Preface: International Workshop on Positron Physics at Jefferson Lab (JPos17)

An experimental program with positron beams, both polarized and unpolarized, may provide valuable opportunities in the future program at Jefferson Lab (JLab). In the context of Hadronic Physics, it can provide the required complementary tool for a precise and unambiguous understanding of the electromagnetic structure of the nucleon, both in the elastic and deep-inelastic domains. At higher energies the potential for positrons at an electron-ion collider (EIC) may provide a unique window of investigation to electroweak physics that offers new pathways in search of physics beyond the Standard Model.

In this framework, the International Workshop on Positron Physics at Jefferson Lab (JPos17) was organized in Newport News (VA, USA), September 12-17, 2017, to discuss the new opportunities offered by the prospect of a polarized positron beam at CEBAF and JLEIC, and to explore the associated technical challenges. The workshop gathered about 80 physicists with a large spectrum of expertise from Accelerator Physics, Materials Science, Hadronic and High Energy Physics. About 50 oral and poster presentations were made and are freely available from the workshop website (www.jlab.org/conferences/JPos2017).

The application of polarized positron beams within high energy accelerators has, until recently, been limited to the self-polarizing Sokolov-Ternov effect of stored positron beams. In the context of the International Linear Collider project, the creation of prompt polarized positrons has been demonstrated with the use of very high energy GeV electron beams to produce polarized gamma rays, with subsequent polarized positron production via e^+e^- pair production on heavy nuclear

targets. Very recently, the PEPPo (Polarized Electrons for Polarized Positrons) experiment at the CEBAF injector demonstrated an alternative method that opens access to prompt polarized positron beams using much lower MeV electron beam energies. Consequently, a new technology pathway for the JLab and EIC scientific community to exploit highly polarized positron beams is available for consideration. This includes:

- ***Interference Physics*** - In the energy range currently available at JLab, there is no specific difference with respect to the scientific information obtained with an electron or a positron probe. However, when more than one QED-based mechanism contributes to a reaction process, the comparison between lepton beams of opposite charges allows one to uniquely distinguish the quantum interference between these mechanisms. This feature is expressed for example in the experimental measurement of the electromagnetic form factors of the nucleon, or the determination of the generalized parton distributions of the nucleon;

- ***Charged Current Physics*** - Charged $W^{\pm}$ currents (CC) differentiate electron and positron beams as essentially different experimental probes, able to uniquely isolate positively or negatively charged quarks. CC Deep Inelastic Scattering (DIS) accesses combinations of quark flavors different from those measured with purely electromagnetic DIS, providing an alternative and novel source of information about parton distribution functions (PDFs), particularly for the unpolarized and polarized strange and to some extent charm PDFs;

- ***Tests of the Standard Model*** - Electromagnetic and electroweak interactions with polarized electron and positron beams provide new possibilities to probe the existence of physics beyond the Standard Model (SM). Comparison between a left-handed electron beam and a right-handed positron beam would provide the first measurement of a charge-conjugation violation observable, the effective electron-quark coupling C_{3q}. Furthermore, the beam longitudinal polarization sensitivity of the total CC cross section constitutes a natural SM test through the search for right-handed W-boson exchange. The $e^{+}e^{-}$ annihilation, on the other hand, is a promising channel in search of a U-boson or heavy photon, candidate of SM-Dark Matter interaction mediator. The combination of high energy and high intensity positron beam would provide the best reach achievable in terms of mass range and coupling constant in the invisible decay channel $e^{+}e^{-} \rightarrow \gamma U$. Polarization observables are here expected to leverage a significant role for suppressing background to identify the experimental physics signal of interest;

- ***Positron Applications*** - Positron annihilation spectroscopy (PAS) is a well-known technique for investigating the structural properties of materials. Because of the purity of the signal produced from the annihilation of positrons with atomic electrons, this technique is a very sensitive probe of material defects and constitutes an accurate method for the measurement of the momentum distribution of electrons. Nevertheless, the globally poor availability of intense slow positron beams precludes efficient use of PAS. An MeV electron accelerator production of positrons, like that used in the PEPPo experiment, can easily provide two orders of magnitude greater beam intensities than the most powerful nuclear reactor-based facility. Adding controlled and flexible polarization capabilities with the PEPPo technique would constitute a technological breakthrough for PAS;

- ***Positron Production and Beam Physics*** - The efficient transfer of polarization from electrons to positrons via the PEPPo technique offers a new pathway to use low energy polarized electron beams (10-100 MeV/*c*) to promptly produce polarized positrons suitable for acceleration. A challenging aspect of the positron injector is the optimization required to achieve the desired beam characteristics such as beam intensity, transverse emittance, bunch length and energy spread necessary, and be well-matched to the accelerator design.

Within the general context of the Jefferson Lab Positron Working Group, this workshop enabled a successful scientific agenda to begin formalizing a *White Paper for Positron Physics at Jefferson Lab*.

The workshop organizers are thankful to the Jefferson Lab support staff for making the workshop program a success and for the financial support by Jefferson Lab, the Jefferson Science Associates, and the Institute of Nuclear Physics at Orsay (France) for making this workshop possible.

On behalf of the JPos17 Organizing Committee,

Joe Grames and Eric Voutier

COMMITTEES

Organizing Committee

J. Arrington (ANL)
M. Battaglieri (INFN Genova)
T. Forest (ISU)
Y. Furletova (JLab)
J. Grames (co-chair, JLab)
C. Hyde (ODU)
W. Melnitchouk (JLab)
V. Morozov (JLab)
F. Selim (BGSU)
B. Vlahovic (NCCU)
E. Voutier (co-chair, IPNO)
X. Zheng (UVa)

Advisory Committee

Jim Alexander (Cornell University Ithaca)
Peter Blunden (University of Manitoba)
David Cassidy (University College London)
Abhay Deshpande (Stony Brook University)
Markus Diehl (DESY Hamburg)
Andrew Hutton (JLab)
Atsuo Kawasuso (QST Takasaki)
Uta Klein (University of Liverpool)
Franck Maas (Helmholz Institute Mainz)
Zein-Eddine Meziani (Temple University)
Richard Milner (MIT)
Alessandro Polini (INFN Bologna)
Jianwei Qiu (JLab)
Frank Sabatié (CEA Saclay)
Anthony Thomas (University of Adelaide)
Paolo Valente (INFN Frascati)
Andreas Wagner (Helmholtz-Zentrum Dresden-Rossendorf)
Ferdinand Willeke (BNL)
Rikutaro Yoshida (JLab)
Franck Zimmermann (CERN)

Positrons at JLab
Advancing Nuclear Science in Hall B

Volker D. Burkert[1,a)]

[1]*Jefferson Laboratory, 12000 Jefferson Avenue, Newport News, Virginia, 23606, USA*

[a)]Corresponding author: burkert@jlab.org

Abstract. In this talk I address two high impact physics programs that require the use of polarized and unpolarized positron beams in addition to using electron beams of the same energy. First, I address what will be gained from using positron beams in addition to electron beams in the extraction of the Compton Form Factors (CFFs) and generalized parton distributions (GPDs) from Deeply Virtual Compton Scattering (DVCS) on a proton target. As a second high impact science program I discuss an experimental scenario using unpolarized positrons to measure elastic scattering on protons in an effort to determine definitively the 2-photon exchange contributions in order to resolve a longstanding discrepancy in the determination of the proton's electric and magnetic form factors.

INTRODUCTION

The challenge of understanding nucleon electromagnetic structure still continues after six decades of experimental scrutiny. From the initial measurements of elastic form factors to the accurate determination of parton distributions through deep inelastic scattering, the experiments have increased in statistical and systematic accuracy. During the past two decades it was realized that the parton distribution functions represent special cases of a more general, much more powerful, way to characterize the structure of the nucleon, the generalized parton distributions (GPDs) (see [1, 2] for reviews).

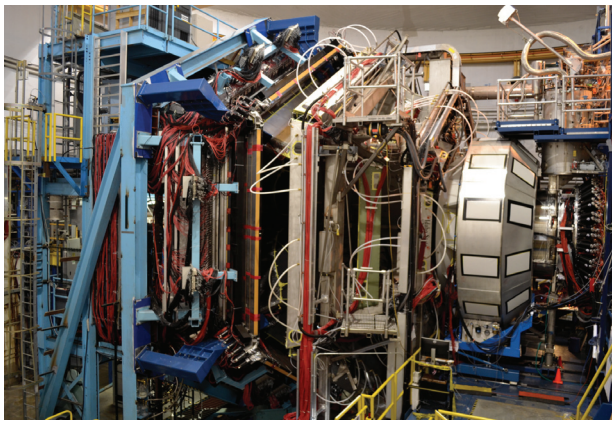

FIGURE 1. The `CLAS12` detector in Hall B. The detector was designed for inclusive, semi-inclusive, as well as exclusive processes such as DVCS. The construction and commissioning of the detector system was completed recently. `CLAS12` is part of the DOE funded energy upgrade of the Jefferson Lab CEBAF accelerator from 6 GeV to 12 GeV, and may play an important role in programs that make use of positron beams at Jefferson Lab..

The GPDs are the Wigner quantum phase space distribution of quarks in the nucleon describing the simultaneous distribution of particles with respect to both position and momentum in a quantum-mechanical system. In addition to the information about the spatial density and momentum density, these functions reveal the correlation of the spatial

and momentum distributions, *i.e.* how the spatial shape of the nucleon changes when probing quarks of different momentum fraction of he nucleon.

The concept of GPDs has led to completely new methods of "spatial imaging" of the nucleon in the form of (2+1)-dimensional tomographic images, with 2 spatial dimensions and 1 dimension in momentum [3, 4, 5]. The second moments of GPDs are related to form factors that allow us to quantify how the orbital motion of quarks in the nucleon contributes to the nucleon spin, and how the quark masses and the forces on quarks are distributed in transverse space, a question of crucial importance for our understanding of the dynamics underlying nucleon structure and the forces leading to color confinement.

The four leading twist GPDs H, $\tilde{H}$, E, and $\tilde{E}$, depend on the 3 variable x, ξ, and t, where x is the longitudinal momentum fraction of the struck quark, ξ is the longitudinal momentum transfer to the quark ($\xi \approx x_B/(2 - x_B)$), and t is the invariant 4-momentum transfer to the proton. The mapping of the nucleon GPDs, and a detailed understanding of the spatial quark and gluon structure of the nucleon, have been widely recognized as key objectives of nuclear physics of the next decades. This requires a comprehensive program, combining results of measurements of a variety of processes in electron–nucleon scattering with structural information obtained from theoretical studies, as well as with expected results from future lattice QCD simulations. The CLAS12 detector, shown in Fig. 1, has recently been completed and has begun the experimental science program in the 12 GeV era Jefferson Lab.

ACCESSING GPD IN DVCS

The most direct way of accessing GPDs at lower energies is through the measurement of Deeply Virtual Compton Scattering (DVCS) in a kinematical domain where the so-called handbag diagram shown in Fig. 2 makes the dominant contributions. However, in DVCS as in other deeply virtual reactions, the GPDs do not appear directly in the cross section, but in convolution integrals, e.g.

$$\int_{-1}^{+1} \frac{H^q(x,\xi,t)dx}{x-\xi+i\epsilon} = \int_{-1}^{+1} \frac{H^q(x,\xi,t)dx}{x-\xi} + i\pi H^q(\xi,\xi,t)\,, \tag{1}$$

where the first term on the r.h.s. corresponds to the real part and the second term to the imaginary part of the scattering amplitude. The superscript q indicates that GPDs depend on the quark flavor. From the above expression it is obvious that GPDs, in general, can not be accessed directly in measurements. However, in some kinematical regions the Bethe-Heitler (BH) process where high energy photons are emitted from the incoming and scattered electrons, can be important. Since the BH amplitude is purely real, the interference with the DVCS amplitude isolates the imaginary part of the DVCS amplitude. The interference of the two processes offers the unique possibility to determine GPDs directly at the singular kinematics $x = \xi$. At other kinematical regions a deconvolution of the cross section is required to determine the kinematic dependencies of the GPDs. It is therefore important to obtain all possible independent information that will aid in extracting information on GPDs. The interference terms for polarized beam I_{LU}, longitudinally polarized target I_{UL}, transversely (in scattering plane) polarized target I_{UT}, and perpendicularly (to scattering plane) polarized target I_{UP} are given by the expressions:

$$I_{LU} \sim \sqrt{\tau'}[F_1 H + \xi(F_1 + F_2)\tilde{H} + \tau F_2 E] \tag{2}$$

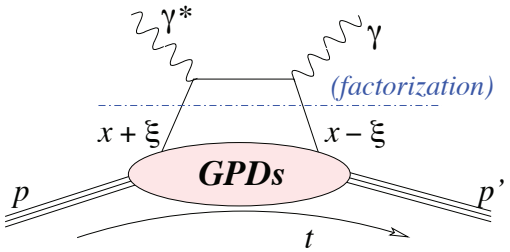

FIGURE 2. Leading order contributions to the production of high energy single photons from protons. The DVCS handbag diagram contains the information on the unknown GPDs.

$$I_{UL} \sim \sqrt{\tau'}[F_1\tilde{H} + \xi(F_1 + F_2)H + (\tau F_2 - \xi F_1)\xi\tilde{E}] \quad (3)$$

$$I_{UP} \sim \tau[F_2 H - F_1 E + \xi(F_1 + F_2)\xi\tilde{E} \quad (4)$$

$$I_{UT} \sim \tau[F_2\tilde{H} + \xi(F_1 + F_2)E - (F_1 + \xi F_2)\xi\tilde{E}] \quad (5)$$

where $\tau = -t/4M^2$, $\tau' = (t_0 - t)/4M^2$. By measuring all 4 combinations of interference terms one can separate all 4 leading twist GPDs at the specific kinematics $x = \xi$. Experiments at JLab using 4 to 6 GeV electron beams have been carried out with polarized beams [6, 7, 8, 9, 10] and with longitudinal target [11, 12, 13], showing the feasibility of such measurements at relatively low beam energies, and their sensitivity to the GPDs. Techniques of how to extract GPDs from existing DVCS data and what has been learned about GPDs can be found in [14, 15]. In the following sections we discuss what information may be gained by employing both electron and positron beams in deeply virtual photon production.

Differential cross section for polarized electrons and positrons (leptons)

The structure of the differential cross section for polarized beam and unpolarized target is given by:

$$\sigma_{\vec{e}p\to e\gamma p} = \sigma_{BH} + e_\ell\sigma_{INT} + P_\ell e_\ell\tilde{\sigma}_{INT} + \sigma_{VCS} + P_\ell\tilde{\sigma}_{VCS} \quad (6)$$

where σ is even in azimuthal angle ϕ, and $\tilde{\sigma}$ is odd in ϕ. The interference terms $\sigma_{INT} \sim \mathrm{Re}A_{\gamma^*\mathrm{N}\to\gamma\mathrm{N}}$ and $\tilde{\sigma}_{INT} \sim \mathrm{Im}A_{\gamma^*\mathrm{N}\to\gamma\mathrm{N}}$ are the real and imaginary parts, respectively of the Compton amplitude. Using polarized electrons the combination $-\tilde{\sigma}_{INT} + \tilde{\sigma}_{VCS}$ can be determined by taking the difference of the beam helicities. The electron-positron charge difference for unpolarized beams determines σ_{INT}. For fixed beam polarization and taking the electron-positron difference one can extract the combination $P_\ell\tilde{\sigma}_{INT} + \sigma_{INT}$. If only a polarized electron beam is available one can separate $\tilde{\sigma}_{INT}$ from $\tilde{\sigma}_{VCS}$ using the Rosenbluth technique [16]. This requires measurements at two significantly different beam energies which reduces the kinematical coverage that can be achieved with this method. With polarized electrons and polarized positrons both σ_{INT} can be determined and $\tilde{\sigma}_{INT}$ can be separated from $\tilde{\sigma}_{VCS}$ in the full kinematic range available at the maximum beam energy.

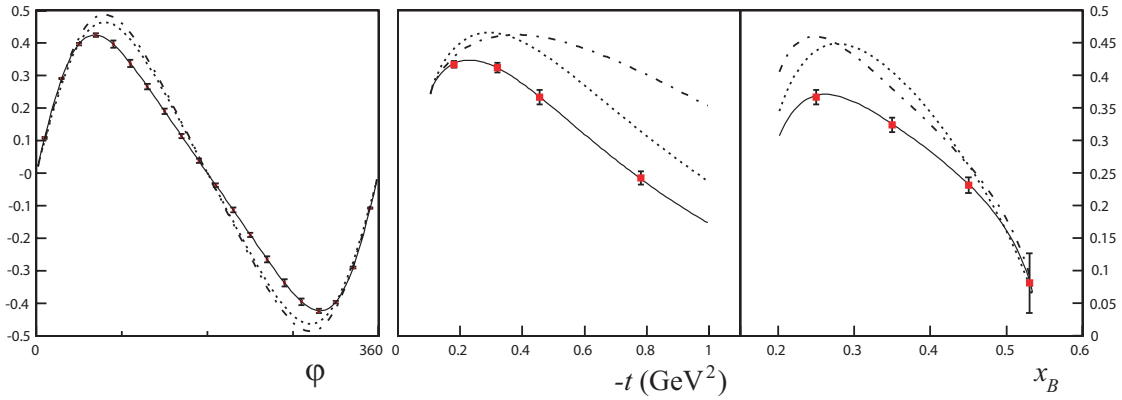

FIGURE 3. The beam spin asymmetry showing the DVCS-BH interference for 11 GeV beam energy [17]. Left panel: $x = 0.2$, $Q^2 = 3.3\mathrm{GeV}^2$, $-t = 0.45\mathrm{GeV}^2$. Middle and right panels: $\phi = 90°$, other parameters same as in left panel. Many other bins will be measured simultaneously. The curves represent various parameterizations within the VGG model [18]. Projected uncertainties are statistical.

Differential cross section for polarized proton target

The structure of the differential cross section for polarized beam and polarized target contains the polarized beam term of the previous section and an additional term related to the target polarization [19, 20]:

$$\sigma_{\vec{e}\vec{p}\to e\gamma p} = \sigma_{\vec{e}p\to e\gamma p} + T[P_\ell\Delta\sigma_{BH} + e_\ell\Delta\tilde{\sigma}_{INT} + P_\ell e_\ell\Delta\sigma_{INT} + \Delta\tilde{\sigma}_{VCS} + P_\ell\Delta\sigma_{VCS}] \quad (7)$$

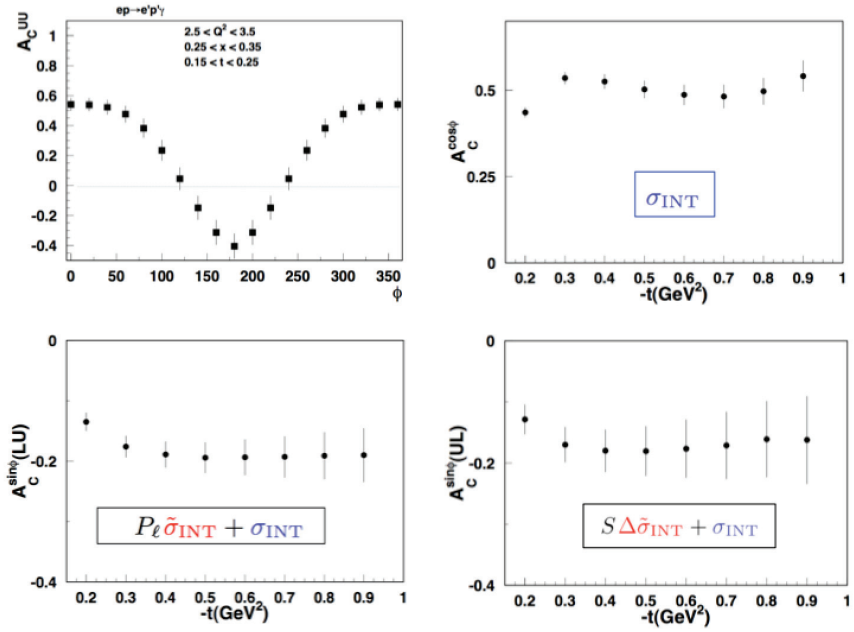

FIGURE 4. Electron-positron DVCS charge asymmetries: Top-left: Azimuthal dependence of the charge asymmetry for positron and electron beam at 11 GeV beam. Top-right: Moment in cos(ϕ) of the charge asymmetry versus momentum transfer t to the proton. Bottom-left: Charge asymmetries for polarized electron and positron beams at fixed polarization (LU). Bottom right: Charge asymmetry for longitudinally polarized protons at fixed polarization (UL). The error bars are estimated for a 1000 hrs run with positron beam and luminosity $L = 2\times10^{34}$ cm^{-2}sec^{-1} at a beam polarization $P = 0.6$. Electron luminosity $L = 10\times10^{34}$ cm^{-2}sec^{-1}, and electron beam polarization $P = 0.8$. The error bars are statistical for a single bin in Q^2, x, and t as shown in the top-left panel. Other bins are measured simultaneously.

where the target polarization T can be longitudinal or transverse. If only unpolarized electrons are available, the combination $-\Delta\tilde{\sigma}_{INT}+\Delta\tilde{\sigma}_{VCS}$ can be measured from the differences in the target polarizations. If unpolarized electrons and unpolarized positrons are available the combination $T\Delta\tilde{\sigma}_{INT}+\sigma_{INT}$ can be determined at fixed target polarization. With both polarized electron and polarized positron beams, the combination $T\Delta\tilde{\sigma}_{INT} + TP_\ell\Delta\sigma_{INT} + P_\ell\tilde{\sigma}_{INT} + \sigma_{INT}$ can be measured at fixed target polarization. Availability of both polarized electron and polarized positron beams thus allows the separation of all contributing terms. If only polarized electron beams are available a Rosenbluth separation with different beam energies can separate the term $\Delta\tilde{\sigma}_{INT}$ from $\Delta\tilde{\sigma}_{VCS}$, again in a much more limited kinematical range and with likely larger systematic uncertainties. The important interference term $\Delta\sigma_{INT}$ can only be determined using the combination of polarized electron and polarized positron beams.

Estimates of charge asymmetries for different lepton charges

For quantitative estimates of the charge differences in the cross sections we use the acceptance and luminosity achievable with CLAS12 as basis for measuring the process $ep \to e\gamma p$ at different beam and target conditions. A 10 cm long liquid hydrogen is assumed with an electron current of 40nA, corresponding to an operating luminosity of 10^{35}cm^{-2}sec^{-1}. For the positron beam a 5 times lower beam current of 8nA is assumed. In either case 1000 hours of beam time is used for the rate projections. For quantitative estimates of the cross sections the dual model [21, 22] is used. It incorporates parameterizations of the GPDs H and E. As shown in Fig. 4, effects coming from the charge asymmetry can be large. In case of unpolarized beam and unpolarized target the cross section for electron scattering has only a small dependence on azimuthal angle ϕ, while the corresponding positron cross section has a large ϕ modulation. The difference is directly related to the term σ_{INT} in equation (6).

Experimental Setup for DVCS Experiments

Figure 5 shows generically how the electron-proton and the positron-proton DVCS experiments could be configured. Electrons and positrons would be detected in the forward detection system of CLAS12. However, for the positron run the Torus magnet would have the reversed polarity so that positron trajectories would look identical to the electron trajectories in the electron-proton experiment, and limit systematic effects in acceptances. The recoil proton in both cases would be detected in the Central Detector at the same solenoid magnet polarity, also eliminating most systematic effects in the acceptances. However, there is a remaining systematic difference in the two configuration, as the forward scattered electron/positron would experience different transverse field components in the solenoid, which will cause the opposite azimuthal motion in ϕ in the forward detector. A good understanding of the acceptances in both cases is therefore important. The high-energy photon is, of course, not affected by the magnetic field configuration.

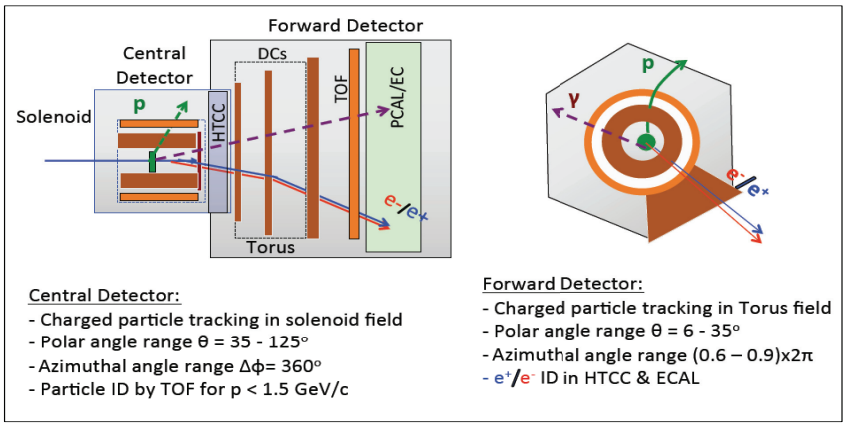

FIGURE 5. CLAS12 configuration for the two electron and positron experiments (generic). The central detector will detect the protons, and the bending in teh magnetic solenoid field will be identical for the same kinematics. The electron and the positron, as well as the high-energy DVCS photon will be detected in the forward detector part. The electron and positron will be deflected in the Torus magnetic field in the same way as the Torus field direction will be opposite in the two experiments. The deflection in ϕ due to the solenoid fringe field will be of same magnitude $\Delta\phi$ but opposite in direction. The systematic of this shift can be controlled by doing the same experiment with opposite solenoid field directions that would result in the sign change of the $\Delta\phi$.

In the next section we discuss a possible solution to the, so-far, not conclusive experimental studies of two-photon effects in elastic electron-proton scattering and their effect on the ratio of electric to magnetic form factors G_E/G_M versus Q^2.

2-PHOTON EFFECTS IN ELASTIC SCATTERING OFF PROTONS

In the electromagnetic physics community it is well known that two experimental approaches, the Rosenbluth separation and the beam polarization transfer approach results in conflicting values for the G_E/G_M ratio when plotted as a function of Q^2. The results of the different experimental methods are compiled in Fig. 6. The trends of the two data sets are inconsistent with each other, although there is a large spread in the Rosenbluth data samples. The latter seem to be more consistent with near Q^2-independent behavior, while the polarization data have a strong downward behavior with Q^2. Furthermore, the uncertainties in the former are much larger and within the individual data sets there seem to be discrepancies as well. The difference of the two methods may been attributed to 2-photon exchange effects, which are expected to be much more important in the cross section subtraction method than in the polarization transfer method.

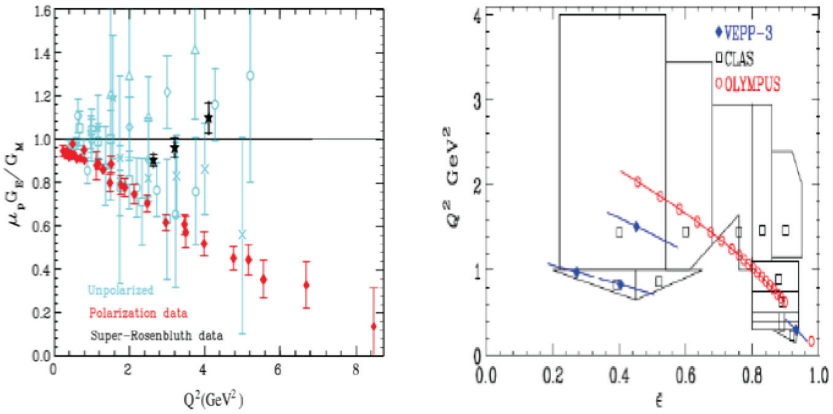

FIGURE 6. Left panel: The ratio of the proton electric and magnetic form factors G_E/G_M. The cyan markers are results of experiments based on the Rosenbluth method. The red markers are from JLab Hall A experiments. Right panel: Kinematics covered by the three recent experiments to measure the 2-photon exchange contribution to the elastic ep cross section. Both figures are taken from a recent review article [27].

Recent efforts to quantify 2-photon exchange contributions

It is obviously important to resolve the discrepancy with experiments that have sensitivity to 2-photon contributions. The most straightforward process to evaluate 2-photon contribution is the measurement of the ratio of elastic e^+p/e^-p scattering, which in leading order is given by the expression: $R_{2\gamma} = 1 - 2\delta_{\gamma\gamma}$. Several experiments have recently been carried out to measure the 2-photon exchange contribution in elastic scattering: the VEPP-3 experiment at Novosibirsk [23], the CLAS experiment at Jefferson Lab [24, 25], and the Olympus experiment at DESY [26]. The kinematic reach of each experiment is shown in the right panel of Fig. 6. The kinematic coverage is much smaller in these experiments $Q^2 < 2$ GeV^2, and $\epsilon > 0.5$, where the 2-photon effects are expected to be small, and systematics of the measurements must be extremely well controlled. The combined evaluation of all three experiments led the authors of the review article Ref. [27] to the conclusion that the results of the experiments are inconsistent with the $\delta_{\gamma\gamma} = 0$ hypothesis at 99.5% confidence. At the same time, they state that *"the results of these experiments are by no means definitive"*, and *"there is a clear need for similar experiments at larger Q^2 and at $\epsilon < 0.5$."*

Conclusions From Previous Experiments

In the following I discuss a possible experiment with CLAS12 at Jefferson Lab that may be able to remedy the shortcomings of the previous measurements. What are these shortcomings?

- Kinematics coverage in Q^2 and in ϵ are mostly where 2-photon effects are expected to be small
- Systematic uncertainties are marginal in some cases
- Higher Q^2 and small ϵ corresponding to high energy and large electron scattering angles were out of reach

Can we do better with a setup using the modified CLAS12 detector? To address this question we begin with the close to ideal kinematic coverage that this setup provides. Figure 7 shows the angle coverage for both the electron (left) and for the proton (right). There is a one-to-one correlation between the electron scattering angle and the proton recoil angle. For the kinematics of interest, say $\epsilon < 0.6$ and $Q^2 > 2$ GeV^2 for the chosen beam energies from 2.2 to 6.6 GeV, nearly all of the electron scattering angles fall into a polar angle range from 40° to 125°, and corresponding to the proton polar angle range from 8° to 35°. While these kinematics are most suitable for accessing the 2-photon exchange contributions, the setup will be able to also measure the reversed kinematics with the electrons at forward angle and the protons at large polar angles. This is in fact the standard CLAS12 configuration of DVCS and most other experiments, however it will not cover the kinematics with highest sensitivity to the 2-photon exchange contributions.

Figure 8 shows the expected elastic scattering rates covering the ranges of highest interest, with $\epsilon < 0.6$ and $Q^2 = 2 - 10$ GeV^2. Sufficiently high statistics of $\sigma_N/N < 1\%$ can be achieved within 10 hrs for the lowest energy and within 1000 hrs for the highest energy, to cover the full range in kinematics. Note that all kinematic bins will be measured simultaneously at a given energy, and the shown rates are for the individual bins in Q^2 - ϵ space.

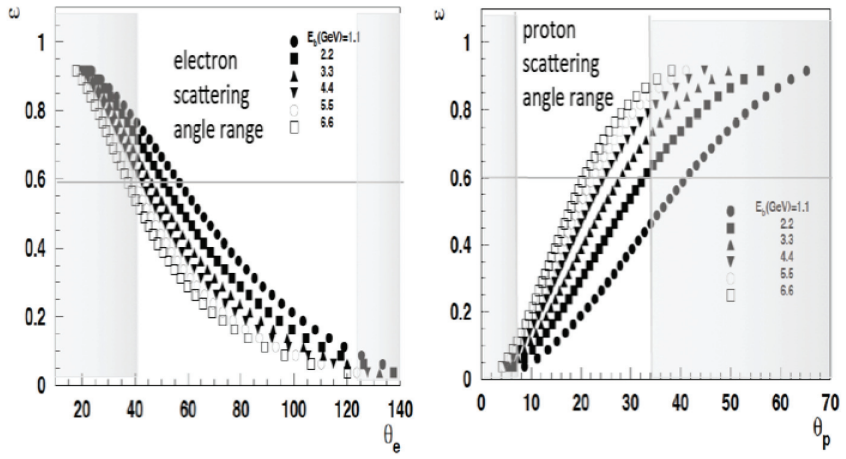

FIGURE 7. Polar angle and ϵ coverage for electron detection (left) and for proton detection (right).

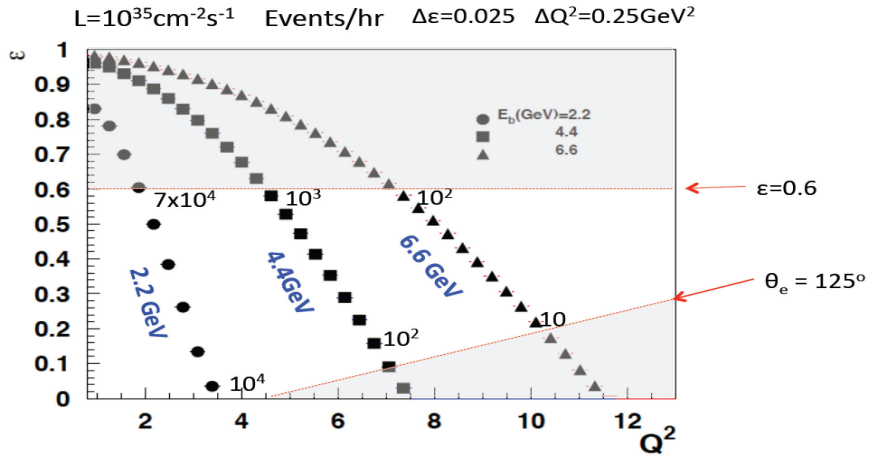

FIGURE 8. Estimated elastic event rates per hour for selected standard CEBAF beam energies of 2.2, 4.4, 6.6 GeV in the ϵ - Q^2 plane. Rates are given only for the lowest and highest Q^2 bin.

A New Experimental Setup - Kinematic Coverage and Rate Estimates

In order to achieve the desired reach in Q^2 and ϵ the CLAS12 detection system has to be used with reversed detection capabilities for electrons. The main modification will involve replacing the current Central Neutron Detector (CND) with a central electromagnetic calorimeter (CEC) . The CEC will not need very good energy or angle resolution (both are provided by the tracking detectors) but will be used for trigger purposes and to aid in electron/pion separation. The over constrained kinematics of measured scattered electrons and recoil protons should be sufficient to select the elastic kinematics and eliminated any background (this will have to be demonstrated by detailed simulations).
For the rate estimates and the kinematical coverage we have made a number of assumptions that are not overly stringent:

- Positron beam currents (unpolarized): $I_{e^+} \approx 60$ nA.
- Beam profile: $\sigma_x,\ \sigma_y < 0.4$ mm.
- Polarization: not required, so phase space at the source maybe chosen for optimized yield and beam parameters.
- Obtain the electron beam from the same source as the positrons to keep systematic under control.
- Switching from e^+ to e^- operation should be doable in reasonable time frame (< 1 day) to keep machine stable, and systematics under control.

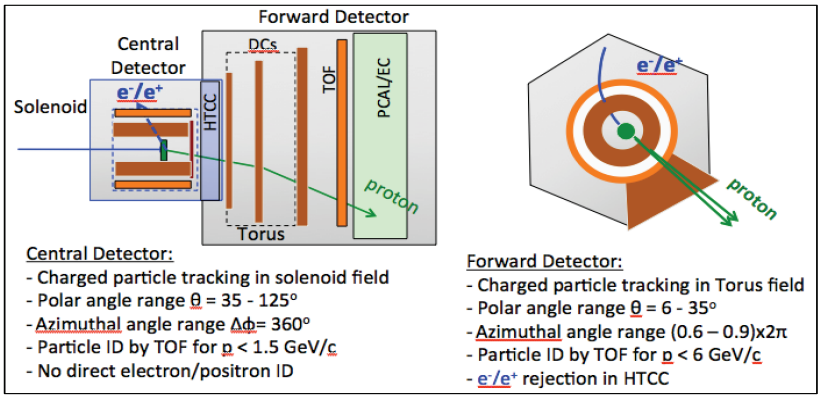

FIGURE 9. CLAS12 configuration for the elastic $e^- p/e^+ p$ scattering experiment (generic). The central detector will detect the electron/positrons, and bending in the solenoid magnetic field will be identical for the same kinematics. The proton will be detected in the forward detector part. The Torus field direction will be the same in both cases. The deflection in ϕ due to the solenoid fringe field will be of same in magnitude of $\Delta\phi$ but opposite in direction. The systematic of this shift can be controlled by doing the same experiment with opposite solenoid field directions that would result in the sign change of the $\Delta\phi$.

- Operate experiment with 5cm liquid H_2 target and luminosity of 0.8×10^{35} cm^{2}sec^{-1}
- Use the CLAS12 Central Detector for lepton (e^+/e^-) detection at $\Theta_l = 40 - 125°$.
- Use CLAS12 Forward Detector for proton detection at $\Theta_p = 7° - 35°$

The CLAS12 configuration suitable for this experiment is shown in Fig. 9.

SUMMARY

Availability of a 11 GeV positron beam at JLab can significantly enhance the experimental program using the CLAS12 detector in Hall B [28]. I discussed two high profile programs that would very significantly benefit from a high performance polarized positron source and accelerated beam. The first program fits well into the already developed 3D-imaging program with electron beams, where the imaginary part of the DVCS amplitude can be extracted. The program with polarized positrons enables access to the azimuthally even BH-DVCS interference terms that are directly related to the real part of the scattering amplitude. Moreover, by avoiding use of the Rosenbluth separation technique, the leading contributions to the cross sections may be separated in the full kinematical range available at the JLab 12 GeV upgrade. Even at modest polarized positron beam currents of 8nA good statistical accuracy can be achieved for charge differences and charge asymmetries. For efficient use of polarized targets higher beam currents of up to 40nA are needed to compensate for the dilution factor of ~ 0.18 inherent in the use of currently available polarized proton targets based on ammonia as target material, and to allow for a more complete DVCS and GPD program at 12 GeV. The second program requiring positron beams is the measurement of the 2-photon exchange contributions in the elastic electron-proton scattering. The measurements we outlined, if properly executed with excellent control of systematic uncertainties, should close the book on the discrepancies in the ratio of electric to magnetic form factors when measured with two different methods.

In this talk we have focussed on experiments with a large acceptance detector, which may be the only option given the low current expected for polarized positron beams of high polarization and good beam parameters. Positron currents in excess of $1\mu A$ may be required to make positron beams attractive for an experimental program with focusing, high resolution magnetic spectrometers.

Acknowledgments

I like to thank Harut Avakian for providing me with the experimental projections for the DVCS experiment, and the elastic ep scattering cross sections and rate calculations. This work has been supported by the US Department of Energy under contract DE-AC05-060R23177.

REFERENCES

[1] M. Diehl, Phys. Rept. **388**, 41 (2003) [hep-ph/0307382].
[2] A. V. Belitsky and A. V. Radyushkin, Phys. Rept. **418**, 1 (2005) [hep-ph/0504030].
[3] A. V. Belitsky, X. d. Ji and F. Yuan, Phys. Rev. D **69**, 074014 (2004) [hep-ph/0307383].
[4] X. d. Ji, Phys. Rev. Lett. **91**, 062001 (2003) [hep-ph/0304037].
[5] M. Burkardt, Int. J. Mod. Phys. A **18**, 173 (2003) [hep-ph/0207047].
[6] H. S. Jo *et al.* [CLAS Collaboration], Phys. Rev. Lett. **115**, no. 21, 212003 (2015) [arXiv:1504.02009].
[7] G. Gavalian *et al.* [CLAS Collaboration], Phys. Rev. C **80**, 035206 (2009) [arXiv:0812.2950 [hep-ex]].
[8] F. X. Girod *et al.* [CLAS Collaboration], Phys. Rev. Lett. **100**, 162002 (2008) [arXiv:0711.4805 [hep-ex]].
[9] C. M. Camacho *et al.* [Jefferson Lab Hall A], Phys. Rev. Lett. **97**, 262002 (2006) [nucl-ex/0607029].
[10] S. Stepanyan *et al.* [CLAS Collaboration], Phys. Rev. Lett. **87**, 182002 (2001) [hep-ex/0107043].
[11] S. Pisano *et al.* [CLAS Collaboration], Phys. Rev. D **91**, no. 5, 052014 (2015) [arXiv:1501.07052 [hep-ex]].
[12] E. Seder *et al.* [CLAS Collaboration], Phys. Rev. Lett. **114**, no. 3, 032001 (2015) Addendum: [Phys. Rev. Lett. **114**, no. 8, 089901 (2015)] [arXiv:1410.6615 [hep-ex]].
[13] S. Chen *et al.* [CLAS Collaboration], Phys. Rev. Lett. **97**, 072002 (2006) [hep-ex/0605012].
[14] M. Guidal, H. Moutarde and M. Vanderhaeghen, Rept. Prog. Phys. **76**, 066202 (2013) [arXiv:1303.6600].
[15] K. Kumericki and D. Mueller, arXiv:1205.6967 [hep-ph].
[16] M. N. Rosenbluth, Phys. Rev. **79**, 615 (1950).
[17] JLab experiment E12-06-119, F. Sabatie et al. (spokespersons).
[18] M. Vanderhaeghen, P. A. M. Guichon and M. Guidal, Phys. Rev. D **60**, 094017 (1999) [hep-ph/9905372].
[19] A. V. Belitsky, D. Mueller and A. Kirchner, Nucl. Phys. B **629**, 323 (2002) [hep-ph/0112108].
[20] M. Diehl and S. Sapeta, Eur. Phys. J. C **41**, 515 (2005) [hep-ph/0503023].
[21] V. Guzey and T. Teckentrup, Phys. Rev. D **79**, 017501 (2009) [arXiv:0810.3899 [hep-ph]].
[22] V. Guzey and T. Teckentrup, Phys. Rev. D **74**, 054027 (2006) [hep-ph/0607099].
[23] I. A. Rachek *et al.*, Phys. Rev. Lett. **114**, no. 6, 062005 (2015) [arXiv:1411.7372 [nucl-ex]].
[24] D. Rimal *et al.* [CLAS Collaboration], Phys. Rev. C **95**, no. 6, 065201 (2017) [arXiv:1603.00315 [nucl-ex]].
[25] D. Adikaram *et al.* [CLAS Collaboration], Phys. Rev. Lett. **114**, 062003 (2015) [arXiv:1411.6908 [nucl-ex]].
[26] B. S. Henderson *et al.* [OLYMPUS Collaboration], Phys. Rev. Lett. **118**, no. 9, 092501 (2017) [arXiv:1611.04685 [nucl-ex]].
[27] A. Afanasev, P. G. Blunden, D. Hasell and B. A. Raue, Prog. Part. Nucl. Phys. **95**, 245 (2017) [arXiv:1703.03874 [nucl-ex]].
[28] V. D. Burkert, Proc. Int. Sch. Phys. Fermi **180**, 303 (2012) [arXiv:1203.2373 [nucl-ex]].

Measurement of TPE with electron/positron elastic scattering off the proton

Brian Raue[1,a)]

[1]*Florida International University, Miami, FL, U.S.A. 33199, USA*

[a)]baraue@fiu.edu

Abstract. Three recent experiments have used the ratio of e^+p to e^-p elastic scattering to directly determine the two-photon exchange (TPE) contribution to the elastic-scattering process. These experiments by CLAS, VEPP-3 and OLYMPUS were motivated by the discrepancy between Rosenbluth separation and polarization transfer measurements of the electromagnetic form factors of the proton. The results of these experiments cover $Q^2 < 2$ GeV^2 and collectively agree well with TPE model predictions that largely explain the form factor discrepancy.

INTRODUCTION

The electromagnetic form factors are the fundamental observables that contain information about the spatial distribution of the charge and magnetization inside the proton. The electric ($G_E(Q^2)$) and magnetic ($G_M(Q^2)$) form factors have been extracted by analyzing data from both unpolarized [1, 2, 3, 4, 5, 6] and polarized [7, 8, 9, 10, 11] electron scattering experiments assuming an exchange of a virtual photon between the electron and the proton while accounting for soft radiative effects and external hard photons. The ratio of the electric to magnetic form factors, $\frac{\mu_p G_E(Q^2)}{G_M(Q^2)}$, where μ_p is the proton magnetic moment, extracted from these two experimental methods shows a significant discrepancy that grows with Q^2, as seen in Fig. 1.

One explanation for the observed discrepancy results from neglecting hard two-photon exchange (TPE) corrections [14, 15, 16, 17], a higher-order contribution to the radiative corrections [18, 19, 20]. A model-independent way of measuring the size of the TPE effect is by comparing e^-p and e^+p elastic scattering cross sections [21]. The interference between one- and two-photon exchange diagrams has the opposite sign for electrons and positrons while most of the other radiative corrections are identical for electrons and positrons and cancel to first order in the ratio

$$R = \frac{\sigma(e^+p)}{\sigma(e^-p)}. \tag{1}$$

Correcting for other radiative effects that do not cancel in the ratio, one obtains

$$R_{2\gamma} \approx 1 - 2\delta_{2\gamma}. \tag{2}$$

TPE EXPERIMENTS

In the 1960s and 1970s there were several attempts to measure $R_{2\gamma}$. Early measurements comparing electron and positron elastic-scattering cross sections (see Ref. [21] for a global comparison) were largely limited to low Q^2 and/or high ε, where calculations [22, 23, 24] suggest that TPE contributions are small. Given the limited experimental sensitivity of these early measurements, none of the experiments observed a significant deviation from $R_{2\gamma} = 1$ and the search for TPE effects was dormant. However, the form-factor discrepancy inspired a new round of experiments by the CLAS [25, 13], VEPP-3 [26], and OLYMPUS [27] collaborations. These three experiments used different techniques and each had its own advantages and disadvantages.

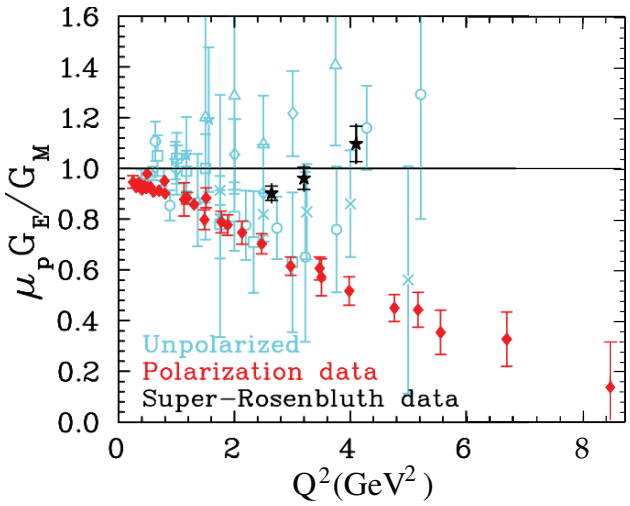

FIGURE 1. Ratio of $\frac{\mu_p G_E(Q^2)}{G_M(Q^2)}$ from Rosenbluth [12] (open cyan symbols) and "Super Rosenbluth" [6] (black stars) measurements and from polarization measurements [7, 8, 9, 10, 11] (filled red diamonds) measurements. Figure adapted from Ref. [13].

The CLAS experiment conducted in Hall B at Jefferson Lab utilized a simultaneous mixed beam of electrons and positrons with a continuous distribution of usable beam energies from 0.85 to 3.5 GeV and the CEBAF Large Acceptance Spectrometer (CLAS) to detect the scattered leptons and protons over a wide range of scattering angles. The mixed beam was produced by a 5.5 GeV primary electron beam incident upon a radiator to produce a secondary photon beam. The photon beam was then incident upon a converter foil that pair-produced the electrons and positrons in the tertiary mixed beam. This conversion process led to large backgrounds in the hall and a large-diameter tertiary beam that together limited the luminosity, which in turn limited the statistical precision of the data. The large acceptance of CLAS led to a wide range of kinematic coverage as shown in Figure 2. By using a simultaneous e^+ e^- beam, there was no need for absolute luminosity normalization in the measured e^+/e^- ratio. A total of 12 independent data points for $R_{2\gamma}$ were measured by CLAS.

The VEPP-3 experiment was conducted on the Novosibirisk storage ring with an internal hydrogen gas target and took data with beam energies of 1.6 and 1.0 GeV during two separate running periods. The experiment used non-magnetic spectrometers, which guarantees identical acceptances for e^+p and e^-p events. This constituted a relative

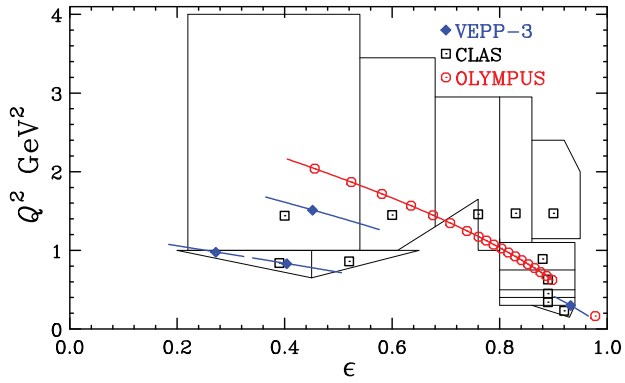

FIGURE 2. Kinematic regions probed by the three two-photon experiments showing the Q^2 and ε plane. Symbols indicate values at which data points were reported by the respective experiments. The boxed regions show the bins over which the CLAS data are summed and the blue curves indicate the kinematic region over which the VEPP-3 data points are summed to obtain the results at the data points shown by the symbols. The binning of the OLYMPUS data are binned such that the gaps between bins are not visible in the red curve. Figure adapted from Ref. [28].

advantage for the VEPP-3 experiment compared to the CLAS and OLYMPUS experiments, which both used magnetic spectrometers and can lead to acceptance differences for the two types of events. The experiment alternated between running with positron and electron beams but did not determine an absolute positron/electron normalizations. Instead, luminosity normalization points were take at small angles where hard TPE effects are expected to be small and $R_{2\gamma} = 1$. This leads to an unknown relative normalization with the measured ratios requiring scaling such that the luminosity normalization points agree with any model predictions. Running with fixed beam energies and fixed spectrometer angles led to high precision results, but at only four kinematic points (see Figure 2).

The OLYMPUS experiment was conducted using the DORIS storage ring at DESY with a 2.01 GeV beam on an internal gas target. Scattered particles were detected with the BLAST detector giving a large coverage of scattering angles from 25° to 75° (see Figure 2). As with the VEPP-3 experiment, the separate electron/positron running required relative normalization. However, unlike VEPP-3, OLYMPUS measured an absolute normalization [29], which was claimed to be good to less than 0.5%. The OLYMPUS experiment resulted in 20 high precision data points.

RESULTS

A direct comparison of all of the results from this new generation of TPE experiments is not straightforward because the data span a large range in both Q^2 and ε. However, comparisons can be made at similar kinematics. Figure 3 shows the ε dependence of the results at $Q^2 = 0.85$ and 1.45 GeV^2 and Figure 4 shows the Q^2 dependence at $\varepsilon = 0.45$ and $\varepsilon = 0.88$. It is clear from the figures that the new results show an marked improvement over the older world data. There is very good agreement between the CLAS and VEPP-3 results but they do not agree well with the OLYMPUS results. CLAS and VEPP-3 results also agree well with the calculations of Zhou and Yang [30] as well as that of Blunden *et al.* [31].

GLOBAL ANALYSIS

In order to better understand the significance of the new results, a global analysis was performed in a recent review article [28]. One way to compare the data is to plot each data point's difference from a given model, $R_{2\gamma}^{\text{data}} - R_{2\gamma}^{\text{model}}$. However, this does not present the entire picture since CLAS and OLYPUS data both have scale-type, or normalization uncertainties that could move the entire data sets up or down.To account for the normalization uncertainty a statistical analysis was preformed in which the CLAS and OLYMPUS data normalization was allowed to float independently but

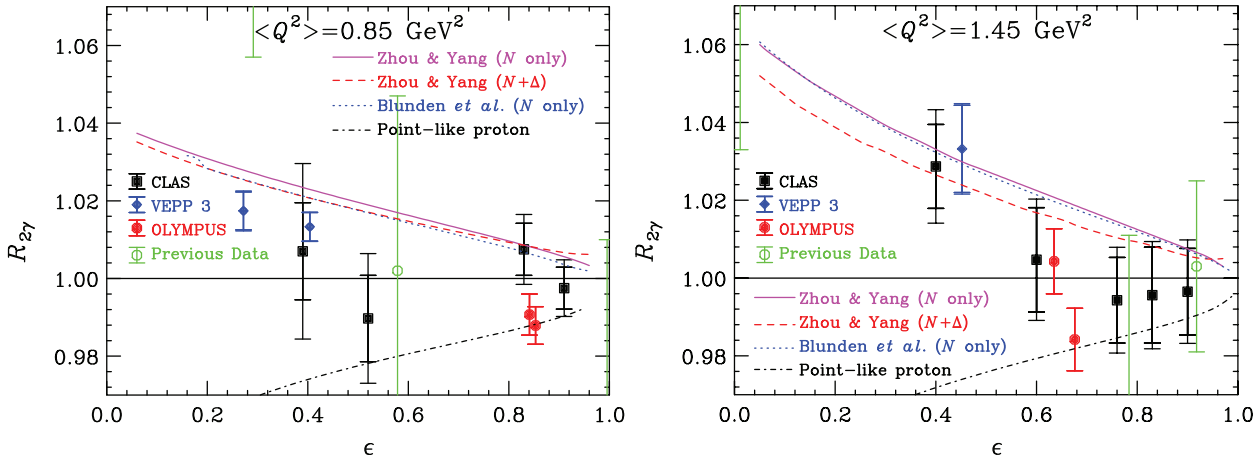

FIGURE 3. World data for $R_{2\gamma}$ at fixed Q^2. The filled black squares are from CLAS [13], the blue diamonds are from VEPP-3 [26], the red circles are from OLYMPUS [27], and the green diamonds are the earlier world data. The line at $R_{2\gamma} = 1$ is the limit of no TPE. The magenta solid and red dashed curves show the calculation by Zhou and Yang [30] including N only and $N + \Delta$ intermediate states, respectively. The blue dotted curve shows the calculation by Blunden *et al.* [31]. The black dot-dashed line shows the calculation of TPE effects on a structureless point proton [20].

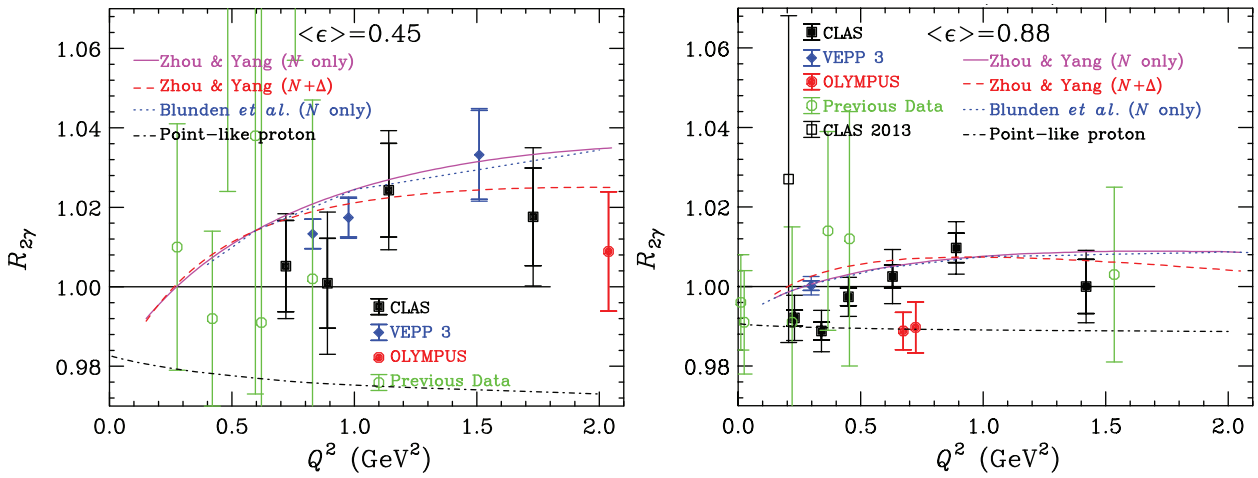

FIGURE 4. World data for $R_{2\gamma}$ at fixed ε. The symbols and curves are the same as in Figure 3 with an additional data point from a CLAS TPE test run [32].

with a penalty determined by the normalization uncertainty. A normalization factor, N, is determined that minimizes a modified χ^2 defined by

$$\chi^2 = \sum_n \left(\frac{R_{2\gamma} N - R_{2\gamma}^{\text{calc}}}{\delta R_{2\gamma}^{\text{total}}} \right)^2 + \left(\frac{N-1}{\delta R_{2\gamma}^{\text{norm}}} \right)^2 , \tag{3}$$

where $R_{2\gamma}$ is the value reported by the experiments, $\delta R_{2\gamma}^{\text{total}}$ is the quadrature sum of the statistical and uncorrelated systematic uncertainties, $R_{2\gamma}^{\text{calc}}$ is the calculated value for a particular model, and $\delta R_{2\gamma}^{\text{norm}}$ is the normalization uncertainty. The number of degrees of freedom, ν, is then number of data points, n, in the set minus one. In total, 34 data points were used for the comparison with two normalization factors leading $\nu = 32$. The analysis for the VEPP-3 data requires a normalization so that the luminosity normalization data point to agrees with the calculation at that point.

For this analysis the comparisons made were to the no-TPE hypothesis ($R_{2\gamma} = 1$) and hadronic model calculations of Blunden and Melnitchouk [33] and by Borisyuk and Kobushkin [34]. The Blunden and Melntichouk calculation determines the TPE correction assuming proton and Δ intermediate states in a dispersive model while the Borisyuk and Kobushkin calculation includes πN intermediate states with $J = 1/2$ and $3/2$. These models largely reconcile the difference between the Rosenbluth and polarization transfer measurements of the form factor ratio.

The difference $R_{2\gamma}^{\text{norm}} - R_{2\gamma}^{\text{calc}}$ is shown in Figure 5 as a function of ε and the results of the statistical analysis is shown in Table 1. A large difference is clearly seen for the no TPE hypothesis. Statistically, it is excluded at the 99.5% confidence level. There is good agreement with the hadronic models of Reference [33, 34] with confidence levels of 53% and 48%, respectively. However, large upward normalizations are required for the OLYMPUS data that is about a factor of two larger than the normalization uncertainty.

CONCLUSIONS

While the statistical analysis excludes the no TPE hypothesis and seems to indicate a good agreement between the data and leading models, the current state of affairs is by no means definitive. The OLYMPUS data requires a normalization that is about twice as large as the quoted normalization uncertainty. Furthermore, the current data are all below where the form factor discrepancy is significant ($Q^2 > 2$ GeV^2). Clearly, more data at larger Q^2 are needed.

A dedicated positron beam at Jefferson Lab could lead to these much needed data. In addition to Rosenbluth separations using a positron beam in either Hall A or C, one could conduct an OLYMPUS-style experiment with CLAS12. With an 11 GeV beam, the large acceptance ($5^\circ \leq \theta_{CM}^e \leq 122^\circ$) of CLAS12 could extend measurements of $R_{2\gamma}$ to Q^2 up to ~ 10 GeV^2, and possibly once and for all resolve the form factor discrepancy.

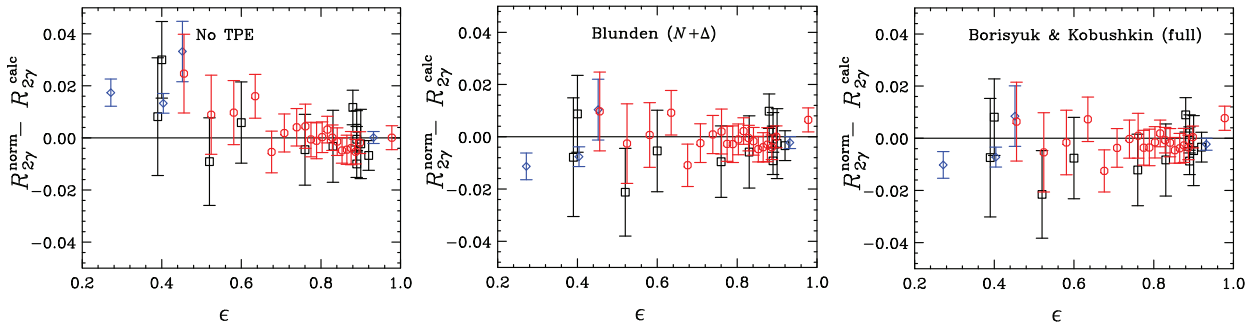

FIGURE 5. Difference between normalized $R_{2\gamma}$ and predictions. Blue diamonds are VEPP-3, black boxes are CLAS, and red circles are OLYMPUS. Figure adapted from Ref. [28].

TABLE 1. Comparison of VEPP-3, CLAS, OLYMPUS, and the combined data set (All) to various TPE calculations showing the reduced χ^2 value and the normalization factor N derived from the fit.

Data set	χ^2_ν	ν	N	$\left(\frac{N-1}{\delta R_{2\gamma}^{\rm norm}}\right)$
Model: $R_{2\gamma} = 1$				
VEPP-3	7.97	4	–	–
CLAS	1.25	11	1.0012	0.40
OLYMPUS	0.68	19	1.0034	0.76
All	1.73	34	–	–
Model: Blunden & Melnitchouk [33]				
VEPP-3	2.62	4	–	–
CLAS	0.91	11	1.0032	1.07
OLYMPUS	0.64	19	1.0082	1.82
All	0.96	34	–	–
Model: Borisyuk & Kobushkin [34]				
VEPP-3	2.28	4	–	–
CLAS	0.94	11	1.0038	1.27
OLYMPUS	0.75	19	1.0097	2.16
All	1.00	34	–	–

ACKNOWLEDGMENTS

This work is supported by the U.S. Department of Energy under grant DE-FG02-99EF41065.

REFERENCES

[1] R. C. Walker *et al.*, Phys. Rev. D **49**, p. 5671 (1994).
[2] L. Andivahis *et al.*, Phys. Rev. D **50**, p. 5491 (1994).
[3] C. Berger, V. Burkert, G. Knop, B. Langenbeck, and K. Rith, Phys. Lett. B **35**, p. 87 (1971).
[4] J. Litt *et al.*, Phys. Lett. B **31**, p. 40 (1970).
[5] M. E. Christy *et al.*, Phys. Rev. C **70**, p. 015206 (2004).
[6] I. A. Qattan *et al.*, Phys. Rev. Lett. **94**, p. 142301 (2005).
[7] V. Punjabi *et al.*, Phys. Rev. C **71**, p. 055202 (2005).
[8] A. J. R. Puckett *et al.*, Phys. Rev. Lett. **104**, p. 242301 (2010).
[9] A. J. R. Puckett *et al.*, Phys. Rev. C **85**, p. 045203 (2012).
[10] X. Zhan *et al.*, Phys. Lett. **B705**, 59–64 (2011).

[11] G. Ron *et al.*, Phys. Rev. C **84**, p. 055204 (2011).
[12] J. Arrington, Phys. Rev. C **68**, p. 034325 (2003).
[13] D. Rimal *et al.* (CLAS), Phys. Rev. **C95**, p. 065201 (2017).
[14] P. A. M. Guichon and M. Vanderhaeghen, Phys. Rev. Lett. **91**, p. 142303 (2003).
[15] P. G. Blunden, W. Melnitchouk, and J. A. Tjon, Phys. Rev. Lett. **91**, p. 142304 (2003).
[16] Y. C. Chen, A. Afanasev, S. J. Brodsky, C. E. Carlson, and M. Vanderhaeghen, Phys. Rev. Lett. **93**, p. 122301 (2004).
[17] J. Arrington, Phys. Rev. **C69**, p. 022201 (2004).
[18] J. Arrington, W. Melnitchouk, and J. A. Tjon, Phys. Rev. C **76**, p. 035205 (2007).
[19] C. E. Carlson and M. Vanderhaeghen, Ann. Rev. Nucl. Part. Sci. **57**, p. 171 (2007).
[20] J. Arrington, P. Blunden, and W. Melnitchouk, Prog. Part. Nucl. Phys. **66**, 782–833 (2011).
[21] J. Arrington, Phys. Rev. C **69**, p. 032201 (2004).
[22] S. D. Drell and M. Ruderman, Phys. Rev. **106**, p. 561 (1957).
[23] S. D. Drell and S. Fubini, Phys. Rev. **113**, p. 741 (1959).
[24] G. K. Greenhut, Phys. Rev. **184**, p. 1860 (1969).
[25] D. Adikaram *et al.* (CLAS), Phys. Rev. Lett. **114**, p. 062003 (2015).
[26] I. A. Rachek *et al.*, Phys. Rev. Lett. **114**, p. 062005 (2015).
[27] B. S. Henderson *et al.* (OLYMPUS), Phys. Rev. Lett. **118**, p. 092501 (2017).
[28] A. Afanasev, P. G. Blunden, D. Hasell, and B. A. Raue, Prog. Part. Nucl. Phys. **95**, 245–278 (2017).
[29] A. Schmidt, C. O'Connor, J. C. Bernauer, and R. Milner, Nucl. Instrum. Meth. **A877**, 112–117 (2018).
[30] H.-Q. Zhou and S. N. Yang, Eur. Phys. J. **A51**, p. 105 (2015).
[31] P. G. Blunden, W. Melnitchouk, and J. A. Tjon, Phys. Rev. C **72**, p. 034612 (2005).
[32] M. Moteabbed *et al.*, Phys. Rev. C **88**, p. 025210 (2013).
[33] P. G. Blunden and W. Melnitchouk, Phys. Rev. **C95**, p. 065209 (2017).
[34] D. Borisyuk and A. Kobushkin, Phys. Rev. **C92**, p. 035204 (2015).

Overview of Recent Theoretical Work on Two-Photon Exchange

Peter G. Blunden

Department of Physics and Astronomy, University of Manitoba, Winnipeg, MB Canada R3T 2N2

blunden@physics.umanitoba.ca

Abstract. *In this contribution I give an overview of recent progress in theoretical calculations of two-photon exchange (TPE) effects in elastic electron-proton scattering. TPE effects are relevant for extractions of proton form factors at high Q^2, and of the proton radius at very low Q^2. Recent experiments to directly measure hard TPE effects by comparing positron and electron scattering are discussed from a theoretical perspective.*

INTRODUCTION

Electromagnetic form factors are fundamental observables characterizing the composite nature of the nucleon. In the standard one-photon exchange (OPE) approximation, the reduced Born cross section can be written as

$$\sigma_R = \tau G_M^2(Q^2) + \varepsilon G_E^2(Q^2) \,, \tag{1}$$

where $G_E(Q^2)$ and $G_M(Q^2)$ are the electric and magnetic form factors, $\tau = Q^2/4M^2$ characterizes the four-momentum transfer to the nucleon Q^2, and ε is the virtual photon polarization ($\varepsilon \to 1$ at forward angles, and $\varepsilon \to 0$ at backward angles). The assumption of OPE as the underlying reaction mechanism in electron-proton scattering has been the foundation of the field since the 1950s.

A major paradigm shift occurred around the turn of the last century with the observation of a significant discrepancy between the ratio $G_E(Q^2)/G_M(Q^2)$ measured using the relatively new polarization transfer (PT) technique [1, 2], and previous extractions of the same quantity from cross section measurements via longitudinal-transverse (LT) separation [3–5] (the Rosenbluth technique). It was soon realized [6, 7] that a large part of the discrepancy could be understood in terms of additional, hadron structure-dependent two-photon exchange (TPE) contributions, which had not been included in the standard treatments of electromagnetic radiative corrections [8, 9]. If we denote the OPE amplitude as $\mathcal{M}_\gamma$, and the TPE amplitude as $\mathcal{M}_{\gamma\gamma}$, then to leading order in α, the correction $\delta_{\gamma\gamma}$ to the reduced cross section arises from the interference term

$$\delta_{\gamma\gamma} = \frac{2\mathrm{Re}\left\{\mathcal{M}_\gamma^\dagger \mathcal{M}_{\gamma\gamma}\right\}}{\left|\mathcal{M}_\gamma\right|^2} \,, \qquad \sigma_R \to \sigma_R(1 + \delta_{\gamma\gamma}) \,. \tag{2}$$

In a hadronic model, the TPE process includes both elastic (nucleon) and inelastic intermediate hadronic states, as shown in Figure 1. Hadronic models are expected to be valid at low to moderate Q^2, typically less than 5 or 6 GeV^2. Early explicit calculations of the elastic contribution [6, 10] showed that $\delta_{\gamma\gamma}$ has a strong ε (*i.e.* angular) dependence which is of the right magnitude and sign to explain a large part of the discrepancy between the LT and PT results. Reliable calculations of the inelastic contributions have been a major focal point of theorists in the field for the past decade. A summary of the early experimental and theoretical work was given in a 2011 review [11]. A 2017 review [12] includes the most recent theoretical and experimental work.

Early calculations of TPE effects were based on direct evaluation of loop integrals for the box and crossed-box TPE diagrams [6, 10, 13–19]. To facilitate this, transition form factors at the photon-hadron vertices were modelled by a sum of monopoles, allowing for analytic evaluation of the loop integrals. However, a problem that emerged with this

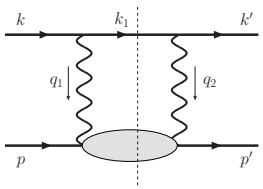

FIGURE 1. The imaginary part of the TPE amplitude. The shaded area corresponds to all possible intermediate elastic and inelastic hadronic states. The dashed line indicates that the intermediate states are taken to be on their mass shells. The real part of the TPE amplitude is constructed from the imaginary part by dispersion relations.

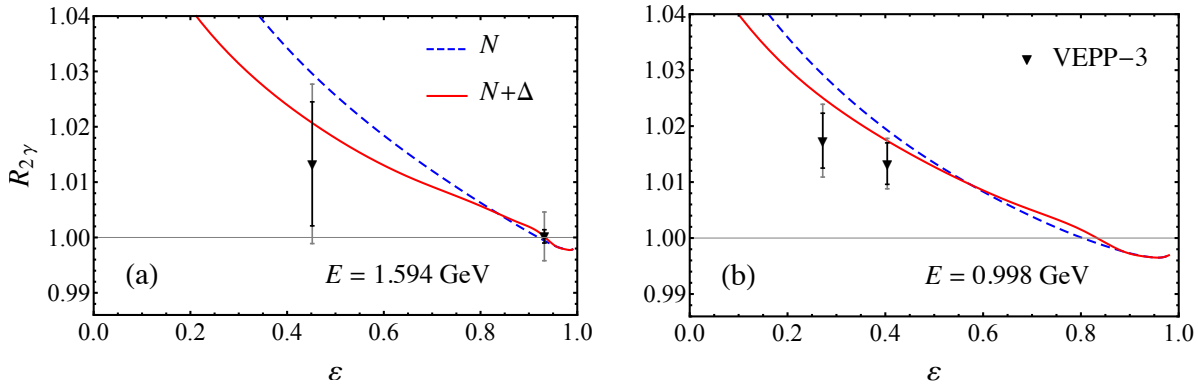

FIGURE 2. Ratio $R_{2\gamma}$ of e^+p to e^-p cross sections as a function of ε for fixed energy (a) $E = 1.594$ GeV, and (b) $E = 0.998$ GeV. The contributions with nucleon only (dashed blue curves) and the sum of nucleon and Δ (solid red curves) intermediate states are compared with data from the VEPP-3 experiment (triangles) [25], with the statistical and systematic uncertainties indicated by the (black) inner and (gray) outer error bars, respectively. Calculations taken from [20].

approach is that for transitions to excited states, described by effective interactions involving derivative couplings, the off-shell dependence leads to divergences in the $\varepsilon \to 1$ (or high energy) limit. This signals a violation of unitarity [20].

Recent approaches avoid this problem through the use dispersive methods to construct the real part of the TPE amplitude from its imaginary part [20–24] (see Figure 1). Because the intermediate states are on their mass-shells, the dispersive method involves the exclusive use of on-shell transition form factors, thereby avoiding the problem of unphysical violation of unitarity in the high energy limit. Integrals over the virtualities of the two exchanged photons can also be done using numerical contour integration [20], which allows for the use of a more general class of transition form factors at the photon-hadron vertices than a sum of monopole form factors.

e^+p TO e^-p RATIO

One of the observables that is most sensitive to the effects of TPE is the ratio of e^+p to e^-p elastic cross sections, which in the OPE approximation is unity. Since the TPE terms enter the e^+p cross section with opposite sign to that in the e^-p reaction, the ratio

$$R_{2\gamma} \;=\; \frac{\sigma(e^+p)}{\sigma(e^-p)} \;\approx\; 1 - 2\,\delta_{\gamma\gamma}, \tag{3}$$

where $\sigma(e^\pm p) \equiv d\sigma(e^\pm p \to e^\pm p)/d\Omega$, provides a direct measure of effects beyond the Born approximation. Earlier data from elastic e^+p and e^-p experiments in the 1960s gave some hints of a small enhancement of $R_{2\gamma}$ at backward angles, but most of the data were in the region of large ε, where TPE effects are relatively small. Within experimental uncertainties, these results were consistent with $R_{2\gamma} = 1$.

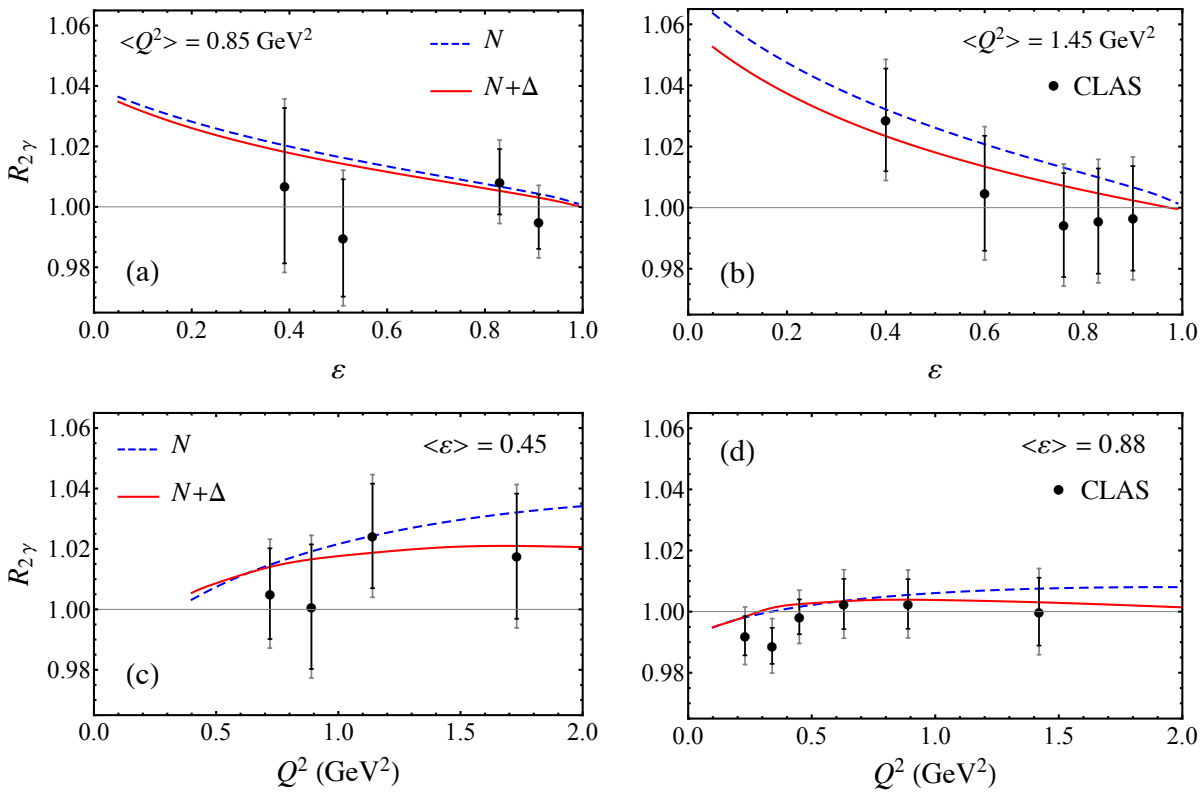

FIGURE 3. Ratio $R_{2\gamma}$ of e^+p to e^-p cross sections as a function of ε for (a) fixed $\langle Q^2\rangle = 0.85$ GeV^2 and (b) fixed $\langle Q^2\rangle = 1.45$ GeV^2, and as a function of Q^2 for (c) fixed $\langle\varepsilon\rangle = 0.45$ and (d) fixed $\langle\varepsilon\rangle = 0.88$. The contributions with nucleon only (dashed blue curves) and the sum of nucleon and Δ (solid red curves) intermediate states are compared with data from CLAS at Jefferson Lab (circles) [26], with the statistical and systematic uncertainties indicated by the (black) inner and (gray) outer error bars, respectively.

More recently, several dedicated e^+p to e^-p ratio experiments performed by VEPP-3 at Novosibirsk [25], CLAS at Jefferson Lab [26], and OLYMPUS at DESY [27], aimed at providing measurements of $R_{2\gamma}$ over a larger range of ε and Q^2 with significantly reduced uncertainties. Data from the VEPP-3 experiment at Novosibirsk [25], taken at energies $E \approx 1$ GeV and 1.6 GeV, are shown in Figure 2 as a function of ε. The data correspond to a Q^2 range between ≈ 0.3 GeV^2 and ≈ 1.5 GeV^2, with ε down to ≈ 0.3. The ratio at the low ε values shows an effect of magnitude 1% – 2%, slightly below but still consistent with our calculated TPE result at the $\approx 1\sigma$ level [20].

In Figure 3 the $R_{2\gamma}$ ratio from the CLAS experiment is shown as a function of ε at averaged Q^2 values of $\langle Q^2\rangle = 0.85$ GeV^2 and $\langle Q^2\rangle = 1.45$ GeV^2 [Figures 3(a) and (b), respectively], and as a function of Q^2 at averaged ε values of $\langle\varepsilon\rangle = 0.45$ and $\langle\varepsilon\rangle = 0.88$ GeV^2 [Figures 3(c) and (d), respectively]. Most of the data at the larger ε values are consistent with unity within the errors, but suggest a nonzero ratio, $\approx 2\% - 4\%$ greater than unity, at the lowest ε value for the higher-Q^2 set. The trend is consistent with our calculated ratio [20], which shows a rising $R_{2\gamma}$ with decreasing ε. At these kinematics the calculated TPE correction is dominated by the nucleon elastic intermediate state, with the Δ contribution reducing the ratio slightly.

The same trend is seen when the $R_{2\gamma}$ data are viewed as a function of Q^2 for fixed ε. At the larger average ε value, $\langle\varepsilon\rangle = 0.88$, the effects are consistent with zero as well as with the small predicted TPE correction. At the smaller value $\langle\varepsilon\rangle = 0.45$, on the other hand, the larger predicted effect is consistent with the larger $R_{2\gamma}$ values with increasing Q^2. Again the effects of the Δ intermediate state are small at low Q^2 values, but become visible at larger Q^2, where they improve the agreement between the theory and experiment.

Most recently, the OLYMPUS experiment at DESY [27] measured the ratio $R_{2\gamma}$ at an energy $E = 2.01$ GeV over a large range of $\varepsilon \sim 0.45 - 1$, corresponding to a Q^2 range from ≈ 0.2 GeV^2 to 2 GeV^2. The results for the ratio $R_{2\gamma}$ are shown in Figure 4. Interestingly, in contrast to the results from the VEPP-3 and CLAS experiments in Figures 2

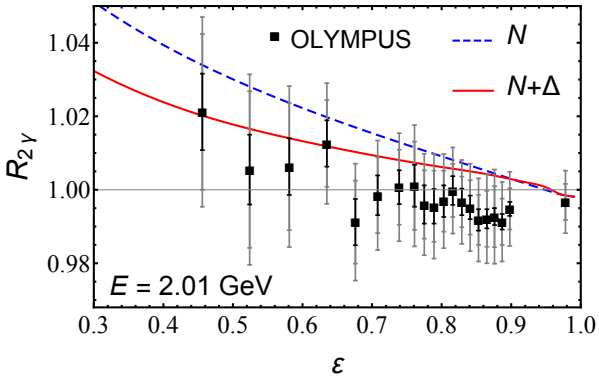

FIGURE 4. Ratio $R_{2\gamma}$ of e^+p to e^-p cross sections as a function of ε for fixed energy $E = 2.01$ GeV. The contributions with nucleon only (dashed blue curves) and the sum of nucleon and Δ (solid red curves) intermediate states are compared with data from the OLYMPUS experiment [27] (squares). The statistical and systematic uncertainties (correlated and uncorrelated) are indicated by the (black) inner and (gray) outer error bars, respectively.

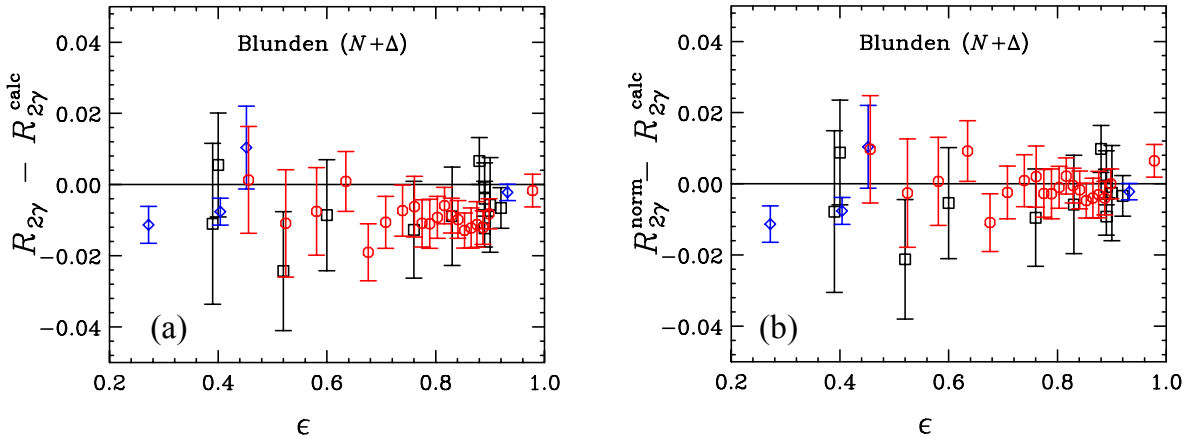

FIGURE 5. Difference between $R_{2\gamma}$ and model predictions as a function of ε [12]. The blue diamonds are VEPP-3, the black boxes are from CLAS, and the red circles are from OLYMPUS. Error bars reflect the quadrature sum of statistical and uncorrelated systematic uncertainties. In the right panel the normalizations of the CLAS and OLYMPUS data sets have been allowed to float.

and 3, at large ε values the trend in the data is towards values of the ratio slightly below unity, whereas the calculated dispersive TPE corrections give a ratio that has a small, $\lesssim 1\%$ enhancement above unity. At the lower ε values, the trend is toward increasing values of $R_{2\gamma}$, consistent with the TPE calculation.

Figure 5(a) shows the difference between $R_{2\gamma}$ and model predictions as a function of ε for the combined datasets [12]. It suggests that the data lie systematically below theory by $\approx 1\%$, independent of kinematics. If the normalization of the CLAS and OLYMPUS data are allowed to float independently, but with a penalty determined by the normalization uncertainty of each data set, the fit to the data gives the results shown in Figure 5(b), with $\chi^2_\nu = 0.96$.

The relatively large overall uncertainties on all of the currently available $R_{2\gamma}$ data unfortunately precludes any definitive conclusions about TPE effects that can be reached, other than that the effects are generally consistent with the signs and magnitudes expected from the dispersive TPE calculations. In addition, the negative values of the slope in ε predicted by the TPE calculations are generally consistent with the data from each of the VEPP-3 [25], CLAS [26], and OLYMPUS [27] e^+p/e^-p experiments.

This scenario calls for an urgent need for new measurements of e^+p to e^-p ratios at large Q^2, $Q^2 \gtrsim 2$ GeV^2, and over a range of ε values below $\varepsilon \sim 0.5$, where the TPE effects are predicted to be large enough ($\sim 2\%$) to be more clearly identified experimentally. As an example, Figure 6(a) shows the combined $N + \Delta$ result for $\delta_{\gamma\gamma}$ vs. Q^2 and ε. The vertical surfaces correspond to fixed electron (or positron) energies E. An experiment with $E = 3$ GeV would nicely cover the full kinematic range $0 < \varepsilon < 1$ and $0 < Q^2 < 5$ GeV^2, where hadronic models are expected to be

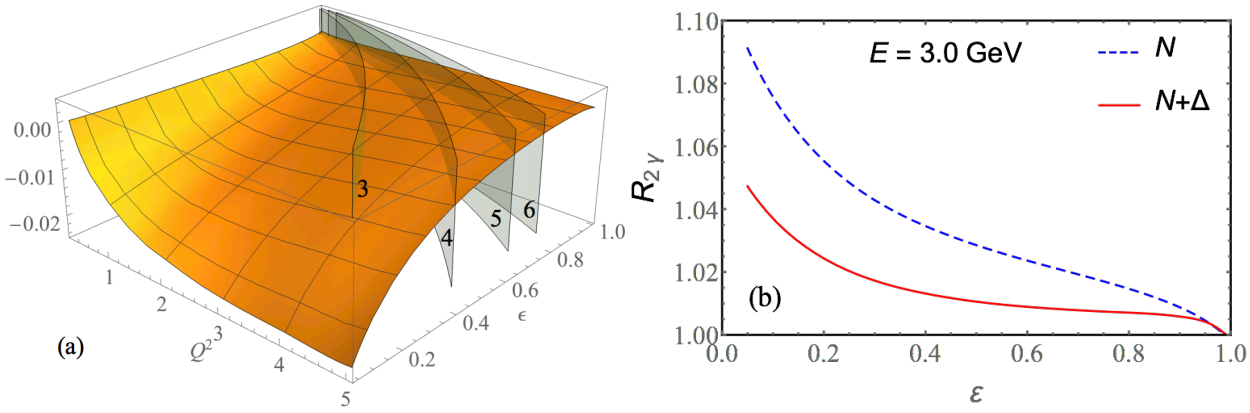

FIGURE 6. (a) Surface plot of $\delta_{\gamma\gamma}$ vs. ε and Q^2 (in GeV^2). Vertical surfaces correspond to fixed electron energies E (in GeV). (b) $R_{2\gamma}$ for the "optimal" energy $E = 3$ GeV, which covers the range $0 < Q^2 < 5$ GeV^2 over the full range $0 < \varepsilon < 1$.

valid. Figure 6(b) shows the model calculation for $R_{2\gamma}$ at fixed $E = 3$ GeV, indicating an effect of a few percent at backward angles.

ACKNOWLEDGMENTS

I thank my collaborator W. Melnitchouk for his contributions to this work. This work was supported in part by NSERC (Canada). I thank Jefferson Lab for support during a sabbatical leave, where part of this work was completed.

REFERENCES

[1] M. K. Jones *et al.*, Phys. Rev. Lett. **84**, 1398–1402 (2000).
[2] O. Gayou *et al.*, Phys. Rev. Lett. **88**, p. 092301 (2002).
[3] R. C. Walker *et al.*, Phys. Rev. **D49**, 5671–5689 (1994).
[4] M. E. Christy *et al.* (E94110), Phys. Rev. **C70**, p. 015206 (2004).
[5] I. A. Qattan *et al.*, Phys. Rev. Lett. **94**, p. 142301 (2005).
[6] P. G. Blunden, W. Melnitchouk, and J. A. Tjon, Phys. Rev. Lett. **91**, p. 142304 (2003).
[7] P. A. M. Guichon and M. Vanderhaeghen, Phys. Rev. Lett. **91**, p. 142303 (2003).
[8] Y.-S. Tsai, Phys. Rev. **122**, 1898–1907 (1961).
[9] L. W. Mo and Y.-S. Tsai, Rev. Mod. Phys. **41**, 205–235 (1969).
[10] P. G. Blunden, W. Melnitchouk, and J. A. Tjon, Phys. Rev. **C72**, p. 034612 (2005).
[11] J. Arrington, P. G. Blunden, and W. Melnitchouk, Prog. Part. Nucl. Phys. **66**, 782–833 (2011).
[12] A. Afanasev, P. G. Blunden, D. Hasell, and B. A. Raue, Prog. Part. Nucl. Phys. **95**, 245–278 (2017).
[13] S. Kondratyuk, P. G. Blunden, W. Melnitchouk, and J. A. Tjon, Phys. Rev. Lett. **95**, p. 172503 (2005).
[14] S. Kondratyuk and P. G. Blunden, Phys. Rev. **C75**, p. 038201 (2007).
[15] K. Nagata, H. Q. Zhou, C. W. Kao, and S. N. Yang, Phys. Rev. **C79**, p. 062501 (2009).
[16] K. M. Graczyk, Phys. Rev. **C88**, p. 065205 (2013).
[17] I. T. Lorenz, U.-G. Meissner, H. W. Hammer, and Y. B. Dong, Phys. Rev. **D91**, p. 014023 (2015).
[18] H.-Q. Zhou and S. N. Yang, Eur. Phys. J. **A51**, p. 105 (2015).
[19] H.-Q. Zhou, Phys. Rev. **C95**, p. 025203 (2017).
[20] P. G. Blunden and W. Melnitchouk, Phys. Rev. **C95**, p. 065209 (2017).
[21] M. Gorchtein, Phys. Lett. **B644**, 322–330 (2007).
[22] D. Borisyuk and A. Kobushkin, Phys. Rev. **C78**, p. 025208 (2008).
[23] D. Borisyuk and A. Kobushkin, Phys. Rev. **C92**, p. 035204 (2015).
[24] O. Tomalak and M. Vanderhaeghen, Eur. Phys. J. **A51**, p. 24 (2015).
[25] I. A. Rachek *et al.* (VEPP-3), Phys. Rev. Lett. **114**, p. 062005 (2015).
[26] D. Rimal *et al.* (CLAS), Phys. Rev. **C95**, p. 065201 (2017).
[27] B. S. Henderson *et al.* (OLYMPUS), Phys. Rev. Lett. **118**, p. 092501 (2017).

Super-Rosenbluth Measurements with Electrons and Protons

Mikhail Yurov[1] and John Arrington[2,a)]

[1]*University of Virginia, Charlottesville, VA, USA*
[2]*Physics Division, Argonne National Laboratory, Argonne, IL, USA*

[a)]johna@anl.gov

Abstract. Precise measurements of the proton form factor ratio $\mu_p G_E^p/G_M^p$ from Rosenbluth separation measurements can be combined with Polarization based extractions to provide significant constraints on two-photon exchange contributions to the elastic e-p cross section. We present an overview of JLab experiment E05-017, the high-precision 'Super-Rosenbluth' measurements of the proton form factor taken in Hall C of Jefferson Lab. We then examine what precision could be obtained for Super-Rosenbluth measurements using a low-intensity positron beam at Jefferson Lab.

INTRODUCTION

Historically, the proton electromagnetic form factors have been measured in unpolarized elastic e-p scattering, using the Rosenbluth separation technique. This technique has limited sensitivity to the charge form factor, G_E^p, at large Q^2, and so recoil polarization techniques have been used to extend measurements of G_E^p to large Q^2 at Jefferson Lab [1, 2, 3]. However, the polarization measurements yielded a significant decrease in $\mu_p G_E^p/G_M^p$ with increasing Q^2, while the Rosenbluth results indicated a roughly constant ratio [4, 5, 6, 7]. Initial attempts to understand the discrepancy [8, 9] suggested that it was a systematic difference, and could not be explained by an error in one or two experiments, and a high-precision 'Super-Rosenbluth' separation [10], using proton rather than electron detection, provided Rosenbluth extractions of the form factor ratio with precision comparable to the polarization measurements, confirming the discrepancy. Figure 1 shows a comparison of polarizations measurements in blue and Rosenbluth measurements in red.

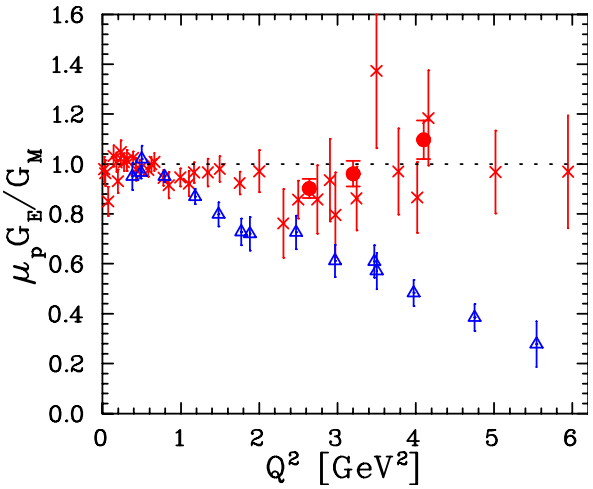

FIGURE 1. Comparison of Rosenbluth and polarization extractions of $\mu_p G_E^p/G_M^p$. The blue triangles are from polarization transfer extractions [11, 12], the red crosses are from a global analysis of Rosenbluth measurements [9], and the solid red circles are from the E01-001 'Super-Rosenbluth' experiment [10] discussed below. Figure adapted from Ref. [10]

The discrepancy is now generally attributed to the contribution of two-photon exchange (TPE) corrections [13, 14, 15, 16, 6, 17], which have minimal impact on polarization measurements but can have a significant impact when extracting G_E^p from the small, angle-dependent contribution to the unpolarized cross section. A combined analysis of existing electron-proton and positron-proton scattering comparisons [18], where the TPE contribution is expected to change sign with the sign of the lepton, provided some evidence for an angle-dependent correction. However, the indication for TPE contributions was only observed at the 3-sigma level, and only when combining all world's data for $Q^2 < 2$ GeV^2 - below the region where a clear discrepancy in the form factor extractions was observed. New measurements of electron-proton and positron-protons scattering [19, 20, 21, 22, 23] provide indications of TPE contributions for Q^2 up to 2 GeV^2. The data provide evidence of TPE contributions and are consistent with calculations of the TPE contributions in hadronic models [24, 25] but the precision of the data and the limited Q^2 range provide limited ability to validate these calculations [17], and further measurements at higher Q^2 are needed.

If the discrepancy between Rosenbluth and Polarization measurements is explained entirely by TPE contributions and these contributions are nearly linear in ε [26], the combination of cross section and polarization measurements can be used to extract the form factors without being dominated by uncertainty in the TPE corrections [16, 27]. However, these assumptions must be tested, and for other high-precision measurements, in particular at low Q^2 values [28, 29, 30, 31, 32], we must rely on calculated corrections and so it is important to test calculations of the TPE contributions.

An examination of world's unpolarized cross section data was consistent with the linear dependence on ε that is expected in the single photon (Born) approximation. It also provided limits on deviations from this linear behavior coming from contributions beyond the Born approximation, such as TPE contributions. While the analysis set significant limits on non-linear contributions [26], these were not precise enough to rule out many of the calculations of TPE corrections, which typically predict relatively modest deviations from linearity. The best limits on non-linear contributions from TPE come from the initial Super-Rosenbluth experiment [10]. These data also provided measurements of $\mu_p G_E^p/G_M^p$ from 2.6-4.1 GeV^2 with precision comparable to polarization measurements, allowing for the most precise extraction of the TPE contribution to the cross section from comparisons of Rosenbluth and Polarization data [33, 34, 35]. With the inclusion of measurements of the polarization ratio as a function of ε [36], it is possible to make similar, but still model-dependent, extractions of the full TPE amplitudes [37, 38].

THE SUPER-ROSENBLUTH TECHNIQUE

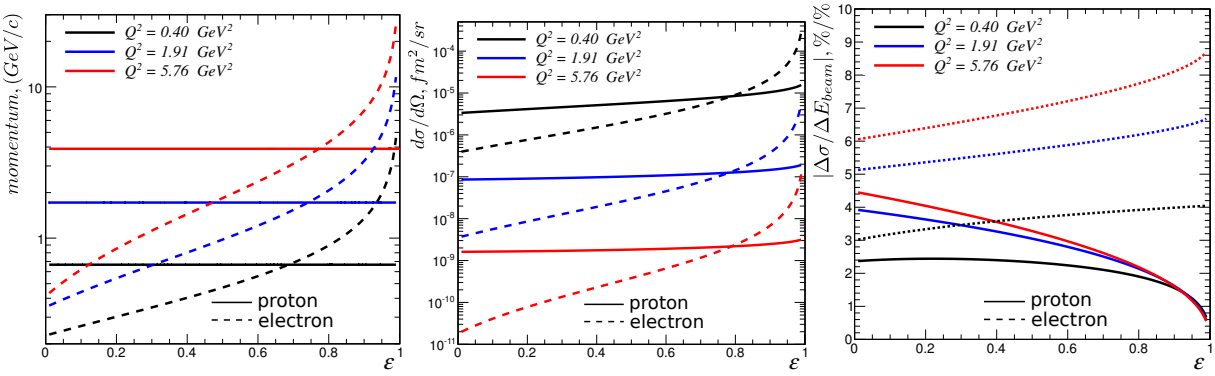

FIGURE 2. Detected particle momentum (left panel), cross section (middle panel), and sensitivity to beam energy (right panel) for Q^2 values of 0.4, 1.91, and 5.76 GeV^2 for proton detection (solid lines) and electron detection (dashed lines). At fixed Q^2, the proton momentum is fixed, while the electron momentum varies over an order of magnitude to cover a ε range from 0.2-0.8. The cross section for proton detection is nearly constant, while the electron cross section varies by 1-2 order of magnitude. In addition, the proton cross section at $\varepsilon = 0.2$ is a factor of 5-20 larger than for electron detection. The sensitivity of the cross section to a possible shift in beam energy is also smaller for proton detection.

JLab experiment E01-001 [10] made high-precision measurements of $\mu_p G_E^p/G_M^p$ using the Rosenbluth technique to provide confirmation of the Rosenbluth-Polarization discrepancy, and to provide better sensitivity to deviations from the linear behavior required in the Born approximation. The improved precision was achieved by minimizing the relative uncertainty between points taken at different values of ε but at the same Q^2. In a conventional Rosenbluth

separation experiment, data at fixed Q^2 but different ε values are taken by making measurements at different beam energy and varying the electron scattering angle to maintain a fixed Q^2 value. This means that the beam energy, detected electron energy, and cross sections change significantly when covering a large range in ε. As such, any corrections that depend on event rate or particle momentum must be corrected for precisely or they will introduce a false ε dependence. In addition, the cross section drops rapidly as the scattering angle increases (to achieve small ε values), limiting the statistics and often leading to use of higher beam currents for the low cross section kinematics, potentially introducing additional corrections that depend on the beam current.

JLab experiment E01-001 attempted to minimize these corrections by detecting protons rather than electrons and by applying a tight solid angle cut to limit the measurement to the very high acceptance region of the High Resolution Spectrometer (HRS)in Hall A. At fixed Q^2, protons have fixed momentum and nearly identical distributions in the detector, minimizing variation in efficiency or detector response, while limiting events to a small solid angle limits potential changes in acceptance for an extended cryogenic target. In addition, the cross section for proton detection has very little dependence on the proton angle, meaning that data can be taken at fixed beam current to minimize current-dependent corrections in the target, the rates in the spectrometer stay nearly constant over the full ε range, and the cross section for small ε values are significantly higher than for electron detection. Finally, the ε dependence of radiative corrections and the sensitivity of the cross section to small changes in beam energy or scattering angle are generally smaller for proton detection. Figure 2 compares detected particle momentum, cross section, and sensitivity to beam energy for electron and proton detection for a selection of Q^2 values from 0.4 to 5.8 GeV^2.

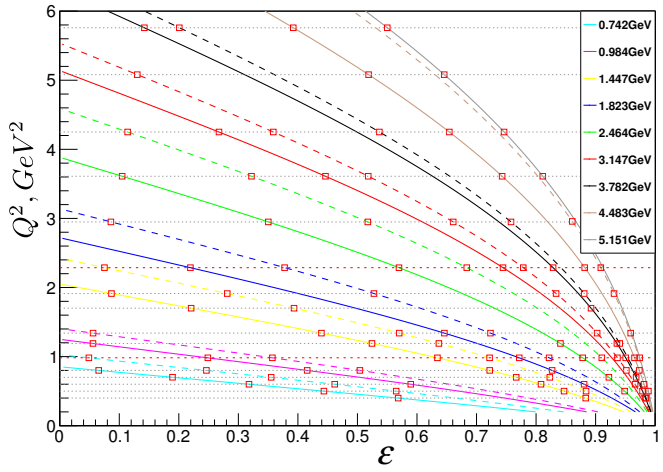

FIGURE 3. Kinematics of the E05-017 experiment. The solid and dashed lines indicate beam energies used in the measurement, with the solid lines corresponding to the energies given in the label. The short-dashed horizontal lines indicate fixed Q^2 values where LT separations were performed and the red boxes indicate the specific kinematics where elastic cross section measurements were made.

Experiment E05-017 used the High Momentum Spectrometer (HMS) in Hall C with the goal of expanding the Q^2 range of precise Super-Rosenbluth measurements (from 0.4-5.8 GeV^2), while also increasing the ε range and density of points to better constrain non-linear TPE contributions. Figure 3 shows the beam energies and kinematic points measured in the E05-017 experiment. Analysis of the data is nearly complete.

Super-Rosenbluth measurements with positrons

The Super-Rosenbluth technique is extremely well suited for making comparisons of electron-proton and positron-protons scattering at Jefferson Lab. Because we are detecting the struck protons, we do not have to change the polarity of the spectrometer used to detect the protons, meaning that we do not have to worry about the backgrounds changing when switching from electron to positron detection. In addition, because the technique focuses on minimizing the relative uncertainty between fixed Q^2 measurements at different ε values, precise extractions of $\mu_p G_E^p/G_M^p$ can be obtained independently for positron and electron scattering, and potential differences between the measurements should cancel in the extraction of the ratio. For example, while positron beam measurements will have much lower event rates, due

to use of a lower intensity positron beam, this rate is nearly constant as a function of ε and so rate-dependent effects will cancel in the extraction of $\mu_p G_E^p/G_M^p$ before comparing electron and positron results, as any normalization uncertainty impacts both G_E^p and G_M^p identically. Thus, the issue of precisely normalizing the luminosity between electron and positron beams is of less significance than for other measurements. Similarly, the experiment is not sensitive to changes in detector performance between electron and positron runs, as long as the conditions are stable within the individual measurements. Finally, the significantly increased cross section for low-ε measurements means that one can still make measurements at relatively large Q^2 values even with a significantly reduced beam current.

We take the run times and statistics achieved in the E05-017 measurement and use this to make projections for the kinematic coverage achievable in a very modest (18 day) run with a beam current of 1 μA. Because we detect protons, the only change with a positron beam is the reduction of beam current, from 30-80 μA for E05-017 to an assumed 1 μA. The E05-017 measurement is generally systematics limited, so we allow for statistical uncertainties of up to 1% at high Q^2, giving only a slight increase in the total uncertainty. Under these conditions, with the same 4 cm cryotarget as used in E05-017, a positron measurement with 1 μA unpolarized beam could cover a Q^2 range from 0.4-4.2 GeV^2 with better than 1% statistical uncertainty, yielding precision comparable to previous Super-Rosenbluth experiments. With an increase to 5 μA positron current or with use of a 10 cm hydrogen target, this could be extended to >5 GeV^2. These estimates assume that we measure at roughly half of the Q^2 points shown in Figure 3, and have fewer ε points for some of the larger Q^2 values.

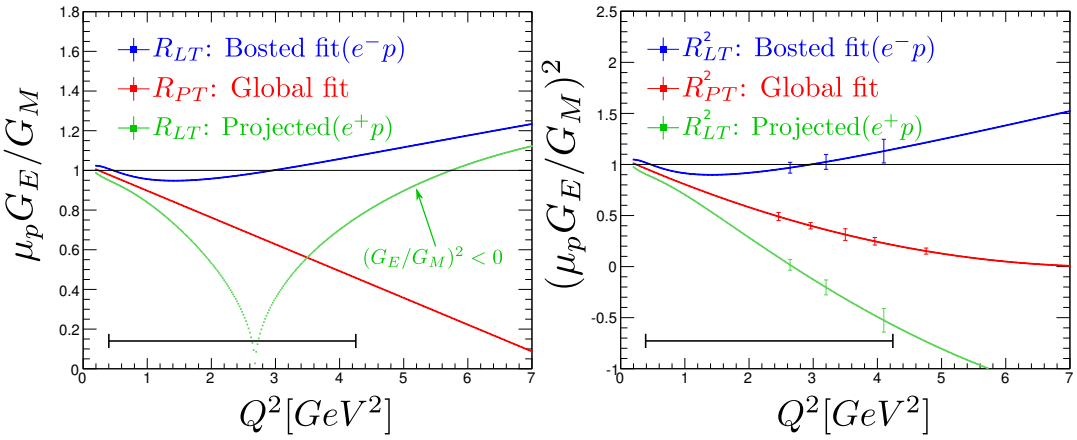

FIGURE 4. The left figure shows parameterization of global Rosenbluth extractions of $\mu_p G_E^p/G_M^p$ (top blue line), recoil polarization measurements (middle red line), and the expected ratio for positron measurements (bottom green line). Note that the ratio goes to zero at $Q^2 \approx 2.6$ GeV^2, and becomes imaginary at higher Q^2, as $(\mu_p G_E^p/G_M^p)^2$ goes negative. The right figure shows $(\mu_p G_E^p/G_M^p)^2$, for which the value is always real. The uncertainties shown on the PT and LT lines correspond to existing data in the 2-5 GeV^2 region, from the Super-Rosenbluth experiments E01-001 [10] for LT. The point on the projected e+p curve shows the uncertainties based on the precision achieved in the E01-001 experiment. The black band at the bottom indicates the range over which precision positron measurements can be made.

Figure 4 shows parameterizations of $\mu_p G_E^p/G_M^p$ from polarization measurements and from electron and positron Rosenbluth separations. The right figure includes the uncertainties from the E01-001 Super-Rosenbluth measurement, with projected uncertainties for positrons assuming comparable precision. Our estimates based on E05-017 would allow for several more Q^2 values than shown in Figure 4, from 0.4-4.2 GeV^2, but with slightly larger uncertainties.

Comparisons of electron and positron LT separations provide several improvements on existing TPE constraints. Under the assumption that TPE fully explains the Rosenbluth-Polarization difference, the difference between the electron Rosenbluth and polarization data can be used to constrain the linear contribution from TPE corrections. Comparison of positron and electron scattering yields twice the difference, improving our sensitivity to TPE contributions. More importantly, this comparison is only sensitive to TPE contributions, providing direct evidence that the discrepancy is caused by TPE rather than making this assumption as a starting point for the comparison. In fact, at $Q^2 = 4$ GeV^2, the contribution to the ε dependence from G_E^p is estimated to be roughly one sixth of the contribution coming from TPE, meaning that measurements with positrons will yield an ε dependence of a similar magnitude but of the opposite slope, as can be seen in the high-Q^2 region of Figure 4.

In addition to comparing electron and positrion extractions of $(\mu_p G_E^p/G_M^p)^2$ to constrain the linear part of the

TPE corrections, we can also compare the detailed ε dependence of electron and positron Rosenbluth separations to achieve improved sensitivity to non-linear contributions from TPE [26].

Conclusions

In summary, comparisons of precise Rosenbluth separation measurements for electrons and positrons can provide direct evidence of TPE contributions, and an improved extraction of the size of the TPE corrections, particular at large Q^2 where there is a clear discrepancy between electron Rosenbluth and polarization extractions of $\mu_p G_E^p/G_M^p$. In addition, these measurements would allow for improved constraints on non-linear contributions from TPE.

Using the Super-Rosenbluth technique, where only the struck proton is measured, such precise comparisons can be made between electrons and positrons, with no contribution to the uncertainty coming from differences in electron and positron beam currents. Projections based on the data from E05-017 suggest that positron LT separations can be performed for 8-9 Q^2 from 0.4 to 4-5 GeV^2, with comparable precision to the electron measurements which covered 16 Q^2 values from 0.4-5.8 GeV^2.

ACKNOWLEDGMENTS

This work was supported by the U.S. Department of Energy Office of Science, Office of Nuclear Physics, under contracts DE-AC02-06CH11357 and DE-FE02-96ER40950.

REFERENCES

[1] V. Punjabi *et al.*, Phys. Rev. C **71**, p. 055202 (2005), Erratum-ibid. C **71**, 069902 (2005).
[2] A. J. R. Puckett *et al.*, Phys. Rev. C **85**, p. 045203 (2012).
[3] A. J. R. Puckett *et al.*, Phys. Rev. C **96**, p. 055203 (2017).
[4] J. Arrington, C. D. Roberts, and J. M. Zanotti, J. Phys. **G34**, p. S23 (2007).
[5] C. F. Perdrisat, V. Punjabi, and M. Vanderhaeghen, Prog. Part. Nucl. Phys. **59**, p. 694 (2007).
[6] J. Arrington, P. G. Blunden, and W. Melnitchouk, Prog. Part. Nucl. Phys. **66**, p. 782 (2011).
[7] V. Punjabi, C. F. Perdrisat, M. K. Jones, E. J. Brash, and C. E. Carlson, Eur. Phys. J. A **51**, p. 79 (2015).
[8] J. Arrington, Phys. Rev. C **68**, p. 034325 (2003).
[9] J. Arrington, Phys. Rev. C **69**, p. 022201 (2004).
[10] I. A. Qattan *et al.*, Phys. Rev. Lett. **94**, p. 142301 (2005).
[11] M. K. Jones *et al.* (Jefferson Lab Hall A), Phys. Rev. Lett. **84**, p. 1398 (2000).
[12] O. Gayou *et al.* (Jefferson Lab Hall A), Phys. Rev. Lett. **88**, p. 092301 (2002).
[13] P. A. M. Guichon and M. Vanderhaeghen, Phys. Rev. Lett. **91**, p. 142303 (2003).
[14] P. G. Blunden, W. Melnitchouk, and J. A. Tjon, Phys. Rev. Lett. **91**, p. 142304 (2003).
[15] A. V. Afanasev, S. J. Brodsky, C. E. Carlson, Y.-C. Chen, and M. Vanderhaeghen, Phys. Rev. **D72**, p. 013008 (2005).
[16] J. Arrington, W. Melnitchouk, and J. A. Tjon, Phys. Rev. C **76**, p. 035205 (2007).
[17] A. Afanasev, P. G. Blunden, D. Hasell, and B. A. Raue, Prog. Part. Nucl. Phys. **95**, 245–278 (2017).
[18] J. Arrington, Phys. Rev. C **69**, p. 032201 (2004).
[19] M. Moteabbed *et al.* (CLAS Collaboration), Phys.Rev. **C88**, p. 025210 (2013).
[20] D. Adikaram *et al.*, Phys. Rev. Lett. **114**, p. 062003 (2015).
[21] I. A. Rachek *et al.*, Phys. Rev. Lett. **114**, p. 062005 (2015).
[22] D. Rimal *et al.*, Phys. Rev. C **95**, p. 065201 (2017).
[23] B. S. Henderson *et al.*, Phys. Rev. Lett. **118**, p. 092501 (2017).
[24] P. G. Blunden, W. Melnitchouk, and J. A. Tjon, Phys. Rev. C **72**, p. 034612 (2005).
[25] D. Borisyuk and A. Kobushkin, Phys. Rev. C **74**, p. 065203 (2006).
[26] V. Tvaskis *et al.*, Phys. Rev. C **73**, p. 025206 (2006).
[27] Z. Ye, J. Arrington, R. J. Hill, and G. Lee, Phys. Lett. B **777**, p. 8 (2017).
[28] A. V. Afanasev and C. E. Carlson, Phys. Rev. Lett. **94**, p. 212301 (2005).
[29] J. Arrington and I. Sick, Phys. Rev. C **76**, p. 035201 (2007).
[30] J. A. Tjon, P. G. Blunden, and W. Melnitchouk, Phys. Rev. **C79**, p. 055201 (2009).
[31] H. Q. Zhou, C. W. Kao, S. N. Yang, and K. Nagata, Phys. Rev. **C81**, p. 035208 (2010).

[32] J. Arrington, J. Phys. **G40**, p. 115003 (2013).
[33] J. Arrington, Phys. Rev. C **71**, p. 015202 (2005).
[34] I. A. Qattan, A. Alsaad, and J. Arrington, Phys. Rev. C **84**, p. 054317 (2011).
[35] I. A. Qattan, J. Arrington, and A. Alsaad, Phys. Rev. C **91**, p. 065203 (2015).
[36] M. Meziane *et al.*, Phys. Rev. Lett. **106**, p. 132501 (2011).
[37] D. Borisyuk and A. Kobushkin, Phys. Rev. D **83**, p. 057501 (2011).
[38] J. Guttmann, N. Kivel, M. Meziane, and M. Vanderhaeghen, Eur. Phys. J. A **47**, p. 77 (2011).

Deeply Virtual Compton Scattering with a Positron Beam

François-Xavier Girod[1,a)], Latifa Elouadrhiri[1] and Volker D. Burkert[1]

[1]*Thomas Jeson National Accelerator Facility, Newport News, VA 23606, USA*

[a)]Corresponding author: fxgirod@jlab.org

Abstract. The hard electroproduction of a photon off a hadron in the Bjorken regime, Deeply Virtual Compton Scattering, unravels three-dimensional information on the partonic structure of the hadron. The imaginary part of the amplitude is more particularly sensitive to the spatial distribution of quarks as functions of the light cone momentum fraction. On the other hand, the real part of the amplitude is less constrained experimentally, and provides access to the D-term. Here we present preliminary results for the extraction of the D-term from unpolarized cross-sections and beam spin asymmetries measured with the CEBAF Large Acceptance Spectrometer at 6 GeV. We discuss some aspects of the associated physics interpretation, and give prospects for future measurements. The availability of a Positron beam at Jefferson Lab will provide access to the Beam Charge Asymmetry for this reaction, which will crucially enable us to keep under control the systematical and model uncertainties in this framework.

INTRODUCTION

The hard electroproduction of a photon off a hadron can proceeds *via* the Bethe-Heitler (BH) process or the Deeply Virtual Compton Scattering (DVCS) process. In the BH process, the photon is emitted by the incoming or outgoing electron, and the amplitude is parameterized byt the hadron ElectroMagnetic Form Factors (FFs). In the DVCS process, the photon is emitted by the active parton in the Bjorken regime, and the amplitude is paramterized by the Generalized Parton Distributions (GPDs). The BH and DVCS processes are indistinguishable, and interfere at the amplitude level of the full reaction.

The GPDs contains the information of the FFs as well as of the ordinary Parton Distribution Functions (PDFs), in a sense bridging the gap between them. But access to the GPDs also promises to unravel a new three dimensional picture of the nucleon, at zero momentum transfer where they provide the spatial distributions of partons in the transverse plane as functions of light cone momentum fraction. Another exciting aspect of GPDs is that they also provide access to the energy-momentum tensor of partons inside a nucleon. At a fundamental level, the energy-momentum tensor is what couples to gravity, and access to this tensor would naively require a beam of gravitons. This however is a rather impractical experimental requirement. Fortunately, the DVCS process coupling simulatenously two spin-1 photons to the nucleon can actually provide the same information as coupling to one spin-2 graviton. The energy-momentum tensor (EMT) of partons inside a nucleon can be parameterized [1, 2] by the three Gravitational Form Factors (GFFs) M_2^q, J^q, and d_1^q, according to the Lorentz structures :

$$\langle p'|\hat{T}^q_{\mu\nu}|p\rangle \quad = \quad \bar{N}(p')\left[M_2^q(t)\frac{P_\mu P_\nu}{M} + J^q(t)\frac{\imath(P_\mu\sigma_{\nu\rho}+P_\nu\sigma_{\mu\rho})\Delta^\rho}{2M} + d_1^q(t)\frac{\Delta_\mu\Delta_\nu - g_{\mu\nu}\Delta^2}{5M}\right]N(p)$$

The form factor J^q parameterizes the time-space components of the EMT, and appears in the well-known Ji sum rule, as it encodes the distribution of angular momentum inside the hadron and is related to the GPDs *via* :

$$J^q(t) \quad = \quad \frac{1}{2}\int_{-1}^{1} \mathrm{d}x\, x\left[H^q(x,\xi,t) + E^q(x,\xi,t)\right]$$

The two other GFFs parameterize respectively the time-time and the space-space components of the EMT, and they appear in the sum rule relating the distributions of mass and of shear forces and pressure inside the nucleon *via* :

$$M_2^q(t) + \frac{4}{5} d_1^q(t) \xi^2 \quad = \quad \frac{1}{2} \int_{-1}^{1} \mathrm{d}x \, x H^q(x, \xi, t)$$

In this talk we will describe a strategy to access the GFF d_1, its interpretation, as well as existing and future experimental constraints.

Experimental Access to the GFF $d_1(t)$

Although the term d_1 appears directly in a sum rule involving the second Mellin moment of the GPD H, experimentally it is more practical to obtain this GFF *via* its relation to the D-term [3]. The GFF d_1 is the first coefficient of the Gegenbauer expansion of the D-term :

$$D(\xi, t) = \left(1 - \xi^2\right) \left[d_1(t) C_1^{3/2}(\xi) + d_3(t) C_3^{3/2}(\xi) + d_5(t) C_5^{3/2}(\xi) + \cdots \right]$$

The D-term itself can be obtained as it appears in a dispersion relation between the imaginary and real parts of the amplitudel [4, 5, 6] :

$$\mathrm{Re}\mathcal{H}(\xi, t) \quad = \quad D(t) + \mathcal{PV} \int \mathrm{d}x \left(\frac{1}{\xi - x} - \frac{1}{\xi + x} \right) \mathrm{Im}\mathcal{H}(\xi, t)$$

A complete analysis of all the ingredients in the DVCS amplitude will require a long program combining many observables together. Here we report on the minimum number of observables, working with the assumption of leading order and leading twist, and using a model dependent approach. The beam spin asymmetry $\mathrm{A_{LU}}$, beam charge asymmetry $\mathrm{A_C}$ and unpolarized cross-section σ_U are schematically related to the imaginary and real parts of the Compton Form Factors $\mathcal{H}$ using :

$$\begin{aligned}
A_{\mathrm{LU}} &= \frac{d^4\sigma^{\rightarrow} - d^4\sigma^{\leftarrow}}{d^4\sigma^{\rightarrow} + d^4\sigma^{\leftarrow}} \overset{\text{twist-2}}{\approx} \frac{\alpha \sin\phi}{\beta \cos\phi + \gamma} \\
\mathcal{H}(\xi, t) &= i\pi H(\xi, \xi, t) + \mathcal{PV} \int_{-1}^{1} \mathrm{d}x \, \frac{H(x, \xi, t)}{x - \xi} \quad \text{Compton Amplitude} \\
\alpha &\propto \mathcal{I}\mathrm{m}\left(F_1 \mathcal{H} + \cdots\right) \quad \rightarrow A_{\mathrm{LU}} \\
\beta &\propto \mathcal{R}\mathrm{e}\left(F_1 \mathcal{H} + \cdots\right) \quad \rightarrow A_{\mathrm{C}} \\
\gamma &\propto 4\left(1 - x_B\right)\left(\mathcal{H}\mathcal{H}^* + \cdots\right) + \cdots \quad \rightarrow \sigma_U
\end{aligned}$$

ANALYSIS

We make use of the dispersion relation to analyze simultaneously the DVCS beam spin asymmetries [7] and cross-sections [8]. The imaginary part of the amplitude is parameterized according to [9, 10] and adjusted to the data. The real part of the amplitude is computed using the dispersion relation from the imaginary part and the D-term as a subtraction constant. We first perform a local fit to the data using only individual kinematical bins, then the obtained parameters are fitted globally. The comparison between the beam spin asymmetries and the unpolarized cross-sections is illustrated in Figure 1 and 2.

RESULTS

In figure 3 left we illustrate the results of our local fits (black points) and our global fit (curve) for the GFF d_1. As we already mentioned, this GFF encodes the shear forces and pressure on partons inside the nucleon. Using a Fourier transformation, we can extract the pressure distribution as shown by the central curve on the right in Figure 3.

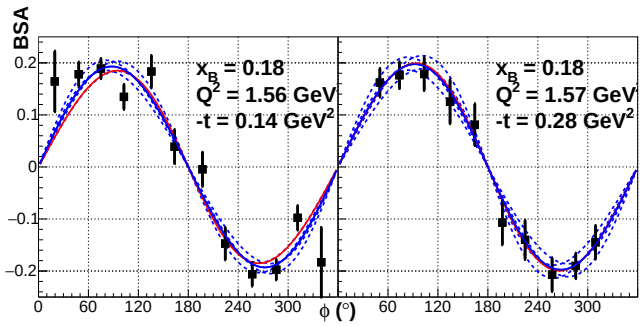

FIGURE 1. The beam spin asymmetries from [7] compared to the local fit (blue and dashed curves), and the global fit (red curves)

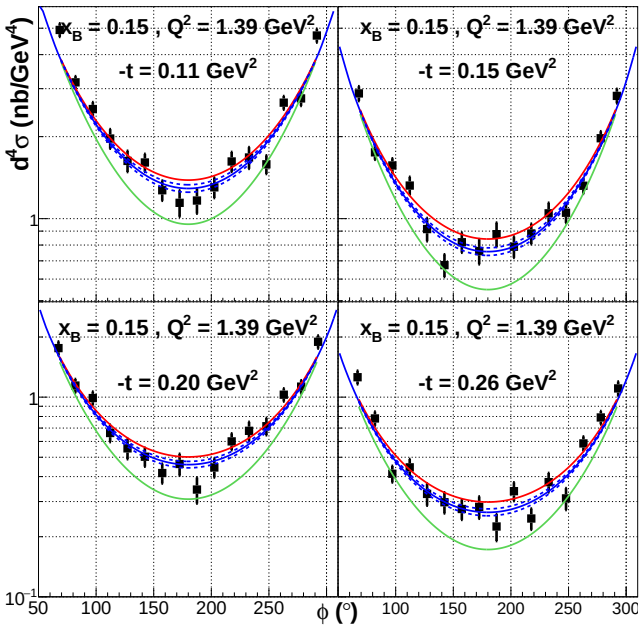

FIGURE 2. The cross-sections from [8] compared to the pure BH (bottom green curve), the local fits to the points (blue and dashed curves), and the global fit to the D-term (red curves)

The outer red band shows the uncertainties from results of global a fit to the world data in [9, 10]. The green band shows the uncertainties associated with our fit on the data from [7] and [8]. The inner blue band shows the projected uncertainties from the completion of the program with CLAS12 at Jefferson Lab.

The pressure as a three-dimensional scalar function, weighted by the square of the radius, should have a vanishing integral on account of the nucleon being a stable object. This pressure displays a positive core interpreted as repulsive forces between valence quarks, and a negative periphery, interpreted as an attractive force from the pion cloud. These features now derived for the first time from experimental data were already observed in chiral quark soliton and Skyrme model calculations [11, 12].

The availability of a positron beam would allow a direct extraction of the real part of the amplitude, thereby greatly simplifying the analysis and reducing the uncertainties associated with higher order/twist and other modeled contributions.

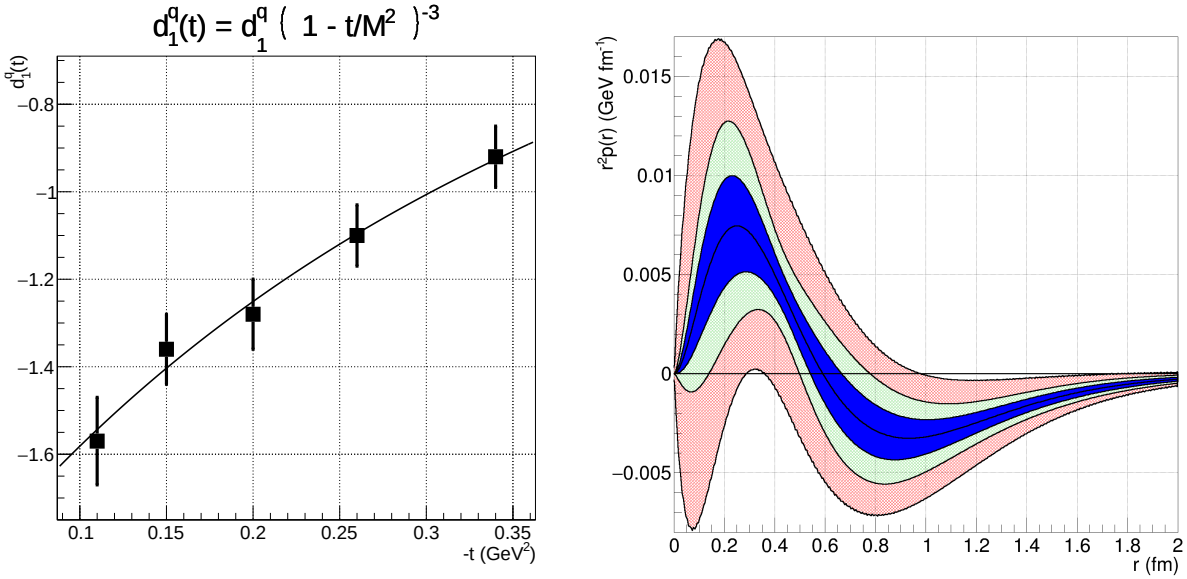

FIGURE 3. The GFF d_1 (left) and associated pressure (right) and uncertainties.

ACKNOWLEDGMENTS

We are grateful to Maxim Polyakov and Peter Schweitzer for numerous discussions on the subect of this work. This material is based upon work supported by the US Department of Energy, Office of Science, Office of Nuclear Physics under contract DE-AC05-06OR23177.

REFERENCES

[1] X.-D. Ji, Phys. Rev. **D55**, 7114–7125 (1997), arXiv:hep-ph/9609381 [hep-ph] .
[2] M. V. Polyakov, Phys. Lett. **B555**, 57–62 (2003), arXiv:hep-ph/0210165 [hep-ph] .
[3] M. V. Polyakov and C. Weiss, Phys. Rev. **D60**, p. 114017 (1999), arXiv:hep-ph/9902451 [hep-ph] .
[4] M. Diehl and D. Yu. Ivanov, Eur. Phys. J. **C52**, 919–932 (2007), arXiv:0707.0351 [hep-ph] .
[5] I. V. Anikin and O. V. Teryaev, *Hadron structure. Proceedings, 1st Joint International Conference, Hadron Structure '07, HS'07, Modra-Harmonia, Slovakia, September 3-7, 2007*, Fizika **B17**, 151–158 (2008), arXiv:0710.4211 [hep-ph] .
[6] B. Pasquini, M. V. Polyakov, and M. Vanderhaeghen, Phys. Lett. **B739**, 133–138 (2014), arXiv:1407.5960 [hep-ph] .
[7] F. X. Girod *et al.* (CLAS), Phys. Rev. Lett. **100**, p. 162002 (2008), arXiv:0711.4805 [hep-ex] .
[8] H. S. Jo *et al.* (CLAS), Phys. Rev. Lett. **115**, p. 212003 (2015), arXiv:1504.02009 [hep-ex] .
[9] K. Kumeriki and D. Mueller, Nucl. Phys. **B841**, 1–58 (2010), arXiv:0904.0458 [hep-ph] .
[10] D. Mller, T. Lautenschlager, K. Passek-Kumericki, and A. Schaefer, Nucl. Phys. **B884**, 438–546 (2014), arXiv:1310.5394 [hep-ph] .
[11] K. Goeke, J. Grabis, J. Ossmann, M. V. Polyakov, P. Schweitzer, A. Silva, and D. Urbano, Phys. Rev. **D75**, p. 094021 (2007), arXiv:hep-ph/0702030 [hep-ph] .
[12] C. Cebulla, K. Goeke, J. Ossmann, and P. Schweitzer, Nucl. Phys. **A794**, 87–114 (2007), arXiv:hep-ph/0703025 [HEP-PH] .

Polarization Observables using Positron Beams

Axel Schmidt[1]

[1]*Massachusetts Institute of Technology, Cambridge, MA, USA*

schmidta@mit.edu

Abstract. The discrepancy between polarized and unpolarized measurements of the proton's electromagnetic form factors is striking, and suggests that two-photon exchange (TPE) may be playing a larger role in elastic electron-proton scattering than is estimated in standard radiative corrections formulae. While TPE is difficult to calculate in a model-independent way, it can be determined experimentally from asymmetries between electron-proton and positron-proton scattering. The possibility of a polarized positron beam at Jefferson Lab would open the door to measurements of TPE using polarization observables. In these proceedings, I examine the feasibility of measuring three such observables with positron scattering. Polarization-transfer, specifically the ϵ-dependence for fixed Q^2, is an excellent test of TPE, and the ability to compare electrons and positrons would lead to a drastic reduction of systematics. However, such a measurement would be severely statistically limited. Normal single-spin asymmetries (SSAs) probe the imaginary part of the TPE amplitude and can be improved by simultaneous measurements with electron and positron beams. Beam-normal SSAs are too small to be measured with the proposed polarized positron beam, but target-normal SSAs could be feasibly measured with unpolarized positrons in the spectrometer halls. This technique should be included in the physics case for developing a positron source for Jefferson Lab.

Introduction

The discrepancy between the proton's electromagnetic form factor ratio, $\mu_p G_E/G_M$, extracted from polarization asymmetry measurements and the ratio extracted from unpolarized cross section measurements leaves the field of form factor physics in an uncomfortable state (See [1] for a recent review). On the one hand, there is a consistent and viable hypothesis that the discrepancy is caused by non-negligible hard two-photon exchange (TPE) [2, 3], the one radiative correction omitted from the standard radiative correction prescriptions [4, 5]. On the other hand, three recent measurements of hard TPE—at VEPP-3, at CLAS, and with OLYMPUS—found that the effect of TPE is small in the region of $Q^2 < 2\ \mathrm{GeV}^2/c^2$ [6–9]. The TPE hypothesis is still viable; it is possible that hard TPE contributes more substantially at higher momentum transfers. However, the three recent TPE experiments were challenging measurements, and the idea that a subsequent suite of follow-on measurements could quickly map out hard TPE over a large kinematic space with small uncertainty does not seem realistic.

In the face of this challenge, it may be more productive to concentrate experimental effort on constraining and validating model-dependent theoretical calculations of TPE. There are multiple theoretical approaches, with different assumptions and different regimes of validity [10–14]. If new experimental data could validate and solidify confidence in one or more theoretical approaches, then hard TPE could be treated in the future like any of the other standard radiative corrections, i.e., a correction that is calculated, applied, and trusted.

VEPP-3, CLAS, and OLYMPUS all looked for hard TPE through measurements of the positron-proton to electron-proton elastic scattering cross section ratio. After applying radiative corrections, any deviation in this ratio from unity indicates a contribution from hard TPE. However, this is not the only experimental signature one could use. Hard TPE can also appear in a number of polarization asymmetries. Having constraints from many orthogonal directions, i.e., from both cross section ratios and various polarization asymmetries would be valuable for testing and validating theories of hard TPE. As with unpolarized cross sections, seeing an opposite effect for electrons and positrons is a clear signature of TPE.

In the following sections, I examine the feasibility of measuring three different types of polarization asymmetries with a hypothetical future positron beam at Jefferson Lab. I find that polarization transfer would be a systematically clean technique, but would be hampered by poor statistical precision. Beam normal single spin asymmetries would

not be feasible due to the high luminosities required. Target normal single spin asymmetries are feasible from the perspective of statistics; the challenge would then become finding ways to reduce systematic uncertainty.

Polarization Transfer

The polarization transfer technique is the most accurate way of measuring the proton's form factor ratio. A polarized electron beam is scattered from an unpolarized proton target, and the polarization of the recoiling proton is then measured using a secondary scattering reaction. The ratio of transverse polarization to longitudinal polarization (within the scattering plane) is proportional to the form factor ratio. This technique has been employed in experiments covering a wide range of momentum transfers, including those at MIT Bates [15], Mainz [16], and Jefferson Lab [17–21], including three experiments, GEp-I [22], GEp-II [22], and GEp-III [23] that pushed to high momentum transfer. Another experiment, GEp-2γ, looked for hints of TPE in the ϵ-dependence in polarization transfer [23]. Two other experiments made equivalent measurements by polarizing the proton target instead of measuring recoil polarization [24, 25].

While polarization transfer is less sensitive to the effects of hard TPE, it is not immune. Following the formalism of Ref. [26], one finds that

$$\frac{P_t}{P_l} = \sqrt{\frac{2\epsilon}{\tau(1+\epsilon)}}\frac{G_E}{G_M} \times \left[1 + \mathrm{Re}\left(\frac{\delta\tilde{G}_M}{G_M}\right) + \frac{1}{G_E}\mathrm{Re}\left(\delta\tilde{G}_E + \frac{\nu}{M^2}\tilde{F}_3\right) - \frac{2}{G_M}\mathrm{Re}\left(\delta\tilde{G}_M + \frac{\epsilon\nu}{(1+\epsilon)M^2}\tilde{F}_3\right) + O(\alpha^4)\right], \quad (1)$$

where M is the mass of the proton, $\tau \equiv Q^2/4M^2$, $\epsilon^{-1} \equiv 1 + 2(1+\tau)\tan^2\frac{\theta}{2}$, $\nu \equiv (p_e + p_{e'})_\mu(p_p + p_{p'})^\mu$, and where $\delta\tilde{G}_E$, $\delta\tilde{G}_M$, and $\delta\tilde{F}_3$ are additional form factors that become non-zero when moving beyond the one-photon exchange approximation. This particular dependence on new form factors is slightly different than one what finds when taking a positron to electron cross section ratio:

$$\frac{\sigma_{e^+p}}{\sigma_{e^-p}} = 1 + 4G_M\mathrm{Re}\left(\delta\tilde{G}_M + \frac{\epsilon\nu}{M^2}\tilde{F}_3\right) - \frac{4\epsilon}{\tau}G_E\mathrm{Re}\left(\delta\tilde{G}_E + \frac{\nu}{M^2}\tilde{F}_3\right) + O(\alpha^4). \quad (2)$$

A measurement of the difference in polarization transfer between electron and positron scattering therefore adds information about TPE in addition to what can be learned from cross section ratios alone.

The GEp-2γ experiment looked for the effects of TPE in polarization transfer by making measurements at three kinematic points with varying values of ϵ, but with Q^2 fixed at 2.5 GeV$^2/c^2$ [23]. Since in the absence of hard TPE the ratio G_E/G_M has no ϵ-dependence, any variation with ϵ is a sign of hard TPE. The GEp-2γ measurement was statistically consistent with no ϵ-dependence, though their measurement of purely the longitudinal component showed deviations from the one-photon exchange expectation.

Positron scattering has the potential to improve the capabilities of a polarization transfer measurement. The largest systematic uncertainties, spin precession in the magnetic spectrometer and polarimeter alignment, are associated with proton polarimetry. These effects will largely cancel when taking a super ratio $(P_t/P_l)_{e^+p}/(P_t/P_l)_{e^-p}$, producing a systematically clean measurement. Ideally one would measure polarization transfer in both beam species for points at fixed Q^2 and look for ϵ-dependence as a signature. The figure-of-merit for such a measurement would be

$$\text{F.o.m.} \sim AP_e\sqrt{\frac{\mathrm{d}\sigma}{\mathrm{d}\Omega}\Omega\mathcal{L}T\varepsilon}, \quad (3)$$

where A is the spectrometer analyzing power, P_e is the lepton beam polarization, $\mathrm{d}\sigma/\mathrm{d}\Omega$ is the elastic cross section, Ω is the spectrometer acceptance, $\mathcal{L}$ is the luminosity, T is the run time, and ε is the running efficiency, i.e., the ratio of the live-time to wall-time.

I have attempted to gauge the reach of such an experiment with a hypothetical future positron beam at Jefferson Lab. I envisioned an experiment in Hall C, along the same lines as GEp-III and GEp-2γ, but using both the HMS and SHMS spectrometers to detect recoiling protons. Both spectrometers would need to be equipped with focal plane polarimeters. As in GEp-III and GEp-2γ, a non-magnetic, calorimetric detector, such as BigCal, could be used to detect scattered leptons in coincidence. I envisioned using two BigCals, each paired to match the acceptance of one of the spectrometers. Rather than calculate the statistical precision directly, I have scaled the statistical uncertainty from GEp-III and GEp-2γ using the figure-of-merit from equation 3, i.e., matching the analyzing power and running efficiency from those experiments. There are two parameters in the figure-of-merit that would have significantly

different values from the previous experiments. The achievable positron polarization would be ≈ 60%, down from the ≈ 80% polarization of the current CEBAF beam. The positron beam would also be limited to 100 nA. GEp-III and GEp-2γ used 80 μA. These two effects mean that a future positron scattering experiment would have a factor 38 worse statistical uncertainty before run time and cross section are taken into account.

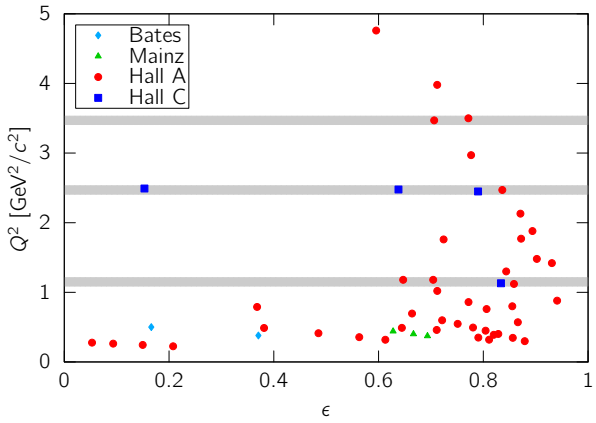

FIGURE 1. Q^2 = 1.15, 2.5, and 3.5 GeV$^2/c^2$ already have multiple prior polarization transfer measurements, and would therefore be sensible targets for an experiment with positrons.

It would be sensible to measure at values of Q^2 where there have already been prior polarization transfer experiments with which to compare. The values of ϵ and Q^2 for all previous polarzation transfer measurements are shown in figure 1. Because of prior measurements at these values, I initially selected Q^2 = 1.15, 2.5, and 3.5 GeV$^2/c^2$ as candidate kinematics. The experiment would need to cover several different ϵ points. The SHMS, which is limited to more forward scattering angles, could stay fixed for entire run to detect protons at ϵ = 0.2, while the HMS could move between ϵ = 0.5 and 0.8, where cross sections are higher and statistics can be accumulated more quickly.

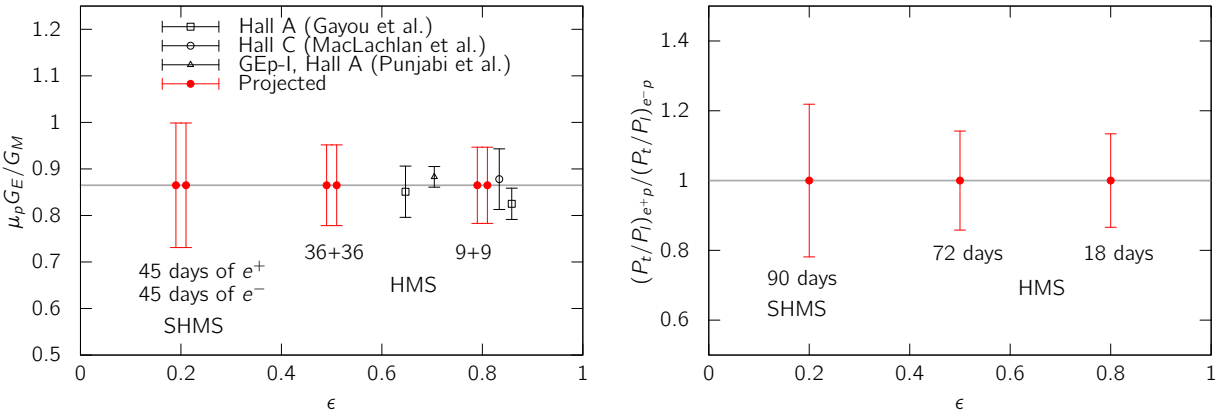

FIGURE 2. Even with a 90-day measurement at a limited Q^2 of only 1.15 GeV$^2/c^2$, a polarization transfer measurement with positrons would be limited to 10–20% statistical precision, hardly enough to constrain a percent level TPE effect.

The GEp-2γ experiment collected data for 40 days. The projected uncertainty for a 90-day experiment with both electrons and positrons at Q^2 = 1.15 GeV$^2/c^2$ is shown in figure 2. Even in 90 days and at reduced Q^2, the projected uncertainties are on the order of 10% on $\mu_p G_E/G_M$ and 10–20% on $(P_t/P_l)_{e^+p}/(P_t/P_l)_{e^-p}$. This would be insufficient for constraining a percent-level TPE effect. For larger Q^2, where the elastic cross section is considerably lower, these projections become even more pessimistic. Despite the polarization transfer ratio between positrons and electrons being a systematically clean technique, it would not be feasible statistically, given the design parameters for a future positron beam at Jefferson Lab.

A measurement of the ratio of tranverse to longitudinal polarization transfers is equivalent to a measurement of the ratio of transverse to longitudinal beam-target double spin asymmetries, where the longitudinal and transverse directions are relative to the momentum transfer vector. Because of this equivalence, one could imagine taking advantage of the large acceptance of the CLAS12 spectrometer and performing such a measurement in Hall B. Unfortunately, this technique relies on having some component of the target polarization being transverse to the beam direction, so that the double spin asymmetry manifests as an azimuthal asymmetry for constant scattering angle. As of now, the CLAS12 solenoid, which has a 5 T field parallel to the beam direction, prevents the use of any non-longitudinal target polarizations, making this technique unfeasible for now.

Beam-Normal Single Spin Asymmetries

Single spin symmetries (SSAs) normal to the reaction plane are zero in the limit of one-photon exchange, and thus make an excellent signature for detecting two-photon exchange. There are two such asymmetries: beam-normal, in which a transversely polarized lepton beam is scattered from an unpolarized target, and target-normal, in which an unpolarized lepton beam is scattered from a transversely polarized target. Both of these asymmetries are sensitive to the imaginary parts of the additional multi-photon exchange form factors. The imaginary parts do not contribute at α^3 order to the elastic cross section, meaning that they do not play any role in the proton form factor discrepancy. However, they can provide valuable orthogonal constraints to theories of TPE.

The beam-normal SSA, B_n, depends on the additional form factors in the following way:

$$B_n = \frac{4mM\sqrt{2\epsilon(1-\epsilon)(1+\tau)}}{Q^2(G_M^2 + \frac{\epsilon}{\tau}G_E^2)} \times \left[-\tau G_M \mathrm{Im}\left(\tilde{F}_3 + \frac{\nu}{M^2(1+\tau)}\tilde{F}_5\right) - G_E \mathrm{Im}\left(\tilde{F}_4 + \frac{\nu}{M^2(1+\tau)}\tilde{F}_5\right)\right] + O(\alpha^4), \quad (4)$$

where m represents the electron mass, and $\tilde{F}_4$ and $\tilde{F}_5$ are yet additional new form factors. Beam-normal effects are helicity suppressed, hence the leading factor of the electron mass, and, as a result, beam-normal SSAs are approximately three orders of magnitude smaller than target-normal SSAs, on the order of 10–100 ppm. Nevertheless, beam normal SSAs have been measured in electron scattering by several experiments and have been shown conclusively to be non-zero. Beam-normal SSAs are a possible source of false asymmetry in parity-violating electron scattering (PVES) experiments, and because of this, nearly every major PVES experiment has produced beam-normal SSA measurement as well, including, but not limited to, SAMPLE [27], G0 [28, 29], A4 [30, 31], HAPPEX/PREX [32, 33], and Q-Weak [34]. The data from previous B_n measurements are shown in figure 3.

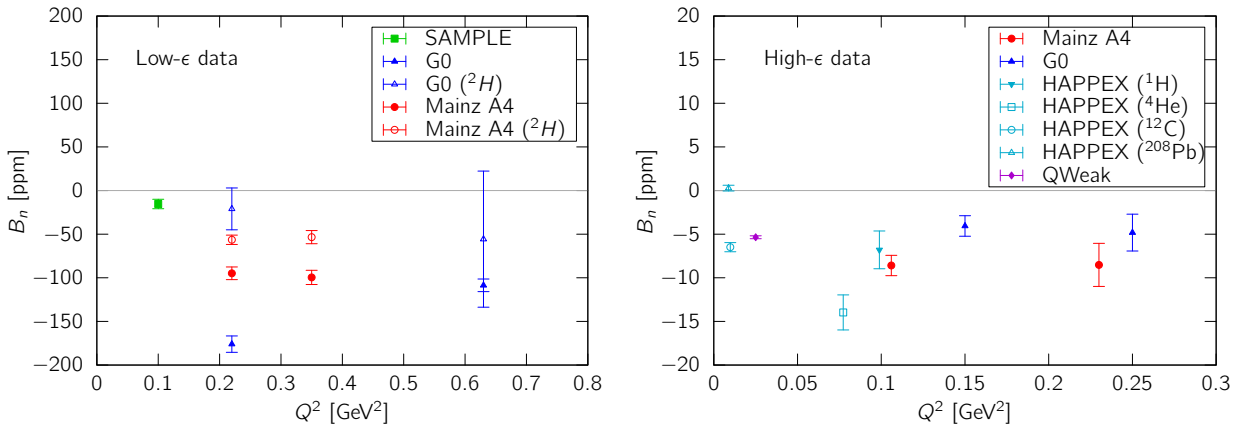

FIGURE 3. Previous B_n measurements at low-ϵ (left panel) have found asymmetries on the order of 100 ppm, while at high-ϵ (right panel), the asymmetries are even smaller.

While a 100 ppm asymmetry is far easier to measure than a 0.1 ppm parity-violating asymmetry, a measurement with a 100 nA polarized positron beam at Jefferson Lab would not be practical. PVES experiments typical use beam currents with many tens if not hundreds of μA. Furthermore, a positron beam does not provide any benefit in reducing the main systematic uncertainties: uncertainty in beam polarimetry and false asymmetries produced by the detectors.

Target-Normal Single Spin Asymmetries

The target-normal SSA, A_n, depends on the additional form factors in the following way:

$$A_n = \frac{\sqrt{2\epsilon(1+\epsilon)}}{\sqrt{\tau}\left(G_M^2 + \frac{\epsilon}{\tau}G_E^2\right)} \times \left[-G_M \mathrm{Im}\left(\tilde{G}_E + \frac{\nu}{M^2}\tilde{F}_3\right) + G_E \mathrm{Im}\left(\tilde{G}_M + \frac{2\epsilon\nu}{M^2(1+\epsilon)}\tilde{F}_3\right)\right] + O(\alpha^4). \quad (5)$$

Since this is also a unique combination of new form factors, a measurement of A_n would provide new constraints on TPE. Previous measurements of A_n with electron scattering have either been made with inelastic scattering [35–39], or in quasielastic scattering from polarized ^{3}He [40]. There are currently no published results from elastic electron scattering from polarized hydrogen. Ref. [40] measured an asymmetry of a few parts per thousand in ^{3}He, which corresponds to an asymmetry of a few percent from polarized neutrons. It would be reasonable to expect an asymmetry of similar size from polarized protons.

Since A_n is zero in the one-photon exchange approximation, any measurement of non-zero A_n, either in positron scattering or in electron scattering, would reveal either TPE, or a contribution from a T-violating process. As an asymmetry from TPE will flip sign when switching between electrons and positrons, a measurement with both electrons and positrons can distinguish between T-violation and the effects of TPE. Unfortunately, unlike in the case of polarization transfer, positrons do not offer any avenues for reducing the systematic uncertainties, which, for a measurement of A_n, are associated with the target polarization (including dilution factors), target alignment, live-time asymmetry, and radiative corrections.

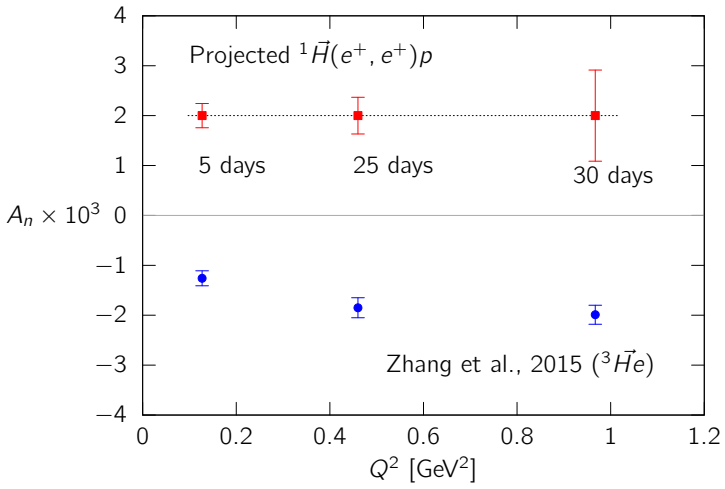

FIGURE 4. A measurement of A_n using positrons on a polarized proton target would be a feasible from the perspective of statistics. However, the challenge remains to successfully rein in systmatic uncertainties.

I have attempted to gauge the feasibility of measurement of A_n in elastic scattering from transversely polarized protons using a hypothetical CEBAF positron beam. The highest achievable luminosity with a polarized proton target would be attained using a frozen ammonia target, such as the one developed for the g_2^p and G_E^p experiments [41]. Such a target would be limited to 100 nA of current, but would allow running with $\mathcal{L} = 10^{35}$ cm^{-2}s^{-1}, with a dilution factor of 12%. I assumed an experimental set-up along the same lines as ref. [40], with both Hall A HRS spectrometers used simultaneously to double the acceptance for scattered positrons. The projected statistical uncertainty is shown in figure 4, assuming a two month measurement with 50% live-time, with data points for 1.2, 2.4, and 3.6 GeV beams and both HRSs positioned at 17°. The projections indicate that such a measurement could attain adequate statistics. The challenge would remain to control systematic uncertainties. As the frozen spin target polarization decays due to irradiation by the beam, frequent and accurate polarimetric measurements would be critical. If the measurement were combined with an electron scattering measurement (which would not be essential), frequent flipping between e^- and e^+ modes would be desired.

Conclusions

Polarization asymmetries in positron scattering would provide valuable new information that can test theories of hard TPE. I have considered three possible asymmetries and assessed the feasibility of measurements in the spectrometer halls with a future positron beam at Jefferson Lab. In the first category of polarization transfer measurements, positrons can dramatically improve the systematic uncertainties. However, with a polarized positron beam current of 100 nA, only 10–20% measurements would be possible, due to limited statistics. The second category, beam-normal single spin asymmetries, an enormous luminosity is needed to resolve the 1–100 ppm asymmetry. The third category, target-normal single spin asymmetry, holds some promise. Though positrons do not offer any avenue to reducing systematic uncertainty, such a measurement would be feasible from the perspective of statistics with a 100 nA beam and a frozen ammonia target. By comparing asymmetries in positron- and electron-scattering, the effects of TPE could be definitely identified, and contributions from possible T-violation could be ruled out. This avenue deserves further study and should be included as part of the physics case for building a positron source at CEBAF.

Acknowledgements

This work was supported by the Office of Nuclear Physics of the U.S. Department of Energy, grant No. DE-FG02-94ER40818.

REFERENCES

[1] A. Afanasev, P. G. Blunden, D. Hasell, and B. A. Raue, Prog. Part. Nucl. Phys. **95**, 245–278 (2017), arXiv:1703.03874 [nucl-ex] .
[2] P. A. Guichon and M. Vanderhaeghen, Phys.Rev.Lett. **91**, p. 142303 (2003), arXiv:0306007 [hep-ph] .
[3] P. Blunden, W. Melnitchouk, and J. Tjon, Phys.Rev.Lett. **91**, p. 142304 (2003), arXiv:0306076 [nucl-th] .
[4] L. W. Mo and Y.-S. Tsai, Rev. Mod. Phys. **41**, 205–235Jan (1969).
[5] L. C. Maximon and J. A. Tjon, Phys. Rev. C **62**, p. 054320Oct (2000), arXiv:0002058 [nucl-th] .
[6] I. A. Rachek *et al.*, Phys. Rev. Lett. **114**, p. 062005 (2015), arXiv:1411.7372 [nucl-ex] .
[7] D. Adikaram *et al.* (CLAS), Phys. Rev. Lett. **114**, p. 062003 (2015), arXiv:1411.6908 [nucl-ex] .
[8] D. Rimal *et al.* (CLAS), Phys. Rev. **C95**, p. 065201 (2017), arXiv:1603.00315 [nucl-ex] .
[9] B. S. Henderson *et al.* (OLYMPUS), Phys. Rev. Lett. **118**, p. 092501 (2017), arXiv:1611.04685 [nucl-ex] .
[10] Y. Chen, A. Afanasev, S. Brodsky, C. Carlson, and M. Vanderhaeghen, Phys.Rev.Lett. **93**, p. 122301 (2004), arXiv:0403058 [hep-ph] .
[11] A. V. Afanasev, S. J. Brodsky, C. E. Carlson, Y.-C. Chen, and M. Vanderhaeghen, Phys.Rev. **D72**, p. 013008 (2005), arXiv:0502013 [hep-ph] .
[12] O. Tomalak and M. Vanderhaeghen, Eur. Phys. J. **A51**, p. 24 (2015), arXiv:1408.5330 [hep-ph] .
[13] P. G. Blunden and W. Melnitchouk, Phys. Rev. **C95**, p. 065209 (2017), arXiv:1703.06181 [nucl-th] .
[14] E. A. Kuraev, V. V. Bytev, S. Bakmaev, and E. Tomasi-Gustafsson, Phys. Rev. **C78**, p. 015205 (2008), arXiv:0710.3699 [hep-ph] .
[15] B. D. Milbrath *et al.* (Bates FPP), Phys. Rev. Lett. **80**, 452–455 (1998), [Erratum: Phys. Rev. Lett.82,2221(1999)], arXiv:9712006 [nucl-ex] .
[16] T. Pospischil *et al.* (A1), Eur. Phys. J. **A12**, 125–127 (2001).
[17] O. Gayou *et al.*, Phys. Rev. **C64**, p. 038202 (2001).
[18] G. MacLachlan *et al.*, Nucl. Phys. **A764**, 261–273 (2006).
[19] G. Ron *et al.* (Jefferson Lab Hall A), Phys. Rev. **C84**, p. 055204 (2011), arXiv:1103.5784 [nucl-ex] .
[20] M. Paolone *et al.*, Phys. Rev. Lett. **105**, p. 072001 (2010), arXiv:1002.2188 [nucl-ex] .
[21] X. Zhan *et al.*, Phys. Lett. **B705**, 59–64 (2011), arXiv:1102.0318 [nucl-ex] .
[22] V. Punjabi *et al.*, Phys. Rev. **C71**, p. 055202 (2005), [Erratum: Phys. Rev.C71,069902(2005)], arXiv:0501018 [nucl-ex] .
[23] A. J. R. Puckett *et al.*, Phys. Rev. **C96**, p. 055203 (2017), arXiv:1707.08587 [nucl-ex] .
[24] M. K. Jones *et al.* (Resonance Spin Structure), Phys. Rev. **C74**, p. 035201 (2006), arXiv:0606015 [nucl-ex] .
[25] C. B. Crawford *et al.*, Phys. Rev. Lett. **98**, p. 052301 (2007), arXiv:0609007 [nucl-ex] .
[26] C. E. Carlson and M. Vanderhaeghen, Ann. Rev. Nucl. Part. Sci. **57**, 171–204 (2007), arXiv:0701272 [hep-ph] .

[27] S. P. Wells *et al.* (SAMPLE), Phys. Rev. **C63**, p. 064001 (2001), arXiv:0002010 [nucl-ex] .
[28] D. S. Armstrong *et al.* (G0), Phys. Rev. Lett. **99**, p. 092301 (2007), arXiv:0705.1525 [nucl-ex] .
[29] D. Androic *et al.* (G0), Phys. Rev. Lett. **107**, p. 022501 (2011), arXiv:1103.3667 [nucl-ex] .
[30] F. E. Maas *et al.*, Phys. Rev. Lett. **94**, p. 082001 (2005), arXiv:0410013 [nucl-ex] .
[31] D. B. Ros *et al.*, Phys. Rev. Lett. **119**, p. 012501 (2017).
[32] L. J. Kaufman, *Proceedings, 3rd International Workshop on From parity violation to hadronic structure and more (PAVI 2006): Milos, Greece, May 16-20, 2006*, Eur. Phys. J. **A32**, 501–503 (2007).
[33] S. Abrahamyan *et al.* (HAPPEX, PREX), Phys. Rev. Lett. **109**, p. 192501 (2012), arXiv:1208.6164 [nucl-ex] .
[34] B. P. Waidyawansa (QWeak), "Beam Normal Single Spin Asymmetry Measurements from QWeak," (2016) arXiv:1604.04602 [nucl-ex] .
[35] J. R. Chen *et al.*, Phys. Rev. Lett. **21**, 1279–1282 (1968).
[36] J. A. Appel *et al.*, Phys. Rev. **D1**, 1285–1303 (1970).
[37] S. Rock *et al.*, Phys. Rev. Lett. **24**, 748–752 (1970).
[38] A. Airapetian *et al.* (HERMES), Phys. Lett. **B682**, 351–354 (2010), arXiv:0907.5369 [hep-ex] .
[39] J. Katich *et al.*, Phys. Rev. Lett. **113**, p. 022502 (2014), arXiv:1311.0197 [nucl-ex] .
[40] Y. W. Zhang *et al.*, Phys. Rev. Lett. **115**, p. 172502 (2015), arXiv:1502.02636 [nucl-ex] .
[41] J. Pierce, J. Maxwell, and C. Keith, Nucl. Instrum. Meth. **A738**, 54–60 (2014).

Facilities For Dark Forces Searches in Italy and USA

Paolo Valente[1, a)] and Jim Alexander[2, b)]

[1]*INFN Sezione di Roma, P.le Aldo Moro, 2, I-00185 Rome (Italy).*
[2]*Cornell University, Ithaca, NY 14853, USA.*

[a)]Corresponding author: paolo.valente@roma1.infn.it
[b)]jim.alexander@cornell.edu

Abstract. The Dark Matter elusiveness could be explained by speculating that it lives in a separate sector with respect to the Standard Model (SM) and that interacts with it only by means of messengers. The simplest model foresees just one messenger: a possibly massive vector boson given by a new U(1) symmetry. This mediator can faintly mix with the photon and, hence, interact with SM charged particles, seeing an effective charge equal to $\varepsilon \cdot e$, but also the production of axion-like particles or dark scalars can be explored. In searching such mediators at accelerators, the fixed-target approach is favored over colliding beams because of the higher luminosity; among the different classes of experiment the e^+e^- annihilation is the less model-dependent approach, and has the potential of positively identifying new particles, regardless from its final state. Producing high-energy, high-intensity positron pulses from a LINAC or extracting them from a e^+ ring have been both considered: the different available time structure, repetition rate, maximum energy and beam intensity reflect in different sensitivities for dark sector searches, a panorama of the available facilities in Italy and USA is given.

DARK SECTOR SEARCHES WITH POSITRONS

Physicists do not know what the dark matter (DM) is made of, but astrophysics and cosmology indicate that Standard Model (SM) particles account for less than 5% of the total content of the Universe. Failing to find DM in the form of weakly interacting massive particles (WIMP) has stimulated the alternative hypothesis of "hidden sectors": one or more families of new particles disconnected from the ordinary matter, except from some mediator states, very weakly coupled, acting as "portals" to the SM [1,2].

A much larger spectrum of masses and couplings is in this case allowed: the dark mediator itself can be light and yet have been undetected so far. An indication on the coupling and mass can be derived by demanding this new particle be the only justification of the well-known muon *g*-2 anomaly [3]. Many models have been built, but in general the portal can be a fermion (e.g. a sterile neutrino), a scalar, a vector (dark photon), or a axion-like particle, and it can be part of a complex sector, rich in new (heavy or light) states.

Many experiments have been devoted to searching for a dark photon (*A'*) kinetically mixed with the ordinary photon, and radiated in the interaction of an electron beam with the nuclei of a target, or coming from the decay of a meson. While a large number of results accumulated in last few years in the "visible" decays, i.e. when *A'* decays to SM final states (e^+e^- if $m_{A'} < 2m_\mu$), much less has been explored in the more general case in which the mediator can decay "invisibly", i.e. to dark particles χ (only possible if $m_{A'} > 2\, m_\chi$).

When searching for such a new particle with accelerator-based experiments, generally a number of assumptions are needed on the production mechanism and on the decay channels: does it couple to leptons? And to quarks? Is it the lightest particle in the hidden sector? Moreover, since the coupling to the SM is very weak, very high luminosity is required: the fixed-target approach is thus favored over colliding beams because the number of target atoms is much higher than the number of particles in an accelerator beam; moreover the atomic number of the target can be $Z > 1$), but the advantage comes at the price of a reduced center of mass energy.

On the other hand, among the different classes of experiment, the e^+e^- annihilation is the less model-dependent approach. Moreover, it has the potential of positively identifying a new particle, regardless of its final state: this is not the case for the missing momentum nor missing energy experiments, which only have an exclusion power.

It is possible to join the two aspects by performing e^+ annihilation on the atomic electrons of a fixed-target [4], as in the case of the PADME [5-7] experiment, approved at Frascati LINAC [8], and MMAPS [9], proposed at the Cornell synchrotron. In both cases a dark vector *A'* can be searched for in a model-independent way, as a peak in the missing mass spectrum, obtained by precisely measuring the momentum of the recoil photon in γ + invisible final states, **or** by measuring the electron-positron pair resulting from the dark photon decay. The energy of the positron beam from the Frascati LINAC is limited to 550 MeV (see next section), so that the mass range extends to 24 MeV/c^2 (as shown in Fig. 1), while up to $M_{A'} = 78$ MeV/c^2 could be explored with the proposed 6 GeV extracted positron beam at Cornell.

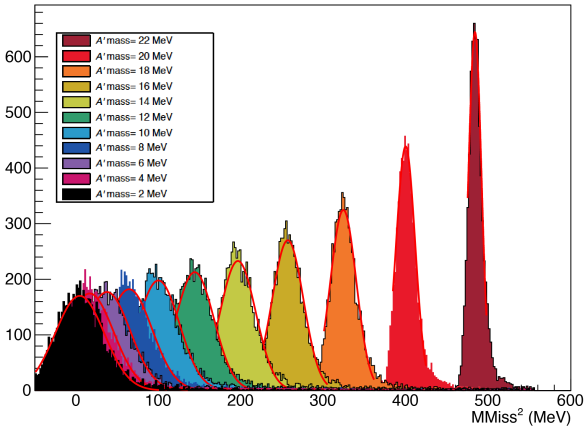

FIGURE 1. Missing mass distributions for dark photons of masses spanning from 2 to 22 MeV/c^2, expected for the PADME experiment.

The excellent missing mass resolution of the PADME experiment is achieved thanks to the characteristics of the setup (the MMAPS proposal is based on a similar concept, although with slightly different technical solutions), which is composed of (see Fig. 2):

- An active low-*Z* target (diamond with graphite strips for the beam monitoring), in which positrons annihilate; the 0.1 mm thickness is optimized taking into account the beam intensity with respect to the annihilation and Bremsstrahlung cross-sections, in order both to limit double-interaction probability and to keep the rate in the detector at a manageable level.
- An analysing dipole magnet, sweeping away the non-annihilated positrons of the incoming beam from the main calorimeter, but also enabling the rejection of Bremsstrahlung background events by vetoing on positrons losing energy by radiation.
- Scintillating bars measuring the momentum of the radiating positrons, bent in the magnetic field; the bars are read-out with wavelength-shifting fibers coupled to Silicon photo-multipliers.
- The main calorimeter, made of 600 BGO crystals (21×21×230 mm^3, i.e. 21 radiation lengths), with the main purpose of precisely measuring the recoiling photon energy and position.
- A fast Cherenkov forward calorimeter, detecting high-energy low-angle photons, mainly from the copious Bremsstrahlung background.

All detectors are acquired by fast switched-capacitor array digitizers, and the waveform data (1024 samples/channel at 1 GS/s) are transmitted to the acquisition for each positron beam pulse (at the maximum rate of 50 Hz).

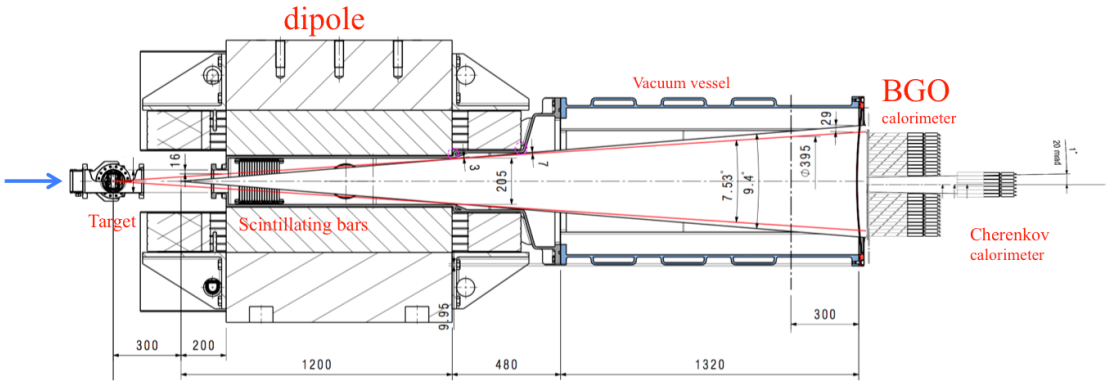

Figure 2. PADME experiment setup.

The first physics run of PADME will be in 2018 (six months of data taking), aiming at 10^{13} positrons on target, in order to reach a sensitivity at the 10^{-6} level in the coupling $\varepsilon^2 = \alpha/\alpha'$ (where the new coupling α' is expressed in terms of the electromagnetic one α), up to a mass for a kinetically mixed dark photon of 24 MeV/c^2. The sensitivity can be pushed further, by accumulating $4 \cdot 10^{13}$ positrons on target in two years or running, thus reaching $\varepsilon^2 \sim 5 \cdot 10^{-7}$, as shown by the red-dashed line in Fig. 3, compared with the exclusions from past experiments (like BaBar [10]) and from present (NA64 [11]) and planned (MMAPS, VEPP-3 [12]) ones: even though the band favored by the muon $g-2$ anomaly is excluded, a large part of parameter plane (mass vs. coupling) remains still unexplored.

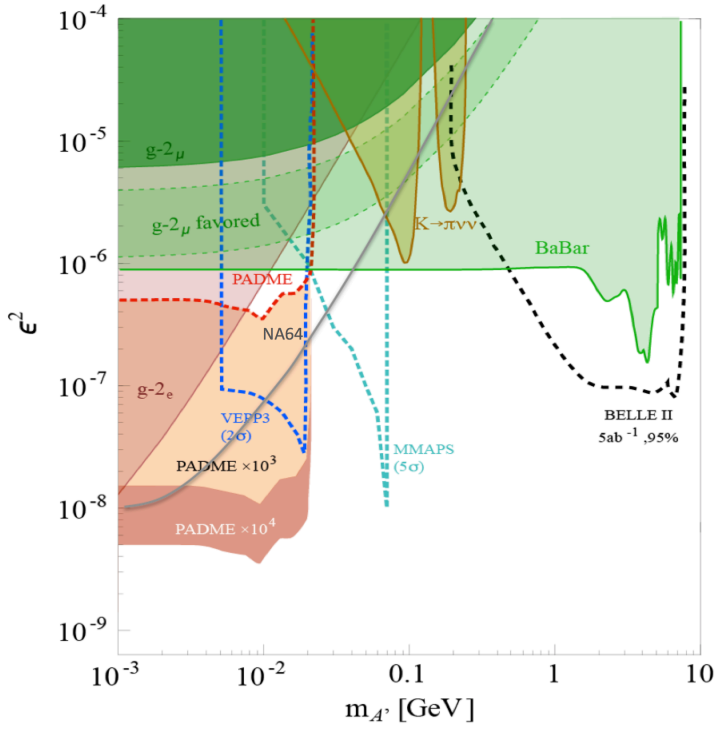

FIGURE 3. Sensitivity of experimental searches of a dark photon decaying to invisible (dark) final states in the plane coupling $\varepsilon^2 = \alpha'/\alpha$ vs. mass: PADME sensitivity is shown by the red dashed line, compared with the existing limits (BaBar mono-photon result is shown in green). The projected sensitivity of an improved PADME experiment using DAΦNE ring as pulse stretcher of the Frascati LINAC (brown area) is also shown compared to future experiments, both approved like Belle-II, and proposed like VEPP3 at Novosibirsk and MMAPS at Cornell.

POSITRON FACILITIES

The Frascati accelerator complex is centred around the DAΦNE e^+e^- collider, running at 1.02 GeV centre of mass energy, using a high-current, S-band warm LINAC, capable of producing up to nC positron pulses at 50 Hz repetition rate, at a maximum energy of 550 MeV, which can be deflected towards the BTF (Beam-Test Facility) beam-line and experimental area [13]. For the PADME experiment the intensity of the positron beam is not limited by the LINAC current, but by the pile-up probability in the calorimeters, measuring the position and energy of the recoil photon, and the veto probability in the scintillating bars hit by positrons undergoing a Bremsstrahlung in the target.

This reduces the particle density impinging on the target to $\sim 10^3 e^+/\text{ns}$, so that the maximum intensity is determined by the longest possible beam pulse from the LINAC. For the DAΦNE collider operations electrons and positrons from the LINAC are injected into the damping ring in ~ 10 ns long pulses (since the radio-frequency is ~ 74 MHz), with a structure of 2856 MHz micro-bunches.

In order to achieve the highest possible luminosity for PADME, the LINAC setup has been modified for accelerating longer positron macro-pulses, despite the accelerating field exhibits a very peaked time structure, due to the compression of the RF power from the klystrons (by means of the so-called SLED device), needed to get relatively high gradients with S-band structures: pulses of >200 ns have been produced [14].

It is clear that for getting significant improvements of the sensitivity of this kind of experiments, such a low duty-cycle (200 ns/20 ms= 10^{-5}) has to be largely improved, indeed the ideal machine would be a continuous-wave accelerator, like a superconducting LINAC.

The possibility of increasing the pulse length by 3-4 orders of magnitude using the DAΦNE ring as pulse stretcher of the LINAC, has been recently proposed [15], using the slow extraction: exciting a 1/3 of integer tune resonance and using the synchrotron radiation losses to drive positrons out of the stable phase-space region, it will be possible to produce ~ 0.4 ms positron bunches. This corresponds to a corresponding improvement in the sensitivity for PADME, shown by the brown-shaded area in Fig. 3). Unfortunately, the small size of the ring does not allow increasing the beam energy, so that no improvement in the explored dark photon mass range is instead possible. A possible layout of the extraction line and PADME location in the main DAΦNE hall is shown in Fig. 4.

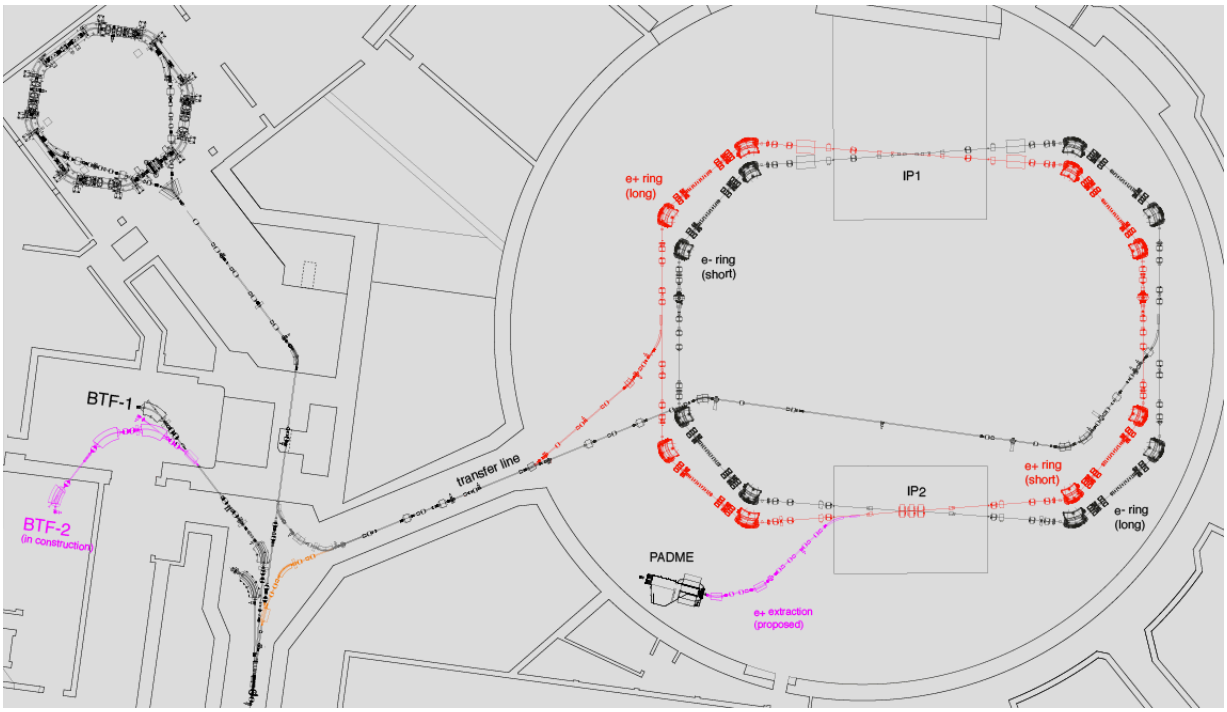

FIGURE 4. Proposed positron extraction line from the Frascati electron-positron collider DAΦNE.

The pulse stretcher project in Frascati has been inspired by a similar project at Cornell University of using resonant extraction of positrons from a storage ring. The CESR storage ring is presently used as synchrotron radiation facility: prior to be stored in the storage (outer) ring, positrons produced by a 150 MeV LINAC are accelerated to 5.3 GeV (6 GeV after the on-going upgrade) by a synchrotron. The two circular rings are one inside the other, positrons are extracted from the inner synchrotron to the outer storage ring, where the undulators and photon beam-lines are installed (in the south region of the accelerator campus).

The idea is again to use 1/3 resonant extraction, excited by sextupoles and driven by ramping quadrupoles, and in order to perform positron fixed-target experiments, an extraction line from the synchrotron has to be realized. A possible layout of the extraction line and of a dark photon experiment modelled on the PADME setup (in particular using the same BGO calorimeter or a very similar one), in the north region of the accelerator campus is shown in Fig. 5.

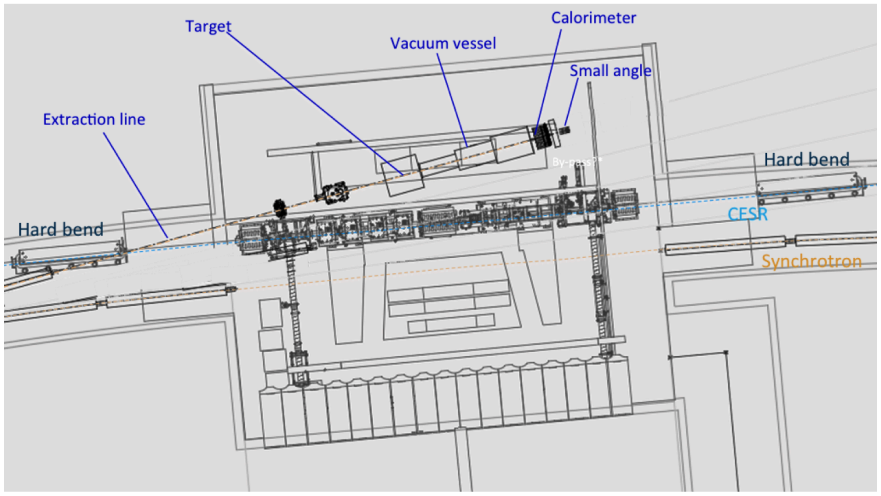

FIGURE 5. A possible scheme for the positron extraction line and dark photon experiment in the north region of the Cornell accelerator campus.

Also in the case of an extracted, stretched beam, the intensity of positrons is limited by the need of keeping the pile-up probability in the detectors (in particular the main BGO calorimeter) at an acceptable level:

- In the case of an improved PADME experiment with ~550 MeV positron beam, 0.4 ms long, extracted at 50 Hz from the DAΦNE ring, the maximum duty-cycle would be of the order 2%;
- For MMAPS using a 6 GeV positron beam extracted from the Cornell synchrotron in 12,000 bunches, spaced by 168 ns and repeated at 60 Hz, the maximum resulting duty-factor is still ~10%.

An alternative approach is to use an internal target, onto which the positron beam circulating in an accelerator ring impinges. This is the approach of the VEPP3 proposal at the Budker Institute in Novosibirsk. In this case the limitation comes from the need of realizing a low-Z, very thin target, in order to reduce the impact on the beam lifetime. The project aimed at building a dedicated by-pass line of the VEPP3 storage ring, for installing a gaseous H_2 target and a dark photon experiment is described in Ref. [12].

CONCLUDING REMARKS

Positron annihilation searches for a dark mediator (dark photon, ALP, or other exotic particles) independent from the final states with missing mass technique, have a two-fold interest:

- It is possible to make model-independent exclusions.
- If the missing mass resolution is good enough, this kind of experiment has a discovery potential of a new (super-weak) force of nature.

In the future (mid and long term) experimental panorama, the Belle-II experiment at SuperKEKB will explore the high-mass range in a few years, but limits in the most interesting range below 100 MeV will be far from the "thermal" DM bounds by several orders of magnitude, until the LDMX experiment at SLAC will reach its ultimate

sensitivity [2].

In order to have a real break-through with respect to the present experiments (PADME, in particular) there are two possibilities:

- Increase the mass sensitivity, by increasing the beam energy. In this respect, the Cornell project of a 6 GeV extracted positron beam would allow extending the range up to 78 MeV$/c^2$.
- Increase the luminosity, keeping in mind that this kind of experiment is limited by the pile-up probability.

The improved PADME proposal, using the DAΦNE ring as a positron beam stretcher, and the Cornell facility, both aim at extending the duty-factor by increasing the pulse length/repetition rate ratio, but can hardly exceed the 10^{16} (Frascati) to 10^{17} (Cornell) positrons on target/year.

In this respect, the best option would be a super-conducting machine like CEBAF, which can easily provide an adequate beam quality: 1% energy resolution, sub-mm spot, 0.1 mrad divergence. A dedicated study on the potential sensitivity of a positron annihilation experiment at 11 GeV at TJNAF is reported in [16].

ACKNOWLEDGMENTS

This work supported by the Italian Minister of Foreign Affairs and International Cooperation (MAECI), CUP I86D16000060005.

REFERENCES

1. J. Alexander et al., "Dark Sectors 2016 Workshop: Community Report," arXiv:1608.08632 [hep-ph].
2. M. Battaglieri et al., "US Cosmics Visions: New Ideas in Dark Matter 2017: Community Report," arXiv:1707.04591 [hep-ph].
3. M. Pospelov, Phys. Rev. D **80**, 095002 (2009).
4. B. Wojtsekhowski *et al.*, arXiv:1207.5089 [hep-ex].
5. M. Raggi and V. Kozhuharov, Adv. High Energy Phys. 2014, 959802 (2014).
6. M. Raggi, EPJ Web Conf. **142**, 01026 (2017).
7. P. Valente et al., PoS ICHEP2016, 204 (2016).
8. R. Boni et al., Conf. Proc. C980622 (1998) 764
9. J. Alexander, EPJ Web Conf. **142**, 01001 (2017).
10. J.P. Lees et al.. Phys. Rev. Lett. **119** no.13, 131804 (2017).
11. D. Banerjee et al., Phys. Rev. Lett. **118** no.1, 011802 (2017).
12. B. Wojtsekhowski et al., "Searching for a dark photon: Project of the experiment at VEPP3," arXiv:1708.07901 [hep-ex].
13. B. Buonomo et al., Nuovo Cim. C **40** no.1, 69 (2017).
14. P. Valente et al., J. Phys. Conf. Ser. **874** no.1, 012017 (2017).
15. P. Valente, "POSEYDON - Converting the DAFNE Collider into a double Positron Facility: a High Duty-Cycle pulse stretcher and a storage ring," arXiv:1711.06877 [physics.acc-ph].
16. L. Marsicano, these proceedings.

Searching For Dark Photon With Positrons At Jefferson Lab

Luca Marsicano[1,2,a)]

[1]*INFN, Sezione Di Genova, Via Dodecaneso, 33 - 16146 - Genova - Italy*
[2]*Universita' Di Genova, Via Balbi, 5 - 16126 - Genova - Italy*

[a)]luca.marsicano@ge.infn.it

Abstract. The interest in the Dark Photon (A' or U) has recently grown, since it could act as a light mediator to a new sector of Dark Matter particles. In this paradigm, the electron-positron annihilation can rarely produce a $\gamma A'$ pair. Various experiments (e.g. PADME@LNF [1], VEPP-3 [2]) have been proposed to detect this process using positron beams impinging on fixed targets. In such experiments, the energy of the photon from the $e^+e^- \rightarrow \gamma A'$ process is measured with an electromagnetic calorimeter and the missing mass is computed (the A' interacts weakly with Standard Model matter so it can't be detected). However, the A' mass range that can be explored with this technique is limited by the accessible energy in the center of mass frame, which goes as the square root of the beam energy.

The realization of a 11 GeV positron beam at Jefferson Lab would allow to search for A' masses up to $\sim$ 100 MeV, reaching unexplored regions of the A' parameter space. A preliminary study on the feasibility of a PADME-like experiment at Jefferson Lab has been carried out, assuming a 11 GeV positron beam with a $\sim 100\,nA$ current. The achievable sensitivity was estimated, studying the main sources of background (positron bremsstrahlung, annihilation into 2 gammas) using CALCHEP [3] and GEANT4 [4] simulations.

INTRODUCTION

Dark Matter (DM) existence is highly motivated by various astrophysical observations but its fundamental properties (interactions with the Standard Model, mass...) remain to date unknown. Experimental efforts have been mainly focused, until today, in the WIMPs search (Weakly Interacting Massive Particles): in this paradigm Dark Matter is made of particles with mass of order of $\sim 100 - 1000$ GeV interacting with the Standard Model via Weak force. However, no unequivocal evidence of WIMP has been found to date.

Recently, the interest in new scenarios predicting DM particles with lower masses has grown. Various models [5] postulate the existence of a hidden sector of χ particles (with masses in the MeV-GeV range) interacting with the visible world through new mediators, offering well-motivated opportunities for experimental exploration.

The simplest hidden sector model introduces one extra U(1) gauge symmetry [5] and a new gauge boson, the "Dark Photon" (A' or U). The interaction between the hidden sector and the SM can be generated effectively by a "kinetic mixing" mechanism between the SM photon and the A':

$$L_{mix} = -\frac{\epsilon}{2} F^{\mu\nu} F'_{\mu\nu},$$

where $F_{\mu\nu}$ is the usual electromagnetic tensor, $F'_{\mu\nu}$ is the Dark Photon tensor and ϵ is the mixing coupling constant. In this scenario, SM particles acquire a dark "millicharge" proportional to ϵ^2. The value of ϵ can be so small as to preclude the discovery of the A' in the experiments carried out so far.

The decay of the A' depends on the ratio between its mass and the mass of the dark sector particles: if the dark photon mass is smaller than twice the muon mass and no dark sector particle lighter than the A' exist, it can only decay to e^+e^- pairs ("Visible Decay"). If the mass of the A' is higher than twice the mass of the χ, it may also decay to $\chi\bar{\chi}$ pairs ("Invisible Decay"). In this work we'll address this last scenario (see Fig. 1).

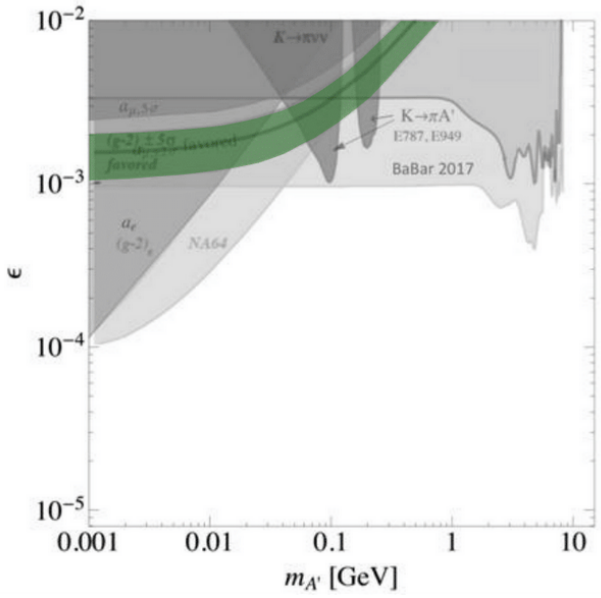

FIGURE 1. Current exclusion limits for A' invisible decay.

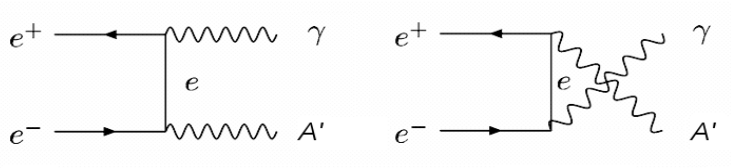

FIGURE 2. A' production via e^+e^- annihilation.

Searching For A' With Positrons - The PADME Experiment

A' can be produced in e^+e^- annihilation, via the process (see Fig. 2):

$$e^+e^- \to \gamma A';$$

several experiments have been proposed to search for the production of A' in this process. PADME (Positron Annihilation into Dark Matter Experiment) [1] is one of the first e^+ on target experiment searching for A'. It uses the 550 MeV positron beam provided by the *DAΦNE* linac at LNF (Laboratori Nazionali di Frascati) impinging on a thin diamond target.

The outline of the experiment is the following: the photon from the annihilation is detected with a BGO electromagnetic calorimeter placed $\sim$ 2 m downstream the target, while the A' leaves the detector area without interacting. A magnetic field of $\sim$ 1 T bends away from the calorimeter the positron beam and all the charged particles produced in the target. A single kinematic variable, the missing mass, is computed for each event:

$$M^2_{miss} = (P_{e^-} + P_{beam} - P_{\gamma})^2$$

its distribution is peaked at $M^2_{A'}$ for the process $e^+e^- \to \gamma\gamma$.

All processes resulting in a single γ hitting the calorimeter represent the background for the experiment:

- Bremsstrahlung
- Annihilation into 2γ: $e^+e^- \to \gamma\gamma$

- Annihilation into 3γ: $e^+e^- \rightarrow \gamma\gamma\gamma$

To reduce the bremsstrahlung background, the PADME detector features an active veto system composed of plastic scintillating bars: positrons losing energy via bremmstrahlung in the target are detected in the vetos, allowing to reject the event. However the high bremsstrahlung rate is an issue for this class of experiments, limiting the maximum viable beam current. For this reason, a beam with a continuous structure would be the best option for PADME-like experiments.

Moreover, the sensitivity of PADME in the A' parameter space is constrained by the available energy in the center of mass frame: with a beam energy of $\sim$ 500 MeV PADME can search for masses up to 22.5 MeV. Higher energy positron beams are required to exceed these limits. In the following section, the achievable sensitivity of a Dark Photon experiment using a continuous 11 GeV e^+ beam is discussed.

Searching For A' With Positrons At Jefferson Lab

Detector Setup

The setup considered in this work, shown in Figure 3, features the following elements:

1. 100 μm carbon target: carbon is a good compromise between density and a low Z/A ratio to minimize bremsstrahlung events.
2. 50 cm radius highly segmented ($1 \times 1 \times 20\ cm^3$ crystals) electromagnetic calorimeter placed 10 m downstream the target. Assumed energy resolution: $\frac{\sigma(E)}{E} = \frac{0.02}{\sqrt{E(GeV)}}$
3. Active veto system with a detection efficiency higher than 99.5% for charged particles.
4. Magnet capable of a field of 1 T over a region of 2 m downstream the target to bend the positron beam.

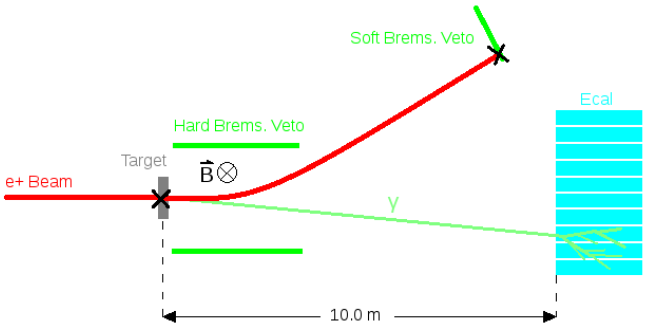

FIGURE 3. Outline of the proposed experiment at Jefferson Lab.

Beam Parameters

The following beam parameters are assumed:

- Current: 10-100 nA;
- Energy: 11 GeV (corresponding to a maximum mass value for the A' of $\sim$ 106 MeV
- Momentum dispersion: $< 1\%$
- Angular dispersion: < 0.1 mrad

It is important to note that momentum and angular dispersion are critical parameters for this kind of experiment, since a good knowledge of the beam particles initial state is fundamental to the missing mass computation.

Background Evaluation

In order to evaluate the sensitivity of the experiment it is necessary to study the reconstructed missing mass distribution for the background events. As discussed previously, main background processes for such an experiment are bremsstrahlung and electron-positron annihilation into 2 or 3 gammas, which can result in a single hit in the calorimeter. To study these processes, different strategies were adopted.

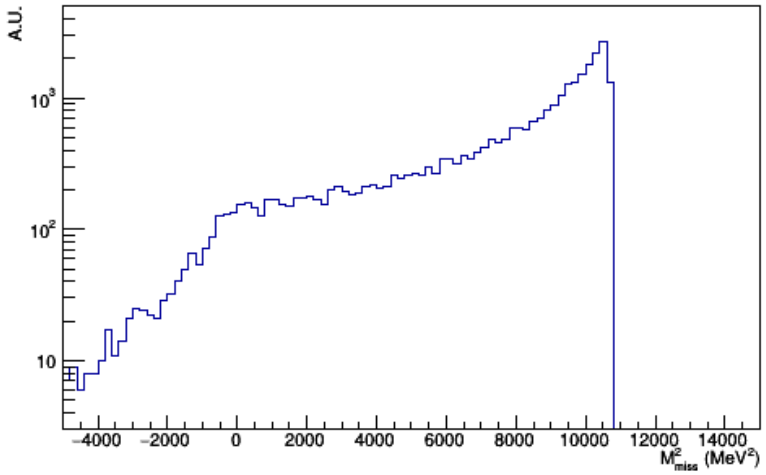

FIGURE 4. Computed missing mass spectrum from bremsstrahlung events.

For the bremsstrahlung background, a full GEANT4 [4] simulation of the positron beam impinging on the target was performed. For all bremsstrahlung photons reaching the calorimeter volume, the missing mass was computed, accounting for the detector angular and momentum resolution. Figure 4 shows the obtained spectrum. The total rate of expected bremsstrahlung events for positron on target (POT) was scaled accounting for the effect of the veto system.

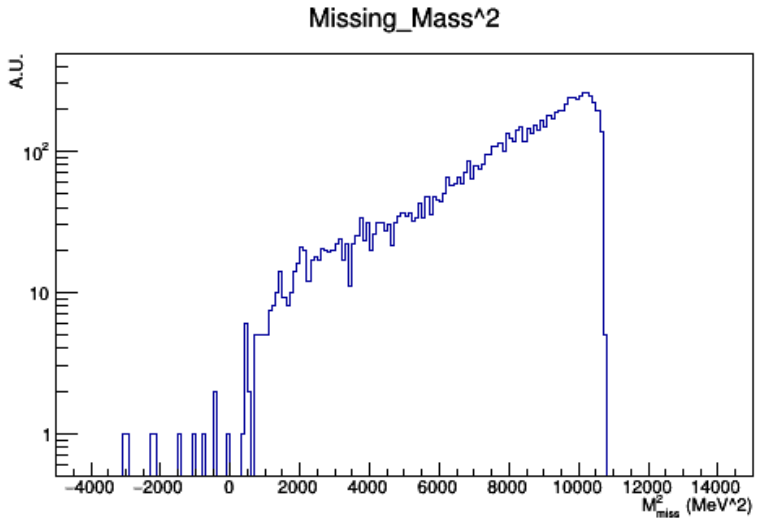

FIGURE 5. Computed missing mass spectrum from annihilation into 3 gammas events.

The annihilation into 2 or 3 gammas is much less frequent than bremsstrahlung and was therefore studied in a different way: events were generated directly using CALCHEP [3] which provided also the total cross sections for

the processes. As in the case of bremsstrahlung, missing mass spectrum was computed for event with a single gamma hit in the calorimeter. This study proved that, if an energy cut of 600 MeV is applied, the 2 gammas background becomes negligible. This is due to the closed kinematics of the $e^+e^- \to \gamma\gamma$ process: asking for only one photon to hit the detector translates in a strong constraint on its energy. This argument is not valid for the 3 gammas: the number of background events from this process is in fact not negligible (see Fig. 5 for the missing mass spectrum).

Signal Simulation

Signal events were simulated using CALCHEP. The widths $\sigma(m_{A'})$ of the missing mass distributions of the measured recoil photon from the $e^+e^- \to \gamma A'$ process were computed for six different values of the A' mass in the 1-103 MeV range. Figure 6 shows results for 4 mass values: the missing mass resolution for the signal is maximum for high A' masses and low for a "light" A' ($M_A < 50$ MeV).

As for the annihilation background, CALCHEP provides the total cross section of the process, for $\epsilon = 1$. To obtain the cross section for different values of ϵ, it is necessary to multiply it for ϵ^2.

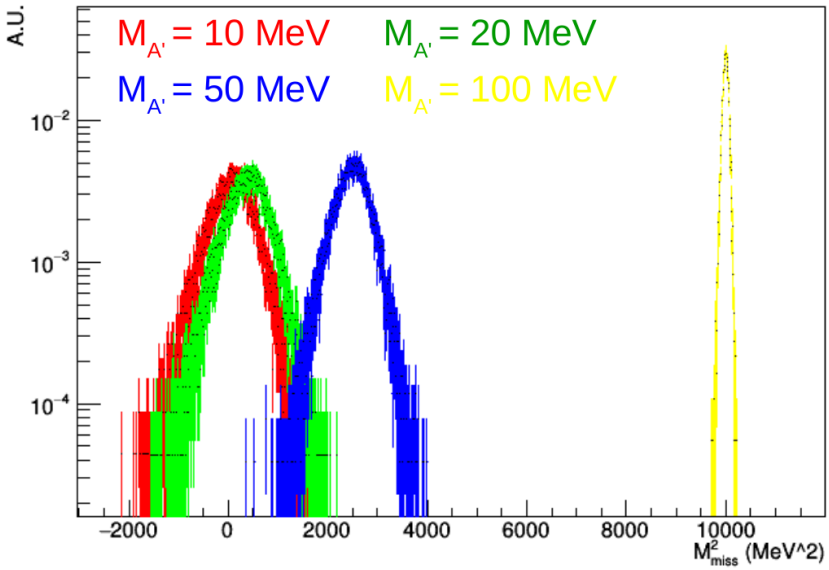

FIGURE 6. Computed missing mass spectrum for signal events with 4 different values of $m_{A'}$.

Evaluation Of The Experimental Reach

To obtain the reach of the experiment, the signal and background spectra discussed in the previous sections were used as follows:

- A measurement run of 180 days at 10 and 100 nA beam current is considered.
- Be $N_s(m_{A'})$ the number of expected signal events for a given mass value $m_{A'}$ and for $\epsilon = 1$
- Be $N_B(m_{A'})$ the number of expected background events (both from bremsstrahlung and 3 gammas annihilation) with computed missing mass in the interval:

$$[m^2_{A'} - 2\sigma(m^2_{A'}),\ m^2_{A'} + 2\sigma(m^2_{A'})]$$

The minimum measurable ϵ^2 value is given by:

$$\epsilon^2_{min}(m_{A'}) = 2\frac{\sqrt{N_B(m_{A'})}}{N_S(m_{A'})}$$

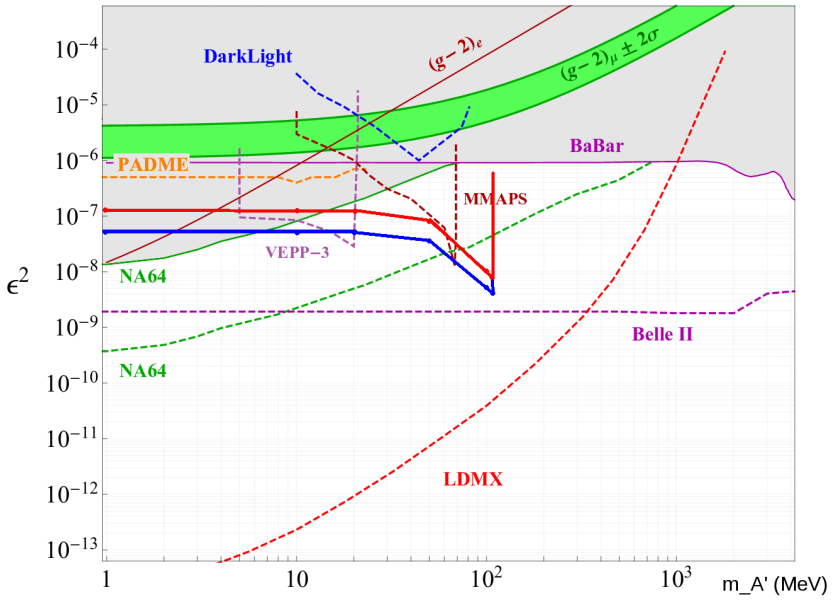

FIGURE 7. Projected exclusion limits in the A' invisible decay parameter space for a 180 days experiment with a 10 nA (red curve) and 100 nA (blue curve) 11 GeV positron beam at Jefferson Lab.

Curves indicating the obtainable reach are shown in Fig. 7: even with a current of 10 nA, a positron experiment searching for A' at Jefferson Lab would exceed the sensitivity of others current experiment, probing a significant region of the unexplored parameter space.

Conclusions

A preliminary study of the achievable sensitivity for a Dark Photon experiment with a 11 GeV positron beam at Jefferson Lab was carried out. The assumptions made on the detector performance (electromagnetic calorimeter resolution, veto system efficiency) are consistent with existing detectors. This work proves that this experiment would probe unexplored regions of the parameter space, exceeding in sensitivity other missing mass experiments. The unique features of a positron beam at Jefferson Lab (high energy, continuous structure, good angular and momentum resolution) would make it the best option for this class of experiments.

REFERENCES

[1] M. Raggi and V. Kozhuharov, Adv. High Energy Phys. **2014**, p. 959802 (2014), arXiv:1403.3041 [physics.ins-det] .

[2] B. Wojtsekhowski *et al.*, (2017), arXiv:1708.07901 [hep-ex] .

[3] A. Pukhov, (2004), arXiv:hep-ph/0412191 [hep-ph] .

[4] S. Agostinelli *et al.* (GEANT4), Nucl. Instrum. Meth. **A506**, 250–303 (2003).

[5] B. Holdom, Physics Letters B **166**, 196 – 198 (1986).

Positron Beams and Two-Photon Exchange: The Key to Precision Form Factors

Jan C. Bernauer[1,a)]

[1]*Massachusetts Institute of Technology, 77 Massachusetts Avenue, Cambridge, MA 02139, USA*

[a)]Corresponding author: bernauer@mit.edu

Abstract. The proton elastic form factor ratio can be measured either via Rosenbluth separation in an unpolarized beam and target experiment, or via the use of polarization degrees of freedom. However, data produced by these two approaches show a discrepancy, increasing with Q^2. The proposed explanation of this discrepancy—two-photon exchange—has been tested recently by three experiments. The results support the existence of a small two-photon exchange effect but cannot establish that theoretical treatment at the measured momentum transfers are valid. At larger momentum transfers, theory remains untested. This paper investigates the possibilities of measurements at DESY and Jefferson Lab to measure the effect at larger momentum transfers.

INTRODUCTION

Over more than half a century, proton elastic form factors have been studied in electron-proton scattering with unpolarized beams. These experiments have yielded data over a large range of four-momentum transfer squared, Q^2. The form factors were extracted from the cross sections via the so-called Rosenbluth separation. Among other things, they found that the form factor ratio $\mu G_E/G_M$ is in agreement with scaling, i.e., that the ratio is constant. Somewhat more recently, the ratio of the form factors was measured using polarized beams, with different systematics and increased precision especially at large Q^2. However, the results indicate a roughly linearly fall-off of the ratio. This discrepancy can be seen in Fig. 1, which includes a selection of unpolarized and polarized beam measurements and recent fits.

The resolution of this "form factor ratio puzzle" is crucial to advance our knowledge of the proton form factors, and with that, of the distribution of charge and magnetization inside the proton.

TWO-PHOTON EXCHANGE

As a possible explanation for the form factor ratio discrepancy, Blunden et al. [14] suggested that hard two-photon exchange (TPE), neglected in standard radiative corrections, could be an important effect in Rosenbluth-type experiments. Two-photon exchange corresponds to a group of diagrams in the second order Born approximation of lepton scattering, namely those where two photon lines connect the lepton and proton. The so-called "soft" case, when one of the photons has negligible momentum, is included in the standard radiative corrections, like ref. [15, 16], to cancel infrared divergences from other diagrams. The "hard" part, where both photons can carry considerable momentum, is not. It is important to note here that the division between soft and hard part is arbitrary, and different calculations use different prescriptions.

Theoretical calculations

A full description of the available theoretical calculations are outside of the scope of this paper. Suffice it to say that they can be roughly divided into two groups: hadronic calculations, e.g. [17], which should be valid for Q^2 from 0 up to a couple of GeV^2, and GPDs based calculations, e.g. [18], which should be valid from a couple of GeV^2 and up.

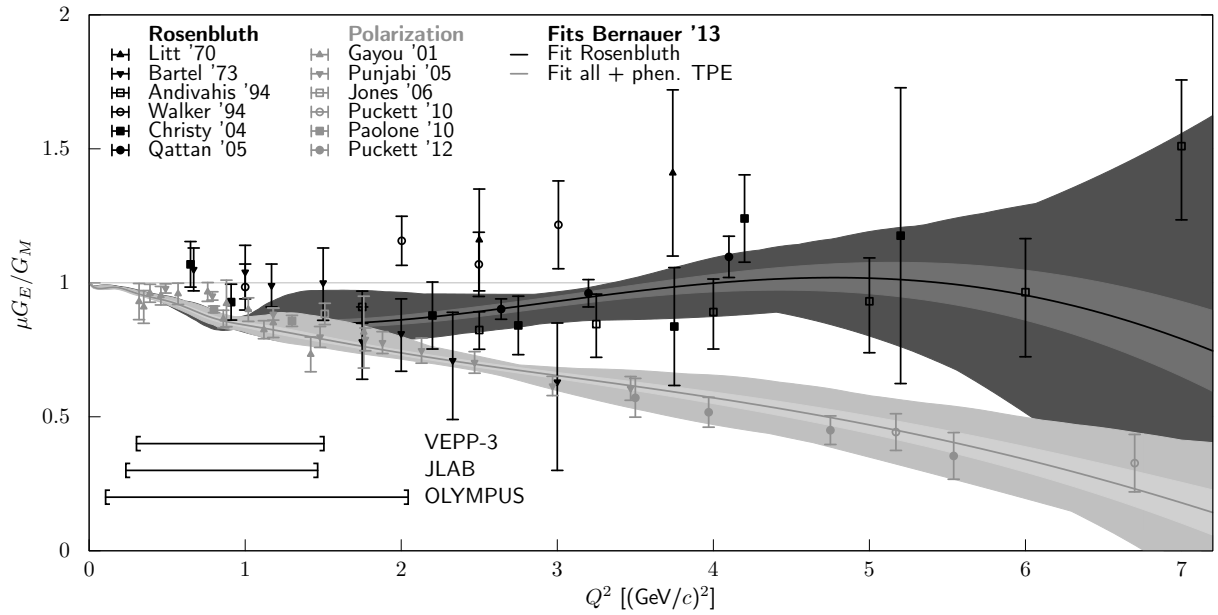

FIGURE 1. The proton form factor ratio $\mu G_E/G_M$, as determined via Rosenbluth-type (black points, from [1–6]) and polarization-type (gray points, from [7–12]) experiments. While the former indicate a ratio close to 1, the latter show a distinct linear fall-off. Curves are from a phenomenological fit [13], to either the Rosenbluth-type world data set alone (dark curves) or to all data, then including a phenomenological TPE model.

Phenomenological extraction

Assuming that TPE is indeed the only (or at least the dominant) source of the discrepancy, it is possible to extract the size of the effect directly from the available data. For example, in [13], the authors built a model based on the following assumptions:

- TPE dominantly affects the Rosenbluth-type experiments, leaving polarization data unchanged.
- The effect is roughly linear in ϵ. This is supported by the fact that no strong deviations from a straight line have been found in Rosenbluth separations so far.
- The effect vanishes for forward scattering, i.e., for $\epsilon = 1$.
- For $Q^2 \to 0$, TPE is given by the Feshbach Coulomb correction [19]. Modern theoretical calculations have the same limit.

Assuming a correction of the form $1 + \delta_{TPE}$ to the cross section, with

$$\delta_{TPE} = \delta_{\text{Feshbach}} + a(1-\epsilon)\ln(1 + b * Q^2), \tag{1}$$

the authors could fit the combined world data set with excellent χ^2. This extraction will be used in the following to predict the size of the effect.

THE CURRENT STATUS

Three contemporary experiments have tried to measure the size of TPE, based at VEPP-3 [20], Jefferson Lab (CLAS, [21]) and DESY (OLYMPUS, [22]) The next order correction to the first order Born calculation of the elastic lepton-proton cross section contains terms corresponding to the product of the diagrams of one-photon and two-photon exchange. These terms change sign with the lepton charge sign. It is therefore possible to determine the size of TPE by measuring the ratio of positron to electron scattering: $R_{2\gamma} = \frac{\sigma_{e^+}}{\sigma_{e^-}} \approx 1 + 2\delta_{TPE}$.

Figure 2 depicts the difference of the data of the three experiments to the calculation by Blunden et al. [17] and the phenomenological prediction by Bernauer et al. [23]. It can be seen that the three data sets are in good agreement

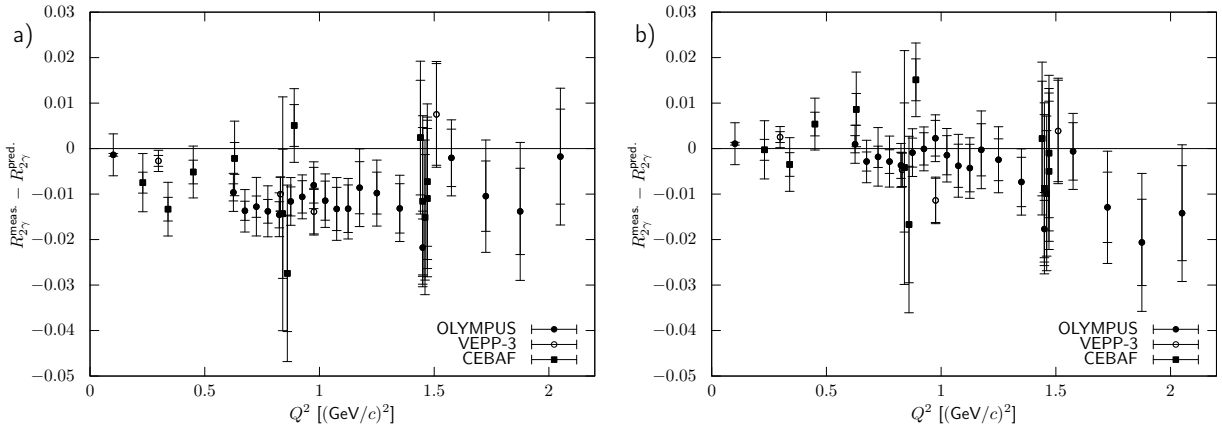

FIGURE 2. Difference of the data of the three recent TPE experiments [20–22] to the calculation in [17] (a) and the phenomenological prediction from [23] (b).

which each other, and appear about 1% low compared to the calculation. The prediction appears closer for most of the Q^2 range, however over-predicts the effect size at large Q^2. This is worrisome, as this coincides with the opening of the divergence in the fits depicted in Fig. 1 and might point to an additional effect beyond TPE that drives the difference.

The combination of the experiments prefer the phenomenological prediction with a reduced χ^2 of 0.68, the theoretical calculation achieves a red. χ^2 of 1.09, but is ruled out by the normalization information of both the CLAS experiment and OLYMPUS to a 99.6% confidence level. No hard TPE is ruled out with a significantly worse red. χ^2 of 1.53.

The current status can be summarized as such:

- TPE exists, but is small in the covered region.
- Hadronic theoretical calculations, supposed to be valid in this kinematical regime, might not be good enough yet.
- Calculations based on GPDs, valid at higher Q^2, are so far not tested at all by experiment.
- A comparison with the phenomenological extraction allows for the possibility that the discrepancy might not stem from TPE alone.

We refer to [24] for a more in-depth review. The uncertainty in the resolution of the ratio puzzle jeopardizes the extraction of reliable form factor information, especially at high Q^2, as covered by the Jefferson Lab 12 GeV program. Clearly, new data are needed. In the following, we will discuss experimental possibilities.

NEXT GENERATION EXPERIMENTS

Effect size and figure of merit

As can be seen from Eq. 1, the size of TPE scales linearly with $1-\epsilon$, but only weakly with Q^2. The strongest signal is therefore at large Q^2 and small ϵ. The cross section, however, drops fast in the same limit. To find the optimal kinematics, a figure of merit can be constructed by the ratio of expected deviation of $R_{2\gamma}$ from 1 and the expected uncertainty:

$$FOM = \frac{\left|R_{2\gamma} - 1\right|}{\sqrt{\Delta^2_{\text{stat.}} + \Delta^2_{\text{syst.}}}} \tag{2}$$

Here, we split the total uncertainty into a statistical and a systematical part. We fix the latter to 1% for the following discussion.

Unfortunately, accelerators with positron beams in the relevant energy range are not very common. We discuss now the possibilities at two locations, DESY and Jefferson Lab.

Measurement at DESY

At DESY, a test beam facility is currently being proposed which would allow to do TPE measurements with a 60 nA beam. Due to constraints of allotted space and installation time, non-magnetic calorimetric detectors, such as the those designed for PANDA, would make suitable detectors. We assume five detector elements covering 10 msr each. The beam impinges on a 10 cm liquid hydrogen target. Figure 3 a) shows the FOM plot for 15 days per species. With a 2.85 GeV beam, the experiment could test TPE up to a Q^2 of about 4.5 GeV^2 with more than 5σ. The projected errors for such a measurement are shown in Fig. 3 b).

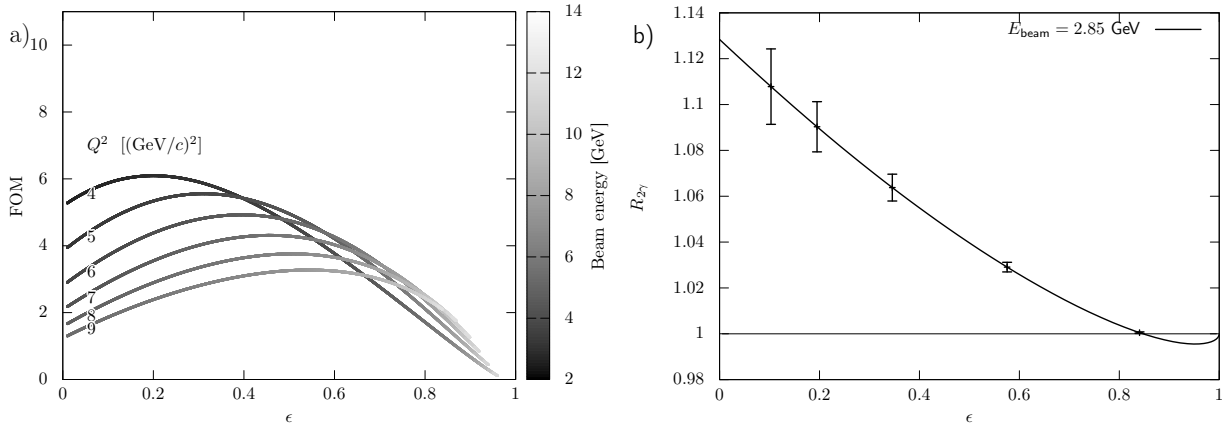

FIGURE 3. a) Figure of merit as a function of ϵ, for various Q^2, for 15 days of beam per species at DESY. b) Expected statistical error of data points and predicted effect size.

Measurement at Jefferson Laboratory

Jefferson Lab is evaluating the construction of a positron source for CEBAF. We assume that such a source would enable CEBAF to deliver up to 1 μA of unpolarized positrons into the experiment halls. We further assume a 10 cm liquid hydrogen target. This combination yields a luminosity of $\mathcal{L} = 2.6\,\text{pb}^{-1}\,\text{s}^{-1}$.

For the purpose of this work, we looked at the possibilities in Hall A and C. The main spectrometers of Hall A, with 6.7 msr acceptance, and the HMS spectrometer in Hall C are very versatile. The SHMS in Hall C is limited to forward angles, but could be used to detect the protons instead of the leptons, with the benefit of different systematical uncertainties. BigBite in Hall A is limited in the maximum momentum. However, the large acceptance allows measurements at very low values of ϵ with excellent figures of merit. Figure 4 depicts the figure of merit for 1 day per species, with the smaller-acceptance spectrometers represented by sub-figure a), and BigBite by sub-figure b).

A sketch of a possible measurement program for Hall A and Hall C is listed in Tab. 1 and Tab. 2, respectively.

TABLE 1. Proposed measurement program for Hall A

E_{beam}	3.1 GeV			3.55 GeV			4.01 GeV		
Spectrometer angles*	30°	70°	110°	52.7°	70°	110°	42.55°	70°	110°
Q^2 [(GeV/c)^2)]	1.79	3.99	4.75	3.99	4.75	5.56	3.99	5.55	6.4
ϵ	0.82	0.32	0.1	0.49	0.30	0.09	0.60	0.28	0.08
Time [days/species]		1			2			3	

* Central angles of the two main spectrometers followed by the central angle of BigBite.

Figure 5 show the estimated errors and predicted effect size for Hall A (a) and Hall C (b). A high-impact measurement is possible with a comparatively small amount of beam time. Even in the case the final positron beam current is lower than assumed here, the experiment remains feasible.

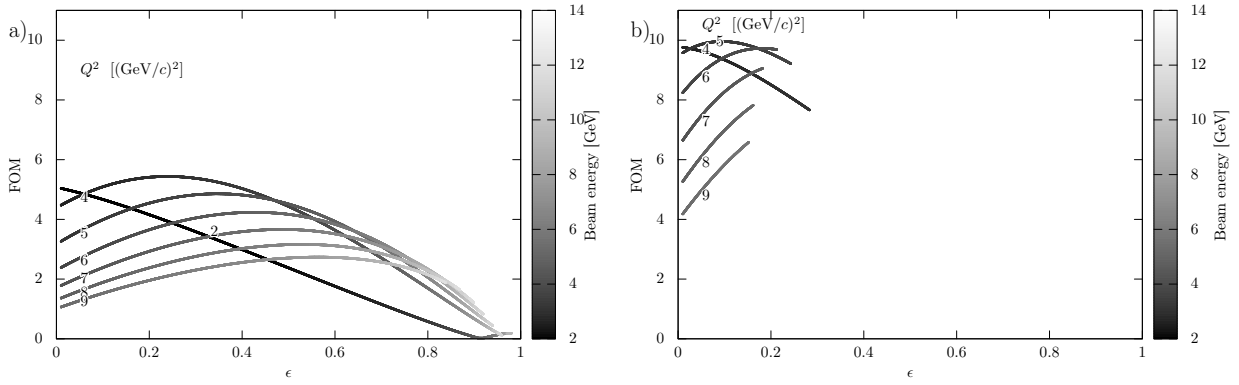

FIGURE 4. Figures of merit as a function of ϵ, for various Q^2, for 1 day of beam per species at Jefferson lab. Small acceptance spectrometers are represented by a), BigBite is represented by b).

TABLE 2. Proposed measurement program for Hall B

E_{beam}	3.1 GeV		3.55 GeV		4.01 GeV	
Spectrometer angles*	79.7°	7.64° (120°)	70°	9.95° (100°)	18°	16.57° (65°)
Q^2 [(GeV/c)^2)]	4.25	4.84	4.76	5.43	1.3	5.35
ϵ	0.244	0.06	0.302	0.122	0.935	0.33
Time [days/species]	3		2		1	

* Central angles for HMS (leptons) and SHMS (protons), with the equivalent lepton angle in parenthesis.

Systematic errors

The main benefit to measure both lepton species in the same beam time is the cancellation of many systematics which would affect the result if data of a new positron scattering measurement is compared to existing electron scattering data. For example, one can put tighter limits on the change of detector efficiency and acceptance changes between the two measurements if they are close together in time, or optimally, interleaved.

For the ratio, only relative effects between the species types are relevant; the absolute luminosity, detector efficiency, etc. cancel. Of special concern here is the luminosity. While an absolute luminosity is not needed, a precise determination of the species-relative luminosity is crucial. Precise relative measurement methods, for example based on Møller scattering, exist, but only work when the species is not changed. Switching to Bhabha scattering for the positron case and comparing with Møller scattering is essentially as challenging as as an absolute measurement. More suitable is a measurement of the lepton-proton cross section itself at extreme forward angles, i.e., $\epsilon \approx 1$, where TPE should be negligible small and the cross section is the same for both species. In OLYMPUS, a method exploiting the detection of multiple scattered particles from the same beam bunch has been used with great success [25].

CONCLUSION

The discrepancy in the form factor ratio is a serious obstacle in the exact determination of the proton form factors and a dedicated measurement program is needed to address this pressing issue. The proposed test beam area at DESY could host a first experiment to investigate TPE at larger momentum transfers on a short time line, but is ultimately limited in reach by the luminosity. At Jefferson Lab, an upgraded CEBAF would make more precise experiments at even larger momentum transfers possible. This would test both hadronic and GPD-based theoretical calculations of TPE, and allow us to extract a phenomenological model precise enough to analyze contemporary and future form factor measurements.

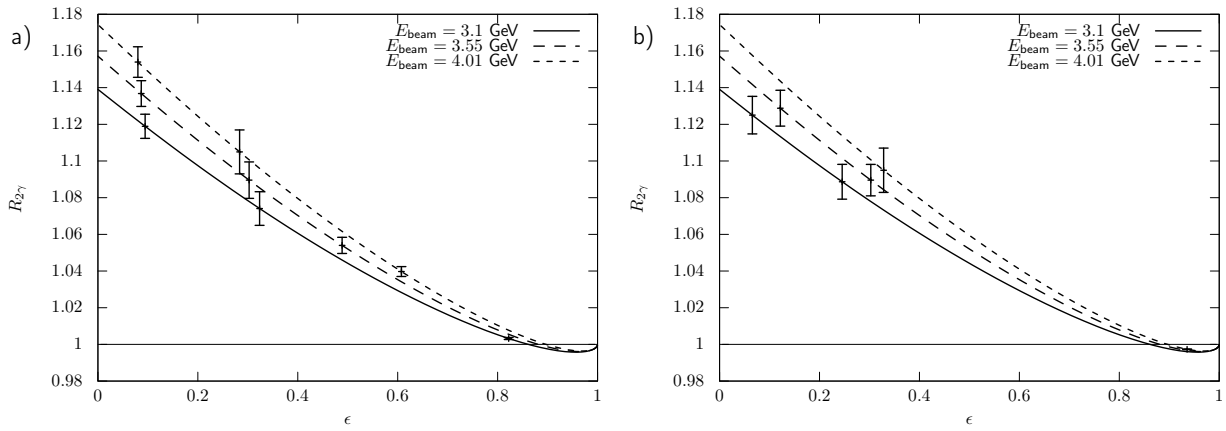

FIGURE 5. Predicted effect size and estimated errors for the proposed measurement program in Hall A (a) and Hall C (b).

ACKNOWLEDGMENTS

This work was supported by the Office of Nuclear Physics of the U.S. Department of Energy, grant No. DE-FG02-94ER40818.

REFERENCES

[1] J. Litt *et al.*, Phys. Lett. **B31**, 40–44 (1970).
[2] W. Bartel *et al.*, Nucl. Phys. **B58**, 429–475 (1973).
[3] L. Andivahis *et al.*, Phys. Rev. **D50**, 5491–5517 (1994).
[4] R. C. Walker *et al.*, Phys. Rev. **D49**, 5671–5689 (1994).
[5] M. E. Christy *et al.*, Phys. Rev. **C70**, p. 015206 (2004).
[6] I. A. Qattan *et al.*, Phys. Rev. Lett. **94**, p. 142301 (2005).
[7] O. Gayou *et al.*, Phys. Rev. **C64**, p. 038202 (2001).
[8] V. Punjabi *et al.*, Phys. Rev. **C71**, p. 055202 (2005).
[9] M. K. Jones *et al.* (Resonance Spin Structure Collaboration), Phys. Rev. **C74**, p. 035201 (2006).
[10] A. J. R. Puckett *et al.*, Phys. Rev. Lett. **104**, p. 242301 (2010).
[11] M. Paolone *et al.* (E03-104 Collaboration), Phys. Rev. Lett. **105**, p. 072001 (2010).
[12] A. J. R. Puckett *et al.*, Phys. Rev. **C85**, p. 045203 (2012).
[13] J. C. Bernauer *et al.* (A1 Collaboration), Phys. Rev. C **90**, p. 015206 (2014).
[14] P. G. Blunden, W. Melnitchouk, and J. A. Tjon, Phys. Rev. Lett. **91**, p. 142304 (2003).
[15] L. W. Mo and Y.-S. Tsai, Rev. Mod. Phys. **41**, 205–235 (1969).
[16] L. C. Maximon and J. A. Tjon, Phys. Rev. **C62**, p. 054320 (2000).
[17] P. G. Blunden and W. Melnitchouk, Phys. Rev. **C95**, p. 065209 (2017).
[18] A. V. Afanasev *et al.*, Phys. Rev. **D72**, p. 013008 (2005).
[19] W. A. McKinley and H. Feshbach, Phys. Rev. **74**, 1759–1763 (1948).
[20] I. A. Rachek *et al.*, Phys. Rev. Lett. **114**, p. 062005 (2015).
[21] D. Adikaram *et al.* (CLAS), Phys. Rev. Lett. **114**, p. 062003 (2015).
[22] B. S. Henderson *et al.* (OLYMPUS), Phys. Rev. Lett. **118**, p. 092501 (2017).
[23] J. C. Bernauer *et al.* (A1), Phys. Rev. **C90**, p. 015206 (2014).
[24] A. Afanasev *et al.*, Prog. Part. Nucl. Phys. **95**, 245–278 (2017).
[25] A. Schmidt *et al.*, Nucl. Instrum. Meth. **A877**, 112–117 (2018).

Measuring the Coulomb Sum Rule at JLab

Michael Paolone[1,2]

[1]*Temple University, USA*
[2]*(For the Jefferson Lab Hall-A E05-110 Collaboration)*

Abstract. In order to determine the Coulomb sum in nuclei, a precision measurement of inclusive electron scattering cross sections in the quasi-elastic region was performed at Jefferson Lab. Incident electrons with energies ranging from 0.4 GeV to 4 GeV scattered from ^4He,^{12}C,^{56}Fe and ^{208}Pb nuclei at four scattering angles ($15°, 60°, 90°, 120°$) and scattered energies ranging from 0.1 GeV to 4 GeV. The Rosenbluth separation method is used to extract the transverse and longitudinal response functions at three-momentum transfers in the range 0.55 GeV/c $\leq$ $|\mathbf{q}|$ $\leq$ 1.0 GeV/c. The impact of a similar positron beam measurement, and its importance in testing coulomb corrections used to extract the Born cross-section, will be discussed.

PHYSICS MOTIVATION

The question of how and by how much the structure of constituent nucleons bound in a nucleus are modified has intrigued the nuclear physics community for many decades now. One experimental method of testing medium modifications of the electric Sachs form-factor of bound nucleons involves testing the Coulomb Sum Rule (CSR) through inclusive quasi-elastics lepton scattering off of nuclear targets. The CSR is defined as the integral of the longitudinal response divided by the charge-weighted electric form-factor for a fixed virtual photon momentum $|q|$ over all possible virtual photon energies ω, see Equation 1. At momentum transfer well above the fermi-momentum one would expect the CSR to be unity in the absence of short-range correlations, relativistic effects, and medium modified nucleon structure. In the kinematic regime where short-range correlations and relativistic effects are expected to be small, then any significant deviation of the CSR from unity would be evidence of a modified electric form-factor.

$$S_L(|\mathbf{q}|) = \frac{1}{Z}\int_{\omega^+}^{|\mathbf{q}|} \frac{R_L(\omega,|\mathbf{q}|)}{\tilde{G}_E^2} d\omega \tag{1}$$

E05-110 EXPERIMENTAL DESIGN

Jefferson Lab Hall-A experiment E05-110 [1] ran from October 23rd 2007 to January 16th 2008. It used an electron beam at energies between 0.4 and 4.0 GeV incident on targets ^{4}He, ^{12}C, ^{56}Fe, and ^{208}Pb. Data was collected in two spectrometer arms, independently, and at scattering angles of 15°, 60°, 90°, and 120° to allow for a high precision extraction of the longitudinal response function through the Rosenbluth separation method. A large range of beam energies and scattered-electron momenta were used to allow for interpolation of cross-sections over a range of constant-$|q|$ between 550 to 1000 MeV/c.

COULOMB DISTORTIONS AND THE EFFECTIVE MOMENTUM APPROXIMATION

One complication in extracting a clean CSR measurement is correctly accounting for the coulomb screening and focusing that is known to occur when an incident electron approaches a highly charged nucleus. The scattering result can be calculated, quite tediously, through solving the Dirac equation radially for each term in a partial wave expansion of the nuclear field. A complete calculation for each scattering event becomes unrealistic for large data samples such as those found in E05-110. Instead, an effective momentum approximation (EMA) is used, which

applies a correction to the virtual photon momentum (q_{eff}), based on a mean potential calculated from the radius and charge of the nucleus, see Equation 2.

$$V_0 = \frac{3\alpha Z}{2r_c} \tag{2}$$

$$Q^2_{eff} = 4(k_i - \kappa_A V_0/c)(k_f - \kappa_A V_0/c)\sin^2(\theta/2) \tag{3}$$

$$q_{eff} = \sqrt{\omega^2 + Q^2_{eff}} \tag{4}$$

The potential is then tuned against full Dirac calculations (using κ_A in Eq. 3)[2]. EMAs have been widely used on many nuclear scattering experiments and methods have been cross-checked between different theoretical groups [3]. All CSR data is corrected using the EMA. The corrections are largest with the heaviest nuclei and lowest momentum-transfer. For E05-110, the 120° data on ^{208}Pb have the largest coulomb corrections, which result in corrections to the cross-section above $\approx 10\%$, see Fig. 1.

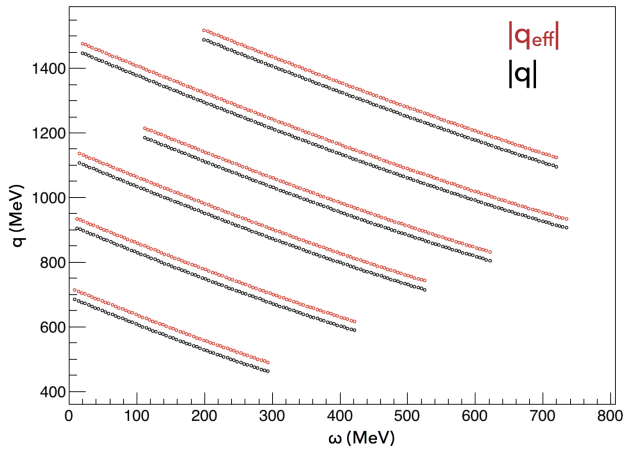

FIGURE 1. The adjustment to the $|q|$-ω phasespace from the expected EMA correction on ^{208}Pb 120° data from E05-110.

EXISTING VERIFICATION OF THE EMA

The most straight-forward way to test the validity of EMA is through comparing positron to electron scattering off of heavy nuclei. By keeping the same beam energy and angle, one can see the direct result of the coulomb field on the scattering process. Such an analysis has been performed by Gueye *et. al.* at Saclay [4]. For positron and electron beams at 420 MeV incident on lead targets, the scattered lepton was detected at 60°. A comparison of the reduced cross-sections show a clear difference between the data. Furthermore, after applying the expected EMA correction to the positron data, both cross-sections come into agreement, see Fig. 2.

CSR AND FUTURE POSSIBILITIES WITH POSITRON BEAMS

Although coulomb corrections are largest at low beam energies on heavier targets, the correction is applied to all data when calculating the CSR. At larger momentum transfer, there is no existing positron data to confirm EMA. It is important to test the validity of the EMA corrections in this regime, especially in kinematic regions where the slope of the Rosenbluth fit may be susceptible to slight changes in the cross-section. For this reason, collecting inclusive positron scattering data at large momentum transfer would be invaluable to validate the currently used EMA corrections.

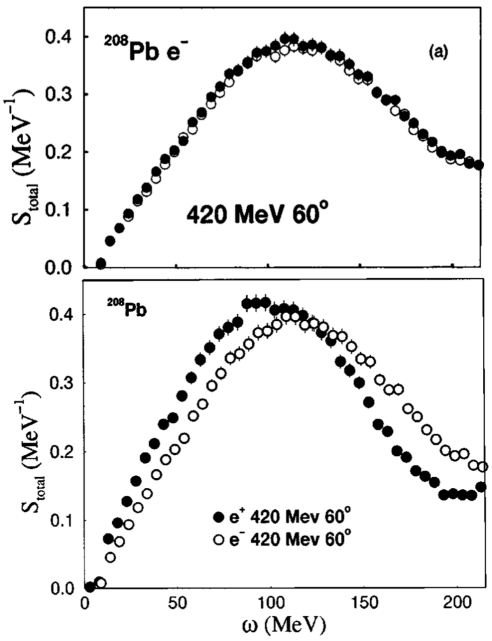

FIGURE 2. Figures are from Gueye *et. al.* [4], 420 MeV beam energy incident on ^{208}Pb target with scattered lepton detected at 60°. Top plot: Positron and electron beam cross-section comparison after EMA corrections on positron data ($E_{e-} = E_{e+} - 2|V_C|$). Bottom plot: Positron and electron cross-sections before EMA correction.

ACKNOWLEDGMENTS

This work is supported in part by the U.S. Department of Energy Grant Award DE-FG02-94ER4084.

REFERENCES

[1] The E05-110 proposal can be found at https://www.jlab.org/exp_prog/proposals/05/PR05-110.pdf.
[2] A. Aste and D. Trautmann, Can. J. Phys. **83**, 1001–1006 (2005), arXiv:gr-qc/0509007 [gr-qc] .
[3] S. J. Wallace and J. A. Tjon, Phys. Rev. **C78**, p. 044604 (2008), arXiv:0808.2029 [nucl-th] .
[4] P. Gueye *et al.*, Phys. Rev. **C60**, p. 044308 (1999).
[5] P. Gueye *et al.*, Phys. Rev. **C57**, 2107–2110 (1998).

Charge and spin asymmetries in elastic lepton-nucleon scattering

Oleksandr Koshchii[1,a)] and Andrei Afanasev[1]

[1]*The George Washington University, Washington, D.C. 20052, USA*

[a)]Corresponding author: koshchii@gwmail.gwu.edu

Abstract. Elastic lepton scattering off of a nucleon has proved to be an efficient tool to study the structure of the hadron. Modern cross section and asymmetry measurements at Jefferson Lab require effects beyond the leading order Born approximation to be taken into account. Availability of unpolarized beams of both electrons and positrons in respective experiments would enable to reduce systematic uncertainties due to higher-order charge-odd contributions. In addition, information on an unpolarized electron-to-positron cross section ratio could serve as a test for theoretical models that provide predictions for charge-dependent radiative corrections to elastic lepton-nucleon scattering. Availability of polarized beams of leptons would allow for even more comprehensive study of higher-order effects as some of them are dominant in polarized lepton-nucleon scattering asymmetries. We present a brief overview of effects due to the lepton's charge and target's polarization on elastic lepton-nucleon scattering measurements.

INTRODUCTION

Generally, most of unpolarized elastic electron/positron scattering measurements are analyzed in a framework of the one-photon exchange (OPE) approximation, shown in Fig. 1(a). This means that, in order to extract an equivalent OPE form, one needs to apply radiative corrections to the measured cross sections. These corrections include contributions that are generated by exchanges of virtual particles (Fig. 1(f)-(k)), as well as by unavoidable background contributions coming from the emission of real photons, called bremsstrahlung (Fig. 1(b)-(e)). Due to the infrared-divergent nature of radiative corrections, it is common to separate "soft" and "hard" photon radiation events. It should be mentioned here that there is no unique approach in separating the photon phase space into soft and hard regions - the most common prescriptions are those of Tsai [1] and Maximon and Tjon [2].

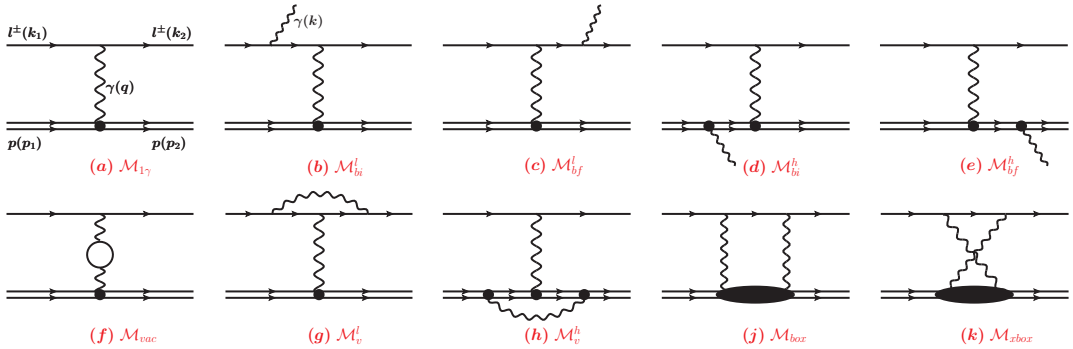

FIGURE 1. Leading and next-to-leading-order QED Feynman diagrams describing elastic lepton-nucleon scattering: (a) One-photon exchange, (b)-(c) Lepton bremsstrahlung, (d)-(e) Nucleon bremsstrahlung, (f) Vacuum polarization, (g) Lepton vertex correction, (h) Proton vertex correction, (j)-(k) Two-photon exchange.

The soft-photon contributions are infrared-divergent and independent of the structure of the hadron. They are generally well-understood and can be calculated analytically. In contrast, the hard-photon contributions are finite

and nucleon structure dependent. In practice of data analysis, the hard photon radiation effects can be minimized by experimental methods. However, due to finite detector resolution, a complete removal of such effects by pure experimental methods is not possible. In addition, accounting for a realistic detector geometry requires a complicated integration over the phase space of the emitted hard photon. As a result, we are constrained and must use the Monte Carlo (MC) technique to deal with this problem (see, e.g., Ref. [3, 4, 5]).

Recently, in unpolarized electron-proton scattering, a lot of attention [6, 7, 8, 9, 10, 11] has been brought to the two-photon exchange (TPE) corrections (Fig. 1(j)-(k)) beyond the soft-photon approximation contributions, which are usually incorporated in standard radiative corrections. These hard TPE contributions, which can provide a percent-level correction to the Born cross section, are believed to affect significantly the discrepancy in proton's electric-to-magnetic form factor ratio [12, 13, 14] and possess a proper magnitude to be included in future precision measurements. Despite substantial theoretical efforts being directed at understanding of the physics of TPE there is currently no complete calculation valid at all kinematics. More investigation on both theoretical and experimental forefront is needed.

Besides affecting significantly unpolarized lepton-proton scattering, TPE plays an important role in polarized scattering measurements. As it was pointed out by de Rujula et al. about three decades ago in Ref. [15], the imaginary part of the TPE amplitude dominates single-spin asymmetry (SSA) observables when either the beam or target is polarized perpendicularly to the lepton scattering plane in respective elastic scattering. This property of transverse SSAs opens up a unique opportunity to study TPE, as well as provides a direct access to effects beyond TPE, given that the beams of both polarities are available.

Lepton mass effects in unpolarized lepton-proton scattering

The square of the amplitude that describes elastic lepton-proton scattering and includes all the leading order radiative corrections can schematically be written as

$$\left|M\right|^2 = \left|M_{1\gamma}\right|^2 + \left|M_b^l\right|^2 + \left|M_b^h\right|^2 + 2\mathrm{Re}\left[M_{1\gamma}^\dagger M_{vac}\right] + 2\mathrm{Re}\left[M_{1\gamma}^\dagger M_v^l\right] + 2\mathrm{Re}\left[M_{1\gamma}^\dagger M_v^h\right] + 2\mathrm{Re}\left[M_{1\gamma}^\dagger M_{2\gamma}\right] + 2\mathrm{Re}\left[(M_b^l)^\dagger M_b^h\right]. \quad (1)$$

It appears that among all the summands in Eq. (1) only the interference between OPE and TPE amplitudes and between lepton and proton bremsstrahlung radiation (the last two terms) are the only charge-odd contributions. This means that hard TPE corrections can be directly extracted by studying the charge asymmetry between elastic l^+p and l^-p scattering cross sections after respective radiative corrections are applied. Until recently, radiative corrections calculated according to [1] or [2], which both assume the ultra-relativistic approximation (the lepton's mass m is much smaller than its energy ε_1), were sufficient enough. However, due to advances in technologies and increasing precision requirements of modern experiments, there is an ongoing demand in updating existing MC codes with contributions that do not employ the $m \ll \varepsilon_1$ approximation. In the following subsections we present the results of our update to a MC generator called Elradgen 2.0 [3] that accounts for the mass of the lepton in elastic $l^\pm p$ scattering. The update is essential for the future MUSE experiment [16] that is going to measure simultaneously elastic $e^\pm p$ and $\mu^\pm p$ scattering.

Soft TPE and bremsstrahlung

In the soft-photon exchange approximation, both charge-odd terms in Eq. (1) can be factorized by the square of the one-photon exchange amplitude, which means that we can write down the charge-dependent cross sections as

$$d\sigma^\pm = d\sigma_{1\gamma}(1 \pm \delta_{ch}), \quad (2)$$

where the charge-odd contribution is given by the respective asymmetry

$$\delta_{ch} = \frac{d\sigma^+ - d\sigma^-}{d\sigma^+ + d\sigma^-}. \quad (3)$$

We have accounted for the influence of the lepton's mass on model-independent contributions to the charge asymmetry δ_{ch} in unpolarized $l^\pm p$ scattering [17]. The calculation was performed according to the approach of Tsai. The graphical representation of our results for the asymmetry in kinematics of MUSE is shown in Fig. 2(c). Moreover, our MC generator had been re-adjusted to account for the lepton mass effects in charge-even contributions that consist of vacuum polarization, lepton vertex, and lepton bremsstrahlung corrections. Respective radiative corrections, which also include charge-odd contributions [17], are shown in Fig. 2(a)-(b).

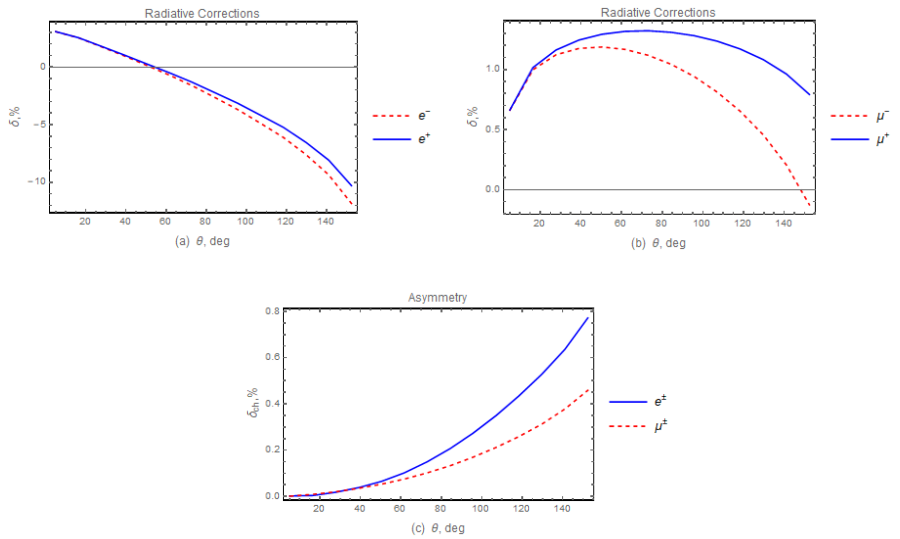

FIGURE 2. Radiative corrections and the soft-photon approximation asymmetry in unpolarized $l^{\pm}$ scattering. The beam's momentum is $|\vec{k}_1| = 115$ MeV.

It can clearly be seen from Fig. 2(c) that the lepton mass effects cannot be neglected in the considered kinematical setting whenever the precision goal is set on a sub-percent level. Moreover, the results shown in Fig. 2(a)-(b) demonstrate that the non-zero mass of the lepton considerably suppresses the emission of bremsstrahlung radiation.

Helicity-flip meson exchange estimations for $Q^2 \lesssim 0.5$ GeV^2

Besides affecting conventional radiative corrections, which are represented by the QED diagrams in Fig. 1(a)-(k), lepton mass effects in precision measurements of elastic $l^{\pm}p$ scattering with $\varepsilon_1 \lesssim m$ are expected to play a decisive role in t channel meson exchanges that are mediated by the two-photon coupling of the meson (see, e.g., Fig. 3). Such contributions are called helicity-flip transitions because of a direct proportionality to the mass of the lepton and appear to be charge-odd whenever their interference with the OPE amplitude (Fig. 1(a)) is considered. If not estimated properly for the scattering of non-ultra-relativistic leptons, e.g. in case of muon scattering in the MUSE experiment, helicity-flip transitions would lead to substantial theoretical uncertainties. In our study [18], we showed that in the kinematical region of MUSE the largest inelastic helicity-flip contribution is expected from the respective scalar σ meson exchange in the t channel. This contribution was computed to be at most $\sim 0.1\%$ for muons, and it appeared to be about three orders of magnitude larger than for electrons (see Fig. 4 for details). This supports an idea that at the given level of precision, one can safely neglect respective contributions in scattering of ulra-relativistic electrons/positrons. To perform our estimation, we parameterized the coupling of the meson to two virtual photons by making use of the vector meson dominance model, which is well justified at $Q^2 \lesssim 0.5$ GeV^2, including the kinematic region of MUSE. The calculation was done in part analytically and in part numerically using the LoopTools software [19]. Besides estimations of the respective charge-odd correction, we provided a first estimation of the effective coupling of the meson to the lepton. This estimation accounts only for the coupling of the virtual σ meson

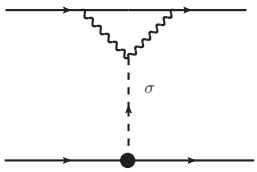

FIGURE 3. σ meson exchange in the t channel.

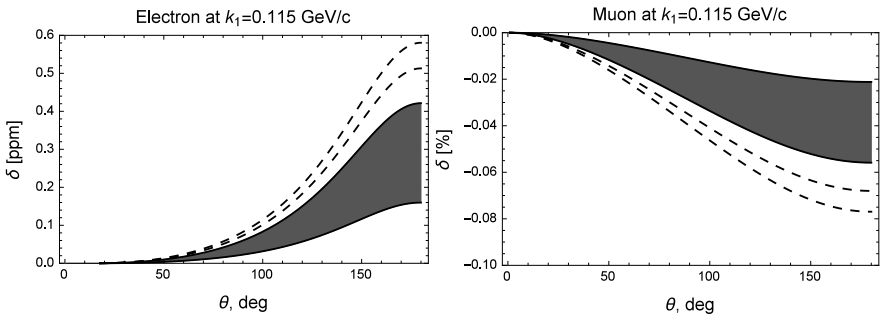

FIGURE 4. Charge-dependent correction due to the interference between the OPE and σ meson exchange in the t channel amplitudes (shaded and transparent regions represent different models that were used to perform the calculation; see Ref. [18] for details).

to the transversely polarized photons in the vector meson dominance model.

Transverse single-spin asymmetries in elastic electron-nucleon scattering

Due to time-reversal invariance of the electromagnetic interaction, the transverse SSA observable A_y^N in elastic lepton-nucleon scattering is zero in the Born approximation. Moreover, it can be shown [15] that the leading contribution to this asymmetry is given by the following expression:

$$A_y^N = \frac{\mathrm{Im}\left[T_{1\gamma}^{\dagger} \cdot \mathrm{Abs}(T_{2\gamma})\right]}{|T_{1\gamma}|^2} \sim \int d^3\vec{K}^* \, \mathrm{Im}\left(L^{\mu\alpha\beta} H_{\mu\alpha\beta}\right), \tag{4}$$

where $L^{\mu\alpha\beta}$ and $H_{\mu\alpha\beta}$ are the leptonic and hadronic tensors, the integral is performed over the phase space of the intermediate lepton, and the proportionality coefficient is well-known. It is also convenient to split $H_{\mu\alpha\beta}$ into two pieces: an elastic piece $H^{el}_{\mu\alpha\beta}$, which describes the intermediate nucleon state in the TPE loop (Fig. 1(j)), and an inelastic piece $H^{in}_{\mu\alpha\beta}$, which describes the intermediate state in the TPE loop that is not given by the nucleon. The greatest challenge in calculations of transverse asymmetries Eq. (4) is the lack of knowledge about the hadronic inelastic tensor $H^{in}_{\mu\alpha\beta}$. This stems from the fact that in the most general case of scattering at non-forward angles the hadronic tensor consists of 18 gauge invariant tensor structures and 18 independent amplitudes [20], which we have little information about. As a result, a number of models and approaches exist that parameterize the respective tensor in different kinematical settings [21, 22, 23, 24, 25]. These models employ the knowledge on the behavior of certain amplitudes in various kinematical limits (see, e.g., Ref. [26, 27]) and have been used to describe the measurements of beam-normal SSAs [28, 29, 30, 31].

Recently, a first non-zero target-normal SSA measurement was performed at Jefferson Lab on a polarized ^{3}He target [32]. By using the fact that this target can be considered as an effective polarized neutron target, the authors of Ref. [32] were able to extract a non-zero neutron-normal SSAs. The obtained asymmetries $A_y^n = -3.32 \pm 0.4 \pm 0.72\%$, $A_y^n = -1.78 \pm 0.2 \pm 0.66\%$, and $A_y^n = -1.38 \pm 0.14 \pm 0.24\%$, which correspond to $\varepsilon_1 = 1.245$ GeV and $Q^2 = 0.127$ GeV^2, $\varepsilon_1 = 2.425$ GeV and $Q^2 = 0.460$ GeV^2, and $\varepsilon_1 = 3.605$ GeV and $Q^2 = 0.967$ GeV^2, respectively, indicate that the inelastic TPE loop contribution is dominant in the considered kinematical region (our estimations of the elastic contribution are shown in Fig. 5). Currently, there exist no theoretical model that could be used for the description of neutron-normal SSAs at GeV beam energies and nearly forward scattering angles, including the results of Ref. [32]. The development of respective unitarity-based approach is underway.

Measurements of transverse SSAs in elastic lepton-nucleon scattering provide an extremely valuable information on the imaginary part of the TPE amplitude and can be used to improve our understanding of the structure of the hadron, thus contributing to advances in theory. Moreover, since transverse SSAs are expected to be of an opposite sign for beams of positively and negatively charged leptons, future experimental data on such asymmetries would lead to studies of multi-photon exchange physics beyond TPE.

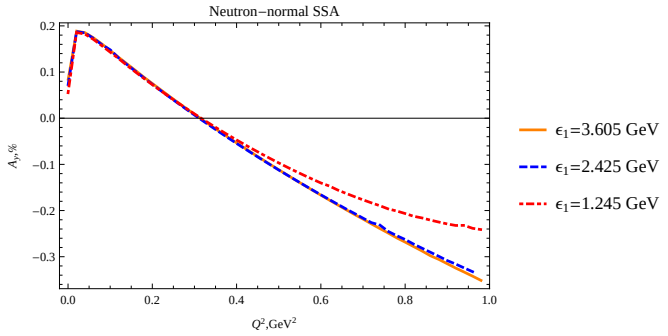

FIGURE 5. Intermediate elastic contribution to the neutron-normal SSA.

ACKNOWLEDGMENTS

O.K. is grateful to the organizers of the workshop for the financial support during his stay at JLab. This work was supported in part by the Gus Weiss Endowment of The George Washington University and in part by a JSA/JLab Graduate Fellowship Award 2016/2017.

REFERENCES

[1] Y.-S. Tsai, Phys. Rev. **122**, 1898–1907 (1961).
[2] L. C. Maximon and J. A. Tjon, Phys. Rev. C **62**, p. 054320 (2000).
[3] I. Akushevich, O. Filoti, A. Ilyichev, and N. Shumeiko, Comp. Phys. Comm. **183**, 1448 – 1467 (2012).
[4] A. V. Gramolin, V. S. Fadin, A. L. Feldman, R. E. Gerasimov, D. M. Nikolenko, I. A. Rachek, and D. K. Toporkov, J. Phys. G **41**, p. 115001 (2014).
[5] I. Akushevich, H. Gao, A. Ilyichev, and M. Meziane, Eur. Phys. J. A **51**, p. 1 (2015).
[6] C. E. Carlson and M. Vanderhaeghen, Annu. Rev. Nucl. Part. Sci. **57**, 171–204 (2007).
[7] J. Arrington, P. Blunden, and W. Melnitchouk, Prog. Part. Nucl. Phys. **66**, 782 – 833 (2011).
[8] A. Afanasev, P. Blunden, D. Hasell, and B. Raue, Prog. Part. Nucl. Phys. **95**, 245 – 278 (2017).
[9] I. A. Rachek *et al.*, Phys. Rev. Lett. **114**, p. 062005 (2015).
[10] D. Rimal *et al.* (CLAS Collaboration), Phys. Rev. C **95**, p. 065201 (2017).
[11] B. S. Henderson *et al.* (OLYMPUS Collaboration), Phys. Rev. Lett. **118**, p. 092501 (2017).
[12] P. G. Blunden, W. Melnitchouk, and J. A. Tjon, Phys. Rev. Lett. **91**, p. 142304 (2003).
[13] Y.-C. Chen, A. Afanasev, S. J. Brodsky, C. E. Carlson, and M. Vanderhaeghen, Phys. Rev. Lett. **93**, p. 122301 (2004).
[14] A. V. Afanasev, S. J. Brodsky, C. E. Carlson, Y.-C. Chen, and M. Vanderhaeghen, Phys. Rev. D **72**, p. 013008 (2005).
[15] A. D. Rjula, J. Kaplan, and E. de Rafael, Nucl. Phys. B **35**, 365 – 389 (1971).
[16] R. Gilman *et al.* (MUSE Collaboration), (2013), arXiv:1303.2160 .
[17] O. Koshchii and A. Afanasev, Phys. Rev. D **96**, p. 016005 (2017).
[18] O. Koshchii and A. Afanasev, Phys. Rev. D **94**, p. 116007 (2016).
[19] T. Hahn and M. Prez-Victoria, Comp. Phys. Comm. **118**, 153 – 165 (1999).
[20] R. Tarrach, Nuovo Cimento Soc. Ital. Fis. **28**, 409–422 (1975).
[21] A. V. Afanasev and N. Merenkov, Phys. Lett. B **599**, 48 – 54 (2004).
[22] B. Pasquini and M. Vanderhaeghen, Phys. Rev. C **70**, p. 045206 (2004).
[23] A. Afanasev, I. Akushevich, and N. P. Merenkov, "Nucleon Compton scattering with two space - like photons," (2002), pp. 142–150, arXiv:hep-ph/0208260 [hep-ph] .
[24] D. Borisyuk and A. Kobushkin, Phys. Rev. C **73**, p. 045210 (2006).
[25] M. Gorchtein and C. J. Horowitz, Phys. Rev. C **77**, p. 044606 (2008).
[26] D. Drechsel, B. Pasquini, and M. Vanderhaeghen, Phys. Rep. **378**, 99 – 205 (2003).
[27] F. Hagelstein, R. Miskimen, and V. Pascalutsa, Prog. Part. Nucl. Phys. **88**, 29 – 97 (2016).
[28] S. P. Wells *et al.*, Phys. Rev. C **63**, p. 064001 (2001).
[29] F. E. Maas *et al.*, Phys. Rev. Lett. **94**, p. 082001 (2005).
[30] D. S. Armstrong *et al.* (G0 Collaboration), Phys. Rev. Lett. **99**, p. 092301 (2007).
[31] S. Abrahamyan *et al.* (HAPPEX and PREX Collaborations), Phys. Rev. Lett. **109**, p. 192501 (2012).
[32] Y.-W. Zhang *et al.* (Jefferson Lab Hall A Collaboration), Phys. Rev. Lett. **115**, p. 172502 (2015).

Constraints On Parton Distribution Functions From Charged Current Deep Inelastic Scattering

J.F. Owens[1,a)]

[1]*Physics Department, 77 Chieftan Way, Florida State University, Tallahassee FL 32306, USA*

[a)]owens@hep.fsu.edu
URL: http://www.hep.fsu.edu/˜owens

Abstract. Progress in the determination of parton distribution functions (PDFs) relies on the ability to separately determine the PDFs corresponding to different parton flavors. In this talk I present some examples of what is currently known and discuss ways to improve the state-of-the-art using charged current deep inelastic scattering.

INTRODUCTION

It is well recognized that PDFs are important for precision calculations of large momentum transfer processes. Further, they are important for obtaining an understanding of the internal structure of hadrons. Hadronic observables may involve single PDFs or products of PDFs:

$$\sigma_A(x) = \sum_a \int dy\, G_{a/A}(x/y, Q)\, \hat{\sigma}_a(y) \tag{1}$$

or

$$\sigma_{AB}(x) = \sum_{a,b} \int dy \int dz\, G_{a/A}(y, Q)\, G_{b/B}(z, Q) \hat{\sigma}_{ab}(y, z) \delta(x - yz). \tag{2}$$

The challenge is to obtain data for appropriate observables in order to constrain PDFs over as large a kinematic region as possible. PDFs are obtained by fitting such data sets in what are known as Global Fits. Most such analyses have many features in common: DGLAP evolution, dependence on α_s, the order of perturbation theory used - next-to-leading order or, increasingly, next-to-next-to-leading order, target mass corrections, higher twist contributions, and nuclear corrections, as needed.

There are, however, some areas of difference which can include the treatment of heavy flavors, parametrization dependence, treatment of PDF errors, the choice of data sets, the choice of kinematic cuts, and the method of incorporating nuclear corrections. These differences can lead to variations in the resulting PDFs and their estimated errors. I will touch on some of these differences in the following.

The critical issues of current interest in PDF determinations can be summarized as all being related to "flavor separation." In the following I will discuss three areas: the behavior of the d/u ratio at large values of x, the determination of the $\bar{d}/\bar{u}$ ratio, and the determination of the $s \pm \bar{s}$ PDFs.

d/u AT LARGE VALUES OF x

In choosing lepton deep inelastic scattering (DIS) data sets to be included in a global fit one must specify cuts on both Q^2 and the squared mass of the produced hadronic system

$$W^2 = M^2 + Q^2\left(\frac{1}{x} - 1\right). \tag{3}$$

These cuts will limit the maximum reach in x for the data included in the fit. At fixed Q^2, lowering the W^2 cut increases the range of x that is included. One must lower these minimum values in order to be able to use data from lower energy experiments and to get to the large-x region [1]. This is shown explicitly in Fig. 1.

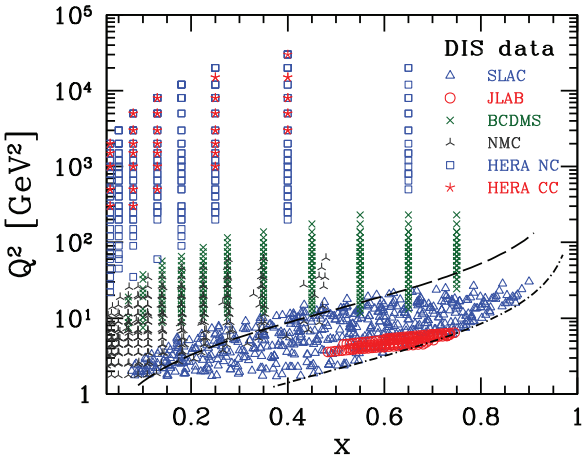

FIGURE 1. Kinematic coverage of various data sets. The lower curve shows the effect of $Q^2 > 1.69$ GeV^2 and $W^2 > 3$ GeV^2 while the dashed curve corresponds to $W^2 > 14$ GeV^2.

One can see that the reach in x is limited by the larger cut on W^2. Note that for the JLab 12 GeV program the maximum reach in Q^2 will almost double so that the reach in x will get close to $x = 0.85$.

An examination of the relative PDF errors in typical global fits shows that the errors increase significantly as one goes to larger values of x. The large-x region is dominated by the u and d PDFs , but the relative error on the d PDF is typically much larger than that on the u PDF. This is due to the charge weighting factors of 4/9 and 1/9 for the u and d PDFs, respectively, along with the fact that the d PDF falls more rapidly as x increases than does the u PDF. Ideally, one would like DIS data on a neutron target where the weighting factors would be reversed. However, the closest one can come to this is to use a deuterium target. This requires corrections for nuclear effects reflecting the fact that deuterium is a bound state of a proton and a neutron. These effects, especially those due to Fermi motion, can be significant, especially in the region above $x \sim 0.6$. Nuclear corrections for deuterium are model dependent, reflecting the choices made for the nuclear wavefunction, off-shell corrections, etc. Thus, even with lowered cuts on Q^2 and W^2 significant uncertainty on the d PDF remains.

To significantly reduce the error on the d PDF in the large-x region one needs a way to constrain the d PDF in the absence of nuclear corrections. The classic solution is to use neutrino DIS data taken with a proton target. At leading order one has as $x \to 1$

$$F_2^{\nu p} = 2x(d + s + \bar{u} + \bar{c}) \to 2xd \tag{4}$$

and

$$F_2^{\bar{\nu} p} = 2x(u + c + \bar{d} + \bar{s}) \to 2xu \tag{5}$$

so that at large values of x, $F_2^{\nu p}/F_2^{\bar{\nu} p} \sim d/u$. However, data on hydrogen from early bubble chamber experiments have low statistics and provide little constraint on d/u at large values of x. More recent high statistics experiments are performed on nuclear targets, thereby providing information on *nuclear* PDFs. However, extracting *nucleon* PDFs again requires the use of model-dependent nuclear corrections. Moreover, it is highly unlikely that experiments on a hydrogen target will be performed using modern high luminosity neutrino beams due to safety concerns.

One solution is to use the charged current interaction in the form of W production in $\bar{p}p$ interactions since the

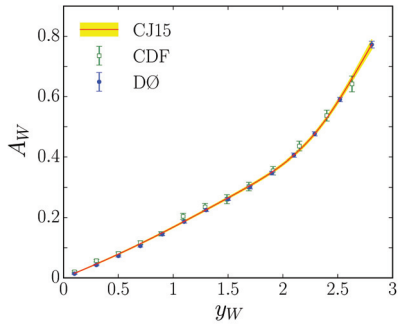

FIGURE 2. W asymmetry compared to the results from the CJ15 PDFs [2].

charged W asymmetry

$$A(y) = \frac{\sigma(W^+) - \sigma(W^-)}{\sigma(W^+) + \sigma(W^-)} \sim \frac{1 - d/u(x_1)}{1 + d/u(x_1)} \text{ with } x_1 \sim \frac{M_W}{\sqrt{s}} \exp(y) \tag{6}$$

at large W rapidity is sensitive to the d/u ratio.

The advantage here is that no nuclear corrections are needed. Indeed, since different nuclear models for the deuterium corrections result in different d PDFs, such collider data can help constrain the choice of the model used for the nuclear corrections [2].

Another solution, also based on using the charged current interaction, is to use line-reversed DIS processes. Again, for large values of x one has at leading order

$$e^+ p \to \overline{\nu} + X \text{ for which } F_2^{e^+ p,cc} \propto xd \tag{7}$$

and

$$e^- p \to \nu + X \text{ for which } F_2^{e^- p,cc} \propto xu. \tag{8}$$

Such measurements would allow the direct extraction of d/u at large values of x without the need for nuclear corrections. These processes were measured at HERA out to $x \simeq 0.4$. It is important to note that one would need good statistics at large values of x for these processes to provide useful constraints on the d PDF.

PROGRESS ON $\overline{d}$ AND $\overline{u}$ PDFs

The perturbative $g \to q\overline{q}$ vertex might lead one to expect that all the antiquark PDFs would be the same. However, this ignores various nonperturbative effects. For example, consider fluctuations involving pions such as

$$p \to \pi^+ n \text{ versus } p \to \pi^- \Delta^{++}$$

or, at the quark level

$$uud \to (u\overline{d})(ddu) \quad uud \to (d\overline{u})(uuu).$$

The latter is suppressed by mass effects so that one might expect $\overline{d} > \overline{u}$. This is confirmed by a measurement of the Gottfried Sum Rule by the NMC experiment [3] whereby

$$\int_0^1 \frac{dx}{x}(F_2^p(x) - F_2^n(x)) = \frac{1}{3} - \frac{2}{3}\int_0^1 dx(\overline{d}(x) - \overline{u}(x)) = 0.235 \pm 0.026.$$

A classic way for constraining antiquark PDFs is to use lepton pair production as in $pp \to \mu^+\mu^- + X$ or $pd \to \mu^+\mu^- + X$ which, at lowest order, are driven by the subprocess $q\overline{q} \to \mu^+\mu^-$. These processes yield information on the antiquark PDFs at low values of x and valence PDFs at large values of x. Experiment E866 at Fermilab measured this process using both p and d targets. The results are most easily interpreted using the approximate relation

$$\frac{\sigma^{pd}}{2\sigma^{pp}} \approx \frac{1}{2}(1 + \frac{\overline{d}}{\overline{u}}).$$

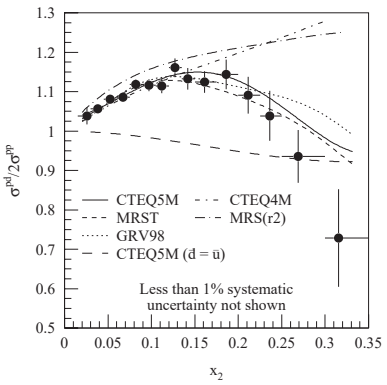

FIGURE 3. Data from E806 showing $\bar{d} > \bar{u}$ at low values of x.

The results[4] showed that $\bar{d} > \bar{u}$ over much of the measured range in x. However, the last few points suggested that $\bar{d} < \bar{u}$, something that is hard to accommodate in any physical picture of nonperturbative inputs. A new experiment, E906, is expected to have improved statistics and kinematic coverage.

It would be beneficial to have another way of constraining the $\bar{d}/\bar{u}$ ratio. Again, consider charged current structure functions in lowest order.

$$F_2^{e^+p,cc}(x, Q) = 2x(d + s + \bar{u} + \bar{c}),$$

$$F_2^{e^-p,cc}(x, Q) = 2x(u + c + \bar{d} + \bar{s}),$$

$$xF_3^{e^+p,cc}(x, Q) = 2x(d + s - \bar{u} - \bar{c}),$$

and

$$xF_3^{e^-p,cc}(x, Q) = 2x(u + c - \bar{d} - \bar{s}).$$

One can then separate the combinations $u + c$, $d + s$, $\bar{u} + \bar{c}$, and $\bar{d} + \bar{s}$. To the extent that $s \sim \bar{s}$ and $c \sim \bar{c}$, then one can obtain information on the valence combinations $u - \bar{u}$ and $d - \bar{d}$. When combined with other information on the u and d PDFs, one can obtain constraints on the $\bar{u}$ and $\bar{d}$ PDFs.

PROGRESS ON STRANGE QUARKS AND ANTIQUARKS

Historically, the best constraint on the strange PDF has come from neutrino production of muon pairs

$$\nu_\mu s \to \mu^- c \text{ followed by } c \to s\mu^+\nu_\mu$$

The opposite sign dimuon cross section is thus sensitive to the s PDF. Similarly, using a $\bar{\nu}_\mu$ beam gives sensitivity to the $\bar{s}$ PDF. Results[5] from the CCFR experiment suggests that

$$\kappa = \frac{s + \bar{s}}{\bar{u} + \bar{d}} \approx 0.4$$

However, some collider results for $W^\pm, Z$ production suggest a ratio closer to one[6] while Alekhin, Blümlein, and Moch[7] attribute at least some of the difference to a less flexible parametrization in the ATLAS analysis.

Is there an argument based on nonperturbative ideas that might shed some light on this? Consider

$$p \to K^+\Lambda$$

$$uud \to (u\bar{s})(sud).$$

The intermediate state is heavier than $\pi^+ n$ or $\pi^- \Delta^{++}$, thereby suggesting a nonperturbative $s\bar{s}$ contribution that is suppressed relative to the $\bar{d}$ and $\bar{u}$ PDFs [8]. This argument is in line with the neutrino DIS results. However, it should be kept in mind that the neutrino results are based on data taken with an iron target so that one is learning about iron PDFs, not those of a free nucleon. Furthermore, there are unknown nuclear corrections for the propagation of the produced charm meson through the nucleus. Therefore one would like to have a process free from nuclear effects.

Suppose that one were to measure charged current DIS processes with a muon tag to select charm final states:

$$e^+ s \to \bar{\nu} c \text{ followed by } c \to s\mu^+ \nu_\mu$$

and

$$e^- \bar{s} \to \nu \bar{c} \text{ followed by } \bar{c} \to \bar{s}\mu^- \bar{\nu}_\mu.$$

Note that the sign of the muon is the same as the sign of the initial state lepton. These processes are potentially capable of providing information on the strange PDFs and of separating s from $\bar{s}$.

CONCLUSIONS

Charged current measurements in $e^{\pm} p$ DIS are potentially capable of improving our knowledge of PDFs by providing:

1. Better constraints on d/u in the large x region
2. Additional constraints on $\bar{d}/\bar{u}$ to complement information from lepton pair production
3. Constraints on $\frac{s+\bar{s}}{\bar{u}+\bar{d}}$ without the need for nuclear corrections.

ACKNOWLEDGMENTS

I would like to thank Alberto Accardi for presenting this talk in my absence - hurricane Irma was passing by my house at the time I was scheduled to give this talk!

REFERENCES

[1] J. F. Owens, A. Accardi, and W. Melnitchouk, Phys. Rev. **D87**, p. 094012 (2013), arXiv:1212.1702 [hep-ph] .
[2] A. Accardi, L. T. Brady, W. Melnitchouk, J. F. Owens, and N. Sato, Phys. Rev. **D93**, p. 114017 (2016), arXiv:1602.03154 [hep-ph] .
[3] M. Arneodo *et al.* (New Muon), Phys. Rev. **D50**, R1–R3 (1994).
[4] R. S. Towell *et al.* (NuSea), Phys. Rev. **D64**, p. 052002 (2001), arXiv:hep-ex/0103030 [hep-ex] .
[5] J. Yu (NuTeV CCFR /), "Strange sea and alpha(s) measurements from neutrino N deep inelastic scattering at CCFR / NuTeV," in *QCD and high energy hadronic interactions. Proceedings, 33rd Rencontres de Moriond, Les Arcs, France, March 21-28, 1998* (1998), pp. 375–380, arXiv:hep-ex/9806030 [hep-ex] .
[6] G. Aad *et al.* (ATLAS), Phys. Rev. Lett. **109**, p. 012001 (2012), arXiv:1203.4051 [hep-ex] .
[7] S. Alekhin, J. Blumlein, and S. Moch, (2017), arXiv:1708.01067 [hep-ph] .
[8] A. W. Thomas, Phys. Lett. **126B**, 97–100 (1983).

Possibilities for learning about the nucleon spin structure with positrons and electrons

C. Van Hulse[1,a)]

[1] *University of the Basque Country – UPV/EHU, Spain*

[a)] Corresponding author: cvhulse@mail.desy.de

Abstract. In these proceedings, the possibilities for studying the nucleon spin structure with positrons and electrons are presented. An overview of existing results based on the usage of charged-lepton beams of both charges is given, and the corresponding advantages are highlighted. Also, possibilities for future experiments with an electron and a positron beam are discussed.

Introduction

In deep-inelastic scattering (DIS), the structure of the nucleon can be studied in terms of distributions of partons as a function of their longitudinal momentum fraction of the nucleon only or in combination with either their transverse momentum or their transverse position. The longitudinal momentum is here defined as the direction of the probe used to study the nucleon, i.e., the boson exchanged between the beam lepton and the nucleon. The spin-independent parton distribution functions that only depend on the longitudinal momentum fraction (PDFs) are rather well known within a delimited longitudinal-momentum range. The helicity PDFs are less known, especially those of the sea quarks, while for transversity only recently first phenomenological extractions have been performed [1, 2]. The transverse-momentum-dependent PDFs (TMD PDFs) are not well known, but based on data from semi-inclusive DIS measurements at the COMPASS and HERMES experiments and experiments at Jefferson Lab, in combination with measurements from e^+e^- annihilation, first extractions of some of these TMD PDFs have been undertaken [3, 4]. There are eight leading-twist TMD PDFs. They describe different configurations of the quark and nucleon polarization state and correlations between the quark transverse momentum and the quark or nucleon spin.

The distribution of partons in terms of longitudinal momentum fraction and transverse position can be accessed through generalized parton distributions (GPDs). There are eight leading-twist GPDs. Four of them involve parton-helicity conservation, while the other four are chiral-odd. A further differentiation of GPDs relies on the polarization state of the partons. Two GPDs, i.e., GPDs E and H are related to the parton total angular momentum via the Ji relation [5]. Information on GPDs can be accessed through deeply virtual Compton scattering (DVCS) and exclusive meson production. The former process provides the theoretically cleanest access to GPDs, since contrary to meson production there is no need for an additional non-perturbative object that is the meson distribution amplitude. On the other hand, meson production probes various types of GPDs with different sensitivity and in different flavour combinations compared to the DVCS process. The DVCS process allows to probe chiral-even GPDs, while in exclusive meson production also chiral-odd GPDs can be accessed, depending on the type of the produced meson. Different parametrizations of GPDs are available and tested against data from exclusive meson production and DVCS [6–11].

Asymmetries in DVCS

Experimental access to DVCS is provided through hard exclusive leptoproduction of real photons. In this DVCS process, a quark emitted from a nucleon absorbs the virtual photon exchanged between the scattering lepton and the nucleon, emits a real photon and subsequently returns to the nucleon, leaving it intact yet with a different momentum. The quark emission and quark absorption from the nucleon is described by GPDs. These GPDs depend on x, ξ, and t, with x the average longitudinal momentum fraction of the struck quark, ξ a measure for the longitudinal momentum

transfer in the process, and t the square of the four-momentum transfer to the nucleon. The variable x is an internal variable that can not be accessed experimentally, whereas ξ can be related to the Bjorken scaling variable x_B. There is an additional dependence of the GPDs on Q^2, the negative virtual-photon four-momentum squared, through evolution.

The Bethe–Heitler (BH) process, where a real photon is emitted from the initial or scattered lepton rather than by a quark, has exactly the same initial an final state as the DVCS process and therefore interferes with it. The cross section for hard exclusive leptoproduction of photons can thus be written as

$$\sigma = |\tau_{BH}|^2 + |\tau_{DVCS}|^2 + \mathcal{I}, \tag{1}$$

where τ_{BH} and τ_{DVCS} are the amplitudes for respectively the BH and the DVCS processes and $\mathcal{I} = \tau_{DVCS}\tau^*_{BH} + \tau^*_{DVCS}\tau_{BH}$ is the interference between both processes. For scattering from an unpolarized nucleon, each of the three terms appearing in Equation 1 can be decomposed into Fourier components [12]:

$$\begin{aligned}
|\tau_{BH}|^2 &= \frac{K_{BH}}{\mathcal{P}_1(\phi)\mathcal{P}_2(\phi)}\left\{\sum_{n=0}^{2} c_n^{BH}\cos(n\phi)\right\} \\
|\tau_{DVCS}|^2 &= K_{DVCS}\left\{\sum_{n=0}^{2} c_n^{DVCS}\cos(n\phi) + \lambda\, s_1^{DVCS}\sin(\phi)\right\} \\
\mathcal{I} &= \frac{-e_l\, K_{\mathcal{I}}}{\mathcal{P}_1(\phi)\mathcal{P}_2(\phi)}\left\{\sum_{n=0}^{3} c_n^{\mathcal{I}}\cos(n\phi) + \lambda\sum_{n=1}^{2} s_n^{\mathcal{I}}\sin(n\phi)\right\}.
\end{aligned} \tag{2}$$

Here, ϕ is the azimuthal angle between the plane formed by the incoming and scattered leptons and the plane formed by the real and virtual photons, $P_1(\phi)$ and $P_2(\phi)$ represent the BH lepton propagators, K_{BH}, K_{DVCS} and K_I group kinematic variables, e_l is the beam charge, and λ the beam helicity. The BH amplitude can be calculated exactly in QED, with knowledge of the Pauli and Dirac form factors, while the other contributions are non-perturbative QCD quantities that need to be extracted from measurements.

The coefficients from the DVCS and interference amplitudes provide access to GPDs. The sine and cosine coefficients of the interference term depend linearly on Compton form factors, while those of $|\tau_{DVCS}|^2$ are bilinear combinations of Compton form factors. The Compton form factors themselves are convolutions of GPDs and the hard scattering amplitude. For example, the coefficient $c_1^{\mathcal{I}}$ provides access to the real part of the amplitude $M^{1,1}$, with:

$$M^{1,1} = F_1(t)\mathcal{H}(\xi,t) + \frac{x_B}{2-x_B}(F_1(t)+F_2(t))\tilde{\mathcal{H}}(\xi,t) - \frac{t}{4M_p^2}F_2(t)\mathcal{E}(\xi,t). \tag{3}$$

Here, $F_1(t)$ and $F_2(t)$ are respectively the Dirac and Pauli form factors, M_p the proton mass, and $\mathcal{H}$, $\tilde{\mathcal{H}}$, and $\mathcal{E}$ are the Compton form factors associated with the GPDs H, $\tilde{H}$ (the polarized partner of H), and E, respectively. The coefficient $s_1^{\mathcal{I}}$ provides access to the imaginary part of $M^{1,1}$. At leading order in α_S, the real part of this amplitude gives access to the GPDs through a convolution integral over x and to the D-term [13], while the imaginary part provides direct access to the GPDs at the point $x = \pm\xi$.

Important to note in Equation 2 is the dependence of the interference term on the beam charge and the dependence of both $|\tau_{DVCS}|^2$ and the interference term on the beam helicity. The latter affects the sine modulations. These different dependencies on the beam charge and the beam helicity allow to separate various contributions in measurements of cross section differences and asymmetries.

In the case of an experiment that can collect data with an electron and a positron beam, a beam-charge asymmetry can be constructed:

$$\mathcal{A}_C(\phi) \equiv \frac{d\sigma^+ - d\sigma^-}{d\sigma^+ + d\sigma^-} = \frac{-\frac{K_I}{\mathcal{P}_1(\phi)\mathcal{P}_2(\phi)}\sum_{n=0}^{3} c_n^{\mathcal{I}}\cos(n\phi)}{\frac{K_{BH}}{\mathcal{P}_1(\phi)\mathcal{P}_2(\phi)}\sum_{n=0}^{2} c_n^{BH}\cos(n\phi) + \frac{1}{Q^2}\sum_{n=0}^{2} c_n^{DVCS}\cos(n\phi)}, \tag{4}$$

where $d\sigma^{+(-)}$ is the cross section (differential in kinematic variables) of the process measured with a positron (electron) beam. This asymmetry provides access to the coefficients $c_n^{\mathcal{I}}$, and thus linear access to GPDs through a convolution integral with the hard scattering amplitude. Experimentally, an asymmetry A_C is constructed based on the number of measured DVCS events (normalized to the number of DIS events) collected with a positron and electron beam. This is

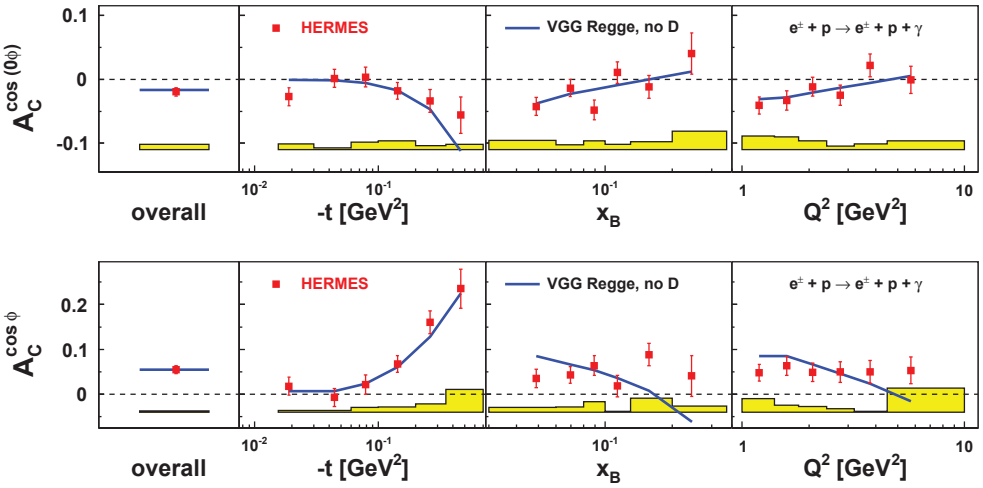

FIGURE 1. Beam-charge asymmetry amplitudes $A_C^{\cos(0\phi)}$ (upper row) and $A_C^{\cos\phi}$ (lower row), integrated over the full kinematic region (left), as a function of $-t$ (middle-left), x_B (middle-right), and Q^2 (right). The error bars represent the statistical uncertainties; the error bands represent the systematic uncertainties. Also shown are model calculations based on double-distributions [14, 15] (blue, continuous lines).

then fit with a function of the form $\sum_{n=0}^{3} A_C^{\cos(n\phi)} \cos(n\phi)$. As is clear from Equation 4, each of the coefficients $A_C^{\cos(n\phi)}$ is related to the corresponding $c_n^{\mathcal{I}}$. However, there are also contributions from BH and from DVCS, which come from the denominator of Equation 4. The first term in the denominator is calculable, while the second is suppressed as $1/Q^2$, and in addition c_n^{DVCS} can be small, depending on the kinematic region. If an experiment is capable of controlling luminosity measurements and detector effects very well, cross section differences can be measured instead of asymmetries, and as such the BH and DVCS contributions from the denominator are eliminated.

The beam-charge asymmetry was measured by the HERMES [16] and H1 experiments [17]. The first two coefficients of the asymmetry as measured by the HERMES experiment are shown in Figure 1. The $A_C^{\cos(\phi)}$ coefficient is positive and increases with $-t$. This amplitude provides access to the real part of the amplitude $\mathcal{M}^{1,1}$, and thus in particular to the twist-2 GPD H, while access to the twist-2 GPDs $\tilde{H}$ and E is suppressed, as can be seen from Equation 3. The amplitude $A_C^{\cos(0\phi)}$ is related to $c_0^{\mathcal{I}}$, itself proportional to $-k\, c_1^{\mathcal{I}}$, where k is a suppression factor. Consistent with this, the amplitude $A_C^{\cos(0\phi)}$ is observed to be smaller than $A_C^{\cos(\phi)}$, of opposite sign, and mirroring accordingly the dependence as a function of $-t$. The amplitudes $A_C^{\cos(2\phi)}$, which provides access to twist-3 GPDs, and $A_C^{\cos(3\phi)}$, which provides access to twist-2 gluon helicity-flip GPDs, have also been extracted and are found to be compatible with zero. Note that on average there is a 12% background contribution to the extracted asymmetries coming from associated-DVCS production $ep \to eN\pi$, where π is a soft pion. Note also that c_n^{DVCS} is expected to be small at HERMES, which also in view of the $1/Q^2$ suppression, justifies it to be neglected in Equation 4, allowing thus to extract the coefficients $c_n^{\mathcal{I}}$ from the measured asymmetry.

In an analogous way, the beam-helicity asymmetry measured from an unpolarized target can be constructed:

$$\mathcal{A}_{LU}(\phi) \equiv \frac{d\sigma^{\rightarrow} - d\sigma^{\leftarrow}}{d\sigma^{\rightarrow} + d\sigma^{\leftarrow}} = \frac{-e_l \frac{K_{\mathcal{I}}}{\mathcal{P}_1(\phi)\mathcal{P}_2(\phi)} \left[\sum_{n=1}^{2} s_n^{\mathcal{I}} \sin(n\phi)\right] + \frac{1}{Q^2} s_1^{DVCS} \sin(\phi)}{\frac{1}{\mathcal{P}_1(\phi)\mathcal{P}_2(\phi)} \left[K_{BH} \sum_{n=0}^{2} c_n^{BH} \cos(n\phi) - e_l K_{\mathcal{I}} \sum_{n=0}^{3} c_n^{\mathcal{I}} \cos(n\phi)\right] + \frac{1}{Q^2} \sum_{n=0}^{2} c_n^{DVCS} \cos(n\phi)}, \quad (5)$$

where $d\sigma^{\rightarrow(\leftarrow)}$ denotes the cross section for positive (negative) beam helicity. In the numerator, now, not only the coefficients of the interference term appear, but there is also a contribution from $|\tau_{DVCS}|^2$. The coefficient s_1^{DVCS} is, however, of twist-3 and is suppressed as $1/Q^2$, so that its contribution to the numerator is expected to be small. In the denominator, again the BH terms are present as well as the cosine modulations from the pure DVCS term. In addition, the cosine modulations from the interference term contribute, and as seen from Figure 1, the coefficients $c_0^{\mathcal{I}}$ and $c_1^{\mathcal{I}}$ are clearly non-zero. Of course, also here, if experimentally feasible, cross-section differences rather than asymmetries can be extracted in order to eliminate the contributions present in the denominator. Nevertheless, even then, the $\sin(\phi)$ modulation receives a contribution from $s_1^{\mathcal{I}}$ and s_1^{DVCS}, which cannot be disentangled.

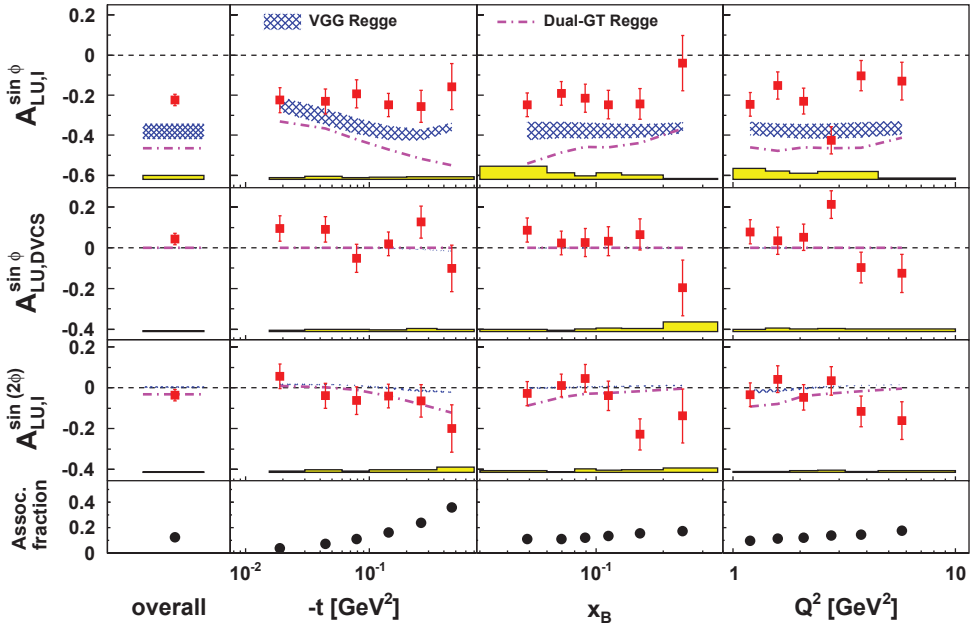

FIGURE 2. Charge-separated beam-helicity asymmetry amplitudes $A_{LU,I}^{\sin\phi}$ (first row), $A_{LU,DVCS}^{\sin\phi}$ (second row), $A_{LU,I}^{\sin(2\phi)}$ (third row), and fractional associated-DVCS background contribution (last row), integrated over the full kinematic region (left), as a function of $-t$ (middle-left), x_B (middle-right), and Q^2 (right). The error bars represent the statistical uncertainties; the error bands represent the systematic uncertainties. Also shown are model calculations based on double-distributions [14, 15] (blue, continuous lines) and a dual-parametrization GPD model [18, 19] (magenta, dashed lines).

In order to remediate this, charge-difference beam-helicity asymmetries and charge-average beam-helicity asymmetries can be constructed. They are respectively defined as

$$\mathcal{A}_{LU,I}(\phi) \equiv \frac{(d\sigma^{+\rightarrow} - d\sigma^{+\leftarrow}) - (d\sigma^{-\rightarrow} - d\sigma^{-\leftarrow})}{(d\sigma^{+\rightarrow} + d\sigma^{+\leftarrow}) + (d\sigma^{-\rightarrow} + d\sigma^{-\leftarrow})} \tag{6}$$

$$\mathcal{A}_{LU,DVCS}(\phi) \equiv \frac{(d\sigma^{+\rightarrow} - d\sigma^{+\leftarrow}) + (d\sigma^{-\rightarrow} - d\sigma^{-\leftarrow})}{(d\sigma^{+\rightarrow} + d\sigma^{+\leftarrow}) + (d\sigma^{-\rightarrow} + d\sigma^{-\leftarrow})}, \tag{7}$$

where again the superscripts indicate the beam charge $(+/-)$ and beam helicity state $(\rightarrow / \leftarrow)$. As can be deduced from Equation 2, for $\mathcal{A}_{LU,I}(\phi)$ only the term containing the s_n^I coefficients survives in the numerator, while for $\mathcal{A}_{LU,DVCS}$, only the s_1^{DVCS} term is present in the numerator. For both asymmetries, the term containing the c_n^I coefficients disappears in the denominator. The $\mathcal{A}_{LU,I}(\phi)$ asymmetry provides linear access to the GPDs, while $\mathcal{A}_{LU,DVCS}$ provides bilinear access.

These asymmetries have been extracted by the HERMES experiment [16], and are shown in Figure 2. As can be seen, there is a sizeable asymmetry amplitude $A_{LU,I}^{\sin\phi}$. This asymmetry provides via the imaginary part of $\mathcal{M}^{1,1}$ primarily access to the twist-2 GPD H. The amplitude $A_{LU,DVCS}^{\sin\phi}$, which provides acces to the twist-3 GPDs, is as anticipated small, compatible with zero. Also $A_{LU,I}^{\sin(2\phi)}$, which probes twist-3 GPDs, is compatible with zero. Finally, also here there is a contribution from associated DVCS, the fraction of which is given in the bottom panel of Figure 2.

Measurements with both beam charges for a clean separation of the different contributions to the asymmetry are not only necessary for the beam-helicity asymmetry, but also for the target-spin asymmetry. Indeed, for the latter similar considerations are of application and measurements were performed along that line [20, 21].

Finally, measurements with electrons and positrons can also be of interest when measuring on nuclear targets. Measuring DVCS on nuclear targets may allow to probe (anti-)shadowing, the EMC effect, and Fermi motion. It may also be sensitive to new nuclear effects, which are absent in the imaginary part of the forward virtual-photon–nucleon amplitude probed in inclusive DIS [22]. Moreover, measuring beam-charge asymmetries on nuclear targets may offer

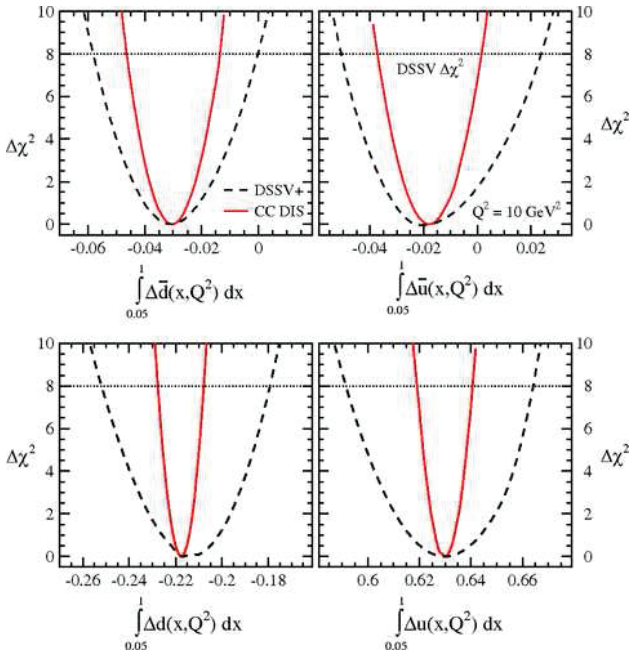

FIGURE 3. Profile function $\Delta\chi^2$ as a function of the first moment of the helicity PDFs $\Delta\bar{d}$ (upper left), $\Delta\bar{u}$ (upper right), Δd (lower left), and Δu (lower right), truncated to the region $0.05 < x_B < 1.0$. The dashed, black line corresponds to the global DSSV+ analysis, and the red, continuous line corresponds to the DSSV+ analysis with inclusion of simulated charged-current DIS data. The horizontal, dotted line indicates the tolerated value of $\Delta\chi^2$ in the DSSV analysis [24].

sensitivity to the mesonic degrees of freedom in the nucleus. It is predicted that mesons in the nucleus cause a significant increase with atomic mass of the DVCS amplitude probed through coherent scattering compared to that probed on nucleons through incoherent scattering [22]. This increase with atomic mass is also expected for the D-term. In particular, an increase of the beam-charge asymmetry and a slow decrease of the beam-helicity asymmetry as a function of the atomic mass is predicted for HERMES kinematics. It is argued that in case of absence of mesonic degrees of freedom, no atomic-mass dependence should be visible. The HERMES experiment performed measurements on nuclear targets [23]. Isolating a coherent-enriched sample, no atomic-mass dependence is observed.

Helicity PDFs

Inclusive DIS with longitudinally polarized charged-lepton beam and longitudinally polarized hydrogen target allows to probe the $g_{1,p}$ proton structure function. This provides access to a combination of quark helicity distributions:

$$g_{1,p}(x) = \frac{1}{2} \sum_{q=u,d,s} e_q^2 \left[\Delta q(x) + \Delta\bar{q}(x)\right]. \tag{8}$$

Here, e_q represents the quark electric charge, and $\Delta q(x)$ and $\Delta\bar{q}(x)$ respectively the quark and anti-quark helicity PDFs. Note that for (semi-)inclusive DIS x coincides with x_B at leading order in α_S.

Semi-inclusive DIS, where a final-state hadron is identified, allows to disentangle the helicity distributions for the different quark flavours. The additional complication in this process results from the inclusion of an additional non-perturbative object, which describes the parton-to-hadron fragmentation. It is possible to extract fragmentation functions from e^+e^--annihilation data in combination with data from semi-inclusive DIS and proton-proton collisions.

On the other hand, it is also possible to study charged-current DIS, where a $W^\pm$ boson is exchanged between the beam lepton and the target. Since, in the process, the electron (positron) splits into a (anti-)neutrino ν_e ($\bar{\nu}_e$) and a W^- (W^+), where the neutrino stays undetected, the inclusive kinematic variables, such as Q^2 and x_B, are reconstructed from the initial-state lepton and the hadronic final-state particles, via the Jacquet-Blondel method [25]. The resolution

of the kinematic variables depends of course on the amount of undetected final-state hadrons. The advantage of studying charged-current DIS is that flavour combinations different from those accessible in purely electromagnetic DIS are probed. As such, one has improved flavour sensitivity without the need for fragmentation functions. Moreover, since the $W^{\pm}$ only couples to left-handed quarks and right-handed anti-quarks because of the weak interaction's parity-violating nature, flipping the target polarization provides automatically access to helicity distributions, without the need for a polarized beam. The spin-dependent structure functions probed with an electron beam, through W^- exchange, and a positron beam, through W^+ exchange, are at leading order in α_S for four active quark flavours respectively

$$\begin{aligned} g_{1,p}^{W^-}(x) &= \Delta u(x) + \Delta\bar{d}(x) + \Delta c(x) + \Delta\bar{s}(x) \\ g_{5,p}^{W^-}(x) &= -\Delta u(x) + \Delta\bar{d}(x) - \Delta c(x) + \Delta\bar{s}(x) \\ g_{1,p}^{W^+}(x) &= \Delta\bar{u}(x) + \Delta d(x) + \Delta\bar{c}(x) + \Delta s(x) \\ g_{5,p}^{W^+}(x) &= \Delta\bar{u}(x) - \Delta d(x) + \Delta\bar{c}(x) - \Delta s(x). \end{aligned} \tag{9}$$

The charged-current DIS process is only accessible for experiments with high enough energy (or at neutrino-scattering experiments). There exist measurements on charged-current DIS with unpolarized protons [26, 27], by the HERA experiments, but there are no measurements with polarized nucleons. Such measurements would be possible at an electron-ion collider (EIC) [28, 29], where longitudinal target-spin asymmetries can be extracted. For electron scattering, these probe at leading-order accuracy the combination $2bg_{1p}^{W^-} - ag_{5p}^{W^-}$, where a and b are functions of the fractional energy of the W^- with respect to the beam-lepton energy. Analogously, positron scattering permits to acces $g_{1p}^{W^+}$ and $g_{5p}^{W^+}$. Estimates of the impact of such measurements on the determination of helicity PDFs have been performed [30]. They make usage of the DJANGOH generator, which has been extended to include longitudinally polarized nucleons, and include electroweak radiative effects, while realistic detector performance parameters have been assumed. The estimates are based on the 'DSSV' analysis at next-to-leading order in α_S [24]. In order to evaluate the impact of charged-current DIS data, the results of the global DSSV+ fit [31], where quark helicity distributions are extracted from data from inclusive and semi-inclusive DIS as well as from proton-proton collisions, are compared to this same DSSV+ fit, but now including the generated charged-current DIS Monte-Carlo data from the present study. In Figure 3, the increase in the χ^2 value away from its minimum value, $\Delta\chi^2$, is presented as a function of the truncated moment of the quark helicity distribution obtained in the fit. The black, dashed line represents the $\Delta\chi^2$ profile function of the DSSV+ fit [31], while the red, continuous line includes the charged-current DIS simulated data. The horizontal dotted line delimits the $\Delta\chi^2$ value that is tolerated and at which the uncertainty of the truncated helicity-PDF moment is defined. As can be seen, the inclusion of charged-current DIS events has a strong impact on the reduction of the uncertainty.

Similar consideration as the ones presented for the determination of the g_1 structure function are applicable to its twist-3 partner, the g_2 structure function. This g_2 structure function probes quark-gluon-quark correlations. Its genuine twist-3 contribution, obtained in the Wandzura-Wilczek decomposition [32], can be related to the force exerted by the nucleon remnant at the exact moment that the quark absorbs the gauge boson, for the case of an unpolarized quark in a transversely polarized nucleon [33]. In addition, this structure function has been shown recently to also provide access to the transversity PDF [34]. The g_2 function is accessible in longitudinal double-spin asymmetries in DIS, but is there suppressed with respect to the contribution from g_1. Instead, it is not suppressed and can be extracted in double-spin asymmetries with a longitudinally polarized lepton beam and a transversely polarized proton target. Measurements of this asymmetry have been performed in purely electromagnetic DIS by the experiments E143 [35], E155 [36], SMC [37], and HERMES [38], and the non-zero asymmetries measured by the different experiments are found to be compatible with each other. As for the asymmetries for the g_1 structure function, no charged-current DIS measurements exist for g_2.

TMD PDFs and fragmentation functions

Partly, the above considerations about charged-current DIS can be extended to TMD PDFs. Although, here, a final-state hadron needs to be reconstructed, and thus, parton-to-hadron fragmentation functions need to be included, one can again profit in charged-current semi-inclusive DIS from the parity violating nature of the weak interaction to obtain automatic helicity selection for the TMD PDFs for which this is relevant, such as, e.g., to access the helicity TMD

PDF and the worm-gear $g_{1T}^{\perp}$ TMD PDF. In addition, given the flavour-changing nature of the $W^{\pm}$ interaction, different combinations of TMD PDFs and TMD fragmentation functions can be probed compared to the existing measurements in purely electromagnetic semi-inclusive DIS (see [39, 40] for reviews). The crucial point in the measurements is the reconstruction of transverse momenta, where the transverse momentum of the hadron with respect to the $W^{\pm}$ needs to be determined. For the reconstruction of the $W^{\pm}$ direction Monte-Carlo techniques might be considered. At present, neither charged-current semi-inclusive DIS measurements with a polarized nucleon nor simulations are at hand.

The availability of both positively and negatively charged lepton beams is also of interest for the measurement of fragmentation functions. For example, the determination of quark-spin-dependent twist-2 and twist-3 fragmentation functions of a polarized Λ can again profit from the parity-violating nature of the weak interaction without the need for a longitudinally polarized lepton beam.

Conclusion

There is a vast series of measurements that can profit from a positron and an electron beam to study the (spin) structure of the nucleon. Beam-charge asymmetries in combination with beam-spin and target-spin asymmetries in DVCS allow to disentangle various Fourier coefficients that provide access to twist-2 and higher-twist GPDs, through the real or imaginary part of the Compton form factors. There are existing measurements from the HERMES collaboration as well as one from the H1 collaboration.

In order to extend the kinematic coverage of the DVCS measurements, both to higher and lower regions in x_B and Q^2, measurements at an EIC or lower-energy facilities would be highly welcome, especially that GPDs appear in convolution integrals and are in general not directly accessible. Thus, measurements spanning an as large as possible kinematic region are needed.

At higher energies, one can profit from charged-current interactions and access helicity PDFs in combinations that are different from those probed in purely electromagnetic DIS. Such measurements would be highly beneficial, as seen from the here presented impact studies, and have the advantage that one eliminates the need for fragmentation functions, which themselves are not yet known with very high precision. Finally, although there are at present no existing studies, also the determination of TMD PDFs could profit from charged-current DIS measurements, since again different flavour combinations are probed, and the weak interaction allows for an automatic helicity-state selection.

ACKNOWLEDGMENTS

The author is supported by Grant No. IT956-16 (Basque Government) and MINECO (Juan de la Cierva), Spain.

REFERENCES

[1] M. Anselmino *et al.*, Phys. Rev. D **87**, p. 094019 (2013).
[2] Z. Kang *et al.*, Phys. Rev. D **93**, p. 014009 (2016).
[3] M. Anselmino *et al.*, arXiv: **1107.4446** (2011).
[4] C. Lefky and A. Prokudin, Phys. Rev. D **91**, p. 034010 (2015).
[5] X. Ji, Phys. Rev. D **78**, p. 610 (1997).
[6] K. Kumericki and D. Mueller, Nucl. Phys. B **841**, p. 1 (2010).
[7] K. Kumericki *et al.*, Phys. Part. Nucl. **45**, p. 723 (2014).
[8] T. Lautenschlager *et al.*, arXiv: **1312.5493** (2013).
[9] S. Goloskokov and P. Kroll, Eur. Phys. J C **50**, p. 829 (2007).
[10] S. Goloskokov and P. Kroll, Eur. Phys. J C **53**, p. 367 (2008).
[11] S. Goloskokov and P. Kroll, Eur. Phys. J A **50**, p. 146 (2014).
[12] A. Belitsky *et al.*, Nucl. Phys. B **629**, p. 323 (2002).
[13] M. V. Polyakov and C. Weiss, Phys. Rev. D **60**, p. 114017 (1999).
[14] P. Guichon *et al.*, Phys. Rev. D **60**, p. 094017 (1999).
[15] K. Goeke *et al.*, Prog. Part. Nucl. Phys. **47**, p. 401 (2001).
[16] A. Airapetian *et al.* (HERMES), JHEP **11**, p. 083 (2009).
[17] F. D. Aaron *et al.* (H1), Phys. Lett. B **681**, 391–399 (2009).
[18] V. Guzey and T. Teckentrup, Phys. Rev. D **74**, p. 054027 (2006).

[19] V. Guzey and T. Teckentrup, Phys. Rev. D **79**, p. 017501 (2006).
[20] A. Airapetian *et al.* (HERMES), JHEP **06**, p. 066 (2008).
[21] A. Airapetian *et al.* (HERMES), Phys. Lett. B **704**, 15–23 (2011).
[22] V. Guzey and M. Siddikov, J. Phys. G **32**, p. 251 (2006).
[23] A. Airapetian *et al.* (HERMES), Phys. Lev. C **81**, p. 035202 (2010).
[24] D. de Florian *et al.*, Phys. Rev. Lett. **101**, p. 072001 (2008).
[25] F. Jacquet and A. Blondel, Proceedings of The Study Group On Detectors For Charged Current Events, edited by U. Amaldi et al. (DESY, Hamburg, 1979) p. 391 (1979).
[26] F. D. Aaron *et al.* (H1), JHEP **09**, p. 061 (2012).
[27] H. Abramowicz *et al.* (ZEUS), Eur. Phys. J. C **70**, p. 945 (2010).
[28] D. Boer *et al.*, arXiv: **1108.1713** (2011).
[29] A. Accardi *et al.*, arXiv: **1212.1701** (2012).
[30] E. C. Aschenauer *et al.*, Phys. Rev. D **88**, p. 114025 (2013).
[31] D. de Florian *et al.*, Prog. Part. Nucl. Phys. **67**, p. 251 (2012).
[32] S. Wandzura and F. Wilczek, Phys. Lett. **72B**, 195–198 (1977).
[33] M. Burkardt, arXiv: (2008).
[34] A. Accardi and A. Bacchetta, Phys. Lett. B **773**, 632–638 (2017).
[35] K. Abe *et al.* (E143), Phys. Rev. D **58**, p. 112003 (1998).
[36] P. L. Anthony *et al.* (E155), .
[37] D. Adams *et al.* (SMC), Phys. Rev. D **56**, p. 5330 (1997).
[38] A. Airapetian *et al.* (HERMES), Eur. Phys. J. C **72**, p. 1921 (2012).
[39] H. Avakian *et al.*, Eur. Phys. J. **A52**, p. 150 (2016), [Erratum: Eur. Phys. J.A52,no.6,165(2016)].
[40] H. Avakian *et al.*, Eur. Phys. J. **A52**, p. 165 (2016).

Pion and Kaon Structure Functions at an Electron-Ion Collider

Tanja Horn[1,2,a)]

[1]*Catholic University of America, Washington, DC 20064, USA*
[2]*Jefferson Lab, Newport News, VA, 23606, USA*

[a)]Corresponding author: hornt@cua.edu

Abstract. Pions and kaons are, along with protons and neutrons, the main building blocks of nuclear matter. They are connected to the Goldstone modes of dynamical chiral symmetry breaking, the mechanism thought to generate all hadron mass in the visible universe. The distribution of the fundamental constituents, the quarks and gluons, is expected to be different in pions, kaons, and nucleons. However, experimental data are sparse. As a result, there has been persistent doubt about the behaviour of the pion's valence quark structure function at large Bjorken-x and virtually nothing is known about the contribution of gluons. The Electron-Ion Collider (EIC) with an acceptance optimized for forward physics could provide access to structure functions over a larger kinematic region. This would allow for measurements testing if the origin of mass is encoded in the differences of gluons in pions, kaons, and nucleons, and measurements that could serve as a test of assumptions used in the extraction of structure functions and the pion and kaon form factors. Measurements at an EIC would also allow to explore the effect of gluons at high x.

INTRODUCTION

Pions and kaons occupy a special role in nature [1] and thus have a central role in our current description of nucleon and nuclear structure. The pion is the lightest quark system, with a single valence quark and a single valence antiquark. It is also the particle responsible for the long range character of the strong interaction that binds the atomic nucleus together. A general belief is that the rules governing the strong interaction are left-right, *i.e.* chirally, symmetric. If this were true, the pion would have no mass. The chiral symmetry of massless Quantum Chromodynamics (QCD) is broken dynamically by quark-gluon interactions and explicitly by inclusion of light quark masses, giving the pion and kaon mass. The pion and kaon are thus seen as the key to confirm the mechanism that dynamically generates nearly all of the mass of hadrons and central to the effort to understand hadron structure.

Experimental knowledge of the partonic structure of the pion is very limited due to the lack of a stable pion target. Our current knowledge of the pion structure function in the valence region is obtained primarily from pionic Drell-Yan scattering [2, 3, 4], and in the pion sea region at low Bjorken-x, from hard diffractive processes measured on $e - p$ collisions at HERA [5]. These data seem to indicate that the pion sea has approximately one-third of the magnitude of the proton sea, while from the parton model one expects the pion sea to be two-thirds of the proton sea.

The distribution of the fundamental constituents, the quarks and gluons, is expected to be different in pions, kaons, and nucleons. However, as discussed above experimental data on the pion structure function are sparse and there are no data on the kaon structure function to date. As a consequence of the lack of pion data, there has been persistent doubt about the behavior of the pion's valence quark structure function at large Bjorken-x and virtually nothing is known about the contribution of sea quarks and gluons [6]. The Electron-Ion Collider (EIC) with an acceptance optimized for forward physics has the potential for accessing pion and kaon structure functions over a large kinematic region through the Sullivan process [7]. This would allow for measurements testing if the origin of mass is encoded in the differences of gluons in pions, kaons, and nucleons [8], and measurements that could serve as a test of assumptions used in the extraction of structure functions and the pion and kaon form factors.

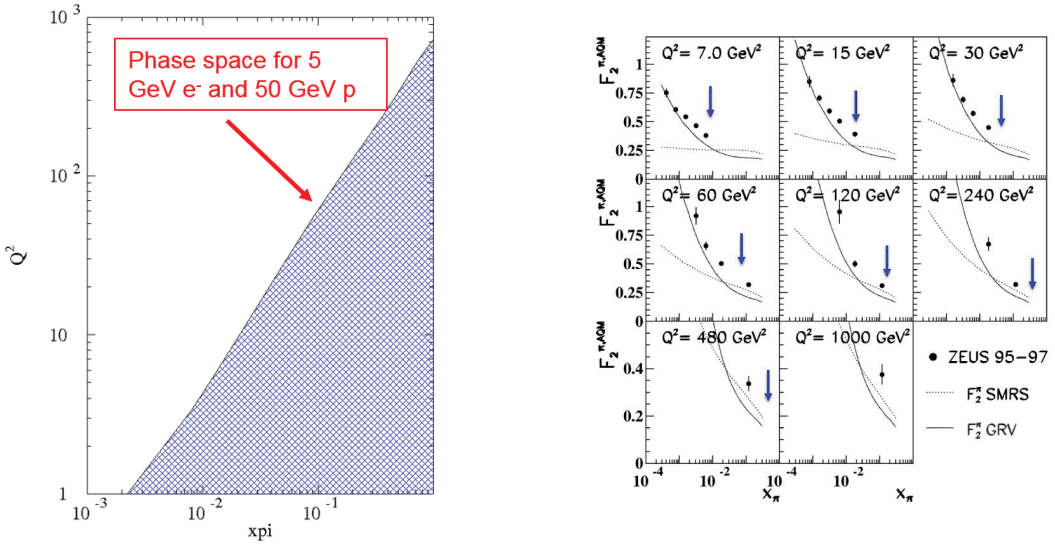

FIGURE 1. EIC kinematic reach.

Experimental Considerations

In the Sullivan process, one measures the contribution to the electron Deep Inelastic Scattering (DIS) of the meson cloud of a proton target. An immediate consequence is that the nucleon parton distributions contain a component which can be attributed to the meson cloud. Note that in the Sullivan process, the mesons in the nucleon cloud are virtual (off-shell) particles. For the process to provide reliable access to a meson target, the pole associated with that meson must be the dominant process. Recent calculations [9] estimate the impact of off-shellness in the Bethe-Salpeter Equation/Dyson-Schwinger Equation (BSE/DSE) framework. It was found that the meson can be considered on-shell for pions up to $t < 0.6$ GeV^2 and for kaons up to $t < 0.9$ GeV^2. This suggests that pion and kaon structure functions can be accessed through the Sullivan process.

To experimentally determine the off-shellness correction, one can use a procedure similar to that used for corrections in studies of the neutron in deuterium. There, interactions in the medium have to be taken into account, which is done through nuclear binding corrections. By binning in t up to the projected on-shell/off-shell limit, an off-shellness correction could be determined in a similar fashion.

Pion and Kaon Structure Functions at an EIC

The Electron-Ion Collider will provide a large (x, Q^2) landscape for both pion and kaon structure measurements. The acceptance at the EIC is ideal for structure function measurements, essentially covering the full forward region and also covering much higher x than previous measurements. The projections in the present report assume roughly a year of running, which corresponds to 26 weeks at 50% efficency and a geometric detection efficiency for forward going particles at small t of 20%. The EIC kinematic reach in x is shown in Fig. 1 for electron and proton beam energies of 5 GeV and 50 GeV, at a luminosity of 10^{34} s^{-1} cm^{-2}. The kinematic coverage reaches down to $x_{\pi,K}$=0.01 or even smaller values for both pion and kaon. The small $x_{\pi,K}$ region will be constrained by structure functions obtained at HERA. The blue arrows in Fig. 1 indicate the x_{min} values for future EIC data at the same Q^2 values as the HERA data.

The projections of kaon structure functions were obtained from those of the pion case by scaling with the coupling constants of Ref. [10] and the geometric detection efficiencies. The resulting kaon structure function projections are of roughly similar quality as the pion structure functio projections for small t, forward particle detection acceptances of JLEIC. Detector similations have shown that the decay particles from Λ decay can be distinguished from the beam particles near the 7th or 8th downstream dipole. Fig. 2 shows the kaon structure function projections for beam energies of 5 GeV electrons and 100(left) GeV and 50(right) GeV protons as a function of Q^2 and for different values of x, at

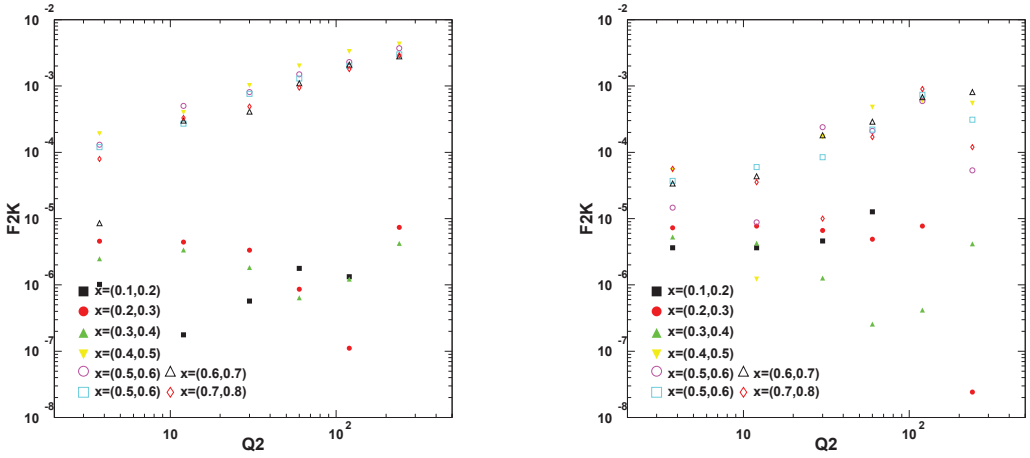

FIGURE 2. Kaon structure function projections for beam energies of 5 GeV electrons and 100(left) GeV and 50(right) GeV protons as a function of Q^2 and for different values of x. A luminosity of 100 fb^{-1} is assumed.

a luminosity of 100 fb^{-1}. To constrain gluons the Q^2 evolution is important. As one can see, for small ranges in x the Q^2 evolution may not be sufficient, however, and other techniques may need to be explored to supplement.

Towards Flavour Decomposition

Parity-violating probes may provide a way to make progress towards a full flavour decomposition. These include neutral- and charged-current probes. Observables from charged-current processes can be obtained through a comparison of electron versus positron interactions. Neutral-current processes include measurements of the xF_3 nucleon structure functions (γZ interference contribution) and the neutral-current conserving parity-violating asymmetry, which can be expressed through the coefficients $a_{2\pi}(x)$ and $a_{2K}(x)$,

$$a_{2\pi}(x) = \frac{2\sum_q e_q g_V^q (q+\bar{q})}{\sum_q e_q^2 (q+\bar{q})} \sim \frac{6u_\pi^+ + 3d_\pi^+}{4u_\pi^+ + d_\pi^+} - 4sin^2\theta_W \tag{1}$$

$$a_{2K}(x) = \frac{2\sum_q e_q g_V^q (q+\bar{q})}{\sum_q e_q^2 (q+\bar{q})} \sim \frac{6u_K^+ + 3s_K^+}{4u_K^+ + s_K^+} - 4sin^2\theta_W \tag{2}$$

Fig. 3(a) shows the DSE parton distributions from Ref. [11]. One can see that the valence quarks in the kaon carry much more of the kaon's momentum than is stored in the pion's valence-quarks. Fig. 3(b) shows the resulting coefficients $a_{2\pi}$ and a_{2K} as a function of x. The different colors denote different scales, e.g., a_{2K} at the hadronic scale ζH=0.51 (green curve), a_{2K} at scale ζ=2 GeV (green curve), and a_{2K} at scale ζ=5.2 GeV (blue curve). At x=1, a_{2K} is independent of the scale, while at x=0 a_{2K} approaches $9/5 - \sin^2\theta_W$ because all valence-quark PDFs become identical at x=0 under evolution. Simulation studies to project the feasibility of such measurements at EIC are currently ongoing.

Summary

In summary, nucleons and the lightest mesons, pons and kaons, are the basic building blocks of nuclear matter. We should know their structure functions. The distribution of quarks and gluons in pions, kaons, and nucleons is expected to be different. Measurements of the structure functions at low to moderate x could shed light on the question if the origin of mass is encoded in differences of gluons in pions, kaons and nucleons (at non-asymptotic values of Q^2). Using electroweak processes, e.g., through parity-violating probes or neutral vs. charged-current interactions, disentangling flavour dependence seems possible.

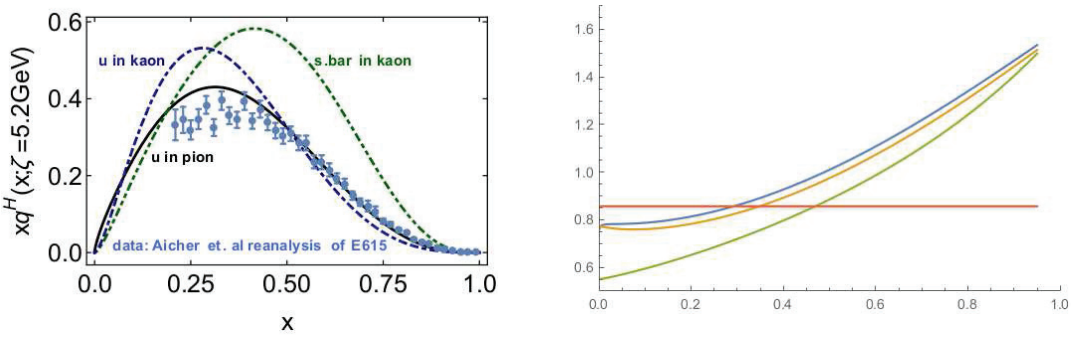

FIGURE 3. (a) DSE Parton Distribution Functions from Ref. [11]; (b) $a_{2\pi}(x)$ and $a_{2K}(x)$ at different scales.

REFERENCES

[1] T. Horn and C.D. Roberts, J. Phys. **43** (2016) no. 7, 073001.
[2] J.S. Conway et al., Phys. Rev. D **39** (1989) 39.
[3] J. Badier et al., Z. Phys. C**18** (1983) 281.
[4] B. Betev et al., Z. Phys. C**28** (1985) 9.
[5] H1 Collaboration, C. Adloff et al., Eur. Phys. J. C**6** (1999) 587; V. Andreev et al., arxiv:1312.4821.
[6] R.J. Holt, C.D. Roberts, Rev. Mod. Phys. **82**, 2991 (2010).
[7] J.D. Sullivan, Phys. Rev. **D5** (1972) 1732.
[8] C.D. Roberts, Few Body Syst. **58** (2017) no.1, 5.
[9] S.-X. Qin, C. Chen, C. Mezrag, C.D. Roberts, arXiv:1702:06100 (2017).
[10] S. V. Goloskokov and P. Kroll, Eur. Phys. J. A **47**, 112 (2011) [arXiv:1106.4897 [hep-ph]].
[11] C. Chen, L. Chang, C.D. Roberts, S. Wang, H.-S. Zong, Phys. Rev. D **93** (2016) no.7, 074021.

Probing Strangeness via Charm Production in Charged Current DIS at HERA

Jae D. Nam[1,2,a)]

[1]*Temple University, 1925 N. 12th St., Philadelphia, PA 19122-1801, U.S.*

[2]*Deutsches Elektronen-Synchrotron DESY, Hamburg, Germany*

[a)]Corresponding author: jae.nam@temple.edu

Abstract. We present an overview of an ongoing analysis at HERA on charm production at high Q^2 charged current DIS. The measurements taken after the HERA shutdown period are categorized as HERA II data. In order to fully exploit the improvements made during this period, this analysis only considers HERA II data. The improvements include a higher luminosity and enhanced heavy particle identification capabilities and are discussed in the present paper. Secondary vertices are extracted in order to distinguish charm production events in charged current DIS. The significance of the decay length associated with each secondary vertex is used to discriminate charm events from light flavor events. Event selection criteria from previous analyses as well as the expected number of surviving events are presented.

INTRODUCTION

The analysis from the ATLAS collaboration published in 2017 reports the strange quark content in the proton sea to be $R_s = \frac{s+\bar{s}}{\bar{u}+\bar{d}} = 1.13 \pm 0.05$ in the kinematic region $x = 0.023, Q^2 = 1.9\,GeV^2$ [1]. This result not only suggests the strange quark content to be equal to or possibly larger than the lighter quark content, but is also about twice as large as the result from the CCFR/NuTeV analysis in 1995 where the strange content in the global kinematic region $\kappa = \int_0^1 dx(xs + x\bar{s}) / \int_0^1 dx(x\bar{u} + x\bar{d}) = 0.477^{+0.063}_{-0.053}$ at $Q^2 \sim 10\,GeV^2$ [2]. The discrepancy between these observations compels a need to revisit this topic with a new approach.

During its operation from 1992 to 2007, HERA served as the only high energy electron(positron)-proton collider in the world. The ZEUS experiment has collected measurements from unpolarized ($P_e \lesssim 3\%$) e^+p and e^-p collisions with lepton beam energy $E_e = 27.5\,GeV$ and proton beam energy $E_p = 920\,GeV$[1], corresponding to a center-of-mass energy $\sqrt{s} = 318\,GeV$. The experiment has provided insights into the inner structure of the proton. The accumulated data can still be accessed for new analyses. Due to its similarity with the physics of the upcoming Electron-Ion Collider project (EIC), the measurement taken from the ZEUS collaboration offers a great testing ground for exploring the potential of the EIC.

The data stored at ZEUS is largely divided into two subsets; HERA I and HERA II. The former includes measurements taken during 1992 - 2000 with integrated luminosity $L \sim 130\,pb^{-1}$, whereas the latter includes measurements taken during 2002 - 2007 with $L \sim 390\,pb^{-1}$. The large improvement in luminosity was due to a major upgrade to the ZEUS detector during the shutdown period in 2000 - 2001. This analysis considers the HERA II data to exploit the increased luminosity as well as the enhanced tagging capabilities.

[1] $E_p = 820\,GeV$ in 1994-1997

HEAVY FLAVOR DIS AT HERA

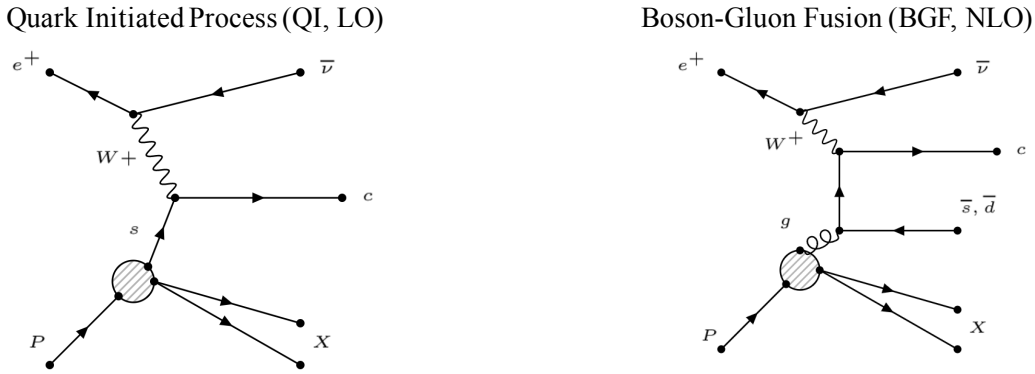

FIGURE 1. Charm Production in e^+p CC DIS; On the left is the LO Feynman diagram of charm production in CC DIS. The incoming positron loses it charge by emitting a W^+. The W^+ then couples to the strangeness and produces a charm (Quark-Initiated Process, QI). On the right is one of the NLO diagrams. Here the W^+ couples to a gluon and produces a charm and an anti-strange or anti-down (Boson-Gluon Fusion, BGF).

In charged current DIS in positron(electron)-proton collisions $e^+(e^-)p \rightarrow \overline{\nu}(\nu)X$, a charm flavor is produced from the coupling between $W^+(W^-)$ and (anti-)strange quark in the proton sea, as shown in Figure 1 (left). The same is also possible via down or beauty flavor; however, these are Cabibbo-suppressed [3]. Also shown in Figure 1 (right) is one of the NLO processes where the W couples to a gluon. Since this scheme does not involve the strangeness, it will be treated as background in this analysis. The contribution from this process becomes significant in the small x kinematic region where the gluon content is dominant. A study by Ingelman and Schuler made predictions for the inclusive cross section for charm flavor production at HERA, as listed in Table 1 [4]. The large BGF contribution is due to the kinematic reach of HERA in the small x region. In this analysis, the mid x ($0.01 \lesssim x \lesssim 0.20$) will be considered.

TABLE 1. List of Predicted Cross Section for Charm Production at HERA.

	QI		**BGF**	
e^+p	$\sigma(s \rightarrow c)(pb)$ 3.3	$\sigma(d \rightarrow c)(pb)$ 0.75	$\sigma(c\bar{s})(pb)$ 8.2	$\sigma(c\bar{d})(pb)$ 0.46
e^-p	$\sigma(\bar{s} \rightarrow \bar{c})(pb)$ 3.3	$\sigma(\bar{d} \rightarrow \bar{c})(pb)$ 0.26	$\sigma(\bar{c}s)(pb)$ 8.2	$\sigma(\bar{c}d)(pb)$ 0.46

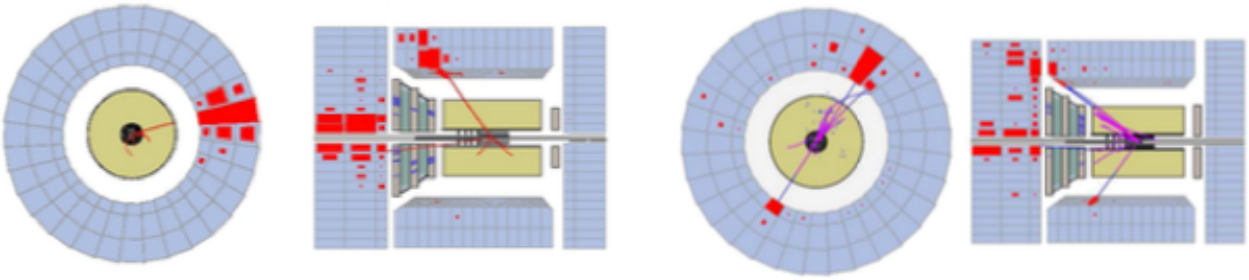

FIGURE 2. Event Display of CC DIS (left) and NC DIS (right); The final state neutrino in CC DIS escapes the detector undetected. As a result, a large missing transverse momentum is observed in the calorimeter (CAL).

Due to the final state neutrino, the information on the leptonic final state is lost, as shown in Figure 2. The invariant variables are redefined by employing the Jacquet-Blondel method in which the four momentum of the exchanged gauge boson q is not only the change in leptonic momentum $k - k'$, but also that in hadronic momentum $p - p'$ [3]. Substituting this relation into the definitions of the variables, one finds the following relations.

$$y_{JB} = \frac{\sum_h (E - p_z)_h}{2E_e}, \tag{1}$$

$$Q^2_{JB} = \frac{p^2_{T,h}}{1 - y_{JB}}, \tag{2}$$

$$x_{JB} = \frac{Q^2_{JB}}{s y_{JB}}. \tag{3}$$

CC DIS collisions only involve weak interaction. This makes the CC cross section highly sensitive to the flavor-specific parton distribution functions (PDFs). In the naive quark parton model (QPM), the proton consists of three quarks in the valence and quark-antiquark pairs as well as gluons in the proton sea. The differential CC cross section $d\sigma^{e^\pm p}_{CC,P_e}/dxdQ^2$ is expressed in terms of the structure functions W_2, W_3 and W_L, as shown in equations (4-5)

$$\frac{d\sigma^{e^\pm p}_{CC,P_e}}{dxdQ^2} = (1 \pm P_e)\frac{G_F^2}{4\pi x}\left(\frac{M_W^2}{M_W^2 + Q^2}\right)^2 \tilde{\sigma}^{e^\pm p}_{CC}, \tag{4}$$

$$\tilde{\sigma}^{e^\pm p}_{CC} = Y_+ W_2^\pm(x, Q^2) - y^2 W_L^\pm(x, Q^2) \mp Y_- x W_3^\pm(x, Q^2), \tag{5}$$

where $\tilde{\sigma}^{e^\pm p}_{CC}$ is the reduced cross section and the structure function W_L given by $W_L = W_2 - 2xW_1$ vanishes [3]. At the leading order in QCD, the remaining structure functions may be written in terms of sums and differences of quark and anti-quark PDFs, as shown in equations (6-7).

$$W_2(x, Q^2) = \sum_i x\,[\, q_i(x, Q^2) + \bar{q}_i(x, Q^2)]\,, \tag{6}$$

$$xW_3(x, Q^2) = \sum_i x\,[\, q_i(x, Q^2) - \bar{q}_i(x, Q^2)]\,. \tag{7}$$

In the Standard Model, the $W^-(W^+)$ only interacts with left (right) (anti-)particles. Therefore, the reduced cross section may be written, as shown in equations (8-9)

$$\tilde{\sigma}^{e^+ p}_{CC} = x[\,\bar{u} + \bar{c} + (1 - y)^2(d + s)]\,, \tag{8}$$

$$\tilde{\sigma}^{e^- p}_{CC} = x[\,u + c + (1 - y)^2(\bar{d} + \bar{s})]\,. \tag{9}$$

In this analysis, secondary vertexing method is used to distinguish the (anti-)strange contribution from the lighter-flavor contribution, which we collectively call the background.

The signature of events whose final state contains heavy flavor is that the final state hadron travels a certain distance before it decays, leaving a secondary vertex [5]. Secondary vertices are reconstructed by 3D fitting tracks coming from jets, as shown in Figure 3. The 2D decay length L_{xy} associated with a secondary vertex is then projected onto the corresponding jet axis. Due to the finite resolution of the detector, the distribution around zero decay length is highly symmetric for the background and slightly asymmetric for the charm signal. Hence, the background can be suppressed by subtracting the negative signal from the positive. In this analysis, the subtracted significance of the decay length is used as the discriminating variable.

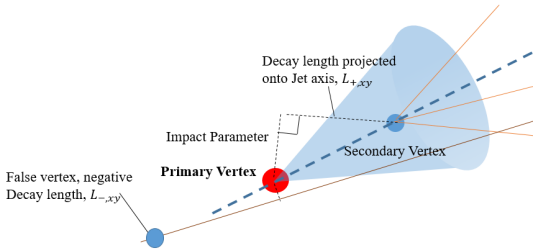

FIGURE 3. Schematic Diagram of Secondary Vertex Reconstruction; When there are more than two tracks associated to a jet, they are fitted to a secondary vertex. Due to the finite resolution of the MVD, false vertices with a negative decay length are observed.

EXPERIMENT

HERA underwent a shutdown period for a luminosity upgrade and installation of new components in ZEUS, including a silicon Micro Vertex Detector (MVD). The improvement in the luminosity was largely achieved by modifying the HERA interaction region to allow for smaller beam spot at the collision point [6].

The MVD has silicon microstrip sensors arranged around an elliptical beam pipe. It dramatically improved the tagging capabilities for heavy quarks by identifying displaced vertices [7]. In order to fully exploit the enhanced tagging capabilities and large statistics, this analysis only focuses on the data taken during the HERA II period. Table 2 lists beam parameters of the lepton and proton for each run period.

TABLE 2. List of Beam Parameters for HERA I and HERA II Measurements.

	HERA I			**HERA II**		
Period	94-97	98 - 99	99-00	03-04	04-06	06-07
Collision	e^+p	e^-p	e^+p	e^+p	e^-p	e^+p
$E_e, E_p(GeV)$	27.5, 820	27.5, 920	27.5, 920	27.5, 920	27.5, 920	27.5, 920
e, p beam current (mA)	50, 100	50, 100	50, 100	38, 140	38, 140	38, 140
Beam size (mm^2)	190×50	190×50	190×50	112×30	112×30	112×30
$L_{inst}\,(10^3 1cm^{-2}s^{-1})$	1.78	1.78	1.78	7.57	7.57	7.57
$L\,(pb^{-1})$	~ 45	~ 15	~ 65	~ 40	~ 190	~ 140

The kinematic reach of HERA allows for a measurement at a large Q^2 ($> 200\,GeV^2$). The combination of measurements from the positively and negatively charged collisions enables a direct comparison between the strange and anti-strange content in the proton sea. The data used in this analysis total about $180\,pb^{-1}$ of e^+p data and $190\,pb^{-1}$ of e^-p data.

EVENT SELECTION

The selection cuts presented in this section are based on the previous analyses on CC DIS and heavy flavor at high Q^2 range [8, 9, 10]. It should be noted that they are subject to change in this analysis.

A kinematic cut at $Q^2_{JB} > 200\,GeV^2$ and $y_{JB} < 0.9$ confines our data into a well-understood region with optimal resolution and low background. Charged current events at high Q^2 should have a large missing transverse momentum $P_{T,miss}$ measured in the calorimeter (CAL) due to the final state neutrino. Events with $P_{T,miss} > 12\,GeV$ and $P'_{T,miss} > 10\,GeV$ are accepted where $P'_{T,miss}$ represents the missing transverse momentum measured excluding the ones from CAL cells adjacent to the forward beam hole. The signature of photoproduction events is the high ratio of antiparallel and parallel components of hadronic transverse moment V_{AP}/V_P where $V_{AP(P)} = -(+)\sum_h \vec{P}_{T,h} \cdot \vec{P}_T/P_T$. Events with $V_{AP}/V_P \geq 0.35$ are rejected. Events with $P_T < 20\,GeV$ are further resitricted to satisfy $V_{AP}/V_P \leq 0.25$. Large missing transverse momentum can be observed in Neutral Current DIS (NC DIS) as a result of poorly measured hadronic jet or charged lepton. Such events are identified and rejected by evaluating $\delta = \sum_h (E - P_z)_h = 2E_e y_{JB}$.

Further selection processes are performed in order to ensure jet and track quality and restrict the light flavor contribution in the decay length signal. Jets are reconstructed by using the jet clustering algorithm and are required

to have transverse energy $E_T^{jet} > 5\,GeV$ in $-2.5 < \eta < 2.5$ pseudo-rapidity region. Tracks are associated with a jet if the proximity satisfy the condition $\Delta R < 1$ where $\Delta R = \sqrt{(\phi^{trk} - \phi^{jet})^2 + (\eta^{trk} - \eta^{jet})^2}$. The tracks are then selected if $P_T^{trk} > 0.5\,GeV$. The total number of hits in the MVD was required to be $N_{MVD} \geq 4$ as well as $N_{CTD} \geq 3$ or $N_{STT} \geq 1$.[2] If more than two tracks associated to a jet survive these criteria, they are fitted to a secondary vertex by using the deterministic annealing filter [12]. The reconstructed secondary vertices are required to satisfy $\chi^2/N_{dof} < 6, |Z_{secvtx}| < 30\,cm$ and the proximity to the beam spot $\sqrt{\Delta x^2 + \Delta y^2} < 1\,cm$.

We expect approximately 4000 e^+p events and 9000 e^-p events to satisfy these criteria. These numbers were obtained by extrapolating the value from the previous analysis with the luminosity of this analysis [8]. The difference in the estimated sample size is largely due to the difference in the integrated luminosity among the run periods as well as the difference in the number of light flavor events which arises from the factor of two larger up flavor content in the proton valence level. About 100 events are expected to survive after the decay length subtraction.

SUMMARY

The present analysis at the ZEUS collaboration attempts to measure the charm cross section by using CC DIS in $e^{\pm}p$ collisions at $\sqrt{s} = 318\,GeV$. This measurement will provide high Q^2 data that is sensitive to the strangeness in the proton sea. The ZEUS result will serve as a complementary measurement to CCFR/NuTeV and ATLAS. The HERA II data set includes measurements from e^+p and e^-p collisions which correspond to approximately 180 pb^{-1} and 190 pb^{-1} of data, respectively. These measurements benefit from a major upgrade to the ZEUS detector which enhanced the integrated luminosity as well as the heavy flavor tagging capabilities.

REFERENCES

[1] ATLAS Collab., Eur. Phys. J. **C 77**, p. 367 (2017).
[2] CCFR Collab., A.O. Bazarko et al., Z.Phys. **C 65**, 189–198 (1995).
[3] Abramowicz and Caldwell, Rev.Mod.Phys. **71**, 1275–1410 (1999).
[4] DESY, Ingelman and Schuler, Z.Phys. **C 40**, p. 299 (1988).
[5] ZEUS Collab., H. Abramowicz et al., Eur.Phys.J. **C 71**, p. 1659 (2011).
[6] M. Minty, "Hera performance upgrade: Achievements and plans for the future," in *EPAC2004 EPAC04 04*, edited by L. R. Geneva (EPS-AG, Lucerne, Switzerland, 2004), pp. 93–97.
[7] ZEUS Collab., A. Polini et al., Nucl. Instrum. Meth. **A 581**, 656–686 (2007).
[8] ZEUS Collab., H. Abramowicz et al., Eur.Phys.J. **C 70**, 945–963 (2010).
[9] ZEUS Collab., H. Abramowicz et al., JHEP **1409**, p. 127 (2014).
[10] ZEUS Collab., H. Abramowicz et al., Eur.Phys.J **C 71**, p. 1659 (2011).
[11] ZEUS Collab., U. Holm, *The ZEUS Detector*, Status Report (unpublished), DESY (1993), available on http://www-zeus.desy.de/bluebook/bluebook.html.
[12] K. Rose, E. Gurewitz and G.C. Fox, Phys. Rev. Lett. **65**, p. 945 (1990).

[2] The Central Tracking Detector (CTD) is a cylindrical wire chamber which measures the trajectories of charged particles [11]. Another upgrade to the ZEUS detector during the shutdown period was the Straw-Tube Tracker (STT) which was designed to improve tracking capabilites in the forward direction [7].

Using Polarized Positrons to Probe Physics Beyond the Standard Model

Yulia Furletova[1,a)] and Sonny Mantry[2,b)]

[1]*Jefferson Lab, Newport News, VA, 23606, USA*
[2]*The University of North Georgia, Dahlonega, GA, 30597, USA*

[a)]yulia@jlab.org
[b)]Sonny.Mantry@ung.edu

Abstract. A high intensity polarized positron beam, as part of the JLAB 12 GeV program and the proposed electron-ion collider (EIC), can provide a unique opportunity for testing the Standard Model (SM) and probing for new physics. The combination of high luminosity with polarized electrons and positrons incident on protons and deuterons can isolate important effects and distinguish between possible new physics scenarios in a manner that will complement current experimental efforts. A comparison of cross sections between polarized electron and positron beams will allow for an extraction of the poorly known weak neutral current coupling combination $2C_{3u} - C_{3d}$ and would complement the proposed plan for a precision extraction of the combination $2C_{2u} - C_d$ at the EIC. Precision measurements of these neutral weak couplings would constrain new physics scenarios including Leptoquarks, R-parity violating supersymmetry, and electron and quark compositeness. The dependence of the charged current cross section on the longitudinal polarization of the positron beam will provide an independent probe to test the chiral structure of the electroweak interactions. A polarized positron can probe charged lepton flavor violation (CLFV) through a search for $e^+ \to \tau^+$ transitions in a manner that is independent and complementary to the proposed $e^- \to \tau^-$ search at the EIC. A positron beam incident on an electron in a stationary nuclear target will also allow for a dark-photon (A') search via the annihilation process $e^+ + e^- \to A' + \gamma$.

INTRODUCTION

The 12 GeV Jefferson Lab (JLAB) program [1] and the proposed electron-ion collider (EIC) [2] are primarily focused on detailed studies of quantum chromodynamics (QCD) and nuclear structure. However, in both of these programs precision tests of the Standard Model (SM) and the search for new physics form vital components as part of the wider effort to search for physics beyond the SM at the "Intensity/Precision Frontier". It is the combination of high luminosity and the availability of polarized electrons and nuclei, a variety of nuclear targets, and a wide kinematic range that allows for a robust program of physics beyond the SM in a manner that complements efforts at the "Energy Frontier". The EIC design calls for a luminosity of $\mathcal{L} \sim 10^{33-34}$ cm$^{-2}s^{-1}$, about a hundred to a thousand times greater than the luminosity achieved at HERA. The SoLID (Solenoidal Large Intensity Detector) [3] program, as part of the 12 GeV upgrade, will be capable of handling luminosities of up to $\mathcal{L} \sim 10^{39}$ cm$^{-2}s^{-1}$.

In this contribution, we explore the possibility of the addition of a polarized positron beam to complement efforts at the Intensity/Precision Frontier at the proposed EIC and the 12 GeV JLAB program. A polarized positron beam is essential for an extraction of the poorly known C_{3q} weak neutral current couplings, providing an independent test of the electroweak structure of the SM and complementing existing measurements of the C_{1q}, C_{2q} neutral weak couplings. It will also mark the first time the C_{3q} couplings are extracted through the use of electron and positron beams. Precision measurements of these neutral weak couplings couplings will constrain new physics scenarios including Leptoquark models, R-parity violating supersymmetry, and electron and quark compositeness. The charged current process $e^+ + p \to \bar{\nu}_e + X$ will allow for a test of the chiral structure of the charged current interactions in the SM in a manner that is independent and complementary to the process $e^- + p \to \nu_e + X$. These charged current tests could improve upon the limits set by HERA. A polarized positron beam will also allow for a search of charged lepton flavor violation (CLFV) through searches for $e^+ \to \tau^+$ transitions, complementing CLFV searches at the EIC through $e^- \to \tau^-$. It will also allow one to distinguish between different states that might contribute to CLFV processes or a modification of the

SM electroweak couplings. A positron beam incident on an electron in a stationary nuclear target will also allow for a dark-photon (A') search via the annihilation process $e^+ + e^- \to A' + \gamma$. [1]

NEUTRAL WEAK COUPLINGS

For electron-hadron scattering, the weak neutral current can be parameterized in terms of contact interactions

$$\mathcal{L} = \frac{G_F}{\sqrt{2}} \sum_{\ell,q} \Big[C_{1q}\, \bar{\ell}\gamma^\mu\gamma_5\ell\bar{q}\gamma_\mu q + C_{2q}\ \bar{\ell}\gamma^\mu\ell\bar{q}\gamma_\mu\gamma_5 q + C_{3q}\, \bar{\ell}\gamma^\mu\gamma_5\ell\bar{q}\gamma_\mu\gamma_5 q \Big], \tag{1}$$

in the region where the virtuality of the exchanged boson satisfies $Q^2 \ll M_Z^2$, where M_Z is the Z-boson mass and G_F denotes Fermi's constant. The C_{iq} coefficients denote the effective couplings and in the single boson exchange approximation in the Standard Model (SM), they take the form $C_{1q} = g_A^e g_V^q, C_{2q} = g_V^e g_A^q, C_{3q} = g_A^e g_A^q$. The electron ($g_{A,V}^e$) and quark ($g_{A,V}^q$) couplings are given in terms of their respective weak isospin (T_3) and electric charge (Q) quantum numbers and the weak mixing angle θ_W: $g_A^{e,q} = T_3, g_V^{e,q} = T_3 - 2Q\sin^2\theta_W$. The SM tree-level expressions for the C_{iq} coefficients are then given by

$$C_{1u} = -\frac{1}{2} + \frac{4}{3}\sin^2\theta_W, \qquad C_{2u} = -\frac{1}{2} + 2\sin^2\theta_W, \qquad C_{3u} = \frac{1}{2}, \tag{2}$$

$$C_{1d} = \frac{1}{2} - \frac{2}{3}\sin^2\theta_W, \qquad C_{2d} = \frac{1}{2} - 2\sin^2\theta_W, \qquad C_{3d} = -\frac{1}{2}. \tag{3}$$

Going beyond the single boson exchange approximation, the effective couplings can no longer be written as products of the electron and quark weak couplings and are instead denoted by $C_{1q} = g_{AV}^{eq}, C_{2q} = g_{VA}^{eq}, C_{3q} = g_{AA}^{eq}$. A comparison of the measured values of the C_{iq} couplings with the SM predictions can be used to set limits of the scale Λ at which new interactions may arise. At low energies, well below the scale Λ, these new interactions can be parametrized by the effective Lagrangian:

$$\delta\mathcal{L} = \frac{g^2}{\Lambda^2} \sum_{\ell,q} \Big\{ \eta_{LL}^{\ell q}\, \bar{\ell}_L\gamma_\mu\ell_L\bar{q}_L\gamma_\mu q_L + \eta_{LR}^{\ell q}\, \bar{\ell}_L\gamma_\mu\ell_L\bar{q}_R\gamma_\mu q_R + \eta_{RL}^{\ell q}\, \bar{\ell}_R\gamma_\mu\ell_R\bar{q}_L\gamma_\mu q_L + \eta_{RR}^{\ell q}\, \bar{\ell}_R\gamma_\mu\ell_R\bar{q}_R\gamma_\mu q_R \Big\}, \tag{4}$$

where the mass limit for Λ is defined with the convention $g^2 = 4\pi$. The coefficients $\eta_{ij}^{\ell q}$ take on the values of $+1$, 0, or -1, allowing for the possibility of constructive or destructive interference with the SM contributions. The C_{iq} coefficients can now be written as the sum of the SM and new physics contributions $C_{iq} = C_{iq}(\mathrm{SM}) + \Delta C_{iq}$, where:

$$\Delta C_{1q} = \frac{g^2}{\Lambda^2} \frac{\eta_{LL}^{\ell q} + \eta_{LR}^{\ell q} - \eta_{RL}^{\ell q} - \eta_{RR}^{\ell q}}{2\sqrt{2}G_F}, \tag{5}$$

$$\Delta C_{2q} = \frac{g^2}{\Lambda^2} \frac{\eta_{LL}^{\ell q} - \eta_{LR}^{\ell q} + \eta_{RL}^{\ell q} - \eta_{RR}^{\ell q}}{2\sqrt{2}G_F}, \tag{6}$$

$$\Delta C_{3q} = \frac{g^2}{\Lambda^2} \frac{-\eta_{LL}^{\ell q} + \eta_{LR}^{\ell q} + \eta_{RL}^{\ell q} - \eta_{RR}^{\ell q}}{2\sqrt{2}G_F}. \tag{7}$$

$$\tag{8}$$

Precision measurements of the C_{iq} constrain the possible deviations ΔC_{iq} which can be converted into a mass limit for Λ. For example, a new physics scenario with chiral structure $\eta_{LL}^{\ell q} = 1$ and $\eta_{RR}^{\ell q} = \eta_{RL}^{\ell q} = \eta_{LR}^{\ell q} = 0$, results in a particular pattern of shifts $\Delta C_{1q} = \Delta C_{2q} = -\Delta C_{3q} = g^2/(2\sqrt{2}\Lambda^2 G_F)$ relative to the SM values which can be used to set limits on Λ. Precision measurements of the C_{iq} couplings constrain new physics scenarios including Leptoquark models, R-parity violating supersymmetry, and electron and quark compositeness.

[1] Dark photon searches will be discussed in a separate contribution to proceedings of this conference and will not be discussed here.

The C_{1q}, C_{2q} couplings are parity-violating and various combinations of these couplings, appearing in different observables, have been measured with increasing precision over the past two decades. Combinations of the C_{1q} coefficients have best been measured through atomic parity violation [4] and elastic parity violating electron scattering [5]. The C_{2q} couplings are more challenging due to their relatively small values in the SM (since $\sin^2\theta_W \approx 1/4$, implying $g_V^e \approx 0$). They can be accessed through parity violating deep inelastic scattering on a deuteron target which uses polarized electron beams to measure the cross section asymmetry between left-handed and right-handed electrons

$$A_{PV} = \frac{d\sigma_L - d\sigma_R}{d\sigma_L + d\sigma_R}. \tag{9}$$

Recently [6] at JLAB, 6 GeV polarized electrons incident on a unpolarized deuteron target were used to extract the combination $2C_{2u} - C_{2d} = -0.145 \pm 0.068$ at $Q^2 = 0$, showing for the first time that this combination is non-zero at the 95% confidence level. The mass limit [6] on the new physics scale corresponding this measurement is $\Lambda_+ > 5.7$ TeV and $\Lambda_- > 4.5$ TeV for constructive and destructive interference of the new physics with the SM respectively. The SoLID [3] spectrometer as part of the JLAB 12 GeV program is expected to further improve the precision of this measurement. The EIC can provide even further improvement due to its wide kinematic range coupled with high luminosity, allowing for enhanced sensitivity to the combination $2C_{2u} - C_{2d}$ over a wide range of Q^2.

By contrast, experimental data on the C_{3q} couplings are quite sparse. They are parity-conserving but charge-conjugation-violating (charge conjugation of the lepton charge) and can be accessed through a comparison of cross sections of polarized leptons and anti-leptons scattering off a nuclear target. The only experiment to measure a charge conjugation asymmetry was at CERN [7] and used polarized muon and anti-muon beams scattering off a Carbon target. A muon/anti-muon beam energy of 200 GeV was used to extract the combination $0.81(2C_{2u} - C_{2d}) + 2C_{3u} - C_{3d} = 1.53 \pm 0.45$. Using the current experimental value [6] of $2C_{2u} - C_{2d} = -0.145 \pm 0.068$, we can extract the combination of C_{3q} couplings as $2C_{3u} - C_{3d} = 1.65 \pm 0.453$.

The availability of a polarized positron beam will provide a unique opportunity to significantly improve upon the current uncertainty in the C_{3q} couplings through a measurement of the charge conjugation asymmetry [8]:

$$A^{e_L^- - e_R^+} = \frac{d\sigma(e_L^- N) - d\sigma(e_R^+ N)}{d\sigma(e_L^- N) + d\sigma(e_R^+ N)}. \tag{10}$$

It will also be the first time that the C_{3q} couplings would be extracted through the use of polarized electron and positron beams. To a good approximation, the asymmetry for scattering off a proton target is given by [9]:

$$A_p^{e_L^- - e_R^+} = \frac{3G_F Q^2}{2\sqrt{2}\pi\alpha} \frac{y(2-y)}{2} \frac{2C_{2u}u_V - C_{2d}d_V + 2C_{3u}u_V - C_{3d}d_V}{4u + d}, \tag{11}$$

where $q_V \equiv q - \bar{q}$ are the valence quark parton distribution functions and $y = \nu/E$ with E being the lepton energy and ν the energy transferred to the proton target. For the isoscalar deuteron target, the asymmetry takes the form:

$$A_d^{e_L^- - e_R^+} = \frac{3G_F Q^2}{2\sqrt{2}\pi\alpha} \frac{y(2-y)}{2} \frac{(2C_{2u} - C_{2d} + 2C_{3u} - C_{3d})R_V}{5}, \tag{12}$$

where $R_V \equiv (u_V + d_V)/(u + d)$. The isoscalar deuteron target is preferred over the proton target since it provides access to the combination $2C_{3u} - C_{3d}$ and minimizes the uncertainty from the d/u ratio of parton distribution functions. However, both the proton and deuteron targets can be used in order to extract the C_{3q} couplings.

It was estimated that [10] that this asymmetry off a deuteron target can be measured to a 3% statistical precision (for a 6 GeV lepton beam) allowing for an extraction of the combination $2C_{3u} - C_{3d}$ to within 3% relative uncertainty. This level of precision can be converted into a 95% CL mass limit of $\Lambda \gtrsim 6.2$ TeV, assuming that the measurement of $2C_{3u} - C_{3d}$ agrees with the SM value of $(2C_{3u} - C_{3d})^{\rm SM} = 1.4973$. The SM value was obtained from Table 6 of Ref. [11] using the condition $0.81(2C_{2u} - C_{2d})^{\rm SM} + (2C_{3u} - C_{3d})^{\rm SM} = 1.4204$ and $(2C_{2u} - C_{2d})^{\rm SM} = -0.0949$. Note that the mass limit of $\Lambda \gtrsim 6.2$ TeV was obtained only taking into account a relative statistical uncertainty of 3%. A detailed study that includes systematic errors, including differences in beam quality for electron and positron beams, is required. A revised estimate of the statistical precision for a 12 GeV lepton beam is also required. The new overall uncertainty that includes systematic errors will correspondingly lower the projected 95% CL mass limit. For an overall uncertainty of 5%, 10%, 20%, and 50% the corresponding 95% CL mass limit will be $\Lambda \gtrsim 4.8$ TeV, 3.4 TeV, 2.4 TeV, and 1.5 TeV respectively.

CHARGED CURRENT CROSS SECTIONS

The chiral structure of the electroweak interactions dictates that only the left-handed electrons (e_L^-) and the right-handed positrons (e_R^+) couple to the W-boson. Consequently, the SM predicts that the cross section for the charged current processes $e^- + p \to \nu_e + X$ and $e^+ + p \to \bar{\nu}_e + X$ will have a linear dependence on the lepton beam polarization:

$$\sigma^{e^\pm p}_{\rm SM}(P_e) = (1 \pm P_e)\sigma^{e^\pm p}_{\rm SM}(P_e = 0), \tag{13}$$

where P_e denotes the lepton beam polarization:

$$P_e = \frac{N_R - N_L}{N_R + N_L}, \tag{14}$$

and N_R and N_L denote the number of right-handed and left-handed leptons (electrons or positrons) respectively. In particular, the SM predicts $\sigma^{e^\pm p}_{\rm SM}(P_e = \mp 1) = 0$. The charged current differential cross section has the general form:

$$\frac{d^2\sigma^{e^\pm p}_{SM}(P_e)}{dx\,dQ^2} = (1 \pm P_e)\frac{G_F^2}{4\pi x}\left[\frac{M_W^2}{M_W^2 + Q^2}\right]^2\left\{Y_+ F_2^{W^\pm} - y^2 F_L^{W^\pm} \pm Y_- x F_3^{W^\pm}\right\}, \tag{15}$$

where $Y_\pm = 1 \pm (1-y)^2$, the virtuality of the exchanged boson is $Q^2 = xys$, and x, y denote the standard Bjorken variables and s is the center of mass energy squared. At the Born level, $F_L^{W^\pm} = 0$ and the the structure functions $F_{2,3}^{W^\pm}$ simplify so that the total charged current cross-sections become:

$$\frac{\sigma^{e^+ p}_{\rm SM}(P_e)}{dx\,dQ^2} = (1 + P_e)\frac{G_F^2}{2\pi}\left(\frac{M_W^2}{M_W^2 + Q^2}\right)^2\left[\bar{u}(x,Q^2) + \bar{c}(x,Q^2) + (1-y)^2\Big(d(x,Q^2) + s(x,Q^2)\Big)\right], \tag{16}$$

$$\frac{\sigma^{e^- p}_{\rm SM}(P_e)}{dx\,dQ^2} = (1 - P_e)\frac{G_F^2}{2\pi}\left(\frac{M_W^2}{M_W^2 + Q^2}\right)^2\left[u(x,Q^2) + c(x,Q^2) + (1-y)^2\Big(\bar{d}(x,Q^2) + \bar{s}(x,Q^2)\Big)\right]. \tag{17}$$

As seen from Equation 16 and 17, the electron and positron beams couple to different combinations of the parton distribution functions, providing independent probes of the linear polarization dependence of the charged current cross section. Thus, a positron beam will complement the electron beam in providing an independent test of the chiral structure of the charged current interactions of the SM.

Polarized electron and positron beams allow measurements of the charged current cross sections for few different values of the beam polarization P_e. A straight-line fit of this polarization dependence can be extrapolated to obtain the charged current cross section at $P_e = \mp 1$ and compared to the SM prediction $\sigma^{e^\pm p}_{\rm SM}(P_e = \mp 1) = 0$. Any observed deviation could indicated the presence of new physics that couples to couples to right-handed electrons and left-handed positrons. A non-zero value for $\sigma^{e^\pm p}(P_e = \mp 1)$ could arise from the coupling of a right-handed W-boson (W_R) of mass M_R to a right-handed electron and a right-handed neutrino. Such a W_R-boson arises in Left-Right Symmetric models that restore the symmetry between left-handed and right-handed quarks and leptons at higher energies such that the SM electroweak sector arises from the spontaneous symmetry breaking $SU(2)_L \otimes SU(2)_R \otimes U(1)_{B-L} \to SU(2)_L \otimes U(1)_Y$. In the presence of a W_R-boson and a light right-handed neutrino, the polarization dependence of the charged current cross section takes the form:

$$\sigma^{e^\pm p}(P_e) = (1 \pm P_e)\,\sigma^{e^\pm p}_{\rm SM}(P_e = 0) + (1 \mp P_e)\,\sigma^{e^\pm p}_{\rm SM}(P_e = 0, M_W \to M_R), \tag{18}$$

where the second term above arises from W_R exchange and is the same as the SM result except for the replacement $M_W \to M_R$, assuming equal coupling strengths between the left-handed and right-handed currents. The second term now allows for a non-zero value for $\sigma^{e^\pm p}(P_e = \mp 1)$ which depends on the W_R-boson mass M_R as:

$$\sigma^{e^\pm p}(P_e = \mp 1) = 2\,\sigma^{e^\pm p}_{\rm SM}(P_e = 0, M_W \to M_R) \neq 0. \tag{19}$$

From the extrapolation of the straight-line fit of $\sigma^{e^\pm p}(P_e)$ to the points $P_e = \pm 1$, one can obtain a 95% CL upper bound, $\sigma^{e^\pm p}_{\text{upper bound}}(P_e = \mp 1)$, which can be converted into a W_R-boson mass limit by requiring:

$$\sigma^{e^\pm p}_{\rm SM}(P_e = 0, M_W \to M_R) < \frac{\sigma^{e^\pm p}_{\text{upper bound}}(P_e = \mp 1)}{2}\,. \tag{20}$$

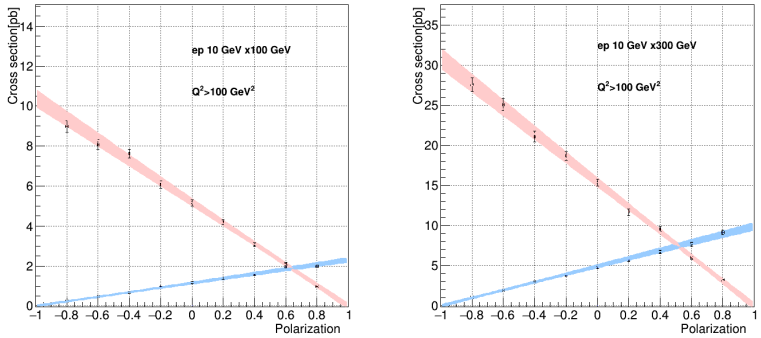

FIGURE 1. Polarization (P_e) dependence of the charged current cross section for $\sqrt{s}$ = 63.25 GeV (left panel) and $\sqrt{s}$ = 109.5 GeV (right panel) based on Monte Carlo simulations using HERWIG 6.5. The red (blue) bands correspond to electron and positron beams respectively. The simulation assumed an integrated luminosity of $\mathcal{L}$ = 100 fb^{-1}, a relative polarization uncertainty of 1%, and a measurement systematic uncertainty of 3%. As explained in the text, these results were used to derive mass limits on the right-handed W_R boson.

Although the EIC will have smaller cross sections compared to HERA due to its lower center of mass energy, its higher luminosity and degree of lepton beam polarization can allow for a more precise extraction of $\sigma^{e^\pm p}_{\text{upper bound}}(P_e = \mp 1)$, allowing for the possibility of stronger limits. Preliminary results simulating such an analysis, using HERWIG 6.5 [12, 13], are shown in Figure 1. The simulation assumed a relative uncertainty on the lepton beam polarization of $\Delta P_e/P_e \sim 1\%$, a systematic uncertainty $\sim 3\%$ in the measured cross-section in addition to the statistical uncertainty, and an integrated luminosity of $\mathcal{L}$ = 100 fb^{-1}. For the case of a 10 GeV positron beam colliding with a 100 GeV proton beam ($\sqrt{s}$ = 63.25 GeV) with cut of $Q^2 > 100$ GeV^2, a 95% CL upper bound of $\sigma^{e^+p}(P_e = -1) < 0.0207$pb is obtained giving the limit of $M_R \gtrsim 270$ GeV. For the case of a 10 GeV positron beam colliding with a 300 GeV proton beam ($\sqrt{s}$ = 109.5 GeV) with cut of $Q^2 > 100$ GeV^2, a 95% CL upper bound of $\sigma^{e^+p}(P_e = -1) < 0.0776$pb is obtained giving the limit of $M_R \gtrsim 285$ GeV. Although more detailed studies are required, these preliminary results indicate that the EIC can compete and make modest improvements on the HERA limits [14] which require $M_R > 208$ GeV. These bounds can be further improved with higher luminosity ($\mathcal{L}$ = 1000 fb^{-1}) or center of mass energy ($\sqrt{s} \sim 150$ GeV). While the Tevatron and the LHC have already set more stringent limits on M_R (in the TeV range) by looking for deviations in the transverse mass distribution of the Drell-Yan process $pp \to W \to \ell\nu_\ell$, the observed distribution is sensitive to a time-like charged boson and in general can be affected by physics that involves a different combination of chiral and flavor structures. Thus, new limits from the EIC can provide complementary information to limits from colliders.

CHARGED LEPTON FLAVOR VIOLATION

The discovery of neutrino oscillations imply lepton flavor violation (LFV) which can also mediate charged lepton flavor violating (CLFV) processes such as $\mu \to e\gamma$, although highly supressed, Br($\mu \to e\gamma$) $\lesssim 10^{-54}$. However, many beyond the SM scenarios predict significantly higher CLFV rates that are within the reach of current or future planned experiments. While CLFV between the first two generations is severely constrained, for example Br($\mu^+ \to e^+\gamma$) $< 4.2 \times 10^{-13}$ [15], the limits on CLFV involving the $e \leftrightarrow \tau$ transition are worse by several orders of magnitude. This motivated extensive searches for CLFV at HERA [16, 17] through the processes $e^\pm p \to \tau^\pm + X$. Theoretical and simulation studies [18, 19] have been now been performed for the EIC. These studies indicate that with 1000 fb^{-1} of integrated luminosity, the EIC can improve upon the HERA limits by a factor between 10 and 200. A polarized positron beam would complement these planned studies at the EIC, providing an independent probe that can help distinguish between different CLFV mechanisms.

It is convenient to study CLFV within the Leptoquark (LQ) framework. LQs are color triplet particles that couple to leptons and quarks and arise in many beyond the standard model scenarios. Unlike most other models, LQs can mediate CLFV processes at tree-level allowing for larger cross sections. The Buchmüller-Rückl-Wyler (BRW)

parameterization classifies the LQs into 14 different types according to their spin (scalar or vector), fermion number F=3B+L (0 or ±2), chiral couplings to leptons (left-handed or right-handed), $SU(2)_L$ representation (singlet, doublet, or triplet), and $U(1)_Y$ hypercharge.

In the region where the LQ mass $M_{LQ} \gg \sqrt{s}$, the CLFV process is mediated via a contact interaction. In this approximation, for an electron beam, the cross-section for $e^- N \to \tau^- + X$ takes the form:

$$\sigma^{e^- p}_{F=0} = \sum_{\alpha,\beta} \frac{s}{32\pi}\left[\frac{\lambda_{1\alpha}\lambda_{3\beta}}{M^2_{LQ}}\right]^2 \left\{ \int dx \int dy\, x\bar{q}_\alpha(x, xs) f(y) + \int dx \int dy\, x q_\beta(x, -u) g(y) \right\}, \tag{21}$$

$$\sigma^{e^- p}_{|F|=2} = \sum_{\alpha,\beta} \frac{s}{32\pi}\left[\frac{\lambda_{1\alpha}\lambda_{3\beta}}{M^2_{LQ}}\right]^2 \left\{ \int dx \int dy\, x q_\alpha(x, xs) f(y) + \int dx \int dy\, x\bar{q}_\beta(x, -u) g(y) \right\}, \tag{22}$$

where $u = x(y-1)s$ and for a scalar LQ $f(y) = 1/2, g(y) = (1-y)^2/2$ and for a vector leptoquark $f(y) = 2(1-y)^2, g(y) = 2$. The lepton-quark-LQ couplings λ_{ij} are assumed to be real and the first and second indices denote the lepton and quark generations respectively. In the above expressions for the cross section, the first and second terms arise from an s-channel and u-channel LQ-exchange respectively. Similarly, for a positron beam, the cross section for $e^+ N \to \tau^+ + X$ takes the form:

$$\sigma^{e^+ p}_{F=0} = \sum_{\alpha,\beta} \frac{s}{32\pi}\left[\frac{\lambda_{1\alpha}\lambda_{3\beta}}{M^2_{LQ}}\right]^2 \left\{ \int dx \int dy\, x q_\alpha(x, xs) f(y) + \int dx \int dy\, x\bar{q}_\beta(x, -u) g(y) \right\}, \tag{23}$$

$$\sigma^{e^+ p}_{|F|=2} = \sum_{\alpha,\beta} \frac{s}{32\pi}\left[\frac{\lambda_{1\alpha}\lambda_{3\beta}}{M^2_{LQ}}\right]^2 \left\{ \int dx \int dy\, x\bar{q}_\alpha(x, xs) f(y) + \int dx \int dy\, x q_\beta(x, -u) g(y) \right\}. \tag{24}$$

From the above expressions for the cross sections, we see that the s-channel process for an F=0 (|F|=2) LQ is larger with a positron (electron) beam since it involves the parton distribution function of initial state quark as opposed to an anti-quark. Thus, the positron and electron beams can be used to enhance the F=0 and $|F|$=2 LQ channels respectively. The polarization of the electron and positron beams can be used to distinguish between LQs that couple to left-handed electrons and right-handed positrons and those that couple to right-handed electrons and left-handed positrons. A wide kinematic range allows distinguishing between scalar and vector LQs through the difference in the y-dependence of the corresponding cross sections. Furthermore, depending on the couplings and electroweak quantum numbers, the production of LQ states might be dominated via lepton scattering from an u-quark ("eu" LQ) or a d-quark ("ed" LQ) within the nuclear target. A comparison of cross sections between a proton and deuteron target can help distinguish between these LQ states. We summarize these points below:

- electron vs. positron beams: distinguish between F=0 and |F|=2 LQs
- polarized electron/positron beams: distinguish between left-handed and right-handed LQs
- wide kinematic range: distinguish between scalar and vector LQs.
- proton vs. deuteron targets: distinguish between "eu" and "ed" LQs.

A more detailed analysis of these points to distinguish between various LQ states can be found in [20]. An updated analysis corresponding the EIC machine parameters is needed in order to further quantify these ideas.

As an example, Figure 2 illustrates the use of polarized electron and positron beams to distinguish between the $S^{\rm R}_0$ (|F|=2) and $S^{\rm L}_{1/2}$ (F=0) scalar LQ states. The dominant partonic s-channel production process for these LQs are $e^-_R u_R \to S^{\rm R}_0$ and $e^+_R u_R \to S^{\rm L}_{1/2}$. Thus, one expects a larger cross section for the $S^{\rm R}_0$ ($S^{\rm L}_{1/2}$) LQ states in the case of an electron (positron) beam with right-handed polarization. In Figure 2, we plot the cross section ($\sqrt{s}$ = 90 GeV) for the production of $S^{\rm R}_0$ ($S^{\rm L}_{1/2}$) states as a function the variable $z \equiv \lambda_{1\alpha}\lambda_{3\beta}/M^2_{LQ}$ divided by the corresponding HERA limit [16, 17]. Thus, $z = 1$ corresponds to the ratio $\lambda_{1\alpha}\lambda_{3\beta}/M^2_{LQ}$ precisely at the HERA limit, yielding the largest allowed cross section. We choose $\alpha = \beta = 1$, corresponding to the contribution from first generation quarks. The most stringent limit in this case comes from the $\tau \to e\pi$ process, yielding $\lambda_{11}\lambda_{31}/M^2_{LQ} < 0.4$ TeV^{-2} [16] for both $S^{\rm R}_0$ and $S^{\rm L}_{1/2}$. Thus, in terms of the z variable one obtains identical cross sections for $S^{\rm R}_0$ with right-handed electron (left-handed positron) beams and $S^{\rm L}_{1/2}$ with right-handed positron (left-handed electron) beams. The dotted lines in Figure 2 correspond to the cross sections for unpolarized ($P_e = 0$) lepton beams. The bands correspond to the linear variation of the cross section with the respective lepton beam polarization, $\sigma(P_e) = (1 \pm P_e)\sigma(P_e = 0)$, due to the chiral lepton couplings of the LQs. The bands correspond to the lepton beam polarization P_e being varied between [-80%,80%]. Thus, we see that the complementary use of polarized electron and positron beams can be effective in constraining the contribution from different LQs or different mechanisms that might contribute to CLFV.

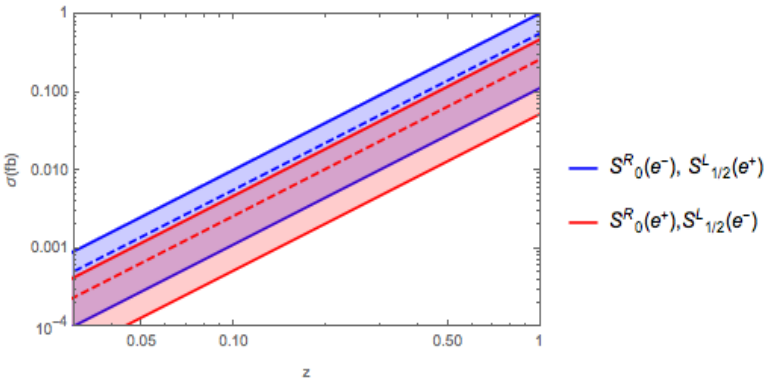

FIGURE 2. Production cross section ($\sqrt{s} = 90$ GeV) for the $S^{\rm R}_0$ and $S^{\rm L}_{1/2}$ LQ states using polarized electron and positron beams as a function of the variable $z = \lambda_{11}\lambda_{31}/M^2_{LQ}$. The blue (red) dotted line gives the unpolarized, $P_e = 0$, cross section for $S^{\rm R}_0$ using an e^- (e^+) beam or $S^{\rm L}_{1/2}$ using an e^- (e^+) beam. The blue and red bands correspond to the variation of the respective cross section when the beam polarization is varied between [-80%,80%] and can be used to distinguish between different LQ states. For example, the top solid blue line corresponds to the cross section for $S^{\rm R}_0$ using a 80% right-polarized electron beam or $S^{\rm L}_{1/2}$ using a 80% right-polarized positron beam. Similarly, the bottom solid red line corresponds to the cross section for $S^{\rm R}_0$ using a 20% left-polarized positron beam or $S^{\rm L}_{1/2}$ using a 20% left-polarized electron beam.

Conclusions

A polarized positron beam can play an important role in the search for physics beyond the SM at the Intensity/Precision Frontier. It will complement the efforts of the 12 GeV JLAB program and the EIC in precision measurements of the weak neutral couplings to constrain new physics scenarios and distinguishing between them, testing the structure of the charged current interactions, searching for charged lepton flavor violation, and dark photon searches.

REFERENCES

[1] J. Dudek *et al.*, Eur. Phys. J. **A48**, p. 187 (2012), arXiv:1208.1244 [hep-ex] .
[2] A. Accardi *et al.*, Eur. Phys. J. **A52**, p. 268 (2016), arXiv:1212.1701 [nucl-ex] .
[3] J. P. Chen, H. Gao, T. K. Hemmick, Z. E. Meziani, and P. A. Souder (SoLID), (2014), arXiv:1409.7741 [nucl-ex] .
[4] C. S. Wood, S. C. Bennett, D. Cho, B. P. Masterson, J. L. Roberts, C. E. Tanner, and C. E. Wieman, Science **275**, 1759–1763 (1997).
[5] D. Androic *et al.* (Qweak), Phys. Rev. Lett. **111**, p. 141803 (2013), arXiv:1307.5275 [nucl-ex] .
[6] D. Wang *et al.*, Phys. Rev. **C91**, p. 045506 (2015), arXiv:1411.3200 [nucl-ex] .
[7] A. Argento *et al.*, Phys. Lett. **120B**, p. 245 (1983).
[8] S. M. Berman and J. R. Primack, Phys. Rev. **D9**, p. 2171 (1974), [Erratum: Phys. Rev.D10,3895(1974)].
[9] X. Zheng, R. Michaels, P. Reimer, and et al., Jefferson Lab E08-011 (2008).
[10] X. Zheng, *Positrons at Jefferson Lab. Proceedings, International Workshop, JPOS 09, Newport News, USA, March 25-27, 2009*, AIP Conf. Proc. **1160**, 160–163 (2009).
[11] J. Erler and M. J. Ramsey-Musolf, Prog. Part. Nucl. Phys. **54**, 351–442 (2005), arXiv:hep-ph/0404291 [hep-ph] .
[12] G. Corcella, I. G. Knowles, G. Marchesini, S. Moretti, K. Odagiri, P. Richardson, M. H. Seymour, and B. R. Webber, JHEP **01**, p. 010 (2001), arXiv:hep-ph/0011363 [hep-ph] .
[13] G. Corcella, I. G. Knowles, G. Marchesini, S. Moretti, K. Odagiri, P. Richardson, M. H. Seymour, and B. R. Webber, (2002), arXiv:hep-ph/0210213 [hep-ph] .
[14] A. Aktas *et al.* (H1), Phys. Lett. **B634**, 173–179 (2006), arXiv:hep-ex/0512060 [hep-ex] .
[15] A. M. Baldini *et al.* (MEG), Eur. Phys. J. **C76**, p. 434 (2016), arXiv:1605.05081 [hep-ex] .
[16] S. Chekanov *et al.* (ZEUS), Eur. Phys. J. **C44**, 463–479 (2005), arXiv:hep-ex/0501070 [hep-ex] .
[17] A. Aktas *et al.* (H1), Eur. Phys. J. **C52**, 833–847 (2007), arXiv:hep-ex/0703004 [hep-ex] .

[18] M. Gonderinger and M. J. Ramsey-Musolf, JHEP **11**, p. 045 (2010), [Erratum: JHEP05,047(2012)], arXiv:1006.5063 [hep-ph] .
[19] D. Boer *et al.*, (2011), arXiv:1108.1713 [nucl-th] .
[20] P. Taxil, E. Tugcu, and J. M. Virey, Eur. Phys. J. **C14**, 165–178 (2000), arXiv:hep-ph/9912272 [hep-ph] .
[21] C. Patrignani *et al.* (Particle Data Group), Chin. Phys. **C40**, p. 100001 (2016).
[22] Y. X. Zhao, A. Deshpande, J. Huang, K. S. Kumar, and S. Riordan, Eur. Phys. J. **A53**, p. 55 (2017), arXiv:1612.06927 [nucl-ex] .

Weak Neutral Current Studies with Positrons

Seamus Riordan[1,a)]

[1]*Argonne National Laboratory*
Argonne IL, USA 60439, USA

[a)]Corresponding author: sriordan@anl.gov

Abstract. Weak neutral current interactions with charged leptons have offered unique opportunities to study novel aspects of hadronic structure and search for physics beyond the standard model. These studies in the medium energy community have been primarily through parity-violating processes with electron beams, but with the possibility of polarized positron beams, new and complementary observables can be considered in experiments analogous to their electron counterparts. Such studies include elastic proton, deep inelastic, and electron target scattering. Potential positron neutral current experiments along with their potential physics reach, requirements, and feasibility are presented.

Introduction and Formalism

Weak neutral current studies with electron beams have been a powerful method to study unique properties of nucleons and nuclei as well as provide a method to search for new physics outside of the standard model. At low momentum transfers, an exchanged neutral Z boson will interfere with a virtual photon producing a parity-violating violating observable which can be separated from the parity-conserving electromagnetic interaction. The measured quantity is typically a parity violating asymmetry A_{PV} generated by the two helicities of a lepton beam on an unpolarized target taking a form

$$\frac{\sigma_R - \sigma_L}{\sigma_R + \sigma_L} = A_{\text{PV}} \propto \frac{G_F Q^2}{\sqrt{2}\pi\alpha} \times ... \tag{1}$$

where $\sigma_{R,L}$ are the right and left-handed lepton cross section, G_F is the Fermi coupling constant, Q^2 is the negative four-momentum transfer squared, and α is the electromagnetic fine structure constant. The ellipses represent the terms which carry the details and structure of a particular interaction. This asymmetry at the momentum transfers available with modern electron beams on fixed targets is typically in the range of 10^{-6} to 10^{-3}, which requires significant experimental control to observe.

From the unique couplings in the interference, these asymmetries provide measurements of the standard model couplings involving $\sin^2\theta_W$ [1, 2], charge-symmetry breaking contributions to nucleon elastic form factors, e.g. [3, 4, 5, 6], and the neutron distributions within nuclei [7]. From general helicity considerations, the parity violating asymmetries from an unpolarized target can be divided into forward and backwards components

$$A = \frac{\sigma_R - \sigma_L}{\sigma_R + \sigma_L} \approx \frac{G_F Q^2}{\sqrt{2}\pi\alpha}\left[D_{\text{f}}(\theta) g_A^e g_V^{\text{target}} + D_{\text{b}}(\theta) g_V^e g_A^{\text{target}}\right] \tag{2}$$

where $D_{\text{f,b}}$ are forward and backwards components depending on the interaction and g_A and g_V are the vector and axial couplings in the neutral current weak interaction. The vector coupling of the electron is $g_V^e = -\frac{1}{2} + 2\sin^2\theta_W \approx 0.04$ which is small by the value nature has chosen for the weak mixing angle, θ_W. This intrinsically suppresses the backwards part of the asymmetry which contains the axial structure of the target and are typically less well known than the vector counterparts. This also must be done using kinematic separation of the forward and backwards parts requiring multiple measurements in different experimental configurations. These axial components are also less constrained due to the fact that axial currents are not conserved.

With the additional consideration of positron beams, new possibilities become available. Under charge conjugation of the leptonic vertex, the overall structure of the $\gamma - Z$ interference is effectively modified by the electron axial

coupling undergoing a sign change [8]. In principle the positron parity-violating asymmetry contains similar levels of information, so the aforementioned studies by themselves do not dramatically change the experimental reach. However, when combinations of both electron and positron data are made, the methods of extracting specific quantities changes and new observables become available. The electron vector-target axial component can be extracted in the sum of the two parity violating asymmetries

$$A_{\rm PV}^{+} - A_{\rm PV}^{-} = \frac{\sqrt{2} G_F Q^2}{\pi\alpha} g_V^e G_A^{\rm target} \tag{3}$$

with G_A containing the general axial structure of the interaction. This object is the same size as the individual parity violating asymmetry contribution and subject to the same experimental issues, but at tree level provides a method of extraction that does not require kinematic separation of the forward and backwards parts. Decades of effort have been put into controlling the production of electron beam suitable for parity-violating measurements would need to be reexamined given a different polarized positron production method. Aside from this very serious issue, the reduced available current and polarization puts severe restrictions on possible measurements. For a parity violating measurement, the figure of merit is proportional to NP^2 where N is the detected number of counts in a process and P is the beam polarization. Given a typical electron beam parity violating experiment with 60 μA beam current and 85% polarization, the approximate relative figure of merit for positron parity violating measurements using 100 nA beam with 60% polarization is 10^{-3}, i.e. requires 1000 times longer experiments, or absolute statistical error bars which are 30 times larger with equivalent measurement time.

The unpolarized charge asymmetry gives access to new non-parity violating axial-axial couplings which are not suppressed

$$\frac{\sigma^{+} - \sigma^{-}}{\sigma^{+} + \sigma^{-}} = \frac{G_F Q^2}{\sqrt{2}\pi\alpha} g_A^e G_A^{\rm target} \tag{4}$$

where σ^{+} and σ^{-} refers to the positron or electron cross section, respectively.

The extreme experimental challenge of this quantity is the charge normalization between electrons and positrons as this asymmetry is similar in scale to the parity violating asymmetry. For example in the parity violating asymmetries, rapid flipping of the lepton helicity and feedback mechanisms are required to control for slow drifts in the beam properties which may introduce false asymmetries. An analogous method would be to rapidly flip between charge states, which is technically difficult to do and would have to be done minimizing the change of other properties of the beam. The advantage to this technique is higher available beam current when no polarization is required and a larger asymmetry containing the axial part. Despite these issues, we consider several experimental scenarios.

Potential Experiments and Reach

Elastic Proton Scattering

Elastic scattering of the proton using the electroweak interaction gives information about that static structure of the proton and is invaluable to the understanding of the strong nuclear force. In particular, by considering electromagnetic and weak processes together, tests of the standard model can be devised and nucleon properties such as charge symmetry violating contributions (e.g. strange quark contributions) and the axial charge can be measured. The parity-violating asymmetry at the Born level is given by [9]

$$A = \left[\frac{-G_F Q^2}{4\pi\alpha\sqrt{2}}\right]\left[\frac{\epsilon G_E^{\gamma} G_E^{\rm Z} + \tau G_M^{\gamma} G_M^{\rm Z} + 2 g_V^e \epsilon' G_M^{\gamma} G_A^{\rm Z}}{\epsilon\left(G_E^{\gamma}\right)^2 + \tau\left(G_M^{\gamma}\right)^2}\right] \tag{5}$$

where $G_{E,M}^{\gamma}$ are the electric and magnetic Sachs form factors, $G_A^{\rm Z}$ is the axial form factor of the proton, $G_{E,M}^{\rm Z}$ are the vector form factors which couple to the Z, ϵ is the virtual photon transverse polarization

$$\epsilon = \left[1 + 2(1+\tau)\tan^2\frac{\theta}{2}\right]^{-1} \tag{6}$$

and $\epsilon' = \sqrt{\tau(1+\tau)(1-\epsilon^2)}$ with $\tau = Q^2/4M^2$. The proton vector-coupling form factor with the Z-boson is given by

$$G_{E,M}^{p{\rm Z}} = (1 - 4\sin^2\theta_W) G_{E,M}^{p\gamma} - G_{E,M}^{n\gamma} - G_{E,M}^{s\gamma} \tag{7}$$

and in the limit of vanishing Q^2 the Z electric form factor reduces to $1 - 4\sin^2\theta_W$ or colloquially the "weak charge" of the proton. The axial charge is related to the isovector charge found in neutron β decay under the assumption of SU(3) symmetry, often using input from processes such as hyperon decays. The SU(3) axial components are related to the spin structure measured in deep inelastic scattering processes [10]

$$\Gamma_1^p = \frac{1}{2}\int_0^1 \sum e_i^2 \Delta q_i(x) dx \sim \frac{1}{12} g_A^{(3)} + \frac{1}{36} g_A^{(8)} + \frac{1}{9} g_A^{(0)} + ... \tag{8}$$

with Δq the deep inelastic spin structure functions, e_i the quark electric charges, and higher order QCD corrections represented by the ellipses. This quantity is critical to evaluating the spin contributions of quarks of the nucleon and is an important area of study in hadronic physics. The axial form factor suffers from poorly-constrained radiative corrections [11]

$$G_A^p(Q^2 = 0) = g_A^{(3)}\left(1 + R_A^{T=1}\right) + \frac{3F - D}{2} R_A^{T=0} + \Delta s\left(1 + R_A^{(0)}\right) \tag{9}$$

where $\Delta s = g_A^{(8)} - g_A^{(0)}$, R_A^T are the isovector and isoscalar radiative corrections and $R_A^{(0)}$ is the isosinglet. In particular the isovector and isoscalar components can have large multiquark (anapole) corrections which give an overall uncertainty of as much as 30% to the value in this channel. The parity-violating asymmetry differences between positron and electrons would provide useful data, but would likely take decades of running in a configuration similar to G0 backwards running for meaningful constraint. The radiative corrections for the asymmetry difference in principle can have different cancellations [12] which would need to be studied for this channel.

The charge asymmetry is dominated by two-photon effects which are orders of magnitude larger, difficult to calculate or predict, and objects of their own study. It may be possible to go to sufficiently low momentum transfer where the nucleon structure properties are unimportant [13] but the asymmetry may become unobservably small.

Deep Inelastic Nucleon Scattering

Parity violating deep inelastic scattering on fixed targets offers information on the longitudinal momentum quark distributions with new effective couplings complementary to those obtained by electromagnetic processes. In addition, due to the fact that quarks themselves are highly constrained to be point-like, the scattering rates are much more favorable for high energies. The parity-violating asymmetry for electron scattering is given by

$$A_{\mathrm{PV}} \approx \frac{G_F Q^2}{4\sqrt{2}\pi\alpha}\left[a_1(x) + \frac{1 - (1-y)^2}{1 + (1-y)^2} a_3(x)\right] \tag{10}$$

with $y = 1 - \frac{E'}{E}$, E' the final lepton energy, E the lepton beam energy and

$$a_1(x) = 2\frac{\sum C_{1q} e_q (q + \bar{q})}{\sum e_q^2 (q + \bar{q})} \tag{11}$$

$$a_3(x) = 2\frac{\sum C_{2q} e_q (q - \bar{q})}{\sum e_q^2 (q + \bar{q})} \tag{12}$$

with q the quark parton distribution functions, $C_{1,2q}$ the effective quark couplings in the interference

$$C_{1q} = \mp\frac{1}{2} + 2e_q \sin^2\theta_W \tag{13}$$

$$C_{2q} = \mp\frac{1}{2} \pm 2\sin^2\theta_W \tag{14}$$

where the upper sign is taken for u-type quarks and lower sign for d-type quarks, q representing the quark flavor, and e_q the quark electric charge. Again, the parity-violating asymmetry difference offers direct access to the axial-electron vector-quark coupling without the requirement of kinematic separation from the larger forward term. Of note are that the C_2 terms contain the differences between the quark and anti-quark distributions, offering an enticing channel of exploration. A relative figure of merit that is three orders of magnitude worse requires useful measurements of this quantity prohibatively long.

The charge asymmetry difference provides access to a new axial-axial coupling termed C_{3q}

$$\frac{\sigma^+ - \sigma^-}{\sigma^+ + \sigma^-} = \frac{G_F Q^2}{4\sqrt{2}\alpha\pi} \frac{1-(1-y)^2}{1+(1-y)^2} \frac{\sum C_{3q} e_q (q - \bar{q})}{\sum e_q^2 (q + \bar{q})} \tag{15}$$

with $C_{3q} = \pm\frac{1}{2}$ with the upper sign taken for u-type quarks and lower sign for d-type quarks. These are also proportional to the quark-antiquark differences. These have been measured once at CERN using μ^+ and μ^- on carbon nuclei to a relative precision of about 25% and were in agreement with the standard model prediction [14].

For 12 GeV Jefferson Lab, the asymmetries can be much larger than any parity-violating experiment performed there before. For the proposed SoLID PVDIS experiment [15] they are on the order of 10^{-4} and for the charge asymmetry, would need to have charge normalization controlled to a level much better than this. A few percent measurement of $2C_{3u} - C_{3d}$ would take approximately six months of running with 1 μA of sufficiently controlled positron-electron running.

An evaluation of neutral current asymmetries for various electron-ion collider configurations was recently performed [16]. The asymmetries may become as large as a few percent and real opportunities for measurements may exist. The $q-\bar{q}$ extraction, or backwards component, could be improved by an order of magnitude given equal positron integrated luminosity through the charge asymmetry due to circumventing the electron vector coupling suppression.

Fixed Target Electron-Positron Annihilation

High energy polarized positrons on an electron target would offer a unique opportunity to study low energy parity violation in pair produced leptons. In terms of standard model interactions, Bhabha scattering at tree level provides identical information to Møller scattering. However for sufficient center of mass energies, a fixed target electron-positron annihilation experiment could provide information on electroweak couplings to heavier leptons. For muon production with an electron beam of energy E_b, $s = \sqrt{2m_e E_b} \geq 2m_\mu$ or $E_b \geq 43.7$ GeV, which is outside the reach of the accelerators under considering.

However, if such a machine were to be constructed, it offers an interesting option complementary to the electroweak programs near the Z pole, such as at LEP at CERN or SLD at SLAC. Here as with the other low energy parity violating programs, the luminosity available with fixed targets is exploited to overcome the intrinsically small observables. A polarized positron beam could be used to form a left-right forwards-backwards asymmetry of muon pair production that is sensitive to the ratio of the vector to axial coupling ratio [17]

$$A_{\mathrm{LRFB}} = \frac{(\sigma_{\mathrm{LF}} - \sigma_{\mathrm{RF}}) - (\sigma_{\mathrm{LB}} - \sigma_{\mathrm{RB}})}{\sigma_{\mathrm{LF}} + \sigma_{\mathrm{RF}} + \sigma_{\mathrm{LB}} + \sigma_{\mathrm{RB}}} \sim \frac{g_V/g_A}{1+(g_V/g_A)^2} \tag{16}$$

where forwards (F) and backwards (B) are integrated over the $\theta < \pi/2$ and $\theta > \pi/2$ hemispheres in the polar angle θ center-of-mass frame.

The muon the vector coupling has uncertainties an order of magnitude larger relative to the electron [18]. If lepton universality is violated, such as in some of the beyond the standard model explanations for the muon $g-2$ anomaly [19] and proton radius puzzle [20], better measurements of this coupling would be critical in constraining new physics.

Parity-violating Elastic Nuclear Scattering from Lead with Coulomb Distortions

Coulomb distortion effects are critical when studying parity-violating processes on high-Z nuclei, such as in the PREX experiment [21] which measures the neutron skin thickness of lead-208. Such an experiment optimizes the sensitivity to the skin thickness at a momentum transfer slightly below the first diffraction peak, the position of which is modified by these distortions. Prior studies of the lead form factors using elastic electron and positron scattering have confirmed that the diffraction minima for positrons are at larger angle relative to electron scattering [22]. The ability to perform such an experiment at larger angle has many technical advantages over the proposed PREX configuration using the high resolution spectrometers in Hall A at Jefferson Lab. A cursory evaluation of the Coulomb distortion effects on these measurements using electrons or positrons showed such a difference was likely negligable for the proposed measurements at small angles [23].

Summary

While a positron beam offers very interesting possibilities for neutral weak current studies and access to new information complementary to the existing electron programs, the proposed positron beam current and polarization make such measurements extremely challenging. Further, the charge asymmetry measurements have asymmetries which are of similar magnitude to the parity-violating analogs and would require a charge normalization of incredible precision which is outside of technical capabilities. Even if such limitations were overcome, a host of beam-related systematic effects, such as control over the beam properties between charge or helicity states, have not been evaluated and would represent an incredible experimental effort requiring many years of dedicated work. Of the experiments presented, an electron (positron)-ion collider offers the best opportunities for the nearest term progress due to the fact it is at the highest energies and offers the largest asymmetries.

ACKNOWLEDGMENTS

The author is grateful for productive and stimulating discussions with C. J. Horowitz, P. A. Souder, and K. S. Kumar over the different possibilities of this program. This work was supported by the U.S. Department of Energy, Office of Science, Office of Nuclear Physics, under contract number DE-AC02-06CH11357.

REFERENCES

[1] R. D. Carlini *et al.*, Jefferson Lab PAC21 Proposal E02-020 (2002).
[2] P. L. Anthony *et al.* (SLAC E158), Phys. Rev. Lett. **95**, p. 081601 (2005), arXiv:hep-ex/0504049 [hep-ex] .
[3] D. T. Spayde *et al.* (SAMPLE), Phys. Lett. **B583**, 79–86 (2004), arXiv:nucl-ex/0312016 [nucl-ex] .
[4] D. S. Armstrong *et al.* (G0), Phys. Rev. Lett. **95**, p. 092001 (2005), arXiv:nucl-ex/0506021 [nucl-ex] .
[5] K. A. Aniol *et al.* (HAPPEX), Phys. Rev. **C69**, p. 065501 (2004), arXiv:nucl-ex/0402004 [nucl-ex] .
[6] Z. Ahmed *et al.* (HAPPEX), Phys. Rev. Lett. **108**, p. 102001 (2012), arXiv:1107.0913 [nucl-ex] .
[7] S. Abrahamyan *et al.*, Phys. Rev. Lett. **108**, p. 112502 (2012), arXiv:1201.2568 [nucl-ex] .
[8] S. M. Berman and J. R. Primack, Phys. Rev. D **9**, 2171–2173Apr (1974).
[9] D. Armstrong and R. McKeown, Annual Review of Nuclear and Particle Science **62**, 337–359 (2012), https://doi.org/10.1146/annurev-nucl-102010-130419 .
[10] S. D. Bass, Rev. Mod. Phys. **77**, 1257–1302Nov (2005).
[11] J. Erler and M. J. Ramsey-Musolf, Phys. Rev. D **72**, p. 073003Oct (2005).
[12] A. V. Afanasev and C. E. Carlson, Phys. Rev. Lett. **94**, p. 212301Jun (2005).
[13] W. A. McKinley and H. Feshbach, Phys. Rev. **74**, 1759–1763Dec (1948).
[14] A. Argento *et al.*, Physics Letters B **120**, 245 – 250 (1983).
[15] P. A. Souder *et al.*, Jefferson Lab PAC35 Proposal E12-10-007 (2010).
[16] Y. X. Zhao, A. Deshpande, J. Huang, K. S. Kumar, and S. Riordan, Eur. Phys. J. **A53**, p. 55 (2017), arXiv:1612.06927 [nucl-ex] .
[17] A. Blondel, B. Lynn, F. Renard, and C. Verzegnassi, Nuclear Physics B **304**, 438 – 450 (1988).
[18] The ALEPH, DELPHI, L3, OPAL, SLD Collaborations, the LEP Electroweak Working Group, the SLD Electroweak and Heavy Flavour Groups, Phys. Rept. **427**, p. 257 (2006), hep-ex/0509008 .
[19] G. W. Bennett *et al.* (Muon g-2), Phys. Rev. **D73**, p. 072003 (2006), arXiv:hep-ex/0602035 [hep-ex] .
[20] R. Pohl, R. Gilman, G. A. Miller, and K. Pachucki, Annual Review of Nuclear and Particle Science **63**, 175–204 (2013), https://doi.org/10.1146/annurev-nucl-102212-170627 .
[21] C. J. Horowitz, S. J. Pollock, P. A. Souder, and R. Michaels, Phys. Rev. C **63**, p. 025501Jan (2001).
[22] V. Breton *et al.*, Phys. Rev. Lett. **66**, 572–575Feb (1991).
[23] C. J. Horowitz, Private communication.

Testing Lorentz symmetry in deep inelastic scattering with an electron-ion collider

Nathan Sherrill

Department of Physics, Indiana University
Bloomington, IN 47405, USA

Abstract. We investigate the prospects for detecting tiny violations of Lorentz symmetry in deep inelastic scattering in the context of the future electron-ion collider. Preliminary results suggest estimated bounds on quark-sector coefficients for Lorentz violation can be extracted at sensitivities of parts in $10^3 - 10^6$.

INTRODUCTION

Lorentz invariance is a global symmetry of the Standard Model (SM) of particle physics and a local symmetry of General Relativity. While both theories have been fantastically successful in describing physics at currently attainable energies, it is widely expected that a fully quantum-theoretical description of all known physics including gravity will emerge at the Planck scale. One interesting possible consequence of this unification is the violation of Lorentz invariance. It has been shown that Lorentz violation can occur via spontaneous symmetry breaking in string field theory [1]. In this setting, a low-energy theory can gain terms in its Lagrange density that violate Lorentz symmetry, e.g.,

$$\mathcal{L}_{LV} \sim \frac{\lambda}{m_P^k} \langle T \rangle \cdot \bar{\psi} \Gamma (i\partial)^k \psi + h.c., \tag{1}$$

where λ is a dimensionless coupling constant, k is an integer exponent, and m_P is the Planck mass. The object $\langle T \rangle$ is a nonzero vacuum expectation value (vev) of a tensor field with suppressed spacetime indices, and Γ is a generic gamma-matrix structure. In Eq. (1), Lorentz symmetry is violated through the vev, which has orientation dependence. Even though the underlying theory is Poincaré invariant, interactions can destabilize the vacuum and generate effective background fields that induce Lorentz violation.

Given that the gap between currently accessible energies and the presumed scale of quantum gravity spans roughly 15 orders of magnitude, probing Planck-scale physics directly is infeasible. An alternative approach is to search for suppressed signals at attainable energies. Probing Nature in this way suggests the use of a low-energy, effective quantum field theory which completely accounts for all possible residual Lorentz-violating effects that presumably originate from mechanisms in a more fundamental theory. This framework is known as the Standard-Model Extension (SME) [2, 3, 4]. By construction, the SME contains the field content from all known fundamental physics with the addition of all possible terms built from fundamental fields that break Lorentz and CPT symmetry. These additional terms take the form of coefficients contracted with products of SM and gravitational fields. For example, one term in the quantum electrodynamics (QED) sector of the SME is given by

$$\mathcal{L}_{QED}^{SME} \supset -a_\mu \bar{\psi} \gamma^\mu \psi. \tag{2}$$

Here, the coefficient for Lorentz (and CPT) violation a_μ is a real quantity that can be thought of as a combination of a coupling constant, mass suppression scale, and tensor vev. An important property of the coefficients for Lorentz violation is that they transform as four-vectors under general coordinate transformations, called Lorentz observer transformations, but as scalars under transformations of the physical system itself, called Lorentz particle transformations. Because these coefficients represent preferred directions in spacetime, their presence implies a violation of

Lorentz symmetry. Since CPT symmetry is related to Lorentz symmetry through the CPT theorem [5], CPT-violating effects are also completely parametrized by the SME. Thus, the SME is the general phenomenological framework used to search for Lorentz- and CPT-violating suppressed signals arising from a more fundamental theory.

Constraints on many coefficients across all sectors of the SME have been placed to date [6]. Despite the large amount of work that has been carried out thus far, comparatively little attention has been paid to the quantum chromodynamics (QCD) sector of the SME. This is primarily due to the difficulties in bypassing the observed spectrum of states to access the fundamental degrees of freedom of QCD. Very recently, there has been a push towards exploring Lorentz violation in this sector [7, 8, 9, 10]. Much of this work may ultimately be relevant to the proposed electron-ion collider (EIC) [12], which is expected to usher in a new era of precision QCD studies of the hadrons. Since the EIC will have a unique ability to study QCD, it is interesting to consider the prospects for detecting Lorentz-violating QCD effects. This is the basis for the current document, which reports on forthcoming research that examines the prospects for detecting Lorentz violation at the EIC through the process of unpolarized electron-proton deep inelastic scattering (*e*-*p* DIS).

LORENTZ-VIOLATING EFFECTS IN UNPOLARIZED DIS

We now focus our attention on tree level Lorentz-violating effects in *e*-*p* DIS. This process was recently studied in the context of HERA collider data [11], and the discussion that follows is largely a summary of those results [10]. The general process is depicted in Fig. 1. For sufficiently large momentum transfer $-q^2 \gg M^2$, with M being the proton mass, interactions among the partons within the proton can be neglected due to asymptotic freedom. At zeroth order in the strong-interaction coupling constant g_s, the partons predominantly interact electromagnetically with the incident electron. Note that, at large enough $-q^2$, effects of Z^0 exchange have also been considered [10]. The dominant Lorentz-violating contributions here appearing in the quark-sector of the SME QCD lagrangian are

$$\mathcal{L}_{QCD}^{SME} \supset \sum_{f=u,d} \frac{1}{2}\left(\eta^{\mu\nu} + c_f^{\mu\nu}\right)\bar{\psi}_f \gamma_\mu i\overleftrightarrow{D}_\nu \psi_f, \tag{3}$$

where $i\overleftrightarrow{D}_\nu = i\overleftrightarrow{\partial}_\nu - 2q_f A_\nu$ is the usual QED covariant derivative. The coefficients $c_f^{\mu\nu}$ control the magnitude of Lorentz violation for each quark flavor f and are fixed in a given observer frame. In considering the Lorentz-violating contributions as written in Eq. (3), a number of additional factors have been taken into account. First, for simplicity, only the up- and down-quark flavor content is considered, as this is the dominant proton flavor content. Second, photon- and electron-sector bounds are constrained at much higher sensitivities than can be probed in this process [6], so these effects are neglected. Considering further only flavor-conserving couplings for the quarks and the fact that spin-dependent coefficients average to zero for unpolarized scattering leaves the written class of CPT-even coefficients in Eq. (3). Taking the right-hand side of Eq. (3) as the effective model, we treat the coefficients $c_f^{\mu\nu}$ as small perturbations and calculate the differential cross section at tree level for the unpolarized scattering process. The inclusion of

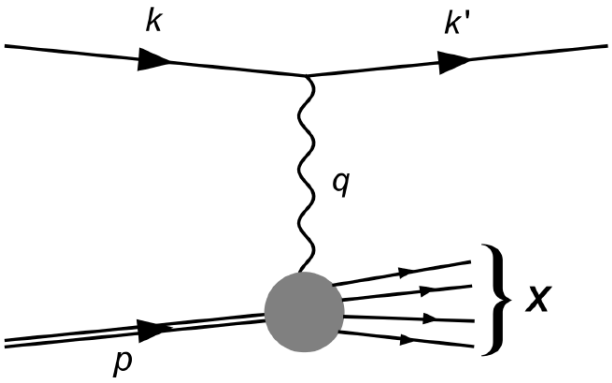

FIGURE 1. DIS: an electron with momentum k scatters off a proton of momentum p producing a generic final hadronic state $|X\rangle$. Figure taken from Ref. [10].

these Lorentz-violating effects leads to a modified quark current

$$J^\mu(x) = q_f \bar{\psi}_f(x) \Gamma_f^\mu \psi_f(x), \tag{4}$$

with $\Gamma_f^\mu \equiv \gamma^\mu + c_f^{\mu\nu}\gamma_\nu$. The scattering amplitude $\mathcal{M}$ for the DIS process illustrated in Fig. 1 is given by

$$i\mathcal{M} = (-ie)\bar{u}(k')\gamma_\mu u(k)\frac{-i}{q^2}(ie)\int d^4x\, e^{iq\cdot x}\langle X|\, J^\mu(x)\,|p\rangle\,. \tag{5}$$

To compute the cross section, the squared modulus of Eq. (5) must be calculated along with the flux factor $F = N_1 N_2 |\vec{v}_1 - \vec{v}_2|$, where N_i and $\vec{v}_i$ are the colliding beam densities and group velocities, respectively. Effects of Lorentz violation on the flux factor are expected to be negligible for the DIS process [13]. The main difficulty here lies in the computation of the hadronic matrix element $\langle X|\, J^\mu(x)\,|p\rangle$, as the current contains quark creation and annihilation operators operating on hadronic states. This can be circumvented by first defining the hadronic tensor as the spin-average of the following quantity:

$$W^{\mu\nu}(p,q) = i\int d^4x\, e^{iq\cdot x}\langle p|\, T\{J^\mu(x)J^\nu(0)\}\,|p\rangle\,. \tag{6}$$

The optical theorem can now be applied to the hadronic tensor to reveal

$$2\mathrm{Im}\left[W^{\mu\nu}(p,q)\right] = \sum_X \int d\Pi_X \langle p|\, J^\mu(-q)\,|X\rangle\langle X|\, J^\nu(q)\,|p\rangle\,, \tag{7}$$

with $d\Pi_X$ being the final hadronic state phase space. Using Eq. (7), and recognizing that the squared modulus of the electon-photon vertex is essentially the leptonic tensor $L^{\mu\nu} = 2\left(k^\mu k'^\nu + k^\nu k'^\mu - k\cdot k'\eta^{\mu\nu}\right)$, leads to a compact form for the triply differential cross section

$$\frac{d^3\sigma}{dxdyd\phi} = \frac{\alpha^2 y}{2\pi q^4} L^{\mu\nu}\mathrm{Im}[W_{\mu\nu}], \tag{8}$$

where $y = p\cdot q/p\cdot k$ and α is the fine-structure constant. In the usual SM calculation of the cross section, there is no complicated dependence on the final-state electron azimuthal angle. However, in the presence of Lorentz violation, the angular dependence is nontrivial. What remains is to choose how to evaluate $\mathrm{Im}[W_{\mu\nu}]$. Here, the parton model can be used to approximate photon-proton scattering as a photon interacting with a parton of flavor f carrying a momentum fraction ξp of the proton's four-momentum p. The hadronic tensor can thus be approximated as

$$W_{\mu\nu} \approx i\int d^4x\, e^{iq\cdot x}\int_0^1 d\xi \sum_f \frac{f_f(\xi)}{\xi}\langle \xi p|\, T\{J_\mu(x)J_\nu(0)\}\,|\xi p\rangle\,, \tag{9}$$

where $f_f(\xi)$ is the parton distribution function (PDF) for a given flavor f. Evaluating the time-ordered product and subsequent Wick contractions and traces leads directly to the expression of the modified γ-exchange differential cross section in terms of SM and Lorentz-violating contributions,

$$\begin{aligned}\frac{d^3\sigma}{dxdyd\phi} = {}& \frac{\alpha^2 s}{q^4}\sum_f q_f^2 x f_f(x)\left[1+(1-y)^2\right] \\ & + \frac{\alpha^2}{q^4}\sum_f q_f^2 x f_f(x)\left[[C''] - \frac{2(1+(1-y)^2)}{y}\left([C'] + \left(\frac{1}{x} + \frac{d\ln f_f(x)}{dx}\right)[C]\right)\right],\end{aligned} \tag{10}$$

where

$$\begin{aligned}[C] &= c_f^{\mu\nu}\left[q_\mu q_\nu + x\left(q_\mu p_\nu + q_\nu p_\mu\right) + x^2 p_\mu p_\nu\right], \\ [C'] &= c_f^{\mu\nu}\left(p_\mu q_\nu + p_\nu q_\mu + 2x p_\mu q_\nu\right), \\ [C''] &= \frac{2y}{x}[C] \\ &\quad + c_f^{\mu\nu}\left[4\left(k'_\mu p_\nu + p_\mu k'_\nu\right) - \frac{4M^2}{s}\left(k_\mu k'_\nu + k'_\mu k_\nu\right) + \frac{4}{x}(1-y)k_\mu k_\nu + 4(1-y)\left(k_\mu p_\nu + p_\mu k_\nu\right) - 4xy p_\mu p_\nu - \frac{4}{x}k'_\mu k'_\nu\right].\end{aligned} \tag{11}$$

The first line of Eq. (10) is the usual leading-order SM contribution. The second line, which is proportional to $c_f^{\mu\nu}$, is the contribution from Lorentz-violating effects. In choosing a frame to analyze Eq. (10), special care must be taken because the coefficients for Lorentz violation depend on choice of observer frame. This implies that an Earth-based experiment will exhibit a sidereal time dependence in the cross section. It is therefore important to work initially in a suitable (approximately) inertial frame.

THE SUN-CENTERED CELESTIAL-EQUATORIAL FRAME AND HERA ANALYSIS

The standard choice of frame used for reporting bounds on coefficients for Lorentz violation is known as the Sun-centered celestial-equatorial frame (SCF) [16]. This frame is effectively inertial over the time scale of most Earth-based experiments. For simplicity, it is convenient to take the coefficients for Lorentz violation as constants in this frame, which preserves energy and momentum conservation. A series of rotations relates the SCF to the laboratory

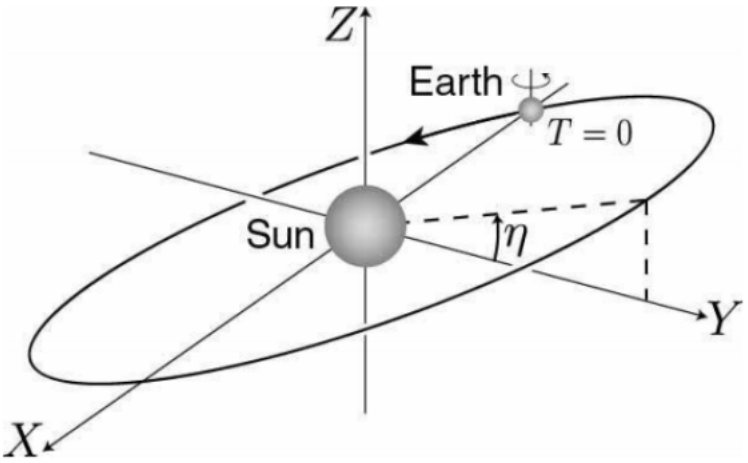

FIGURE 2. The SCF: in this frame the Z axis is taken to be parallel with the rotation axis of the Earth, and the X axis points towards the 2000 vernal equinox. Figure taken from Ref. [17].

frame on Earth that depend on three angles: the colatitude of the laboratory, the orientation of the colliding beamline relative to the cardinal points, and the product of Earth's sidereal frequency with the local sidereal time. Once the coefficients have been transformed to the laboratory frame, they exhibit a time dependence by virtue of the local sidereal time. More precisely, for a given flavor f, only six combinations of the nine independent components of $c_f^{\mu\nu}$ obtain time dependence after the transformation from the SCF to the laboratory frame. The first estimates of bounds on the time-dependent coefficients were placed in the study of HERA collider data [10]. The best estimated bounds obtained in this work are at at low $(x, -q^2)$ values and on the order of $10^{-4} - 10^{-6}$. A complete description of these results is contained in Table 1 of Ref. [10]. Sensitivity to the kinematical region of low $(x, -q^2)$ is convincing when examining the Lorentz-violating contribution to the cross section in Eq. (10). We also mention that these bounds are estimates obtained from binning the time-dependent contribution of the cross section in bins of sidereal time. For real bounds to be placed on the coefficients, time stamps of the events culminating in each measurement are needed, which are unavailable. We now turn our attention to a preliminary analysis of simulated EIC data.

PRELIMINARY RESULTS FOR THE EIC

The EIC is scheduled to be constructed at either Jefferson Lab (JLab) or Brookhaven National Lab (BNL). Initial design parameters for the JLab EIC (JLEIC) and BNL EIC (eRHIC) suggest a similar reach in terms of kinematic phase space [12, 15]. The main distinction between the two proposed designs is that JLEIC has lower center-of-mass system (CMS) energy range than eRHIC, but a higher luminosity. Whether the EIC is eventually built at JLab or BNL, each machine is capable of being upgraded to a similar maximum CMS energies and luminosity.

Simulated inclusive *e-p* DIS data can be used to estimate the sensitivities to Lorentz violation attainable at the future EIC [14]. Thus far, only a full analysis of JLEIC simulated data has been performed. Our preliminary results suggest estimated bounds on the time-dependent *and* time-independent coefficients on the order of $10^3 - 10^6$. We remark that bounds on the time-independent coefficients will be the first estimates placed to date. These coefficients can be examined for the future EIC because the simulated cross section data does not enter into the construction of the PDFs used to build the cross section. Because of this, there is no concern of the PDFs being contaminated with potential Lorentz-violating effects as in the case of real data. The sensitivities obtained for the time-dependent coefficients are at the a similar level to what was obtained in the analysis of HERA data. Nevertheless, as HERA and both potential EIC colliders have a unique geographic location, the linear combination of coefficients within the cross section for each orientation are unique. This implies that the level of sensitivity to a particular coefficient obtainable in one experiment is not necessarily indicative of the sensitivity in another. This fact further supports the case for exploring the sensitivities of an EIC to Lorentz violation with two distinct locations.

ACKNOWLEDGMENTS

I thank Enrico Lunghi for his collaboration on the work for which this current document is based on. Simulated data for the JLEIC and eRHIC collider was generated and supplied by A. Accardi (Hampton U./JLab) and Y. Furletova (JLab), and by E. C. Aschenauer (BNL) and B. Page (BNL), respectively. This work was supported in part by the United States Department of Energy under grants DE-AC05-06OR23177, DE-FG0287ER40365, DE-SC0010120, and by the Indiana University Center for Spacetime Symmetries.

REFERENCES

[1] V.A. Kostelecký and S. Samuel, Phys. Rev. D **39**, 683 (1989).
[2] D. Colladay and V.A. Kostelecký, Phys. Rev. D **55**, 6760 (1997).
[3] D. Colladay and V.A. Kostelecký, Phys. Rev. D **58**, 116002 (1998).
[4] V.A. Kostelecký, Phys. Rev. D **69**, 105009 (2003).
[5] O.W. Greenberg, Phys. Rev. D **89**, 231602 (2002).
[6] *Data Tables for Lorentz and CPT Violation,* V.A. Kostelecký and N. Russell, Rev. Mod. Phys. **83**, 11 (2011); 2017 edition arXiv:0801.0287v10.
[7] M.S. Berger, V.A. Kostelecký, and Z. Liu, Phys. Rev. D **93**, 036005 (2016).
[8] R. Kamand, B. Altschul, and M. Schindler, Phys. Rev. D **95**, 056005 (2017).
[9] J.P. Noordmans, Phys. Rev. D **95**, 075030 (2017).
[10] V.A. Kostelecký, E. Lunghi, and A.R. Vieira, Phys. Lett. B **769**, 272 (2017).
[11] H. Abramowicz *et al.*, Eur. Phys. J. C **75**, 580 (2015).
[12] A. Accardi *et al.*, Eur. Phys. J. A **52**, 268 (2016).
[13] D. Colladay and V.A. Kostelecký, Phys. Lett. B **511**, 209 (2001).
[14] E. Lunghi and N. Sherrill, in preparation.
[15] *eRHIC Design Study: An Electron-Ion Collider at BNL,* E.C. Aschenauer *et al.*; arXiv:1409.1633.
[16] V.A. Kostelecký and M. Mewes, Phys. Rev. D **66**, 056005 (2002).
[17] Q.G. Bailey and V.A. Kostelecký, Phys. Rev. D **74**, 045001 (2006).

Spin-Polarized Positron Beams with ^{22}Na and ^{68}Ge and Their Applications to Materials Research

K. Wada, A. Miyashita, M. Maekawa, S. Sakai, A. Kawasuso [a)]

National Institutes for Quantum and Radiological Science and Technology, 1233, Watanuki, Takasaki, Gunma 370-1292 JAPAN

[a)]kawasuso.atsuo@qst.go.jp

Abstract. We introduce our research and development of spin-polarized positron beams with ^{22}Na and ^{68}Ge sources and their applications to spin-related materials research in the period of 2008 to 2017. We also discuss the prospects of spintronics study with spin-polarized positron spectroscopy.

INTRODUCTION

Positrons emitted from radioisotopes are longitudinally spin-polarized due to the parity non-conservation in the weak interaction [1-3]. After this discovery, using angular correlation of annihilation radiation (ACAR) technique, the investigation of ferromagnetic band structures had been started. However, in the late 1960, the other competitive tools, such as magnetic Compton profiling and photoemission electron spectroscopy, were developed one after another. Consequently, the study of magnetism with spin-polarized positron spectroscopy turned out to be minor.

In 1979, the role of spin-polarized positron spectroscopy was again paid the attention due to the invention of spin-polarized 'slow' positron beam by the Michigan group [4]. At that time, the surface physics was rapidly progressing accompanying the technological innovation such as ultra-high vacuum technology and the scanning tunneling microscopy. Novel phenomena were anticipated to occur at solid surfaces due to the dimension lowering. Magnetic dead layer hypothesis that means the disappearance of magnetic moment at surfaces of ferromagnets [5], was argued in such tendency. To confirm new hypothesis, the further development of experimental techniques were required. The spin polarization of the Michigan ^{58}Co-based beam was 22 %. They reported that, by rejecting low energy positrons from the source, the spin polarization could be enhanced to ~70 %. In 1982, they found that Ni surface is in magnetically 'live' layer against the dead layer hypothesis [6]. This demonstrated the superiority of spin-polarized slow positron beam in the study of surface magnetism. However, leaving this paper, no further researches had been conducted. From 1997 to 1999, the Tokyo Metropolitan University [7] and RIKEN [8] groups attempted to generate spin-polarized slow positron beams with ^{27}Si and ^{18}F sources.

Recently, towards the innovation of electronic devices by using electron charge and spin together, so-called spintronics research is brisk. The discovery of giant magnetoresistance giving rise to the tremendous increase of hard disk memory capacity is a representative outcome of the spintronics. Currently, half-metals that have ideally 100 % spin polarization at the Fermi level, and magnetic semiconductors in which the magnetism is controllable using electric field and light are extensively investigated. The further intriguing phenomena and materials, such as the spin-Hall effect, the Rashba effect, topological insulators and graphene-related monoatomic layer materials are also explored enthusiastically. Discovery of new phenomena and materials stimulates the development of more advanced new experimental techniques.

Taking advantage of the spin sensitivity of positron, the traditional positron spectroscopies will become state-of-the-art techniques. In light of the above-mentioned circumstances, the spin-polarized positron spectroscopy may be revived, improved and applied to the research of spintronics materials. In this article, we introduce our research and development of spin-polarized positron beam. We also discuss the prospects of this method including anticipation to the development of intense and highly spin-polarized positron beam.

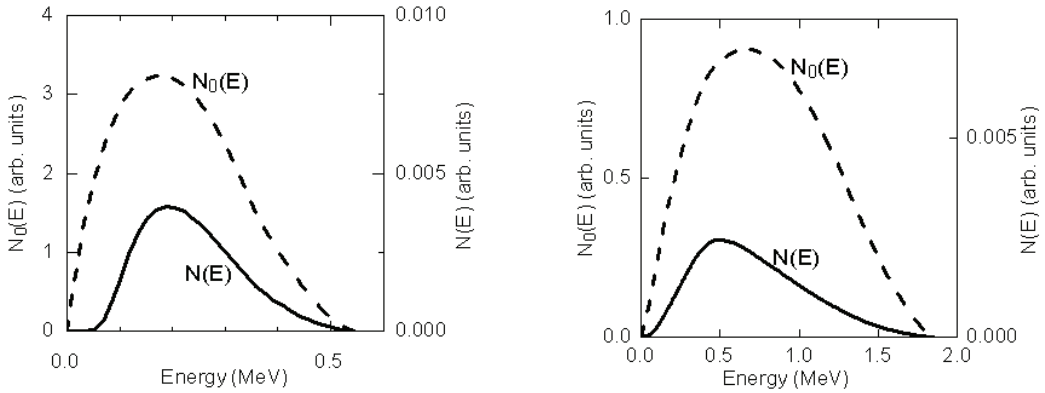

FIGURE 1. Intrinsic energy distribution of positrons, $N_0(E)$, and effective energy distribution of positrons converted to slow positrons from the source to the moderator, $N(E)$ for (a) ^{22}Na source of d_S=0.1 mm and (b) ^{68}Ge source of d_S=0.5 mm and with a tungsten moderator of d_M=1 μm and no absorber

DEVELOPMENT AND APPLICATION OF SPIN-POLARIZED POSITRON BEAM

Expected beam spin polarization

Longitudinal spin polarization of positrons emitted from radioisotopes (RIs) is given as the helicity (v/c), where v and c are the speeds of positrons and light, respectively. Since normally nuclear spins of radioisotopes are randomly oriented, positrons are isotropically (4π direction) emitted. Average spin polarization of positrons into a cone with an open angle of θ and in the energy range from E_1 to E_2 is given by

$$\langle P_+ \rangle = \frac{\langle v \rangle}{c}\frac{1+\cos\theta}{2} = \int_{E_1}^{E_2}\sqrt{1-\frac{1}{[1+E/(mc^2)]^2}}N(E)dE\frac{1+\cos\theta}{2},$$

where $\langle v \rangle$ and $N(E)$ are the average speed and the energy distribution, respectively, of positrons. From this, higher spin-polarization is obtained by using RIs with higher Q values, restricting the cone angle and backscattering, and selecting the higher energy component. If the nuclear spins can be aligned in one direction, both spin-polarization and emission probability to that direction can be enhanced simultaneously.

Spin polarization also depend on the details of experiment. Firstly, the effective energy distribution of positrons is no longer the same as the intrinsic one ($N_0(E)$) because of (i) the energy dependent absorption of positrons in the source material and the intentional absorber, (ii) the energy selection by the moderator for slow positron generation. Secondly, various depolarization effects should be considered. The major processes are (i) the backscattering of positrons by the source substrate and (ii) the spin-flipping during scattering processes in the moderator.

Let us assume that slow positrons are generated by a source-absorber-moderator alignment. The energy distribution of positrons that are moderated and reemitted as slow positrons may be given by

$$N(E) = \frac{1}{2}\int_0^{d_S} N_0(E)[A(z)/A_0]T_S(E,z)dz \times T_A(E,d_A)\times\varepsilon_M(E,d_M),$$

where z is the depth from the surface, $A(z)$ is the source activity (total amount of A_0 in d_s thick) distribution, $T_{S,A}(E, z)$ is the transmittance of positrons in the source and the absorber with d_A thick, and $\varepsilon_M(E, d_M)$ is the efficiency of moderator of d_M thick. Figure 1 shows $N_0(E)$ and $N(E)$ for ^{22}Na source of d_S=0.1 mm and ^{68}Ge source of d_S=0.5 mm with tungsten moderator of d_M=1 μm and no absorber (T_A=1). The spin polarizations after the moderation are 41% (^{22}Na) and 53% (^{68}Ge) with a realistic open angle θ = 78° [9].

Backscattering processes of positrons that occur in the source-absorber-moderator component is very complicated, since the energy and angle dependent backscattering probability, the transmission after backscattering in the series of materials, and their multiple processes should be taken into account. Here, we simply assume that the backscattering by the source substrate is the major depolarization process. The backscattering probability for ^{22}Na and ^{68}Ge on a Z material is given empirically as R = 0.342log Z – 0.146 [10]. Assuming that positrons with any angles and energies are backscattered at a carbon substrate (Z=6), R~10 % and hence 10 % polarization will be lost.

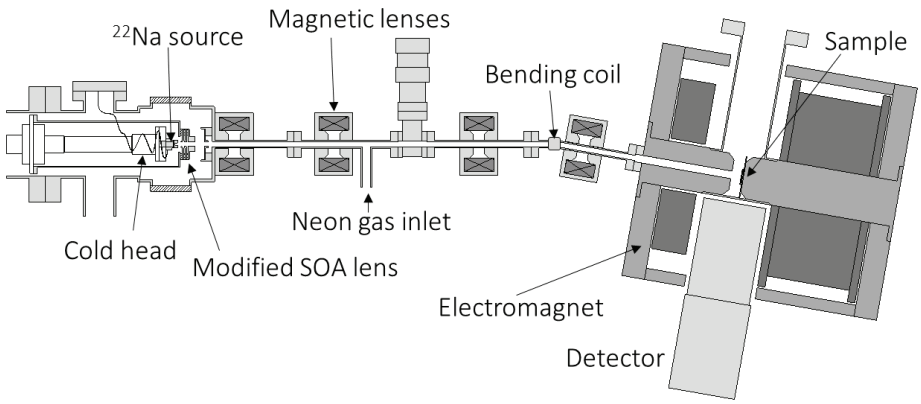

(a)

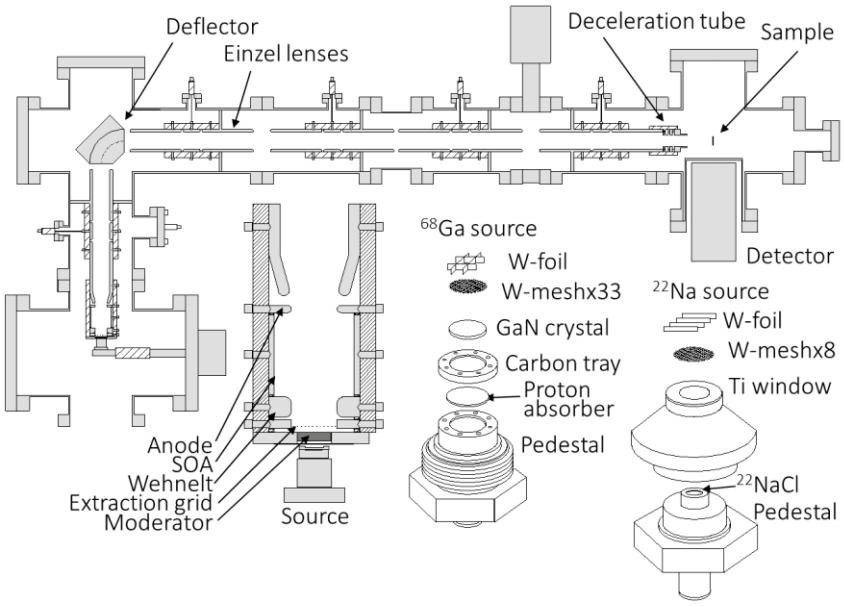

(b)

FIGURE 2. Slow beam apparatuses with ^{22}Na and ^{68}Ge sources developed by the authors: (a) Electromagnetic beam and (b) Electrostatic beam

Interaction between positrons and materials may be classified into the electromagnetic interaction (bremsstrahlung and Bhabha scattering), dielectric interaction (electron-hole and plasmon excitations), phonon excitation and elastic Mott-Coulomb scattering. The stopping power of the bremsstrahlung is $EZ/800$ of that of the Bhabha scattering and hence it is not so important in the case of RI positrons. Positrons injected into a material lose the most of energy through the ionization of the Bhabha scattering. When the energy reaches ~keV range, the electron-hole and plasmon excitations become major energy loss processes. In ~eV range, positrons are thermalized through the phonon excitation. During the above slowing-down processes, in the Bhabha scattering, positron spins are flipped. In the quantum electromagnetic dynamics theory, the spin-flipping probability of positron is given as a function of positron energy and the energy transfer [11]. From $N(E)$ in Fig. 1, the mean positron energies, that are converted to slow positrons from ^{22}Na and ^{68}Ge sources, are ~0.2 MeV and ~0.7 MeV, respectively. The mean energy transfer per scattering is ~500 eV in tungsten [12]. The spin-flipping probabilities are approximately 3×10^{-4} (^{22}Na) and 8×10^{-5} (^{68}Ge) per scattering. About 400 (^{22}Na) and 1400 (^{68}Ge) scattering events may occur until zero energy. Thus, about 6% (^{22}Na) and 5 % (^{68}Ge) polarizations may be lost. In the Mott scattering, due to the spin-orbit interaction, spin is rotated to the direction of scattering. For electron, the depolarization amount is given as an

analytical formula [13]. Assuming that it is applicable to positron, too, 5% (^{22}Na) and 3 % (^{68}Ge) polarizations may be lost in the tungsten moderator with d_M=1 μm.

Thus, in total, the spin polarizations of slow positron beams may be 41 % (absorption) ×0.9 (backscattering) ×0.94 (Bhabha) ×0.95 (Mott) = 33 % (^{22}Na) and 53 % (absorption) ×0.9 (backscattering) ×0.96 (Bhabha) ×0.95 (Mott) = 43 % (^{68}Ge). No significant depolarization occurs as long as light materials are used as source substrate. Use of absorber will enhance the final spin polarization.

Examples of beam apparatus

Spin-polarized positron beam can be generated with RIs and no special devices. The simplest way may be direct injection of fast positrons emitted from the source into the sample without moderation. This method may be suited for out-of-plane magnetized bulk ferromagnets [14, 15]. The authors developed slow beam apparatuses with ^{22}Na and ^{68}Ge sources as shown in Fig. 2 [16, 17]. The apparatus of Fig. 2(a) is based on electromagnetic lenses. In this method, the beam direction and the field direction of beam focusing are the same and hence the longitudinal spin polarization is conserved well. Relatively strong magnetic field (~a few Tesla) can be applied to the sample. The apparatus of Fig. 2(b) is based on electrostatic lenses. By bending the beam 90° by an electrostatic deflector, transversely spin-polarized beam is obtained.

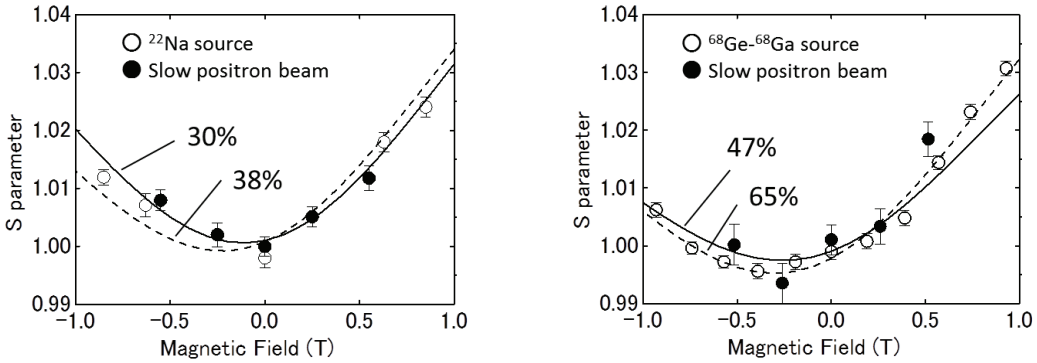

(a) (b)

FIGURE 3. DBAR *S* parameter in a fused silica obtained using (a) ^{22}Na source itself and its electrostatic beam and (b) ^{68}Ge source itself and its electrostatic beam as a function of magnetic field. The evaluated spin polarizations are also shown

Measurement of spin-polarization with positronium

Positron spin-polarization can be measured through the spin-dependent transmission into ferromagnets and the Mott scattering by gold target. After the Michigan group [4], the method using the magnetic quenching of positronium is also available. We determined the spin-polarization of our beams by the Nagai's method based on the positronium magnetic quenching in fused silica [18]. In this method, the spin polarization is determined using the fact that the *S* parameter of the Doppler broadening of annihilation radiation (DBAR) spectrum is the first order function of the two-photon annihilation intensity in magnetic field. That is, the magnetic field dependence of *S* parameter is given by

$$S = (S_{Ps} - S_{SiO_2})I(B) + S_{SiO_2} = (S_{Ps} - S_{SiO_2})\left(\frac{F_{|00\rangle'}}{\lambda_{|00\rangle'}}\frac{\kappa\lambda_p}{1+y^2} + \frac{F_{|10\rangle'}}{\lambda_{|10\rangle'}}\frac{\kappa y^2\lambda_p}{1+y^2}\right) + S_{SiO_2}\ .$$

Here, S_{Ps} is the *S* parameter of self-annihilation of perturbed positronium, S_{SiO2} is the *S* parameter of other two-photon annihilation events, $I(B)$ is the fraction of perturbed positronium as a function of magnetic field, $F_{|00\rangle'}$ and $F_{|10\rangle'}$ are the fractions of perturbed para- and ortho-positronium, respectively, λ_p, $\lambda_{|00\rangle'}$, $\lambda_{|10\rangle'}$ are the annihilation rates of para-, perturbed para- and ortho- positronium, respectively, $y=x/[(1+x^2)^{1/2}+1]$, $x=4\mu_B B/\Delta E$ (μ_B: Bohr magneton, B: magnetic field, ΔE: hyperfine interaction energy (8.4×10^{-4}eV) and κ is the contact density which is the ratio of square of positronium wave-functions in materials and vacuum ($=|\Psi_m(0)|^2/|\Psi_v(0)|^2$). By fitting the above equation to experimental field dependence of *S* parameter, P_+ is obtained. The details are described elsewhere [9].

Figure 3 shows the magnetic field dependences of *S* parameter in a fused silica by directly implanting fast positrons from ^{22}Na and ^{68}Ge sources and by the slow positrons. The separation between the sample and the source is 7 mm. By the above-mentioned Nagai's method, the spin-polarizations are determined to be 38 % (^{22}Na) and 65 % (^{68}Ge) for fast positrons and 30 % (^{22}Na) and 47 % (^{68}Ge) for slow positrons. These values agree well with those estimated in the previous subsection.

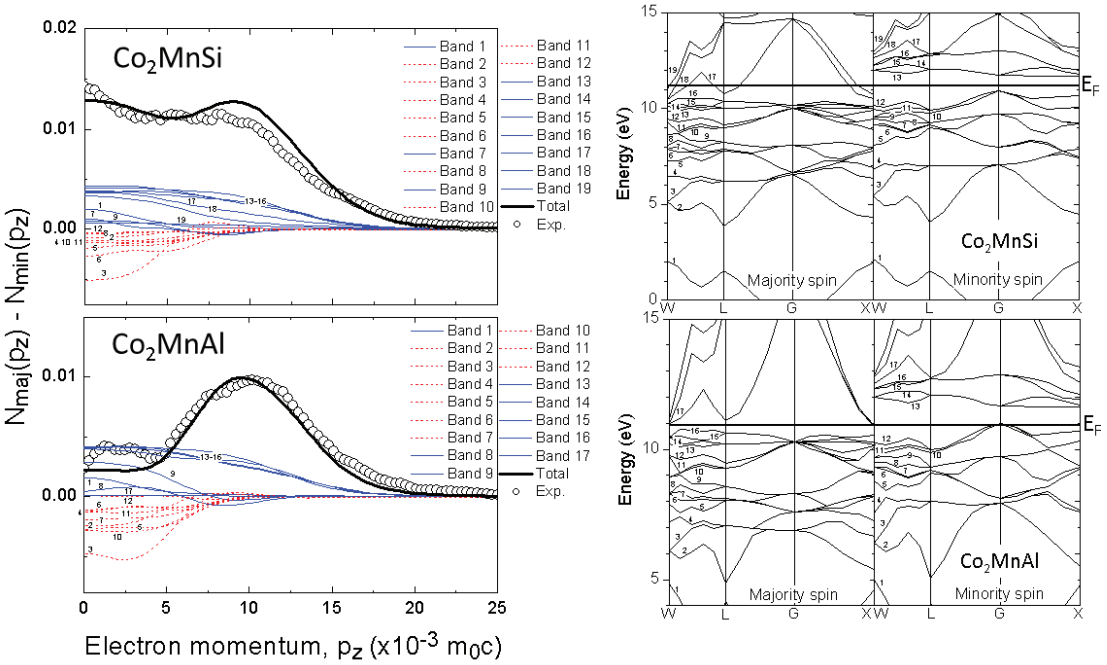

FIGURE 4. (Left): Differential DBAR spectra between majority and minority spin bands obtained for Co_2MnSi (CMS) and Co_2MnAl (CMA). Right: Band structures of CMS and CMA calculated by the ABINIT code

Application of spin-polarized positron spectroscopy

Ferromagnetic band structure

Here, as an example, we pick up the Heusler alloys. Some of the Heusler alloys are thought to be half-metals. Half-metal is a metal having a gap in either majority or minority spin bands, i.e., ideally 100 % spin-polarization at the Fermi level. Because of this novel property, half-metals are extensively studied in spintronics as promising materials to give rise to very large magnetoresistance. Spin-polarized positron spectroscopy based on ACAR and DBAR spectra may be useful to examine the ferromagnetic band structures and hence the half-metallicity.

As shown in Fig. 4 (left), for two Heusler alloys (Co_2MnSi (CMS) and Co_2MnAl (CMA)) that are expected to be half-metals, we obtained the differential DBAR spectra between majority and minority spin bands, which is directly comparable to theoretical calculation, as

$$N^{maj}(p_z) - N^{\min}(p_z) = [N_+(p_z) - N_-(p_z)] + P_+[(\lambda^{\uparrow} - \lambda^{\downarrow})/(\lambda^{\uparrow} + \lambda^{\downarrow})][N_+(p_z) + N_-(p_z)],$$

where $\lambda^{\uparrow(\downarrow)}$ is the annihilation rate of spin up (down) positrons, and $N_{\pm}(p_z)$ is the DBAR spectrum in positive and negative magnetic field [19]. For the CMS sample, a bump at around p=0 m_0c and a shoulder at around p=10 m_0c are seen. For the CMA sample, the intensity at around p=0 m_0c is significantly lost. Contrarily to the CMS sample having $L2_1$ structure, the CMA sample was in fully disordered B2 structure. Therefore, one may consider that the reduced intensity of the CMA sample at around p=0 m_0c is due to the B2 disordering. Furthermore, the above difference between the CMS and CMA samples may be correlated with the general trend that CMS has a higher half-metallicity as compared to CMA. However, the above argument is not true as explained below. The solid lines in Fig. 4 are theoretical curves assuming $L2_1$ structure. The blue (thin solid) and red (broken) lines represent positive and negative polarizations, respectively. Agreement between experiment and theory is good even if the CMA

sample was in fully B2 structure. This indicates that the band structure and hence the electron momentum distribution is not dramatically changed between $L2_1$ and B2 structures. Actually, our calculation supported this assumption. The bump at around p=0 m_0c and the shoulder at around p=10 m_0c for the CMS sample are interpreted as that, the total intensity of the positively polarized 17 th to 19 th bands having *sp*-like dispersion and the 13 th to 16 th bands having *d*-like dispersion overcompensate the total intensity of the other negatively polarized bands. In the case of CMA, the 13 to 16 th bands are similarly positively polarized, but, the 17 th to 19 bands have nearly no states. Consequently, their total intensity does not exceed the total intensity of the other negatively polarized bands and hence the valley at around p=0 m_0c appears. As seen from the calculated band structures in Fig. 4 (Right), CMS has theoretically better half-metallicity as compared to CMA. Thus, considering the above arguments, it is concluded that, (i) from the agreement between experiment and theory, the CMS sample has a higher half-metallicity than the CMA sample and (ii) the half-metallicity is robust for the disordering from $L2_1$ to B2 structures.

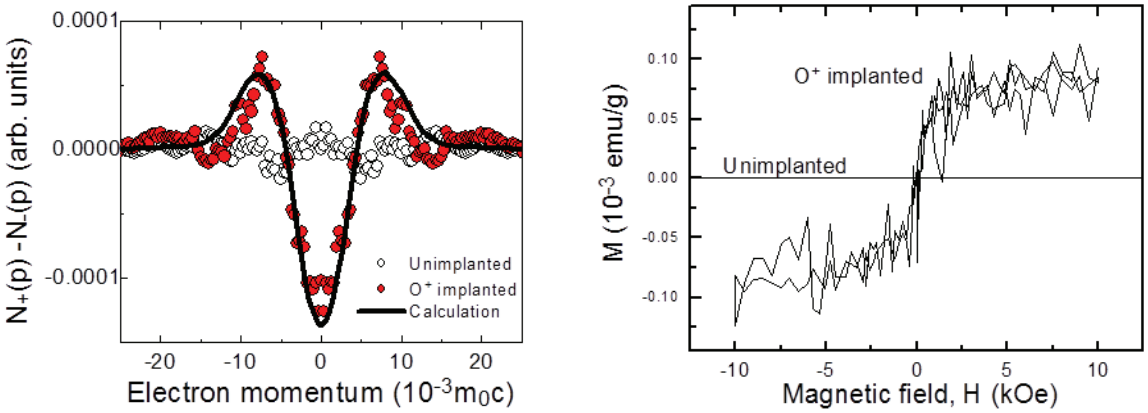

FIGURE 5. (a) Differential DBAR spectra in positive and negative magnetic fields and (b) the M-H curve, obtained for a hydrothermally-grown ZnO before and after oxygen irradiation ZnO. Sold line in (a) is the theoretical DBAR spectrum for electrically neutral zinc vacancy

Vacancy-induced ferromagnetism

It is demonstrated that ferromagnetism appears in originally non-magnetic materials without intentional doping of magnetic elements. Many subsequent investigations demonstrated that such ferromagnetism is a common feature of metal oxides, nitrides and carbides. Zinc oxide (ZnO), which is a wide-bandgap semiconductor, is one of such materials. The origin of the ferromagnetism is speculated to be due to atomic vacancies. However, no direct evidences for this speculation have been obtained. Since positrons are preferentially trapped by atomic vacancies in solids, spin-polarized positron spectroscopy may be a powerful tool to confirm the existence of magnetic moments at vacancies, i.e., vacancy-induced ferromagnetism.

Figures 5(a) and 5(b) show the differential DBAR spectra in positive and negative magnetic fields and the M-H curve, respectively, obtained for a hydrothermally-grown ZnO before and after oxygen irradiation [20]. After oxygen irradiation, the DBAR spectrum shows clear field reversal symmetry. The M-H curve also shows a ferromagnetic history. After oxygen irradiation, most of positrons get trapped by zinc vacancies. The solid line in Fig. 5(a) is the calculated differential DBAR spectrum for electrically neutral zinc vacancies. It reproduces the experiment quite well. The finite differential intensity is due to the high spin state associated with zinc vacancies. For oxygen vacancies and nearest neighbor divacancies, no differential curves (only horizontal lines) are obtained. The above results allow us to conclude that electrons at zinc vacancies are spin-polarized contributing to the macroscopic ferromagnetism.

There are many other potential candidates of vacancy-induced ferromagnetism such as doped or irradiated GaN, AlN, SnO_2, CeO_2, etc. Spin-polarized positron spectroscopy may also be applied to these systems. Development of spin-polarized positron lifetime spectroscopy will be more helpful to promote this kind of studies.

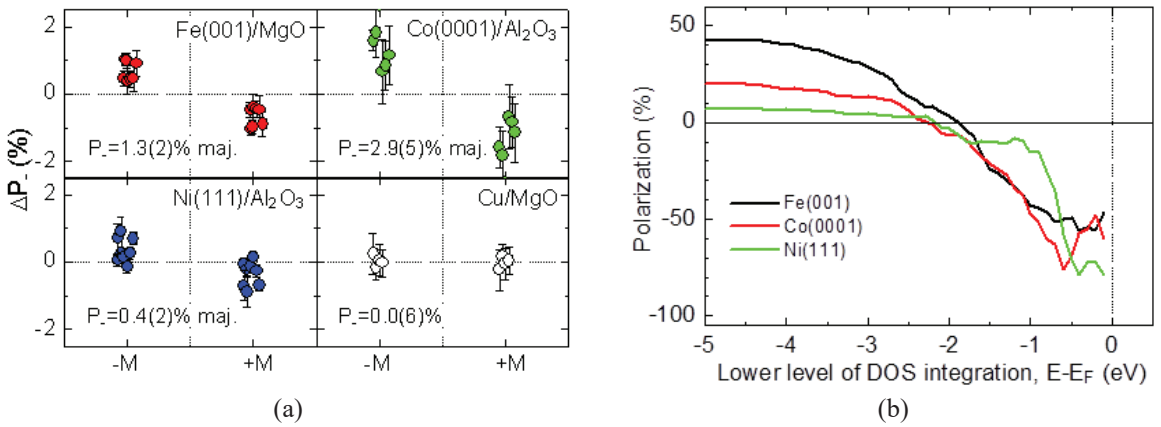

(a) (b)

FIGURE 6. (a) Surface spin polarizations observed for bcc-Fe(001)/MgO(001), hcp-Co(0001)/Al_2O_3(0001), fcc-Ni(111)/Al_2O_3(0001) and polycrystalline Cu/MgO(001). $\pm$M denotes that the magnetization of sample is parallel (antiparallel) to the positron spin polarization. (b) Theoretical spin polarizations of the vacuum region of Fe(001), Co(0001) and Ni(111) surfaces as a function of the lower energy level of density of states. That is, positrons are assumed to pick-up electrons from the lower level to E_F

Surface spin polarization

In spintronics, surface and interface are extremely important concerning spin injection into non-magnetic layer from ferromagnetic substrate, and spin current/accumulation induced via strong spin-orbit interaction. That is, surface spin polarization should be evaluated with less disturbances from deep layers. However, conventional methods such as photoemission spectroscopy and magneto-optical effect measurement are not necessarily sufficient for the above requirements. Spin-polarized positron spectroscopy based on surface positronium formation will be an alternative method since positronium is assured to be formed at the first surface layer. When both positrons and electrons are spin-polarized, from the change of positronium intensity upon spin reversal, surface spin polarization can be obtained [6].

Figure 6(a) shows the spin polarizations obtained for clean bcc-Fe(001)/MgO(001), hcp-Co(0001) and fcc-Ni(111) on Al_2O_3(0001) and polycrystalline Cu/MgO(001) with the film thicknesses of 30-100 nm. The spin polarization of the Cu sample is under the detection limit, while all the other samples exhibit finite spin polarizations. From the signs of the spin-polarizations, majority spin electrons are detected. Figure 6(b) shows the calculated spin polarizations in the vacuum regions of Fe(001), Co(0001) and Ni(111) surfaces as a function of lower energy level of integration below the Fermi level. From this, if electrons located only above E_F-1.5 eV are picked-up by positrons, the observation of majority spins is not explained. Probably, positrons pick up electrons in deeper levels, too.

We have also evaluated the surface spin polarizations induced on metals known as spin-Hall and Rashba systems [21-23]. The topological insulators and graphene-related monoatomic layer materials are also the potential applications. For more quantitative discussion, positronium formation mechanisms should be revealed both in experiment and theory. Spin-, energy- and angle-resolved positronium spectroscopy is required ultimately.

PERSPECTIVE OF SPIN-POLARIZED POSITRON SPECTROSCOPY

Early studies of ferromagnetic band structures were performed with ACAR method. Though ACAR is useful for the Fermi surface mapping, at present, only bulk study is possible since slow positron beams with enough intensity (>10^9 e^+/sec) and spin polarization (>50 %) have not yet been in use. We demonstrated that DBAR method can also be used for studying ferromagnets. This measurement is possible even with low beam flux (10^4-10^5 e^+/sec) from RI sources. Also, magnetic moments of vacancies in thin films and subsurface regions can be detected. Spin-polarized and pulsed positron beam may also be a powerful probe for detecting magnetic moments of vacancies, since lifetime spectroscopy provides more direct information about open volumes and electron densities associated with vacancies.

For the study of surface spin polarization, currently, only a simple positronium spectroscopy (gamma-ray energy and lifetime measurements) is available. This method has an advantage about selectivity of the first surface layer that the other methods are hardly accessible. But, to deduce more detailed information about spin-polarized

electronic state, energy- and angle-resolvability is also required. If the surface positronium spectroscopy with spin, energy and angle resolutions is realized, it is possible to determine spin polarization at the Fermi level, spin-polarized density of states and band dispersion that are practically of importance. We may call this technique "spin and angle-resolved positronium spectroscopy". Surface spin polarization can also be studied through positron surface state since it has characteristic long lifetimes (>500 ps) which is distinguishable from bulk annihilation. For doing this, spin-polarized and pulsed positron beam is again needed.

The above experiments can be conducted somehow even using RI-based beams. But, as mentioned above, in ACAR experiments of thin films, spin-polarized 'intense' beam is absolutely needed. This may be difficult with RIs. Spin-polarized intense positron beam can open other possibilities, too, such as micro-probing of spin polarization. Obviously, higher beam spin polarization gives better results in spin-polarized positron spectroscopy experiments. Beam intensity of 10^{10} e^{+}/sec plus spin-polarization of more than 90 % would be an ultimate goal of positron beam development.

ACKNOWLEDGMENTS

This work was partly supported by JSPS KAKENHI under Grant No. 24310072, 15K14135, 17K19061.

REFERENCES

1. C. S. Wu, E. Ambler, R. W. Hayward, D. D. Hoppes, R. P. Hudson, Phys. Rev. **105**, 1413-1415(1957).
2. T. D. Lee, C. N. Yang, Phys. Rev. **104**, 254-258(1956).
3. S. S. Hanna and R. S. Preston, Phys. Rev. **106**, 1363-1364(1957).
4. P. W. Zitzewitz, J. C. Van House, A. Rich and D. W. Gidley, Phys. Rev. Lett. **43**, 1281-1284(1979).
5. L. M. Liebermann, D. R. Fredkin and H. B. Shore, Phys. Rev. Lett. **22**,539-541(1969), L. M. Liebermann, J. Chilton, D. M. Edwards, J. Mathon, Phys. Rev. Lett. **25**,232-235(1970).
6. D. W. Gidley and A. R. Koymen, Phys. Rev. Lett. **49**, 1779-1783(1982).
7. T. Kumita, M. Chiba, R. Hamatsu, M. Hirose, T. Hirose, H. Iijima, M. Irako, N. Kawasaki, Y. Kurihara, T. Matsumoto, H. Nakabushi, T. Omori, Y. Takeuchi, M. Washio and J. Yang, Appl. Surf, Sci. **116**, 1-6(1997).
8. F. Saito, T. Hyodo, Y. Nagashima, T. Kurihara, N. Suzuki, Y. Itoh, and A. Goto, "Intense Radioisotope Sources for Spin Polarized Positron Beams" in *New Directions in Antimatter Chemistry and Physics*, edited by C. M. Surko and F. A. Gianturco (Kluwer Academic Publishers, The Netherlands, 2001)pp.35-45.
9. M. Maekawa, Y. Fukaya, A. Yabuuchi, I. Mochizuki, A. Kawasuso, Nucl. Inst. Meth. Phys Res. B**308**, 9-14(2013).
10. I. K. MacKenzie, C. W. Shulte, T. Jackman and L. Campbell, Phys. Rev. **A7**, 135-145(1973).
11. C. K. Iddings, G. L. Shaw and Y. S. Tsai, Phys. Rev. **135**, B1388-B1397 (1964).
12. R. M. Sternheimer, Phys. Rev. B **103**, 511-515(1956).
13. M. E. Rose and H. A. Bethe, Phys. Rev. **55**, 277-289(1939).
14. A. Kawasuso, M. Maekawa, Y. Fukaya, A. Yabuuchi, and I. Mochizuki, Phys. Rev. B **83**, 100406(R) (2011), Phys. Rev. B**83**, 100406(R)-1-3(2011).
15. A. Kawasuso, M. Maekawa, Y. Fukaya, A. Yabuuchi and I. Mochizuki, Phys. Rev. B**85**, 024417-1-6(2012).
16. M. Maekawa, Y. Fukaya, H. Zhang, H. Li and A. Kawasuso. J. Phys.: Conf. Ser., **505**, 012033-1-4(2014).
17. M. Maekawa, H. Zhang, H. Li, Y. Fukaya, A. Kawasuso, Jpn. J. Appl. Phys. Conf. Proc. **2**, 011305-1-6(2014).
18. Y. Nagai, Y. Nagashima, J. Kim, Y. Itoh, and T. Hyodo, Nucl. Instrum. Meth. Phys. Res. B **171**, 199-203(2000).
19. H. Li, M. Maekawa, A. Miyashita, A. Kawasuso, Defect and Diffusion Forum, **373**, 65-70 (2016).
20. M. Maekawa, H. Abe, A. Miyashita, S. Sakai, S. Yamamoto, A. Kawasuso, Appl. Phys. Lett., **110**, 172402-1-5(2017).
21. A. Kawasuso, Y. Fukaya, M. Maekawa, H. Zhang, T. Seki, T.Yoshino, E. Saitoh, K. Takanashi, J. Mag. Mag. Mater. **342,** 139-143(2013).
22. H. J. Zhang, S. Yamamoto, Y. Fukaya, M. Maekawa, H. Li, A. Kawasuso, T. Seki, E. Saitoh& K. Takanashi, Scientific Reports **4,** 04844-1-5(2014).
23. H. J. Zhang, S. Yamamoto, B. Gu, H. Li, M. Maekawa, Y. Fukaya, and A. Kawasuso Phys. Rev. Lett. **114**, 166602-1-5(2015).

Proposal for a slow positron facility at Jefferson National Laboratory

Allen P. Mills, Jr.[1,a)]

[1] *University of California Riverside, Riverside CA 92521 USA*
[a)] *Corresponding author: allen.mills@ucr.edu*

Abstract. One goal of the JPos-17 International Workshop on Physics with Positrons was to ascertain whether it would be a good idea to expand the mission of the Thomas Jefferson National Accelerator Facility (JLab) to include science with low energy (i.e. "slow") spin polarized positrons. It is probably true that experimentation with slow positrons would potentially have wide-ranging benefits comparable to those obtained with neutron and x-ray scattering, but it is certain that the full range of these benefits will never be fully available without an infrastructure comparable to that of existing neutron and x-ray facilities. The role for Jefferson Laboratory would therefore be to provide and maintain (1) a dedicated set of machines for making and manipulating high intensity, high brightness beams of polarized slow positrons; (2) a suite of unique and easily used instruments of wide utility that will make efficient use of the positrons; and (3) a group of on-site positron scientists to provide scientific leadership, instrument development, and user support. In this note some examples will be given of the science that might make a serious investment in a positron facility worthwhile. At the same time, the lessons learned from various proposed and successful positron facilities will be presented for consideration.

I. INTRODUCTION

Positrons are the antiparticles of the electrons that are part of all the matter we observe in daily life. Slow positrons are positrons produced in vacuum with a few eV energy by moderating energetic (greater than a few 100 keV) positrons produced by beta decay or pair production. Slow positrons may be accelerated to any desired energy and focused and manipulated in phase space as needed. A positron interacts with ordinary matter in many ways, including scattering, annihilating with electrons, and forming bound states such as the hydrogen-like electron-positron atom positronium (Ps). These interactions can be used to study fundamental physics as well as the properties of matter in ways that are complementary to the more usual methods that probe matter using neutrons, electrons, X-rays and so forth. About 25 years ago the US Department of Energy (DOE) decided that positron spectroscopy had become sufficiently important to justify the initiation at Lawrence Livermore National Laboratory (LLNL) of a high intensity positron source and user facility based on their working 150 MeV electron LINAC. Unfortunately, the non-completion of a complex initial flagship instrument [1] after more than five years of effort led to the cancellation of the project, which otherwise would likely have gradually grown into a valuable enterprise with many instruments and users. Today the case for establishing an intense positron source and user facility in the USA has become even stronger than before with the development of several new types of positron spectroscopies and more advanced theories that would be very valuable to US science and industry given a positron source of sufficient intensity and a suite of instruments that could be easily employed by outside users. Briefly described here are some of the capabilities that would be possible with a new slow positron facility at Jefferson National Laboratory (JLab). This facility would be the best of its kind in the world by at least an order of magnitude in all respects, including providing beams of more than 10^8 polarized or 10^9 unpolarized positrons emanating from 1 mm diameter areas with initial energies of less than 1 eV. In this document we are concentrating on the new science and useful materials analysis that could be done at JLab and the reasonably achieved characteristics of the proposed intense slow positron sources that would make it possible.

II. WHAT ARE SLOW POSITRONS?

Energetic positrons are produced in beta decay and pair production interactions. Typical beta-decay radioactive sources like ^{22}Na, ^{13}N, ^{79}Kr, and ^{68}Ge are produced via reactions such as ^{27}Al(p,X) $\rightarrow ^{22}$Na, ^{12}C(d,n) $\rightarrow ^{13}$N, ^{78}Kr+n$^{0}\rightarrow ^{79}$Kr, etc. These particular nuclei emit positrons with energies ranging from 0.54 to 1.95 MeV. The positrons have a continuous distribution of velocities v because the total radioactive decay energy is shared with a neutrino. The positrons are emitted with helicities $h = \hat{s} \cdot \hat{v} = v/c$ [2], where $\vec{s}$ is the positron's spin angular momentum, due to the non-conservation of parity in the weak interaction [3]. If a restricted solid angle of the directions of the emitted particles is collected into a beam, the beam will be spin-polarized along the average emission direction. A typical polarization for a positron beam from the most common isotope, ^{22}Na, has a polarization of about 30% [4, 5], which can be increased by filtering out the lower energies and restricting the positrons to those emitted more closely to the beam direction.

Pair production occurs when an energetic photon is able to turn into an electron and a positron in close proximity to an atomic nucleus which conserves the momentum of the interaction by absorbing a virtual photon. The energetic photons are either obtained from the bremsstrahlung emitted by relativistic electrons passing through a material absorber or Cd(n,γ) neutron capture gamma rays in a nuclear reactor.

Slow positrons are obtained in vacuum with eV energies when they escape from the surface of a solid moderator that is being bombarded with fast positrons [6, 7]. The usual positron moderators are solid Ne with a fast-positron to slow positron conversion efficiency $\varepsilon \approx 1\%$ for ^{22}Na [8]. For single crystal W [9], which can work at high temperatures, the efficiency is $\varepsilon \approx 0.1\%$ and Ni(111) thin single crystals can be used to efficiently moderate low energy positron beams to increase their brightness [10, 11, 12, 13]. Once produced, slow positrons are accelerated and focused directly onto a target used in an experiment, or manipulated in phase space before being used in an experiment by remoderation, trapping, bunching, etc. A multitude of experiments are done involving e^+ interactions with matter, via the annihilation photons, scattering, optical spectroscopy, positronium formation, secondary particle emission, and other mechanisms.

III. OVERVIEW

There is now even more science and probably a greater user base to justify a DOE slow positron user facility unique in the world for intensity and for having polarized positrons. On September 12-15, 2017 a group of scientists met in Newport News, VA to discuss the possibility of JLab being the host for a new US-based positron facility that might include the generation of high energy positrons for study of nuclear structure as well as slow positrons for studying the structure of ordinary materials. The possibility that the same high energy electron LINAC could profitably be used for generating both high energy positron and slow positrons was seriously entertained, especially because of the highly successful facility of this type that has been operated at Dresden for many years [14]. One possibility for having a source of polarized slow positrons was suggested by JLab's recent demonstrated ability to make 3-6 MeV highly polarized positrons in a small momentum band [15]. The consensus of the group that was considering the possibilities, was that there was more than enough science to be done with unpolarized positrons to justify a facility that would start out with an unpolarized intense bremsstrahlung source, and that a polarized source of lesser intensity based on ^{22}Na should also be made for the facility. This polarized source could in fact be of greater intensity than that of any other existing unpolarized positron facility in the world and it would thus have great utility complementing the main unpolarized source. In addition the polarized source would not be constrained by the schedules of high energy experiments, and maintenance and development that is usual for high energy machines.

The advantages to US Science for developing the slow positron component of the proposed facility are (1) that it would be the best positron facility in terms of available quantity of data anywhere in the world by more than a factor of ten; (2) that it would make available in the US a number of new valuable spectroscopies competitive in sensitivity and precision, and complementary in point of view, to standard methods using neutron and x-ray scattering and photoemission; (3) that it would provide these spectroscopies without our scientists having to go overseas; and (4) that the great intensity would mean there will be sufficient beam time for making detailed and precise measurements that could not be done anywhere else. One of the most forceful arguments in favor of the present proposal is that beam

time is scarce at the current best places in the world for this kind of work, namely in Germany at the Munich reactor [16] and at the ELBA LINAC facility in Dresden.

There was some concern expressed by the attendees that there is a long path from 100 MeV to 1 eV and while many have attempted it, none have succeeded in getting 10^{10} slow e^+/s in a useful beam diameter and energy. This concern was met by consideration of the proposal from NCCU [17] of a way to use the highly efficient solid Ne moderator [8] to get slow positron intensities much greater than 10^{10} slow e^+ per sec. Another concern was that the Jefferson Lab has no onsite history, expertise, or leadership in slow positron physics. This objection would be easily rectified by hiring the right persons. Some worries that there might be competition for space, personnel, and funding between the high and low energy aspects of the project were nullified by the spectacular success of the Dresden LINAC which successfully incorporates both aspects of science into its operations.

IV. SCIENTIFIC ARGUMENT IN FAVOR OF A JLAB LOW ENERGY POSITRON FACILITY

The main argument in favor of a JLab low energy positron Facility is that one could do lots of great experiments with a 1 mm diameter beam of 3×10^{10} unpolarized and 3×10^{8} polarized thermal energy slow positrons per second at Jlab. The following is a list of some of the positron spectroscopies that have been established for studying the electronic structure of solids and surfaces and that would be enormously more useful with the proposed high intensity positron beams.

1. 2D-ACAR is the two dimensional angular correlation of annihilation radiation spectroscopy that produces a 3D momentum space density profile of the electrons in a solid [18, 19]. This method probes the same information as Compton scattering with much better resolution and detail and with much less unwanted signal from the inner core electrons, but with some distortions due to the positron wave function in the solid. With modern theory, especially the theorem of Biasini and Rusk [20], which shows how to largely remove such probe effects from the measurements, and the Lock-Crisp-West theorem [21], which shows how to remove the effects of the filled electron bands, one could obtain a momentum density map with both 10× better precision and 10× better resolution given a high intensity positron beam and a matching high resolution and high efficiency detector. Measurements of this kind would reveal spectacular detail never before observed in momentum space. At the present time the best 2D-ACAR measurements are obtained with a 50 mCi ^{22}Na source in close proximity to a sample. The resolution in the direction normal to the crystal surface can be very good, but in the direction parallel to the surface the resolution is determined by the size of the positron illumination spot. As a result of the low intensity and limited resolution, the data being taken today, although useful as far as it goes, is no better than experiments from 25 years ago or more. To really take advantage of the tremendous capabilities of this type of spectroscopy we need both a high intensity source and a detector of high efficiency and high resolution. The latter has never been made because there was never a source that would have justified building it. Nevertheless, the technology for making a great ACAR instrument is available. With the new source and detector, a full 3D image of the momentum density in a crystalline solid at low temperature, with momentum resolution of roughly 1% of the size of the Brillouin zone and statistical precision of the occupation number of the various bands at better than 0.003 out of the maximum value of 1, could be obtained in a few days.

2. TRHEPD is total reflection high energy positron diffraction [22], which is like its electron counterpart known as reflection high energy electron diffraction, RHEED. The latter is routinely used to gauge the layer by layer growth of crystals via molecular beam epitaxy or MBE. High energy positron diffraction at grazing angles is predominantly affected by the top monolayer because the positrons are repelled by the inner potential because the attractive polarization potential becomes invisible to the high speed probe particles. This allows one to unambiguously see the precise arrangement of the surface atoms without a theory by a simple Fourier transform of the data. A high intensity version of TRHEPD would permit scanning a large area sample using a small area beam to see details of the surface structure made visible at each location sampled from its local diffraction intensity distribution. For a non-crystalline surface the top layer atom positions could be determined using a microscopic probe beam area even though there are no regularly spaced narrow diffraction spots.

3. LEPD is low energy positron diffraction [23], similar to the familiar low energy electron diffraction, LEED, discovered by Davison and Germer at Bell Labs in 1927 [24]. With high intensity a LEPD diffraction pattern could

be obtained in a few seconds rather than over a period of days, allowing one to make a 2D image of a surface with crystal order as the contrast. Although this type of positron diffraction requires a complicated analysis, its interpretation is more reliable than LEED in determining the structure of the first few layers of a crystalline surface [25].

4. ARPsES is angle resolved positronium emission spectroscopy [26], which is the analog of angle-resolved photoelectron spectroscopy (ARPES) [27]. A Ps atom is emitted from a metal surface when a thermal energy positron that was implanted within the solid comes up to the surface and tunnels out to the vacuum, having captured one of the electrons from the solid. The momentum parallel to the surface and the total energy of the resulting positronium atom tell us what the parallel momentum and total energy of the electron was when it was inside. ARPsES differs from ARPES in that only the electrons near the Fermi energy are imaged and there are probably less competing processes for the electron leaving the surface to complicate the analysis. While normal emission ARPsES has just been made possible by time of flight detection of Rydberg positronium atoms [28], a full 3D image of the electronic structure near a crystal surface could be made in a few minutes using a high intensity positron source.

5. PAES is positron annihilation induced Auger electron spectroscopy [29, 30]. This technique allows one to be free of the defect of ordinary Auger spectroscopy, in which the core hole is created near the surface by bombardment with electrons. As a consequence, the secondary electrons from bombardment are confused with the emitter Auger electrons, and it is difficult to extend the Auger electron energy spectrum to low energies. The positron version of this spectroscopy allows one to see nothing but Auger electrons and would be a much sought-after method of looking at surface atoms if there were a high intensity positron beam.

6. Positron microscopes or microprobes can be implemented by bringing a beam of positrons to a tiny focus after the brightness of the beam has been enhanced by repeated stages of acceleration, focusing, and remoderation [10]. The possibilities enabled by a primary positron beam include the following.

7. Positron reemission microscope. One could illumintate a 20 μm spot on a metal crystal sample in ultrahigh vacuum with 10^8 10 keV e^+/s to obtain a reemitted positron immersion optics image able to detect 1% contrast variations with 10 nm resolution in about 10^3 s. One would be able to see crystal defects, grain boundaries [31], and surface objects larger than 10 nm. With one further stage of brightness enhancement one could illuminate a 150 nm thick single crystal Ni(100) foil such that about 10^6 e^+/s would be emitted from the other side [13] from a half micron diameter spot. With suitable electron optics one could examine single molecules with nm resolution, 1% contrast and 1 h exposure. Ordinarily one would suppose that such a long exposure would completely burn up the molecules, even though the probing re-emitted positrons from the back of the Ni film have only 1 eV of kinetic energy. On the contrary, it has been suggested that the electronic excitations of a molecule in close contact with a metal surface will be transmitted to the electronic degrees of freedom of the metal, thus permitting a long term exposure of delicate protein molecules for example [32, 33].

8. Variable energy scanning defect positron microprobe. By scanning a sample surface with a focused positron beam [34] of variable energy one may obtain images with depth resolution of about 50% and with a contrast dependent on the positron lifetime [35] or the S- or W- parameters for detecting vacancies in metals [36], voids in polymers [37], etc.

9. A positron field emission microscope is also a possibility but has not been implemented yet [38].

10. Other applications of high intensity positrons include fundamental physics studies such as precision 1S-2S spectroscopy of Ps for testing QED, searches for Ps antigravity, production of positron plasmas, and storage of vast quantities of positrons for making portable positron sources or for studies of positron systems at high densities. The latter topic includes studies of the Ps BEC, the e^+ superconductor, the e^+ FET, the annihilation gamma laser, and density probes of laser fusion capsules and exploding foils.

Conclusion. With 10× the count rate of the current best place in the world, a lot of these spectroscopies, which are currently seen as novelties, suddenly become very practical!

V. PROPOSAL FOR A HIGH INTENSITY POSITRON FACILITY

1. Lessons from previous attempts to make a Facility.

Twenty years after the discovery of the first practical slow positron moderator [39] there were already dozens of successful US positron researchers who wanted a high intensity US Positron Facility. Besides numerous Positron meetings, the formal evidence of the need for a facility at that time included:

(1) 1991 Symposium on the need for a US Positron Facility at the Fall Meeting of the Materials Research Society at Boston MA.

(2) 1992 Sept 9-11 (25 years ago) DOE Rancho Mirage CA workshop on the Application of Positron Spectroscopy to Materials Sciences, assessing the need for a US Positron Facility [40].

(3) 1992 DOE BESAC panel on neutron sources requests Report on Positron Spectroscopy [41].

(4) 1994 Proposal for a US positron facility at the ORNL (Oak Ridge National Laboratory) ANS (Advanced Neutron Source) [42].

(5) 1994 Proposal for a US Positron Facility at CEBAF (JLab) [43].

(6) 1997 Nov 5-7 DOE Workshop on Applications of positron beam spectroscopy was held at LLNL and gave a positive answer to the questions: (1) Is there a need for a national center for materials analysis using positron techniques and (2) Can the capabilities at Lawrence Livermore National Laboratory serve this need? [44]

By the mid 1990's there were 3 medium intensity DOE slow positron machines that had been operating in the US for about 10 years [45]:

(1) BNL had a ^{64}Cu source made in their reactor that produced 6×10^{7} slow e^{+}/s from a 5 mm diameter spot [46].

(2) ORNL was using its ORELA LINAC operating at 3 kW to produce 7.8×10^{6} slow e^{+}/s [47, 48].

(3) LLNL reported they were developing a 100 MeV LINAC positron microprobe [49, 1]. The measured raw slow e^{+} intensity was $(5\pm1)\times10^{8}$ e^{+}/s [50] and perhaps could have been more than an order of magnitude higher but for target heating problems.

2. What Happened?

Despite Scientific Justification for there being a US Positron Facility at a DOE Lab, it did not happen. There were several problems that may have prevented going forward to facility status for the three high intensity DOE positron machines. Both the ORNL and LLNL LINAC's never reached the claimed possible intensities of 10^{10} slow e^{+}/s because the LINAC's primary purposes were for producing neutrons and therefore the positron producing target geometries could not be optimized. The ^{64}Cu source at BNL used a self-moderating ^{64}Cu single crystal evaporated on a clean W single crystal. The source perhaps could have simplified and reached the desired intensity by using a solid Ne moderator, but before that could be implemented the operation ceased when the reactor was permanently shut down. While the BNL reactor source produced lots of good physics, the LLNL positron microprobe project never worked due to a complicated design and a failure to ever obtain preliminary results along the way.

To prevent this type of failure, the present proposal is based on (1) a noncontroversial facility, and (2) a small group of expert collaborators in the field who will ensure (a) that a reasonable route is taken to the fast and slow positron production and (b) that useful and interesting preliminary and continuing experimental results will unambiguously verify progress.

3. Expectations that there will be a significant user base.

(1) The existing slow positron facilities at the Munich Reactor [16], the Dresden superconducting electron accelerator [14], and the KEK (Japan) electron LINAC [22] between them have ~10 beam lines and a significant and oversubscribed user base. With 10× higher useful intensity at JLab the user base and data rate could be much larger.

(2) The many new positron techniques that have been developed in the last 50 years using weak positron beams are now ripe for exploitation in hundreds of new applications given sufficient intensity.

(3) Advances in theory and computation speed now make it practical to analyze and understand in detail various new types of measurements with large amounts of data.

(4) A well-staffed and well equipped slow positron facility would allow hundreds of researchers who ordinarily use neutron or x-ray scattering to obtain complementary information using positrons, without having to become experts in positron beam technology.

4. Proposal elements.

(1) The primary solid Ne moderated slow positron source will be based on the proposal by S. Golge, B. Vlahovic, and B. Wojtsekhowski [17] and will be implemented by collaborators at JLab.

(2) Positron beam transport to the slow positron experiment hall will implemented be via solenoids, and positron instruments will be set up, starting with the simplest (scanning microprobe) and progressing up to building instruments for PAES and 2D ACAR.

(3) To permit rapid development, testing, and first applications of the instrumentation so that it will be ready when the JLab positrons are available, the UCR polarized positron beam would be moved to the JLab slow positron experiment hall. The three existing beam lines will eventually be set up to accept either the ^{22}Na beam or the JLab beam. Experiments on the positronium BEC, measuring the positronium 1S-2S interval, and measuring Rydberg positronium gravitational free fall will be set up and continued as they were at UCR.

(4) In order that there will be positrons available with significant intensities for set up and for preliminary experiments when the JLab positron source is not available (availability may only be about 30%) a 1 Ci ^{22}Na capsule will be prepared at LANL and installed in the UCR beam. Eventual upgrade to 3 Ci will provide 10^9 polarized 10 keV e^+ on a 1 mm spot for bulk magnetic 2D ACAR.

ACKNOWLEDGMENTS

The author is indebted to many colleagues over the years for discussions and experimental efforts toward creating a US Low Energy Positron Facility. This work was supported in part by the US National Science Foundation Grants PHY 1404576 and PHY 1505903.

REFERENCES

1. W. Stoeffl, Asoka-Kumar, and R. H. Howell, "The positron microprobe at LLNL", *Appl. Surf. Sci.* **149**, 1-6 (1999).
2. J. D. Jackson, S. B. Treiman and H. W. Wyld, Jr., "Possible tests of time reversal invariance in beta decay, *Phys. Rev.* **106**, 517 (1957).
3. T. D. Lee and C. N. Yang, "Question of parity conservation in weak interactions", *Phys. Rev.* **104**, 254 (1956).
4. P. W. Zitzewitz, J. C. Van House, A. Rich, and D. W. Gidley, "Spin polarization of low-energy positron beams", *Phys. Rev. Lett.* **43**, 1281 (1979).
5. D. B. Cassidy, V. E. Meligne, and A. P. Mills, Jr., "Production of a fully spin-polarized ensemble of positronium atoms", *Phys. Rev. Lett.* **104**, 173401 (2010).
6. L. Madansky and F. Rasetti, "An attempt to detect thermal energy positrons", *Phys. Rev.* **79**, 397 (1950).

7. W. H. Cherry, Doctoral Dissertation, Princeton University (1958).
8. A. P. Mills, Jr. and E. M. Gullikson, "Solid Neon Moderator for Producing Slow Positrons", *Appl. Phys. Lett.* **49**, 1121 (1986).
9. A. Vehanen, K. G. Lynn, Peter J. Schultz, and M. Eldrup, "Improved slow-positron yield using a single crystal tungsten moderator", *Appl. Phys. A* **32**, 163 (1983). doi: 10.1007/BF00616613
10. A. P. Mills, Jr., "Brightness Enhancement of Slow Positron Beams", *Appl. Phys.* **23**, 189 (1980).
11. K. F. Canter and A.P. Mills, Jr., "Slow Positron Beam Design Notes", *Can. J. Phys.* **60**, 551 (1982).
12. W. E. Frieze, D. W. Gidley, and K. G. Lynn, "Positron-beam-brightness enhancement: Low energy positron diffraction and other applications", *Phys. Rev. B* **31**, 5628 (1985).
13. P. J. Schultz, E. M. Gullikson, and A.P. Mills, Jr., "Transmitted Positron Re-emission from a Thin Single-Crystal Ni(100) Foil", *Phys. Rev. B* **34**, 442 (1986).
14. A. Wagner, et al., "Positron annihilation lifetime spectroscopy at a superconducting electron accelerator", *J. Phys.: Conf. Ser.* **791**, 012004 (2017).
15. D. Abbott, et al., "Production of Highly Polarized Positrons Using Polarized Electrons at MeV Energies", *Phys. Rev. Lett.* **116**, 214801 (2016).
16. C. Hugenschmidt, "Positrons in surface physics", *Surf. Sci. Reports* **71**, 547 (2016).
17. S. Golge, B. Vlahovic, and B. Wojtsekhowski, "High-intensity positron microprobe at the Thomas Jefferson National Accelerator Facility", *J. Appl. Phys.* **115**,234907 (2014).
18. S. Berko, "Positron annihilation experiments in metals; electronic structure and Fermi surface studies", *Scripta Metallurgica* **14**, 23-29 (1980).
19. S. Berko, "Momentum density and Fermi-surface measurements in metals by positron annihilation", in *Positron Solid-State Physics*, W. Brandt and A. Dupasquier, eds. (Soc. Italiana di Fisica, Bologna, 1983), pp. 64-145.
20. M. Biasini and J. Rusz, "Cancellation of probe effects in measurements of spin-polarized momentum density by electron-positron annihilation", *J. Phys.: Cond. Mat.* **18**, L289 (2006).
21. D. G. Lock, V. H. C. Crisp, and R. N. West, "Positron annihilation and Fermi surface studies: a new approach", *J. Phys F: Metal Physics* **3**, 561 (1973).
22. Fukaya Y, Maekawa M, Kawasuso A, Mochizuki I, Wada K, Shidara T, Ichimiya A and Hyodo T, *Appl. Phys. Express* **7**, 056601 (2014).
23. I. J. Rosenberg, A. H. Weiss, and K. F. Canter, "Low energy positron diffraction from a Cu(111) surface", *Phys. Rev. Lett.* **44**, 1139 (1980).
24. C. Davisson and L. H. Germer, "Diffraction of electrons by a crystal of nickel", *Phys. Rev.* **30**, 705 (1927).
25. T. N. Horsky, G. R. Brandes, K. F. Canter, C. B. Duke, S. F. Horng, A. Kahn, D. L. Lessor, A. P. Mills, Jr., A. Paton, K. Stevens, and K. Stiles, "Observation of differences between low-energy electron- and positron-diffraction structural determinations of the cleavage faces of CdSe", *Phys. Rev. Lett.* **62**, 1876 (1989).
26. A. C. L. Jones, H. J. Goldman, T. H. Hisakado, A. M. Pinero, H. W. K. Tom, A. P. Mills, Jr., B. Barbiellini, and J. Kuriplach, "Angle-resolved spectroscopy of positronium emission from a Cu(110) surface", *Phys. Rev. Lett.* **117**, 216402 (2016).
27. J.H. Dil, J. Phys.: Condens. Matter 21, 403001 (2009).
28. A. C. L. Jones, H. J. Goldman, Q. Zhai, P. Feng, H. W. K. Tom, and A. P. Mills, Jr., "Monoenergetic positronium emission from metal-organic framework crystals", *Phys. Rev. Lett.* **114**, 153201 (2015).
29. K. H. Lee, Gimo Yang, A. R. Koymen, K. O. Jensen, and A. H. Weiss, "Positron annihilation induced Auger electron spectroscopy studies of submonolayer Au on Cu(100): Direct evidence for positron localization at sites containing Au atoms", *Phys. Rev. Lett.* **72**, 1866 (1994).
30. S. Mukherjee, K. Shastry, C. V. Anto, P. V. Joglekar, M. P. Nadesalingam, S. Xie, N. Jiang, and A. H. Weiss, "Time of flight spectrometer for background-free positron annihilation induced Auger electron spectroscopy", *Rev. Sci. Instrum.* **87**, 035114 (2016); doi: 10.1063/1.4943858
31. G. R. Brandes, K. F. Canter, and A.P. Mills, Jr., "Sub-micron Resolution Study of a Thin Ni Crystal Using a Brightness-Enhanced Positron Re-emission Microscope", *Phys. Rev. Lett.* **61**, 492 (1988).
32. A.P. Mills, Jr. and P. M. Platzman, "New experiments with bright positron and positronium beams", *New Directions in Antimatter Chemistry and Physics*, edited by C. M. Surko and F. A. Gianturco (Kluwer Academic, 2001), 115-126.
33. B. Barbiellini and P. M. Platzman, "The healing mechanism for excited molecules near metallic surfaces", *New J. Phys.* **8**, 020 (2006).
34. G. R. Brandes, P. H. Lippel. T. Horsky, K. F. Canter, and A.P. Mills, Jr., "Scanning Positron Microbeam", *Rev. Sci. Instrum.* **59**, 228 (1988).

35. W. Stoeffl, P. Asoka-Kumar, and R. H. Howell, "The positron microprobe at LLNL", *Appl. Surf. Sci.* **149**, 1-6 (1999).
36. I. K. MacKenzie, T. L. Khoo, A. B. McDonald, and B. T. McKee, "Temperature dependence of positron mean lives in metals", *Phys. Rev. Lett.* **19**, 946 (1967).
37. D. W. Gidley, W. E. Frieze, T. L. Dull, A. F. Yee, E. T. Ryan, and H. M. Ho, "Positronium annihilation in mesoporous thin films", *Phys. Rev. B* **60**, R5157 (1999).
38. A. P. Mills, Jr., "Physics with many positrons", *Rivista del Nuovo Cimento* **34**, 151-252 (2011).
39. K. F. Canter, P. G. Coleman, T. C. Griffith, and G. R. Heyland, *J. Phys. B Atom Molec. Phys.* 5, L167 (1972).
40. L. D. Hulett, Jr. and Y. Chen, DOE CONF-9209221 (1993).
41. A. P. Mills, Jr., "Report on e+ spectroscopy for BESAC Panel", *AIP Conf. Proc.* 303, 335 (1994).
42. L. D. Hulett, Jr. and C. Eberle, "High intensity slow e+ facility at the ANS", Conf-9405170 (1994).
43. W. J. Kossler, A. J. Greer, and L. D. Hulett, Jr., "Positrons at CEBAF", *AIP Conf. Proc.* **303**, 296 (1994).
44. R. H. Howell https://www.osti.gov/scitech/biblio/302868 (1997).
45. K. G. Lynn and F. Jacobssen, "Intense low energy positron beams", *Hyp. Int.* **89**, 19-29 (1994).
46. P. J. Peng, K. G. Lynn, et al., "Study of SiO_2-Si interface…", *Phys. Rev. Lett.* **76**, 2157 (1996).
47. J. Xu, R. Suzuki, L. D. Hulett, and T. A. Lewis, "Production of slow positron bunches at ORELA and their applications", *Appl. Surf. Sci.* **116**, 34-38 (1997).
48. L. D. Hulett, T. A. Lewis, and J. Xu, "Generation of slow positron beams with the Oak Ridge Electron Linear Accelerator (ORELA)", in *Accelerator-Based Atomic Physics Techniques and Applications, S. M. Shafroth and J. C. Austin, editors,* (AIP Press, Woodbury, NY, 1997) *ISBN 1-56396-484-8*, pp 637-647.
49. R. H. Howell, Thomas E. Cowan, Jay H. Hartley, and Philip A. Sterne, "Positron Beam Lifetime Spectroscopy at LLNL", *AIP Conf. Proc.* **392**, 451 (1997). https://doi.org/10.1063/1.52486
50. D. B. Cassidy, A. W. Hunt, P. Ashoka-Kumar, B. V. Bhat, T. E. Cowan, R. H. Howell, K. G. Lynn, A.P. Mills, Jr., J. C. Palathingal, and J. A. Golovchenko, "Resonant versus nonresonant nuclear excitation of ^{115}In by positron annihilation", *Phys Rev C* **64**, 054603 (2001).

Positron Annihilation Lifetime and Doppler Broadening Spectroscopy at the ELBE Facility

Andreas Wagner[1, a)], Maik Butterling[1], Maciej O. Liedke[1], Kay Potzger[2], and Reinhard Krause-Rehberg[3]

[1]*Helmholtz-Zentrum Dresden-Rossendorf, Institute of Radiation Physics*
Bautzner Landstraße 400, 01328 Dresden, Germany
[2]*Helmholtz-Zentrum Dresden-Rossendorf, Institute of Ion Beam Physics and Materials Research*
Bautzner Landstraße 400, 01328 Dresden, Germany
[3]*Martin-Luther Universität Halle-Wittenberg, Institut für Physik, 06099 Halle, Germany*

[a)]Corresponding author: a.wagner@hzdr.de

Abstract. The Helmholtz-Zentrum Dresden-Rossendorf operates a superconducting linear accelerator for electrons with energies up to 35 MeV and average beam currents up to 1.6 mA with bunch charges up to 120 pC. The electron beam is employed to produce several secondary beams including X-rays from bremsstrahlung production, coherent IR light in a Free Electron Laser, superradiant THz radiation, neutrons, and positrons. The secondary positron beam after moderation feeds the Monoenergetic Positron Source (MePS) where positron annihilation lifetime (PALS) and positron annihilation Doppler-broadening experiments in materials science are performed. The adjustable repetition rate of the continuous-wave electron beams allows matching of the pulse separation to the positron lifetime in the sample under study. The energy of the positron beam can be set between 0.5 keV and 20 keV to perform depth resolved defect spectroscopy and porosity studies especially for thin films. Bulk materials, fluids, gases, and even radioactive samples can be studied at the unique Gamma-induced Positron Source (GiPS) where an intense bremsstrahlung source generates positrons directly inside the material under study. A ^{22}Na-based monoenergetic positron beam serves for offline experiments and additional depth-resolved Doppler-broadening studies complementing both accelerator-based sources.

INTRODUCTION

Positron annihilation lifetime spectroscopy (PALS) serves as a unique tool for the characterization of lattice defects in materials science. While the annihilation lifetime yields characteristic information about the size of open-volume defects ranging from single atomic vacancies up to even porous microstructures, the kinematical Doppler-broadening of annihilation radiation tells about the local electron momentum distribution at the annihilation site. Long annihilation lifetimes in the order of ns result from production of positronium, especially in porous media and in polymers. The well-established technique of employing radionuclides simultaneously emitting gamma-rays and positrons of typically up to several hundreds of keV is widely applied. Annihilation lifetimes are monotonously related to the void size with a surprisingly low dependence on the material surrounding the void [1]. The quantitative determination of positron annihilation lifetimes nevertheless is hampered when thin films or layered structures with sub-µm thicknesses which are of high technological relevance are considered. The isotropic emission and the high energy of common positron emitters cause penetration depths which are on the mm-scale. The installation described here overcomes this limitation by using mono-energetic positron beams with kinetic energies between 0.5 keV and 20 keV thus enabling depth-dependent thin film studies on the nm to µm scale [2].

THE MONOENERGETIC POSITRON SOURCE

The Mono-energetic Positron Source MePS has been set up at the superconducting electron linear accelerator ELBE (Electron LINAC with high Brilliance and low Emittance) [3] at Helmholtz-Zentrum Dresden-Rossendorf in a collaborative effort between Martin-Luther University Halle-Wittenberg and the Helmholtz-Zentrum Dresden-Rossendorf. Figure 1 shows the layout of the system schematically. Some of the details of the installation are described below.

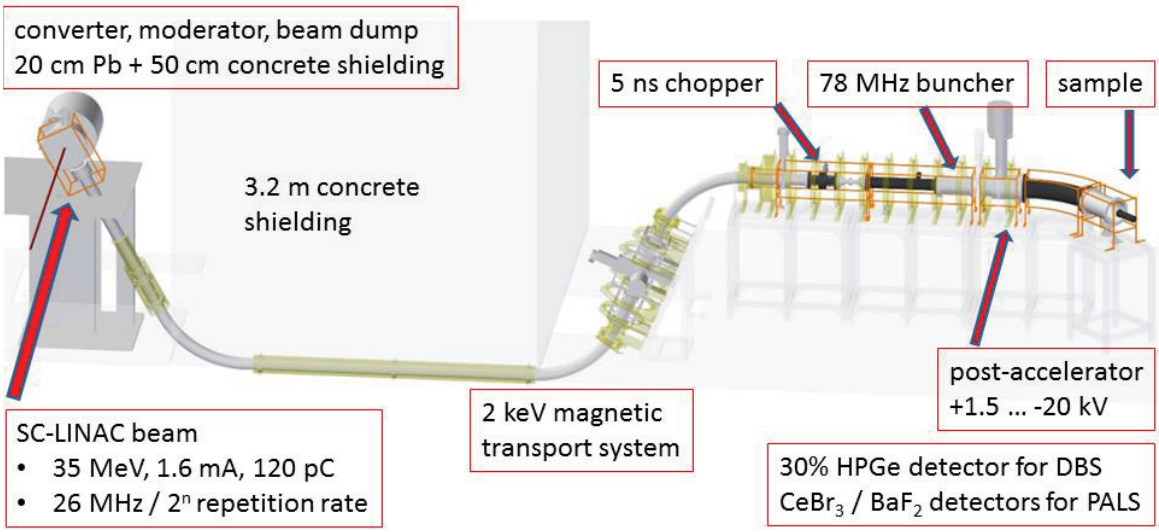

FIGURE 1: Layout of the Monoenergetic Positron Source at ELBE. DBS stands for Doppler-broadening Spectroscopy and PALS stands for Positron Annihilation Lifetime Spectroscopy.

The incident electron beam is delivered by the superconducting (SC) electron linear accelerator ELBE with energies up to 35 MeV. In contrast to conventional normal conductive accelerators superconducting technology makes possible the application of continuous radio-frequency accelerating electromagnetic fields with electric field gradients up to 20 MV/m. The injection of electrons from an injector can be done in principle with any divisor of the base frequency which is 1.3 GHz for ELBE. However, pulse-preforming by the electron beam bunching system prior to injection restricts the maximum applicable pulse repetition rate to 260 MHz. For positron annihilation studies repetition rates of 1.625 MHz, 6.5 MHz, 13 MHz, and 26 MHz have been employed up to now. The repetition rates have been selected in order to match to the annihilation lifetimes in the samples. Minimization of the effect of pulse-overlap (lower repetition rate favored) has been done while maximizing the detection efficiency (higher repetition rate favored) at given electron beam bunch charges. If we request a pulse-overlapping fraction of not more than one part in a 10^5, maximal annihilation lifetimes should be 54 ns, 14 ns, 7 ns, and 3 ns for the canonical repetition rates given above. The electron beam is directed towards a water-cooled tungsten bremsstrahlung converter consisting of 50 foils of 100 µm thickness each with a separation of 100 µm each as shown in figure 2, (a). The converter is enclosed in a stainless steel casing with attached stainless steel cooling pipes as shown in figure 2, (b). The converter has been designed to cope with average beam powers of up to 40 kW out of which only 4 kW have been used by now. Electron bremsstrahlung with a continuous spectrum up to the electron beam energy is then converted in turn by pair production into electrons and positrons inside the converter and also inside the following tungsten moderator.

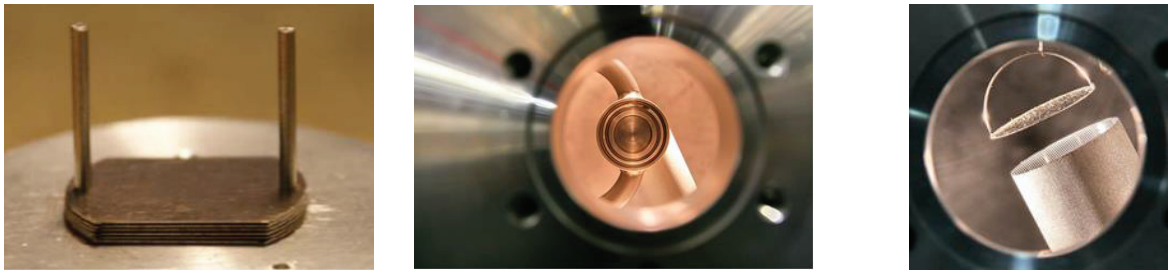

(a) (b) (c)

FIGURE 2: The bremsstrahlung converter and positron moderator. (a) Partially assembled stack of 50 Tungsten foils with 100 µm thickness each. (b) Assembled converter as viewed by the electron beam. (c) Moderator foil suspended above the accelerating grid at the entrance to an electrostatic lens.

Thermalized positrons from the moderator are being accelerated with a bias potential of +2 kV towards a conductive mesh at a few mm distance shown in figure 2, (c). Further positron transport is accomplished by a longitudinal magnetic field of 8 mT with variations of less than 10%. More than 3 m of iron-enriched concrete and 20 cm of lead shield the accessible laboratory from the positron generating converter. A water-cooled aluminium beam catcher of 600 mm length absorbs most of the radiation penetrating the converter and the moderator. Pure aluminium has been selected in order to minimize photo-neutron production owing the neutron separation energy of 13 MeV for ^{27}Al. The design of the beam catcher has been derived from the liquid lead photo-neutron source which is operated at ELBE [4].

After transporting the beam through the radiation shielding the beam is sent through a double beam chopper which imposes a transversal electric field of up to 500 V/cm, see figure 3, (a). The pulsed electric field has a Gaussian shape with a FWHM of 5 ns while the electrodes are separated by 6 mm. Out-of-phase positrons are deflected towards an adjustable aperture after half a gyration length of 126.3 mm. After removal of those non-phase matched positrons the beam is further longitudinally compressed with a double-slit buncher operating at a frequency of 78 MHz. A resonant circuit drives the central isolated drift tube while generating an electric field strength of up to 2.5 kV/cm at the two gaps, see figure 3, (b). The two buncher gaps are separated by 509 mm which matches to 3/2 times the buncher period at 2 keV positron transport energy.

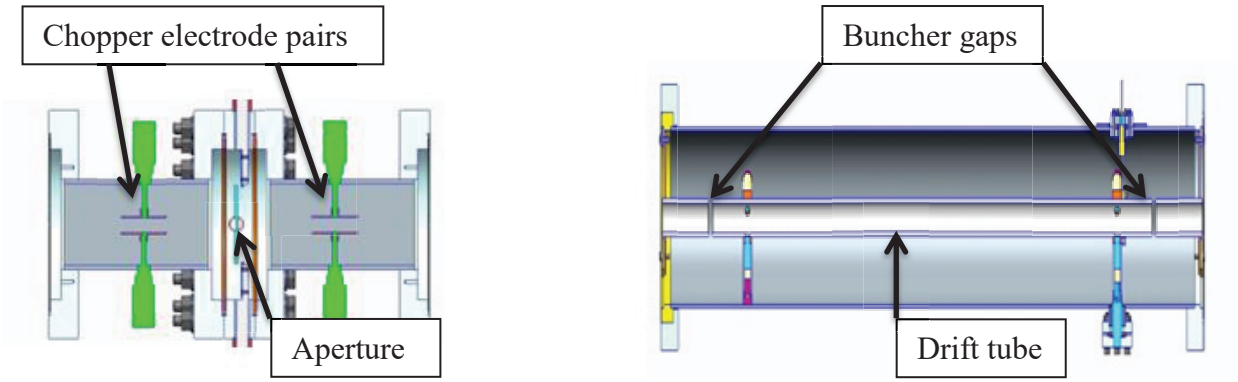

(a) (b)

FIGURE 3: (a) Beam chopper and (b) double-slit buncher. The beam enters from the left and additional beamline sections are omitted.

After longitudinal bunch compression by the chopper a 6-stage electrostatic acceleration structure follows which allows the positron kinetic energy and thus the penetration depth inside the sample to be varied. Prior to the target the magnetic guiding system is bent by 45° thus suppressing positrons reflected from the sample and bounced by the accelerator field to impact again onto the sample.

The sample station is kept at a potential of up to 25 kV. About 3 cm behind the sample a µ-metal shielded BaF_2 scintillation detector is employed for annihilation lifetime measurements. The detector has been recently substituted

by a $CeBr_3$ scintillation detector offering significant improvements with respect to disturbances from long scintillation lifetime components in BaF_2. The timing reference is derived from the precision master oscillator of the superconducting accelerator and is phase-matched to the electron bunches of the beam with a temporal jitter of 14 ps (FWHM). The signal-to-noise ratio is above 10^4 while lifetime resolutions of around 230 ps (FWHM) have been obtained. Figure 4 shows the positron annihilation lifetime of two reference samples with well-known annihilation lifetimes for an incident positron kinetic energy of 10 keV. On the left side, single crystalline Y_2O_3-stabilized ZrO_2 (YSZ) is shown together with a Gaussian distribution with a derived time resolution of 230 ps FWHM. On the right hand side, mono-crystalline silicon is shown. In both cases, the annihilation lifetimes of 181 ps and 218 ps, respectively, which were determined in conventional lifetime studies are well reproduced. Besides the main contribution an additional stable background lifetime of 720 ps of unknown origin is visible which is subtracted in all subsequent analysis. For both samples a signal to noise ratio of $5x10^5$ is obtained.

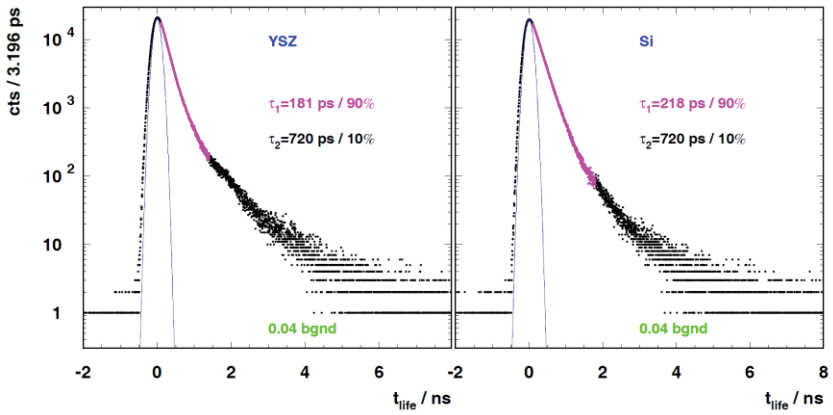

(a) (b)

FIGURE 4: Positron annihilation lifetime distributions for Y2O3-stabilized ZrO2 (a) and wafer-grade silicon (b). A Gaussian distribution with 230 ps FWHM (blue) is included in order to visualize the timing resolution.

An example for longer positron annihilation lifetimes is shown in figure 5, (a). It shows the variation of ortho-positronium lifetimes with the incident positron energies for nano-porous glasses. The µm-thin glass films have been produced by stimulated phase separation in sodium borosilicate glass into silica and an alkali borate phase thus generating sponge-like porous structures with unknown porosity [5]. Nano-porous glasses feature a tunable pore width and adjustable surface properties which makes them ideal candidates for separation membranes, chemo-sensors, drug delivery, optical coatings, and many other applications. Determination of porosity is hampered when employing conventional porosimetry methods. Both, Hg intrusion or LN2 sorption methods fail in the case of thin films due to weak signals from small surface areas and small porous volumes. Furthermore, systems with closed porosity cannot be investigated by means of intrusion techniques. In contrast, PALS serves as an ideal tool in such cases. Experimentally, the lifetime distributions are almost free from distortions and the peak to background ratios are between $5x10^4$ and $8x10^4$ due to a slight pulse-to-pulse overlap with the selected beam repetition rate of 1.625 MHz which corresponds to 615 ns pulse-to-pulse spacing.

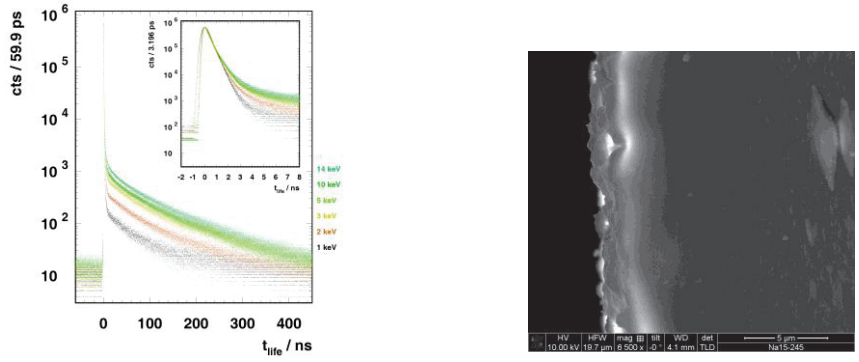

(a) (b)

FIGURE 5: (a) Positron annihilation lifetime distributions for nano-porous glasses (inset shown with increased time dispersion). (b) SEM picture of the nano-porous film with the surface on the right side and the non-porous structure extending from the center to the right side.

Due to imperfect bunching the timing resolution decreases for positron beam energies below 2 keV. The sample had been covered with a thin carbon layer to prevent positronium from escaping the surface. Figure 5, (b) shows a scanning electron microscope picture of a sample cut. The nano-porous film has a thickness of about 4 µm.

MePS has also been employed successfully for porosity studies of ultra low-k dielectric thin films as promising materials for advanced inter-connects scheme of ultra-large scale integrated devices. The aim is the reduction of resistance-capacitance delay and cross-talk noise by the introduction of nano-scale voids inside the insulating SiO_2 [6,7].

THE GAMMA-INDUCED POSITRON SOURCE

A second accelerator-driven positron source is realized in the so-called Gamma-induced Positron Source (GiPS) [8]. A pioneering technology called "accelerator-based γ-ray-induced PAS" or AGAPS at a normal conducting electron LINAC had been developed at Idaho State University and it was used for Doppler-broadening spectroscopy experiments [9]. The setup employs high-energy bremsstrahlung for pair production right inside the sample under study. The GiPS setup additionally allows annihilation lifetime experiments, as well, and it is especially suited for extended bulk samples, or samples which cannot be exposed to external positrons sources like positron beams or radioactive sources or because they are imposing hazardous conditions (high pressure, high temperature, intrinsic radioactivity), or if the sample handling imposes difficulties (fluids, gases, organic samples).

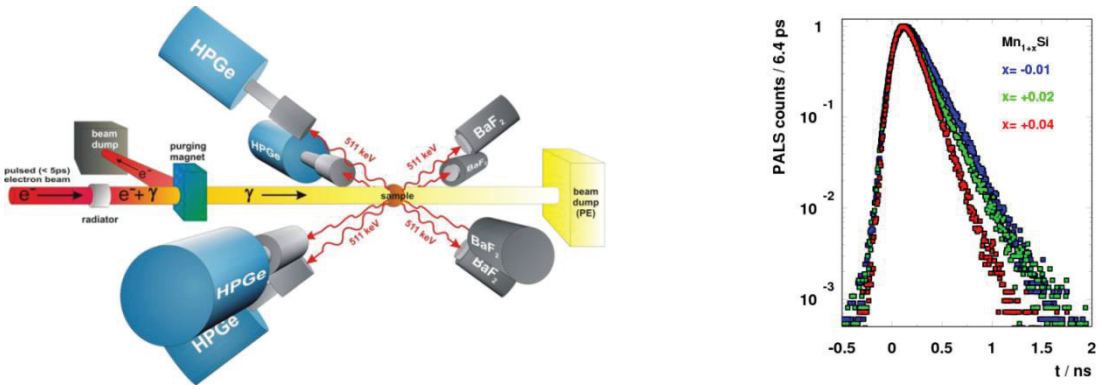

(a) (b)

FIGURE 6: (a) The Gamma-induced Positron Source at ELBE. Four identical pairs of High-Purity Germanium (HPGe) detectors for high energy resolution and BaF2 scintillation detectors for high timing resolutions are arranged around the sample. (b) Example of annihilation lifetime distributions (scaled) for three cases of slightly over- and under-stoichiometric contents of Mn in MnSi alloys.

Derived from a setup for nuclear resonance fluorescence studies [10] special emphasis has been put on background reduction and shielding. Recently, positron annihilation lifetime studies on point defects in the skyrmion-lattice compound MnSi [11] and on the origin of luminescence and scintillation in ZnO [12] have been published. Figure 6, (b) shows three annihilation lifetime distributions for slightly under- and over-stoichiometric Mn contents in MnSi alloys. For $x<0$, a single lifetime component of 185(4) ps agrees very well with the calculated lifetime of 181 ps for a single Mn vacancy in MnSi acting as a positron trap. For $x>0$, the lifetime distributions tend to become narrower while approaching the calculated bulk lifetime of 111 ps. Both features are in line with Coincidence Doppler-Broadening Spectroscopy results as discussed in [11].

As for the MePS source the beam repetition rate can be matched to the positron annihilation lifetime thus optimizing for high average intensity and low detector pile-up distortions.

THE SLOW POSITRON SYSTEM OF ROSSENDORF

While the accelerator-driven positron sources require sharing beam time with users of other beam lines, complementary Doppler-broadening spectroscopy studies are being performed at the ^{22}Na-based mono-energetic positron beam SPONSOR (Slow POsitroN System Of Rossendorf) [13]. The setup is shown in figure 7, (a). Here, Doppler-broadening studies are performed with higher statistics and more energy steps. Additionally, with both Germanium detectors arranged face-to-face and perpendicular to the beam line coincidence Doppler-broadening experiments are performed which allow for a two order of magnitude improvement in signal to noise ratio.

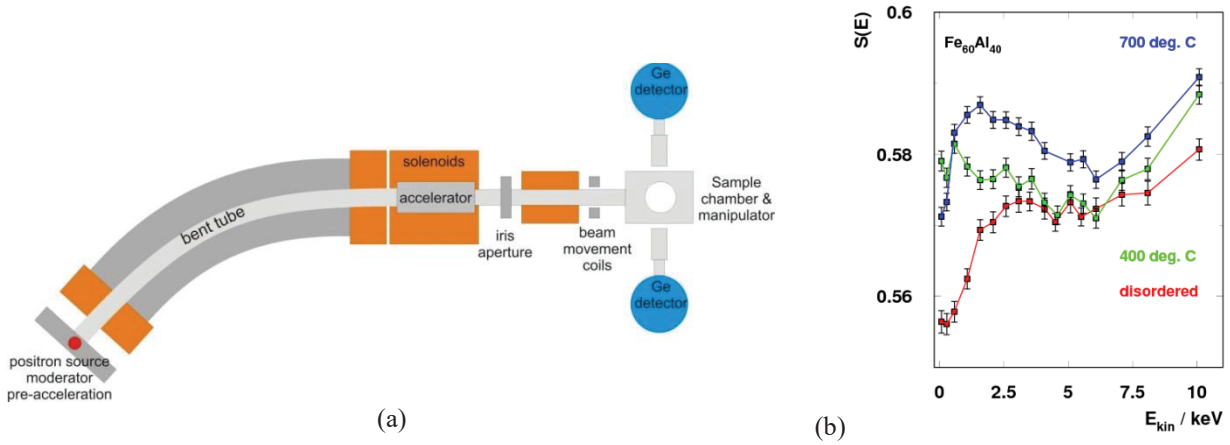

FIGURE 7: (a) The Slow Positron System at Rossendorf (SPONSOR). (b) Energy-dependent line-shape parameter variations for thin $Fe_{60}Al_{40}$ films after in-situ temperature treatments.

One of the main motivations for the additional setup is that it allows studying samples independently from available beam time at the main accelerator prior to measurements there. E.g., positron energy ranges for Positron Annihilation Lifetime experiments at MePS are determined using Doppler-broadening studies DBS at SPONSOR. Being a quite reliable and versatile stand-alone setup, many publications in various defect studies have successfully demonstrated the need for such a complementary setup. Most recently, post-growth treatment studies on defects in ALD-grown thin ZnO films [14] and the role of Zn vacancies in sol-gel prepared ZnO films [15] have been investigated. ^{22}Na-based lifetime experiments for bulk materials can be performed at a conventional lifetime setup.

THE APPARATUS FOR IN-SITU DEFECT ANALYSIS (AIDA)

In the future, MePS will be complemented by an ultra-high vacuum system for in-situ defect studies called Apparatus for In-Situ Defect Analysis (AIDA). Here, the introduction and the annealing of defects during ion-irradiation, temperature treatment and during thin film growth will be studied with a focus on novel energy-related materials. The AIDA system allows investigating of defects near the surface of a material, i.e. in an early stage of defect development, as well as in-situ "live" measurements. Currently, the interaction of such defective materials with hydrogen is investigated.

As a precursor for the MePS installation a pre-stage of AIDA has been implemented at the SPONSOR beam and in-situ experiments on the influence of defects on magnetic phase transitions in $Fe_{60}Al_{40}$ alloys [16] and on Cr_2O_3 which is used in a purely antiferromagnetic magneto-electric random access memory have been performed [17]. As an exemplary result figure 7, (b) shows the energy-dependent shape parameter variations for thin $Fe_{60}Al_{40}$ films after in-situ temperature treatments. The line-shape parameter *S* measures the ratio between those annihilation gamma-rays in a narrow energy region around 511 keV and all annihilation photons. Larger *S* parameters indicate larger molecular free volumes. Increase of S evidences an emerging ordered paramagnetic B2-phase containing vacancy complexes located in the Fe-sublattice as compared to the disordered A2-phase where randomly distributed mono-vacancies are expected. In addition, segregation of Al has been found for higher temperatures. The AIDA system (see figure 8) consists of an ultra-high vacuum system for annealing, metallic thin film deposition, and low-temperature ion irradiation. A four-point resistometry setup and an X-ray photoelectron spectroscopy (XPS) unit are optional characterization methods while maintaining vacuum conditions and temperature. Parts of the system are already installed at the 6 MV ion accelerator at HZDR where it is being used in Hydrogen-depth profiling studies employing the $^{1}H(^{15}N,\alpha\gamma)^{12}C$ reaction [19]. The positron beam transport system is currently under construction.

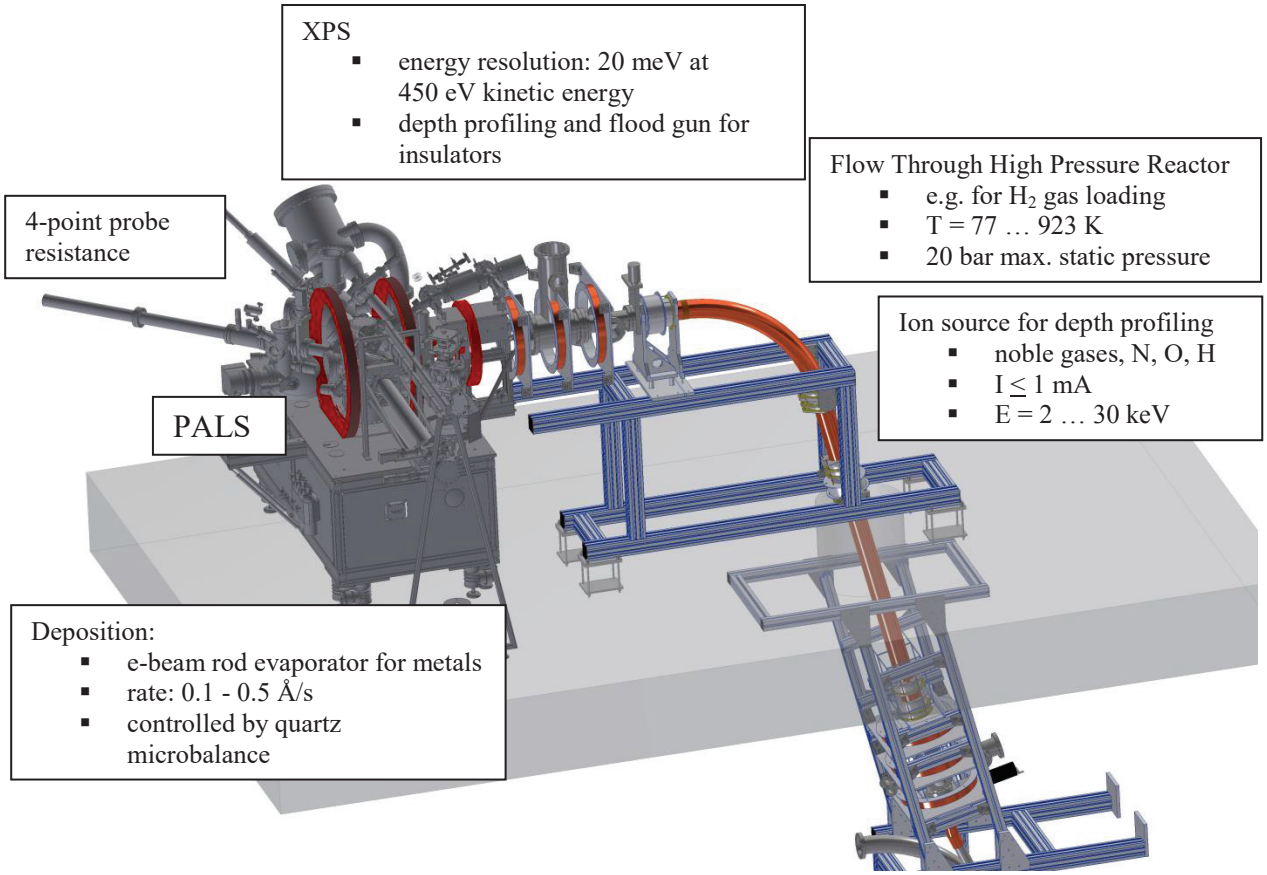

FIGURE 8: The Apparatus for In-situ Defect Analysis (AIDA) which is currently being set up on top of the monoenergetic positron beam MePS at ELBE.

CONCLUSIONS

The monoenergetic positron source MePS and the Gamma-induced Positron Source GiPS represent the first accelerator-based setups for positron annihilation lifetime, Doppler-broadening and age-momentum correlation measurements operated at a superconducting RF accelerator in a continuous wave mode. Adjustable beam repetition rates are selected to match annihilation lifetimes in order to obtain efficient measurements and low pile-up distortions. Conventional positron sources complement the accelerator-based setups for in-depth and precursor studies. Positron annihilation lifetime and Doppler-broadening experiments are complemented by new facilities for defect analysis during in-situ material modifications and thin film growth.

ACKNOWLEDGEMENTS

The pre-stage system of AIDA was funded by the Initiative and Networking Fund of the Helmholtz-Association. (FKZ VH-VI-442 Memriox). Thanks go to the ELBE accelerator crew for providing stable beams, to M. Görler, A. Hartmann, A. Müller, D. Stach, and G. Staats for their contributions to the beam transport, buncher and chopper system, and especially to M. Jungmann for his invaluable contributions to the MePS setup.

REFERENCES

1. K. Wada and T. Hyodo, Journal of Physics: Conf. Series **443**, 012003 (2013).
2. R. Krause-Rehberg, G. Brauer, M. Jungmann, A. Krille, A. Rogov, K. Noack, Appl. Surf. Sci. **255,** 22 (2008).
3. F. Gabriel, P. Gippner, E. Grosse, D. Janssen, P. Michel, H. Prade, A. Schamlott, W. Seidel, A. Wolf, R. Wünsch, Nuclear Instruments and Methods in Physics Research B **161**, 1143 (2000).
4. E. Altstadt, C. Beckert, H. Freiesleben, V. Galindo, E. Grosse, A. R. Junghans, J. Klug, B. Naumann, S. Schneider, R. Schlenk, A. Wagner. F.-P. Weiss, Annals of Nuclear Energy **34**, 36 (2007).
5. H. Uhlig, G. Adouane, C. Bluhm, S. Zieger, R. Krause-Rehberg, D. Enke, Journal of Porous Materials **23**, 139 (2016).
6. M. Jungmann, J. Haeberle, R. Krause-Rehberg, W. Anwand, M. Butterling, A. Wagner, J. M. Johnson, T. E. Cowan, Journal of Physics: Conference Series **443**, 012088 (2013)
7. A. Uedono, S. Armini, Yu. Zhang, T. Kakizaki, R. Krause-Rehberg, W. Anwand, A. Wagner, Applied Surface Science **368**, 272 (2016)
8. M. Butterling, W. Anwand, T. E. Cowan, A. Hartmann, M. Jungmann, R. Krause-Rehberg, A. Krille, A. Wagner, Nuclear Instruments and Methods in Physics Research B **269**, 2623 (2011).
9. F. A. Selim, D. P. Wells, J. F. Harmon, J. Williams, Journal of Applied Physics **97**, 113539 (2005)
10. R. Schwengner, R. Beyer, F. Dönau, E. Grosse, A. Hartmann, A. R. Junghans, S. Mallion, G. Rusev, K.-D. Schilling, W. Schulze, A. Wagner, Nuclear Instruments and Methods in Physics Research A **555**, 211 (2005).
11. M. Reiner, A. Bauer, M. Leitner, T. Gigl, W. Anwand, M. Butterling, A. Wagner, P. Kudejova, C. Pfleiderer, C. Hugenschmidt, Scientific Reports **6**, 29109 (2016).
12. J. Ji, A. M. Colosimo, W. Anwand, L. A. Boatner, A. Wagner, P. S. Stepanov, T. T. Trinh, M- O. Liedke, R. Krause-Rehberg, T. E. Cowan, F. A. Selim, Scientific Reports **6**, 31238 (2016).
13. W. Anwand, G. Brauer, M. Butterling, H. R. Kissener, A. Wagner, Defect and Diffusion Forum **331**, 25 (2012).
14. M. Haseman, P. Saadatkia, D. J. Winarski, F. A. Selim, K. D. Leedy, S. Tetlak, D. C. Look, W. Anwand, A. Wagner, Journal of Electronic Materials **45**, 6337 (2016).
15. D. J. Winarski, W. Anwand, A. Wagner, P. Saadatkia, F. A. Selim, M. Allen, B. Wenner, K. Leedy, J. Allen, S. Tetlak, D. C. Look, AIP Advances **6**, 095004 (2016).
16. M. O. Liedke, W. Anwand, R. Bali, S. Cornelius, M. Butterling, T. T. Trinh, A. Wagner, Journal of Applied Physics **117** 163908 (2015).
17. T. Kosub, M. Kopte, R. Hühne, P. Appel, B. Shields, P. Maletinsky, R. Hübner, M. O. Liedke, J. Fassbender, O. G. Schmidt, D. Makarov, Nature Communications **8**, 13985 (2017).
18. J. Čížek, F. Lukáč, I. Procházka, R. Kužel, Y. Jirásková, D. Janičkovič, W. Anwand, G. Brauer, Physica B **407**, 2659 (2012).
19. T. P. Reinhardt, S. Akhmadaliev, D. Bemmerer, K. Stöckel, L. Wagner, Nuclear Instruments and Methods in Physics Research B **381**, 58(2016).

Slow positron applications at Slow Positron Facility of Institute of Materials Structure Science, KEK

Toshio Hyodo [1, a)], Izumi Mochizuki [1, b)], Ken Wada [1, 2], NobukazuToge [3], and Tetsuo Shidara [3]

[1]*Institute of Material Structure Science, High Energy Accelerator Research Organization* (*KEK*), *Japan*
[2]*Present Address*: *Takasaki Advanced Radiation Research Institute, National Institutes for Quantum and Radiological Science and Technology (QST), Japan*
[3]*Accelerator Laboratory, High Energy Accelerator Research Organization* (*KEK*), *Japan*

[a)]Corresponding author: hyodot@post.kek.jp
[b)]mochizu@post.kek.jp

Abstract. Slow Positron Facility at High Energy Accelerator Research Organization (KEK) is a user dedicated facility with an energy-tunable (0.1 - 35 keV) slow positron beam created by a dedicated ~ 50 MeV linac. It operates in a short pulse (width 1-12 ns, variable, 5×10^6 e^+/s) and a long pulse (width 1.2 μs, 5×10^7 e^+/s) modes of 50 Hz. High energy positrons from pair creation are moderated by reemission after thermalization in W foils. The reemitted positrons are then electrostatically accelerated to a desired energy up to 35 keV and magnetically transported. A pulse-stretching section (pulse stretcher) is installed in the middle of the beamline. It stretches the slow positron pulse for the experiments where too many positrons annihilating in the sample at the same time has to be avoided. Four experiment stations for TRHEPD (total-reflection high-energy positron diffraction), LEPD (low-energy positron diffraction), Ps^- (positronium negative ion), and Ps-TOF (positronium time-of-flight) experiments are connected to the beamline branches, SPF-A3, SPF-A4, SPF-B1 and SPF-B2, respectively. Recent results of these stations are briefly described.

INTRODUCTION

Positrons are widely used as a probe for solid state and atomic phenomena. Positron annihilation in condensed matter is most popular. Use of the positrons from radioisotopes (β^+rays) has a long history. Since the cross section for the positron-electron pair annihilation is by far smaller than those for the positron scatterings in atomic and solid state processes, it is safe to say that the positrons annihilate with an electron only after reaching thermal equilibrium with the material (thermalization). Positron annihilation method relies on this fact in obtaining the information of material electrons.

Since the advent of a technique to produce energy-tunable slow positrons efficiently [1, 2] the samples to be investigated have expanded to include thin films and interfaces [3]. Depth profiling became also possible. Moreover, almost all the experimental techniques developed for the electron are now possible with the positron. It should be pointed out that some of the positron counterparts of the electron techniques show quite different features than the latter. The only drawback of the use of the positron is the difficulty in obtaining a high intensity beam. Use of the pair creation from high energy photons is a solution for this. Such photons are available as the bremsstrahlung form accelerated electrons bombarded on a high Z materials or γ rays from an atomic reactor core or from Cd after absorbing thermal neutrons [3].

In this article production and applications of energy-tunable (0.1 - 35 keV) slow positrons in the Slow Positron Facility (SPF), High Energy Accelerator Research Organization (KEK) is described [4].

PRODUCTION OF AN ENERGY TUNABLE SLOW POSITRON BEAM

Figure 1 shows the layout of the SPF. The slow positron beam is created by a dedicated ~ 50 MeV, 600 W linac [5, 6]. It operates in a short pulse (width 1-12 ns, variable, 5×10^6 e^+/s) and a long pulse (width 1.2 μs, 5×10^7 e^+/s) modes with a repetition frequency of 50 Hz. The accelerated electrons bombard a 4 mm thick Ta plate (converter). The resulting Bremsstrahlung may be converted into electron-positron pairs before going out of the Ta plate. The high-energy positrons thus created are injected into W-foils (moderator) placed nearby. The converter-moderator assembly is shown in Fig. 1 [6]. W foils of 25 μm-thick and 4.8 mm × 21 mm and 4.8 mm × 29 mm are arranged in two sets of lattices. The foils were annealed at temperatures higher than 2600℃ by using an electron beam welder after being set in lattices.

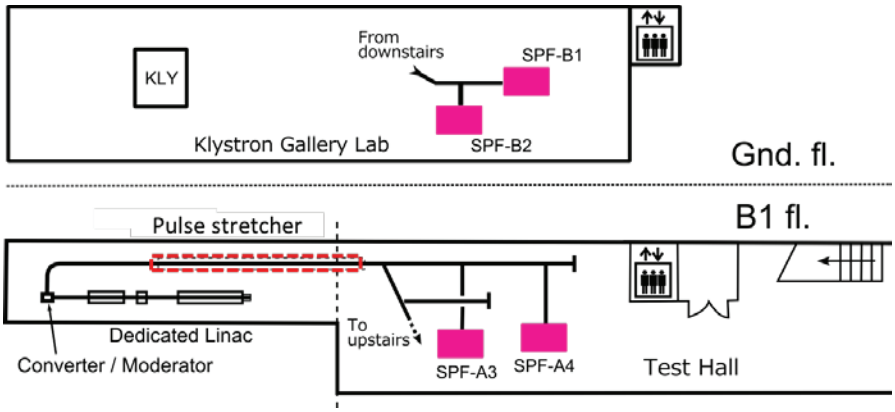

FIGURE 1. The layout of the linac, the slow positron production unit (converter/moderator), the beamline including the pulse-stretching section (pulse stretcher), and the four experiment stations at the Slow Positron Facility (SPF).

Tungsten (W) is one of the metals whose positron work function is negative. Negative work function of a particle means that the particle inside material is spontaneously emitted from the surface even though its kinetic energy inside is zero. This phenomenon, characteristic to positrons, was noticed and interpreted by Mills et al [7, 8]. A fraction of the injected positrons diffuse back to the surface after thermalization and re-emitted with an energy equal to the absolute value of the negative work function. The energy spread is essentially equal to the thermal energy. The positron work function of W is about -3 eV.

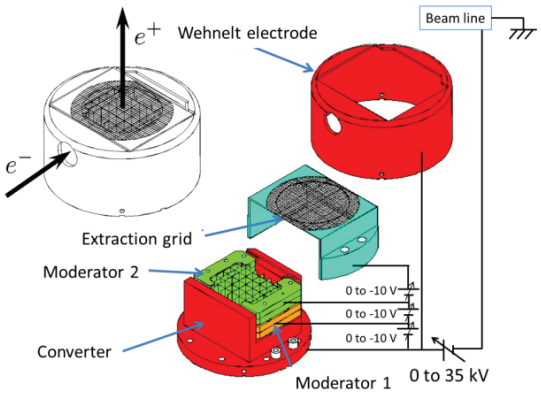

FIGURE 2.
The converter / moderator assembly for the slow positron production at SPF, KEK [6].

The slow positrons emitted from the W foil surface are extracted by the electrostatic voltage of the extraction grid. The Ta converter, W moderator lattices, and the extraction grid are electrically isolated from each other, and connected to a cascade voltage supply. The positrons emitted with an energy of 3 eV are then electrostatically accelerated to a desired energy, which is variable from 0.1 keV to 35 keV after requirement of each individual experiment. The accelerated positrons are then magnetically transported to an experiment station.

A PULSE STRETCHER

An intense pulse beam is not always convenient. Our pulse in the long pulse mode of width 1.2μs contains temporal density of 8×10^{11}/s positrons in a pulse. This is too much for certain experiments such as γ ray energy spectroscopies. A pulse stretcher as shown schematically in Fig. 3 is thus installed in the middle of the beamline. It is a kind of Penning-Malmberg trap. It consists of a short inlet and outlet electrodes and a 6-m long trapping electrode in between. They are all cylindrical and set inside the beamline tube. Currently the energy of the stretched beam is fixed to 5.2 keV, determined by the electrostatic potential of 5.2 kV of the outlet electrode.

When the pulse stretcher operates, the voltage of the converter/moderator unit is kept at 4.8 kV that 4.8 keV positron pulse is transported. Just before the front edge of the pulse reaches the inlet electrode, its voltage, normally kept at 5.75 kV, is temporarily lowered to 4.5 kV; the positrons are introduced into the trapping electrode set at 4.74 kV with a resulting mean kinetic energy of 0.06 keV, or with a speed of 4.6×10^6 m/s. Positrons then travel in the trapping electrode along the solenoid magnetic field down to the outlet electrode and are reflected back. The inlet

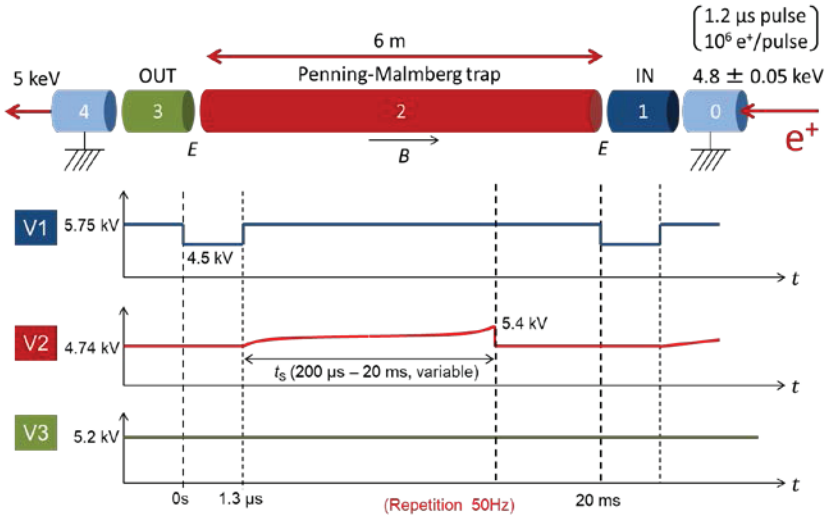

FIGURE 3. The pulse stretcher and the timing chart of the voltage of the electrodes.

electrode voltage is raised back to 5.75 kV after the tail of the pulse is accepted and before the front of the pulse comes back so that all the positrons in the pulse are trapped. The trapping electrode voltage is then raised gradually, letting the positrons spill over the outlet electrode. In this way a stretched pulse of an energy fixed to 5.2 keV is obtained. By varying the sweeping speed of the trapping electrode voltage, the width of the output pulse is adjusted from 200 μs to 20 ms. The minimum stretched width of 200-μs is limited by the time response of the amplifier used for controlling the trapping-electrode voltage, and the maximum of 20 ms is a trivial limit from the linac repetition frequency of 50Hz.

Currently the pulse stretching system is operated for the LEPD measurement which uses a position-sensitive delay-line detector (DLD). It will also be useful for future spectroscopy of the 511 keV annihilation γ rays as well as for the future creation of a short positron pulse for the positron lifetime study.

BRIGHTNESS ENHANCEMENT

For diffraction experiments, the brightness of the beam defined as

$$B = I/r^2\theta^2 E\ ,$$

where I, r, θ, and E are the intensity, radius, angular divergence, and energy of the beam [8], is crucially important because it indicates how parallel and how thin the beam could be made. Liouville's theorem sets that the normalized emittance, $\varepsilon_n = r\theta\sqrt{E}$ is constant in a non-dissipative force field. This means that it is impossible to decrease E without increasing θ and/or r. However, the remoderation process using a metal whose positron work function is

negative involves dissipative forces and overcomes the limit by Liouville's theorem. In the first place, reducing the energy of the positrons created in the converter, of order MeV, to that of the positrons reemitted from the moderator, of order eV (Fig. 1), is certainly a considerable reduction of emittance. How much enhancement of the brightness depends also on the loss of intensity through annihilation inside the moderator and that by passing through.

Positron diffraction experiments need further brightness enhancement, called re-moderation. Figure 4 is a schematic diagram of the transmission type re-moderator with parameters in the brightness enhancement for the total-reflection high-energy positron diffraction (TRHEPD) station [9]. The positrons from the converter/moderator are transported with an energy of 15 keV, guided by a magnetic field, as a beam of a diameter of ~10 mm. It is released into a magnetic-field free region. A magnetic lens focuses it onto a spot of diameter of ~3 mm on a 100 nm-thick W foil re-moderator kept at a voltage of 10 kV. A fraction of the positrons thermalized in the foil are emitted from the surfaces of both sides with a kinetic energy of 3 eV. Those reemitted from the forward side are then accelerated to 10 keV as required for the TRHEPD experiments. This process reduces the normalized emittance by two orders of magnitude, while the intensity is reduced by one order of magnitude owing to the annihilation inside the foil. The brightness is thus enhanced by three orders of magnitude.

For low-energy positron diffraction (LEPD) experiments, the re-moderator is a 150 nm thick Ni foil, whose

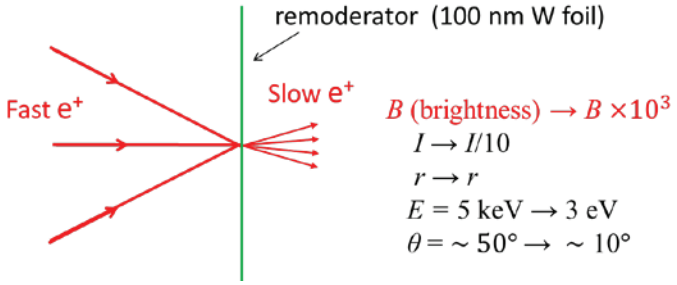

FIGURE 4. Schematic diagram of brightness enhancement by transmission-type re-moderation.

positron work function is about -1 eV. The positrons are transported with an energy of 5.2 keV. In contrast to TRHEPD, LEPD beam is incident on a sample with a variable energy from ~25 eV to a few hundred eV. The varying kinetic energy is achieved by adjusting the voltage of the foil. As in the re-moderator for the TRHEPD, a beam of an energy around 5keV (variable now) is focused onto the Ni foil. While the re-emission efficiency of the W foil is rather stable, the Ni foil requires occasional atomic-hydrogen flushing to maintain good reemission efficiency.

EXPERIMENT STATIONS

Four experiment stations, TRHEPD, LEPD, Ps^-, and Ps-TOF, connected to the beamline branches in the measurement area are currently available. Only one of them is active at a time because the single primary slow positron source is shared and no quick switching system is implemented. The beam time allocated to an experiment is usually 4-7 days.

TRHEPD

TRHEPD station is connected to the branch SPF-A3. TRHEPD is the positron counterpart of reflection high-energy positron diffraction (RHEED). It is a method for determining the surface atomic structure (detailed arrangement of the atoms on the topmost surface and subsurface) of a crystal. It was proposed by Ichimiya [10] and the first experimental data was obtained by Kawasuso and Okada [11]. It has an exceedingly high surface selectivity [4, 12, 13].

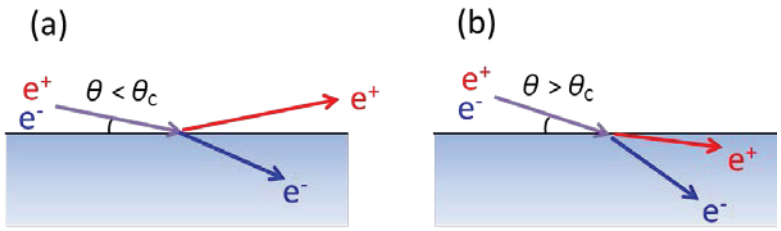

FIGURE 5. Paths of the positron and electron directed on a material surface with different values of glancing angle [4]. Since the electrostatic potential in every crystal is positive, a positron directed to a surface with a glancing angle, θ, smaller than a critical angle, θ_c, is totally reflected (a). When $\theta > \theta_c$, the positron is refracted into the crystal in the direction towards the surface (b). In contrast, an electron is always refracted into the crystal in the direction away from the surface.

The sensitivity of TRHEPD stems from the inelastic scattering, as is the case for electron diffractions. That is, once a particle undergoes inelastic scattering, it loses coherence to contribute to the diffraction pattern. The deeper the particle penetrates into the crystal, the higher is the probability of losing coherence. In addition, TRHEPD has another feature which gives its uniqueness in its surface selectivity, i.e., the electrostatic potential inside every solid is positive and thus the surface is repulsive to a positively charged particle. As shown in Fig. 5, a positron directed at a crystal surface with a glancing angle smaller than a certain critical angle, θ_c, whose value depends on the material and the energy of the incident positron, is totally reflected. In this condition, the diffraction pattern depends only on the kinds and the positions of the atoms on the topmost surface. It is also possible to get information on the immediate subsurface by slightly increasing the glancing angle across θ_c. Then the positrons go into the crystal, refracted in the direction toward the surface, in contrast to the electron which is refracted away from the surface and penetrates deeper. By increasing the glancing angle further, information on the deeper region is also available. TRHEPD is the only diffraction technique in which the critical angle for the total reflection, θ_c, lies in the middle of the measurement angular range. Furthermore, since TRHEPD is based on the self-interference of an elastically scattered positron, just as the other diffraction techniques, it is very sensitive not only to the positions of the atoms but also to the kinds of atoms, even those hidden under the surface.

Recently, TRHEPD has determined the structure of the rutile-TiO_2(110) (1×2) surface [14], which had been under debate over the past 35 years. TiO_2 is a well-known catalyst used in a variety of applications including photo-catalysis, metal-nanoparticle catalyst supports, gas sensors and corrosion-protective coating materials [15, 16]. Its surface is a good example whose structure is too complicated for the other structural analysis method to determine in detail. The rocking curves of the 00-spot obtained from the TRHEPD patterns were compared to the curves for various models calculated based on a dynamical diffraction theory [17]. None of the proposed models with the coordinates as given in the literature gave satisfactory agreement. In practice, however, when the model is essentially correct, small further adjustment of the atomic positions gives a good agreement. In the present case, the model that TRHEPD singled out is the asymmetric added Ti_2O_3 model (Fig. 6) suggested by Wang et al. [18], who reached this model after a global search made by changing both the chemical composition and the atomic positions with the USPEX code

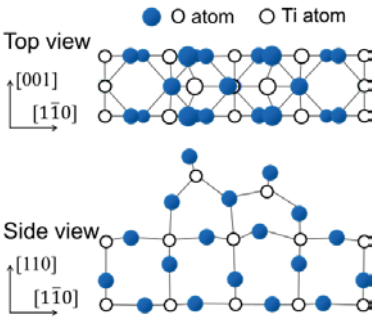

FIGURE 6.
Atomic arrangement of rutile-TiO_2(110) (1×2) surface determined by TRHEPD [14].

Single layer of group 14 elements such as graphene (that of C), silicene (Si) and germanene (Ge) are attracting increasing attention since the isolation of graphene. Graphene is flat as it is a single layer of a layered material, graphite. Since the only stable structure of Si and Ge is the diamond structure, it is expected that silicene and germanene have a buckling. These materials are usually synthesized on a substrate surface. The substrate-single layer material distance and the amount of the buckling are the two major features of these materials; apparently TRHEPD is the most suited method for the experimental analysis of these features. Theoretical calculations on various electronic properties of these materials are of course based on the determination of the atomic positions, although the positions are not necessarily reported explicitly.

Graphene has high carrier mobility, high thermal conductivity and robust mechanical properties [19]. Theoretical calculations demonstrated that the nature of the spacing between graphene and a metal substrate can be classified into two groups, depending on the interaction between them: weak interaction with simple and noble metal substrates; and strong interaction with transition metal substrates [20-22]. TRHEPD has been applied to determine the spacing between graphene and the Cu(111) and Co(0001) substrates [23]. Rocking curve analysis based on the dynamical diffraction theory shows that the spacing between graphene and a Cu(111) substrate is 3.34 Å and that between graphene and a Co(0001) substrate is 2.06 Å (Fig. 7). The former is close to the interlayer spacing in graphite, consistent with a weak interaction with the noble metal substrate, whereas the latter small value is consistent with strong interaction with the transition metal substrate. The analysis let the amount of the buckling be a free parameter and resulted in showing that the buckling is 0 for both cases as expected.

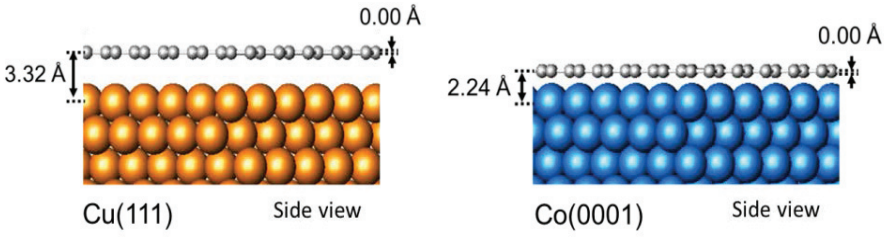

FIGURE 7. The distance between graphene and the substrate surface atoms and the amount of buckling of the graphene of different substrate (Cu(111) and Co (0001)) [23].

First measurement of this kind was performed on silicene on a Ag(111) substrate [24]. It verified that it has certainly a buckling structure of size of 0. 83 Å (distance between the top atomic sublayer and the bottom one within the single layer). The distance between the bottom Si sublayer and the substrate Ag surface is 2.14 Å, and the two bonding angles of the buckled hexagons are also measured to be 112° and 118°. These agree with the theoretical predictions [25].

More recently the structure of germanene on Al(111) was investigated by TRHEPD and revealed that a structure proposed was not consistent with the data, followed by a proposal of a new model [26].

LEPD

LEPD is the positron counterpart of low-energy electron diffraction (LEED). It is also a method for the determination of the surface atomic structure of a crystal. The first LEPD experiment was reported by K. Canter's group in 1980 [27] using a radioisotope-based slow-positron beam. They demonstrated that the LEPD showed better agreement between theoretical and experimental diffraction intensity profiles compared to LEED [28]. Less multiple scattering is expected for positrons than electrons. The atomic scattering factor is simple because of the repulsive force from the core and no exchange interaction with material electrons [29, 30]. These give advantages in atomic structure analysis of high-*Z* materials in particular.

Recently, we have developed a LEPD experiment station connected to the beamline branch SPF-A4, and first diffraction patterns have been recorded [31]. In usual LEED system with a thin filament electron source, back scattered diffraction pattern on a phosphor screen is recorded with a CCD camera. This is difficult in a LEPD system where the positrons are provided through a vacuum beamline duct. Thus we detect the diffracted positrons with a position-sensitive DLD mentioned in a previous section. The brightness of the stretched positron pulse is enhanced with a Ni foil.

It is expected that LEPD works well in the structural analysis of the surfaces containing high-Z atoms such as those of spintronics-related materials whose atomic arrangements are difficult to be analyzed by LEED. Model-free structural analysis employing surface holographic reconstruction [32] and the reconstruction by the surface Patterson function [33] will be attempted.

Ps^- (positronium negative ion)

A Ps^- (positronium negative ion) station was connected to a general-purpose branch, SPF-B1, until very recently. Ps^- is a three-lepton (one positron and two electrons, $e^-e^+e^-$) bound system [34, 35]. It is energetically possible that a fraction of positrons thermalized in a W sample diffuse back to the surface, form Ps^- ions there, and are emitted spontaneously with a small kinetic energy [36, 37] along with the emission of slow positrons and Ps (positronium) atoms. It was found that the emission efficiency is greatly enhanced by coating the surface with sub-monolayer of alkali metals. The proportion of emitted Ps^- ions to the total incident positron flux is reported to be as high as 1.5% [38]. This is much larger than the fraction from a clean W surface and that from a beam-foil process through a carbon film [35].

The ions were used to make an energy-tunable, pulsed positronium beam of practical intensity [39]. The ions are accelerated to a desired energy by an electrostatic field, and then one of the constituent electrons is removed by a laser irradiation (photo-detachment) [40]. A Nd:YAG laser of a 25 Hz pulse with a width 10 ns was synchronized with the ions produced from a positron beam of the 50 Hz pulse with a width of 12 ns,.

The production of plenty of Ps^- ions makes its atomic spectroscopy easy. The ion, made up of leptons with the same mass, provides an excellent testing ground for the three-body problem in quantum mechanics. There have been a lot of theoretical studies since the first calculation of the stability of the ion. Among them are the prediction of the Feshbach resonance and the shape resonance in the photo-detachment process.

The binding energy of Ps^- is only 0.33 eV and no excited state exists [41, 42]. However, quasi-bound states (resonances) are predicted in the vicinities of the formation thresholds of the excited states of Ps (of principal quantum number $n \geq 2$) [43]. This is the shape resonance where the cross section of the photo-detachment is enhanced [43-45]. Laser spectroscopy study of Ps^- verified the shape resonance of $^1P^o$ symmetry near the Ps (n=2) formation threshold 46.

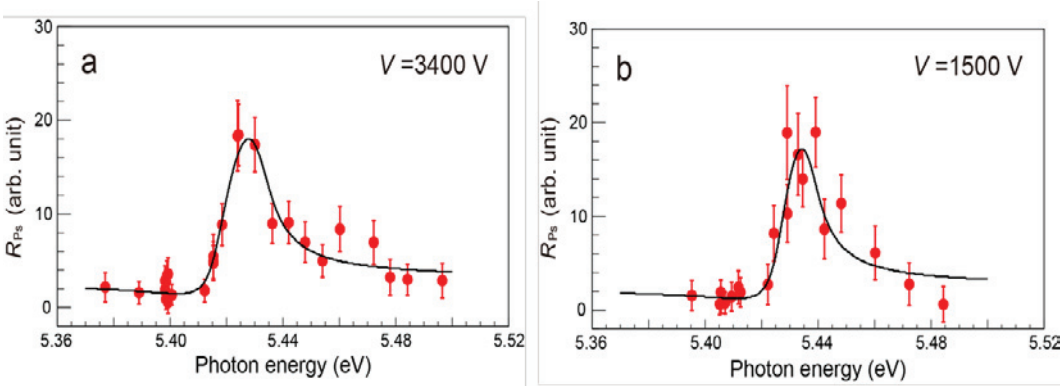

FIGURE 8. The data of the shape resonance (closed circles) for the indicated acceleration voltages [47].

In this experiment, as well as others [39, 48], the positron beam of a kinetic energy of 4.2 keV was deflected by an angle of 45° with a curved magnetic field, and impacted onto a W target coated with a sub-monolayer of Na. The emitted Ps^- ions are accelerated and interact with a synchronized beam of a tunable dye laser. The *ortho*-Ps atoms resulting from the photo-detachment were detected by an MCP placed 0.88 m away from the W target.

Figure 8 shows the count rate of the Ps measured as a function of the laser photon energy for the acceleration voltages of V = 3400 V and 1500 V. Increase in the photo-detachment cross section due to the resonance are clearly seen. The solid lines show the theoretical predictions including the effects of the Doppler-broadening and the longitudinal Doppler-effect. The resonance energy in the rest frame of the ions was deduced to be 5.437(1) eV.

The application of energy-tunable Ps beam has been taken over by a trap-based slow positron apparatus using a radioisotope (^{22}Na) at The Tokyo University of Science. A new research, laser cooling of Ps atoms, has started in the station on the branch, SPF-B1.

Ps-TOF

Positronium time-of-flight (Ps-TOF) station is connected to the beamline branch SPF-B2. Ps-TOF is a method to measure the energy of *ortho*-Ps emitted from the sample surface [49]. In the measurements positrons of a typical energy of 4.5 keV are transported to the Ps-TOF chamber and injected into the sample. If the sample is an insulator, the Ps may be formed in the bulk or on the surface. If the sample is a metal, the Ps is exclusively formed on the surface because the screening of the electron-positron Coulomb attraction by free electrons prevents the Ps formation in the bulk. The energy distribution measured through the time of flight gives information on the positron interactions inside an insulator and on the surface of an insulator and a metal. The station is operated with the beam in the short pulse mode whose width is short enough for the measurement of TOF of the *ortho*-Ps whose lifetime is 142 ns. Ps-TOF spectrum also gives information on the amount of Ps emitted.

One of the γ-rays emerging when ortho-Ps self-annihilate in flight is detected by a scintillation counter behind a lead slit set at a fixed distance from the sample surface. A small fraction of the γ-rays from the positrons annihilation in the sample are also detected even through the lead shield of the detector because large majority of the positrons annihilate in the sample without reaching the surface. This signal indicates the time when the positron pulse is injected in the sample (time zero) because the lifetime of the positrons annihilating in the bulk is around 0.2 ns..

As an example, a recent measurement of Ps-TOF from alkali-metal-coated W surfaces made in an attempt to explore the mechanism of the large enhancement of the Ps^- formation is described here. Coating of a metal surface with an alkali metal is known to reduce the electron work function and increase the positron work function. This may be relevant to the enhancement because Ps^- consists of one positron and two electrons. If this is the main cause of the enhancement of the Ps^- formation, it is conceivable that the coating does not have an effect on the formation fraction of Ps which consists of one electron and one positron.

The measurements revealed that the Ps emission was also remarkably enhanced contrary to the expectation (Fig. 9) [50, 51]. Considering that Ps emission fraction from a clean W surface is already about 25%, that from the coated surface far exceeds those for slow positron emission and the positron trapping on the surface. This is supported by an independent measurement [52].

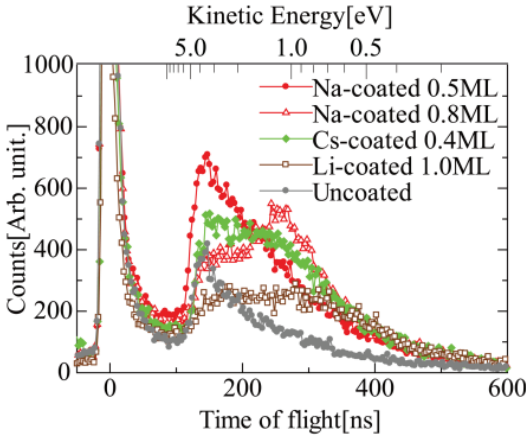

FIGURE 9.
Ps-TOF spectra of W surfaces coated with submonolayer of alkali metals indicated [51].

The mechanism of this enhancement is not clear yet. It is conceivable that the free electron density in the alkali-metal coating layer is not dense enough that it allows the Ps formation. Moreover, this will lead to the enhancement of the Ps^- formation, while it does not contradict with the mechanism related with the change in the work functions.

It was also revealed that the low energy part of the spectra have a component with a specific energy loss that varied with the alkali metals [51], which is also a phenomenon to be explained.

SUMMARY

Overview of the Slow Positron Facility (SPF), Institute of Materials Structure Science, KEK, and some details of the slow positron production unit and the pulse stretcher are presented. The principle of the brightness enhancement is described. Some of the recent results of the researches conducted at the four stations are presented.

ACKNOWLEDGMENTS

Support from the Staff of the Injector group of the Accelerator Laboratory, KEK, the Staff of the Photon Factory, Institute of Materials Structure Science, KEK, and the collaborators of the researches presented here.

The resarches were performed under the PF Proposal No.2016S2-006, 2014S2-004, 2013S2-005 and 2013U002, and the auspices ofa JAEA-KEK Joint Development Research and a QST-KEK Joint Development Research at KEK. It was partly supported by JSPS grants KAKENHI (S)24221006 and (S)24221007 and those for Young Scientists (B) 25800182 and 26800170, Cabinet office Cross-ministerial Strategic Innovation Promotion Program (SIP, unit D66), and by Toray Science and Technology Grant from Toray Science Foundation. One of the authors (T. H.) is grateful to the Foundation for High Energy Accelerator Science for the support for attending JPos17.

REFERENCES

1. A. P. Mills, Jr., in *Positron Solid State Physics*, edited by W. Brandt and A. Dupasquier (North-Holland, Amsterdam, 1983), pp. 432-509.
2. P. J. Schultz and K. G. Lynn, Rev. Mod. Phys., **60**, 701-779 (1988).
3. C. Hugenschmidt, Surf. Sci. Rep **7**, 547-594 (2016).
4. T. Hyodo, *et al*., J. Phys.: Conf. Ser. **791**, 012003-1-8 (2017).
5. T. Hyodo, *et al.*, J. Phys.: Conf. Ser. **262**, 012026-1-5 (2011).
6. K. Wada, *et al*., Eur. Phys. J. D, **66**: 37-1-4 (2012).
7. A.P. Mills, Jr., *et al*., Phys. Rev. Lett. **41**, 1076-1079 (1978).
8. A.P. Mills, Jr., Appl. Phys. **23**, 189-191 (1980).
9. M. Maekawa, *et al*., Eur. Phys. J. D **68**:165, 1-6 (2014).
10. A. Ichimiya, Solid State Phenom. **28-29**, 143-148 (1992).
11. A. Kawasuso and S. Okada, Phys. Rev. Lett., **81**, 2695-2698 (1998).
12. Y. Fukaya, *et al.*, J. Phys.: Conf. Ser. **443**, 012068, 1-6 (2013).
13. Y. Fukaya, *et al.*, Appl. Phys. Express **7**, 056601 (2014).
14. I. Mochizuki *et al*., Phys. Chem. Chem. Phys. **18**, 7085-7092 (2016).
15. A. Fujishima, *et al*., Surf. Sci. Rep. **63**, 515-582 (2008).
16. M. A. Henderson, Surf. Sci. Rep. **66**, 185–297 (2011).
17. A. Ichimiya, Jap. J. Appl. Phys. **22**, 176-180, Jap. J. Appl. Phys. 24, 1356 (1985).
18. Q. Wang *et al*., Phys. Rev. Lett. **113**, 266101-1-5 (2014).
19. A.K. Geim, Science **324** 1530-1534, (2009).
20. G. Giovannetti, *et al*., Phys. Rev. Lett. **101**, 026803-1-4 (2008).
21. M. Batzill, Surf. Sci. Rep. **67**, 83-115 (2012).
22. P.L. Silvestrelli and A. Ambrosetti, Phys. Rev. B **91**, 195405-1-9 (2015).
23. Y. Fukaya, *et al.*, Carbon **103**, 1-4 (2016).
24. Y. Fukaya, *et al.*, Phys. Rev. B **88**, 205413-1-4 (2013).
25. P. Vogt *et al*., Phys. Rev. Lett. **108**, 155501-1-5 (2012).
26. Y. Fukaya, *et al*., 2D Materials, **3**, 035019-1-8 (2016).
27. I. J. Rosenberg, *et al*., Phys. Rev. Lett. **44**, 1139-1142 (1980).
28. T. N. Horsky, *et al*., Phys. Rev. Lett. **62**, 1876-1879 (1989).
29. C. B. Duke and D. L. Lessor, Surf. Sci. **225**, 81-86 (1990).
30. S. Y. Tong, Surf. Sci. Lett. **457**, L432-L436 (2000).
31. K. Wada *et al*., to be published in e-Journal of Surface Science and Nanotechnology (e-JSSNT): Proceedings of ISSS-8 (2018)
32. S. Y. Tong, *et al*., Phys. Rev. Lett. **69**, 3654-3657 (1992).
33. S. Y. Tong and H. Wu, J. Phys.:Condens. Matter **14**, 1231-1236 (2002).
34. J. A. Wheeler, Ann. N. Y. Acad. Sci. **48**, 219–238 (1946).
35. A. P. Mills, Jr., Phys. Rev. Lett. **46**, 717-720 (1981).

36. Y. Nagashima and T. Sakai, New J. Phys. **8**, 319-1-7 (2006).
37. Y. Nagashima, Phys. Rep. **545** 95-123 (2014).
38. H. Terabe, *et al*., New J. Phys. **14**, 015003-1-6 (2012).
39. K. Michishio, *et al.*, Appl. Phys. Lett. **100** 254102-1-4 (2012).
40. K. Michishio, *et al*., Phys. Rev. Lett. **106** 153401-1-4 (2011).
41. A. P. Mills, Jr. Phys. Rev. A **24** 3242-3245 (1981).
42. A. K. Bhatia and R. J. Drachman Phys. Rev. A **28** 2523-2525 (1983).
43. Y. K. Ho, Phys. Rev. A **19** 2347-2352 (1979).
44. J. Botero, and C. H. Greene, Phys. Rev. Lett. **56**, 1366–1369 (1986).
45. A. K. Bhatia, Y. K. Ho, Phys. Rev. A **42**, 1119–1122 (1990).
46. A. Igarashi, *et al*., New J. Phys. **2**, 17.1-17.14 (2000).
47. K. Michishio, *et al*., Nature Communications **7**, 11060-1-5 (2016).
48. K. Michishio, *et al*., Nucl. Instrum. Meth. Phys. Res. A **785**, 5-8 (2015).
49. Y. Nagashima, et al., Phys. Rev. B **58**, 12676-12679 (1998).
50. H. Terabe, et al., *Surf. Sci.*, **641**, 68-71 (2015).
51. S. Iida, et al., *J. Phys.: Condens. Matter* **28**, 475002-1-4 (2016).
52. T. Yamashita, *et al*., Nucl. Insrum. Meth. Phys. Res. B **387**, 115–118 (2016).

Development of Slow Positron Beam lines and Applications

Nagendra Nath Mondal[1, a)]

[1)] Department of Physics, Techno India Batanagar,
B-7/360 Putkhali, Maheshtala, Kolkata 700141, West Bengal, India.

[a)]Corresponding author: nn.mondal2011@gmail.com

Abstract. A positron is an antiparticle of an electron that can be formed in diverse methods: natural or artificial β-decay process, fission and fusion reactions, and a pair production of electron-positron occurred in the reactor and the high energy accelerator centers. Usually a long-lifetime radio isotope is customized for the construction of a slow positron beam lines in many laboratories. The typical intensity of this beam depends upon the strength of the positron source, moderator efficiency, and guiding, pulsing, focusing and detecting systems. This article will review a few positron beam lines and their potential applications in research, especially in the Positronium Bose-Einstein Condensation.

INTRODUCTION

(i) There are two β-decay process: β^+-decay, when a proton (p) decays into a neutron (n); a positron (e^+) and a neutrino (ν) are radiated, i.e., $p \rightarrow n + e^+ + \nu$. Similarly in β^--decay, n decays into p, and e^- and antineutrino ($\bar{\nu}$) are generated. Extracting those elementary charged particles accelerated beam lines are constructed with desirable intensities for various applications. (ii) Reactor based e^+: Many fissile materials, e.g., Th^{232}, U^{238} and Pu^{239} undergo fission reactions when bombarded by thermal neutrons resulting e^+ radiation from the successive decay of daughter nuclei. A common fission reaction in atomic reactor is

$$n + {}^{235}_{92}U \rightarrow {}^{236}_{92}U \rightarrow {}^{140}_{54}Xe + {}^{94}_{38}Sr + 2n$$

Not only the charged particles but also energetic γ- rays (energy $\geq$ 1.022 MeV) are discharged from the decays of daughter nuclei and are forced to create pair productions by smashing the surface of a thin single crystal. Another process is the fusion reaction (naturally occurred in the Sun) stated as follows:

$${}^1_1H + {}^1_1H \rightarrow {}^2_1H + e^+ + \nu$$
$${}^2_1H + {}^2_1H \rightarrow {}^3_2He + \nu$$
$${}^3_2He + {}^3_2He \rightarrow {}^4_2He + {}^1_1H + {}^1_1H$$

After moderation this e^+ can be utilized as a slow positron beam. Pair production can produce high intense e^+ beam provided the intensity of mother beam, efficiencies of target and moderator in the reactor controlling system are very high. In the elementary particle physics e^+ can be extracted from the decay of lepton too. For examples:

$$\pi^+ \rightarrow \mu^+ + \nu_\mu$$
$$\mu^+ \rightarrow e^+ + \nu_e + \overrightarrow{\nu_\mu}$$

Hadrons and Kaon undergo decays into e^+: $K^+ \rightarrow \pi^0 + e^+ + \nu_e$.

(iii) Accelerator based e^+: Innumerable scientists of particle accelerators are working in order to achieve the highest intense slow e^+ beam. Some of the LINAC based centers are BNL (NY), CERN (Geneva), KEK (Tsukuba), SLAC (Stanford), Jefferson (VA) etc. TRIUMF (Vancouver), KFA (Julich), RIKEN (Saitama), JINR & FLNR (Dubna)

LBL (Berkeley), etc. are cyclotron based centers. Those particle accelerators provide energetic γ- rays (> 1.022 MeV) for the pair production. Details of these beam lines with applications are described in the following sections.

SLOW POSITRON BEAM LINES

Radio isotope based slow positron beam lines

Most of the slow positrons beam lines are developed on the basis of Radio Isotope (RI). The moderate lifetime (half-life ~ 2.6 years, measured by the formula, $T_{1/2} = \frac{0.693}{\lambda}$, where λ is called a decay constant.) and intensity (90% of the decay is e^+) of ^{22}Na are made it an ideal runner for the construction of an intense slow e^+ beam line. The typical intensity of this beam is about $10^4 - 10^7$ e^+/s. We had developed a slow positron beam line namely TOPS at Tokyo Metropolitan University, Tokyo, Japan in 1998 and studied many crystalline surfaces in order to justify the highest intense Positronium (Ps) production [1]. A schematic diagram of a "TOPS" is shown in **Figure 1**.

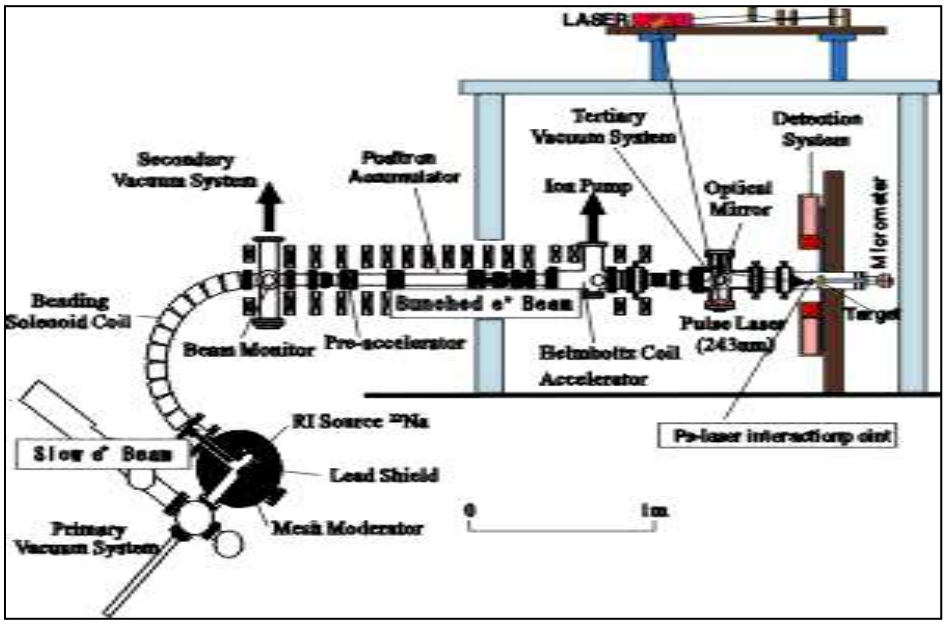

FIGURE 1: A slow positron beam line with laser facilities @ Tokyo Metropolitan University, Tokyo, Japan.

A few world-wide slow positron beam line facilities with intensities are summarized in **Table-1**. Bose-Einstein Condensation (BEC) is one of the moving areas of QED, atomic physics and statistical mechanics. In order to achieve the Ps-BEC (density is about 10^{15} Ps/cm^3 at mK temperature), the highest intense Ps production on the surface of a target or inside the nano-pore materials are vital points. Hence suitable materials, intense source of continuous/pulsed slow e^+s, advanced Laser cooling of ortho-Ps and Ps-BEC detection systems should be developed innovatively [2-14].

A slow e^+ beam line is developed at the University of California, San Diego (UCSD), based on ^{22}Na source whose strength is 50 mCi and is about 3 mm in diameter. The efficiency is measured about 30% with flux of 5×10^8 e^+/s in the forward direction. With solid Neon moderator $6 - 9 \times10^6$ slow e^+/s is found under a 100 Gauss field with a beam diameter of 1.0 - 1.2 cm. Energy spread of the slow e^+ is 1.9 eV (FWHM). They have developed a multi-staged buffer gas trapping system for collecting a large numbers of e^+ [15]. Recently, 10^{15} e^+ can be accumulated by using a Penning-Malmberg trap [16]. This highest intensity e^+ burst allows them atomic physics experiments. Another RI based slow e^+ beam line is developed by A.P. Mills, Jr., at the University of California, Riverside (UCR). The ^{22}Na source strength is 25 mCi, where e^+s are moderated with a solid Neon moderator engendering slow e^+ beam of

intensity ~ 6×10^6 e^+/s. Those moderators are grown at a temperature of 7 K with ultra-pure 99.999% Neon within 7 minutes. The UCR group uses a trapping device to achieve low energy e^+ pulses of intensity about 6×10^7 e^+ with a width of 1 ns [17]. They have done tremendous efforts for the experiment of Ps-BEC [18].

TABLE 1. Summary of a few slow positron beams and applications

Name and place	Contact persons	Positron source	Beam Energy	Beam Intensity e^+/s	Applications
EPOS, Halle, Dresden	Prof. Kraus-Rehberg	40 MeV e^-Linac	0.2 – 100 keV	Moderated: 10^9 and Pulse: 10^6	Defects, AMOC, CDBS, PACS etc.
LLNL, Livermore	Dr. R. H. Howell	Pelletron, 3 MeV	1 – 50 keV	300, 20 MHz	Defects, CDBS, PACS etc.
KEK-B Factory, Tsukuba	Dr. T. Kurihara	2.5 GeV e^- Linac	10 – 100 keV	10^8	2D-ACAR, TOF, Spin polarization
TU-Delft reactor, Amsterdam	Prof. P. J. Schultz	Reactor based	1 eV – 40 keV	10^8	2D-ACAR, 2D-Doppler, Depth profile
MRR-FRM-II, Munich	Prof. G. Kogel	Reactor based	100 eV	10^7 – 10^9	Positron microprobe, defect concentration
TOPS, Tokyo M. University	Dr. N. N. Mondal/ Dr. T. Kumita	^{22}Na (150 mCi) source	1 eV – 250 keV	10^6	BEC, Laser cooling, defects, polarization etc.
GU, Tokyo	Dr. I. Kanazawa	^{22}Na (3 mCi)	30 eV	10^3	Vacancy-type defects
Bonn University	Dr. K. Maier	^{22}Na (10 mCi)	150 eV	10^3	Surface and dislocation of materials
TUS, Tokyo	Dr. Y. Nagashima	^{22}Na (740 MBq)	100 eV	10^5	Ps^-, moderator, defects of materials.
SHI, Tokyo	Dr. M. Hirose	Compact Cyclotron	10 – 150 keV	10^6	Commercial purpose, surface, interface, polarization.
NCSU	Dr. Ayman Hawari	Reactor based	variable	6×10^8	Defect studies of various materials
Jefferson	Joe Grames	LINAC	---	---	Fundamental research

Reactor based slow positron beam lines

There are only a few nuclear reactor-based e^+ sources are available where e^+s are created by pair production from the reactor core. The intensity of slow e^+ not only depends on the power of the core, converter material, and moderator geometry but also on the criticality (k_{eff}), pulsing and guiding system. Reactor core based e^+ source at PULSTAR is a 1-MW located at the North Carolina State University. Main interests of this center are in neutron diffraction, ultra-cold neutron studies, and deliver intense e^+ beams to the users. Positrons are created from a converter-moderator assembly surrounded by cadmium blocks adjacent to the core [19]. Positrons are created by pair productions and also with neutron capture in the Cadmium (Cd). In this reaction 9 MeV radiation energies are released [20]: $^{113}Cd + {}^1n \rightarrow {}^{114}Cd + 9$ MeV. The W target is placed closer to 30 cm of the core. The PULSTAR reactor beam currently uses two W arrays as e^+ converters and moderators. Each array is 22 cm in diameter and 2.5 cm in length. An array is comprised of interlocking W strips of each thickness 250 μm can produce 5×10^8 slow e^+/s.

The NEutron induced POsitron source of MUniCh (NEPOMUC) [21] is a 20 MW reactor-based e^+ beam facility. Reaction process is similar to PULSTAR and a structure of Platinum (Pt) and a stack of W foils are placed for converting the γ-rays into e^+e^- pairs. Platinum is used because e^+e^- production cross-section of Pt is higher than W. Inside the Cd cap, the mean-flux density is expected to be 4.1×10^{13} /cm^2/s. About 15% of the γ-radiation of 6.2×10^{12} /cm^2/s originates from the core. The maximum energy of e^+ spectrum is about 800 keV. The W foils also act as a moderator assembly. After moderation e^+ beams are accelerated by electrostatic lenses and guided by magnetic fields of 6 mT. The beam diameter is about 18 mm (FWHM) and intensity is close to 10^9 e^+/s with average energy of 1 keV [22, 23].

Positron beam line (POSH) at the Interfaculty Reactor Institute in Delft that provides a constant intensity of 0.8×10^8 e^+/s to a 2D-ACAR target chamber [24, 25]. In the reactor core high energy γ-rays are generated when thermal neutrons are captured in Cd foils via the nuclear reaction ^{113}Cd (n,γ) ^{114}Cd that produce pair production in W foils. The POSH was designed installed at the Delft 2 MW research reactor [25] in 1998. An assembly of thin W foils, configured as 4 disks containing 10 × 10 mm square channels, serves to convert the γ-rays into slow down and thermalize the energetic e^+s, and, finally to re-emit slow e^+s (3 eV) from the tungsten surfaces into the vacuum tube containing the source. In March 1999 a beam intensity of 2×10^8 e^+/s was demonstrated.

Accelerated based slow positron beam lines

The highest intense slow positron beam with a variable time structures are developed by pair production facilities. Electron beam is used as a typical driving beam to produce the bremsstrahlung photon of energy ≥ 1.022 MeV that can create pair production on a suitable target. A Van-de-Graff generator can be used to accelerate *p* or deuteron (*d*) up to 4 MeV [26] in order to produce e^+ alternatively. Accelerated *d* beam hits a graphite target and emits e^+ via ^{12}C $(d,n)^{13}$N reaction. In BNL such a facility is exist. In Dresden, ELBE Super Conducting e^- -LINAC (40 MeV) produces one of the highest intense slow e^+ beam (EPOS) of energy 0.2 – 40 keV for materials studies [27]. The bunch structure of the driving beam is 77 ns with repetition cycle 13 MHz and 1 mA current [28]. The entrance diameter of e^- beam is 5 mm and passes next to a stainless steel window (0.3 mm), 0.1 mm of water column, followed by a heap of 50 W foils of thickness 5 mm. The separation gap is 100 μm through which the cooling water runs and simulated intensity of e^- beam is about 5×10^{13} /sec. The W moderator is placed near the converter and projected slow e^+ intensity after moderation is about $5\times10^8 - 10^9$ e^+/s.

In Tsukuba (KEK) there is an e^- accelerator (beam energy 70 MeV , 1 μs pulse with 3 μA average current of cycles 100 Hz) is developed by the group of Advanced Industrial Science and Technology (AIST). This facility is generating a slow e^+ beam for material science experiments to identify the nano scale defects in various applied materials. A similar bremsstrahlung technique is utilized to produce e^+ beam. The fast e^+ s are immediately moderated through W films (25 μm) and using the magnetically guiding system (7 mT) those are transported to the experimental room which is about 20 m long in order to escape the background. The moderated e^+ beam diameter and energy are about 10 eV and 10 mm respectively. The beam intensity at the experimental site is about $2\text{-}3\times10^7$ e^+/s [29]. In order to reduce the spot size they followed the Brightness enhancement method where the beam was extracted from the magnetic field prior to reach the experimental hall. It was focused by a lens on a re-moderator (200 nm thick single crystal W) to enhance its brightness. After re-moderation, the spot size at the target place was measured ~30-100 μm [30]. The efficiency of the transmission in re-moderator is about 5%, which reduces the intensity to ~ 10^6 e^+/s [31].

The primary source of positrons at LLNL is located at the end of a 100 MeV LINAC where e^+ current is ~ 400 mA with repetition rate of 300 Hz. Duration of pulse is 3 μs is obtained by a penning trap system and average beam power is up to 45 kW. The energetic e^-s were stopped in a water-cooled W target from where the shower of photons produced by bremsstrahlung method. The conversion of photons yields a pair of e^+e^-, an intense source of e^+. It was slowed with Venetian blinds type moderator as described earlier. Again it was moderated by a single crystal W and attained the slow e^+ beam (3×10^7/s) which is good for many material studies in conventional PALS systems [32].

Cyclotron based slow positron beam lines

The pair production mechanisms produce a higher intense positron beam in many cyclotron centers world-wide. A high intensity (~ 7.8×10^{21} e^+/s at peak position) pulsed e^+ beam is obtained from the accelerated e^- (energy is a few MeV) at the third generation cyclotron center in Shanghai [33]. The superconducting wiggler with 8-12 Tesla magnetic field of Spring-8 storage ring in RIKEN provides another highest intensity 10^{12} (slow e^+/sec). Sumitomo heavy industries in Japan has been producing different types of compact cyclotron for various purposes. Positron emitting cyclotron, proton therapy cyclotron, and Medical cyclotron for producing radio isotopes for clinical pupose are the most. For examples: ^{18}F, ^{15}O, ^{13}N, ^{11}C etc. are produced for the Positron Emission Tomography (PET) in order to image cancerous cells and tiny brain tumors in the body.

APPLICATIONS OF SLOW POSITRON BEAM LINES

Defect studies of materials

Both the POSH and EPOS beam lines are utilized for performing the high resolution measurements of the electron momentum distribution (2D-ACAR) for depth localized defects, thin layer systems, interfaces and defect depth profiling. It helps to map "vacancy type" defects in a 3-D fashion. The lifetime spectrum can be described as a sum of decaying exponentials as follows:

$$N(t) = \sum_{i=1}^{f} \frac{I_i}{\tau_i} \exp(-t/\tau_i)$$

Where f is a number of different annihilation and τ_i lifetime and I_i intensities respectively are of the i[th] annihilation. In Doppler broadening measurement the detected energy spectrum of annihilation γ-rays will provide the information about the bulk and defects after analyzing the S (sharp) and W (wing) parameters. Those are defined by:

$$S = \frac{B}{A+B+C}, \text{ and } W = \frac{D+F}{D+E+F}, \quad \text{respectively.}$$

The implantation of slow positron beam can be approximated by a Makhovian profile:

$$P(z,E) = \frac{mz^{m-1}}{z_o^m} \exp\left[-\left(\frac{z}{z_o}\right)^m\right]$$

Where m is the shape parameter is set to be 2 and mean implantation depth:

$$\vec{z}\,[nm] = \frac{\sqrt{\pi}}{2}\, z_o = \frac{\alpha}{\rho}\, E^n$$

Where ρ represents the density of the material and α, n are the material independent constants. Positron trapping rate at defect sites is given by:

$$\Gamma_d = \mu\, C_d = \frac{I_2}{I_1}\left(\frac{1}{\tau_b} - \frac{1}{\tau_d}\right)$$

Where μ is trapping coefficient, C_d defect concentration, τ_b is bulk lifetime and τ_d is defect lifetime. It is also possible to know the defect size (volume) by the following formula:

$$v_h(\tau_3) = \frac{4}{3}\,\pi r_h^3(\tau_3)$$

Where, τ_3 is the third component of ortho-Positronium lifetime and r_h is the radius of the volume of a defect. Hence e^+ lifetime measurement is a unique and nondestructive spectroscopy of defect and structures of various materials including nanomaterial.

Medical diagnostics (positron therapy)

An interesting diagnostic system, positron therapy similar to proton therapy has been launched in many institutes in advanced countries. There are four such facilities in Japan and one of them is in Tsukuba University. An intense e^+ beam is extracted from the LINAC of 7 – 250 MeV beam transportation system. About 500 patients are given treatment during the year 2001 – 2004 and each patient is required 10 – 20 min/treatment [34].

Fundamental Research (BEC)

Positronium is a quasi-bound atomic state comprises numerous fundamental researches in advanced atomic and molecular physics. In compare to hydrogen atom the lightest mass makes it possible to achieve of Ps-BEC. Thermal para-Ps and work-function Ps can't be the subject of Ps-BEC because of their shorter life-time (125 ps) than the 1S – 2P transition period and higher kinetic energy (a few eV) respectively. On the other hand thermal ortho-Ps has a life-time of 142 ns and lower kinetic energy (a few meV) is an ideal candidate only if phase space density 10^{15} Ps/cm^3 can be extended. In order to realize the Ps-BEC many laboratories have been trying to reach the e^+ beam intensity more than 10^{12} /sec, e^+ storing (trapping) system, high intense laser (of wavelength 256 nm) and efficient detection system [35-37]. We had accomplished a laser cooling of ortho-Ps by constructing a slow e^+ beam line (**Figure-1**), a Cr:LiSAF laser system, e^+ pulsing system and advanced detection system. A typical spectrum of this measurement depicted in **Figure-2**. A few years back Mills and co-workers at UCR made tremendous efforts to achieve Ps-BEC and Ps molecule [18].

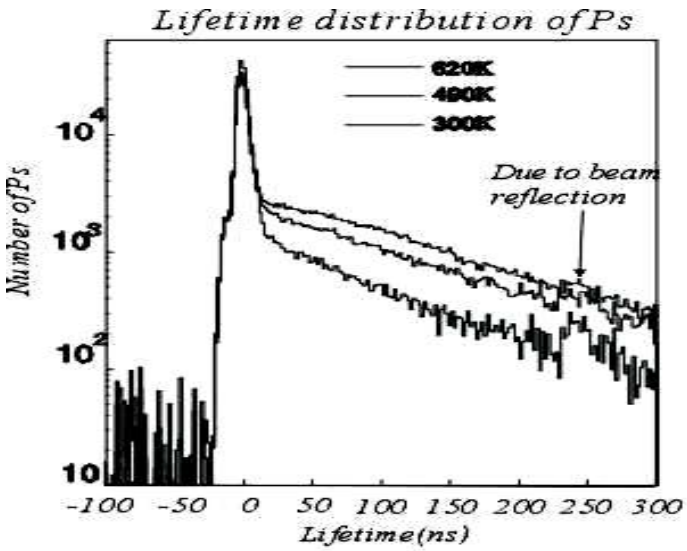

FIGURE 2: Laser cooling of ortho-Ps measurement at different temperature. Spectra show the lifetime effect due to laser-Ps interactions.

IMAGING TECHNIQUES IN VARIOUS FIELDS OF RESEARCH

An array of position-sensitive γ-ray detectors is one of the best detection and imaging system which is convenient for the visualization of Ps-BEC. The size and scintillation materials used in the detectors system play a vital role for the improvement of energy and time resolutions, detection efficiency and imaging without artifacts. Recently we have developed an image reconstruction algorithm (Position vector method) which enables us to take data and process the image in-situ treatment. In this precession measurement tiny brain tumors are imaged within the stipulated period of the diagnosis of the patient [38-40].

DISCUSSIONS AND CONCLUSIONS

In order to achieve Ps-BEC and e^+ therapy many laboratories have been developing higher intense slow e^+ beam lines, efficient and advanced detection, Laser cooling, e^+ accumulator, pulsing, guiding and polarization systems. High density nano-porous materials are relevant for accumulating the huge density Ps production which is advancing too.

ACKNOWLEDGEMENTS

Author is pleased to acknowledge the financial support from his family and thanks the organizers (Prof. Joe Grames and Prof. Farida A Selim) for accepting the Talk in the conference.

REFERENCES:

1. N. N. Mondal, R. Hamatsu, T. Hirose, H. Ijima, M. Irako, T. Kumita, Y. Igura and T. Omori; Appl. Surf.Sci. **149,** 269 (1999).
2. R. Krause-Rehberg, G. Brauer, M. Jungmann, AKrille, A. Rogov, K. Noack, Appl. Surf. Sci. **255,** 22-24 (2008).
3. S. Chu, A.P. Mills, Jr., and C. A. Murray; Phys. Rev. **B 23,** 2060 (1981).
4. S. Chu, A. P. Mills Jr., Phys. Rev. Lett. 48 (1982) 1333 and Phys. Rev. Lett. **52**, (1984) 1689.

5. A. P. Mills Jr., E. D. Shaw, M. Leventhal, R. J. Chichester, and D.M. Zuckerman; Phys. Rev. **B 44,** 5791 (1991).
6. P. M. Platzman and A.P. Mills; Phys. Rev. **B. 49,** 454 (1993).
7. H. Iijima, T. Asonuma, T. Hirose, M. Irako, K. Kadoya, T. Kumita, M. Kajita, B. Matsumoto, N. N. Mondal and K. Wada; Mat. Sci. Forum Vols. **363 – 365,** 670 (2001).
8. H. Iijima, T. Asonuma, T. Hirose, M. Irako, T. Kumita, M. Kajita, K. Matsuzawa and K. Wada; Nucl.Inst. Meth. Phys. Res. **A 455,** 104 (2000).
9. Nagendra Nath Mondal; Nucl. Inst. Meth. Phys. Res. **A 495,** 161 (2002).
10. T. Kumita, T. Hirose, M. Irako, K. Kadoya, B. matsumoto, N. N. Mondal, K. Wada, H. Yabu, K. Kobayashi, M. Kajita; Nucl. Inst. Meth. Phys. Res. **B 192,** 171 (2002) and references therein.
11. P. Asoka-Kumar, K. G. Lynn, and D. O. Welch, J. Appl. Phys. **76**, 4935 (1994).
12. D. B. Cassidy, T. H. Hisakado, H. W. K. Tom, and A. P. Mills, Jr., Photoemission of Positronium from Si, Phys. Rev. Lett. **107**, 033401 (2011).
13. C. V. Falub, S.W. H. Eijt, P.E. Mijnarends, H. Schut and A. van Veen, Nucl. Instr. Meth. Phys. Res. **A 488**, 478 (2002).
14. David W. Gidley, Hua-Gen Peng, and Richard S. Vallery, Annual Review of Materials Research, Vol. **36**, 49-79 (2006).
15. A. P. Mills *et al.*, Rev. of Sci. Instr. **77**, 073106 (2006).
16. C. M. Surko *et al.*, Rad. Phys. and Chem. **68**, 419 (2003).
17. A. P. Mills *et al.*, Phys. Rev. Lett. **104**, 173401 (2010).
18. D. B. Cassidy, P. Crivelli, T. H. Hisakado, L. Liszkay, V. E. Meligne, P. Perez, H. W. K. Tom, and A. P. Mills Jr., Positronium cooling in porous silica measured via Doppler spectroscopy, PHYSICAL REVIEW A **81**, 012715 (2010).
19. A. G. Hathaway *et al*., Nucl. Instr. Meth. Phys. Res. **A 579**, 538 (2007).
20. A. I. Hawari *et al.,* AIP Conf. Proc. **1099**, 862 (2009). Ayman I Hawari1, David W Gidley2, Jeremy Moxom1, Alfred G Hathaway1 and Saurabh Mukherjee, Journal of Physics: SLOPOS-12 Conference Series **262,** 012024 (2011).
21. C. Hugenschmidt *et al.,* Appl. Surf. Sci. **252**, 3098 (2006).
22. C. Hugenschmidt *et al*., Nucl. Instr. Meth. Phys. Res. **A 593**, 616 (2008).
23. C. Hugenschmidt *et al*., Appl. Surf. Sci **149**, 7 (1999).
24. Van Veen, A., F. Labohm, H. Schut, J. De Roode, T. Heijenga, P.E. Mijnarends, Appl. Surf. Sci. **116,** 39-44 (1997).
25. A. van Veen, H. Schut, F. Labohm, J. De Roode, Nucl. Instr. Meth. **A 427,** 266-270 (1999). International symposium on research reactor utilization, safety and management. Book of extended synopses, http://www.iaea.org/inis/collection/NCLCollectionStore/_Public/30/044/30044395.pdf
26. K. G. Lynn et al., Appl. Surf. Sci. **194**, 296 (2002).
27. R. Krause-Rehberg *et al*., Appl. Surf. Sci. **252**, 3106 (2006).
28. R. Krause-Rehberg *et al*., Appl. Surf. Sci. **255**, 22 (2008).
29. AIST, http://unit.aist.go.jp/riif/adcg/english/.
30. R. Suzuki et al., Rad. Phys. and Chem. **78**, 1096 (2009).
31. N. Oshima et al., Mater. Sci. Forum **607**, 238 (2008).
32. W. Stoeffl, P. Asoka-Kumar, and R. Howell, **UCRL-JC**-132420
33. Tongjun Xu, Baifei Shen, Jiancai Xu *et.al.*, Physics of Plasmas **23**, 033109 (2016).
34. Shinkai Yasuhiro, Positron beam therapy of cancer: Genshiryoku Eye; ISSN 1343-3563 v. **50** (10); p. 54 – 57
35. Nagendra Nath Mondal and Tachishige Hirose, Appl. Surf. Sci. **194**, 317 – 324 (2002).
36. Nagendra Nath Mondal, Nucl. Instr. Meth. Phys. Res. **A 495**, 161-169 (2002).
37. T. Kumita, T. Hirose, M. Irako, K. Kadoya, B. Matsumoto, K. Wada, N. N. Mondal, H. Yabu, K. Kobayashi, M. Kajita, Nucl. Instr. Meth. Phys. Res. **B 192**, 171–175 (2002).
38. Nagendra Nath Mondal, Journal of Medical Physics, **33/1**, 9-13 (2008).
39. Nagendra Nath Mondal, Journal of Medical Physics, **34/4**, 212-6 (2009).
40. B. N. Ganguly, N. N. Mondal, Moitryee Nandi and F. Roesch, Journal of Radioanalytical and Nuclear Chemistry, **279/2** 685–698 (Feb, 2009).

Electronic Structure Probed with Positronium: Theoretical Viewpoint

Jan Kuriplach[1,a)] and Bernardo Barbiellini[2,3,b)]

[1]*Department of Low Temperature Physics, Faculty of Mathematics and Physics, Charles University, V Holešovičkách 2, CZ-180 00 Prague 8, Czech Republic*
[2]*School of Engineering Science, Lappeenranta University of Technology, Lappeenranta, Finland*
[3]*Physics Department, Northeastern University, Boston, MA 02115, USA*

[a)]Corresponding author: jan.kuriplach@mff.cuni.cz
[b)]bernardo.barbiellini@lut.fi

Abstract. We inspect carefully how the positronium can be used to study the electronic structure of materials. Recent combined experimental and computational study [A.C.L. Jones et al., Phys. Rev. Lett. **117**, 216402 (2016)] has shown that the positronium affinity can be used to benchmark the exchange-correlation approximations in copper. Here we investigate whether an improvement can be achieved by increasing the numerical precision of calculations and by employing the strongly constrained and appropriately normed (SCAN) scheme, and extend the study to other selected systems like aluminum and high entropy alloys. From the methodological viewpoint, the computations of the positronium affinity are further refined and an alternative way of determining the electron chemical potential using charged supercells is examined.

INTRODUCTION

Positrons strongly interact with electrons in materials. This fact makes the interpretation of positron experiments a difficult task. On the other hand, this strong coupling enables us to inspect not only electron-positron interactions, but also electron-electron interactions, which are usually labeled by the term *exchange-correlation* (XC) effects, as distinct from electrostatic interaction of electrons. A simple example of such probe is the bulk positron lifetime which depends on the electron density (electron only related quantity) and (electron-positron) enhancement factor. Since the positron lifetime is an integral quantity, its sensitivity to XC energy is rather small. Measuring the positron lifetime thus mostly serves as a test of positron annihilation enhancement factors [1].

There are positron related quantities, however, which exhibit more sensitivity with respect to XC effects. In particular, the positronium affinity, which characterizes the ability of a material to form positronia at and emit them from its surface, can be effectively employed to examine various approximations for XC [2]. The Ps affinity (A_{Ps}) is defined through electron (ϕ_-) and positron (ϕ_+) work functions or, alternatively, via electron (μ_-) and positron (μ_+) chemical potentials, in the following way:

$$A_{\mathrm{Ps}} = \phi_- + \phi_+ - E_{\mathrm{Ps}} \quad (1)$$

$$= -(\mu_- + \mu_+) - E_{\mathrm{Ps}} \,, \quad (2)$$

with E_{Ps} being the Ps binding energy in vacuum ($E_{\mathrm{Ps}} \simeq 6.803$ eV). According to Equation 1, A_{Ps} is the sum of electron and positron work functions minus the (vacuum) Ps binding energy and corresponds thus to the negative of the maximum of the kinetic energy (E_{K}) of Ps atoms emitted from a given surface (i.e. $E_{\mathrm{K}} = -A_{\mathrm{Ps}}$). If A_{Ps} is positive, thermalized positrons cannot escape the surface in the form of Ps. Another name for Ps affinity is the Ps formation potential [3] (the more negative A_{Ps} is, the stronger Ps emission can be expected). We note that in atomic physics the Ps affinity is defined in somewhat different way [4].

The relation between the work functions and respective chemical potentials is expressed as $\phi_\pm = \mp D - \mu_\pm$, where D is the surface dipole barrier for electrons [3] (surface dipole barrier has the opposite sign for electrons and

positrons). In this way, Equation 2 is justified, and one can clearly see that the Ps affinity is a bulk property, as are μ_- and μ_+. We should stress that the surface dipole barriers for an electron and positron (forming Ps) mutually cancel when particles go through the (sufficiently clean) surface to vacuum, and the type of the surface becomes irrelevant when Ps atoms are studied in the vacuum region – these entities reflect the bulk state of the material (electronic structure) and thermalized positrons properties.

A recent Ps time of flight (TOF) experiment performed by Jones et al. [2] is essentially the realization of the above explained concept. Namely, the Ps affinity has been determined precisely by measuring the maximum of kinetic energy of Ps atoms emitted from a Cu (110) surface. In order to allow a highly accurate determination of the Ps TOF, the Ps atoms were excited to Rydberg states, which can travel very long before annihilating. The details of experiment are given in Ref. [2], and we discuss A_{Ps} results below in the context of new and improved computational results for Cu.

It is yet useful to mention the relation between the Ps and positron (A_+) affinities. In the context of positron materials research the positron affinity is usually defined as a sum of electron and positron chemical potentials, i.e. $A_+ = \mu_- + \mu_+$. Then, using Equation 2 we obtain that $A_+ = -A_{\mathrm{Ps}} - E_{\mathrm{Ps}}$, and A_+ is also a bulk characteristics. Since the positron work function is negative for many materials, A_+ can be determined from positron reemission experiments using the relation $A_+ = -(\phi_- + \phi_+)$ provided that ϕ_- for the same surface is known. Such type of measurements typically does not bring sufficiently high precision to allow for a reliable testing of electron XC energies.

COMPUTATIONAL PROCEDURES

The background and motivations of our calculations were given in the previous section, and now we proceed with the description of calculations from the practical and technical viewpoints. In order to determine the μ_- and μ_+ quantities, we employ the density functional theory (DFT) [5]. First, the electronic structure of studied materials is determined by solving self-consistently the Kohn-Sham equations [6]:

$$\left[-\frac{1}{2}\Delta_{\boldsymbol{r}} + V_{\mathrm{Coul}}(\boldsymbol{r}) + V_{\mathrm{xc}}[n_-(\boldsymbol{r})]\right]\psi_-^{(i\boldsymbol{k})}(\boldsymbol{r}) = \epsilon_-^{(i\boldsymbol{k})}\psi_-^{(i\boldsymbol{k})}(\boldsymbol{r}) \tag{3}$$

with energy bands $\epsilon_-^{(i\boldsymbol{k})}$ and corresponding wave functions $\psi_-^{(i\boldsymbol{k})}$ (i is the band index and $\boldsymbol{k}$ is the vector from the first Brillouin zone of the corresponding crystal). V_{Coul} and V_{xc} are, respectively, the Coulomb and exchange-correlation potentials. The V_{xc} potential is derived from the XC functional $E_{\mathrm{xc}}[n_-]$: $V_{\mathrm{xc}}(\boldsymbol{r}) = \delta E_{\mathrm{xc}}[n_-(\boldsymbol{r})]/\delta n_-(\boldsymbol{r})$. In all above equations, n_- is the electron density determined by summing all densities corresponding to states with energies smaller than or equal to μ_-. Thus, the highest occupied state energy $\epsilon_-^{(i\boldsymbol{k})}$ is equal to μ_-. The XC energies employed in this study were the most common approximations: local density approximation (LDA) (based on quantum Monte Carlo simulations [7] and parametrized in Ref. [8]), generalized gradient approximation (GGA) after Perdew, Burke and Ernzerhof [9], and the so-called PBEsol functional [10] (based on GGA) designed especially for solids.

Within the DFT framework, one can also find that if the unit cell contains N_{tot} electrons, there is a relation between the total energy $E[n_-, N]$ as a function of the number of electrons (N) and the chemical potential [11]:

$$\mu_- = \left.\frac{\partial E[n_-, N]}{\partial N}\right|_{N=N_{\mathrm{tot}}} , \tag{4}$$

where we suppose that N can be a real (non-integer) number. It can be instructive to check whether Equation 4 can be fulfilled in practical calculations.

In the case of an electron-positron system, there is a generalization of DFT – two component DFT [12] – and here we use it in a simplified form for delocalized positrons which do not influence electronic structure. In this case, we need to solve a Schrödinger equation for positrons:

$$\left[-\frac{1}{2}\Delta_{\boldsymbol{r}} - V_{\mathrm{Coul}}(\boldsymbol{r}) + V_+[n_-(\boldsymbol{r})]\right]\psi_+(\boldsymbol{r}) = \epsilon_+\psi_+(\boldsymbol{r}) \tag{5}$$

considering the ground state characterized by the positron wave function ψ_+ and energy ϵ_+. Since there is typically only one positron in a measured sample at a given moment, we can identify ϵ_+ with μ_+. In Equation 5, the Coulomb potential for positrons has the opposite sign than in Equation 3 due to opposite charges of electrons and positrons. V_{corr} is the so-called positron correlation potential which depends on n_-. There were two approaches to electron-positron

correlations taken into consideration during positron calculations: LDA [13] and parameter free (PF) GGA introduced recently [14].

The practical calculations of the electronic structure of studied systems were carried out using the WIEN2k code [15]. This code implements the augmented plane-wave plus local orbital (APW+lo) method [16], which is considered to be one of the most accurate methods to calculate electronic structure of solids, and is based on the the linearized augmented plane-wave (LAPW) method [17]. The electron density and Coulomb potential were exported on a 3D spatial mesh inside the unit cell after reaching self-consistency and employed subsequently in a real space code in order to solve the positron Schrödinger equation for the ground state (Equation 5). Most of computational details are given in Ref. [1]. Here we mention that parameters of both codes (such as basis set cutoff and 3D mesh spacing) are optimized in order to obtain high precision numerical values of $A_{\mathrm{Ps}}(A_+)$ and positron lifetime, which are typically 0.01 eV and 0.1 ps, respectively. In this paper, we attempt to obtain even a better precision of A_{Ps} (and A_+) values, which is motivated by possible future experiments achieving a higher precision than that in Ref. [2]. For this purpose some of numerical parameters have to be optimized with great care. Special attention has to be paid to basis energy parameters for the *d*-electrons. In some cases a second energy parameter has to be appropriately chosen, which corresponds to the addition of a local orbital to the basis (for *d*-electrons). Since such a procedure is rather based on experience, it introduces some level of arbitrariness into calculations. Similarly, the choice of the muffin-tin radii for atoms requires attention since the linearization of the LAPW basis works reasonably only for some range of these radii. In total, about 10 different numerical parameters have to be optimized in order to achieve well converged values for the quantities of interest.

The Vienna *ab initio* simulation package (VASP) [18, 19] was also employed within the current study. The purpose was threefold. First, we employ VASP to study the validity of Equation 4 in charged supercells. Second, we intend to estimate the effect of the new meta-GGA SCAN (= strongly constrained and appropriately normed) functional [20] on the Ps affinity as this new scheme is self-consistently implemented in VASP, but not yet in the WIEN2k code. This effect can be approximately calculated by using the PBE functional and then the SCAN functional. From the change of μ_- between these two calculations in VASP, the PBE value of A_{Ps} obtained using WIEN2k can be modified to obtain the corresponding SCAN value. The same procedure can be applied to μ_+. However, the results should be taken with caution since VASP probably averages the XC potential though we have not find it mentioned in the description supplied along with the program. Third, we perform the relaxation of atomic positions in model high entropy alloys using VASP.

RESULTS AND DISCUSSIONS

Copper

Copper is a transition metal with a completely filled 3*d*-band and fcc structure. The Ps affinity of Cu has been determined with high precision recently in Ref. [2] using a time of flight experiment at 128 K. The value is $A_{\mathrm{Ps}} = (2.476 \pm 0.010_{\mathrm{stat}} \pm 0.013_{\mathrm{syst}})$ eV; index 'stat' is for the statistical error and 'syst' for systematic (see Ref. [2] for details). Table 1 presents calculated values updated in the present work. The shifts (~ 0.035 eV) with respect to Ref. [2] are mainly due to the detailed examination of the $\boldsymbol{k}$-mesh dependence (see Figure 1). Even if the values for all three XC are slightly shifted, PBEsol + GGA PF remains closest to the experimental value. The estimated SCAN value is also quite close to experiment. The uncertainties of affinity values (except SCAN) are ±0.002 eV, which originates from the $\boldsymbol{k}$-mesh dependence and cumulative effect of other WIEN2k parameters (muffin-tin radius choice is important for Cu). The calculations were done with the Cu lattice constant at 128 K.

TABLE 1. Results of A_{Ps} and A_+ calculations for copper; the bulk positron lifetime is also given. The uncertainty of affinity values is ±0.002 eV (and ±0.02 eV for last two columns) as discussed in the text.

LDA + LDA			**PBE + GGA PF**			**PBEsol + GGA PF**			**SCAN + GGA PF**	
A_{Ps} (eV)	A_+ (eV)	τ (ps)	A_{Ps} (eV)	A_+ (eV)	τ (ps)	A_{Ps} (eV)	A_+ (eV)	τ (ps)	A_{Ps} (eV)	A_+ (eV)
−2.159	−4.644	106.5	−2.726	−4.077	110.1	−2.508	−4.295	109.9	−2.43	−4.37

The experimental value of the positron affinity of Cu is −4.3 eV [21] and was obtained by measuring separately ϕ_+ and ϕ_- for selected surfaces. According to Table 1 the PBEsol + GGA PF scheme gives again the best agreement with experiment, but we should be aware of an experimental uncertainty of about 0.1 eV. We can see that the Ps affinity

provides a higher level of confidence in assessing the most appropriate XC functional for Cu. The positron lifetime for the LDA + LDA is too short when compared to experiment (~ 110 ps) and GGA values differ negligibly only.

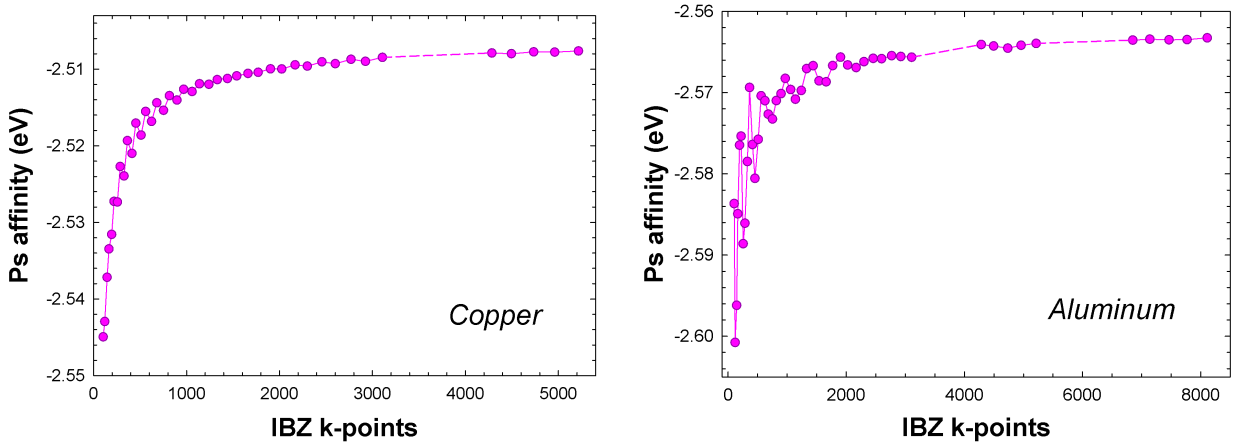

FIGURE 1. The dependence of A_{Ps} for copper (left) and aluminum (right) on the number of $\boldsymbol{k}$-points in the irreducible part of the Brillouin zone (IBZ). The calculations were done within the PBEsol + GGA PF scheme for Cu and LDA + LDA for Al; variations of A_{Ps} for other schemes used look similar to those shown here. The corresponding maximum number of $\boldsymbol{k}$-points in the whole Brillouin zone would be more than 200000 (Cu) and 300000 (Al). The dashed lines are just guide to eyes; no calculations were performed in the corresponding regions.

Charged cells

The electron chemical potential (μ_-) is an important electron, energy-related quantity related to DFT. Namely, the derivative of $E[n, N]$ with respect to the number of electrons (see Equation 4) should result in μ_-. In practical calculations, however, μ_- is routinely determined as the highest occupied level to ensure that the total number of electrons is just N_{tot}, and no derivative is needed. It should be mentioned that in electronic structure calculations V_{Coul} is considered with respect to a level called *crystal zero* [22] since no absolute scale exists. The derivative of $E[n, N]$ with respect to N thus contains implicitly the derivative of this crystal zero (E_{c0}) level with respect to N. The problem is that E_{c0} changes with N (for instance, WIEN2k averages for practical reasons V_{Coul} in the interstitial region and this procedure certainly depends on N). Therefore, it is likely that we do not obtain μ_- from equation 4, but μ_- plus a term $\propto \partial E_{\mathrm{c0}}/\partial N$.

Figure 2 shows the $\boldsymbol{k}$-mesh dependence of $\Delta\mu_-$, which is a difference between μ_-'s for the charged cell and the neutral one, for 1 and 32 atom fcc Cu cells. Indeed, the curves corresponding to WIEN2k do not approach $\Delta\mu_-$ zero level even for very high number o $\boldsymbol{k}$-points. In the case of VASP, the $\Delta\mu_-$ zero level is approached with the increasing number of $\boldsymbol{k}$-points, but there are two things to consider: V_{Coul} is averaged over the cell (i.e. in a different way compared to WIEN2k) and V_{xc} is also averaged (not in in WIEN2k). Thus, μ_- is based on an averaged total potential and does not depend on N in the limit of very dense $\boldsymbol{k}$-mesh. We can thus state that calculating the chemical potential via the derivative of the total energy using the codes devoted to electronic structure calculations is not straightforward and one has to consider the presence of the crystal zero and various schemes of the potential averaging. When the Ps affinity is calculated using the WIEN2k code, the resulting value does not depend on the crystal zero as E_{c0}'s are opposite for electrons and positrons and effectively cancel.

Aluminum

Aluminum is an sp metal without any d- and f-electrons. Its conduction band is dominated by the $3s$ and $3p$ electrons. It would certainly be instructive to see which XC theory describes properly the electronic structure of Al. Table 2 shows results of A_{Ps} and A_+ calculations for Al with the room temperature lattice constant. Several XC approaches for electrons combined with two electron-positron correlation approaches were employed like in the case of Cu.

The only experimental value currently available is for the positron affinity. According to the summary given in Ref. [21], $A_+ = -4.1$ eV, which compares well with the corresponding values in Table 2. This experimental value

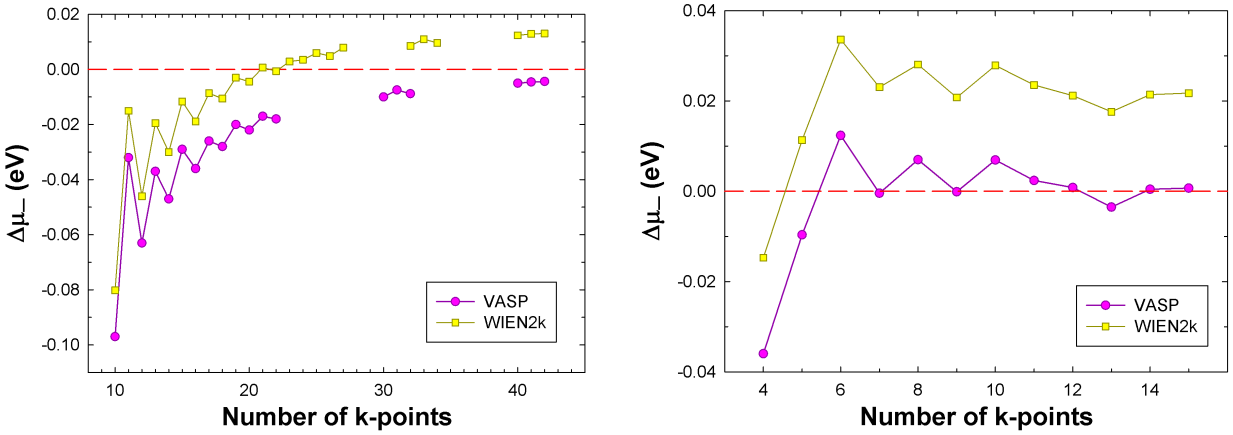

FIGURE 2. The dependence of the chemical potential difference (see the text) on the $\boldsymbol{k}$-mesh sampling for 1 atom (left) and 32 atom (right) fcc Cu cells. The derivative (see Equation 4) was calculated as $(E[N+\delta N] - E[N-\delta N])/2\delta N$ with $\delta N = 0.1$ for 1 atom cell and $\delta N = 1$ fro 32 atom cell. The number of $\boldsymbol{k}$-points characterized by the division of the $\boldsymbol{k}$-space in one direction (e.g. division 10 means that there is approximately 10^3) in the whole Brillouin zone.

of A_+ translates to $A_{\mathrm{Ps}} = -2.7$ eV, which means that the maximum kinetic energy of positronia emitted from an Al surface should be positive. It should be mentioned that the precision of experimental A_+ values is of order 0.1 eV. Current experimental possibilities in measuring positron lifetimes do not allow to differentiate between various XC approaches. Concerning the correction due to the SCAN treatment of the electronic structure (obtained using the VASP code) we can state that the change of the electron chemical potential with respect to the PBE case is rather small and amounts to −0.002 eV. Considering the comments above about the SCAN effect on μ_- and the effect of XC on μ_+, which is very small for Al, we can calculate the SCAN corrected values of A_{Ps} and A_+. They are given in the last two columns of Table 2 and are effectively equal to values obtained for PBE + GGA PF scheme. However, the estimated uncertainty has to be larger, we guess ±0.02 eV.

TABLE 2. Results of A_{Ps} and A_+ calculations for aluminum; the bulk positron lifetime is also given. The precision of affinity values is ±0.002 eV (and ±0.02 eV for last two columns) as discussed in the text.

LDA + LDA			**PBE + GGA PF**			**PBEsol + GGA PF**			**SCAN + GGA PF**	
A_{Ps} (eV)	A_+ (eV)	τ (ps)	A_{Ps} (eV)	A_+ (eV)	τ (ps)	A_{Ps} (eV)	A_+ (eV)	τ (ps)	A_{Ps} (eV)	A_+ (eV)
−2.563	−4.240	161.4	−2.771	−4.031	163.1	−2.713	−4.090	163.1	−2.77	−4.03

Next, we should note that Al has quite complicated Fermi surface [23] with small electron pockets close to the Brillouin zone boundary. We suspect that very slow convergence of the μ_- value in dependence on the $\boldsymbol{k}$-mesh sampling (see Figure 1 where A_{Ps} is plotted) is due to the Fermi surface complexity. From the variation of A_{Ps} we can estimate that the uncertainty of the values of A_{Ps} and A_+ is at the 0.002 eV level considering also effect of other WIEN2k numerical parameters. In Ref. [14] the numerical precision of A_+ was declared to be 0.01 eV. Due to the Fermi surface effects mentioned, the value given there for A_+ of Al (within the PBE+GGA PF scheme) needs to be corrected by 0.02 eV (to −4.03 eV). The reason is that the influence of $\boldsymbol{k}$-mesh sampling was not investigated in sufficient detail in Ref. [14] for Al.

High entropy alloys

We select the HfNbTaTiZr refractory high entropy alloy (HEA) [24] to be examined here. We first discuss results for constituting elements (Hf, Nb, Ta, Ti, and Zr) which are mixed in the ratio 1:1:1:1:1 in the resulting bcc alloy studied next.

Constituting elements

The calculations for Hf, Nb, Ta, Ti, and Zr were done at their experimental crystal structures and corresponding room temperature lattice constants. All studied elements are transition metals; 3*d*, 4*d* and 5*d* electrons are involved. The results of affinity and lifetime calculations are presented in Table 3 where elements are listed according to periods (4–6) and groups (IV, V) in the periodic table in order to see possible trends.

TABLE 3. Results of A_{Ps} and A_+ calculations for Hf, Nb, Ta, Ti, and Zr elements; the bulk positron lifetime is also given. The precision of affinity values is ±0.002 eV (±0.003 for Hf) as discussed in the text.

Element and structure		**LDA + LDA**			**PBE + GGA PF**			**PBEsol + GGA PF**		
		A_{Ps} (eV)	A_+ (eV)	τ (ps)	A_{Ps} (eV)	A_+ (eV)	τ (ps)	A_{Ps} (eV)	A_+ (eV)	τ (ps)
Ti	hcp	−2.216	−4.587	142.7	−2.578	−4.225	145.9	−2.439	−4.364	145.8
Zr	hcp	−2.227	−4.576	154.7	−2.540	−4.263	157.6	−2.400	−4.403	157.6
Hf	hcp	−2.528	−4.275	144.7	−2.893	−3.910	147.4	−2.734	−4.068	147.5
Nb	bcc	−3.057	−3.746	120.9	−3.388	−3.415	123.1	−3.232	−3.571	123.0
Ta	bcc	−3.264	−3.538	115.5	−3.635	−3.168	117.4	−3.465	−3.338	117.4

The Ps affinity decreases (E_{K} increases) in each group (the only exceptions is Zr for electron GGA XC functionals). In addition, A_{Ps}'s in group V are below those in group IV. The same observation can be made for positron lifetimes (but a decrease occurs in group V only). It is approximately valid that the shorter is the lifetime (i.e. higher electron density), the higher is E_{K}. Intuitively, Ps can be emitted with higher kinetic energy from materials with higher electron density. On the other hand, this works for metals in the same part of the periodic table (Cu and Al cases do not perfectly match metals in group IV and V).

To the best of our knowledge, the only affinity known from experiment is $A_+ = -3.8$ eV for Nb [25]. In this case the agreement with experiment is the best for the LDA + LDA scheme. At first sight it may be surprising, but it is well known that electron GGA approaches do not always describe best materials with 4*d* and 5*d* where relativistic effects may play a role (see the discussion in Ref. [14]). In this respect, precise measurements of Ps affinity as in the case of Cu could help to clarify this problem.

The numerical uncertainty of calculated affinity values is about ±0.002 eV except Hf where ±0.003 eV is more appropriate. The point is that *d*-electrons require carefully chosen energy parameters for the basis. It is not necessary to include a local *d*-orbital (in contrast to Cu), but when we do so, some influence on affinity values is observed for Hf. We also note that $\boldsymbol{k}$-mesh sampling sensitivity is apparently smaller for all five studied elements when compared to Cu and Al.

Model alloys

One model alloy was constructed by putting randomly Hf, Nb, Ta, Ti, and Zr atoms into a $4 \times 4 \times 4$ bcc empty lattice supercell. Concentrations of all atoms are equal. The positions of atoms in the supercell were then relaxed using VASP considering the PBEsol XC functional and the experimental (bcc) lattice constant $a = 3.4089$ Å [26] (room temperature). The resulting configuration is marked as alloy R. In order to inspect the effect of possible local order, we also study a supercell of the same size where Ta atoms form a small, approximately spherical cluster in the supercell, whereas all other atoms are located randomly in remaining lattice sites. This supercell is also relaxed as in the case of completely random model alloy and marked as alloy T. The reason for considering Ta precipitation is that preliminary calculations indicate that Ta clusters could be thermodynamically stable at low temperatures [27]. The compositions of alloys R and T are exactly the same. Positron characteristics of relaxed supercells are calculated with the help of WIEN2k code (supplying the electron density and potential) as in the case of alloy constituting elements discussed above.

The results are collected in Table 4. For large supercells, testing various numerical parameters is a difficult task since it requires much more computational time. We have thus performed rather basic testing of $\boldsymbol{k}$-mesh sampling, basis energy cutoff and 3D mesh spacing of the positron program. Based on this, we suppose that affinity values have uncertainty about ±0.01 eV and calculated lifetime should not differ more than 0.2 ps from well converged values.

One can see that regardless of XC approach employed the Ps affinity of alloy R is always smaller (E_{K} larger) than for alloy T. This suggests that such type of local order could be detectable via A_{Ps} measurements. The necessary condition would be to 'calibrate' the measurements first using constituting elements. We also note that A_{Ps} for model

TABLE 4. Results of A_{Ps} and A_+ calculations for HfNbTaTiZr model alloys R and T; the bulk positron lifetime is also given. The estimated numerical uncertainty of affinity values is ±0.01 eV; see the text. The last line (ΔA) lists the difference of affinities (alloy R − alloy T).

Alloy	**LDA + LDA**			**PBE + GGA PF**			**PBEsol + GGA PF**		
	A_{Ps} (eV)	A_+ (eV)	τ (ps)	A_{Ps} (eV)	A_+ (eV)	τ (ps)	A_{Ps} (eV)	A_+ (eV)	τ (ps)
alloy R	−2.40	−4.40	139.7	−2.71	−4.09	142.5	−2.58	−4.22	142.4
alloy T	−2.36	−4.44	141.1	−2.67	−4.13	143.9	−2.54	−4.26	143.8
ΔA	−0.04	+0.04	–	−0.04	+0.04	–	−0.04	+0.04	–

alloy R is not equal to the average of A_{Ps}'s of constituting elements. This effect is due to large relaxations of atoms with respect to ideal (bcc) lattice sites and charge transfer among atoms in the alloy. The final point is that we should also look at other configurations with the same compositions differing just by random atomic arrangement. First calculations for another model alloy R indicate that A_{Ps} does not depend on this arrangement as far as it is really random.

CONCLUSIONS

The electronic structure of materials can be studied via positronium affinity, which can be both calculated using density functional theory and also measured in precise experiments. The comparison of 'theoretical' and experimental values allows to answer the question whether a given exchange-correlation approach is suitable for the description of a studied system. In this context, the series of numerical tests were performed in order to improve the precision of computational predictions of Ps and positron affinity. The $\boldsymbol{k}$-mesh sampling appears to be an important parameter along with a careful choice of energy basis parameters for APW/LAPW method. Predictions for the Ps affinity for Cu were improved, and new calculations were carried out for Al, constituting elements of a HfNbTaTiZr high entropy alloy and the alloy itself, considering also possible local order in the alloy. Several common XC approaches were tested along with SCAN (for Cu and Al), and other XC functionals, like DFT+U, hybrid, and effect of spin-orbit coupling, can in principle be tested using the same computational scheme. Another important aspect of the study is that the Ps (positron) affinity does not depend on the potential reference level (crystal zero), which makes it a true bulk property of materials, in contrast to electron and positron chemical potentials, which have to be always considered with respect to some reference energy level.

ACKNOWLEDGMENTS

Fruitful discussions with A. P. Mills are appreciated. At the Charles University the work was supported by the Czech Science Foundation under project 17-17016S. The computations carried out were supported by The Ministry of Education, Youth and Sports of the Czech Republic from the Large Infrastructures for Research, Experimental Development and Innovations project "IT4Innovations National Supercomputing Center – LM2015070". The work at the Northeastern University was supported by the US Department of Energy (DOE), Office of Science, Basic Energy Sciences grant number DE-FG02-07ER46352 (core research), and benefited from Northeastern Universitys Advanced Scientific Computation Center (ASCC), the NERSC supercomputing center through DOE grant number DE-AC02-05CH11231.

REFERENCES

[1] J. Kuriplach and B. Barbiellini, Phys. Rev. B **89**, p. 155111 (2014).
[2] A. C. L. Jones, H. J. Rutbeck-Goldman, T. H. Hisakado, A. M. Piñeiro, H. W. K. Tom, A. P. Mills, B. Barbiellini, and J. Kuriplach, Phys. Rev. Lett. **117**, p. 216402 (2016).
[3] P. J. Schultz and K. G. Lynn, Rev. Mod. Phys. **60**, p. 701 (1988).
[4] A. Harju, B. Barbiellini, and R. M. Nieminen, Phys. Rev. A **54**, 4849–4853 (1996).
[5] P. Hohenberg and W. Kohn, Phys. Rev. **136**, B864–B871 (1964).
[6] W. Kohn and L. J. Sham, Phys. Rev. **140**, A1133–A1138 (1965).

[7] D. M. Ceperley and B. J. Alder, Phys. Rev. Lett. **45**, p. 566 (1980).
[8] J. P. Perdew and Y. Wang, Phys. Rev. B **45**, p. 13244 (1992).
[9] J. P. Perdew, K. Burke, and M. Ernzerhof, Phys. Rev. Lett. **77**, p. 3865 (1996).
[10] J. P. Perdew, A. Ruzsinszky, G. I. Csonka, O. A. Vydrov, G. E. Scuseria, L. A. Constantin, X. Zhou, and K. Burke, Phys. Rev. Lett. **100**, p. 136406 (2008).
[11] J. P. Perdew, R. G. Parr, . Levy, and J. L. Balduz, Phys. Rev. Lett. **49**, 1691–1694 (1982).
[12] E. Boroński and R. M. Nieminen, Phys. Rev. B **34**, 3820–3831 (1986).
[13] N. D. Drummond, P. L. Ríos, R. J. Needs, and C. J. Pickard, Phys. Rev. Lett. **107**, p. 207402 (2011).
[14] B. Barbiellini and J. Kuriplach, Phys. Rev. Lett. **114**, p. 147401 (2015).
[15] P. Blaha, K. Schwarz, G. K. H. Madsen, D. Kvasnicka, and J. Luitz, *WIEN2k: An Augmented Plane Wave and Local Orbitals Program for Calculating Crystal Properties* (Vienna University of Technology, Austria, 2001).
[16] E. Sjöstedt, L. Nordström, and D. J. Singh, Solid State Commun. **114**, 15–20 (2000).
[17] O. K. Andersen, Phys. Rev. B **12**, 3060–3083 (1975).
[18] G. Kresse and J. Furthmüller, Phys. Rev. B **54**, 11169–11186 (1996).
[19] G. Kresse and D. Joubert, Phys. Rev. B **59**, 1758–1775 (1999).
[20] J. Sun, A. Ruzsinszky, and J. P. Perdew, Phys. Rev. Lett. **115**, p. 036402 (2015).
[21] A. H. Weiss and P. G. Coleman, in *Positron Beams*, edited by P. Coleman (World Scientific, Singapore, 2000), pp. 129–183.
[22] M. J. Puska and R. M. Nieminen, Rev. Mod. Phys. **66**, 841–897 (1994).
[23] H. Nakashima, T. Kubota, H. Kondo, Y. Murakami, and S. Tanigawa, Phys. Stat. Sol. (b) **170**, 171–188 (1992).
[24] O. Senkov, J. Scott, S. Senkova, D. Miracle, and C. Woodward, J. Alloys Compd. **509**, 6043–6048 (2011).
[25] D. W. Gidley and W. E. Frieze, Phys. Rev. Lett. **60**, 1193–1196 (1988).
[26] J. Zýka, J. Málek, Z. Pala, I. Andršová, and J. Veselý, in *METAL 2015: 24th International Conference on Metallurgy and Materials* (TANGER Ltd, 2015) p. 1687.
[27] J. Kuriplach, to be published.

Survey of Beta-Particle Interaction Experiments with Asymmetric Matter

J. David Van Horn[a)] and Fei Wu

Department of Chemistry, University of Missouri-Kansas City, 5110 Rockhill Rd., Kansas City, Missouri 64110 USA

[a)]Corresponding author: vanhornj@umkc.edu

Abstract. Asymmetry is a basic property found at multiple scales in the universe. Asymmetric molecular interactions are fundamental to the operation of biological systems in both signaling and structural roles. Other aspects of asymmetry are observed and useful in many areas of science and engineering, and have been studied since the discovery of chirality in tartrate salts. The observation of parity violation in *beta* decay provided some impetus for later experiments using asymmetric particles. Here we survey historical work and experiments related to electron (e^-) or positron (e^+) polarimetry and their interactions with asymmetric materials in gas, liquid and solid forms. Asymmetric interactions may be classified as: 1) stereorecognition, 2) stereoselection and 3) stereoinduction. These three facets of physical stereochemistry are unique but interrelated; and examples from chemistry and materials science illustrate these aspects. Experimental positron and electron interactions with asymmetric materials may be classified in like manner. Thus, a qualitative assessment of helical and polarized positron experiments with different forms of asymmetric matter from the past 40 years is presented, as well as recent experiments with left-hand and right-hand single crystal quartz and organic compounds. The purpose of this classification and review is to evaluate the field for potential new experiments and directions for positron (or electron) studies with asymmetric materials.

INTRODUCTION

Asymmetry in the universe and the origin of biological chirality are intricate and rich areas of scientific exploration [1-2]. For over four decades, researchers have been interested in the interactions of positron (e^+) particles with asymmetric matter [3-11]. A more general characterization would be to couch the problem in terms of *beta* particle (e^+ or e^-) physical interactions or *beta* particle-molecular reactions with different forms of asymmetric matter. Figure 1 illustrates these facets of *beta* particle interactions; in this conceptual scheme, scattering and a reaction equation are representative of *beta*-molecule physical interactions and reactions, respectively.

In this context, recent polarized *beta* scattering and diffraction experiments [12-14], electron induced reactions that exhibit asymmetry [15-17], and positron interactions with quartz and other materials [18-20] are instructive to categorize and characterize known and expected polarized *beta* particle interactions with both symmetric and asymmetric materials.

In the first instance above, asymmetric scattering of polarized (helical) electron beams from asymmetric organic molecules has been observed [13], while that with positrons has not [12]. Diffraction of electrons from thin films of asymmetric molecules has also been reported [14]. The polarized electron work was extended to the observation of asymmetries in electron-induced dissociative reactions in the gas phase, using halogenated camphor molecules [15-17]. Finally, recent work characterizing the interaction of positron with left and right chiral quartz crystal points to observable asymmetric interactions between positrons and materials [19].

The review, critique, and classification of reported polarized *beta* particle/molecular interactions with symmetric and asymmetric matter presents an opportunity to clarify prior confirmed or uncertain results. To this end, and toward the development of future experimental design and theory, the present paper presents a classification framework for known and potentially observable asymmetric *beta* interactions with matter.

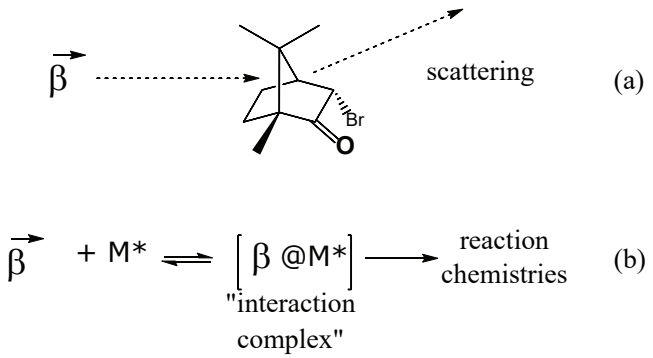

FIGURE 1. General schemes for polarized beta (β) scattering from an asymmetric target (a) or reaction chemistry with asymmetric materials or molecules (M*) (b).

ASYMMETRIC BETA INTERACTIONS WITH MATTER

This section will focus on scattering behavior and reaction interactions of beta particles with matter. In the gas phase at low energies, particles are expected to scatter off of molecular entities. Asymmetric scattering of electrons has been demonstrated, while that for positrons has not been exhibited yet. In terms of reactions, the addition of an electron is an overall chemical reduction in the system, while the positron that will act as an chemical oxidant in a system. If we evaluate the different forms of matter gas liquid and solid we see that the beta particles will give rise to different interactions and reactions the one may consider them to be supplementary.

In the liquid phase, solvated electrons will react quickly with oxygen or other atoms and it is not certain whether these reactions could be distinguished in an asymmetric fashion. For positron interactions in a liquid an asymmetric interaction is not expected due to positronium bubble formation. In this instance, while the surrounding molecules are asymmetric, the environment of the bubble would be quasi-spherical, probably prohibiting any asymmetric interactions or reactions.

Polarized *beta* particles impinging on amorphous solids are not expected to give rise to asymmetric interactions. This would be because the microenvironment is quasi-isotropic and the interactions or reactions would be averaged over all of the possible sites available to the *beta* particle and the resulting interactions.

In contrast, polarized *beta* particles directed into *asymmetric* crystalline forms of matter should give rise to asymmetric interactions. This has been observed for electron backscatter reactions and diffraction and mixed into reduction reaction processes. The interaction of polarized positrons with an asymmetric crystal environment is at the core of our present studies [18-20]. In this context, and taking a page from host-guest chemistry, one might expect the polarized positron to interact differently with the left or right pair of asymmetric host lattices. If an asymmetric physical interaction is observed, this may be extended to possible asymmetric reaction processes in solid crystalline environments that would yield product asymmetries.

TABLE 1. Conceptual interactions of helical *beta* particles or positronium (Ps) with asymmetric materials in different phases.

β	**Gas**	**Liquid**	**Solid (amorphous)**	**Solid (crystalline)**
e^-	Scattering off asymmetric HOMO; Reaction/Interaction with LUMO	Not expected, solvated electrons rapidly react with dioxygen or other atoms	Not expected.	Electron backscatter/ diffraction; reaction process [reduction]…
e^+ / Ps	Not yet observed; residence/ interaction time too small	Not expected, Ps bubble – quasi-spherical environment	Not expected, "isotropic" microstructure	Possible? Helical guest in asymmetric host lattice; reaction process [oxidation]…

BETA / MOLECULAR PHYSICAL STEREOCHEMISTRY

A way of classifying physical stereochemical interactions is threefold, i.e., as stereo*recognition*, stereo*selection* or stereo*induction* processes. In general, one could classify a stereorecognition event or process as one that is able to observe or distinguish between two asymmetric forms of a material, *i.e*. the enantiomeric pair or asymmetric set of left and right stereoisomeric forms (molecular, crystalline, macroscopic, etc.). In contrast, a stereoselection event would be a physical process where one of the stereoisomeric pair of objects is selected and acted upon preferentially. In chemical systems, this might be a separations process or preferential reaction. In this regard, some stereorecognition event may be a part of the stereoselection process, or the stereoselection may be accomplished by the differential stability in the interaction of two asymmetric entities. This type of interaction is termed "diastereomeric" and arises from stability differences in the interactions of L_1/L_2, R_1/R_2, L_1/R_1, R_2/L_2, *etc*. systems of molecules or particles. The last classification, stereoinduction, relates to the impressing of stereochemistry onto a *symmetric* target. Thus, stereoinduction arises from the interaction of an asymmetric entity on a symmetric entity to give rise to an asymmetric product.

As an aside, many reactions will give rise to stereochemical products, however if there is no asymmetric bias in the reaction, the resulting products are a 50/50 mixture of the two stereochemical outcomes. In the regime of stereoinduction, scientists are generally interested in processes that impart asymmetry to a symmetric target. In this regard, perhaps the interaction of polarized beta particles with *prochiral* targets (an object that could give rise to a stereochemical outcome) could be attempted. However, it is conceptually difficult to propose a scheme where the *helicity* of a particle or photon could be transferred to the prochiral target to give an *asymmetric* reaction result.

Table 2 outlines a conceptual framework for the possible interactions of helical particles with asymmetric (or symmetric, prochiral) targets to give rise to one of the physical stereochemical outcomes. The table is not exhaustive and should not be understood to be complete regarding the possible physical interactions of beta particles with matter, or the possible stereochemical outcomes in their interactions with matter. On the left, the helical particle and expected processes are listed and compared to the stereochemical categories. Regarding chemical reactions, the electron and positron necessarily give rise to reductive or oxidative reactions, respectively, in the media that they are found. Working backwards from this fundamental reaction difference and the difference in particle charge lends itself to the understanding that different physical and reactions processes would be expected for each of the *beta* particles. The expected different processes may be considered supplementary to each other, but some "opposite" physical interaction or reaction may not be anticipated as occurring for the opposite *beta* particle in all cases.

A final categorization that can be derived from this classification is that stereorecognition is related to physical interactions, whereas stereoselection or stereoinduction is related to beta particle reactions, *i.e*. a chemical reaction between the particle and the target. To clarify, stereoselection or stereoinduction events may be formally written as thermodynamic or kinetic reaction equations or pathways for the interaction of the *beta* particle with a molecular entity, *e.g*. Fig. 1b.

TABLE 2. Conceptual stereochemical interaction grid for helical particles with condensed phase materials.

Helical particle	Stereo-recognition	Stereo-selection	Stereo-induction
Electron scattering/diffraction	e^- / HOMO repulsion	---	---
Electron/molecule "reaction"	e^- / LUMO interaction	Selective reactions; polarized bremsstrahlung or other hypotheses [?]	[?] Selective *reduction* of a pro-chiral molecule
Positron scattering/diffraction	Presently not observed/detectable. e^+ / HOMO interaction; Z^* or lattice interactions.	---	---
Positron/molecule "reaction"	Host / guest interaction with asymmetric single crystal lattices	Selective oxidation of one stereoisomer [?]	[?] Selective *oxidation* of a pro-chiral molecule

HOMO, highest occupied molecular orbital; LUMO, lowest unoccupied molecular orbital; Z^*, effective nuclear charge.

POSITRON STEREORECOGNITION OF QUARTZ

As an example of positron stereorecognition of an asymmetric material, we studied left- and right-handed quartz crystals [19]. As part of the DBES measurements in our experimental campaign, quartz crystals were evaluated in a number of different orientations. In the first case, DBES depth profiling with a mono-energetic positron beam was completed on the obverse and reverse sides of thin quartz crystal discs. The asymmetry of crystalline quartz is related to a helical arrangement of SiO_4 tetrahedra oriented along the z-axis. The two faces align the helix of the crystal with the incident beam, and should give rise to the same profile, barring any differences in the surface or defect quality of the crystal on the opposite faces. This result is included in Figure 2 for RH quartz. Additionally, the effect of rotating the crystal in the beam to various relative angles (0°, 45°, 90°, 135°) was conceived as a way to test the variability in the depth profile result for a single face. These data are also included in Figure 2 for LH quartz, and the experiment design is shown as a scheme inset. We note that the variability in the S parameter for measurements in the bulk sample region (i.e. >5 keV implantation energy) is less than 0.005 for each type of crystal, whereas the difference between the right-hand and left-hand crystal profiles are approximately 0.01. An estimate of a 5% error in the S-parameter would give error bars that are approximately the same size as the shown data points.

These results taken together, and complementary PALS data [19], is interpreted as indicating stereo*recognition* by the polarized positron of the asymmetric crystals. The observed variability in the profiles of the front and back faces, and in the profiles at varied relative angle, may arise from minute differences in crystal surface and bulk quality, and small variations in the beam impinging on the sample. This variability is much less than the difference observed between right and left quartz.

A report that may parallel our recent left- and right-hand quartz experiment evaluated muonium interactions with a set of chiral quartz crystals [21]. In this experiment, a pair of crystals were probed with forward and reverse polarized muons in *z* and non-*z* orientations. The source of muon was a cyclotron beamline. The results indicated there was no appreciable difference in the amplitude of the triplet muonium signal, evaluated over both crystal orientations, and with the forward or reverse muon beam. The absence of an asymmetric difference with in the error of the experiment may relate to a difference in the muon interaction with the asymmetric crystal (compared to positron). However, we note that the "L quartz" sample (assumed to be LH quartz) was a natural crystal, versus the synthetic "D quartz" sample. This is significant in that natural quartz exhibits 'twinning' and possesses oppositely helical domains within a crystal that may be predominantly RH or LH—identified visually by crystal habit or polarized light microscopy. Thus, an asymmetric observation in the muonium experiment may have been masked by the selection of a natural crystal sample.

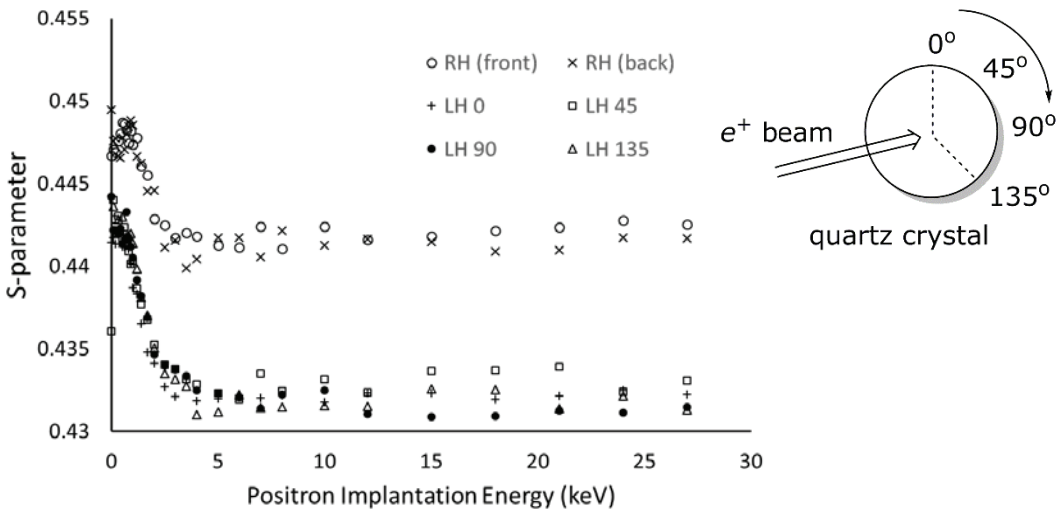

FIGURE 2. DBES profiles at varied positron implantation energies for RH quartz crystal on opposite faces or LH quartz physically rotated at varied relative orientation. Inset: schematic of LH quartz orientation in beam.

BETA POLARIMETRY

As an aside, in the present particle physics literature, the term "polarimetry" relates to the measurement of the helicity found in particles emitted from a radionuclide or the residual or induced helicity of a particle beam [22-25]. This is to be distinguished from the stereochemical technique of "optical polarimetry", which uses polarized light to determine the relative amounts of two asymmetric forms of molecules in a sample. Polarized light microscopy was used in the above quartz studies to verify the chirality of synthetic and natural quartz samples. In the work on positron polarimetry, positron helicity in beam samples has been measured to within 1% for polarizations greater than P = 0.69 at moderate to good e^+ intensity (10^3 - 10^5 /sec). Studies applying polarized positrons range in their selection of material studied, and appear to unsystematic. Convenient access to a dedicated, variable polarity, positron beam would allow for a significant program in materials studies to be conducted. While useful for amorphous, metallic or crystalline materials in general, studies with asymmetric forms of matter may be a more promising avenue for exploration of new positron phenomena.

POLARIZED POSITRON PROSPECTS

Future studies with low-energy polarized *beta* particles, especially the positron, will benefit from combined particle physics, chemical, and theoretical research teams. Opportunities to make advances in the area lie in 1) the generation high helicity, high-intensity *beta* particle beams, 2) the straightforward measurement of particle helicity from various sources, 3) the production of variable-helicity beams, and 4) the theory of helical particle interactions with matter.

Following, in synoptic format, are brief proposals for possible future polarized particle interactions with matter.

- **Gas Phase**. While the recent experiment of Chiari, *et al*. [12], indicated no asymmetry in the scattering of positrons with asymmetric molecules in the gas phase, it may be that this type of reaction should be revisited with different types of asymmetric molecules. Chiral molecules that are larger (*e.g*. camphor [13, 17]) or those in point groups C_n or D_n may give rise to asymmetric scattering results. Disubstituted allenes and biphenyls are examples of possible molecules for this further study, but may have the attendant problem of low vapor pressures, inhibiting gas-phase sample preparation.
- **Liquid Phase**. PALS studies investigating chiral liquids [6-7] should be repeated with a focus on the liquid-to-frozen transition. In the liquid and frozen states, PALS should be studied with molecules that exhibit some order in the liquid phase, or that lend themselves to a high degree of crystallinity in the frozen state. Moving away from pure liquid-state experiments, self-assembled monolayers (SAMs) of chiral molecules, or asymmetric liquid crystals [26] may also offer opportunity to observe asymmetric positron interactions.
- **Solid phase**. The procurement of suitable, large single-crystal enantiomorphs is difficult. Further explorations of asymmetric, solid-phase materials will be best accomplished by using thin films in polarized positron beams. This approach lends itself to depth profiling experiments as in [19], but presents difficulty in obtaining "free positron" annihilation lifetimes, unless novel, high-resolution techniques can be obtained or applied. Studies with asymmetric solids need to be completed using AMOC techniques and 2D-ACAR. Finally, positron/asymmetric material reaction chemistry may be feasible by using homogeneous racemic single crystals or other crystalline materials.
  With the aforementioned classification schemes and the consideration of positron redox chemistry, it seems feasible to design a molecular sample and experiment that exhibits a positron stereo*selection* reaction. This would confirm or deny the possibility of such a reaction, attempted previously [8-9, *etc*.], and may allow the determination of the quantitative range of such a phenomenon.
- **2D-ACAR and AMOC**. Angular correlation of annihilation radiation utilizing a polarized positron beam offers a unique opportunity to study symmetric and asymmetric materials [27-28]. Of priority should be the exploration of asymmetric single crystals in various orientations; thin film asymmetric materials will also be amenable to this technique. In addition, oriented polymers or polymers that exhibit tacticity using well-characterized samples would benefit from dedicated 2D-ACAR studies. Finally, age momentum correlation (AMOC) techniques, either with bulk or thin film samples, in standard or beam experiments, may offer insight into asymmetric positron interactions.

ACKNOWLEDGMENTS

We would like to acknowledge the contributions of past and present students and visiting scientists in the Positron Science Laboratory at UMKC. JDVH especially thanks Professor Emeritus Y. C. Jerry Jean for his mentorship in the Department of Chemistry (2002-present) and encouragement for our current pursuits in positron and material science research.

REFERENCES

1. A. Guijarro and M. Yus, *The Origin of Chirality in the Molecules of Life* (RSC Publishing, Cambridge, 2009).
2. J. M. Hicks, Ed., *Chirality: Physical Chemistry* (Am. Chem. Soc., Washington, DC, 2002).
3. A. S. Garay, L. Keszthekyi, I. Demeter and P. Hrasko, Nature, **250**, 332-333 (1974).
4. M. M. Ulrich and D. C. Walker, Nature, **258**, 418419 (1975).
5. A. Rich, Nature, **264**, 482-483 (1976).
6. Y. C. Jean and H. J. Ache. J. Phys. Chem. **81**, 1157-1162 (1977).
7. Y. C. Jean and H. J. Ache. "Search for Selectivity between Optical Isomers in Interaction of Positrons with Chiral Molecules." in *Origins of Optical Activity in Nature*, edited by D. Walker (Elsevier Scientific Pub. Co.: Amsterdam, 1979), pp.67-83.
8. D. W. Gidley, A. Rich, J. Van House and P. W. Zitzewitz, Nature, **297**, 639-643 (1982).
9. R. A. Hegstrom, Nature, **297**, 643-647 (1982).
10. J. Van House and P. W. Zitzewitz, Phys. Rev. A, 29, 96-105 (1984).
11. W. A. Bonner, Top. Stereochem. **18**, 1-96 (1988).
12. L. Chiari, A. Zecca, S. Girardi, A. Defant, F. Wang, X .G. Ma, M. V. Perkins and M. J. Brunger, Phys. Rev. A, **85**, 052711 (2012).
13. S. Mayer, C. Nolting and J. Kessler, J. Phys. B: At. Mol. Opt. Phys. **29**, 3497-3511 (1996).
14. K. Ray, S. P. Ananthavel, D. H. Waldeck and R. Naaman, Science, **283**, 814-816 (1999).
15. J. M. Dreiling, S. J. Burtwistle and T. J. Gay, Appl. Optics, **54**, 763-769 (2015).
16. J. M. Dreiling and T. J. Gay, J. Phys. Conf. Ser. **635**, 012015 (2015).
17. J. M. Dreiling, F. W. Lewis, J. D. Mills and T. J. Gay, Phys. Rev. Lett. **116**, 093201 (2016).
18. G. A. Corsiglia, "Asymmetric positron annihilation in chiral tartrate and tartaric acid crystals," M.S. Thesis, University of Missouri, 2015.
19. J. D. Van Horn, F. Wu, G. Corsiglia and Y. C. Jean, *Defect. Diffus. Forum* **373**, 221-226 (2016).
20. B. Eren, F. Wu, E. Eren, Y. C. Jean and J. D. Van Horn, *Acta Phys. Pol. A* **132**, *accepted* (2017).
21. D. P. Spencer, D. G. Fleming, J. H. Brewer and R. J. Mikula, "A Search for Chirality Dependent Muonium Formation in Quartz Crystals," in Origins of Optical Activity in Nature, edited by D. C. Walker (Elsevier Science Ltd., New York, 1979), pp. 87-99.
22. P. W. Zitzewitz, J. C. Van House, A. Rich and D. W. Gidley, *Phys. Rev. Lett.* **1979**, *43*, 1281-1284.
23. A. Skalsey, T. A. Girard, D. Newman and A. Rich, *Phys. Rev. Lett*. **1982**, *49*, 708-711.
24. J. C. Van House and P. W. Zitzewitz, *Phys. Rev. A*, **1984**, *29*, 96-105.
25. A. Rich, J. C. Van House, W. Gidley, R. S. Conti, P. W. Zitzewitz, *Appl. Phys. A* **1987**, *43*, 275-281.
26. J. J. Singh, A. Eftekhari and D. S. Parmar, "Positron Lifetime Measurements in Chiral Nematic Liquid Crystals." (NASA, Washington, D.C., 1991).
27. H. Chen, J. D. Van Horn, Y. C. Jean, W.-S. Hung and K.-R. Lee. *AIP Conf. Ser*. **2013**, *1525*, 448-451.
28. Y. C. Jean, J. D. Van Horn, W.-S. Hung and K.-R. Lee. *Macromolecules* **2013**, *46*, 7133−7145.

The PEPPo Method for Polarized Positrons and PEPPo II

Lawrence S. Cardman[1, a)] (for the PEPPo Collaboration)

[1] Thomas Jefferson National Accelerator Facility, 12000 Jefferson Ave., Newport News, VA 23606

[a)] cardman@jlab.org

Abstract. The Polarized Electrons for Polarized Positrons (PEPPo) experiment at the injector of the Continuous Electron Beam Accelerator Facility demonstrated for the first time the efficient transfer of polarization from electrons to positrons via a two-step process: polarized bremsstrahlung radiation is induced by a polarized electron beam in a high-Z target; then the polarized bremsstrahlung produces polarized positrons via the pair-production process in the same target. Positron polarization up to 82% was measured for an initial electron beam momentum of 8.19 MeV/*c*, limited only by the electron beam polarization of 85%. This technique extends polarized positron capabilities from GeV to MeV electron beams, and opens access to polarized positron beam physics to a wide community. We will present the results of the PEPPo experiment and outline tentative plans for a follow-up experiment that would investigate key aspects of an approach based on PEPPo as a polarized positron source for the 12 GeV Upgrade of CEBAF.

INTRODUCTION

Polarized electrons have been key to some of the highest impact results from the JLab program, including: measurements of the strangeness distribution in the nucleon (HAPPEX [1] and G0 [2]); precision tests of the Standard Model (Q_{Weak} [3]); a measurement of the neutron radius of ^{208}Pb (PREx [4]); and the accurate determination of the ratio G_E/G_M for the proton [5] using the polarization transfer technique. During the life of the "6 GeV Program", the quality and intensity of polarized beams has evolved remarkably. Between the first experiment in 1995 and the shutdown in May of 2012 for the start of the 12 GeV Upgrade the Figure of Merit (P^2I) improved by a factor of 42 (from 30 μA beams with 35% polarization to 200 μA beams with 89% polarization) [6].

Positron beams would provide a key tool for pushing the precision of electron scattering experiments further. The comparison of e^- results with the same data taken with e^+ beams tests our understanding of two photon effects in electron scattering, which currently define the limit of precision of these experiments. Furthermore, if the positron beams can be polarized two additional possibilities present themselves. First one could expand the nature and sensitivity of the two photon effect experiments by allowing direct measurements of two photon effects in the polarization transfer experiments (such as G_E/G_M for the proton). Second, they would provide an essential tool for unraveling nucleon structure through the measurement of the charge-sensitive Generalized Parton Distributions (GPDs). This and a number of other very interesting possibilities are the subject of this workshop (and the previous one [7]), so I will not try to be exhaustive here. I note also that there is a great interest in polarized and unpolarized positron beams for condensed matter physics (again, see talks at this workshop and in ref. [7]).

The Polarized Electrons for Polarized Positrons (PEPPo) experiment [8] demonstrated a viable approach to the efficient production of polarized positrons for CEBAF. It used the highly polarized electron beam available from the CEBAF source and generated polarized positrons through a two-step process: bremsstrahlung followed by pair production, with both reactions taking place (in series) in the same physical target. Calculations by Olsen and Maximon [9], generalized to any particle energy Kuraev, *et. al*. [10], demonstrate how these two processes may combine to produce polarized positrons. First the longitudinal polarization of the incident electron beam is transferred to circular polarization of the bremsstrahlung produced early in the target (see Fig. 1a). As can be seen in Fig. 1a, the calculations indicate that the transfer efficiency increases as the photon energy approaches the electron beam energy.

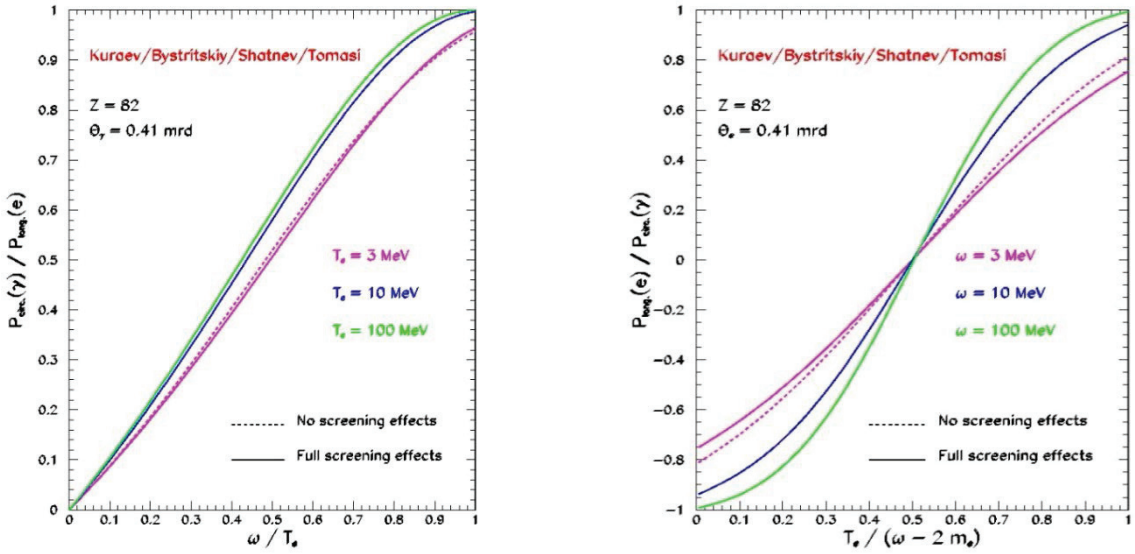

FIGURE 1. **a** (left) the circular polarization of the photons produced by longitudinally polarized electrons at a fixed production angle of 0.41 mrd for several electron beam energies and for the extreme cases of full or no screening as a function of the ratio of the photon energy to the electron energy; **b** (right) the electron/positron longitudinal polarization resulting from the pair production by circularly polarized photons for the extreme cases of full or no screening for several photon beam energies as a function of the ratio of the positron energy to the photon beam energy less the sum of the electron and positron masses [11].

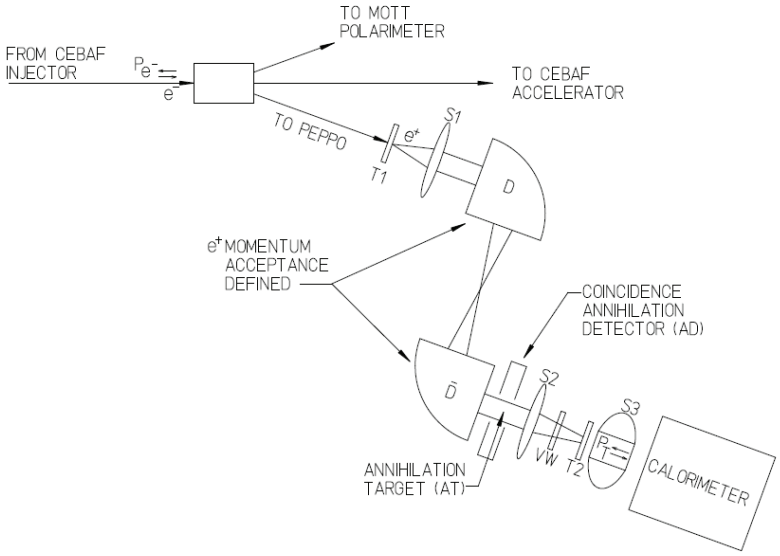

FIGURE 2. Schematic of the PEPPo experiment beamline [8]. T1 is the target in which the incident polarized electron beam produces polarized bremsstrahlung, which, in turn, produces a polarized e^+e^- pair; D and $\bar{D}$ are 90° dipole bending magnets; S1 and S2 are solenoidal lenses; and VW is a vacuum window, isolating the Compton transmission polarimeter. The polarimeter consists of a conversion target (T2), an iron cylinder that has its polarization saturated by solenoid S3, and a calorimeter consisting of a 3x3 array of CsI crystals (see Ref. [8] for a more complete description).

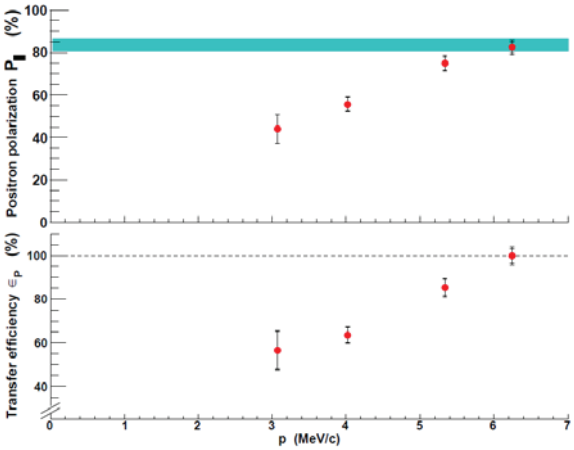

FIGURE 3. PEPPo measurements of the positron polarization (top panel) and polarization transfer efficiency (bottom panel); statistics and systematics are reported for each point, and the shaded area indicates the electron beam polarization [8].

Fig. 1b shows how the polarization is then transferred from the circularly polarized photon to the e^+e^- pair; the efficiency of the polarization transfer increases as the positron energy approaches the energy of the gamma ray (less twice the positron mass).

These calculations were tested by the PEPPo experiment. The layout of the experiment is shown in Fig. 2. After the production of the e^- e^+ pair by the combination of bremsstrahlung and pair production in the same target (T1 in the figure), the beam is passed through a combination of magnets and slits that select a subset of the positrons from the produced pairs, and defines the longitudinal and transverse emittance of the output positron beam. In the PEPPo experiment the intensity of the positron beam was then determined by inserting the annihilation target (AT) and measuring the counting rate in the coincidence annihilation detector (AD). Then the polarization of the positron beam was measured using the Compton Transmission Polarimeter. Results of PEPPo, for an incident polarized electron beam of 8.2 MeV/*c* and 85.2% polarization are shown in Fig. 3. The transfer of the initial electron beam polarization to the extracted positron beam can be very efficient, approaching 100% as the positron beam momentum approaches the initial electron beam momentum.

PEPPo demonstrated convincingly the merits of the polarization transfer technique making it worthwhile to explore the optimization of the technique for the production of positron and polarized positron beams in support of the physics program of the 12 GeV Upgrade. Given the rapid increase in positron production (for positrons within a useful phase volume) with the energy of the electron beam used to produce the positrons, one can speculate that an excellent approach to the production of a very intense positron beam at CEBAF would be to use the 2.2 GeV beam from the first pass through CEBAF to generate positrons, transport this beam to the injection point (adding a phase shift relative to the electron beam) and then accelerate this beam through the full, CEBAF accelerator. This would require the reversal of the fields in all of the recirculation system and the addition of a 6th recirculation path placed below the current system to transport the initial electron beam to the positron production target. It would, however, be a very expensive solution. When polarized positrons are desired it would be essential to investigate the optimization of the Figure of Merit ($P_z^2 I$); based on the calculated behavior seen for lower energy polarized positron production, one can speculate that it would be useful to "tweak" the system so that the energy of the positrons selected for injection into CEBAF would be roughly half of the first pass energy [12]. The acceleration phase of the positron beam in the first (North) linac could then be adjusted so that the energy of the beam after acceleration in that linac was the nominal (1.1 GeV) energy of the usual electron beam at that point. For the case where unpolarized positrons are desired, it is likely that the maximum useful positron flux would be obtained by selecting positrons at energies as low as 123 MeV (the standard energy of the injector for CEBAF at 12 GeV) and to accelerate them through the first linac with full energy gain (i.e. at a phase 180° away from the standard electron phase).

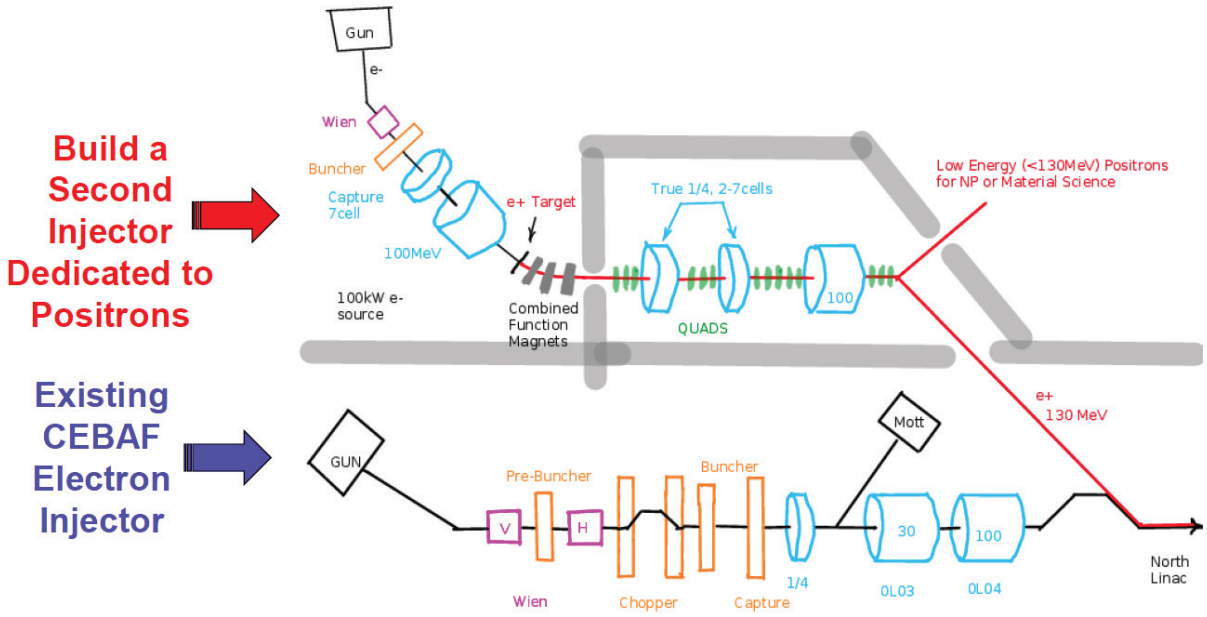

FIGURE 4. The approach to adding positron capability to CEBAF suggested by S. Golge in his thesis [13]; figure developed by A. Freyberger [14].

A second approach to positron beams for CEBAF, proposed by Serkan Golke [13], is shown in Fig. 4. The idea is to build a complete second injector dedicated to positron production. The new injector would be built in a new building located adjacent to the current injector tunnel. A 123 MeV electron linac with a polarized electron source would drive a positron production target. A slit and magnet system that follows the production target would select the positrons to be accelerated. They would then be passed through a second linac, accelerated to 123 MeV for injection into CEBAF (with a 180° phase shift relative to the usual electron injection phase) and accelerated in CEBAF to the desired energy (with all the magnetic fields in the recirculation system reversed). Golke estimated that with a 10 mA electron beam from the first linac this approach would comfortably produce a 3 μA polarized positron beam. One advantage of this approach is that the positrons could also be made available at low energies appropriate for condensed matter research without impacting CEBAF nuclear physics operations by simply operating the positron production system independently and diverting the beam into a low-energy experimental hall that could be constructed adjacent to the positron source.

A third approach, summarized in Fig. 5, would utilize the standard CEBAF injector, modifying it to both produce the positron beam and then accelerate it (via recirculation at the appropriate phase) back through the injector linac to raise the positron beam's energy to the standard electron injection energy of 123 MeV. The standard operation of the injector has a gun energy of 130 keV. In the capture section the energy is increased to 500 keV, and in the Cryounit (¼ of a cryomodule) the energy is increased to 6.3 MeV. This beam is then sent through a pair of standard cryomodules, increasing the energy by 116.7 MeV to bring the beam energy to the 123 MeV used for injection into CEBAF and acceleration to energies up to 12 GeV. As can be seen in the figure, we can modify and extend this system to provide a polarized or unpolarized positron beam. To begin, the 123 MeV polarized electron beam (normally sent to CEBAF to be accelerated to up to 12 GeV) is instead turned 180° back toward the gun and sent through a positron production target. This is followed by a (to be designed) slit and magnet system that selects the appropriate portion of the positron beam (setting the central energy of the beam, its energy spread, and its transverse emittance). This would be followed by a path length adjusting system (basically similar to the path length adjustment systems used in the recirculation of beams through CEBAF) that would permit adjusting the phase of the positrons at the entrance of the injector cryomodules relative to the electron beam. The positrons could then be accelerated to

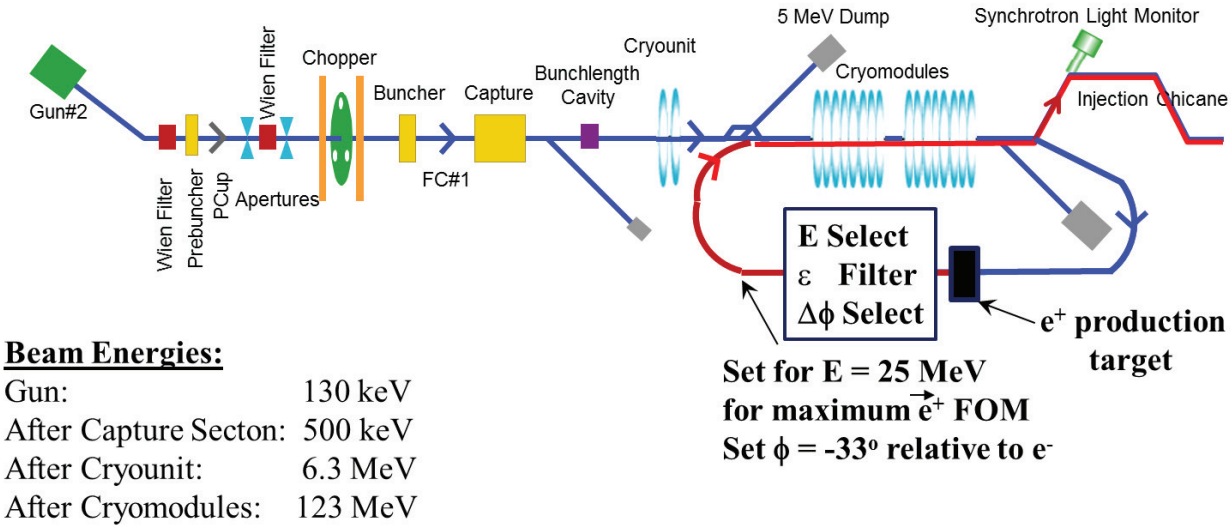

FIGURE 5. An approach to the development of positron capability for CEBAF using the injector linac both to produce the positrons and to accelerate them. The choice of an injected positron energy of 25 MeV is based on the general behavior of the figure of merit for the positron beam that peaks at about ¼ of the production beam energy when beam emittance considerations are taken into account.

123 MeV for injection into CEBAF and then accelerated to the full energy of CEBAF by reversing the fields in the recirculation magnets and setting the phase of the main linacs for positron rather than electron acceleration. This scheme has the advantage that it probably minimizes the cost of developing a positron beam. The low energy of the injector recirculation system means that the cost of the magnetic elements would be modest. To help refine the approach and estimate the positron beams it could produce, J. Grames [15] has used the GEANT4 model developed by J. Dumas [12] that produces results at high energies consistent with the theory of Kuraev, *et al*. [10] to calculate the positron production using the full energy of the 85% polarized electron beams from the injector (123 MeV). For these calculations we examined the positron beams produced by a 0.5 mm diameter polarized electron beam for two phase space acceptances: first with a constant angular acceptance of 10° and an energy spread of 1 MeV (to compare with earlier calculations); and then for an energy spread of 1 MeV and a normalized emittance of 2400 mm mr (to be within the maximum geometric acceptance of 10 mm mr when injecting into CEBAF from the injector linac). The results shown in Figs. 6 and 7.

Figure 6a displays the calculated intensity of the positron beam produced by a 123 MeV polarized electron beam as a function of the positron energy; the positron yield (emerging from the emittance filter) drops by about two orders of magnitude as the positron energy selected increases from 10 MeV to 70 MeV. As shown in Fig. 6b, the polarization increases smoothly from small values at low positron energies to the incident beam polarization as the positron energy approaches the electron beam energy. The combination of these two effects results in the figure of merit (P^2I) for the positron beam shown in Fig. 7 as a function of positron energy. If one could use the full 10° acceptance the optimum occurs at about half the electron beam energy as the decrease in intensity overcomes the increase in positron polarization as the positron energy increases toward the beam energy. This feature, of an optimum FoM at about half the electron beam energy, is a general feature of such calculations for a range of electron energies. However, if the phase space of positrons accepted is reduced to the maximum allowable acceptance of the first CEBAF linac the optimum FoM occurs at a positron energy of 25 MeV, about ¼ of the electron beam energy.

Setting the emittance filter for a positron energy of ~25 MeV for a maximum Figure of Merit for the positron beam, we must then adjust the phase of the positron beam relative to the cryomodule RF to about 33° to provide an energy gain of 98 MeV going through the two cryomodules. This would result in a final positron energy of 123 MeV, which is correct for injection into CEBAF via the standard injection chicane (with its fields reversed, as would be the

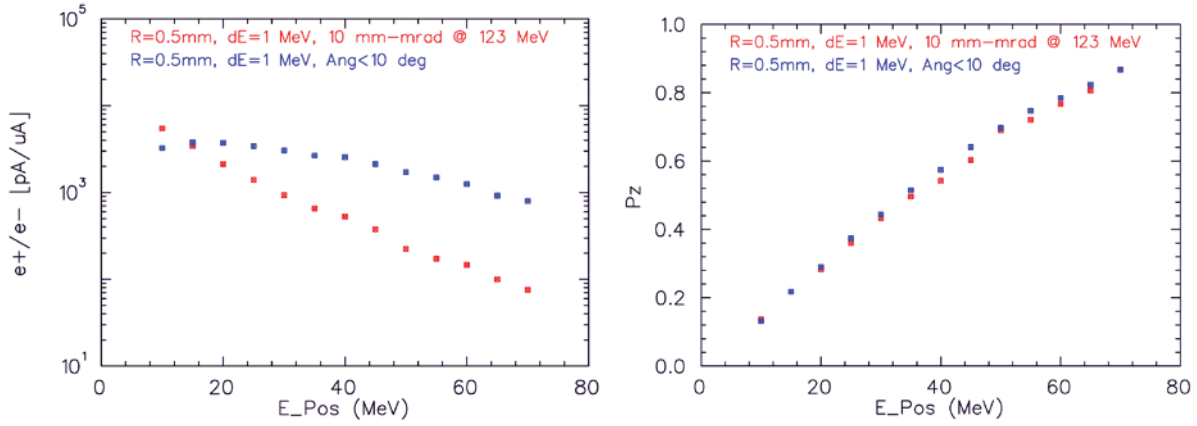

FIGURE 6. **a** (left) calculations [15] of the positron to electron ratio for positron production by a 123 MeV 85% polarized electron beam; **b** (right) the longitudinal polarization of that positron beam; both are shown as functions of the positron beam energy. The red data points correspond to the selection of produced positrons within an energy spread of 1 MeV and a normalized emittance of 2400 mm mr, while the blue data points correspond to selection with the same energy spread but within a constant angular acceptance of 10°.

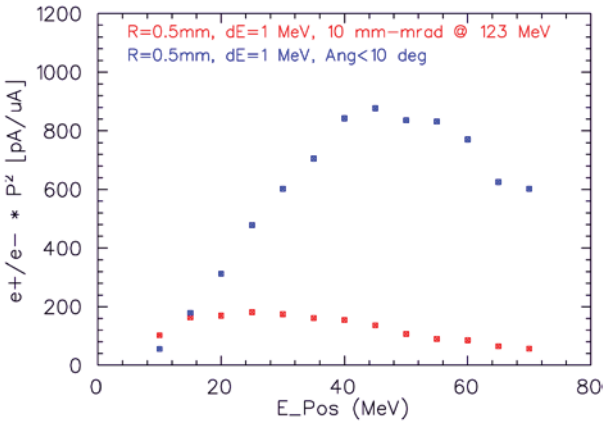

FIGURE 7. the Figure of Merit ($P_z^2 I$) for the positron beam produced by a 123 MeV 85% longitudinally polarized electron beam as a function of the positron energy [15]. As is the case for the curves in Fig. 6, the red data points correspond to the selection of produced positrons within an energy spread of 1 MeV and a normalized emittance of 2400 mm mr, while the blue data points correspond to selection with the same energy spread but within a constant angular acceptance of 10°.

case for all the magnetic fields in CEBAF). It would also permit some energy compression during the acceleration, meaning a larger energy spread could be accepted at the cryomodule entrance. Very rough estimates assuming the standard 100 μA, 85% polarization electron beam used in normal operations of CEBAF suggest that this scheme would produce positron beams with intensities of 100-200 nA and a polarization of about 40%. With the installed RF in the injector it would be straightforward to increase the current available for positron production to about 200 μA, doubling the estimated positron current to 200-400 nA. Further, one could obtain an even higher intensity beam by increasing the intensity of the polarized electron beam. This would require an upgrading of the RF system for the injector cryomodules. A >500 μA electron beam is estimated to provide a microampere polarized positron beam. Of course the details should be calculated precisely so one can be sure that the scheme has indeed been optimized.

If the positron beams needed for a particular experiment do not have to be polarized, we can take advantage of the fact that the positron to electron ratio increases as the positron energy selected is lowered relative to the electron beam energy (see Fig. 6a above). At an extreme, one could set the filter downstream of the positron production target for a positron energy as low as 6.3 MeV (the nominal energy of the polarized electron beam after the ¼ cryomodule), and then set the phase so the positron beam is 180 degrees out of phase relative to the electron beam. It would then get the same acceleration through the cryomodules as the electron beam does, and emerge at 123 MeV for injection into CEBAF. An optimization might well end up with a somewhat higher positron energy so that the acceleration would be off-crest and provide some energy compression in addition to the acceleration of the positron beam. One anticipates that this approach would result in positron beams of order two microamperes with a 200 μA polarized electron beam drive (and a beam of order 5 μA if we increased the drive beam to 500 μA). Currents this high have the advantage that they are visible using the standard beam diagnostics in CEBFAF, so tuning the beam should be straightforward. One interesting possibility that may be worth considering is the use of this beam to tune CEBAF for positron operation and then switch to polarized positrons simply by readjusting the "filter" system for optimum Figure of Merit of the polarized positrons and setting the phase shift of the recirculated positrons in the injector linac correctly relative to the electron phase.

In developing plans for positrons in CEBAF there are a number of issues that must be considered. First, the beam handling system that collects the positrons will have to be set stringently so that the positron beams leaving the injector after acceleration will be fully accepted in CEBAF. This means of order 100 keV energy spread and 10 degrees phase spread for the beam at 123 MeV [16]. In addition, the standard beam monitoring system used to tune full energy CEBAF beams requires about 2 μA of beam current for the necessary accuracy [14]. If we cannot reach this current for polarized positron beams with optimum FoM, it may be interesting to consider using the much higher intensity unpolarized positron beams that could be made available to tune CEBAF, and then switch to polarized positrons for the experiment(s) of interest.

So What Are the Next Steps? To begin, the anticipated yields of polarized and unpolarized positrons feasible with the beams from the 123 MeV CEBAF Injector should be calculated precisely, with the present preliminary investigations extended to include a study of the bunching possible for the positrons in the injector linac and setting precise constraints on the 123 MeV beam longitudinal and transverse emittance to ensure full acceptance in CEBAF. This should be followed by a "PEPPo-II" experiment. Key apparatus (the E Select, ε Filter, and $\Delta\phi$ Select in the figures above, the production target, and the associated electron beam dump) should be designed and built. Then this apparatus should be used (either at the CEBAF injector or at LERF) to measure the polarized and unpolarized positron yields within the acceptance specifications of CEBAF to verify the merits of this approach and prepare for positron beams at 12 GeV. I note that if we have built the apparatus for this test carefully, and the calculations are accurate, it should be straightforward to simply install it on the CEBAF injector.

With a polarized and unpolarized positron source ready to use, there are other issues to discuss and resolve. The first is the magnetic recirculation in CEBAF. The electron beam circulates clockwise. For the positron beam to do the same it will be necessary to reverse all of the unipolar power supplies that drive the recirculation dipoles. The field reversal problem is simpler for the focusing quadrupole and steering correctors as they already have bipolar supplies. If one anticipates significant positron running it would no doubt be valuable to install reversing switches on the dipole power leads rather than having to switch the leads for each positron run.

A second difficulty will be the relatively low current of the positron beams, causing difficulties for both the tuning and maintenance of positron beams. Most of the accelerator and Hall B monitors are blind to currents below 100 nA and key monitors need a few microampere beam for precision setup. As noted earlier, in the event that polarized positrons will not be available with adequate current for machine setup, it may be feasible to use the unpolarized positron beam to setup CEBAF, and then switch to polarized positrons for the experiment of interest. It may also be desirable to add supplemental high-sensitivity monitors to monitor the low intensity positron beam during operation.

On a positive note, work is already underway in many areas relevant to the production of polarized positron beams. A key effort is work on improving the lifetime of the polarized electron source at high beam currents (see, e.g. [17,18]). Related work is improving the photocathodes used for the production of the polarized electron beam. The distributed Bragg reflector approach to photocathodes is of particular importance, and has demonstrated a factor of four improvement in the quantum efficiency relative to the familiar GaAs–GaAsP multilayer photocathodes [19]. Finally,

work is underway at Niowave [20] on the development of high power targets suitable for the polarized positron production; using a liquid metal target they have already demonstrated the 10 kW power level.

To summarize, I note that the PEPPo experiment demonstrated an excellent approach to providing highly spin-polarized positrons from moderate energy polarized electrons, opening a variety of physics possibilities for CEBAF's research program (and in condensed matter physics). This workshop provides both a review of the physics that can be done, and a review of much of the relevant technology being developed to enable a high-energy polarized positron beam program for CEBAF@12 GeV (and JLEIC) based on the PEPPo technique. The possibilities are fascinating and I urge the community to pursue them diligently.

ACKNOWLEDGMENTS

I would like to thank Joe Grames, Eric Voutier, Arne Freyberger, Yves Roblin, Reza Kazimi, and Michael Tiefenback for their help in the preparation of this talk, and Joe Grames and Eric Voutier for a thoughtful critique on the manuscript. This material is based upon work supported by the U.S. Department of Energy, Office of Science, Office of Nuclear Physics under contract DE-AC05-06OR23177.

REFERENCES

1. K.A. Aniol, *et al*., Phys. Rev. C **69,** 065501 (2004), K.A. Aniol, *et al*., Phys. Lett. B **635**, 275 (2006), K.A. Aniol, *et al.*, Phys. Rev. Lett. **96**, 022003 (2006).
2. D. S. Armstrong, *et al.,* Phys. Rev. Lett. **95**, 092001-1-5 (2005).
3. D. Androic, *et al*., Phys. Rev. Lett. **111**, 141803 (2013).
4. C. Horowitz, *et al*., Phys. Rev. C **63**, 025501 (2001).
5. A. J. R. Puckett, *et al.*, Phys. Rev. C **96** (2017) 055203, and references therein to earlier measurements.
6. L. Wei, M. Poelker, M. Stutzman, S. Zhang, A. Moy, Y. Chen, and W. Lueed, Applied Physics Letters **109**, 252 (2016).
7. *Proceedings of the International Workshop on Positrons at Jefferson Lab*, L. Elouadrhiri, T. A. Forest, J. Grames, W. Melnitchouk, and E. Voutier (eds.), March 25-27, 2009, AIP Conf. Proc. **1160**, (2009).
8. (PEPPo Collaboration) D. Abbott, *et al.* , Phys. Rev. Lett. **116,** 214801 (2016)
9. H.A. Olsen and L.C. Maximon, Phys. Rev. **114** (1959) 887.
10. E.A. Kuraev, Y.M. Bystritskiy, M. Shatnev, and E.Tomasi-Gustafsson, Phys. Rev. C **81**, 055208 (2010).
11. E. Voutier and E. Tomasi-Gustafsson (private communication). The calculations shown in the figure were carried out using the code of Kuraev, *et al*. [10].
12. J. Dumas, Ph.D. thesis, l'École Doctorale de Physique de Grenoble, France (2011).
13. Concept S. Golge, Ph.D. thesis, Old Dominion University (2010); Drawing A. Freyberger
14. Arne Freyberger, private communication
15. J. Grames (private communication) using the GEANT4 model developed by J. Dumas [11] that produces results at high energies consistent with the theory of Kuraev, *et al*. [10].
16. Geoff Krafft, private communication
17. R. Suleiman, "*High Current Polarized Electron Source*" (Proceedings of this conference)
18. J. Grames, *et al*., Phys. Rev. ST Accel. Beams **14**, 043501 (2011)
19. W. Liu, *et al*., Appl. Phys. Lett. **109**, 252104 (2016
20. C. Boulware, "*High-flux positron source based on an SRF electron linac and liquid-metal target*" (Proceedings of this conference)

A Proposal for Antiparallel Acceleration of Positrons Using CEBAF

M. Tiefenback[1,a)] and B. Wojtsekhowski[1]

[1]*Thomas Jefferson National Accelerator Facility, Newport News, VA 23606*

[a)]Corresponding author: tiefen@jlab.org

Abstract. We present a scheme for positron beam acceleration in CEBAF antiparallel to the normal electron path, requiring no change in polarity of the magnet systems. This feature is essential to the principal benefit: enabling extremely simple configuration changes between conventional (clockwise) e^- acceleration and counter clockwise e^+ acceleration. Additionally, it appears possible to configure the accelerating cavity phases to support concurrent acceleration of the electron and positron beams. The last mode also may enable use of the higher peak current electron beam for system diagnostics. The inherent penalty of the concurrent mode in acceleration efficiency and increased energy spread may render this a commissioning-only diagnostic option, but the possibility appears worthy of consideration.

INTRODUCTION

A positron beam of 1-2 μA intensity would open a new dimension for hadron physics with electromagnetic probes and also make JLab a most prolific antimatter factory. The JLab physics community proposed an extensive physics program with a positron beam and organized two workshops in 2009 and 2017 [1, 2]. Early studies for a positron beam at JLab were summarized in Ref. [3]. The physics topics are: positron-proton elastic scattering; additional proton structure functions; Compton scattering from a quark; virtual Compton scattering from a proton; positron source technologies and application to linear accelerators; polarized positron sources; positron beam polarimetry; applied research with slow positrons; and new physics with positrons (including dark matter searches and a test of special relativity). During the second workshop, extensive studies were presented about practical aspects of the positron beam acceleration, see [4]. Antiparallel positron acceleration was also presented at JPos2017 [5], motivated by the use of a positron beam in a precision test for speed of light anisotropy, see also [6].

The most direct approach to a positron beam would be to reverse the polarity of the CEBAF magnets, see [7, 8]. This choice maximally leverages the beam handling infrastructure supporting delivery to multiple experiments in all four halls. This apparent virtue may be illusory because there is a very large approved electron physics program which requires beam current 10-100 times higher than is possible for the positron case. Hall D houses essentially photon-only experiments. The principal positron interest lies with the original halls: A, B, and C. However, for low positron current, a large solid-angle detector such as CLAS12 is required to make use of the event rate.

In this paper we outline a system, extensible to Halls A and C, but delivering positrons initially only to Hall B. We examine use of a positron beam with no change of magnet polarity, but a change in the direction of beam motion. Such an approach has advantages operationally, and possibly in capital cost:

- Fast transition between e^- and e^+ operation.
- Supports graded implementation of the e^+ operation.
- Potentially concurrent e^-/e^+ operation (with beam energy reduction).

These features minimize conflict between beam delivery to high luminosity halls and to Hall B (as best suited initially for a positron beam program). Until sufficient e^+ current can be produced to provide high luminosity, it will be available only to Hall B. Transition between e^- and e^+ operation at the same energy should require no magnet changes apart from some "beam switchyard" region deflection magnets and the RF separators. The separator cavities

are not sited longitudinally to support bidirectional operation and would be either turned off as for static magnetic recirculation or re-phased as required at e^-/e^+ transitions.

Items being opened for discussion here include:

- Antiparallel "counter-clockwise" e^+ acceleration.
- Diagnostic capacity and requirements.
- Prospects for e^-/e^+ concurrent operation.

Operational/procedural tradeoffs for different positron source and acceleration path will be compared, including differences in required capital improvements.

OVERVIEW

The positron beam can be produced using the Low Energy Recirculator Facility (LERF) to provide electrons for e^+ conversion local to LERF. The e^+ beam will be collected, re-bunched, accelerated, and collimated for shielded, ground-level transport to the west end of the South Linac. We propose injecting the e^+ beam at an energy tunable up to 123 MeV (equal to the energy of an electron beam injector) into the South Linac. Due to the low beam energy and total power of the injected positron beam (100-200 W), it appears possible to transport the positrons at ground level from LERF to the point from which they will be directed down into accelerator tunnel for injection into CEBAF near the normal exit of the South Linac. For projected 1% localized beam current loss, about 1 meter of concrete shielding may be adequate. The accelerator will have been configured and all magnets set for the desired beam energy with standard diagnostics, using the higher peak current electron beam.

The accelerating cavity phases must be set differently for antiparallel acceleration (see below), but if concurrent e^-/e^+ acceleration proves possible, low duty-factor "tune mode" electron beam current can potentially be used with the positrons to track and correct system parameter drift. A small suite of supplementary diagnostics will be required to monitor essential parameters of the positrons. Synchrotron light monitors and viewers are the simplest additions, but low-current capable Digital Receiver BPMs can be retrofitted as necessary. To the extent that the magnetic system is static, it may be possible to gain most of the necessary information from electron beam signals. Synchrotron Light Monitors configured to gather light from the counter-rotating positrons can be added to the system to verify beam position at critical points, following the general pattern of low-current electron delivery to Hall B.

An injector optimized for installation within LERF has not yet been designed; however, analysis of possible source configuration has been performed several times [9, 10, 11]. For polarized positrons, the problem is strongly constrained. The most straightforward production path would be to collect positrons from the most densely populated regions of phase space into a single "bucket" for acceleration to high energy. For situations with no polarization requirement, however, redistribution of transverse phase space into temporally adjacent buckets may improve the yield of positrons per electron.

ACCELERATION OF THE BEAM AT CEBAF

The CEBAF beam travels from the injector through the "Injection Chicane" into the North Linac (see Fig. 1). With a nominal energy of up to 123 MeV, the electrons undergo a series of 5.5 degree bends to exit the chicane along a trajectory parallel to the linac. The higher-pass beams from previous acceleration passes traverse a parallel "reinjection chicane" using magnets of the same $\int B \cdot dL$). The injection and re-injection chicanes share the same final magnet, all beams entering the linac with parallel trajectories. Separation and recombination of the various momentum beams are accomplished using vertical dipoles. The system is designed for equal energy gain in the two linacs. The tolerance to differential acceleration is useful to maintain total beam energy in case of hardware outages in one linac, or to improve the beam polarization available to users on different acceleration passes.

As normally configured for electron acceleration, the North and South Linac quadrupole set points track the first pass beam momentum. The early North Linac quadrupoles focus only weakly for the higher pass, much higher momentum beams. The usual South Linac lattice retains significant higher-pass focusing along its length, but is far too strong for stable transport of 123 MeV positrons using antiparallel injection. During the CEBAF Energy Recovery Demonstration in March, 2003 [12], the South Linac was configured to support a decreasing beam momentum profile, decelerating the beam to injector energy at the South Linac exit. This is also required for a proposed 5-pass energy recovery demonstration, for which an analogue of the injection chicane has been designed [13] for extraction of the

CEBAF BEAMLINE

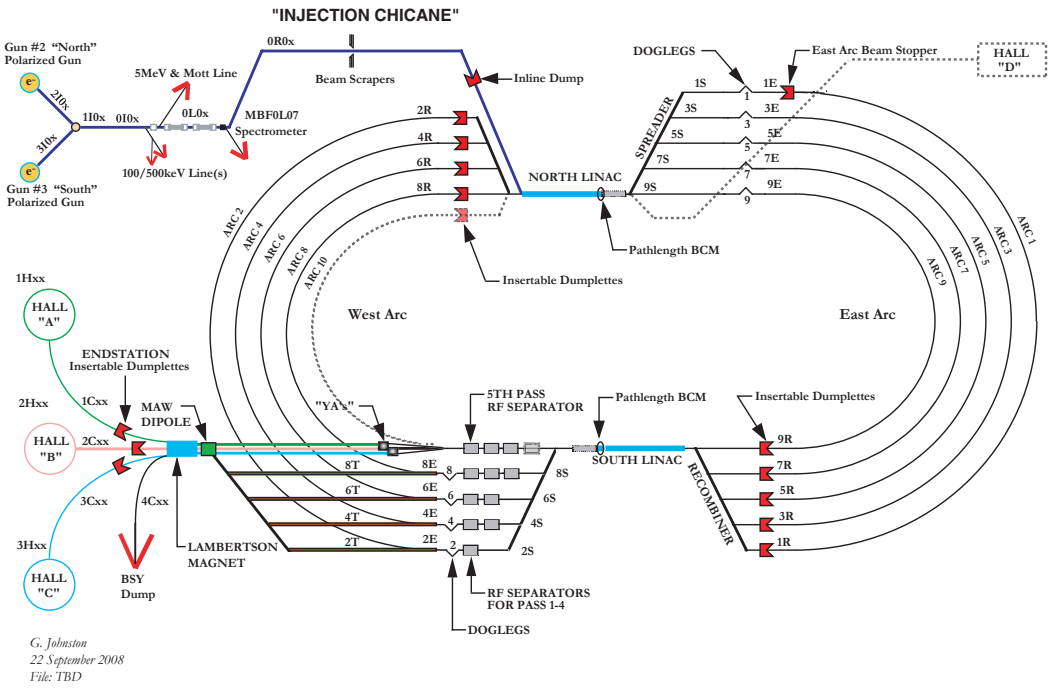

FIGURE 1. CEBAF accelerator schematic, showing the injection chicane merging into the North Linac. Electron propagation is normally clockwise, starting from the injector at the upper left corner. A chicane designed for extraction of an energy recovered beam at the end of the South Linac (see Fig. 2b) would serve well as an injection point for positrons for antiparallel acceleration.

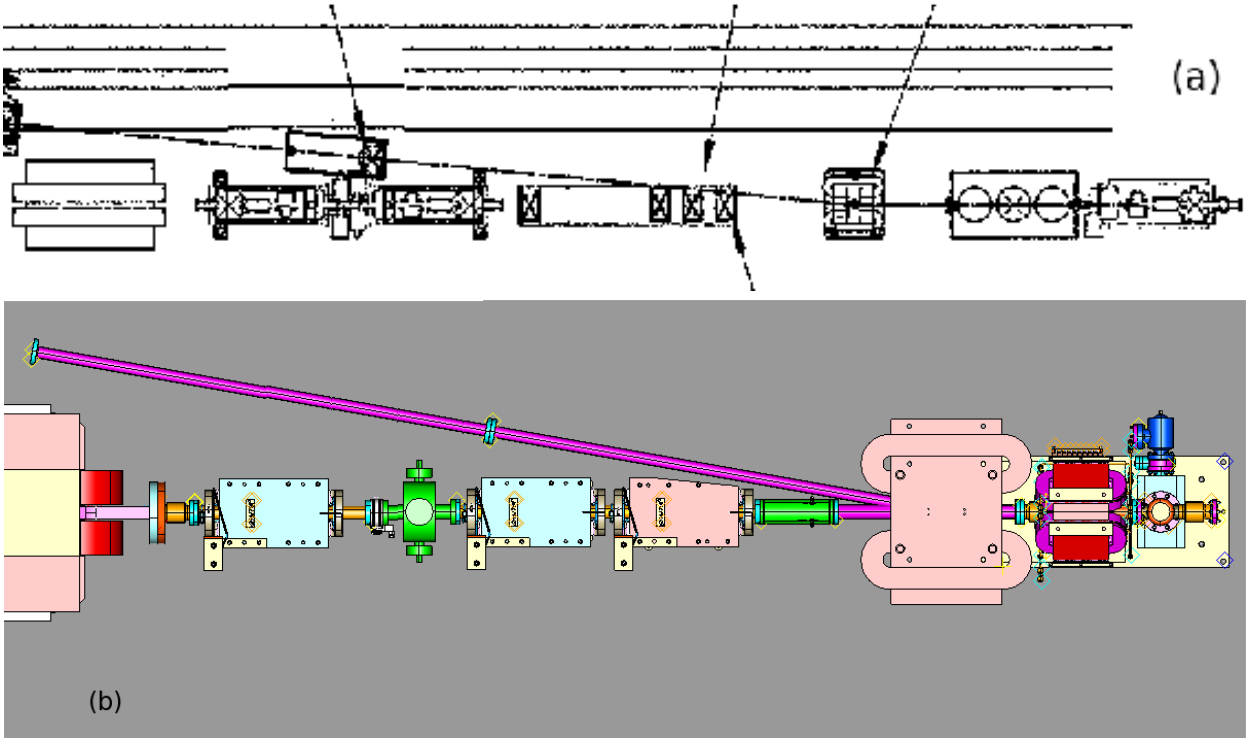

FIGURE 2. The injection chicane (a) provides for beam entrance into the North Linac, propagating from left to right at the top of the diagram. The chicane (b) designed to provide an exit path for injector-energy beam (right to left) at the exit of the South Linac for a proposed energy recovery linac demonstration also enables antiparallel positron injection.

decelerated beam (see Fig. 2b). This design can support antiparallel injection of positrons into the CEBAF South Linac.

Geometry of RF system

Independent phase control for each CEBAF cavity allows the acceleration to be maximized for each cavity independently. The 5- and 7-cell cavities have "π mode" fields, alternating in sign for each half-wave separated cell. The time of flight delay between cells is synchronous with the RF, and each cell maximally accelerates the beam. The phase relationship works bidirectionally for each cavity. However, this symmetry applies to multiple cavities only if the cavities/cells are spaced at integer multiples of half wavelengths. Consider a point along the linac at which counter-rotating bunches cross. For convenience, we will take this to be at the center of some cavity, but this is not essential. Take the phase reference for each cavity to provide peak acceleration ($cos(0) = 1$, maximum acceleration) for the bunch moving clockwise. At a cavity centered a distance dZ from the crossing point, the phase difference between the arrival of the two crossing bunches is $-2k \cdot dZ$, where k is the RF wave number. The relative phase (modulo 2π) can only be zero when the physical separation from the crossing point is a multiple of $\lambda/2$.

Bi-directional acceleration Cavity phases can be set for full acceleration in either direction. To provide simultaneous bidirectional acceleration if the phase difference described above is not zero, shift the cavity phase set point by half of the relative phase to provide equal acceleration for both bunches. The CEBAF 5-cell cavity and cryomodule spacing distribution is sufficiently broad that the average acceleration is about 63% in the bidirectional mode, independent of the choice of relative timing between the counter-rotating bunches (assuming no correlation due to gradient capability of the cavities). This comes from $\langle cos(\theta)\rangle = \int_0^{\pi/2} cos(\theta)d\theta) / \int_0^{\pi/2}(d\theta) = 2/\pi$. The more favorably spaced 7-cell systems (five cryomodules per linac) can be configured in symmetric bidirectional acceleration for $\sim$ 77% of maximum energy gain with bunches crossing at the center of the 7-cell cavity span, assuming equal cavity gradients. It appears possible to increase the C100 cryomodule spacing by 1.25 cm, raising this 77% fraction to $\sim$ 91%.

For each cavity, shifting the phase away from equal acceleration results in a decrease in total energy gain for the two bunches. The bunch gaining energy from the phase shift gains less than is lost by the bunch which loses energy. For symmetric distribution of cavity timing before and after crest for the counter-rotating beams, a global phase shift results in both bunches losing energy, Therefore, for broadly uncorrelated cavity separations, the procedure outlined above results in the net vector sum of RF accelerating fields being on-crest. The energy spread will then be dominated by the incoherent phase noise of the cavities.

Such a configuration opens the option of simultaneous electron and positron counter-rotating acceleration. Many system tests can be made in CEBAF with no need for a counter-rotating beam. The reduced acceleration may appear self-defeating, but enables the application of electron beam diagnostics to solve problems encountered with positron acceleration while changing neither magnetic nor RF configurations. This may be especially useful during commissioning or trouble-shooting.

The phase change from maximal electron acceleration in the conventional clockwise sense to either antiparallel or bidirectional acceleration is determined by the longitudinal placement of the cavities. Download of phase shifts for bidirectional acceleration should provide an on-crest RF vector sum, deviations from which can be measured using the RF global phase shift. The 5-cell system energy gain should be approximately 63% of the maximal acceleration, and the energy spread due to the RF incoherent phase flicker should be measurable using existing accelerator diagnostics. The new acceleration profile can be used to set the linac quadrupoles. Full 5-pass acceleration can test feasibility of operating the system in this mode and would test the capacity of CEBAF to accelerate and control high momentum-spread beams.

The dipole magnet set points for maximal electron acceleration are the same required for positrons at maximal acceleration with the condition of equal energy gain for the two linacs. Transitioning between electron and positron modes requires only changing the RF phases and some beam delivery "beam switchyard" selections. The electron and positron momentum profiles coincide in the arcs, but the different profiles along the linacs may result in the need for small steering corrections. Selected supplemental synchrotron radiation monitors (useful at nanoAmpere average current) and viewers may be adequate to guide re-steering of the beam. CEBAF Digital Receiver BPMs provide useful signal at currents as low as 30 nanoAmperes and could be installed as part of a positron diagnostic supplement.

Acceleration of two beams

Consider the accelerator configured for multi-pass electron acceleration, with the exception of the quadrupoles of the South Linac being arranged for the decelerating momentum profile used for the 2003 Energy Recovery Demonstration. An injection chicane analog at the exit of the South Linac supports antiparallel position injection at MQL2L27. Such an insertion has been designed as part of a study in support of a 5-pass energy recovery demonstration [14]. Positrons will be accelerated through the South Linac as they propagate toward the 2L02 RF zone, mirroring electron beam acceleration through the North Linac, with the caveat that the phases of the SL cavities must be altered to provide peak acceleration in each cavity to the counter-rotating positrons. With equal energy gain in the NL and SL, the positrons will enter Arc 1A at the normal energy and propagate into the NL. With its phases also altered to support antiparallel acceleration of the positrons, the beam will continue into Arc 2A and potentially on multiple successive passes through Arc 10.

Development plan

The project can be arranged in several stages:

- Stage 1: Demonstrate understanding of RF phase and cavity locations.
- Stage 2: Characterize CEBAF electron beam performance with concurrent mode phasing (energy spread/stability).
- Stage 3: Construct 123 MeV 1 μA CW positron source.
- Stage 4: Construct positron transport and injection lines to CEBAF.
- Stage 5: Inject and accelerate the positron beam.
- Stage 6: Accelerate positrons to 11 GeV.
- Stage 7: 1-pass (or other) positron extraction with dedicated transport to Hall B (Hall A/C?) within tunnel to support initial $\sim$ 2 GeV e^+ experiments.
- Stage 8: Construct 11 GeV beam transport to BSY for high-energy experiments.

SUMMARY

Delivery of a positron beam to Hall B and high intensity electron beams to halls A, C, and D is proposed with an "antiparallel" mode. The most expensive part of the proposed approach would be the construction of a beam transport tunnel conducting positrons from the West Arcs to the BSY. Fast and reliable transition between electron mode and positron mode is the main advantage of our proposal. In the case where a lower beam energy is acceptable for an experimental program, it may be possible to deliver electrons and positrons concurrently.

ACKNOWLEDGMENT

The authors are grateful for stimulating discussions with J. Benesch and Y. Roblin over the different possibilities of this program. This material is based upon work supported by the U.S. Department of Energy, Office of Science, Office of Nuclear Physics under contract DE-AC05-06OR23177

REFERENCES

[1] Positrons at Jefferson Lab. Proceedings, International Workshop, JPOS 2009, Newport News, USA, March 25-27, 2009, https://www.jlab.org/conferences/JPOS09/, proceedings published in AIP Conf. Proc. 1160 (2009) 178 p.

[2] The workshop JPOS 2017, https://www.jlab.org/conferences/JPos2017/index.html

[3] Paul Gueye, AIP Conf.Proc. 1160 (2009) 164-169.

[4] JPos 2017 workshop talks, https://www.jlab.org/indico/event/206/timetable/#20170912.detailed

[5] B. Wojtsekhowski, Using a positron beam to measure the speed of light anisotropy, https://www.jlab.org/indico/event/206/session/24/contribution/117/material/slides/0.pdf

[6] B. Wojtsekhowski, Euro Physics Letters, **108**, 31001 (2014); arXiv:1409.6373.

[7] Y. Roblin, Using CEBAF as a positron machine, https://www.jlab.org/indico/event/206/session/19/contribution/90/material/slides/1.pdf

[8] M. Tiefenback, Bipolar Operation of CEBAF Magnets Considerations and Implications. https://www.jlab.org/indico/event/206/session/19/contribution/18/material/slides/0.pdf

[9] S. Golge, B. Vlahovic, B. Wojtsekhowski, High-intensity positron microprobe at the Thomas Jefferson National Accelerator Facility, J.Appl.Phys. 115 (2014) 234907.

[10] S. Golge, Feasibility and conceptual design of a C.W. positron source at CEBAF, Ph.D. thesis, ODU, 2010.

[11] B. Wojtsekhowski, P. Degtiarenko, A. Freyberger, L. Merminga, Search of U boson in electron-positron annihilation in flight, internal report, 2006.

[12] A.P. Freyberger, K. Beard, A. Bogacz, *et al.*, "The CEBAF energy recovery experiment: Update and future plans", in *Proc. 9th European Particle Accelerator Conference (EPAC 2004)* Lucerne, Switzerland, July 5-9, 2004, http://accelconf.web.cern.ch/AccelConf/e04/PAPERS/MOPKF087.PDF,

[13] F. Mot, I. Ben-Zvi, M.E. Bevins, S.A. Bogacz, *et al.*, "ER@CEBAF - A High Energy, Multi-pass Energy Recovery Experiment at CEBAF", in *Proc. 7th Int. Particle Accelerator Conf. (IPAC'16)*, Busan, Korea, May 2016, paper TUOBA02, pp. 1022–1024, http://jacow.org/ipac2016/papers/tuoba02.pdf, doi:10.18429/JACoW-IPAC2016-TUOBA02, 2016.

[14] S.A. Bogacz, D. Douglas, C. Dubbe, A. Hutton, *et al.*, "ER@CEBAF: A test of 5-pass energy recovery at CEBAF", JLAB PAC proposal 2016.

High Energy Polarimetry of Positron Beams

D. Gaskell[1,a)]

[1]*Thomas Jefferson National Accelerator Facility, Newport News, VA, 23606, USA*

[a)]Corresponding author: gaskelld@jlab.org

Abstract. Møller and Compton polarimetry are the primary techniques used for high energy electron polarimetry at Jefferson Lab. In principle, both techniques can also be used for positron polarimetry. However, some modifications to the configuration and/or operating mode of the existing devices will likely be required for use with the types of positron beams currently under consideration at Jefferson Lab.

INTRODUCTION

Polarimetry of high energy electron beams (on the order of 1 GeV or larger) is typically accomplished using Møller and Compton polarimetry. Møller polarimetry makes use of the scattering of the polarized beam electrons from polarized target electrons, the latter usually found in a magnetized ferromagnetic foil. Compton polarimeters make use of collisions between the polarized electron beam and laser photons. The scattered electrons and backscattered photons from the Compton scattering process can both be used to make quasi-independent beam polarization measurements. Since both Møller and Compton scattering are QED processes, their analyzing powers are known to high precision and hence are ideal techniques for electron beam polarimetry.

Compton polarimetry was initially employed at high energy storage rings, but has lately been used at more modest energies and luminosities at fixed target accelerators like CEBAF at Jefferson Lab and MAMI at Mainz. The μA currents and sometimes low beam energies used at fixed target accelerators present certain challenges, but <1% precision measurements have been made at energies as low as ~1 GeV.

Møller polarimetry is easier to employ at fixed-target machines due to the nearly energy-independent analyzing power and the ability to make statistically precise measurements in relatively short amounts of time. The need to use ferromagnetic foil targets leads to the measurements affecting the electron beam such that the polarization measurements become invasive.

Møller polarimeters are deployed in Halls A [1, 2], B [3], and C [4] at Jefferson Lab, while Compton polarimeters are only available in Halls A [5] and C [6]. In principle, Compton and Møller polarimetry can be employed for both electron and positron beam polarization measurements. The discussion here will focus on how the existing polarimeters at Jefferson Lab could be used to measure positron beam polarization. In the context of this discussion, we will assume positron beam currents of 100 nA and polarizations of 60%, with beam properties nearly identical to the existing Jefferson Lab electron beam.

COMPTON POLARIMETRY

The unpolarized cross section and longitudinal analyzing power for Compton scattering of a polarized electron beam colliding nearly head-on with a green laser are shown in Fig. 1. The cross section is nearly independent of beam energy, while the analyzing power changes dramatically between 1 GeV (≈4% at the Compton endpoint) and 11 GeV (≈30%). Note that the cross section and analyzing power are the same for positrons and electrons.

The Hall A and C Compton polarimeters at Jefferson Lab are very similar, and employ the following major components (see Fig. 2):

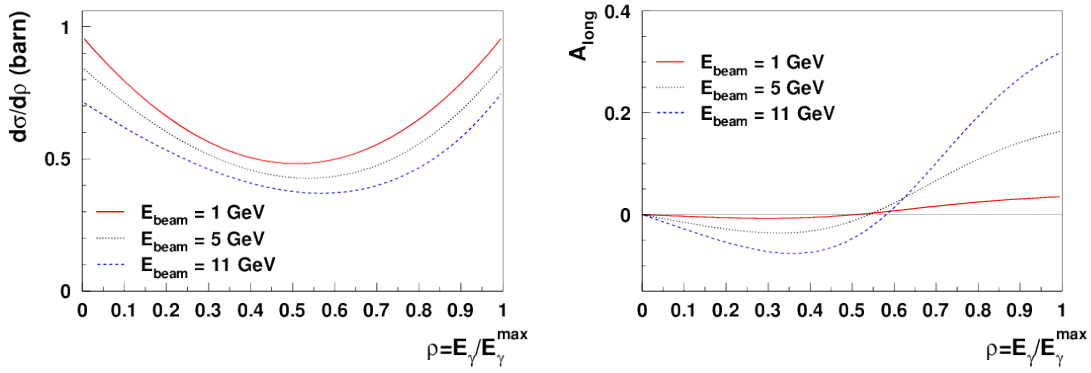

FIGURE 1. Unpolarized cross section (left) and longitudinal analyzing power (right) for GeV-scale electrons colliding with a green laser.

1. 4-dipole magnetic chicane, to first deflect the beam vertically to the laser interaction region and then restore the beam to its nominal trajectory.
2. Laser system consisting of a CW laser coupled to an external Fabry-Pérot cavity.
3. Photon detector downstream of the 3rd dipole (at laser-electron collision height).
4. Segmented strip detector for the scattered electrons, located just upstream of the fourth dipole.

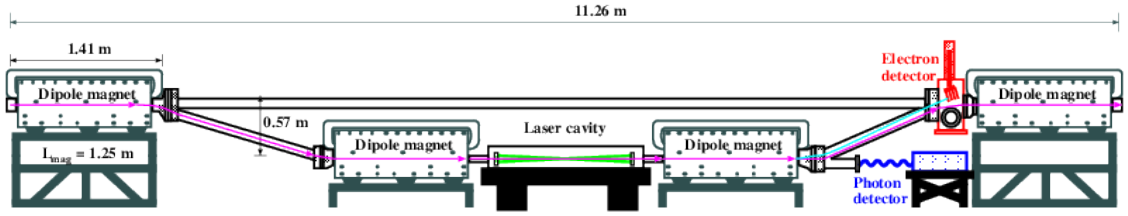

FIGURE 2. Layout of the Hall C Compton polarimeter (as used during the Q_{weak} experiment). The layout of the Hall A Compton polarimeter is similar, although differs in the overall chicane length and vertical beam deflection. Figure from Ref. [6], licensed under CC BY 3.0 [7].

Repurposing either the Hall A or Hall C Compton polarimeters for use with positron beams, to first order, requires no hardware changes; just a simple change of polarity of the dipole chicane. However, the relatively low positron beam currents projected to be feasible at Jefferson Lab will have a significant impact on the practicality of using the existing Compton polarimeters without modification.

The figure-of-merit for a Compton polarimeter can be defined in terms of the time required for a measurement of a given precision, $\Delta P/P$. In the case where the energy of the scattered electron/backscattered photon is determined event-by-event, the time needed is given by,

$$t^{-1} = \mathcal{L}\sigma\left(\frac{\Delta P}{P}\right)^2 P_e^2\langle A^2\rangle, \tag{1}$$

where σ is the Compton cross section, $\mathcal{L}$ is the luminosity of the beam-laser collision, and $\langle A^2\rangle$ is the mean value of the square of the Compton asymmetry. For Gaussian laser and electron beams colliding at a small angle, α_c, the luminosity is given by,

$$\mathcal{L} = \frac{(1+\cos\alpha_c)}{\sqrt{2\pi}}\frac{I_e}{e}\frac{P_L\lambda}{hc^2}\frac{1}{\sqrt{\sigma_e^2+\sigma_\gamma^2}}\frac{1}{\sin\alpha_c}, \tag{2}$$

where I_e is the electron beam current, P_L is the laser power, and σ_e and σ_γ are the electron and laser beam spot sizes. From Equations 1 and 2, it is clear the measurement time is driven by the size of longitudinal asymmetry, the electron beam current, laser power, and laser/electron beam sizes.

The figure-of-merit expression in Equation 1 is a little too simple in that it ignores laser-off periods for background measurements, detector inefficiencies etc. To make a more realistic estimate of expected measurement times using positron beams at Jefferson Lab, we scale using experience with the Hall C Compton polarimeter as used during the $Q_{\rm weak}$ experiment. In that case, the 1.16 GeV beam energy gave an endpoint analyzing power of about 4% and the high beam current (180 μA) resulted in a Compton event rate (in the electron detector) of about 150 kHz at a beam polarization of 89%. For an 11 GeV positron beam, the endpoint analyzing power is 32%, but the rate decreases to 185 Hz (100 nA beam current), and the beam polarization is expected to be no larger than 60%.

In the $Q_{\rm weak}$ case, a 0.47% measurement took about 1 hour. Using Equation 1 to scale to the 11 GeV positron conditions implies that a precision of about 2.5% could be achieved in a similar amount of time. Note that this is a bit optimistic since we are scaling using just the endpoint asymmetry - using the average value of A^2 results in a 3% precision in one hour. A measurement of 1% statistical precision would then take about 9 hours.

While 9 hours is possibly a reasonable amount of time, it does make it challenging to perform systematic studies and track rapid changes in polarization. It would be desirable to make 1% measurements in time scales on the order of one hour. The easiest way to accomplish this is likely an increase in laser power. The Fabry-Pérot cavities used in the JLab Hall A and Hall C Compton polarimeters store 1-5 kW of CW laser power. Higher powers have been achieved at JLab (10 kW), but they are hard to maintain routinely. The effective luminosity of the beam-laser interaction could be enhanced, however, by taking advantage of the electron beam pulse structure. An RF-pulsed laser coupled to a Fabry-Pérot cavity, operating at the same frequency as the electron beam with a comparable pulse width would significantly enhance the effective luminosity, although at the expense of technical complexity. Such laser systems have been accomplished using mode-locked laser systems, but do place some constraints on the Fabry-Pérot cavity geometry, and are not commonplace.

MØLLER POLARIMETRY

As with Compton polarimetry, Møller polarimetry can also be readily applied to both electron and positron beams. The polarized CM cross section ($d\sigma/d\Omega^*$) and longitudinal analyzing power ($A_\parallel$) for Møller scattering are given by,

$$\left(\frac{d\sigma}{d\Omega^*}\right)^{\rm Møller} = \frac{\alpha^2}{\sqrt{2m_e(E_b+m_e)}}\frac{(3+\cos^2\theta^*)^2}{\sin^4\theta^*}[1+P_eP_tA_\parallel(\theta^*)], \quad (3)$$

$$A_\parallel = \frac{-(7+\cos^2\theta^*)\sin^2\theta^*}{(3+\cos^2\theta^*)^2}, \quad (4)$$

where α is the fine structure constant, E_b is the electron beam energy in the lab frame, and θ^* is the CM scattering angle. For Bhabha (positron-electron) scattering, the expression for the unpolarized cross section is a bit different, but the longitudinal analyzing power is the same [8],

$$\left(\frac{d\sigma}{d\Omega^*}\right)^{\rm Bhabha} = \frac{\alpha^2}{4\sqrt{2m_e(E_b+m_e)}}\frac{(3+\cos^2\theta^*)^2}{(1-\cos\theta^*)^2}[1+P_eP_tA_\parallel(\theta^*)]. \quad (5)$$

The magnitude of the longitudinal analyzing power is a maximum value of 7/9 at θ^* =90 degrees and is independent of beam energy for GeV-scale beams. In practice, the analyzing power is diluted by the need to use ferromagnetic foils for the polarized electron target. The effective target polarization is on the order of 8%, so the maximum possible asymmetry is then ~6%.

Møller polarimeters have been built in various configurations and modes of operation. Detection of only the scattered electron results in sometimes non-trivial backgrounds due to Mott scattering. It is now more common to detect the scattered and recoiling electrons in coincidence, which eliminates virtually all physics backgrounds. Møller polarimeters also require magneto-optical systems to steer the electrons to a detector system. Various optical solutions are possible (dipole-only, quadrupole-only, quadrupole+dipole). At Jefferson Lab, experimental Halls B and C use a 2-quadrupole optical system, while Hall A uses multiple quadrupoles with a dipole. The layout of the Hall C system is shown in Fig. 3.

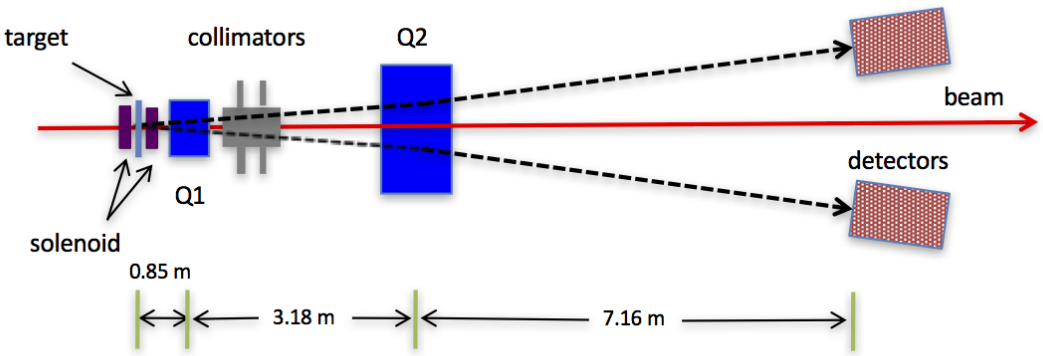

FIGURE 3. Layout of the Hall C Møller polarimeter. The first quadrupole horizontally focuses the scattered and recoil electrons, while the second quadrupole horizontally de-focuses and steers the electrons to the lead-glass detectors, which are separated from the nominal electron beam path by 49 cm. Figure from [9], licensed under CC BY 4.0 [10].

The use of quadrupoles in the Møller polarimeter optics presents a practical challenge for the use of the JLab polarimeters for positron measurements. The magneto-optical systems presume that both the scattered and recoiling particles have the same charge so that the steering effects/focusing from the quadrupoles will be the same. Clearly this is not the case for positron beams and the detection of the scattered positron and recoiling electron in coincidence is not possible with the existing optical configurations. However, there are two relatively simple options that would allow the use of the existing JLab Møller polarimeters with no or relatively modest modification.

Single arm Møller Polarimetry

A simple option for operation of the JLab Møller polarimeters for positron beams would be to operate them in single-arm mode, not requiring a coincidence between the scattered and recoiling particle. This has the advantage of requiring no changes to the magneto-optical systems. However, operation in this mode would result in larger backgrounds due to Mott scattering. Even more problematic is that the optical systems of the JLab polarimeters are not configured for easy fitting and subtraction of the Mott background.

Constraint of the Mott backgrounds in single-arm mode could be perhaps most simply accomplished using electron beam data at the relevant positron beam energy. In this case one could compare the asymmetries extracted in coincidence (background-free) mode to those extracted in single-arm mode. The inferred size of the Mott backgrounds could then be applied to measurements taken under similar conditions with positron beams.

It's worth noting that, even with the Mott backgrounds properly determined, the figure of merit for the measurement will decrease due to the smaller measured asymmetry.

Dipole-only optics

The JLab Møller polarimeters could be operated with positron beams in coincidence mode by replacing the quadrupole-based optical systems with a dipole-only system. In this case, the oppositely-charge particles travel through a vertical magnetic field and are both bent away from the beamline, into detectors. Figure 4 shows an example of this potential implementation in the Hall C system. In this case, the first quadrupole is not used, and the second quadrupole replaced by a large gap (~3.5 inch) dipole with integrated field on the order of 1 T-m. While the example shown here is for the Hall C system, it is likely possible with the Hall B system as well due to the similar layout. Application to the Hall A system would be more problematic since a dipole is already used there to bend both scattered and recoil electrons down, below the nominal beam path.

The drawback to this solution is the requirement for a new magnet. In addition, the system can not be easily swapped between electron and positron mode - some significant installation time is required for switching between the two modes.

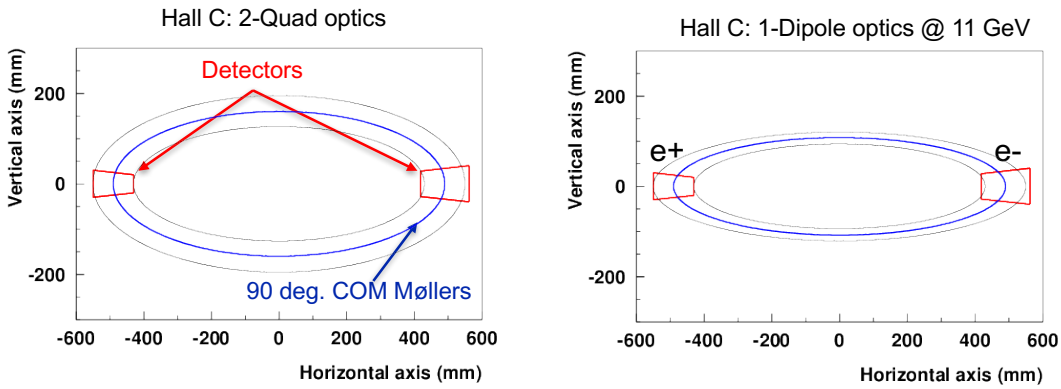

FIGURE 4. Envelope of Møller events at detector plane. Left: 2 quad optics for scattered/recoil electron pair. The quads focus the relevant Møller events to form an ellipse at the detector plane. The acceptance of the detectors is described by the red trapezoids. Right: Single dipole optics for positron/electron detection at 11 GeV. While the height of the ellipse has changed, the particles scattered at 90 degrees in the CM are still steered to the detectors.

SUMMARY

Positron polarimetry of GeV-scale beams can be readily accomplished using the standard techniques of Compton and Møller polarimetry. In particular, the polarimeters at JLab can potentially be used for these measurements, either with some modification or compromise in performance. The primary challenge for the JLab Compton polarimeters is the relatively low beam current (100 nA) projected to be feasible for polarized positron beams at JLab. This low current leads to rather lengthy measurement times. Measurement times could be reduced with improvements to the Compton polarimeter laser systems, although this would require some R&D and expense. The Møller polarimeters at JLab, on the other hand, use magneto-optical systems designed to detect two particles of the same charge in coincidence. Møller polarimetry with positron beams would ideally detect the scattered positron and recoil electron. The JLab Møller polarimeters could be operated in single-arm mode, resulting in non-trivial Mott backgrounds and potentially larger systematic uncertainties (although the Mott backgrounds could potentially be understood by comparing single-arm and coincidence measurements with electrons). Another option would be to replace the quadrupole-based polarimeter optics with a dipole-based system. This would enable the detection of the positrons and electrons in coincidence. Extra time would be needed, though, to switch between positron and electron operating mode.

ACKNOWLEDGMENTS

This work is supported by the United States Department of Energys Office of Science contract number DE-AC05-06OR23177 under which Jefferson Science Associates, LCC operates the Thomas Jefferson National Accelerator Facility.

REFERENCES

[1] A. V. Glamazdin *et al.*, Fizika **B8**, 91–95 (1999), arXiv:hep-ex/9912063 [hep-ex] .
[2] O. Glamazdin, Nuovo Cim. **C35**, 176–180 (2012).
[3] B. A. Mecking *et al.* (CLAS), Nucl. Instrum. Meth. **A503**, 513–553 (2003).
[4] M. Hauger *et al.*, Nucl. Instrum. Meth. **A462**, 382–392 (2001), arXiv:nucl-ex/9910013 [nucl-ex] .
[5] S. Escoffier *et al.*, Nucl. Instrum. Meth. **A551**, 563–574 (2005), arXiv:physics/0504195 [physics] .
[6] A. Narayan *et al.*, Phys. Rev. **X6**, p. 011013 (2016), arXiv:1509.06642 [nucl-ex] .
[7] Creative Commons Attribution 3.0 Unported, `https://creativecommons.org/licenses/by/3.0/`.
[8] G. Alexander and I. Cohen, Nucl. Instrum. Meth. **A486**, 552–567 (2002), arXiv:hep-ex/0006007 [hep-ex] .
[9] J. A. Magee *et al.*, Phys. Lett. **B766**, 339–344 (2017), arXiv:1610.06083 [physics.ins-det] .
[10] Creative Commons Attribution 4.0 International, `http://creativecommons.org/licenses/by/4.0/`.

Opportunities and Challenges of a Low-energy Positron Source in the LERF

Stephen Benson [1,a)], Bogdan Wojtsekhowski[1],
Branislav Vlahovic[2] and Serkan Golge[2]

[1]*Jefferson Lab, 12000 Jefferson Avenue, Newport News, Virginia, USA*
[2]*North Carolina Central University, Durham, NC, USA*

[a)]Corresponding author: felman@jlab.org

Abstract. Though there are many applications of low energy positrons, many experiments are source limited. Using the LERF accelerator at the Thomas Jefferson National Accelerator Facility, it is possible to build a high brightness source of very low-energy positrons. The accelerator requirements are well within the capabilities of the installed hardware. The accelerator can produce 120 kW of beam with a beam energy of up to 170 MeV. For these experiments, we only need run at up to 120 MeV. The gamma-to-positron converter must be able to absorb 20% of the beam power that the linac delivers. At this low an energy the converter, though challenging, is possible. The transport of the low energy positrons from the production target to the next stage, where the energy is reduced even further, must have a very large acceptance to be able to efficiently transport the flux of positrons from the positron production target to the moderator. We propose to accomplish such a transport by means of a guiding solenoidal field with a novel endcap design. In this presentation, we will present the proposed schemes necessary to realize such a high brightness positron source.

INTRODUCTION

As has been pointed out in several papers in this workshop, low energy positrons are a unique probe of materials and surfaces that allow measurements of surface properties not possible with other probes such as electrons or X-rays. Though nuclear decay sources are available for positron studies, accelerator sources can provide higher fluxes and much higher brightness[1]. Spin polarized source can provide even more capability and an accelerator source can produce spin polarized positrons either via production by spin polarized electrons[2] or perhaps via a spin polarized hydrogen converter[3].

THE LOW ENERGY RECIRCULATION FACILITY

The Low Energy Recirculation Facility at Jefferson Lab was originally constructed to study free-electron laser (FEL) systems and was successful in demonstrating record recirculated beam power in an energy recovery linac (ERL) and record power from a free-electron laser[4]. The accelerator system, shown in figure 1, is housed in a heavily shielded underground vault. It consists of a DC photocathode gun providing 350 keV beams to a superconducting booster accelerator that can accelerate up to 9 MeV. This beam is then injected into an energy recovering accelerator system consisting of three superconducting accelerator modules (cryomodules) and two recirculation loops that bring the beam through an FEL and then back to the accelerator for energy recovery. In this energy recovery mode, the ERL has demonstrated up to 1.3 MW of circulating electron beam power. This is far higher than the 192 kW of klystron power available to accelerate the beam. The accelerator is also capable of operating in a non-recirculated mode in which the beam is dumped at high energy. In this case the electron beam power is limited by the klystron power to less than 200 kW and is typicall limited by the target and dump to much less than that.

It is possible to use the electron beam generated by the superconducting linear accelerator of the LERF to generate a beam of positrons with a high flux. A reasonable goal is a flux of 10^{10} positron/sec delivered to a laboratory on the floor above the FEL vault. To produce this flux, one must consider the following: generation and transport of the positron beam, optimization of the positron cooling, radiation shielding, and management of the design, installation and operation of the facility.

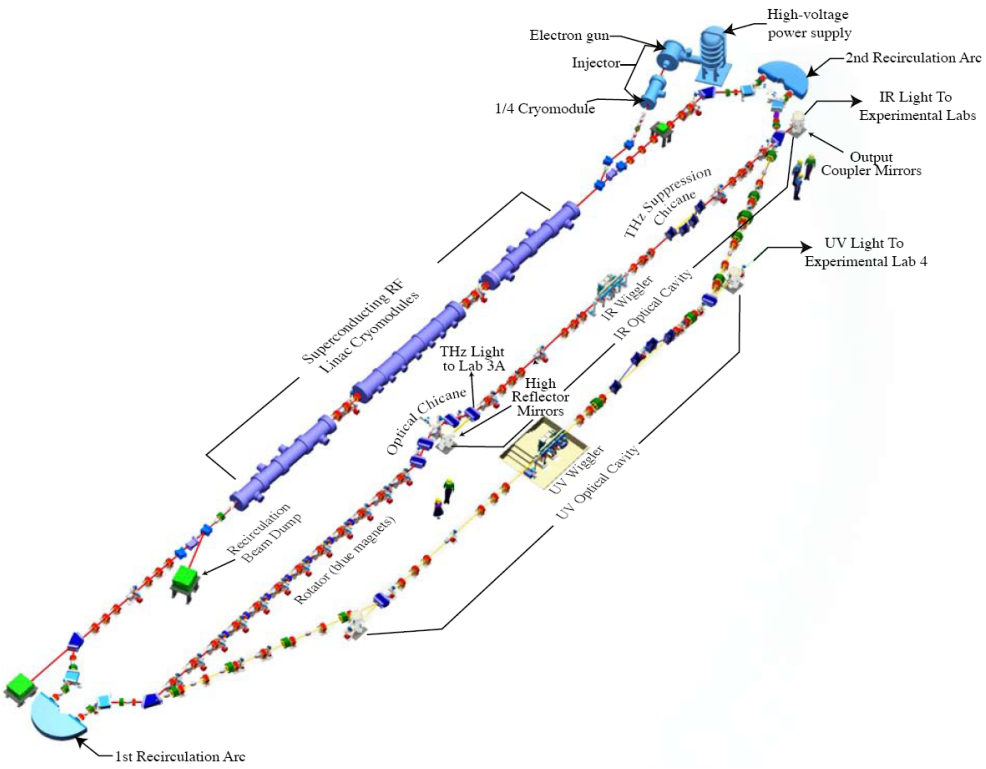

Figure 1. Layout of the accelerator at the LERF with two FEL beamlines. A target for positron production would be just after the first arc

SOURCES OF POSITRONS

Currently there are three different types of positron sources available worldwide:

1. **Radioisotope-based slow positron facilities:** There are many small-sized research and medical labs in the world using positron emitting isotopes, e.g. ^{22}Na ($t_{1/2}$=2.6 yr.), ^{58}Co ($t_{1/2}$=71 d), ^{18}F ($t_{1/2}$=109 min)[5]. These sources are commercially available, have low infrastructure costs and modest radiation shielding requirements. Compared to other sources however they are low-intensity (<10^6 slow positrons/sec.).
2. **Reactor-based slow positron facilities:** Positrons can also be produced via pair-production from the emission of high energy prompt γ-rays after thermal neutron capture i.e. ^{113}Cd (n, γ) ^{114}Cd. The positron intensity is proportional to the reactor core power and the flux can be very high. There are radiation concerns, however, and a high initial cost of the infrastructure. In addition, the source size is rather large so the brightness is not very high. The highest flux source in the world is the Munich Reactor Positron Source[6], which has achieved ~9x10^8 slow positrons/sec.
3. **Electron linac-based slow positron facilities:** Here, positrons are produced via pair production from Bremsstrahlung photons. The positron intensity is proportional to the intensity of the incident electron beam, which can be very high. The positrons also have an adjustable time structure which can be useful for some experiments requiring time-of-flight measurements. As with the reactor-based facility, there are radiation concerns and a high initial cost of infrastructure. A very productive source is the Elbe Positron Source (EPOS) near Dresden, Germany[1]. The projected flux is ~10^8 slow positrons/sec. Due to their small source size, these sources can, in principle, provide very high brightness.

PROPOSED POSITRON GENERATION AND TRANSPORT

A potential source of accelerator positrons is the LERF linac in fixed-target mode. It can provide an electron beam at ~120 MeV and up to 1 milliampere of beam current. The existing JLAB accelerator is ideally suited for this application. The electron beam from the LERF linac is very bright and the time structure is quite flexible, allowing either pulsed or CW electron beams.

The power available to be deposited into the target by the electron beam to produce sufficient positron intensity is very high, 10's of kW. This can be deposited into a very small volume, but the heat from this must be removed promptly to prevent damage to the target. One can mitigate the power density by rotating a solid target and by rastering the incoming electron beam.

Positron Transport

To transport the generated positrons from the target to an experiment we would use a novel high-efficiency Rare Gas Moderator (RGM), such as solid-Neon[7], which is a different moderator type than the ones used in existing linac- and reactor-based facilities. It is experimentally verified that the efficiency of the solid-Neon moderator is more than a factor of 10 higher than the Tungsten moderator (commonly used in existing facilities) with positrons emitted from ^{22}Na. The difference between efficiencies occurs due to the fact that positron diffusion length inside the RGMs is much longer than it is inside metallic moderators.

Using the positron kinetic energy spectrum of the ^{22}Na as a baseline, this design will transport positron with kinetic energy below 600 keV from the converter. It is important to note that cryogenic nature of the RGM mandates that RGM must be positioned away from the high temperature and radiation area around the converter.

Target design

Since we are interested in the positron with kinetic energies below 600 keV for moderation, we optimized the front-end capture field to collect the highest number of positron that we were able to transport. We then optimized the converter thickness and incident e- beam energy to maximize positron intensity that is driven by the transport design. We performed Monte Carlo simulations using GEANT4 to evaluate these parameters. Due to the multiple scattering of charged particles in the converter, both the momentum spread and angular spread of the emitted positron are very large with $x' = p_x/p_z$ up to 1.5 rad. In order to capture a significant fraction of these positron we calculate that a 6-cm diameter channel and a modest longitudinal field of 2 kG are required. This allows one to capture and transport about 50% of the emitted positron within the assumed kinetic energy range. To determine the converter thickness, we varied the incident e- beam energy and used 10, 60 and 120 MeV/c on various thicknesses of tungsten converters to find the highest positron yield. In Fig. 2 (left), the positron-production efficiency ($\eta+$) as a function of converter thickness is shown, where N_{e+} is the number of positrons in the 2π steradian solid angle in the forward direction and with energies up to the spectrum-end (up to 120 MeV/c), and N_{e-} is the number of incident e- on the converter.

As seen in the Fig. 2 (left), there is a broad maximum yield centered at 6 mm thickness with 120 MeV/c incident electron beam, about a factor of 3 higher than 60 MeV/c, and two orders of magnitude higher than peak yield at 10 MeV/c. With 120 MeV/c incident beam on a 6 mm thick converter, the efficiency is 0.3 positron / incident electron. However, from the whole energy spectrum, only positrons that can be moderated to sub-keV energy are useful. Another important parameter when evaluating the converter thickness selection is the normalized brightness, which is defined as the flux divided by the transverse geometrical emittances. In Fig. 2 (right), the positron brightness at the end of the transport channel is compared for positrons emitted from 2 mm and 6 mm thick converter. As is seen, the brightness is about 3 times higher for the 6 mm than the 2 mm thick converter.

A major challenge in a high-power linac-based positron source is the dissipation of the deposited power in the production converter. As mentioned previously, we calculated that higher intensities of slow positron beam can be produced through a novel high-efficiency RGM. Experimental results with this type of moderator (solid-Ne) shows that positrons with below 600 keV can be moderated with 1% efficiency. Thus, we found that the highest yield of positron can be obtained with 120 MeV e- beam incident on a 6 mm tungsten within the provided positron energy constraint. The intensity is highest for this energy range because in the first radiation length, the bremsstrahlung photons are produced whereas the low-energy positrons are mostly produced in the downstream radiation length close to the exit surface of the converter.

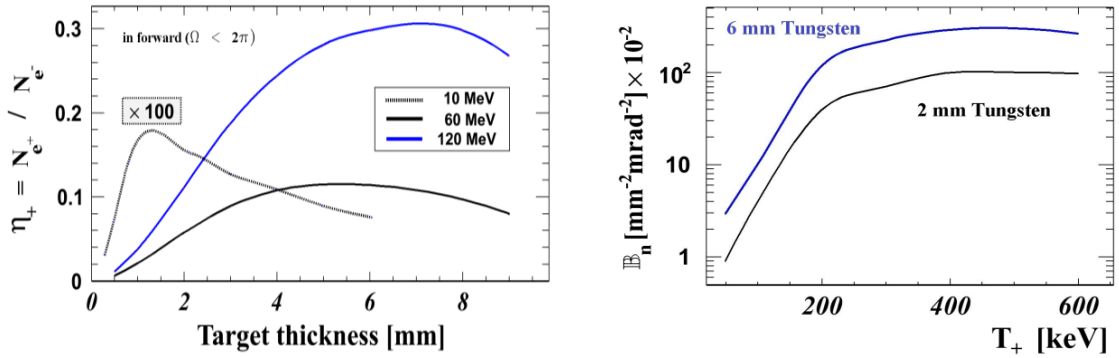

Figure 2. Left: The yield, η_+, as a function of the target thickness. The 10-MeV curve is multiplied by 100 for convenience. Right: Brightness of the positrons at the end of the channel reaching the moderator. We present only e^+ with T_+ below 600 keV.

The incident electron beam on the converter will be 120 MeV, 1 mA which has a total power of 120 kW. We found from full GEANT4-based simulation that 20% (= 24 kW) of this incident power is deposited in a 6 mm plate and 5% (= 6 kW) in 2 mm tungsten plate. As it is seen, the lower thickness results in less deposited power but provides about a factor of 3 less positron intensity on the moderator as plotted in Fig. 2 (right). Although tungsten is a very durable material for high temperature applications, 24 kW deposited power in such a small area will result in melting immediately.

One well-known solution[8-10] to prevent melting of the converter is a combination of a rotating converter target with the incident beam rastering on the converter with magnetic steering elements (a.k.a wobbling). In this way, the effective beam size will be increased by an order of magnitude, thus reducing the power density and increasing the emission area for radiation cooling. In order to preserve positron beam brightness, anti-rastering is done synchronously, where the anti-raster is located immediately downstream of the converter. In addition, the converter is tilted with respect to the incident beam. The raster area is thus increased further. We performed simulations to determine the maximum raster width that allows transportation of positron beam to the moderator without significant loss of intensity. This study showed that with a 45˚ tilted converter and 1.4 cm full width raster size (with positron anti-rastering), about 12% positron intensity is lost when compared to transportation without any rastering.

At high temperature, cooling through radiation emission is the predominant cooling mechanism, so the emission area should be as large as possible. As mentioned, in addition to rastering the electron beam, the effective emission area of the converter is increased by rotating the converter. This type of rotating converters has been used for many years and is well-developed. For the temperature calculations in a rotating converter, we assumed a 45˚ tilted ring type converter with 100 cm outer radius and a radial thickness of 1.4 cm. With 45˚ tilt, the actual converter thickness is reduced to 4.2 mm in order to keep the interaction length 6 mm. The effective emission area is calculated to be A ~ 1746 cm^2 with mass M ~ 14.3 kg. The emissivity coefficient is taken to be =0.26 as provided in the literature[11] for the expected temperature range in our calculations. In steady-state, we calculated that the temperature of the converter will be T ~ 1753 ̊K. In order to obtain a uniform temperature profile, we calculated that the required rotation frequency should be at least 2 Hz (Tangential velocity ~ 12.6 m/s). We also calculated the induced eddy-current power loss and found that the loss is insignificant due to the low speed of the converter.

Pure tungsten is a brittle element which makes it challenging to work with. One study related to the engineering aspects of rotating positron converter targets concluded that tungsten alloy such as, W-Ta(90%) is much easier to work with and more durable to the thermally induced stress loads[12], Therefore, W-Ta(90%) will be used to construct the wheel as Ta has a high-melting temperature and similar emissivity values to W[13].

Positron capture and the transport line to the moderator

The integrated positron beamline layout is shown in Fig. 3. Essentially, two major processes are required to produce slow-positrons. First, a driving electron beam from a linac hits the converter target thus producing positrons. We then capture low-energy positrons (T_+ below 600 keV) and transport them to the moderator. Second, in the moderator, the positrons lose energy and then a fraction of them are able to escape to the surface as slow positrons with T_+ on the order of a few eV. For the transportation of positrons to the moderator we designed an arc-

shaped solenoid capture and transport channel. The purpose of this curved transport channel is to transport positrons away from the high radiation area around the converter. The high-energy photons, electrons and positrons are much more collimated than low-energy particles and they will hit the beam dump along a straight path. The curved channel has a bending radius = 4 m and total arc length is planned to be 6 m with an arc angle 90˚. The required longitudinal field in the solenoid channel is 2 kG, which is enough to capture lower energy positrons at larger opening angles (T_+ up to 600 keV and x' up to 800 mrad). The aperture diameter of the solenoid channel is 6 cm. Corrector dipole magnets are superposed on the channel to allow the positrons to follow the curve.

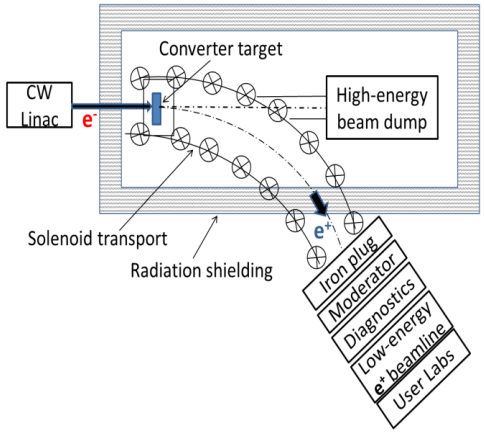

Figure 3. Conceptual layout of the positron beamline. Drawing is not to scale.

The required integrated field along the channel is calculated to be B[G]·ds[cm] = 1350 G-cm. The extraction of the positrons from the channel to a very low magnetic field area will be achieved by a magnetic field terminator ("plug"). In Fig. 4 (a) and (b), the concept of the design is illustrated. The extraction efficiency from the solenoid channel is enhanced with rapid extinction of the guide field. Otherwise, the lowest energy, and most desirable positron, will follow the diverging field lines into material surfaces and be lost.

In Fig. 4(c), the end section of the solenoid (red) and half cross-section of the plug (green) are shown, which has been designed in OPERA-3D (TOSCA solver). We designed and constructed a simpler prototype iron plug to compare magnetic field termination and positron transmission characteristics against our calculations. As we presented in previous work[14] the simulation and data are in good agreement, resulting in a thousand-fold reduction in field. Further reduction of the field to the mG levels can be achieved with metal shielding.

Transport calculations of positrons were performed with GEANT4-based software. A snapshot from the simulation is shown in Fig. 5. In this snapshot, we only present the solenoid transport channel, the plug, and the positrons that are able to penetrate through the plug. For the purpose of presenting a clear picture, other particles are eliminated.

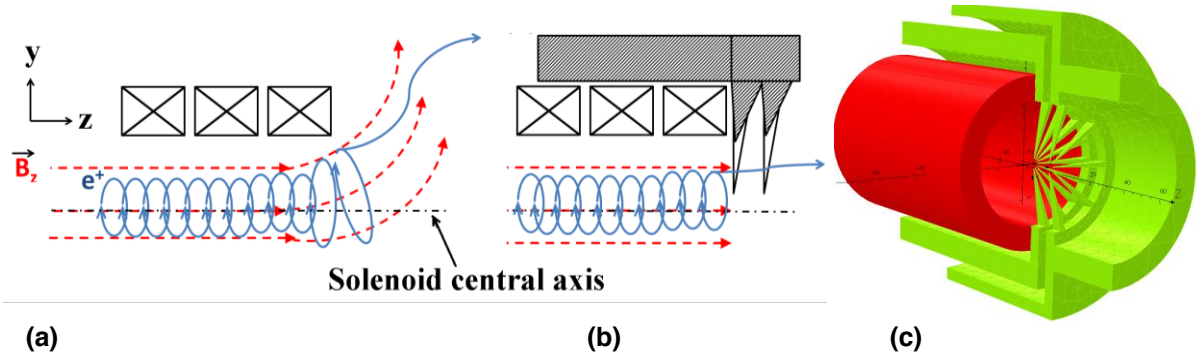

Figure 4. Concept of transport through the solenoid channel (a) without and (b) with the magnetic steel plug. Solid blue lines show positron track. Dashed red lines are magnetic field lines. Only the upper half of solenoid is shown.
(c) OPERA 3D Model of the magnetic plug is shown.

Approximately 25% of the positrons that have reached to the iron plug from the tungsten converter are lost while traversing the plug. The kinetic energy spectrum of the positrons that are able to reach to the moderator is shown in Fig. 6b. The positron efficiency on the moderator is calculated to be 6.6×10^{-4} positron/incident electron. With the assumption of 1 mA incident electron beam current, the intensity on the moderator would be about 4×10^{12} positron/s within a transverse spot size of x,y ~ 8 mm r.m.s as seen in Fig. 6a. By using 1% efficiency with solid neon RGM, the projected slow positron intensity would be 4×10^{10} slow positrons/sec.

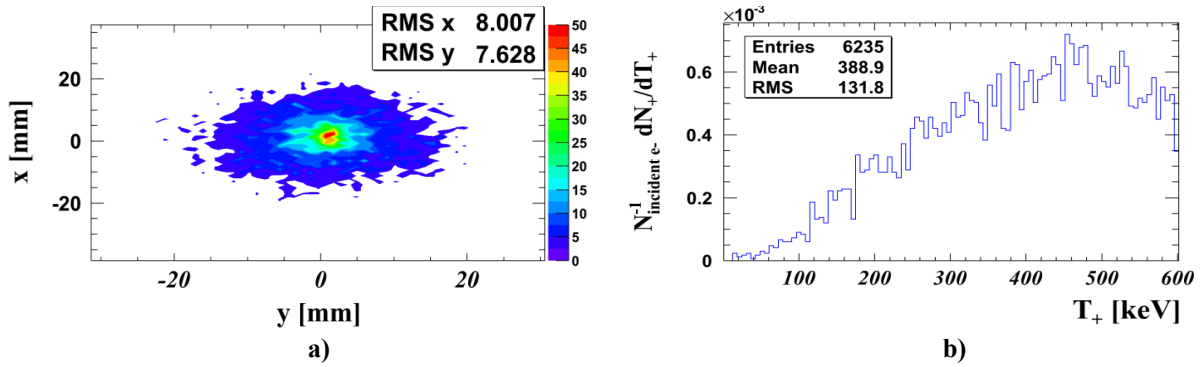

Figure 5. (a) The transverse spot profile of the positron beam on the moderator. Here we present positrons with energies below 600 keV. (b) Kinetic energy of the positrons after the iron plug. Positrons shown here have a cut in energy with T+ < 600 keV.

Focusing and Remoderation of Slow Positrons

Moderated slow-positrons will be extracted from the moderator by the electrostatic focusing elements. Electrostatic focusing is dominant for low speed particles in a low magnetic field environment.

It is known that the energy spread of the emitted slow positron from RGMs is higher than W moderators, thus this will result in lower beam brightness. This low brightness can be offset by higher intensity and through further re-moderation in a very thin W foil a process known as brightness-enhancement[15]. The brightness-enhancement will be done as illustrated previously in Figure 2. Although, after the re-moderation process only 5% of the positrons survive, the brightness of the beam will be increased significantly by at least 3 orders of magnitude due to the reduction in the transverse size and energy spread. As it is shown[16], a slow positron micro-beam can be produced with a transverse size of less than 100 μm on a sample.

Since the solenoid captures both positrons and electrons from the converter, the number of electrons that are able to reach to the moderator is a factor of 10 higher than the number of positrons. There is also a small portion with positron and e- energies up to 2.5 MeV that make it to the moderator. The total power of the particles that reach the moderator is about 20 W (when incident e beam is 120 kW). Simulations with 500 μm thick solid-Neon show that about 10% (~ 2 W) of this power will be deposited in the moderator. With adequate cooling in the moderator, this power can easily be extracted from the system. If the temperature increase in the moderator cannot be prevented due to these electrons, we will implement a small dipole magnet to divert low-energy electrons away from the moderator.

Radiation Aspect and Deposited Power in All Elements with a High-Power High-Energy Electron Beam

The advantage of using an existing accelerator facility for positron production brings extra efforts and costs for radiation protection. JLab's effective radiation administrative dose limit[17] is not to exceed 250 mrem (2.5 mSv)/calendar year for radiation workers and 10 mrem (0.1 mSv)/calendar year for non-radiation workers. In order to reach this design goal, the radiation protection design aspects of the FEL vault was considered not to exceed 0.1% beam loss (1 kW) at 200 MeV-5μA during continuous operation at any point along the beam line[18]. The maximum possible beam loss (100% of the beam) occurs when the beam is sent to the beam dump, where additional

shielding was constructed locally to prevent exceeding the overall design limit. Dose rates at the surface of beam dump areas should not exceed 5 mrem/h (at 30 cm distance).

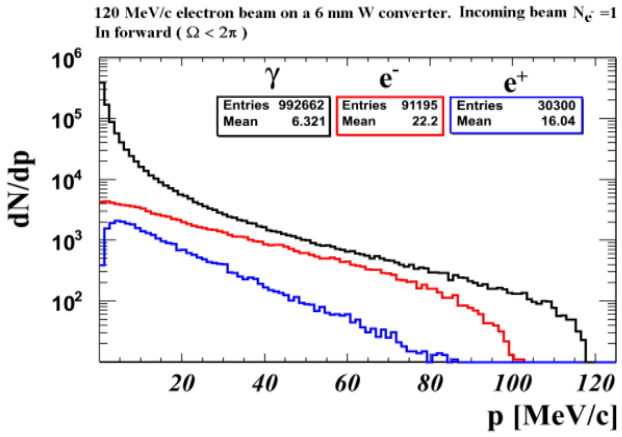

Figure 6. The probability distribution of the emitted particles from the converter.

Local shielding will be required in order to achieve radiation protection design goals at the FEL. In our proposed design, as shown conceptually in Fig. 3, the positron production area mainly consists of the converter, the transport channel, the beam dump, and the radiation shielding elements. We performed simulations to estimate the required thicknesses of the shielding materials and how much power will be deposited in these mentioned elements. In Fig. 6, the momentum spectrums of the γ rays, electrons, and positrons emitted from the W converter are plotted. As is seen, the main concern here is the γ rays as the intensity is a magnitude higher and they are not easily attenuated. Considering the average photon energy which has a broad peak between 1 and 6 MeV, at least 30 cm thick steel (=7.8 g/cm^3 and photon attenuation of ~ 33 g/cm^2)[19] is required to attenuate the intensity of the photons to 0.1% of its initial intensity. A lower thickness of lead could be used but this creates more neutrons. In Table 1, we present the percentage of deposited power in each element around the converter. The absolute deposited power values in the second column are provided for a 120 MeV, 1 mA incident electron beam on a 6 mm thick tungsten converter. Of this 120 kW of power, ~ 57 kW (47.5%) will be deposited in the shield, ~ 30 kW (25%) in the beam dump, ~ 24 kW (20%) in the converter, ~ 9 kW (7.5%) in the solenoid. About 0.1 kW (0.1%) is calculated to escape from the shielding from the aperture where the solenoid channel exits. The calculated power leak from the shielding is well below the radiation dose limit.

TABLE 1. Simulation of deposited power in elements.

Element	Percent (%)	Deposited (kW)
Shield	47.5	57
Beam Dump	25.0	30
Converter	20.0	24
Solenoid	7.5	9
Escaped	0.1	0.1

Conclusions

The Low Energy Recirculation Facility at Jefferson Lab can provide a bright, high power beam for the production of low energy positrons. By using a combination of a rare-gas cryogenic moderator and tungsten final moderator we can provide over 10^{10} positrons/sec. at low energy and can moderate them to 10^7 positrons/sec. with a very small spot size. We should note that polarized positrons are also possible if a polarized hydrogen target is used to eliminate one spin orientation, though the flux would be reduced by a large factor.

ACKNOWLEDGMENTS

This material is based upon work supported by the U.S. Department of Energy, Office of Science, Office of Nuclear Physics under contract DE-AC05-06OR23177.

REFERENCES

1. http://positron.physik.uni-halle.de/EPOS/
2. D. Abbott et al., *Physical Review Letters* **116**, 214801 (2016).
3. Allen Mills noted "The spin polarized gas has to be spin aligned atomic H so the annihilation rate differs by a factor of 372 between positrons polarized parallel and antiparallel to the H spins", in a conversation with the authors.
4. S. Benson, D. Douglas, G. Neil and M. Shinn, "The Jefferson Lab free electron laser program", J. Phys. Conf. Ser. **299** 012014 (2011).
5. See Positron Beams and Their Applications, edited by P. G. Coleman (World Scientific, Singapore, 2000).
6. C. Hugenschmidt et al., *Appl. Phys.* **A 74** [Suppl.], S295–S297 (2002).
7. A. P. Mills et al., Rev. of Sci. Instr. **77**, 073106 (2006).
8. I. R. Bailey, "A Prototype Target Wheel for the ILC Positron Source", Proceedings of EPAC08, Genoa, Italy, 2008.
9. V. Bharadwaj, R. Pitthan, J. Sheppard, H. Vincke, J. W. Wang, "Heat Deposition in Positron Sources for ILC", Proceedings of PAC '05, Knoxville, Tennessee, 2005
10. J. Gronberg, "Positron Source Technology R&D", International Linear Collider PAC meeting –Eugene Oregon, November 11, 2010
11. V. D. Dmitriev and G. K. Kholopov, "Integral Radiant Emissivity of Tungsten in the 1200-2800 K Temperature Range", *Zhurnal Prikladnoi Spektroskopii*, **3** pp. 72- 75 (1965).
12. B. Feerick, "Engineering basis for selection of positron source material", Technical Report, SLAC-CN-250, Url: http://www.osti.gov/bridge/servlets/purl/6901418-5Cd12u/
13. N. D. Milosevic, G. S. Vukovie, D. Z. Pavicid, and K. D. Maglic, "Thermal Properties of Tantalum Between 300 and 2300 °K", *International Journal of Thermophysics*, **20** (1999).
14. S. Golge, B. Vlahovic, and B. Wojtsekhowski "High-Intensity Low-Energy Positron Source at Jefferson Laboratory", Proceedings of IPAC-12, p.1461, New Orleans, Louisiana (2012).
15. A. Mills, "Brightness enhancement of slow positron beams" *Appl. Phys.* **23**, 189-191 (1980).
16. Nagayasu Oshima, Ryoichi Suzuki, Toshiyuki Ohdaira, Atsushi Kinomura, Takamitsu Narumi, Akira Uedono, Masanori Fujinami, "A positron annihilation lifetime measurement system with an intense positron micro beam", *Radiation Physics and Chemistry* **78**, pp. 1096–1098 (2009).
17. Radiological Standards, Ch. 2, ES&H Handbook, Radiation and Control Group, Jefferson Lab, Rev. 4.
18. T. Dunn, G. Neil and G. Stapleton, "Radiation Control Aspects of the Civil Construction for a High Power Free Electron Laser (FEL) Facility", CP392, Application of Accelerators in Research and Industry, p.1405, edited by J. L. Duggan and I L. Morgan, AIP Press, New York (1997).
19. Berger, M.J., Hubbell, J.H., Seltzer, S.M., Chang, J., Coursey, J.S., Sukumar, R., Zucker, D.S., and Olsen, K. (2010), XCOM: Photon Cross Section Database (version 1.5). [Online] Available: http://physics.nist.gov/xcom. National Institute of Standards and Technology, Gaithersburg, MD.

Polarized Positrons in Jefferson Lab Electron Ion Collider (JLEIC)

Fanglei Lin[1, a)], Joe Grames[1, b)], Jiquan Guo[1, c)], Vasiliy Morozov[1, d)], Yuhong Zhang[1, e)]

[1]*Thomas Jefferson National Accelerator Facility, Newport News, VA, 23606, USA*

[a)]fanglei@jlab.org [b)]grames@jlab.org [c)]jguo@jlab.org
[d)]morozov@jlab.org [e)]yzhang@jlab.org

Abstract. The Jefferson Lab Electron Ion Collider (JLEIC) is designed to provide collisions of electron and ion beams with high luminosity and high polarization to reach new frontier in exploration of nuclear structure. The luminosity, exceeding 10^{33} $cm^{-2}s^{-1}$ in a broad range of the center-of-mass (CM) energy and maximum luminosity above 10^{34} $cm^{-2}s^{-1}$, is achieved by high-rate collisions of short small-emittance low-charge bunches with proper cooling of the ion beam and synchrotron radiation damping of the electron beam. The polarization of light ion species (p, d, ^{3}He) and electron can be easily preserved, manipulated and maintained by taking advantage of the unique figure-8 shape rings. With a growing physics interest, polarized positron-ion collisions are considered to be carried out in the JLEIC to offer an additional probe to study the substructure of nucleons and nuclei. However, the creation of polarized positrons with sufficient intensity is particularly challenging. We propose a dedicated scheme to generate polarized positrons. Rather than trying to accumulate "hot" positrons after conversion, we will accumulate "cold" electrons before conversion. Charge accumulation additionally provides a novel means to convert high repetition rate (>100 MHz) electron beam from the gun to a low repetition rate (<100 MHz) positron beam for broad applications. In this paper, we will address the scheme, provide preliminary estimated parameters and explain the key areas to reach the desired goal.

INTRODUCTION

The proposed Jefferson Lab Electron Ion Collider (JLEIC) has been developed to achieve the physics requirements outlined in the EIC white paper [1]. The overall design strategies towards high luminosity and high polarization have not changed over a decade, but technical design aspects have evolved. The design considers a balance of machine performance, technical risk, cost and path for future upgrade. In addition to the electron and ion collision as it is carried out in the JLEIC, physicists also found that collision of polarized positron and ion beams provide more capabilities to study the physics world [2, 3, 4, 5, 6, 7, 8, 9]. From the accelerator design point view, acceleration, accumulation and store of polarized electron and position have no significant difference, as long as polarities of powered magnets are inversed and some charge-related collective effects are solved. The most, probably the only, challenging part is the generation of intense positron beams with high polarization. Several methods to create polarized positrons have been explored and/or applied at different circumstances [10, 11, 12, 13, 14, 15]. However, each scheme has its own advantages and disadvantages, and does not satisfy the JLEIC injection and current requirements.

A new approach, referred to as the Polarized Electrons for Polarized Positrons (PEPPo) technique [16, 17], has been investigated at the Continuous Electron Beam Accelerator Facility (CEBAF) of the Thomas Jefferson National Accelerator Facility. Polarized positrons are generated by the bremsstrahlung radiation of low energy longitudinally polarized electrons within a high-Z target and e^+e^- pair production. The PEPPo concept can be developed efficiently

with a low momentum (10 – 100 MeV/c) and high polarization (>80%) electron beam driver. This opens access to polarized positon beams to a wide community and without creating a highly radioactive environment. The experiment demonstrates highly efficient transfer of polarization from 8.19 MeV/c primary electrons to the produced positrons [18].

In the paper, we first provide an overview of JLEIC baseline design. Then a description of generating high polarized positron beams for the JLEIC on the basis of PEPPo technique is followed, and some key areas to reach the desired performance are discussed.

JLEIC DESIGN OVERVIEW

Physics motivations of electron-ion collisions have been addressed in detail in the EIC white paper [1]. The design performance of JLEIC [19] is consistent with the requirements of the science program in the white paper. The JLEIC is designed as a traditional ring-ring collider. The electron complex is composed of CEBAF and electron collider ring. The existing CEBAF serves as an electron injector of the collider ring. The ion complex is composed of ion source, SRF linac, booster and ion collider ring. The green field new ion complex and electron collider ring provide opportunity for a modern design to achieve highest performance. The central part of JLEIC is two figure-8 shape collider rings that are vertically stacked and housed in the same tunnel. The figure-8 crossing angle is 81.7°, partitioning a collider ring into two arcs and two long straights. The ion beam excuses a vertical excursion to the plane of electron ring for a horizontal crossing during the electron-ion collisions. Two collider rings have nearly identical circumferences and fit well in the Jefferson Lab site. Figure 1 shows a cartoon model of the layout of JLEIC accelerator complex.

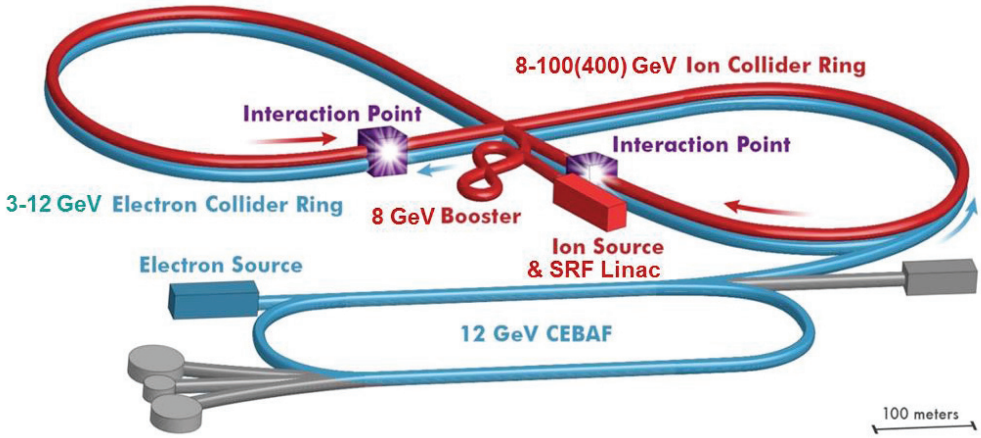

FIGURE 1. A layout of JLEIC accelerator complex.

The design strategy to reach high luminosity in the JLEIC is high bunch repetition rate collision of beams. Both electron and ion beams have very short bunch length and small transverse emittances so that beam sizes at the collision point can be focused to a micrometer level. This configuration, combining with a the high bunch repetition rate, can significantly boost the collider luminosity. This high bunch repetition rate ensures small bunch charge of colliding beams, leading to relatively weak collective and inter-beam scattering effects, while maintains high bunch beam current to provide high luminosity. Such luminosity strategy has been validated by the lepton-lepton B-factory colliders worldwide. For example, the KEK-B factory has reached a world record luminosity of a few of 10^{34} $cm^{-2}s^{-1}$ [20], and Super-KEKB factory is aiming for a luminosity of 10^{36} $cm^{-2}s^{-1}$ [21].

The design strategy to reach high polarization is adopting figure-8 shape ring [22] (ion booster, ion and electron collider rings) to preserve and control the polarization. Because of the opposite dipole fields in two arcs in a figure-8 shape ring, the net spin rotation majorly due to arc dipoles is zero and the whole ring becomes “transparent” for the spin. Any spin orientation at any orbital location repeats every turn, and there is no preferred polarization. In another world, the spin tune in a figure-8 shape accelerator is zero and energy independent. This novel concept eliminates spin despoliation resonances during the acceleration and polarization at the collision point can be easily stabilized and controlled using weak-field compact magnet insertions [23, 24]. This property is universal and does

not depend on the particle type. In particular, the figure-8 shape ring provides a real, perhaps the only, opportunity for obtaining polarized deuteron beams with energies greater than a few tens of GeV [25].

One key feature in the JLEIC is the full detector acceptance to all fragments produced in collisions. The primary detector region [19] is essentially designed to meet such requirement by having scattered particles being detected at the center detector and downstream detectors along the beam lines with close to 100% acceptance and necessary resolution. 50 mrad crossing angle is introduced at the collision point to separate two beams quickly after collision to avoid the parasitic collision. Such large crossing angle also improves the detection by moving spot of poor resolution along the detector solenoid axis into the periphery. In addition, the detector region design also satisfies requirements of beam dynamics and geometric matching.

Table 1 presents the JLEIC baseline design parameters at three representative design points in the low, medium and high CM energy regions, respectively [26]. The luminosity is above 10^{33} $cm^{-2}s^{-1}$ in all these design points, and reaches 2.1×10^{34} $cm^{-2}s^{-1}$ at the medium CM energy of approximately 45 GeV. At the low energies, space charge of the low energy ion beam severely limits the bunch charge, particular for the short bunches in the JLEIC. Therefore, a relatively long bunch length is preferred to accommodate the full bunch charge while still remaining the design limit for the Laslett space charge tune-shift of 0.06. At the high energies, synchrotron radiation of the electron beam is the dominating effect. The electron beam current needs to be scaled down proportionally to the 4^{th} power of the beam energy to reduce the synchrotron radiation power to a reasonable level of 10 MW. To compensate the reduction of electron beam current, a relatively low bunch repetition rate and proportionally increased bunch charge are adopted to boost the luminosity. At the medium CM energies, the strong beam-beam effect dominates the JLEIC luminosity. An optimum luminosity above 10^{34} $cm^{-2}s^{-1}$ can be achieved by combining a high bunch repetition rate, small beam emittance and small β^* at the IP. This energy region delivers the highest luminosity in the JLEIC.

TABLE 1. JLEIC baseline design parameters for e^-p collisions.

	Unit	Beam Parameters					
Center of mass energy	GeV	21.9		44.7		63.3	
Species		p	e^-	p	e^-	p	e^-
Beam energy	GeV	40	3	100	5	100	10
Collision frequency	MHz	476		476		476/4=119	
Particle per bunch	10^{10}	0.98	3.7	0.98	3.7	3.9	3.7
Beam current	A	0.75	2.8	0.75	2.8	0.75	0.71
Polarization	%	80	80	80	80	80	75
Bunch length, RMS	cm	3	1	1	1	2.2	1
Norm. emit., horiz./vert.	μm	0.3/0.3	24/24	0.5/0.1	54/10.8	0.9/0.18	432/86.4
Horizontal & vertical β^*	cm	8/8	13.5/13.5	6/1.2	5.1/1	10.5/2.1	4/0.8
Vert. beam-beam param.		0.015	0.092	0.015	0.068	0.008	0.034
Laslett tune-shift		0.06	7×10^{-4}	0.055	6×10^{-4}	0.056	7×10^{-5}
Detector space, up/down	m	3.6/7	3.2/3	3.6/7	3.2/3	3.6/7	3.2/3
Hourglass (HG) reduction		1		0.87		0.75	
Luminosity/IP, w/HG, 10^{33}	$cm^{-2}s^{-1}$	2.5		21.4		5.9	

The highest CM energy in the JLEIC is mainly dominated by the ion beam energy, which is determined by the maximum arc dipole field. The higher the maximum dipole field is, i.e. the higher the ion beam energy can be reached, the wider the CM energy region will be. The baseline design adopts a cost-effective super-ferric-type superconducting magnet for the arc dipoles. Current maximum field of such magnet is ~3 T, resulting a maximum proton beam energy of 100 GeV. Then, the maximum CM energy is about 63 GeV. For the future energy upgrade, both maximum luminosity and maximum CM energy can be expanded with high dipole field. Figure 2 illustrates general trends of JLEIC luminosity for e^-p collisions in the CM energy region with different maximum arc dipole fields [26].

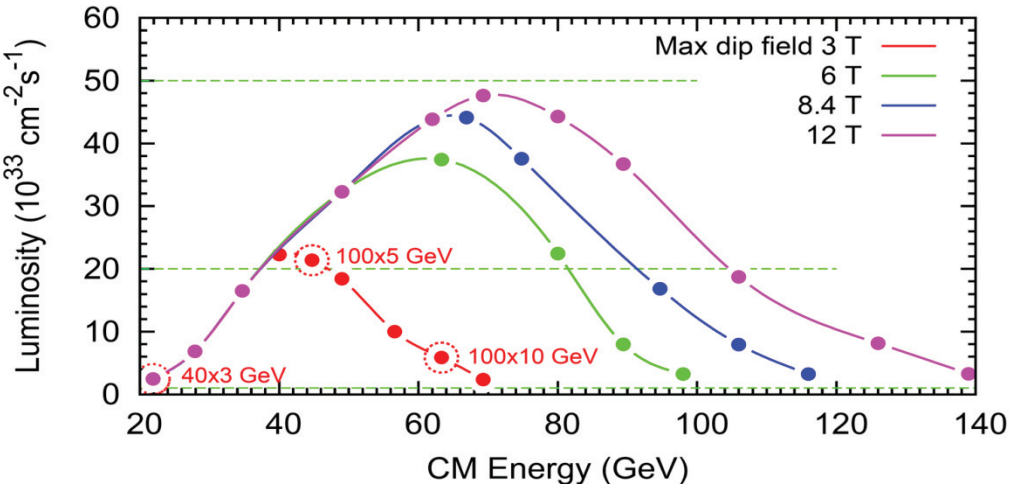

FIGURE 2. Luminosity of e^-p collisions in the JLEIC with different maximum arc dipole fields a) red dots represent the luminosity in the baseline design with a 3 T super-ferric-type maximum arc dipole field, b) green dots represent the luminosity with a 6 T (super-ferric- or cosθ-type) maximum arc dipole field (proton energy up to 200 GeV, CM energy up to ~100 GeV), c) blue dots represent the luminosity with a 8.4 T LHC-type maximum arc dipole field (proton energy up to 280 GeV, CM energy up to ~115 GeV), d) purple dots represent the luminosity with a possible future 12 T maximum arc dipole field (proton energy up to 400 GeV, CM energy up to ~140 GeV).

JLEIC WITH POLARIZED POSITRONS

Physics Interest and Requirements

Recently, an interest in polarized positron-ion collisions at a future EIC has revived. Physicists believe this offers EIC an additional probe to study the substructure of nucleons and nuclei. For instance, with both polarized electron and positron beams at EIC, one could obtain a full flavor decomposition of the nucleon quark and antiquark distributions, as well as provide understanding the meson cloud effects and diffractive contributions to structure functions [2]. The flavor separation of the pion and kaon structure could be achieved by comparing the difference between electron and positron interactions involving the Sullivan process [3] with neutral and charged currents. Note that the availability of positron beams may be the only way to get to quark flavor decomposition of the pion and kaon structure, and allow comparisons of the quark and gluon distributions in the pion, kaon and proton.

The charged-current deep inelastic scattering (DIS) cross section measurements provide possibly the most direct information on the flavor dependence of quark and antiquark distributions. Depending on the charge of the exchanged W boson, the charged current process will be sensitive to either up-type or downtype flavors. Furthermore, charm and anticharm production in charged current DIS offers the best way to obtain information on strangeness in the nucleon, and the availability of polarized positron and electron beams would provide the necessary tools to extract strange and antistrange distributions unambiguously [6, 7]. Likewise to the production of Ds^+ mesons in diffractive charged current DIS, that could provide information on the gluon structure of nucleons and the diffraction mechanism in QCD [8].

In addition, the charged current DIS measurements may provide new possibilities to probe for physics beyond the Standard Model. The Standard Model does not predict right-handed charged currents, so that the cross section for electron (positron)-proton charged current DIS with helicity +1(-1) is expected to vanish. Measuring the beam longitudinal polarization sensitivity of the total charged current cross section allows one to set limits on the right-handed W-boson exchange. This requires polarization measurements with high precision [9]. A longitudinally polarized positron beam also offers sensitivity, for example, to squark production in R-parity violating SUSY models, where only left- (right-) handed electrons (positrons) contribute. For leptoquark searches, different lepton beams and polarizations will allow selective increase in the sensitivity to different leptoquark types.

High luminosity and high polarization are essential to perform these measurements. Ideally, machine performance of positron-ion collisions should be similar to that of electron-ion collisions at the JLEIC, if the polarized positron source has the same efficiency as the current electron source. However, the generation of positron beams with high polarization and high bunch charge is particularly challenging. Considering a balance of accelerator

design and physics requirement, collision luminosity of $\sim 10^{33}$ $cm^{-2}s^{-1}$ and position polarization ~ 40% are proposed as a reasonable low threshold of requirements for valuable science program at an EIC [27].

PEPPo Based Polarized Positron Injector

Schemes for creating polarized positron beams have been explored in the past, and some of them are even applied in an accelerator. Radioactive sources can be used for low energy positrons [10], but the flux is restricted. Storage or damping rings can be used at high energy, taking advantage of the self-polarizing Sokolov-Ternov effect [11], however, this approach is generally not suitable for external beams and continuous wave injection facilities. Two schemes based on the e^+e^- pair creation process from circularly polarized photons [12, 13] have been explored and investigated successfully: the Compton backscattering of polarized laser light from a GeV unpolarized electron beam [14], and synchrotron radiation of a multi-GeV unpolarized electron beam travelling within a helical undulator [15]. Both experiments demonstrated high positron polarization, confirming the transfer efficiency of the pair production process for a polarized positron. However, both techniques require high energy electron beams and further development of challenging technologies.

A new approach, referred to as Polarized Electrons for Polarized Positrons (PEPPo) technique [16, 17, 18], has been investigated at the CEBAF of the Thomas Jefferson National Accelerator Facility. Taking advantage of advances in high polarization, high intensity electron sources [28], it exploits the fact that polarized photons generated by the bremsstrahlung radiation of low energy longitudinally polarized electrons within a high-Z target produce polarized e^+e^--pairs. It is expected that the PEPPo concept can be developed efficiently with a low momentum (10 - 100 MeV/c), high intensity (> 1 mA) and high polarization (>80%) electron beam driver. While the polarization transfer by bremsstrahlung and pair creation is similarly efficient for any incident electron energy, the yield of positrons is not. Rather, the positron yield scales approximately with the beam energy. In the energy range of ~10 – 100 MeV, the positron conversion/collection efficiency is relatively low, ~ 10^{-5} to 10^{-3}.

The strategy to compensate for the low positron efficiency is to accumulate charge on the basis of PEPPo technique. However, rather than accumulating "hot" positrons with large phase space distributions after conversion, we propose to accumulate "cold" dense electrons before conversion. A high-level diagram of the polarized positron injector, satisfying the requirements of luminosity and polarization for the JLEIC [27], is show in Fig. 3 along with preliminary parameters at each step along the injection chain.

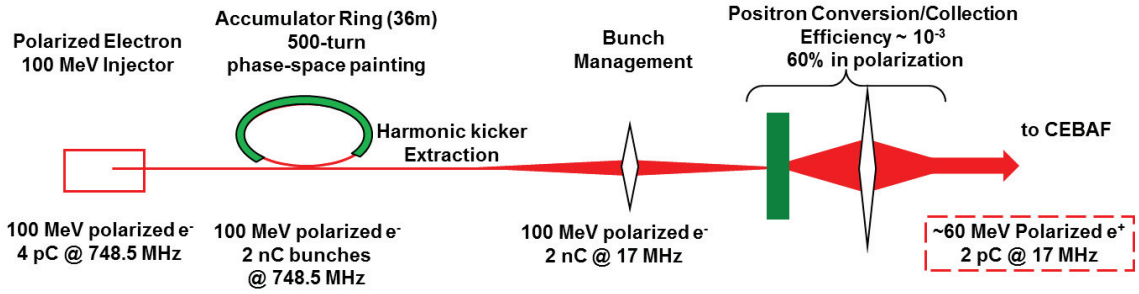

FIGURE 3. Polarized positron injector for the JLEIC.

Accumulation of polarized positrons for the JLEIC collider ring requires an average polarized positron current of about 10 nA, considering a reasonably short injection time and sufficient injected beam current to maintain high equilibrium polarization. Figure 4 shows the polarized positron bunch train pattern injected into the JLEIC collider ring. The 17 MHz micro bunch train from the polarized positron injector matches the RF frequency of CEBAF 1497 MHz (1/88 of 1497 MHz) and the one of JLEIC 476 MHz (1/28 of 476 MHz). The injected beam into the JLEIC collider ring is not exactly a CW fashion because the bunches need on the order of a few tens of millisecond (20 – 85 ms in Fig. 4) to damp to the design orbit. Thus, the key of polarized positron injection into the JLEIC is a positron source that provides a low-duty, relatively high-current micro bunch structure with low average current. As shown in Fig. 3, lowering the duty factor is accomplished by collecting the beam coming from the electron source within an accumulator ring.

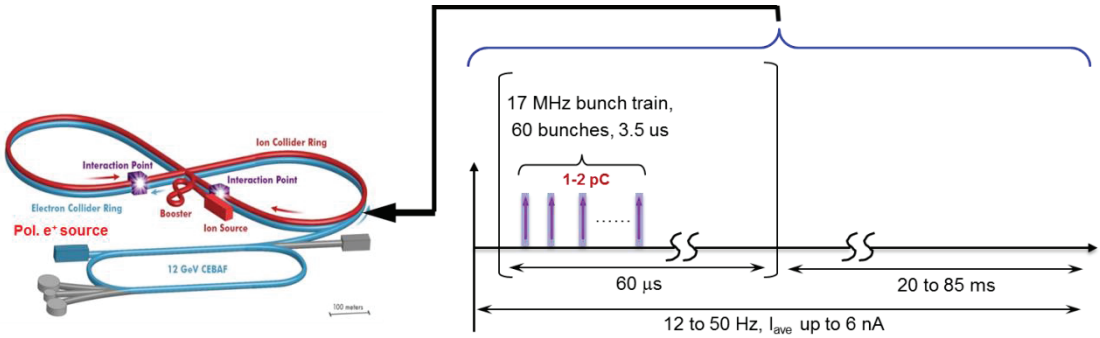

FIGURE 4. Polarized positron injection bunch pattern into the JLEIC electron collider ring.

As the beginning of this injector chain, spin polarized GaAs-based photo-guns must exhibit long photocathode operating lifetimes and can provide a micro pulse current up to 3 mA. A dc-high voltage GaAs photo-gun has been built at Jefferson Lab based on a compact inverted insulator design [29] for high average current photocathode lifetime studies at a dedicated test facility up to 4 mA of polarized beam, which meets the requirement of a 3mA micro pulse current from the polarized electron source in the proposed position injector scheme. In achieving this, the photo-gun employs the best learned practices, e.g. (a) operating with the drive laser beam positioned away from the electrostatic center of the cathode/anode, (b) limiting the photocathode active area to eliminate photoemission by stray light, (c) using a large drive laser beam to distribute ion dam-age over a larger area, (d) applying low bias voltage to the anode to repel ions downstream of the gun, and (e) operating with immeasurable field emission. However, a very high voltage at the photo-gun minimizes the ill-effects of space charge forces which degrade the emittance and introduce beam loss leading to a diminished photo-gun charge lifetime. High voltage increases QE by lowering the potential barrier (Schottky effect) [30] and suppresses the surface charge limit [31]. In addition, a very high bias voltage may enhance the operating lifetime of the photo-gun by quickly accelerating the beam to energy with very small ionization cross section. Further gains are necessary in order for sustained operation of the polarized electron source at milliAmpere currents to be realized.

Beam accumulation in the accumulator ring is the essential step in the positron injector. The main function of the accumulator ring is to convert the high duty factor, low intensity electron bunch train available from the electron gun into low duty factor and high charge per bunch beam, using multi-turn phase painting injection that has been successfully demonstrated for 75 turn injection of Pb^{54+} in the LEIR at CERN [32]. The phase-space painting does not increase the local phase-space density but accumulates the beam at the expense of increasing its 6D emittance. Therefore, rather than accumulating low phase-space density polarized positrons, electron bunches with very small emittances from the photo cathode can be efficiently stacked in the accumulator ring. A high bunch repetition rate, 748.5 MHz shown in Fig. 3, in the accumulator ring is preferred to keep the ring relatively compact. A stripline RF kicker is fired to create 17 MHz pulses with a short pulse width to extract 1 in every 44 bunches in the accumulator ring, leaving the rest bunches unperturbed. The longitudinal dynamics will be managed by a low voltage RF cavity running at 1497 MHz or a sub-harmonic and by an appropriate adjustment of the compaction factor. To preserve the polarization, a full solenoid Siberian snake is placed at the symmetry point $\theta=\pi$ with respect to the injection location in the accumulator ring. This guarantees that the injected beam's polarization is aligned with the store beam's one during the accumulation.

Polarized electron beam strikes a high-Z target, and results in an efficient electro-magnetic shower. Then spin-polarized positrons are generated by transferring spin first from electrons to photons (polarized bremsstrahlung) and second from photons to positrons (polarized pair-creation). In order to handle positrons, electron beam parameters are optimized at the radiator firstly. For any reasonable electron beam size at the target, the positron angular spread greatly dominates over the initial electron angular spread. Therefore, the rms positron emittance $\varepsilon_{x,y}$ in each plane after the target can be written as $\varepsilon_{x,y} \approx \sigma_{x,y}\, \theta_{rms}$, where $\sigma_{x,y}$ is the horizontal/vertical electron beam size at the radiator. Obviously, minimizing the electron beam size at the radiator lowers the final positron emittance, however, leading to a high instantaneous power density at the beam spot location on the target. This problem may be solved by considering a liquid metal design demonstrated by Niowave Inc [33].

The end of the injector chain is the existing CEBAF, which accelerates positron beam from the injected low energy to the desired high energy. Therefore, CEBAF, used as an continuous electron beam facility, needs to be demonstrated that it has the capability to accelerate positron beams. First investigation of CEBAF magnet and

diagnostic system has been performed [34, 35]. For those bipolar powered magnets, most quadrupoles and correctors, they need set point for a polarity inversion only. Given availability of tune-up diagnostics, none of the bipolar magnets have any known problems with polarity inversion. For those unipolar powered magnets, recirculation arc dipoles and spreader/recombiner vertical dipoles, need to swap the lead on the "shunt" controls attached to the magnet string being inverted. They also need swap power leads at the power supply. The concerns of magnet over-temperature sensors, ground fault detection and power supply internal protections are all independent of polarity inversion. All diagnostic systems should work for a positron beam with a pulse current of a few tens of microampere and peak power of 0.6 kW.

The preliminary JLEIC parameters for collision of polarized positron and proton beams at three CM energies are listed in Table 2. The parameters are estimated using the proposed positron generation scheme for the injection of beam to the collider ring. The luminosity below 10^{33} $cm^{-2}s^{-1}$ at the low CM energy 21.9 GeV is limited by the space charge effect of proton beam at the low energy. Figure 5 shows the potential luminosity of e^+p collision at three CM energies given in the Table 1, plus an additional CM energy 33.5 GeV (collision of 70 GeV proton and 4 GeV positron beams). As it is shown, the luminosity is above 10^{33} $cm^{-2}s^{-1}$ when the CM energy is higher than 33.5 GeV. The luminosity degrades at high energies (but still above 10^{33} $cm^{-2}s^{-1}$) due to the large electron beam emittance (resulting in large beam sizes at the collision point).

TABLE 2. Preliminary JLEIC parameters for e^+p collisions.

	Unit	Beam Parameters					
Center of mass energy	GeV	21.9		44.7		63.3	
Species		p	e^+	p	e^+	p	e^+
Beam energy	GeV	40	3	100	5	100	10
Collision frequency	MHz	476/4=119		476/4 = 119		476/4 = 119	
Particle per bunch	10^{10}	1.1	1.1	2.1	1.1	3.9	1.1
Beam current	A	0.2	0.2	0.4	0.2	0.75	0.2
Polarization	%	80	40	80	40	80	40
Bunch length, RMS	cm	3	1	2	1	2	1
Norm. emit., horiz./vert.	μm	0.3/0.3	24/24	0.5/0.1	54/10.8	0.9/0.18	432/86.4
Horizontal & vertical β^*	cm	8/8	13.5/13.5	6/1.2	5.1/1	10.5/2.1	4/0.8
Vert. beam-beam param.		0.004	0.091	0.004	0.144	0.002	0.034
Laslett tune-shift		0.059	3×10^{-4}	0.059	2×10^{-4}	0.061	6×10^{-6}
Detector space, up/down	m	3.6/7	3.2/3	3.6/7	3.2/3	3.6/7	3.2/3
Hourglass (HG) reduction		0.98		0.77		0.77	
Luminosity/IP, w/HG, 10^{33}	$cm^{-2}s^{-1}$	0.18		2.9		1.7	

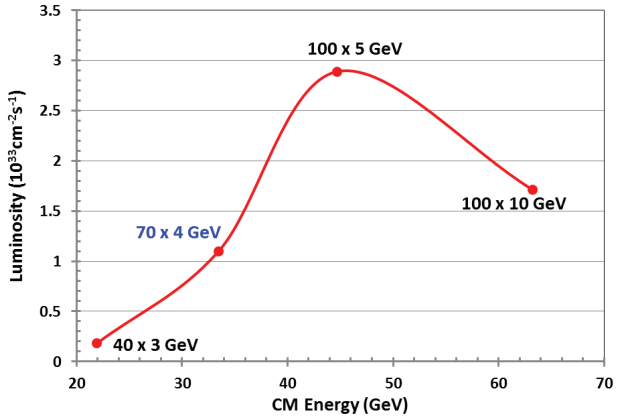

FIGURE 5. Potential luminosity of e^+p collision in the JLEIC.

CONCLUSION

The Jefferson Lab Electron Ion Collider (JLEIC) design parameters meet the science program requirements of high luminosity and high polarization. The baseline design is the result of optimization of machine performance, project cost, technical risk assessment and potential for future upgrades. An overview of JLEIC accelerator design is reported. Considering a rich science program with collision of polarized positron and ion beams, this paper presents a proposal of generating a polarized positron beam for the JLEIC on the basis of PEPPo technique. Preliminary parameters in each step of the injector chain are presented, as well as technical description of each subsystem. Detail simulation and/or experimental demonstration will be performed to validate this polarized positron injection scheme.

ACKNOWLEDGMENTS

Authors would like to thank R. Ent for his inspiration and support of exploration of polarized positrons in the JLEIC, thank Y. Furletova, W. Melnitchouk, F. Selim and E. Voutier for providing physics impact and benefits of studying positrons in a wide physics community.

REFERENCES

1. A. Accardi et al., arXiv:1212.1701 (2014).
2. A. Accardi et al., Eur. Phys. J. A 52, 268 (2016).
3. J.R. Mckenney, N. Sato, W. Melnitchouk and C.-R. Ji, Phys. Rev. D 93, 054011 (2016).
4. V. Chekelian, in *DIS2010* (PoS, 2010) 187 (2010).
5. F.D. Aaron et al. (H1 Collaboration), JHEP 1209, 061 (2012).
6. Z. Zhang (H1 Collaboration), in *ICHEP2012* (PoS, 2013), 289 (2013).
7. V. Barone, U.D' Alesio and M. Genovese, hep-ph/9610211.
8. Z. Song and K.-T. Chao, Phys. Lett. B 529, 77 (2002).
9. U. Stoesslein et al., Tech. Rep. ZEUS-05-003.
10. P.W. Zitzewitz, J.C.V. House, A. Rich and D.W. Gidley, Phys. Rev. Lett. 43, 1281 (1979).
11. A. Sokolov and I.M. Ternov, Sov. Phys. Dokl. 8, 1203 (1964).
12. H. Olsen and L. Maximon, Phys. Rev. 114, 887 (1959).
13. E.A. Kuraev, Y. Bistritskiy, M. Shatnev and E. Tomasi-Gustafsson, Phys. Rev. C 81, 055208 (2010).
14. T. Omori et al., Phys. Rev. Lett. 96, 114801 (2006).
15. G. Alexander et al., Phys. Rev. Lett. 100, 210801 (2008).
16. E.G. Bessonov and A.A. Mikhailichenko, in *EPAC96* (JACoW, 1996), THP071L (1996).
17. A.P. Potylitsin, Nucl. Inst. Meth. A 398, 395 (1997).
18. D. Abbott et al., Phys. Rev. Lett. 116, 214801 (2016).
19. S. Abeyratne et al., arXiv:1504.07961 (2015).
20. Y. Funakoshi et al., in *Proc. of EPAC2004*, 707 (2004).
21. "Super KEKB Design Report", http://www-superkekb.kek.jp/documents.html.
22. Y.S. Derbenev, University of Michigan report UM HE 96-05 (1996).
23. A.M. Kondratenko et al., in *proc. of PSTP 2013*, 026 (2013).
24. A.M. Kondratenko et al., in *proc. of IPAC14*, MOPRO004, (2014).
25. A.M. Kondratenko et al., in *Proc. of IPAC2017*, WEPIK038 (2017).
26. JLEIC Design Update, https://jleic-docdb.jlab.org/DocDB/0000/000031/002/JLEIC-Apr-2017.pdf.
27. R. Ent, Y. Furletova (private communication).
28. P. Adderley et al., Phys. Rev. St Acc. Beams 13, 010101 (2010).
29. R. Suleiman, et al., in *Electron Ion Collider Workshop* (Jefferson Lab, 2014).
30. J.R. Howorth et al., App. Phys. Lett. 23, 123 (1973).
31. G.A. Mulhollan et al., Phy. Lett. A 282, 309 (2001).
32. A. Fowler, K.D. Metzmacher, CERN-PS-CA-Note-98-22-Tech (1998).
33. T. Grimm, C. Boulware, NP SBIR/STTR Exchange Meeting, Gaithersburg, MD (2016).
34. M. Tiefenback, "Bipolar Operation of CEBAF Magnets - Considerations and Implications", in this proceeding.
35. M. Tiefenback, "An Operational Diagnostic Complement for Positrons at CEBAF/JLab", in this proceeding.

Temperature management of photo cathodes at MAMI and MESA

K. Aulenbacher[1,2], S. Friederich[1] and V. Tyukin[1,a)]

[1]*Institut für Kernphysik, Johannes Gutenberg-Universität Mainz, Germany*
[2]*Helmholtz Institut, Mainz, Germany*

[a)]Corresponding author: tioukine@kph.uni-mainz.de

Abstract. Production of highly polarized electron current is limited by cathode heating which leads to the destruction of the active layer. For the new electron accelerator MESA a more efficient solution for the cathode cooling problem is required, with the goal to achieve acceptable temperatures at an incident power of about 1 Watt. The current status of temperature management of photo cathodes at MAMI and MESA is presented.

Spin-polarized operation of MESA in the ERL-mode

MESA is a new electron accelerator which is currently being build at the Johannes Gutenberg-University in Mainz, Germany [1]. Initially, polarized beams were foreseen at MESA only in the external beam mode, but recently demand occurred to use it also for scattering off polarized gas targets in ERL operation. Since polarized gas targets have a very low areal density, a relatively large electron current is needed to achieve sufficient count rate. Preliminary estimations have revealed that a current of 1 mA at 100 MeV would allow to achieve a significant improvement in the accuracy of the magnetic form factor of the proton $G_{m,p}$ at low momentum transfer. In this paper we discuss the resulting challenges for the electron source, in particular we address the issue of controlling the heat introduced into the photocathode by the high laser intensity required.

Lifetime issues at high current

Figure 1 shows typical quantum efficiencies achieved at MAMI during a run time with low current. The curve shows increase towards a maximum and then an exponential decay with time constants of approximately 10 days. A GaAs/GaAsP superlattice cathode with polarizations of about 85% was used. The photo sensitivity of $> 1\,mA/Watt$ - this corresponds to a QE of 0.2% at the laser wavelength of 780 nm - demonstrates that laser powers of about 1 Watt are needed for the upcoming MESA experiments. For intensities in this range, heating of the cathode may occur which in turn leads to an accelerated deterioration of the active surface layer. In experiments [2] where no photo current was drawn but intense laser radiation was applied to a grounded cathode we have observed that the cathode lifetime τ is approximately exponentially decreasing with the laser power P_L

$$\tau = \tau_0 e^{(-k_L P_L)}. \tag{1}$$

With τ_0 the observed lifetime at room temperature (of the order 1000 h)) and typical values of k_L of the order $10\,W^{-1}$. Under this conditions operation with the intended intensities is impossible. In later experiments [3] we observed the rise in temperature related to the laser power, see figure 2. This increase was depending strongly on the mechanical contact between photocathode and its holder and ranged between 35 and $140 K/$Watt. Combining these observations we conclude that the increase of photocathode temperature should be limited to less than $\Delta T = 10\,K$ with respect to room temperature level to avoid a significant reduction of photocathode lifetime.

Note that the actual heating power is lower than the laser power, for instance due to the fact that electrons leave towards the vacuum and carry away the energy that was transferred to them by the laser. Due to the low quantum

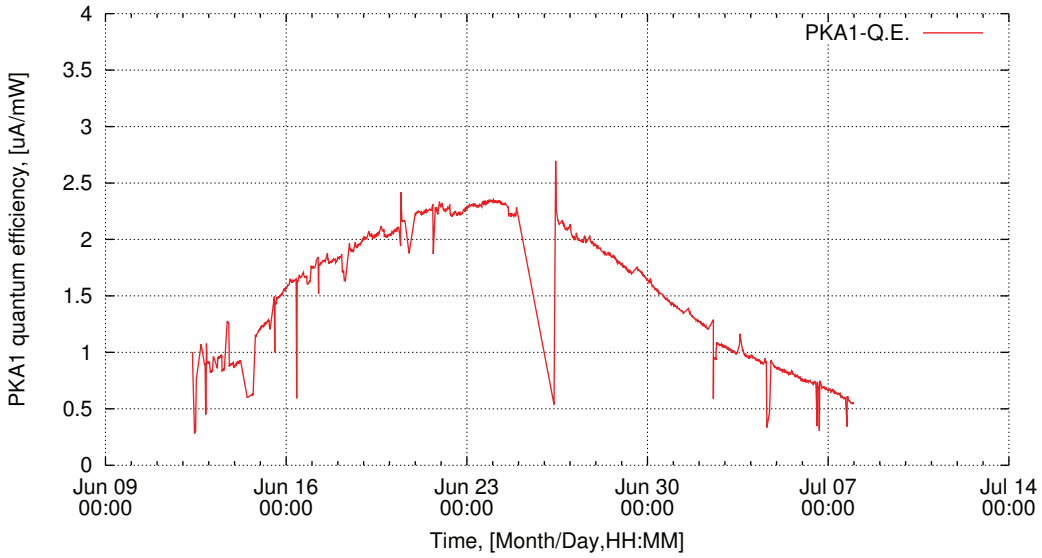

FIGURE 1. Quantum efficiency development of a cathode in source PKA1 during a typical MAMI run time.

efficiency this effect is negligible. All other electrons will recombine in the cathode or at its surface. Radiative recombination could also take away energy from the cathode by the emitted photons, but it seems reasonable to assume that most of the recombinations are non-radiative. We therefore assume the worst case, namely that all absorbed laser light is converted into heat inside the cathode. The thermal power introduced into the bulk of the cathode has to be conducted away from it without rising the cathode temperature above the given limitation.

Improved sources for MESA: 'PKA2'

At high currents cathode lifetime is also limited by ion back-bombardment. The ion current is proportional to the residual gas pressure and the length of the acceleration stage. In figure 3 an improved copy (PKA2) of the MAMI source (PKA1) is shown. The main improvement of PKA2 with respect to the source PKA1[1] are additional NEG modules which are installed in optimized distance to the acceleration stage of the source. With PKA2 longer operational times have been achieved, a curve which is similar to Fig. 1 was observed but with time constants of about 25 days [4]. The charge lifetime is at least as good as in PKA1 where 200 C were observed. Presently, PKA2 is foreseen as source for the MESA accelerator. Note that the 200 C charge lifetime corresponds to an operation interval of 55 hours for one cathode lifetime at 1 mA which is in principle sufficient, since cathode exchange can be done within less than 3 hours. However, this conclusion rests on the assumption that at least 1 Watt of laser power can be applied without excessive temperature increase, which is presently not the case. We discuss the necessary modifications of PKA2 below.

Improved sources for MESA: 'STEAM'

To achieve further improvement, the source 'STEAM' was developed. STEAM stands for 'Small Thermalized Electron-source At Mainz' and is presently used to investigate emission of high peak brightness electron bunches [5]. A low emittance is expected when photons with energies close to band-gap energy are employed [6] which corresponds to the emission of an almost thermalized electron ensemble.

STEAM is based on the inverted source design which was initially tested at SLAC [7] and was later improved and installed at JLAB [8]. Concerning lifetime, STEAM should have considerable advantages compared to PKA1/PKA2

[1] PKA stands for Polarisierte KAnone (german)

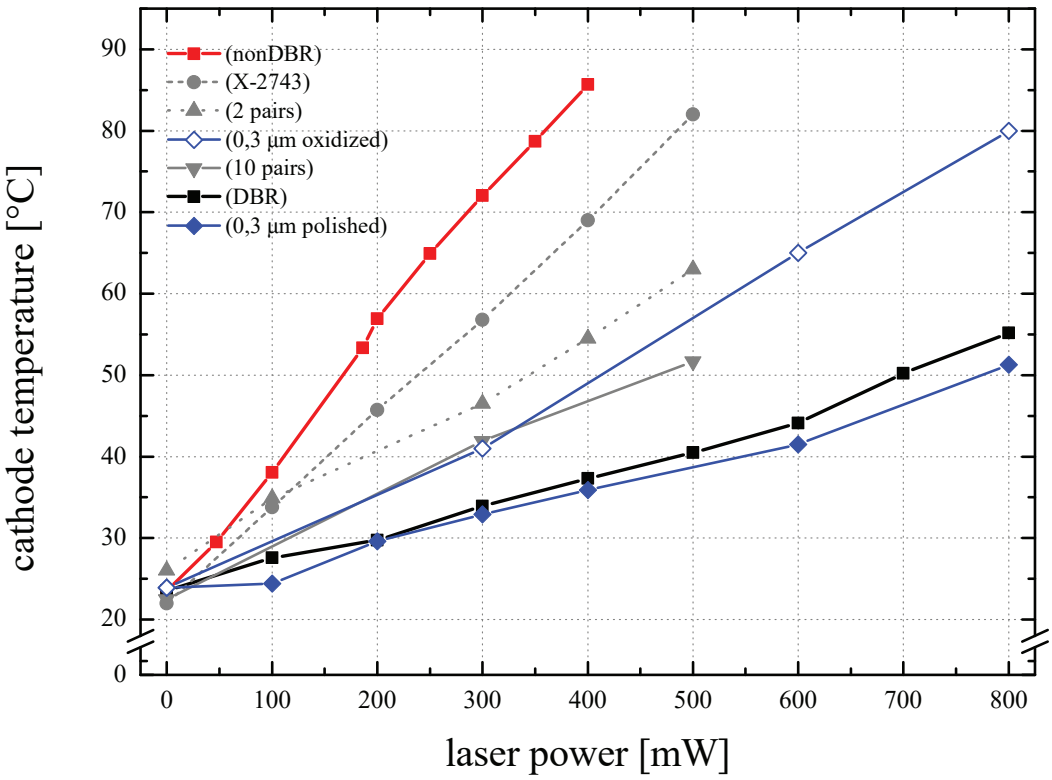

FIGURE 2. Increase of cathode surface temperature with laser power for several cathode/holder combinations with nominally identical geometry. While nonDBR, X-2743, 2 pairs, 0.3 μm, 10 pairs and DBR are internal names for different photo cathode structures, the terms "oxidized" and "polished" refer to the surface condition of the used cathode holder. These measurements where done with a bolometer. Adapted from [3]

since pumping speed to surface ratio is much larger which allows to reduce the base pressure. Moreover, the acceleration stage of STEAM has about half the length of the PKA# types which should reduce ionization correspondingly. In STEAM the conditions for heat transfer are different compared to PKA1/PKA2. This will also be discussed below.

Modification of PKA2 and STEAM for better heat management

For a few Watts of heat flow, active cooling does not seem necessary, but a good heat conductivity is needed. Mechanical interfaces represent regions of potentially high thermal resistance. There are two such interfaces in PKA2 and STEAM. The first one is between the photo-cathode and its holder. The other resides between the cathode holder and the electrode because the holder has to be moved in and out for cathode reactivation.

So far we have only pressed the cathodes into the holder by a tungsten spring which creates a low and not very reproducible conductivity. This can be observed in figure 2. The strong variation of the slope of the curves is caused by different thermal resistance of the interface between cathode and its holder. The variation is probably mainly due to different pressures of the tungsten springs used for fixation of the cathodes in the holders. The smallest slope was achieved with the holder that has the best surface polish at the interface.

This problem can be solved by soldering the cathodes into the holder with indium [9].

The other interface has to be nechanically disconnectable in order to remove the holder for cathode exchange. Weigel et al. [10] have measured the temperature rise of such an interface to depend strongly on the force applied. Their findings indicate that forces of about 100 N are necessary to achieve temperature rises as low as 10 K/W. We have performed studies with copper rods that where pressed into the cathode holders with soldered in GaAs cathodes and have achieved similar results [11].

Since in PKA2 the cathode holder is accessible from the back side, introducing such a copper heat conductor

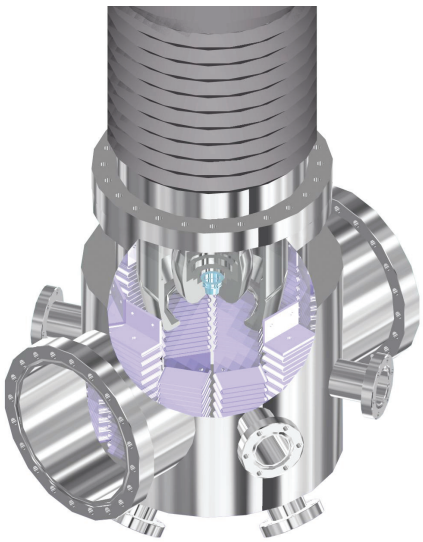

FIGURE 3. The cut away view of source 'PKA2' (see text for details) shows the cathode holder (light blue) in its position in the electrode structure. The mauve colored objects are the NEG strips surrounding the acceleration stage.

from behind is possible. Presently, the so-called elevator which is moved down to allow to extract the cathodes from the side has also a rotational degree of freedom which is not needed in everyday operation. The rotational feedthrough can be replaced with a bellow which allows to press a copper conductor into the cathode holder. The heat will then be transported to the top flange of the source which can be considered as a heat sink at room temperature. Therefore, the modification of the source of the PKA2 type seems feasible.

Cooling the photo cathode in our source of inverse geometry is more demanding. The application of pressure to the holder is possible here also. However, this is not the main concern, since even if the cathode is well connected to the electrode, the latter sits on the insulator (see Fig. 4) which has low thermal conductivity, and only the inner conductor of the high voltage cable is available for efficient heat transfer from the electrode. The conductivity may depend on the contact of the conductor within the inside of the insulator cap and could therefore represent an interface with high thermal resistance.

On the other hand, one may take advantage from the inverted design by using the fact that the electrode is completely surrounded by the vacuum chamber wall. A cooling of this outer wall will establish a temperature difference with respect to the electrode that allows radiative cooling.

A rough estimation for the radiated power can be made. We approximate the situation by a hot inner cylinder inside a cool outer one. The emissivity of the inner surface is low due to the fact that it is polished, whereas the outer wall has higher emissivity due to its less smooth surface. From a NIST database we extract values $\epsilon_{in} = 0.16 - 0.19$, $\epsilon_{out} = 0.4$. Geometric factors can be calculated for the given radii of the cylinders which amount to $\phi_{12} = 1$, $\phi_{21} = 0.28$ These enter into equation 2 in which the heat transfer coefficient (ϵ) is calculated:

$$\epsilon = \frac{1}{(\frac{1}{\epsilon_{in}} - 1)\phi_{12} + (\frac{1}{\epsilon_{out}} - 1)\phi_{21} + 1}. \tag{2}$$

The inner electrode shall be kept at room temperature $T_{in} = 293.15K$, whereas we assume for the outer surface $T_{out} = 258.15K = -15°C$. We can then calculate the power flow from the warm to the cold surface:

$$P_{irradiated} \sim \sigma \, \epsilon \, \phi_{12} \, S_{in} \left(T_{in}^4 - T_{out}^4\right) \sim 1.0W. \tag{3}$$

The inner surface area is S_{in} and the Stefan-Boltzmann constant is indicated by σ. Note that the main limitation of this method results from the low emissivity of the inner surface.

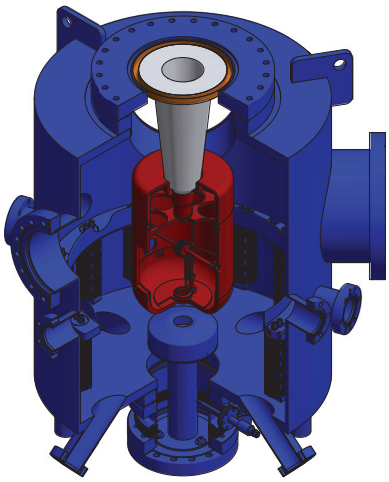

FIGURE 4. Artists view of STEAM. The red part is the metallic electrode that is attached to the cone-shaped insulator - a so-called 'inverted' design.

Conclusion

We have discussed our plans to improve the polarized source for MESA which will have to operate with spin-polarized currents in the 1 mA range. A new challenge is the handling of the heat which is dissipated in the photocathodes by the absorption of the intense laser radiation that will be typically a factor 30 larger than presently used at MAMI. This task requires moderate mechanical modifications of our sources which we can realize before the start of operations at MESA which is foreseen in 2021.

ACKNOWLEDGMENTS

This work was supported by the Deutsche Forschungsgemeinschaft (DFG) through SFB-1044, and through the cluster of excellence PRISMA. The development of the STEAM electron source was supported by funds of the german Ministerium für Bildung und Forschung (BMBF), project HOPE-II (Verbundforschung, FKZ 05K16UMA).

REFERENCES

[1] F. Hug, K. Aulenbacher, R. Heine, B. Ledroit, and D. Simon, "MESA - an ERL Project for Particle Physics Experiments," in *Proceedings, 28th International Linear Accelerator Conference (LINAC16): East Lansing, Michigan, September 25-30, 2016* (2017) p. MOP106012.

[2] E. Riehn et al., "Lifetime measurements of DBR and non-DBR photocathodes at high laser intensities," in *Proceedings of the 13th international workshop Polarized Sources, Targets and Polarimtry* (2009), pp. 241–248.

[3] E. Riehn, "Photokathoden mit internem DBR-Reflektor als Quellen hochintensiver spinpolarisierter Elektronenstrahlen," Ph.D. thesis, University of Mainz 2011.

[4] K. Aulenbacher, I. Alexander, E. Riehn, and V. Tioukine, J. Phys. Conf. Ser. **298**, p. 012019 (2011).

[5] S. Friederich and K. Aulenbacher, "Test electron source for increased brightness emission by near band gap photoemission," in *Proceedings of IPAC2015, Richmond, VA, USA* (JACOW, 2015), pp. 1512–1514.

[6] I. V. Bazarov, B. M. Dunham, F. Hannon, Y. Li, X. Liu, T. Miyajima, D. G. Ouzounov, and C. K. Sinclair, *Particle accelerator. Proceedings, 22nd Conference, PAC'07, Albuquerque, USA, June 25-29, 2007*, Conf. Proc. **C070625**, p. 1221 (2007), [,1221(2007)].

[7] M. Breidenbach, M. Foss, J. Hodgson, A. Kulikov, A. Odian, G. Putallaz, H. Rogers, R. Schindler, K. Skarpaas, and M. Zolotorev, Nuclear Instruments and Methods in Physics Research Section A: Accelerators, Spectrometers, Detectors and Associated Equipment **350**, 1 – 7 (1994).

[8] P. A. Adderley, J. Clark, J. Grames, J. Hansknecht, K. Surles-Law, D. Machie, M. Poelker, M. L. Stutzman, and R. Suleiman, Phys. Rev. ST Accel. Beams **13**, p. 010101 (2010).

[9] V. Schmidt, "Nachweis des Einflusses von optimierter thermischer Ableitung an Halbeiterphotokathoden," Master thesis, University of Mainz 2015.

[10] U. Weigel, D. Orlov, S. Kosolobov, D. Schwalm, A. Terekhov, and A. Wolf, Nuclear Instruments and Methods in Physics Research Section A: Accelerators, Spectrometers, Detectors and Associated Equipment **536**, 323 – 328 (2005), polarized Sources and Targets for the 21st Century. Proceedings o f the 10th International Workshop on Polarized Sources and Targets.

[11] P. Herrmann, "Optimierung der Wämeableitung von Photokathoden für die Hochstrom-Elektronenquelle von MESA," Master thesis, University of Mainz 2014.

High Current Polarized Electron Source

R. Suleiman [a)], P. Adderley, J. Grames, J. Hansknecht, M. Poelker and M. Stutzman

Jefferson Laboratory, *12000 Jefferson Ave, Newport News, VA 23606, USA*

[a)] Corresponding author: suleiman@jlab.org

Abstract. Jefferson Lab operates two DC high voltage GaAs photoguns with compact inverted insulators. One photogun provides the polarized electron beam at the Continuous Electron Beam Accelerator Facility (CEBAF) up to 200 μA. The other gun is used for high average current photocathode lifetime studies at a dedicated test facility up to 4 mA of polarized beam and 10 mA of un-polarized beam. GaAs-based photoguns used at accelerators with extensive user programs must exhibit long photocathode operating lifetime. Achieving this goal represents a significant challenge for proposed facilities that must operate in excess of tens of mA of polarized average current. This contribution describes techniques to maintain good vacuum while delivering high beam currents, and techniques that minimize damage due to ion bombardment, the dominant mechanism that reduces photocathode yield. Advantages of higher DC voltage include reduced space-charge emittance growth and the potential for better photocathode lifetime. Highlights of R&D to improve the performance of polarized electron sources and prolong the lifetime of strained-superlattice GaAs are presented.

INTRODUCTION

CEBAF load lock DC high voltage GaAs photogun employs inverted insulator geometry [1]. This describes a photogun with a ceramic insulator that extends into the vacuum chamber, as shown in Fig. 1. The primary benefit of this approach is that a large metal structure is not required to support the cathode electrode. As a result, there is significantly less metal biased at high voltage, and consequently there is less metal to generate field emission. Another appealing feature of the design is that the insulator is a common element of medical x-ray sources, and therefore relatively inexpensive compared to cylindrical insulators purchased solely for accelerator electron gun applications. A load-locked photogun design with an inverted insulator helps to reduce the surface area of the high voltage vacuum chamber, which in turn reduces the gas load. Finally, because there is no exposed high voltage, corona shields and a tank for dry nitrogen gas or SF_6 are not required. The polarized GaAs photogun operating at CEBAF uses a tee-shaped cathode electrode made of 316L stainless steel polished to sub-micron finish using diamond grit. This gun was high voltage processed to 150 kV without detectable field emission and now provides beam at 130 kV. It has a charge lifetime ~ 200 C at 200 μA with transmission of 95%. Recently, the gun delivered 1800 C of polarized beam to the QWeak experiment [2].

A second inverted gun located at an Injector Test Facility is used for lifetime studies at high currents. It employs a similar tee-shaped cathode electrode but made of large-grain niobium. The first application of high voltage was disappointing, with field emission detected at voltage > 140 kV. By increasing the applied voltage, some field emitters were eliminated but processing was limited to 225 kV, which was the maximum voltage of the high voltage power supply. Not surprisingly, photocathode lifetime was poor while delivering beam at 200 kV due to field emission, which served to degrade the vacuum within the photogun. Moreover, often there were high voltage discharges that completely eliminated photocathode quantum efficiency (QE). The large-grain niobium electrode was removed from the photogun and another surface treatment was performed. Upon re-installation of the cathode electrode into the photogun and vacuum chamber bake-out, no field emission was detected at voltage up to 225 kV.

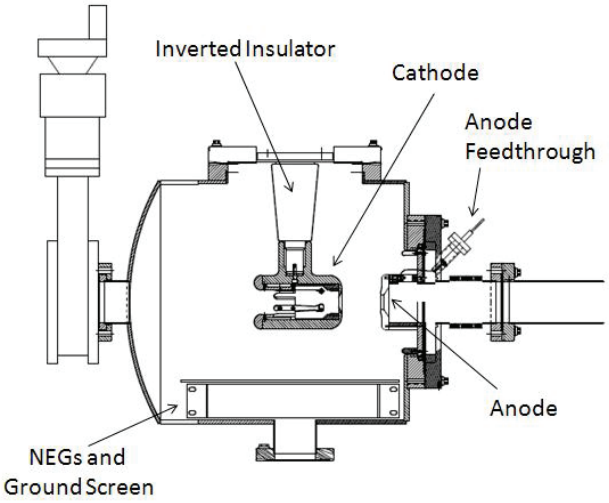

Figure 1: CEBAF inverted gun high voltage chamber.

The previous record of polarized beam from a photogun was 1 mA [3]. This photogun was used to deliver 4 mA average beam current from a high polarization strained-superlattice GaAs photocathode that was illuminated with light from an RF-pulsed fiber-based drive laser operating at 780 nm and with 1500 MHz pulse repetition rate. This is a new record [4] and an important development toward realizing some of the requirements for proposed high current accelerators. Table 1 gives the details of the two polarized high current tests.

Table 1: Parameters of Two Polarized High Current Record Tests at Jefferson Lab

Parameter	Value	Value
Laser Rep Rate	499 MHz	1500 MHz
Laser Pulse Length	30 ps	50 ps
Laser Wavelength	780 nm	780 nm
Laser Spot Size	0.45 mm	0.35 mm
Photocathode	GaAs/GaAsP	GaAs/GaAsP
Gun Voltage	100 kV	200 kV
Beam Current	1 mA	4 mA
Run Duration	8.25 hour	1.4 hour
Extracted Charge	30.3 C	20 C
Charge Lifetime	210 C	80 C
Fluence Lifetime	132 kC/cm^2	83 kC/cm^2
Bunch Charge	2.0 pC	2.7 pC
Peak Current	67 mA	53 mA
Peak Current Density	42 A/cm^2	55 A/cm^2

The operating lifetime of a GaAs-based DC high voltage photogun is set by the vacuum level inside the photogun. Imperfect vacuum leads to ion bombardment, the mechanism where residual gas is ionized by the extracted electron beam and transported backward to the photocathode where the ions adversely affect photocathode yield. Ions with sufficient kinetic energy penetrate the surface of the photocathode, where they might damage the GaAs crystal

structure or serve as trapped interstitial defects that reduce the electron diffusion length. Impinging ions might also sputter away the chemicals (Cs and F) used to reduce the work function at the surface of the photocathode.

The rate of ion production depends strongly on the electron beam energy, which varies across the cathode/anode gap. The peak of electron-impact ionization cross-section for molecular hydrogen (the prevalent gas species in a photogun) occurs at ~ 100 eV, and dropping by nearly three orders of magnitude at 100 keV. It is likely that low and high-energy ions do different things to the photocathode (e.g., sputter versus implant), but the presence of the QE trench suggests that all ions (low and high energy) are problematic and lead to QE decay.

Photocathode QE decays more quickly at high current, compared to low current, since more electrons lead to the production of more ions and consequently, more ion bombardment. If the vacuum level inside the photogun were constant, the QE would decay at a rate inversely proportional to beam current. However, in practice, the vacuum level inside the gun is not constant; rather it varies with beam current for dynamic reasons related to beam loss. QE can drop precipitously at high current, particularly if the electron beam is not efficiently delivered to the desired final location (i.e., a beam dump or target far away). This dynamic QE dependence on beam current makes it very difficult to infer the lifetime at high current based on measurements at low current. However, a crude gun performance can be estimated based on hours-long demonstrations listed in Table 1 from a strained-superlattice GaAs photocathode. During these tests, the QE was monitored and an exponential fit applied to the data. This provides a measure of the photogun "charge lifetime" which is a useful metric describing the amount of charge that can be extracted before QE falls to 1/e of its initial value. Of course, the photogun can continue to operate beyond its charge lifetime if the drive laser is sufficiently powerful. However, now there is the risk of overheating the photocathode and there are experimental measurements that show the beam polarization is lower when the QE becomes very small.

At 4 mA, the photogun can provide 14 C/hour, or 346 C/day. Using the empirically determined photogun charge lifetime of 80 C at 4 mA, and assuming the use of a 10 W laser, a high-polarization photocathode with typical 1% initial QE could operate for 13 hours before running out of laser power and QE. At this point, moving the laser beam to a fresh photocathode location would take 1 hour. Assuming there are 6 spots (since laser spot size is much smaller than active area), this provides 3 days of operation before heat and reactivate is needed (8 hours). Accelerators with dedicated user programs require highly reliable equipment that can operate for days without interruption, including photoguns. Experiments at higher current require photoguns with significantly improved charge lifetime. A suitable charge lifetime R&D goal is 1000s C.

Table 2: Source Parameters for Existing Accelerators (CEBAF and JLab FEL) and Proposed Facilities

Parameter	CEBAF	JLab/FEL	eRHIC	JLEIC	Cornell ERL	LHeC	CLIC	ILC
Polarization	Yes	No	Yes	Yes	No	Yes	Yes	Yes
Photocathode	GaAs/GaAsP	Bulk GaAs			K_2CsSb			
Width of microbunch (ps)	50	35	100	50	2	100	100	1000
Time between microbunches (ns)	2	13	106	1.34	0.77	25	0.5002	337
Microbunch rep rate (MHz)	499	75	9.4	748.5	1300	40	1999	3
Width of macropulse	-	-	-	2.3 μs	-	-	156 ns	1 ms
Macropulse repetition rate (Hz)	-	-	-	20	-	-	50	5
Charge per microbunch (nC)	0.0004	0.133	5.3	0.1735	0.077	0.640	0.960	4.8
Peak current of microbunch (A)	0.008	3.8	53	3.5	38.5	6.4	9.6	4.8
Laser spot size (cm, diameter)	0.1	0.5	0.6	0.3	0.3	0.5	1	1
Peak current density (A/cm^2)	1	19	188	50	500	32	12	6
Average current from gun (mA)	0.2	10	50	0.006	100	25	0.015	0.072

Table 2 lists the parameters of the sources at CEBAF and JLab FEL and of the sources needed for future facilities. Charge per microbunch and average current from the gun are the two most relevant parameters that affect the design of the source. If polarization is not required, then the new facilities are planning to use multi-alkali photocathodes like

K_2CsSb or Na_2KSb. Unlike GaAs, these are positive electron affinity (PEA) bulk photocathodes that do not require an activation layer on the surface and thus not sensitive to ion bombardment. If polarization is required then as of now, there is no choice other than using strained-superlattice GaAs. This photocathode requires surface activation to lower the work function and to generate the negative electron affinity (NEA) needed for photoemission and thus susceptible to ion bombardment that sputters the active layer and damages the supper-lattice structure.

IMPROVING PHOTOGUN VACUUM

In order to minimize ion bombardment and improve the charge lifetime of the photogun, one must improve the vacuum inside the photogun, which is a function of statistic (i.e., no beam) and dynamic (i.e., with beam) conditions. Static vacuum is determined from the gas load from all sources including outgassing and leaks, and the effective pump speed. Obviously, to reduce pressure, the pump speed should be maximized and the gas load minimized. Most, if not all, polarized photoguns today rely on load-locked designs, with the photogun composed of multiple vacuum chambers separated by valves. Load-locked photoguns provide superior vacuum inside the high voltage chamber, where the beam is produced, by moving comparatively poor vacuum tasks like photocathode installation and heating and activation to other chambers where ion bombardment is not a concern. The static vacuum level inside the high voltage chamber at CEBAF is 10^{-12} Torr or better [5].

The cathode/anode gap inside the high voltage chamber of a modern DC high voltage photogun is surrounded by non-evaporable getter (NEG) pumps, which have very high pump speed for hydrogen, the dominant gas species of baked stainless steel vacuum chambers. Modern photoguns also employ an ion pump, which serves to pump gas species not efficiently pumped by the NEG such as methane, carbon monoxide and helium. It is worthwhile to degas the vacuum chamber via an extended 400 °C pre-bake (10 days long) to reduce the outgassing rate by more than an order of magnitude, from typical 2×10^{-12} to 1×10^{-13} $TorrLs^{-1}cm^{-2}$ [6].

The list of potential vacuum improvements that could be applied to the next generation of photoguns is rather meager. One possibility is to replace the ion pump with a cryopump. Another potential vacuum improvement involves using coatings that are considered to be diffusion barriers that limit hydrogen outgassing, such as titanium nitride (TiN) [6].

At Jefferson Lab, the biggest vacuum improvement at the photogun will be realized when improvements are made to the adjoining beamline. The most obvious, but frequently overlooked, assessment of the vacuum condition of the beamline is to monitor the photogun vacuum when the valve to the beamline is opened. Of course, when properly engineered, the photogun vacuum should not increase when the valve is opened. A beamline designed for high current will be pre-baked at 400 °C to achieve low outgassing rate, and it will include a significant level of pumping, both localized, and distributed along the beamline via NEG coating.

Dynamic vacuum is determined by field emission and beam loss. Ion bombardment is greatly enhanced in the presence of field emission from the cathode electrode, even at levels that are difficult to measure. Field emitted electrons strike surfaces near the photocathode, generating a gas load. Field emission is often more problematic for high current applications because these applications frequently require very high bias voltages to overcome space charge forces. Every effort must be made to monitor and eliminate field emission. Monitoring field emission can be accomplished by using an anode that is electrically isolated from ground and attached to a sensitive current meter. An ion pump with a sensitive current monitor can also provide an indication of field emission and x-ray radiation monitors placed near the photogun represent another very useful diagnostic.

Beyond eliminating field emission, other steps can be taken to ensure dynamic vacuum conditions are suitable for high current beam delivery. It is extremely important to effectively manage all extracted beam leaving the photocathode, including beam not intentionally produced, for example, from extraneous laser reflections or background light illuminating the activated surface of the photocathode.

PROLONGING PHOTOCATHODE LIFETIME

It is possible to enhance the operating lifetime of the photocathode at high beam currents by: (a) operating with the drive laser beam positioned away from the electrostatic center of the photocathode, (b) limiting the photocathode active area to eliminate photoemission from regions of the photocathode that do not support efficient beam delivery, (c) using a large drive laser beam to distribute ion damage over a larger area, and (d) by applying a relatively low bias

voltage to the anode to repel ions created within the downstream beam line. These techniques are described in detail in reference [7]. Granted, some of these techniques (a and c) degrade emittance, but the benefits of longer photogun operating lifetime might warrant their implementation.

The reasoning for (c) is that the same number of ions will be produced within the cathode-anode gap regardless if the laser beam was big or small, but for a larger laser beam, the ions will be distributed over a larger area and QE should decrease more slowly. With this in mind, the concept of fluence lifetime, the amount of charge that could be extracted per unit area before QE falls to of its original value, was studied and with the expectation that fluence lifetime would be a constant for each photogun. Furthermore, the fluence lifetime of a gun measured with a small laser spot could be used to predict the charge lifetime of a gun illuminated with a large laser spot.

Lifetime measurements were made over a broad range of currents by illuminating a freshly activated photocathode with 5 mm active area, with small and large laser beam sizes. Results shown in Fig. 2 clearly indicate an improved lifetime when using the larger spot size.

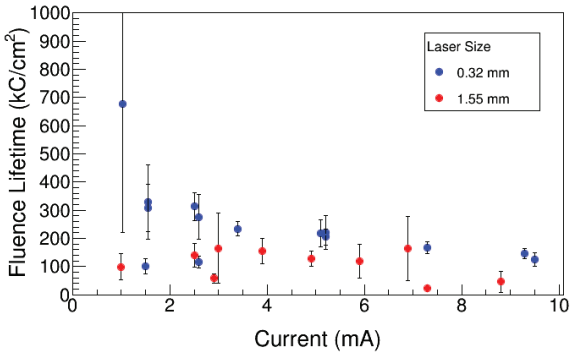

Figure 2: Fluence lifetime vs average beam current for the two laser spot sizes. These measurements were taken with bulk GaAs, 532 nm, and 5 mm active area.

Most of these techniques are routinely employed at CEBAF - only the center portion of the photocathode is activated to negative electron affinity to reduce the likelihood of generating stray electrons that would hit the vacuum chamber walls, and the laser beam is always positioned away from the electrostatic center. During the QWeak experiment, the laser beam spot size was doubled from 0.5 to 1.0 mm. The charge lifetime (Fig. 3) improved by a factor of four while using the 1.0 mm diameter laser spot because the offending ions produced by the extracted beam were distributed over a larger area.

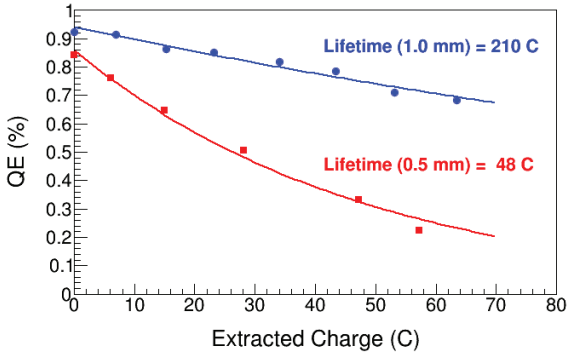

Figure 3: Measured charge lifetime while delivering 200 μA average current during the QWeak experiment using two different laser beam diameters at the photocathode. Different spot sizes were obtained by using different focusing lenses.

Recent dedicated studies at CEBAF confirmed that charge lifetime improves with spot size, as expected but eventually beam size becomes too large for efficient beam transport as can be seen in Fig. 4.

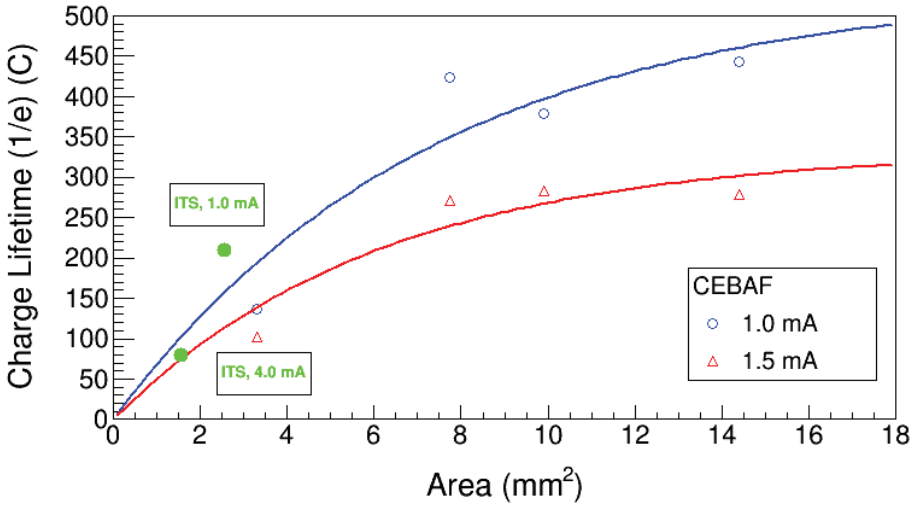

Figure 4: Recent Charge lifetime measurements at CEBAF at few laser spot sizes. Also shown are the two high current tests (1.0 mA and 4.0 mA) described in Table 1.

Fig. 5 shows first measurement of polarization from superlattice photocathode at milliampere current. The polarization was measured by extracting and accelerating a small fraction of the beam to a sub-percent accuracy Mott Polarimeter. The polarization of the beam does not change over the measured current range.

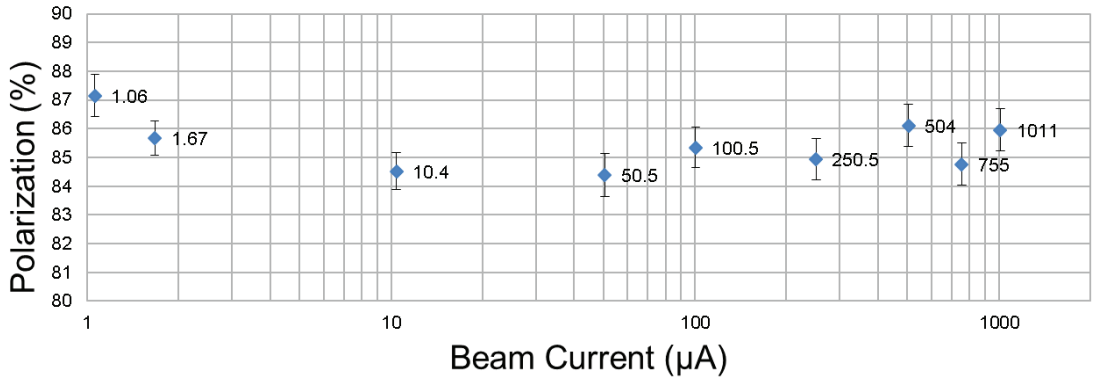

Figure 5: Beam polarization versus beam current from CEBAF polarized photogun. Only very small fraction (~1 μA) of the polarized beam was accelerated to the Mott Polarimeter; the rest of the beam was dumped on a chopping aperture.

HIGHER PHOTOGUN HIGH VOLTAGE

High average current and/or high bunch charge applications benefit from the operation of the photogun at very high voltage, which serves to minimize the ill effects of space charge forces that degrade the emittance and introduce beam loss leading to a diminished photogun charge lifetime. Guns with higher high voltage allow for compact, less-complicated injectors. Higher HV would also increase QE by lowering the potential barrier (Schottky effect) [8] and suppresses the surface charge limit [9]. As an added benefit, operation at very high bias voltage may enhance the operating lifetime of the photogun by quickly accelerating the beam to energy with very small ionization cross section. The total number of ions generated at 500 kV, for example, will be substantially reduced compared to operation at 100 kV, assuming the same cathode/anode gap, see Fig. 6.

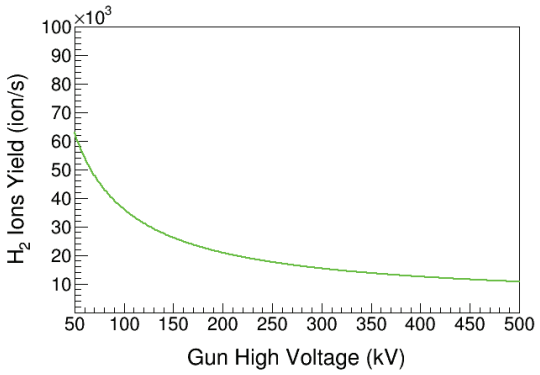

Figure 6: Ions yield assuming electron beam current of 2.0 mA and gun vacuum of 8.0 × 10^{-12} Torr.

A number of photogun groups are working to build 500 kV guns, however without exception; efforts to operate photoguns at 500 kV and maximum field strength greater than 10 MV/m have met with problems due to field emission. At Jefferson Lab, a new photogun is being constructed that will employ proven vacuum techniques such as pre-baking at 400 °C to reduce outgassing, as well as cryopupming if ongoing vacuum tests indicate an improvement over conventional pumping with NEGs and ion pumps. The adjoining beamline will be properly engineered for 10^{-12} Torr operation and techniques will be used to minimize the effect of ion bombardment, in particular the use of a large laser beam at the photocathode. However, the focus of the new photogun design effort is directed at operation at high voltage of 500 kV. The new inverted gun will use a longer ceramic insulator and a spherical cathode.

PHOTOCATHODE RESEARCH

Roughly, 70% of the light incident on the photocathode is absorbed while the remaining 30% is reflected. With high laser power, the photocathode must be cooled. Otherwise, if the photocathode temperature rises above a certain threshold, the activation chemicals (Cs and F) of GaAs or the actual chemical elements of a multi-alkali photocathode start to evaporate which lowers the QE. For strained-superlattice GaAs, another approach would be to reduce the overall laser light absorption in the photocathode material. This can be accomplished by adding a reflector between the superlattice layers and the substrate so no light is absorbed in the substrate and more light is absorbed in the superlattice material when the light is reflected back. It is important to steer the reflected light away from the photocathode so it would not scatter from the surrounding structures and hit the photocathode again to generate halo beam. Recent work at Jefferson Lab [10] demonstrated the highest QE of any reported high polarization photocathode using a GaAS/GaAsP photocathode with GaAsP/AlAsP Distributed Bragg Reflector (DBR). This DBR photocathode achieved 6.4% QE at 776 nm with 84% polarization.

A possible candidate for a new polarized material photocathode is the strained-superlattice GaAsSb/AlGaAsP from SVTA [11]. This new photocathode will provide higher than 90% polarization and 5-10% QE. Sb has three orders of magnitude lower diffusivity than Ga and two orders of magnitude lower diffusivity than As. Diffusion is one of the main reasons for structural and surface decomposition of cathodes, especially during heat cleaning and ion bombardment. Sb based photocathodes can thus be more robust in poor vacuum environment.

In summary, the goals of polarized photocathode R&D are: (a) higher QE (>> 1%) with a thicker superlattice absorber region (with fully strain-compensated structure) and more efficient photon absorption, (b) an effective DBR structure on a GaAs substrate to enhance QE and reduce heating, (c) longer lifetime by reducing structural and surface decomposition and with new photocathode material that is more robust in poor vacuum, and (d) higher polarization with higher-gradient-doping to reduce surface charge limit and depolarization.

ACKNOWLEDGMENTS

Authored by Jefferson Science Associates, LLC under U.S. DOE Contract No. DE-AC05-06OR23177. The U.S. Government retains a non-exclusive, paid-up, irrevocable, world-wide license to publish or reproduce this manuscript for U.S. Government purposes.

REFERENCES

1. P. A. Adderley et al., "Load-locked dc high voltage GaAs photogun with an inverted-geometry ceramic insulator," Phys. Rev. ST Accel. Beams 13, 010101 (2010).
2. D. Androic et al., "First Determination of the Weak Charge of the Proton", Phys. Rev. Lett. 111, 141803 (2013).
3. J. Grames et al., "Lifetime Measurements of High Polarization Strained Gallium Arsenide at Beam Current > 1mA using a new 100kV Load Lock Photogun", Proceedings of the 2007 Particle Accelerator Conference, Albuquerque, NM.
4. R. Suleiman et al., "CEBAF 200 kV Inverted Electron Gun", Proceedings of the 2011 Particle Accelerator Conference, New York, NY.
5. M. Stutzman et al., "Continued Work toward XHV for the Jefferson Lab Polarized Electron Source," presented at the AVS 58th International Symposium and Exhibition, Nashville, TN, 2011.
6. M. A. Mamun, M.L. Stutzman et al., "Effect of heat treatments and coatings on the outgassing rate of stainless steel chamber," Journal of Vacuum Science & Technology A 32, 021604 (2014).
7. J. Grames, R. Suleiman et al., "Charge and fluence lifetime measurements of a DC high voltage GaAs photogun at high average current," Phys. Rev. ST Accel. Beams 14, 043501 (2011).
8. J. R. Howorth et al., "Electric field enhancement of escape probability on negative electron affinity surfaces," Applied Physics Letters 23, 123, (1973).
9. G. A. Mulhollan et al., "Photovoltage effects in photoemission from thin GaAs layers," Physics Letters A 282, 309 (2001).
10. W. Liu et al., "Record-level quantum efficiency from a high polarization strained GaAs/GaAsP superlattice photocathode with distributed Bragg reflector," Applied Physics Letters 109, 252104 (2016).
11. Y. Chen et al., "DOE/SBIR Phase I/II: GaAsSb/AlGaAsP Superlattice Polarized Electron Source," SVT Associates, Inc., Eden Prairie, MN.

High current polarized electron source for future eRHIC

Erdong Wang[1,a)*]

[1]*Brookhaven National Laboratory , Upton, New York, 11973, USA*

[a)] Corresponding author: wange@bnl.gov

Abstract. The high current and high bunch charge polarized electron source is essential for cost reduction of Linac-Ring (L-R) eRHIC. In the baseline design, electron beam from multiple guns (probably 4-8) will be combined using deflection plates or accumulate ring. Each gun aims to deliver electron beam with 10 mA average current and 5.3 nC bunch charge. With total 50 mA and 5.3 nC electron beam, this beam combining design could use for generating positron too. The gun has been designed, fabricated and expected to start commissioning by the mid of this year. In this paper, we will present the DC gun design parameters and beam combine schemes. Also, we will describe the details of gun design and the strategies to demonstrate high current high charge polarized electron beam from this source.

INTRODUCTION

In the eRHIC nominal design, the polarized electron injector needs to provide a beam of 50 mA average current and 5.3 nC bunch charge [1]. Currently, the highest average current of polarized electron source was 4mA achieved by JLab. The highest bunch charge was 12 nC achieved by Stanford linac collider (SLC) by 1990s. The major risk factor stems from the fact that there is no single experiment where both the high charge and high average current have been demonstrated simultaneously and lifetime of the cathode under this condition is yet to be determined. In order to reduce the risk, we proposed to use multiple electron guns to generate high current beam. We considered three beam combining schemes. In the baseline design, electron beam from multiple guns will be combined using multiple deflection plates. Thus each gun should deliver 6.25 mA and 5.3 nC polarized electron beam. The second design is using magnetic field rotatable combiner to combine the electron beam by increasing the repetition frequency. The third design is using a accumulate ring to stacking beam transversely. Then each gun bunch charge only require for 10s pC.

Polarized electron gun has been identified as one of the risk factors in BNL eRHIC design. Primary components of the gun are the high voltage system, the laser system and the design of the gun. The design of the gun itself, along with the cathode, with its ability to deliver high charge and high average current simultaneously, with acceptable lifetime still poses difficulty. Besides the gun difficulties, design an injector for transporting low energy high charge electron beam is another challenge. The L-R eRHIC needs low emittance beam for electron-ion collision. For all above three schemes, the low energy beam manipulations such as combining and compression will increase emittance. In this paper, we will present the high charge high current gun design and eRHIC injector design including beam combining components, beam line design and final beam parameters.

HIGH CURRENT HIGH CHARGE GUN DESIGN

Most of the challenges in meeting the eRHIC polarized beam requirements are related to the photocathode properties, its sensitivity and associated lifetime. The section below lists a few of these challenges and possible mitigation methods based on the existing knowledge base, leading to a set of operational parameters for eRHIC polarized electron gun.

- Extremely high Vacuum

*This work was carried out at Brookhaven Science associates, LLC under Contracts No.DE-AC02-98CH10886 with the U.S.DOE.

The GaAs cathode emission surface is coated by a O(NF_3)-Cs monolayer which is very sensitive to gas contamination including carbohydrate, oxygen, water and other active gases. The active gases degrade the quantum efficiency (QE) by chemical poisoning while Hydrogen degrades the QE during beam operation via ion back bombardment. In above 100 uA high average current operation, the ion back bombardment is the dominated cathode QE degradation mechanism. Thus to obtain long lifetime, the gun chamber dynamics pressure should be in 10^{-12} Torr with Hydrogen being the dominant gas, comprising 99% of the gas load. All chamber material must be low out gassing rate such as high temperature baked or NEG coated stainless steel, Ti or Al.

- Beam loss

One important factor causes the pressure increasing in high current operation is due to beam loss. The main beam loss is from the beam halo. For instance, i) High bunch charge beam in multiple focus lens will generate transverse halo due to betatron mismatching, which typically happen at couple meters away from the gun. ii) The laser transverse halo and longitudinal halo will cause an electron beam halo even at beam emission. We must provide a large beam pipe at the exit the gun to reduce beam loss near the gun. Furthermore, the laser beam profile in both transverse and longitudinal dimensions should be very well defined.

- Heating effect

When the average current goes above the mA level, the high power of the laser may heat the substrate leading to cesium loss, which reduces the lifetime even further. $A^* \tau$, defined as the fluence life time, is no longer a constant. GaAs photocathode usually could survive at temperatures below 90 C. Thus for high current operations, the cathode needs to be cooled either by cooling media or increase heat capacity.

- Ion back bombardment

Ion back bombardment is well-known as a mechanism that limits the cathode lifetime. Both theoretical and experimental work shows that the cathode lifetime is proportional to beam emission area. We could bias the anode or ion clean electrodes to prevent ions generated from downstream beam.

- Edge effect

The emission from the edge of the cathode will take extreme trajectory due to strong transverse kick and can end up hitting the wall creating outgassing. Thus, the emission area should keep at a safe distance from the Pierce geometry cathode. The simulation shows the distance from the emission area to cathode edge to be 3-5 mm. The cathode edge emission came from laser beam halo could be eliminated by masking the cathode in activation or anodizing the edge.

Considering both ion back bombardment effect (2mm offset) and edge effect(4 mm to the edge) and 6mm diameter of the cathode's illuminated spot, we need a cathode with a diameter above 24 mm to match the current density/charge density achieved in state of the art measurements. Following above discussion, a high current/ high charge long operation polarized electron gun needs following features: i) Hydrogen dominated XHV gun chamber; ii) Large aperture beamline; iii) Heavy surface doped superlattice GaAs/GaAsP photocathode; iv) Cooling capability or heat shrink (sink); v) Large photocathode; vi) High voltage. In order to reduce the risk of high average current, high bunch charge polarized electron source, we are working on developing a single cathode inverted high voltage DC gun whose geometry is based on JLab inverted gun [2]. The HV and vacuum components are all commercial parts. The improvements are including:

1. The cathode size is enlarged by a factor of four;
2. Add large copper block at back of cathode as heat sink.
3. Develop a high quality mode-locked fiber laser;
4. Increase beam pipe diameter by 60%.

Table 1 The gun parameters

	Inverted gun (LR)
Electrodes diameter	20 cm
Gap distance (lg)	5.7 cm
Voltage	350 kV
Cathode size	4.98 cm^2
Electrodes angle (α)	22 degs
Cathode gradients	3.8 MV/m
Maximum gradient	9.9 MV/m
Anode radius (la)	1.8 cm
Pumping speed	35000 L/s

The gun DC gap geometry parameters are presented in table 1. Figure 1 shows the Possion statics electrical field simulation. The anode cone angle is same as the Perice angle. The gun geometry is optimized by minimum the emittance and keeping the beam away from the anode aperture. With this design, the expected average current is 10 mA with 1000C charge lifetime if the dynamic vacuum pressure is less than 1e-11 torr.

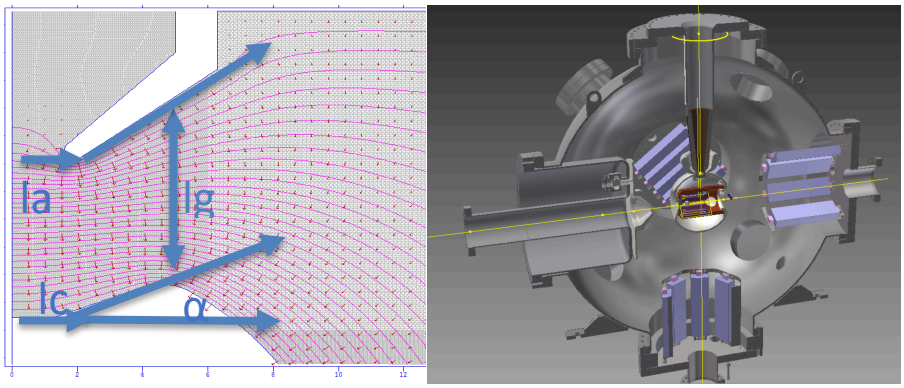

Figure 1. Left: The E-field in the DC gap simulated by the Possion. Right: the gun 3D model including gun vessel, NEG pump and HV electrodes.

STRATEGY OF INJECTOR SCHEMES CHOOSING

The lifetime as the function of charge is unknown when the average current is constant. Based on the gun test results, we will choose the suitable schemes. Recently, there are three injector designs in consideration. The average current, number of guns and total charge per day is common for all three schemes. If the bunch charge could reach 67 pC, then we will choose accumulator ring to accumulate bunch charge up to 5.3 nC and kick into the ERL. If the bunch charge could reach 1.77 nC without significant lifetime degradation, the machine could operate at low charge mode where the ion bunch frequency should increase to 30 MHz. The obvious advantages are : 1. Low peak current reduces the beam loss. 2. Smaller bunch charge helps to maintain the good emittance and compress the bunch length easily. The bunch length could increase up to10 ns, then the peak current is about 177 pC for reducing the risk even more. If the bunch charge reaches 5.3 nC from the gun, then we will operate at nominal mode where using a plate deflector to combine the beam from multiple guns. In the best scenario, the gun performance is better than expect, we can reduce the number of guns for simplify the entire injector design, commissioning and operation.

Table 2 The injector parameters for L-R eRHIC

	Nominal	**Low charge**	**Accumulator ring**
Current/ per gun [mA]		6.25	
Charge lifetime [C]	80	80	80
Bunch charge [nC]	5.3	1.77	0.067
Frequency [MHz]	1.17	3.51	93.8
Bunch length [ns]	1.5	10	0.1
Peak current [A]	3.53	0.177	0.67
Cathodes/ per day		7	
# of guns		8	
Total current [mA]		50	
Total charge [C]		4320	

eRHIC MULTIPLE GUNS INJECTOR DESIGN

The eRHIC electron injector has to produce up to 50mA polarized electron beam with less than 50 mm-mrad normalized transverse beam emittance, bunchlength in 3mm and energy spread less than 1%. The injector will

accelerate the beam up to 20 MeV. It consists of multiple electron gun, beam combining system, 112MHz bunching cavities , a 3rd harmonic cavity, a drift space for ballistic bunch compression and a 647 MHz booster linac.

Around 1ns polarized electron bunches are extracted from the superlattice GaAs photocathode in an inverted HV DC gun, which is adopted as the electron source for beam optics designing. The gun operates at 350kV with the 3.8 MV/m cathode gradient. Long bunches are extracted from the gun to match the surface charge limitation and reduce the beam quality degradation due to space charge limit.

The beam from the gun will be combined by either of three methods of combining section then get into the compression section, which consists of a 112MHz cavity, a 336 MHz cavity and a ballistic drift space. The 112MHz SRF cavity pre-boosts the beam energy and provides a chirp on the bunch. Then a normal conducting 3rd harmonic cavity (336MHz) linearized the bunch longitudinal energy spread. A three meters ballistic compression drift line is applied to shorten the bunch duration to 3 mm. Multiple solenoids are placed on the beamline to maintain the beam size along the beamline. Both energy spread modification cavities are of the quarter wave resonator type. The bunch is under-compression at the entrance of the first booster cavity. The boost cavity use single 5 cell 647MHz SRF cavity which is function as boosting the bunch energy to 20MeV and also de-chirping the bunch reducing the energy spread to 0.1%. This cavity is same as the main linac cavities but has to deliver an RF power of 520 kW. The beam from the booster linac is then transported and injected into the main FFAG-ERL. The beam dynamics simulation of the injector beam line is carried out by GPT. The compression section and boost section are common for the nominal beam parameters. The following section will discuss two combining methods and simulation results.

Nominal option I: Rotatable magnetic field beam combine

The rotatable magnetic field combiner has been studied in Gatling gun development [3]. Eight DC guns will be placed along the rim of a 4 meters radius ring at a potential of -300 kV. A series of fixed magnetic field dipoles first bend the off-axis electron bunches by 90 degrees, then bend by another dipole magnets by -60 degrees. After about 1 meter drift, the beam will be kicked 30 degrees into alignment with the main axis by a rotating magnetic field. The combiner consists of 20 dipole coils and 40 quadruple coils providing both dipole and quadruple field with rotation frequency is 1.17 MHz. The combiner has been tested up to 650kHz . For higher frequency operation, more R&D has to be carried out. We also can place additional eight more guns. In case one of the guns is in failure, other set of 8 guns could be in operation without stop machine significantly. Figure 2 shows the bunch length and normalized transverse emittance of eight guns beam combining injector. The simulated RMS transverse normalized emittance could achieve 47 mm-mrad, which has met the requirements.

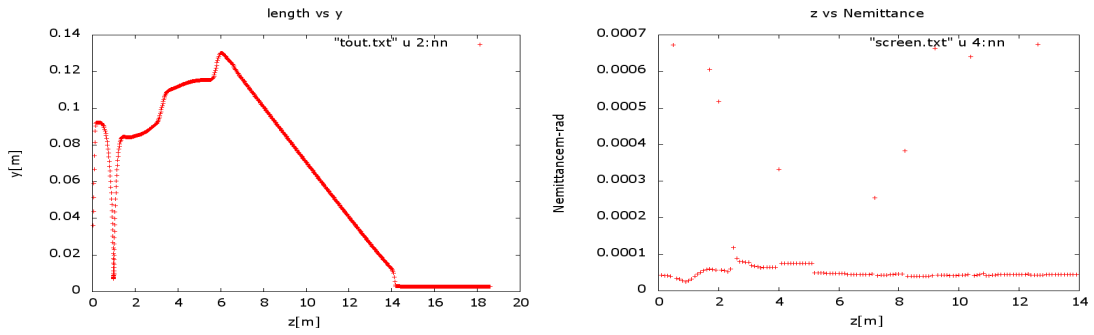

Figure 2. The beam parameters in injector. a) The bunch length as the function is z, finally compressed to 3mm rms. b) the transverse normalized emittnace is 47 mm-mrad at 20 MeV.

Nominal option II: Plate deflector

With an E-field plate deflector, two bunches could be combined in longitudinally. There are two methods to generate transverse deflection electrical field. One is a switch deflector. Another one is a RF deflector. The switch deflector could use PVM-1001 adjustable pulsed voltage source, which could operate at 1-5MHz with 55-10000ns pulse length. It could bend 350 keV beam by 10 degrees. The RF deflector, which is tuned with a resonating inductor and a pair of tunable external capacitors in parallel with the deflection plates, could bend the 350 keV beam

by 15 degrees in maximum. Totally, we need 14 fixed dipoles and 7 deflector combiners to kick all eight beams into the common beamline. The first stage four deflector combiners combine the eight beams into four sets, then into two with other two deflectors at the second stage, finally combine into single beam with the third stage deflector. The RF deflector could provide higher transverse kick gradient while the switch deflector has more uniform field without RF curvature. Figure 3 shows the deflector geometry and the RF deflector circuit parameters. Figure 4 shows the bunch length and normalized transverse emittance of eight guns beam combining injector. The RMS transverse normalized emittance could achieve 57 mm-mrad.

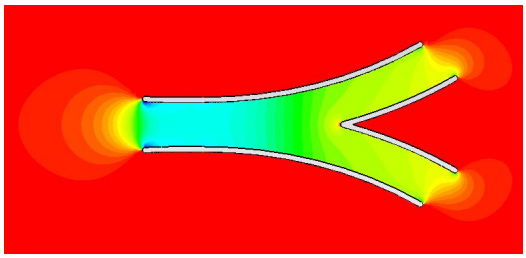

	RF1 - RF4	RF5 - RF6	RF7
Frequency	1.175 MHz	2.35 MHz	4.7 MHz
Gap Volts	9.7kV	9.7kV	9.7kV
Inductance	63 uH	63 uH	63 uH
Capacitance of Plate	17.7 pF	17.7 pF	17.7 pF
Resonance Capacitance	295 pF	73 pF	18.4 pF
Plate Displacement Current	1.27 A	2.55 A	5.1 A
RF Power	344 W	121 W	43 W
Q0	300	423	600

Figure 3 The plate deflector geometry and RF deflector parameters.

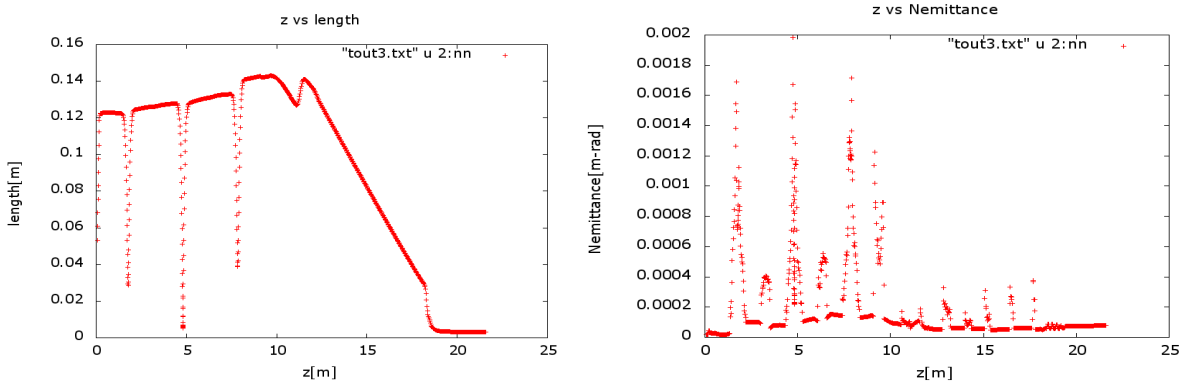

Figure 4 The beam parameters in injector using the pulse switch deflector. a) The bunch length as the function is z, finally compressed to 3.4 mm rms. b) The transverse normalized emittnace is 57 mm-mrad at 20 MeV.

CONCLUSION

The BNL eRHIC L-R version needs a high charge and high current polarized electron source. We have developed three high current beam-combining methods. Two beam combining schemes have been simulated and shown promising. With the results of gun beam test, we will determine which method should be chosen in eRHIC design. We also have designed the large cathode prototype HV inverted gun. The gun recent is in fabrication and will be start to test by the mid of this year. Such high current high bunch charge injector is not only crucial for the eRHIC also will be useful for positron source.

REFERENCES

[1] V. Ptitsyn, in *AIP Conf. Proc.* (American Institute of Physics, 2012), pp. 646–648.

[2] P. A. Adderley, J. Clark, J. Grames, J. Hansknecht, K. Surles-Law, D. Machie, M. Poelker, M. L. Stutzman, and R. Suleiman, Phys. Rev. Spec. Top. - Accel. Beams **13**, 10101 (2010).

[3] I. Ben-Zvi, X. Chang, V. Litvinenko, W. Meng, A. Pikin, and J. Skaritka, Phys. Rev. Spec. Top. - Accel. Beams **14**, 92001 (2011).

[4] E. Wang, I. Ben-Zvi, D. M. Gassner, R. Lambiase, W. Meng, O. Rahman, A. Pikin, T. Rao, B. Sheehy, J. Skaritka, J. Pietz, M. Ackeret, C. Yeckel, R. Miller, E. Dobrin, and K. Thompson, in *6th Int. Part. Accel. Conf. IPAC 2015* (2015).